Novel Integrated Silicon Nanophotonic Structures using Ultra-high *Q* Resonators

A Thesis
Presented to
Academic Faculty

by

Mohammad Soltani

In Partial Fulfillment
of the Requirements for the Degree
Doctor of Philosophy in Electrical and Computer Engineering

School of Electrical and Computer Engineering

Georgia Institute of Technology

December 2009

Novel Integrated Silicon Nanophotonic Structures using Ultra-high *Q* Resonators

Approved by:

Dr. Ali Adibi, Advisor
School of Electrical and Computer Engineering
Georgia Institute of Technology

Dr. Thomas K. Gaylord
School of Electrical and Computer Engineering
Georgia Institute of Technology

Dr. Stephen Ralph
School of Electrical and Computer Engineering
Georgia Institute of Technology

Dr. John Papapolymerou
School of Electrical and Computer Engineering
Georgia Institute of Technology

Dr. Joseph Perry
School of Chemistry and Biochemistry
Georgia Institute of Technology

Date Approved: August 10, 2009

To my wife Leyla and my parents

ACKNOWLEDGMENT

I would like to thank my advisor, Professor Ali Adibi, for his support and encouragement and for giving me the freedom to pursue my academic research. Ali Adibi is one of the smartest people I have ever known. I learned a lot from him. I also thank his family for their warm hospitality.

I would also like to thank Professors Thomas Gaylord, Stephen Ralph, John Papapolymerou, and Joseph Perry for reviewing my thesis and serving on my Ph.D. defense committee.

My research was a very small portion of the beautiful field of electromagnetism, which has a broad scope in science covering DC to gamma rays (and even beyond), from classical to quantum, from non-relativistic to relativistic, all relevant to the known and unknown interactions with matter. I really enjoyed the path I started, which provided a gateway for me to learn many other disciplines of science. During my research, I collaborated with many friends and colleagues, and without their help and vision, this research would not have been accomplished.

I wish to thank Siva Yegnanarayanan, a post-doc member of the group, who joined the group when I started the research on silicon nanophotonics. He has been with me during every step of my research. His vision and expertise in different aspects of photonics and other related disciplines was exemplary. Working with him was one of the best experiences I have had in my research career.

I wish to thank Babak Momeni. Well, what can I say about such an indescribable, humble, and genius person. I have known him for more than 12 years

and I'm still learning and learning from him. He was my colleague, my roommate, my officemate for many years, and the best I can say, he was and is my friend. I learned about many aspects of electromagnetics and photonics from him.

One aspect of my research was the fabrication of ultra-high Q resonators, which required a deep knowledge of nanofabrication. In this regard, I would like to thank Saeed Mohammadi, Murtaza Askari, and Dr. Mohammad Rakhshanderoo for collaborating on developing the steps for the fabrication of the silicon nanophotonic devices. We learned many things from each other and especially from Dr. Rakhshandehroo, who was a great source of knowledge in nanofabrication. Special thanks to Qing Li, who came to the group later and helped me in the fabrication of my devices in the last year of my research. We shared the same office and had many thought-provoking physics discussions from theory to experiment. I envision a bright career for him. I also thank Devin Brown and Raghu Murali for training me in nanolithography. Special thanks to Garry Spinner for managing the MiRC cleanroom and providing all the resources. Also, I would like to thank Pejman Monajemi, Vinh Nguyen, Charlie Suh, and Joel Pikarsky for helping me on different aspects of fabrication and equipment in the cleanroom.

I would like to thank Ali (Reza) Eftekhar, Amir Atabaki, Maysam Chamanzar, and Ehsan Shah-Hosseini for many useful discussions on my research. Special thanks to Reza for participating in many discussions and making valuable suggestions. He built an optical near-field scanning setup, allowing us greater insight into the physics of microresonators.

I would like to thank Omid Momtahan, Arash Karbaschi, Charles Reinke, Saman Jafarpour, and J.D. Huang, who made many contributions to assembling the computation and characterization tools in our labs. Special thanks to Saman for many interesting and productive discussions that we had on different things inside and outside the school. I would also like to express my gratitude to the other group members: Majid Badieirostami, Charles Camp, Pouyan Mohajerani, Payam Alipour, Fengtao Wang, Chaoray Hsieh, Ye Lou, Ali Hashmi, Ali Behrouz, and Reza Pour-Abolghasem.

My photonic research chronology goes back to when I started my M.Sc. studies at Sharif University and joined Prof. Bizhan Rashidian's group. There, I worked with a group of talented people under Bizhan Rashidian's supervision, and they gave me my electromagnetics and photonics foundation. I would like to thank Khashayar Mehrany, Sina Khrasani, and again Babak Momeni who was there also.

During my stay at Georgia Tech, I had the honor of taking courses with many excellent teachers and researchers. I would like to especially thank Thomas Gaylord, Uzi Landman, Brian Kennedy, Rick Trebino, and Michael Pustilnik.

And finally, from bottom of my heart, I would like to thank my parents and my dear wife, Leyla, for all their love, sacrifice, and patience. In the last year of my research, Leyla came to my life. Her love and kindness, her wisdom, and her support were the bright light on the last miles of this journey.

TABLE OF CONTENTS

LIST OF TABLES

Table 8.1: comparison of the parameters of two Si microdisk resonators with radii of 2 μm and 20 μm and with water cladding for the two cases of (a) water loss is absent, and (b) a water loss of ~ 40 dB/cm is present.

LIST OF FIGURES

Fig. 2.6: (a) Spectrum of TWR resonator with two resonances and one FSR is shown. (b) Schematic representation of field enhancement and energy build up in a TWR due to the constructive interference of roundtrips of EM field which results in a steady state resonator field profile as shown in (c).

Fig. 2.7: Different waveguide-based TWR architectures with no circular symmetry. The straight portion of the resonator can enhance its interaction with another waveguide or resonator that is coupled to it along the straight region.

Fig. 2.8: (a) Structure of a 3D Si microring (disk) resonator made of a finite height slab and seated on a substrate and covered by cladding. The outer and inner radii are specified in the figure by R_{out} and R_{in} (R_{in} = 0 for disk). For clarity, on the top-right corner of the figure, the details of the Si slab is shown which is sandwiched between the substrate and cladding and supports a mode with an effective index n_{eff}. (b) Reduced 2D model of the 3D microring (disk) shown in (a).The refractive index of the 2D microring (disk) is n_{eff} calculated for slab shown in (a), and the surrounding has the refractive index of cladding ($n_{cladding}$).

Fig. 2.9: (a) Structure of a Si slab waveguide with a thickness *d* on a SiO_2 substrate. The field components corresponding to TE and TM polarizations are specified in the figure. (b) The dispersion and (c) the effective index of different family modes of the waveguides for both TE and TM are shown. The solid and dashed curves correspond to the cases of air and oxide cladding respectively. For this simulation, refractive indices of Si and SiO2 were 3.475 and 1.444, respectively.

Fig. 2.10: Simulation results for the quasi-TE (H_z) modes of a microdisk resonator with a radius of 10 μm and a thickness of 230 nm, seated on a SiO_2 substrate and covered by air cladding using the effective-index method. Magnetic field (H_z) profile of (a) 1st, (b) 2nd, (c) 3rd, and (d) 4th radial modes along a line in the middle of the disk thickness and in the radial direction. The resonance wavelengths and azimuth number of these field profiles are specified in their figures. (e) Effective indices of the resonance modes for the 1st, 2nd, 3rd, and 4th radial order modes and at different azimuth harmonic numbers *m* as specified in the figure. For this simulation, refractive indices of Si and SiO_2 are 3.475 and 1.444, respectively. The dashed box in (d) is to highlight that in a small wavelength range around 1550 nm, how these four radial modes are located in the spectrum.

Fig. 2.11: (a) Structure of a dielectric microsphere with a refractive index of 3.475 and a radius of 10 μm suspended in air. (b) Cross section of the magnetic field profile of H_z corresponding to TE polarization. (c) Comparison of resonance wavelength of the microsphere for the mode shown in (b) at different azimuth mode numbers *m*.

Fig. 2.12: (a) Cross section of a Si microdisk resonator on an SiO_2 substrate and moderately meshed for FEM analysis. Cross sections of the profiles (b)-(g) all six field components of one of the resonance modes, (h)-(i) electric and magnetic energy densities of the mode, respectively. This mode is 1st radial order TE mode, as u_E has one peak, and electric field is predominantly in-plane (E_z is very small). (j)-(k) Variations of some of the field quantities across a line along the radial direction and passing through the middle of the disk height, e.g. the dash line in (h). For this simulation m= 107, and refractive index of Si and SiO_2 are 3.475 and 1.444, respectively.

Fig. 2.13: (a) Effective indices of 1st, 2nd and 3rd radial quasi-TE modes of a microdisk resonator with a radius of (a) 10 μm and (b) 20 μm, versus wavelength. For both (a) and (b) the microdisk has a thickness of 230 nm and is seated on SiO_2 substrate and covered by air cladding. In (a), the solid and dash curves correspond to effective-index and FEM analysis, respectively, and in (b) all the simulations are based on FEM analysis. In both (a) and (b) the azimuth mode number (m) corresponding to each resonance is shown. Also the effective index of the 1st quasi-TE mode of a waveguide with a width of 500 nm and a thickness of 230 nm is shown in both figures. For this simulation, refractive indices are the same used in Fig. 2.8.

Fig. 2.14: Calculated effective index of the first three radial TE modes of a Si microdisk resonator and the fundamental TE mode of a microring resonator versus their outer diameters, as shown by different markers and colors and specified in the figure. All resonators have a thickness of is 230 nm, and they seated on a SiO_2 substrate and covered by air cladding. The width of the microring is also 500 nm. For both the microdisk and microring, the effective index at the external radius was calculated. The inset shows the cross section of electric energy density for the 1st TE mode of the microring with an external radius of 10 μm, as well as for the 1st, 2nd, and 3rd radial TE modes of a microdisk with a radius of 10 μm. All the simulations were for the resonance wavelength existed in a range of 1550±20 nm.

Fig. 2.15: Calculated effective index of the fundamental quasi-TE mode of a microring resonator versus its external diameter, at two radial distances corresponding to the external radius (solid curve) and the middle of the ring width (dashed curve). For all the simulations the microring has a thickness of 230 nm and a width of 500 nm, and is seated on a SiO_2 substrate and covered by air cladding. The inset shows the cross section of electric energy density profile for the 1st quasi-TE mode of a microring with an external radius of 10 μm (Also the effective indices of this resonator corresponding to the external radius and the middle of the ring are specified by arrows). The red line shows the effective index of the waveguide with a width of 500 nm and a thickness of 230 nm, at the wavelength = 1550 nm. For all the microring simulations the effective index was calculated for one of the

resonance wavelengths (λ_0) which existed in a range of 1550±20 nm (At larger diameters (>40 μm), resonance wavelength λ_0 = 1550±2.5 nm was available for the resonator).

Fig. 2.16: Calculated FSR of the 1st and the 2nd radial quasi-TE modes of a Si microdisk resonator versus its diameter. All the simulations are for resonance wavelengths exist in a range around 1550 nm. The microdisk has a thickness of 230 nm, and is seated on a SiO_2 substrate and covered by air cladding.

Fig. 2.17: (a) Radial distribution of the normalized-to-peak electric energy density u_E of the 1st order radial quasi-TE mode, for Si microdisk resonators with a thickness of 230 nm and different radii R =2 μm, 10 μm, and 20 μm as specified in the figure. The point 0 in the horizontal axis corresponds to the position of edge of the microdisks. All plots are for the variations of u_E across a line in the radial direction and passing through the middle of the microdisk thickness (e.g. see the dash line in Figure 2.12(h)). (b) A zoom view of the variation of the energy at the edge of the microdisk.

Fig. 2.18: Calculated normalized mode volume (V_m /λ_0^3) of the first three radial quasi-TE modes of a Si microdisk resonator, as well as the one for the fundamental quasi-TE mode of a microring resonator versus their outer diameters, as shown by different markers and colors and specified in the figure. Both resonators have their thickness is 230 nm, substrate is SiO_2, and cladding is air. The microring width is 500 nm. For all the simulations the mode volume was calculated for one of the resonance wavelengths (λ_0) existed in a range of 1550±20 nm.

Fig. 2.19: Radial distribution of the normalized magnitude of the radial electric field $|E_r|$ of the 1st and the 2nd order radial TE modes, as specified in the figure, for a Si microdisk resonators with a thickness of 230 nm and a radius of R =1.94 μm. Both cover and substrate are oxide with a refractive index of 1.444, and the refractive index of Si is 3.475. The point 0 in the horizontal axis corresponds to the edge of the microdisks. All plots are across a line, in the radial direction and passing through the middle of the microdisk thickness.

Fig. 2.20: Variation of bulk absorption Q (or Q_b) of a N-doped Si TWR resonator versus (a) free electron density, and (b) resistivity.

Fig. 2.21: (a) Cross section of the structure of and (a) an undercut Si microdisk resonator and (b) a non-undercut Si microdisk resonator in SOI platform. The energy profiles of the 1st radial TE mode inside the resonators are shown.

Fig. 2.22: Variation of the intrinsic radiation Q of a Si microdisk resonator versus its radius. The microdisk has a thickness of 230 nm and its substrate and cladding has

been specified in the figure. The simulation results for three radii 1.53, 2, and 2.47 μm have been shown in the figure. For this simulation the refractive index of Si and oxide were 3.475 and 1.444, respectively. For each resonance the corresponding azimuth mode number (m) and resonance wavelength (λ_0) in nanometer have been specified. Also, the bulk absorption Q of a silicon resonator for a typical resistivity of bigger than 10 Ω-cm has been shown by the gray region.

Fig. 2.23: Calculated intrinsic Q of a Si microdisk resonator with a radius of 2 μm versus its thickness (as shown by red square markers). The simulations were performed for thicknesses of 170, 200, 230, and 260 nm. Also the simulation results for a microdisk with a radius of 5 μm and a thickness of 170 nm is shown (green pentagon markers). For each resonance the corresponding azimuth mode number (m) and resonance wavelength (λ_0) in nanometer have been specified. For all the simulations the cladding and substrate are both oxide. The refractive index of Si and oxide were considered 3.475 and 1.444, respectively. Also, the bulk absorption Q of a silicon resonator for a typical resistivity of bigger than 10 Ω-cm has been shown by the gray region.

Fig. 2.24: Variation of the Q of a TWR versus the thickness of SiO_2 substrate in a SOI platform. The inset shows the cross section of the Si waveguide (that forms the TWR) in a SOI platform. The resonator radius is large enough so that the intrinsic Q of the resonator is limited by the energy leakage to the underneath Si layer. Also, the bulk absorption Q of a silicon resonator for a typical resistivity of bigger than 10 Ω-cm has been shown by the gray region.

Fig. 2.25: Scanning electron microscopy (SEM) image of a Si microdisk resonator that has strong roughness at its sidewall as a result of fabrication imperfection. The microdisk is side-coupled to a Si ridge waveguide.

Fig. 2.26: Cross section of the electric energy of the 1st radial TE mode of a microdonut resonator with internal and external radii 1.2 and 2.5 μm. A thin Si pedestal layer with a thickness of 40 nm is at the interface of the resonator and the underneath oxide substrate. This resonance mode has azimuth mode number m=24, resonance wavelength λ_0 = 1533.045, and Q = 4×10^5. The P-doped and N-doped regions are schematically shown at the proximity of the resonator for the purpose of injecting (removing) free carriers to (from) the resonator. The structure has an oxide cladding. For this simulation, refractive index of Si and oxide were 3.475 and 1.444, respectively.

Fig.3.1: (a) Schematic of waveguide-resonator coupling for a TWR. The structure is excited by a waveguide source S_{in} from left. This source mode couples to the clockwise (CW) mode of the resonator. Interaction of S_{in} and a_{cw} results in the output waveguide amplitude S_{out}. If there is a considerable perturbation in the

resonator, then the counterclockwise (CCW) mode of the resonator can be excited as a result of coupling to the CW mode. The generated CCW mode can couple to the backward waveguide mode and generate a reflection in the waveguide as shown by S_{ref}. When there is no CW-CCW coupling S_{ref} is almost absent.

Fig.3.2: Spectral response of a waveguide-TWR coupling structure. (a) The squared magnitude and (b) the phase of the transmission (T) given by Equation (3.8) for different ratios of Q_0/Q_c as specified in the inset of the figure in (a). (c) The variation of the squared magnitude of T at resonance versus the ratio Q_L/Q_0. The operation regimes of the coupling are specified in (c).

Fig.3.3: Energy of the resonator with (a) the equal quality factors ($Q_{0+}=Q_{0-}$), and (b) unequal quality factors ($Q_{0+}=Q_{0-}$) for the standing-wave modes of the resonator in a waveguide-TWR structure shown in Figures 3.1. The other parameters are specified in the insets of the figures.

Fig.3.4: (a) Squared magnitudes of the transmission ($T = S_{out}/S_{in}$, the blue curves) and the reflection ($R = S_{ref}/S_{in}$, the red curves) and (b) their phases for the equal quality factors ($Q_{0-} = Q_{0+}$, the solid curves), and (b) unequal quality factors ($Q_{0-} = 0.8\ Q_{0+}$, the dash curves) for the standing-wave modes of the resonator in a waveguide-TWR shown in Figure 3.1. The other parameters are specified in the insets of the figures.

Fig.3.5: (a) Squared magnitude and (b) phase response of the transmission of a waveguide-TWR coupling structure when and $Q_c = Q_0$ and under different conditions of Q_{split}/Q_0 as specified by different colors in the figures. The quality factors of the standing-wave modes are $Q_{0+} = Q_{0-} = Q_0$.

Fig.3.6: (a) Squared magnitude and (b) phase response of the transmission of a waveguide-TWR coupling structure under different conditions of Q_{split}/Q_0 and Q_c/Q_0 as designated by different colors in the figures.

Fig.3.7: Spectra of $|T|2$, $|R|2$, and normalized-to-peak of $\omega_0 U/P_{in}$, for (a) $Q_{\text{split}}/Q_0 = 0.25$, and (b) $Q_{\text{split}}/Q_0 = 0.45$, and with Q_c given by Equation (3.43). For the case of $Q_{\text{split}}/Q_0 = 0.45$ as shown in (b), the reflection behaves as singlet.

Fig. 3.8: Spectrum of (a) U, (b) $|T|^2$, (c) phase of T, (d) $|R|^2$, and (e) phase of R, for a waveguide-TWR coupling structure at a fixed $Q_{split}/Q_0 = 0.5$, and at different values of Q_c/Q_0 as specified in the figure. *: $Q_c/Q_0 = 0.6$ corresponds to the condition given by (86) where the doublet peaks of U are maximum. The dashed curve corresponds to the case that structure has no CW-CCW coupling and it is at the critical coupling, i.e. $Q_c = Q_0$.

Fig. 3.17: (a) Calculated Q_c of a the first (o), second (◊), and third (□) radial mode orders of a microdisk resonator for different disk radii, for two cases of pedestal=0 nm (solid curves) and pedestal = 40nm (dash curves). The coupling structure is shown in Figure 3.11 where the ring is replaced by a disk. For this simulation, gap = 150 nm, WW = 500 nm, and H=250 nm. The calculation of Q_c for all resonators was performed at resonance wavelengths ~1550 nm. (b) A table showing the resonance wavelength (λ_0), azimuth mode number (m), waveguide effective index ($n_{eff\text{-}WG}$), and the resonator effective index ($n_{eff\text{-}R}$) for the pedestal structure and for microdisk radii 5 μm, 10 μm, and 20 μm. For each microdisk radius, $n_{eff\text{-}R}$ was calculated at the center of the width of the waveguide when the gap = 150 nm as $n_{eff\text{-}R} = m\lambda_0 / [2\pi(r+gap+WW/2)]$.

Fig. 3.18: Calculated Q_c of the first (*), the second (o), and the third (□) radial mode orders of a microdisk resonator with radius 10 μm in the structure shown in Figure 3.11 where the ring is replaced by a disk. The structure parameters as shown in Figure 3.11 are gap = 150 nm, H=250 nm, pedestal=40 nm, and the waveguide width (WW) is a varying parameter. The calculation of Q_c for all resonators was performed at resonance wavelengths ~1550 nm.

Fig. 3.19: Schematic a waveguide-TWR coupling structure where the waveguide is bent concentric with the resonator to increase the interaction length. If the waveguide mode an the resonator mode are phase-matched then the coupling is enhanced, otherwise, if they are phase-mismatched by increasing the interaction length the coupling may approach zero.

Fig. 3.20: (a) Structure of a racetrack resonator coupled to a waveguide. (b) Detailed structure of the coupling region which is a directional coupler with identical branches. The super-even and super-odd modes of the directional coupler and their propagation constants are shown in the figure.

Fig. 3.21: Structure of a racetrack resonator side coupled to a waveguide. Both waveguide and the resonator have the same waveguiding dimension.

Fig. 3.22: Variation of the normalized Q_c of the waveguide-TWR structure, as shown in Figure 3.20, versus its normalized coupling length $\Delta\beta Z_0$.

Fig. 3.23: Variation of Q_c versus the gap for a coupled waveguide-racetrack structure shown in Figure 3.20. The structure is made of a waveguide with a width of 500 nm and with different pedestal thicknesses as specified in the figure. The cladding is air. The coupling length Z_0 = 5 μm and the bending radius of the racetrack is 6 μm. The simulations are performed for a resonance wavelength ~ 1550 nm.

Fig. 5.4: (a) Transmission spectrum of a Si microdisk resonator with a radius of 20 μm coupled to a ridge waveguide with a width of 550 nm. The measurement is done for the TE polarization. (b) The SEM picture of the structure. The gap between the waveguide and the resonator is 220 nm. (c) An ultra-high Q=2.0×10^6 was observed at λ=1520.188 nm. From the simulation results, this resonance wavelength corresponds to a 2nd radial order mode with azimuth number m=218 and a free spectral range (FSR) of 5.1 nm. The mode order and FSR are found by comparing the experimental results with the theoretical simulation (which agree with the experimental data). (d) Observation of resonance mode splitting at resonance wavelength λ=1533.642 nm for one of the microdisk modes [63].

Fig. 5.5: (a) SEM cross section of the pedestal type structure captured at a sample tilt angle of 30^o. The microdisk radius and thickness are ~ 20 μm and ~ 225 nm, respectively, and the thickness of the shallow pedestal layer is ~ 60 nm. (b) Spectrum of the pedestal microdisk resonator coupled to a waveguide for the TE polarization. (c) Spectrum of the 2nd order radial mode; mode-splitting due to the coupling of CW and CCW is observed. The theoretical Lorentzian spectrum, which is shown as the solid red curve in (c), resulted in unloaded Q's in agreement with the experimental Q's. The disk radius and the input/output coupling waveguide are identical to the conventional microdisk shown in Figure 5.4 [63].

Fig. 5.6: (a) Scanning electron micrograph of a microdisk resonator with a radius of 20 μm coupled to a waveguide with a width of 540 nm. The gap between the waveguide and the resonator is 140 nm and the structure is seated on a 48±2 nm silicon pedestal layer. (b) Transmission spectrum of the structure [85, 86].

Fig. 5.7: Detailed observation of the spectrum of the microdisk shown in Fig. 5.6(b). (a) A zoomed portion of the spectrum containing four resonance modes belonging to four different radial mode orders. These modes are labeled by letters **A**, **B**, **C**, and **D**. The insets in (a) show the details of resonances **B** and **C**. Fabry-Perot fringes resulting from the waveguide facets are observed in the figure. (b) Spectrum of the same four modes at one FSR away from the ones shown in (a). The modes in (b) have their azimuth mode number one less than the modes in (a). The measured FSRs for **A**, **B**, **C**, and **D** are 5.151, 5.149, 5.205, and 5.332 nm, respectively. The insets in (b) show the details of resonances **A**, **B**, and **C**.

Fig. 5.8: Spectrum of the four resonance modes at one wavelength FSR lower from their corresponding ones shown in Fig. 5.7(a). The inset shows the zoomed view of mode B which shows a doublet as a result of resonance splitting.

Fig. 5.9: (a) The measured versus the fitted data for the transmission response of one of the ultra-high Q modes of the microdisk resonator shown in Fig. 5.6(a). This mode is the mode B in Fig. 5.7(b). (b) A zoomed view of Fig. 5.9(a) with the fitted data given in the inset of the figure. The power extinction of this mode is ~18 dB.

(c) Simultaneous plot of the fitted resonator energy transmission response of the resonator mode.

Fig. 5.10: (a) Scanning electron micrograph of a racetrack with an inner bend radius of 7.75 μm and width of 500 nm and a straight length of 24 μm coupled to an external waveguide with a width of 500 nm. The gap between the waveguide and the racetrack is 300 nm. The overall height of the waveguide is H=235 nm. (b) Transmission spectrum of the resonator coupling structure. (c) The zoomed view of one of the resonance modes. Strong Fabry-Perot fringes of the external waveguide are clearly observed in the spectrum in (b) [85, 86].

Fig. 5.11: The cross sections of the simulated electric energy distributions of (a) the 1^{st} and (b) the 2^{nd} radial order mode of a silicon microdisk resonator with a radius of 1.4 μm and a thickness of 200 nm. The resonance wavelengths of the modes are around 1550 nm, and the corresponding azimuth mode numbers are 11 and 8 for the 1^{st} mode and the 2^{nd} mode, respectively. The polarization considered is TE (electric field is predominantly in the plane of the disk).

Fig. 5.12: (a) SEM image of a microdisk resonator with a radius of 1.53 μm coupled to a waveguide with a width of 400 nm. The gap between the waveguide and the resonator is ~ 210 nm. The thickness of the Si microdisk is 230 nm and there is a thin HSQ layer with a thickness of ~ 60 nm on top of the microdisk and the waveguide. (b) Transmission spectrum of the resonator showing the 1^{st} radial order TE mode. (c) Detailed resonance spectrum of the 1^{st} radial mode of this resonator which shows a resonance splitting. By fitting the theory to the experiment, the intrinsic Qs ≈ 110,000 and 88,000 were obtained for the two standing-wave modes. The value of the coupling Q ~ 99,000 in the fitted data is closed to the calculated value from the coupled mode theory. The azimuth harmonic mode of this mode is m=12 and its mode volume is ~ $0.15\ (\lambda_0)^3 = 6.3\ (\lambda_0/n)^3$ with n = 3.475 [50, 87, 88].

Fig. 5.13: (a) Left: Schematic of an array of 32 resonators side-coupled to a waveguide. Right: The SEM image of one of the resonators in the left structure. The structure has oxide- cladding. An inner hole with a radius of 0.6 μm has been perforated at the disk center. The external radius of the resonators in the array is distributed in the range of 1.92 μm to 2 μm. (b) The resonance spectrum of the structure shown in (a) in the left [88].

Fig. 5.14: (a) and (b) show the details of two of the resonance features in Figure 5.13(c), respectively. These resonances belong to two different resonators in the array shown in Figure 5.13(a). In (a), the resonance splitting with a doublet in the transmission is observed. In (b) resonance splitting has resulted in the flattening of the transmission. Strong Fabry-Perot fringes of the waveguide with a period of ~ 31

pm is observed. (b) By fitting theory and experiment in (b) intrinsic Qs of ~ 82,500 and 75,000 were obtained for the standing-wave modes of the resonator [88].

Fig. 5.15: (a) and (b) show the details of two of the resonance features in Fig. 5.13(c), respectively. These resonances belong to two different resonators in the array shown in Fig. 5.13(a). In (a) a weak doublet and in (b) a singlet is observed. In both (a) and (b) the resonance spectrum of the resonator has been loaded by Fabry-Perot fringes of the waveguide.

Fig. 5.16: The SEM image of a miniaturized add-drop filter. The waveguide width and thickness are 400 *nm* and 230 *nm*, respectively. The employed microdisk resonator has a radius of r = 1.97 μm with an inner hole with a radius of r = 0.6 μm perforated at its center. The gap between the waveguide and the resonator is 240 *nm*. (b) Transmission spectrum of the drop port of the filter showing the two resonances belonging to the 1st order radial family modes with azimuth mode numbers specified in the figure [50, 87, 88].

Fig. 5.17**:** (a) A schematic drawing of an array of add-drop resonator filters suitable for in-plane spectral analysis and signal processing. The radius of the resonators varies from 1.92 μm to 1.97 μm with a radial step change of 10 nm. (b) The SEM image of one of the fabricated resonators in the array which has a radius of 1.97 μm. The structure is covered with an oxide cladding. (c) Measured transmission of the drop ports of the array shown in (a). The FSR is ~57 nm and the spectral linewidth was designed to be in the range of 50 to 100 pm [88].

Fig. 5.18: (a) SEM image of an array of 90 microdonut resonators coupled to one bus waveguide (a ridge waveguide with a width of 400 nm). (b) A zoomed view of the structure in (a). (c) Transmission spectrum of the structure. The resonance spectrum at the very right end and the one at the very left end belong to one of the resonators and the spacing between these two resonances is the FSR of that resonator [88].

Fig. 5.19: (a) SEM image of a pedestal microdonut resonator with the internal and external radii of 1.3 μm and 1.5 μm, respectively, coupled to a waveguide with a width of 400 nm. The gap between the waveguide and the resonator is 250 nm. The thickness of the pedestal layer is 33 nm and the overall height of the Si device layer is 216 nm. (b) Transmission spectrum of the resonator shows large extinctions for three resonances belonging to the 1st order radial mode and with different azimuth mode numbers as specified in the figure. (c) A zoomed view of one of the resonance modes [88].

Fig. 6.1: (a) Schematic of the electronic band diagram of Si showing all the absorption and generation mechanisms of photons, phonons and electrons. The TPA process absorbs photons (which results in TPA loss and degrades the Q) and

stimulates the electrons from the valence band and sends them to the higher unstable states. The phonons interplay to send the electrons from the unstable states into the stable conduction band. The generated electrons decrease the refractive index (which results in a resonance blue-shift), adds free-carrier absorption loss (which degrades the Q). The generated loss heats the resonator (which results in a resonance red-shift). (b) A conceptual visualization of processes happens during the circulation of photon in a resonator. (c) A qualitative description of the change of resonance spectrum from the low-power regime (solid curve) to high-power regime (dash curve).

Fig. 6.2: (a) Diagram of the setup used for monitoring the time domain and spectral domain response of the resonator. The SEM image of the measured microdisk is shown in the setup. The microdisk has a radius of 20 μm and a thickness of 230 nm, on a SiO_2 substrate and covered by air.

Fig. 6.3: (a) The resonance spectrum of one of the modes of a Si microdisk close to critical coupling regime for different values of the input optical power as specified in the figure by different colors. For this measurement, the laser wavelength has been swept from the short to the long wavelengths. By increasing the power, resonance linewidth broadening as well as temporal oscillations have appeared in the spectrum. By fixing the laser wavelength at any point in the oscillation regions temporal oscillations in the amplitude of the resonator is observed. Increasing the power has increased the wavelength range that temporal oscillations can occur. (b) Observation of the temporal oscillations in the transmission response of the resonator when the input laser is CW with a fixed wavelength. The microdisk has a radius of 20μm and thickness ~ 230nm coupled to a waveguide with a width of 550 nm. The unloaded Q of this resonance mode is Q_0~1.2x10^6 [96].

Fig. 6.4: (a) Normalized transmission, (b) resonator energy, and (c) Relative resonance shift (with respect to the initial resonance) of a waveguide-TWR structure versus the relative input laser wavelength (with respect to the initial resonance wavelength) in the critical coupling regime ($Q_c = Q_{R0}$) and at different levels of input optical power as shown by different colors. In the red curve depending on sweeping the laser from left to right or vise versa one of the edges of the bi-stability region as shown by the red dash lines is observed.

Fig. 6.5: The threshold (red curve) to observe bistable behavior in the spectrum. No bistable behavior is observed in the shaded region.

Fig. 6.6: The energy spectrum of a Si microdisk resonator (coupled to a waveguide) for an input power of P_{in} = 0.6 mW and at different FC lifetimes, as specified in the figures. The resonator cold Q (i.e. Q_{R0}) is assumed $Q_{R0} = 2\times10^6$, and the structure operates at the critical coupling regime ($Q_c = Q_{R0}$). The other parameters are $K_{eff} = 9.6\times10^{-4}$ and $V_m = 4.5\ (\lambda_0)^3$. These last two parameters correspond to the

fundamental mode of a microdisk in a SOI platform with a BOX thickness of 1 μm. The microdisk has a radius of 20 μm and a thickness of 250 nm, and its cladding is air. In these plots, λ_{R0} is the resonance wavelength of the cold resonator and λ_p is the wavelength of the input power. The arrows in (b) correspond to the allowed directions of moving on the spectrum curve when the laser source is swept from the short wavelength to long wavelength or vice versa.

Fig. 6.7: The normalized transmission spectrum of a Si microdisk resonator (coupled to a waveguide) at different FC lifetimes (τ_{FC}) as specified in the figures. In the figures λ_{R0} is the resonance wavelength of the cold resonator and λ_p is the wavelength of the input power. Other parameters have been described and specified in the caption of Figure 6.6. The dashed curve in the top-left plot is the transmission at low powers where the TPA, FCA, and thermal effects are absent.

Fig. 6.8: The resonance wavelength shift of a Si microdisk resonator (coupled to a waveguide) at different FC lifetimes (τ_{FC}) as specified in the figures. In the figures λ_{R0} is the resonance wavelength of the cold resonator and λ_p is the wavelength of the input power. Other parameters have been described and specified in the caption of Figure 6.6. The dashed curve in the top-left figure is the transmission at low powers where the TPA, FCA, and thermal effects are absent.

Fig. 6.9: The total quality factor (Q_R) of a Si microdisk resonator (coupled to a waveguide) at different FC lifetimes (τ_{FC}) as specified in the figures. In the figures λ_{R0} is the resonance wavelength of the cold resonator, and λ_p is the wavelength of the input power. Other parameters have been described and specified in the caption of Figure 6.6. The dashed curve in the top-left figure is the transmission at low powers where the TPA, FCA, and thermal effects are absent.

Fig. 6.10: The energy (left figures) and the normalized transmission (right figures) spectra of a Si microdisk resonator (coupled to a waveguide) at different input powers as specified in the left figures. For this simulation we assumed $Q_{R0} = 2\times10^6$ and the FC lifetime τ_{fc} = 1 ns, $K_{eff} = 9.6\times10^{-4}$ and $V_m = 4.5\ (\lambda_0)^3$. The last two parameters correspond to the fundamental mode of a microdisk with a radius of 20 μm and a thickness of 250 nm with air cladding in a SOI platform with a BOX thickness of 1 μm.

Fig. 6.11: Effect of resonator scaling on the spectral response of the resonator. (a) Energy and (b) transmission spectrum of a Si microdisk resonator with two different sets of parameters as plotted by red and green colors. These parameters are specified in the inset of (b). The given parameters for the red curve and the green curve correspond to the microdisks with a thickness of 250 nm and radii of 20 μm and 1.53 μm, respectively, and with air cladding. The thickness of the BOX layer is 1

μm. (and for this thickness K_{eff} has been calculated). The dash blue curve in (b) corresponds to the low power transmission spectrum [97].

Fig. 6.12: Experimental measurement of the resonance transmission spectrum at low powers (the solid green curve) and at high powers are shown, when the input laser wavelength is swept from the left to the right (the dot blue curve) and from the right to the left (the dot red curves) side of the resonance wavelength. Strong FC-TPA-thermal oscillations as well as resonance broadening are observed in both sweeping direction at the high power measurement. The microdisk has a radius of 20 μm and a thickness of ~ 230 nm, and it has a thin Si pedestal layer with a thickness ~ 40 nm. The thickness of the BOX layer is 1μm. The effective thermal conductivity of this resonator is $K_{eff} \sim 9.6\times10^{-4}$. See the text for more information on the input powers [97,98].

Fig. 6.13: (a) Experimental measurement of the resonance transmission spectrum at low powers (the dash red curve), and at high powers (the solid blue curve). The laser wavelength is swept from the left to the right side of the resonance wavelength. FC-TPA-thermal oscillations as well as resonance broadening are observed at high powers. (b) Repeating the experiment for another resonance mode of the microdisk. The microdisk structure has the same specifications as the one described in Figure 6.12.

Fig. 6.14: Experimental measurement of the resonance transmission spectrum at low powers (the red curve), and at high powers (the blue curve). The laser wavelength is swept from the left to the right side of the resonance wavelength. At low powers the spectrum shows resonance splitting with a flattening at he bottom of the transmission. Strong FC-TPA-thermal oscillations as well as resonance broadening are observed at the high power. The microdisk structure has the same specifications as the one described in Figure 6.12 with the only difference that the BOX thickness is 3 μm and the pedestal thickness is ~ 50 nm.

Figure 6.15: (a) Transmission response, (b) resonance wavelength change, (c) Temperature change, and (d) free-carrier response of a microdisk resonator coupled to a waveguide. (e) A zoomed view of the transmission response shown in (a) around t ~ 2.04 μs. For this simulation the input power is P_{in} = 3 mW, the microdisk intrinsic $Q_{R0} = 3\times10^6$, the mode volume is $V_m = 4.5\ (\lambda_0)^3$, the thermal lifetime τ_{Th} = 500 ns, the FC lifetime τ_{FC} = 0.6 ns, and the resonator works in the critical coupling regime ($Q_c = Q_{R0}$). The laser wavelength is detuned from the original resonance wavelength of the resonator as with an amount of $\delta\lambda = \lambda_0/Q_0$ where λ_0 is the resonance wavelength.

Figure 6.16: Transmission response of a microdisk resonator with an input power P_{in} = 1 mW, calculated with two different FC lifetimes of τ_{FC} = 0.5 ns (left figures), and 1 ns (right figures), and at different detuning ($\delta\lambda$) of the laser wavelength from the

original resonance wavelength of the resonator as specified at the corner of the figures. The inset in (e) shows a damped fast oscillation. Microdisk has an intrinsic $Q_0 = 4\times10^6$, a thermal lifetime τ_{Th} = 600 ns, and it works in the critical coupling regime ($Q_c = Q_{R0}$).

Figure 6.17: Left figure: Transmission response of a microdisk resonator with three different input powers of P_{in} =0.5 mW, 1mW, and 2 mW. The inset in (e) shows a damped fast oscillation. The right figures are the zoomed views of the regions in the left figures as specified. Microdisk has an intrinsic $Q_0 = 4\times10^6$, a thermal lifetime τ_{Th} = 600 ns, τ_{FC} = 1 ns, and it works in the critical coupling regime ($Q_c = Q_0$). The laser wavelength is detuned from the original resonance wavelength of the resonator as with an amount of $\delta\lambda = 0.5\ \lambda_0/Q_0$ where λ_0 is the resonance wavelength.

Figure 6.18: (a) Transmission response, (b) resonance wavelength change, (c) Temperature change, and (d) free-carrier response of a microdisk resonator with an input power of P_{in} =2 mW. Microdisk has an intrinsic $Q_0 = 4\times10^6$, $V_m = 4.5\ (\lambda_0)^3$, a thermal lifetime τ_{Th} = 500 ns, τ_{FC} = 1 ns, and it works in the critical coupling regime ($Q_c = Q_0$). The effective thermo-optics coefficient of the resonator is one third of that silicon [98].

Fig. 6.19: Experimental results for temporal oscillations of a microdisk resonator. (a) Observation of simultaneous steady-state slow (MHz) and long-sustained fast (GHz) oscillations. (b) A zoomed view of the fast oscillations which has a frequency of 0.52-0.54 GHz. The oscillation is sustained for over 110 periods. (c) Observation of simultaneous steady-state slow (MHz) and damped fast (GHz) oscillations. Bottom: A zoomed view of the damped GHz oscillations in the specified zone. The transmission spectrum and the parameters of this microdisk are given in Figure 6.12 [98].

Figure 6.20: Spectrum of the time-domain measured data shown in Figure 6.18(a). The insets show more details of the spectrum. The left inset shows the spectral components of the slow oscillations shown in Figure 6.18(a), and the right inset shows the spectrum of the fast oscillations. The 3 dB linewidth of the fast oscillations spectrum is 10 MHz [98].

Figure 6.21: Temporal dynamic response of an ultra-high Q microdisk resonator at three laser wavelengths of (a) 1530.447, (b) 1530.457, and (c) 1530.467 detuned from the microdisk cold resonance wavelength. The right figures show the zoomed views of the fast oscillations regions specified in the left figures. The linear spectrum of this microdisk is shown in Figure 6.12 [98].

Fig. 7.1: (a) Schematic of a chain of coupled-resonator structure made of identical traveling-wave resonators and side-coupled to two waveguides at the both ends of

the chain. The simulation of the normalized transmissions response at (b) the drop port and (c) the through port versus the normalized frequency, for the case that the structure consists of six resonators periodically arranged with a resonator-resonator coupling coefficient μ. Strong Fabry-Perot fringes are observed in the response. The coupling lifetime between the waveguides and their adjacent resonators is $\tau_c = 0.27 / \mu$. The resonance frequency of the resonators is ω_0. The resonators have been assumed to have no loss (infinite Q).

Fig. 7.2: (a) Structure of a finite-size CROW with the detailed parameters specified. a_i is the amplitude of the i^{th} resonator normalized such that $|a_i|^2$ represent the energy of the resonator. μi is the coupling coefficient between the resonators with indices i and i+1. τ_{in} and τ_{out} are the coupling lifetimes between the input and the output waveguides and their adjacent resonators. S_{in}, S_{Th}, and S_D are the waveguide amplitude at the input port, through port and the drop port, normalized such that their squared amplitudes represent the power. (b) Structure of an LC circuit ends by to resonators.

Fig. 7.3: Variation of the coupling coefficients between the resonators in a finite-size Butterworth-response CROW made of N=4, 8, 12, 18 and 18 resonators as plotted by different curves. The horizontal axis is the index of the coupling coefficients which varies from 1 to N-1.

Fig. 7.4: (a) Transmission, (b) normalized phase ($\phi/2\pi N$), and (c) normalized group delay $\tau_d /(N \tau_c)$ of the drop port for a finite–size CROW with the Butterworth design parameters. Solid and dash curves are for CROWs with N=7 and N=16 number of resonators respectively. The resonance frequency of the resonators is ω_0. (d) Normalized 3dB bandwidth ($\tau_c \Delta\omega^{3dB}$) of the CROW for different number of resonators for the Butterworth design.

Fig. 7.5: Energy spectrum of the resonators (a_n^2) (scaled with $2/\tau_c$) for a Butterworth CROW with $N = 7$ resonators. The arrow in the figures shows the direction of increasing the resonator index number. The input power from the bus waveguide is unity. The last resonator has the same spectrum as the output power in the drop waveguide.

Fig. 7.6: Transmission responses of the drop port (solid curves) and the through port (dash curve) for a CROW structure made of (a) N=2 resonators, and (b) N=6 resonators. The simulation has been performed for τ_0/τ_c = [10, 20, 40] as plotted by the colors green, red, and blue, respectively. The insets in the figures show the zoomed views of the regions specified in the figure. The coupling coefficients of the CROW have been obtained from Equation (7.4).

Fig. 7.7: The phase response of the transmission at the drop port for a CROW structures made of N = 2 and N = 6 resonators and described in Fig. 7.6. The simulation has been performed for τ_0/τ_c = [10, 20, 40] as plotted by the colors green, red, and blue, respectively. The insets in the figures show the zoomed views of the regions specified in the figure.

Fig. 7.8: (a) Transmission responses of the drop port (solid curves) and the through port (dash curve) and (b) the phase response of the transmission at the drop port for a CROW structure made of N = 2 resonators and with τ_0/τ_c = 20, for the cases that the coupling lifetimes at the input (τ_{in}) and at the output (τ_{out}) ports are imbalanced. The simulations have performed for the cases of τ_{out}= τ_c and τ_{in} = [0.8, 1, 1.2] as plotted by different colors of green, red, and blue, respectively. The inset in (a) show a zoomed view of the regions specified in the figure. The coupling coefficients of the CROW have been obtained from Equation (7.4).

Fig. 7.9: (a) Transmission responses of the drop port (solid curves) and the through port (dash curve) and (b) the phase response of the transmission at the drop port for a CROW structure made of N = 2 resonators and with τ_0/τ_c = 20, for the cases that the coupling coefficient (μ) between the two resonators deviates from its original value. The simulations have performed for the three new coupling coefficients as μ' = [0.8μ, 1 μ, 1.2 μ] which are plotted by different colors of green, red, and blue, respectively. The inset in (a) show a zoomed view of the regions specified in the figure. The original coupling coefficient has been obtained from Equation (7.4).

Fig. 7.10: (a) Transmission responses of the drop port (solid curves) and the through port (dash curve) and (b) the phase response of the transmission at the drop port for a CROW structure made of N=2 resonators and with τ_0/τ_c = 20, for the cases that the resonance frequency of the bottom resonator (close to the input waveguide) has been deviated from its original value (ω_0). The amount shifts are $\Delta\omega_0$ = [-1, -0.5, 0]/τ_c which are plotted by different colors of green, red, and blue, respectively. The inset in (a) show a zoomed view of the regions specified in the figure. The original coupling coefficient has been obtained from Equation (7.4).

Fig. 7.11: Transmission responses of (a) the drop port and (b) the through port of a CROW structure made of N = 4 resonators and with τ_0/τ_c = 20, for the cases the three following cases: 1) the resonance frequency of the all the resonators are the same as ω_0 (the blue curves), 2) only the resonance frequency of the 1st resonator (close to the input waveguide) has been deviated an amount of $1/\tau_c$ (the red curves), 3) only the resonance frequency of the 2nd 1st resonator (close to the input waveguide) has been deviated an amount of $1/\tau_c$ (the green curves). The coupling coefficient has been obtained from Equation (7.4).

is 1μm. (b) The normalized peak temperature of the non-undercut microdisk resonator versus *d* which is the distance between the disk edge and the surrounding silicon layer. The simulation has been performed for air and oxide cladding materials and for two pedestal thickness of zero and 50 nm (as specified in the figure). The temperatures in (b) are normalized to the peak temperature of the undercut microdisk. The undercut microdisk has the same radius and thickness as the non-undercut microdisk. It is seated on a SiO_2 micropost with a radius of 17 μm and a height of 1 μm. For these simulations, the thermal conductivities of Si, SiO_2 and air were 163, 1.38, and 0.02 ($WK^{-1}m^{-1}$).

Fig. G.3: Effective thermal conductance of a microdisk resonator versus its radius. It has been calculated by dividing the total absorbed power (which is one) to the maximum temperature rise. The simulations have been performed for three cases: The BOX (oxide substrate) thickness is 2 μm (the stars), the BOX thickness is 1 μm (the diamonds), the BOX thickness is 1 mm and a Si pedestal layer with a thickness of 50 nm exists. The thickness of the Si microdisk in all the simulations is 250 nm. Cross sections of (b) the electric mode energy and (c) the temperature distribution resulting from heat generated by the mode energy in (b) for a microdisk with a radius of 2.5 μm.

LIST OF ABBREVIATIONS

1D	One Dimensional
2D	Two Dimensional
3D	Three Dimensional
BOE	Buffered Oxide Etchant
CW	Clockwise
CCW	Counterclockwise
DAQ	Data Acquisition
EBL	Electron Beam Lithography
EM	Electromagnetic
FC	Free-Carrier
FCA	Free-Carrier Absorption
FDTD	Finite-Difference Time-Domain
FEM	Finite-Elements Methods
FSR	Free-Spectral-Range
GRIN	Graded Refractive Index
HSQ	Hydrogen Silsequioxane
ICP	Inductively-Coupled Plasma
IR	Infrared
LPCVD	Low-Pressure Chemical Vapor Deposition
MEMS	Micro-Electro-Mechanical Systems

OPO	Optical Parametric Oscillation
PECVD	Plasma-Enhanced Chemical Vapor Deposition
PDMS	Polydimethylsiloxane
PML	Perfectly Matched Layer
QED	Quantum Electrodynamics
SEM	Scanning Electron Microscopy
SM	Single Mode
SWR	Standing-Wave Resonator
SOI	Silicon-On-Insulator
TE	Transverse Electric
TIR	Total Internal Reflection
TM	Transverse Magnetic
TPA	Two-Photon Absorption
TWR	Traveling-Wave Resonator
UV	Ultra Violet
WDM	Wavelength Division Multiplexing
WGM	Whispering Gallery Mode

SUMMARY

Optical traveling-wave resonator architectures have shown promise for the realization of many compact photonic functionalities in different research disciplines. Realizing these resonator structures in high-index contrast silicon enables dense and large scale integration of large arrays of functionalized resonators in a CMOS-compatible technology platform. Based on these motivations, the main focus of this Ph.D. research has been on the device physics, modeling, implementations, and applications of planar ultra-high Q silicon traveling-wave microresonators in a silicon-on-insulator (SOI) platform. Microdisk, microring, and racetrack resonators are the three general traveling-wave resonator architectures of interests that I have investigated in this thesis, with greater emphasis on microdisks. I have developed efficient tools for the accurate modeling of these resonators. The coupling to these resonators has been through a nano-waveguide side coupled to them. For this purpose, I have developed a systematic method for engineering a waveguide-resonator structure for optimum coupling. I have addressed the development of nanofabrication techniques for these resonators with efficient interaction with a nano-waveguide and fully compatible with active electronic integration. The outcome of the theoretical design, fabrication, and characterization of these resonators is a world-record ultra-high Q (3×10^6) with optimum waveguide-resonator interaction. I have investigated the scaling of these resonators toward the ultimate miniaturization and its impact on different physical properties of the resonators. As a result of these investigations, I have demonstrated miniaturized Si

microdisk resonators with radii of ~ 1.5 μm and Q > 10^5 with single-mode operation over the entire large free-spectral range. This is the highest Q (~ one order more than that in previously reported data) that has been obtained for a Si microdisk resonator with this size on a SiO_2 substrate. I have employed these resonators for more advanced functionalities such as large-scale integration of resonators for spectroscopic and filtering applications, as well as the design of flat-band coupled-resonator filter structures. By proposing a systematic method of design, I have shown ultra-compact coupled-resonator filters with bandwidths ranging from 0.4 to 1 nm. I have theoretically and experimentally investigated the performance of ultra-high Q resonators at high powers and in the presence of nonlinearities. At high powers, the presence of two-photon absorption, free-carrier generation, and thermo-optic properties of silicon results in a rich dynamic in the response of the resonator. In both theory and experiment, I have predicted and demonstrated self-sustained GHz oscillation on the amplitude of an ultra-high Q resonator pumped with a continuous-wave laser.

CHAPTER I

INTRODUCTION

Trends toward the integration of silicon-based nanophotonics and microelectronics devices have made much progress during recent years [1-8]. One major driving force behind these trends is the prospect of improved communication and information processing technologies. The MIT Microphotonics Roadmap [9] has suggested that the switch from electronic to photonic technology typically occurs around 10 GHz/m. Figure 1.1 compares a number of application domains and their associated technologies where we see the transition point for the migration from electronics to photonics. As an example in this figure, the bus technologies used on the computer backplane and also in display videos are the areas that could benefit most from improved performance from a transition to photonic links. Among several material platforms for realizing such photonic functionalities, silicon photonics, and its compatibility with CMOS technology, is a potential platform for enabling several of these emerging applications.

While the field of silicon photonics originated in the 1980s [1], the technological advances achieved in recent years have spurred a renaissance in this field. The large refractive index of silicon (Si) and its low material absorption at telecommunication wavelengths have enabled the realization of a variety of optical functionalities in micron and submicron scales. The compatibility of Si photonic devices with silicon-on-insulator (SOI) CMOS fabrication has enabled monolithic integration with active

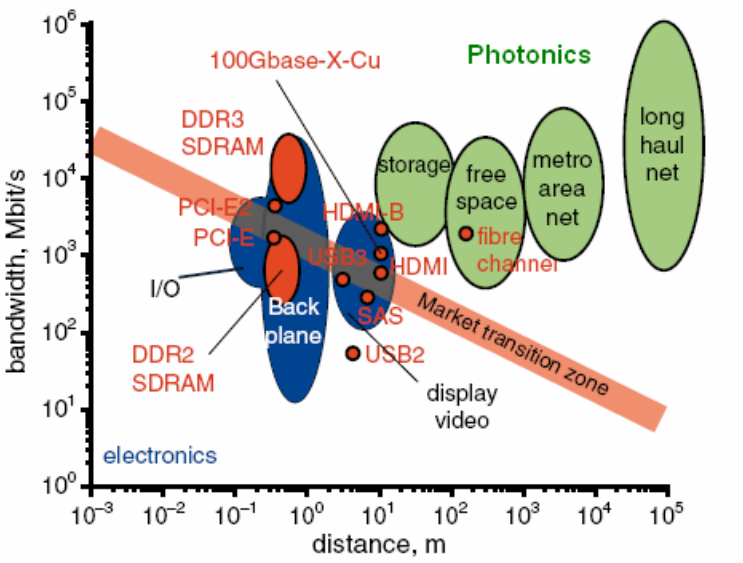

Fig.1.1: Comparison of bandwidth against distance for different technologies [9].

devices (e.g., MOS transistor, p-n junctions, SiGe detectors) in a low-cost, mass-manufacturable (I don't think this is a real word) platform [7,8,10]. In particular, recent advances include the demonstration of high-speed optical modulators [7,10-16], Raman lasers [17,18], WDM filters and buffers [19,22], photodetectors [7,23], and wavelength conversion [24,25]. In addition, in other disciplines such as on-chip sensing [26,27], optofluidics [28,29], and optomechanics [30], silicon photonics has demonstrated its unique properties.

In most of the pursued research, a key building block for compact and large-scale integration of photonics functionalities is an optical microresonator [31, 32]. The key features of an optical microresonator are the localization and storage of electromagnetic energy, both spatially and temporally, at a particular wavelength, within a micron or submicron length scale, and for a considerably long time

Table 1.1: A summary of applications of resonators and the figures of merit related to the resonator parameters.

Bio-chemical sensing	**Finesse (sensitivity)**	$F \sim Q/V$
Nonlinear optics	**OPO threshold**	$P_{NL} \sim V/Q^2$
Cavity QED	**Purcell-factor**	$Fp \sim Q/V$
Analog signal processing and filtering	**Loss**	$1/Q$

compared to the photon time period. The spatial confinement is typically quantified by the mode volume (V), whereas the temporal confinement is described by the quality factor (Q). These two parameters are respectively related to the electric field enhancement and the photon lifetime in the resonators. Table 1.1 summarizes the impact of Q and V for some applications of interest. The implemention of these resonators in a high refractive index contrast and low-loss SOI platform make them ideal candidates for many applications that require chip-scale integration and compact sizes.

In general, optical resonators can be grouped into two broad classes, namely, standing-wave resonators (SWR) and traveling-wave resonators (TWR), as shown schematically in Figures 1.2(a) and 1.2(b), respectively. In a dielectric SWR, the electromagnetic (EM) wave, by bouncing between the two dielectric mirrors, is trapped inside the resonator. In a dielectric TWR structure, the EM wave, by propagating in a roundtrip, is trapped inside the resonator. Examples of SWR-type structures are photonic crystal defects [33-35], and examples of TWR structures are

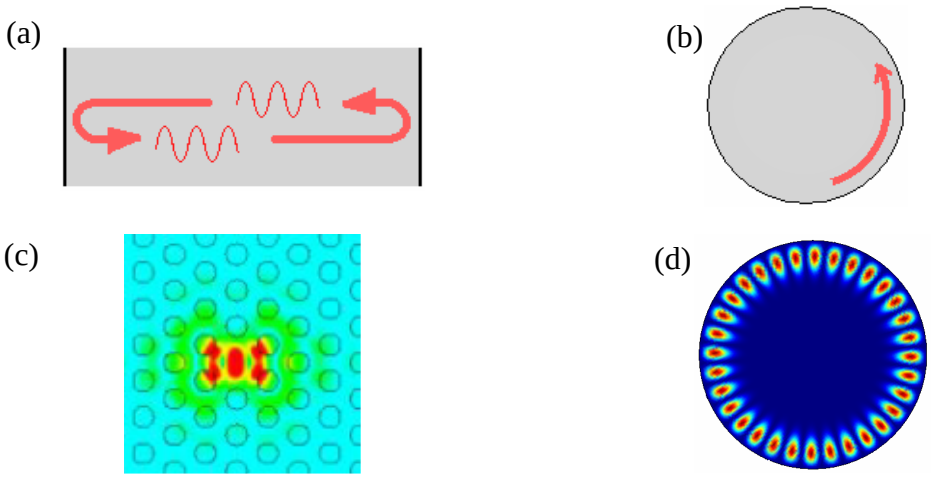

Fig. 1.2: (a) Schematic structure of a SWR in which light at the resonance wavelength is trapped and a standing-wave pattern is formed inside the structure. (b) Structure of TWR in which light is trapped in a roundtrip path. (c) Schematic structure and mode profile of a photonic crystal defect resonator as a SWR example in which light is confined by the Bragg mirrors. The photonic crystal in (c) has been made by the periodic perforation of air holes in silicon. (d) Schematic structure and mode profile of a microdisk resonator as a TWR example in which light does the roundtrip in the vicinity of the resonator perimeter and it is confined by total internal reflection (TIR) from the boundaries.

microring [12], microdisk [14], and micro-racetrack resonators [19]. Figures 1.2(c) and 1.2(d) show the energy profile of the resonator mode trapped in a typical photonic crystal point defect and microdisk resonator, respectively.

Recent advances in the micro- and nanofabrication of silicon photonic components [36, 37] have enabled the demonstration of very high *Q*s (above 1 million) in both SWR [34] and TWR [38] structures. In most recent reports on Si microresonators, such a high Q has required the removal of the oxide substrate underneath the resonator in order to reduce the radiative coupling loss from the resonator to the substrate [33, 37]. Especially, in the case of photonic crystal cavities, the presence of the oxide substrate dramatically degrades the Q compared

to the undercut structures. However, removal of the substrate causes other drawbacks: 1) the integration of active electronic functionalities such as metal-oxide-semiconductor (MOS) transistors and P-N junctions in which the resonator becomes very challenging or almost impossible; 2) the cavity structure becomes thermally isolated. In this dissertation we focus on Si microresonators with the presence of the oxide substrate.

This Ph.D. research focuses on the device physics, modeling, implementation, and application of planar ultra-high Q silicon TWR microresonator structures in a SOI platform. Microdisk, microring, and racetrack resonators are the three TWR resonator architectures of interest in this research, with greater emphasis on microdisk resonators. The theme of this research is to introduce these resonators as an essential fundamental element for dense integrated photonic circuits by theoretically and experimentally addressing the unique properties of these resonators such as the possibility of achieving ultra-high Qs and small mode volumes, efficient interaction with a waveguide or a resonator, and compatibility with large-scale integration. Both single- and coupled-resonator architectures are investigated, and theoretical design, modeling, and experimental techniques for the implementation and demonstration of such planar Si-based microresonators are developed. Scaling microresonators for the purpose of large-scale integration is investigated and the effects of structural size scaling on properties of the resonator are studied. Based on that, high Q microdisk resonators with ultra-small mode volumes, large free-spectral range, and single-mode operation for a large

wavelength range are demonstrated. The performance of high Q resonators at high powers is theoretically and experimentally investigated and the impacts of the resonator mode volume, Q, as well as the input power on the static and dynamic response of the resonator are discussed.

In the next section the organization of the thesis is provided.

1.1 Thesis Organization

In chapter 2, the physical and electromagnetic concepts of TWR structures are reviewed. The impact of Q and V on the performance of single- and coupled-resonator architectures is analyzed. Electromagnetic modeling of these structures for both two-dimensional (2D) and three-dimensional (3D) cases is provided. For the 2D case, the resonance wavelength and mode profile are obtained analytically. For the 3D case, an efficient finite-element technique is presented that provides the resonance frequency and all the field components. Down-scaling microdisk resonators toward the ultimate miniaturization (for the purpose of large-scale and compact integration of many resonators) is investigated. In addition, the impact of down-scaling on other resonator parameters is discussed, and with appropriate design, a miniaturized microdisk with single mode operation condition (similar to microring resonators) is proposed.

In chapter 3, coupling to TWR structures is investigated. In this thesis, the excitation of these resonators is via a nano-scale waveguide side coupled to them, which is the most compatible and flexible technique for on-chip and planar integration. Hence, a systematic method for engineering waveguide-resonator

coupling for microdisk, microring, and racetrack resonators to achieve the optimum waveguide-resonator interaction is presented.

In chapter 4, advanced fabrication techniques with nanometer range control, which we developed for the implementation of ultra-high *Q* Si TWR microresonators in a SOI platform, are presented.

In chapter 5, experimental characterization techniques for studying the performance of the fabricated microresonators are developed and using these techniques, the spectral properties of the microresonators at low powers are presented. Microdisk resonators from large to ultimate miniaturized scales are characterized and very large (Q/V) is obtained in both scaling regimes.

In chapter 6, the static and dynamic behavior of silicon microresonators is theoretically and experimentally investigated at high optical powers in the presence of two-photon absorption (TPA), free-carrier absorption (FCA), free-carrier dispersion, and thermo-optics effects. The result of these phenomena in ultra-high resonators is spectral lineshape distortion and bistability in the static regime, and the appearance of self-sustained oscillations on the resonator amplitude in the dynamic regime. Two regimes of sustained slow (MHz) and fast (~ GHz) oscillations are theoretically and experimentally investigated. Sustained fast oscillations are reported for the first time in this thesis. Also, the thermal properties of the microdisk resonator (with more details in the Appendix) are accurately investigated and methods to improve them are presented.

Chapter 7 is devoted to coupled-resonator structures. A systematic method for the design of a coupled-resonator filter structure with an arbitrary number of resonators and a flat-band response in the optical spectrum is presented. Using miniaturized microdisk resonators (with very large Qs), ultra-compact filters with very large free-spectral range (FSR) are demonstrated.

Chapter 8 addresses the future extension of this research, and chapter 9 provides the conclusion of the thesis.

CHAPTER 2

TRAVELING-WAVE RESONATORS IN SOI PLATFORMS: PHYSICAL CONCEPTS AND ELECTROMAGNETIC MODELING

In this chapter, the fundamental concepts of dielectric optical resonators are presented and, in particular, the electromagnetic properties of traveling-wave resonators (TWR) are discussed. Then, the electromagnetic modeling of these TWR structures is presented to extract the mode profile and the corresponding resonance wavelength. Using the electromagnetic modeling, the physical properties of the resonators in a SOI platform are quantitatively described. The down-scaling of microdisk resonators toward the ultimate miniaturization (for the purpose of large-scale and compact integration of many resonators) is investigated. In addition, the impact of down-scaling on other resonator parameters is discussed, and with appropriate design, a miniaturized microdisk with single-mode operation condition (similar to microring resonators) is proposed. Finally, a general review of non-idealities in Si resonators is discussed; more details are provided in relevant chapters.

2.1 Fundamental Concepts of Optical Microresonators

The key features of an optical microresonator are the spatial and temporal localization of electromagnetic energy (at a particular wavelength) within a micron or submicron length scale and for a considerably long time compared to the photon time period. By assuming a harmonic time dependence, $\exp(+i\omega t)$, for the

electromagnetic field components, Maxwell's curl equations in the frequency domain for a linear dielectric and nonmagnetic material are expressed as

$$\nabla \times E = -i\omega\mu_0 H \,, \tag{2.1}$$

$$\nabla \times H = i\omega\varepsilon_o n^2 E \,, \tag{2.2}$$

where μ_0 and ε_0 are the permeability and permittivity of the vacuum, respectively, and n is the refractive index, which can be a complex number to include loss. Combining Equations (2.1) and (2.2), we reach the Helmholtz equation in terms of E or H as

$$\nabla \times [\frac{1}{p^2} \nabla \times F] = (\frac{\omega}{c})^2 \frac{n^2}{p^2} F \quad , \quad \begin{cases} F = H, \ p = n \\ \quad or \quad \\ F = E, \ p = 1 \end{cases} , \tag{2.3}$$

in which c is the speed of light in vacuum. By solving the above equation for a resonator structure, the resonance frequency and mode profile of the resonator can be obtained.

The temporal localization of energy in a resonator is quantified by photon lifetime (τ_0) or equivalently by quality factor (Q), as will be described later. A major effort in the design and implementation of resonators is to minimize energy loss or leakage to have a long photon lifetime. However, in practice, the photon lifetime in a dielectric resonator is finite and limited because of (1) the resonator geometry that cannot completely confine the optical mode and prohibit any energy leakage to the outside and (2) non-idealities in the material properties and the fabrication of the resonators that cause absorption or leakage of energy. As a result of these cases, a

finite photon lifetime appears, when solving Helmholtz equation, as an imaginary part of the resonance frequency, which represents the loss or energy decay of the resonator. In this case, the complex resonance frequency and field profiles of the resonator mode can be written as follows:

$$\omega_{resonance} = \omega_0 - i/\tau_0, \tag{2.4}$$

$$\begin{pmatrix} E \\ H \end{pmatrix} = \begin{pmatrix} \mathrm{E}(r) \\ \mathrm{H}(r) \end{pmatrix} \exp(j\omega_0 t - t/\tau_0), \tag{2.5}$$

where τ_0 is photon lifetime, and E(r) and H(r) are spatial variation of the electric and magnetic field of the resonator. τ_0 also represents the broadening of the resonator energy spectrum. A figure of merit of a resonator is its quality factor (Q), which is defined as

$$Q_0 = \omega_0 \frac{Resonator\ Stored\ Energy}{Power\ Lost}. \tag{2.6}$$

To quantitatively evaluate Equation (2.6), we note that the total resonator energy is obtained by integrating electric energy (u_E) and magnetic energy (u_H) densities over the entire volume as follows:

$$U = \int (u_E + u_H) dv = \int (\frac{1}{4} E.\varepsilon_0 n^2 .E^* + \frac{1}{4} H.\mu_0 .H^*) dv = U_0 \exp(-2t/\tau_0), \tag{2.7}$$

where U_0 is the volume integration of spatial parts of the energy densities, which is

$$U_0 = \int (\frac{1}{4} \mathrm{E}.\varepsilon_0 n^2 .\mathrm{E}^* + \frac{1}{4} \mathrm{H}.\mu_0 .\mathrm{H}^*) dv. \tag{2.8}$$

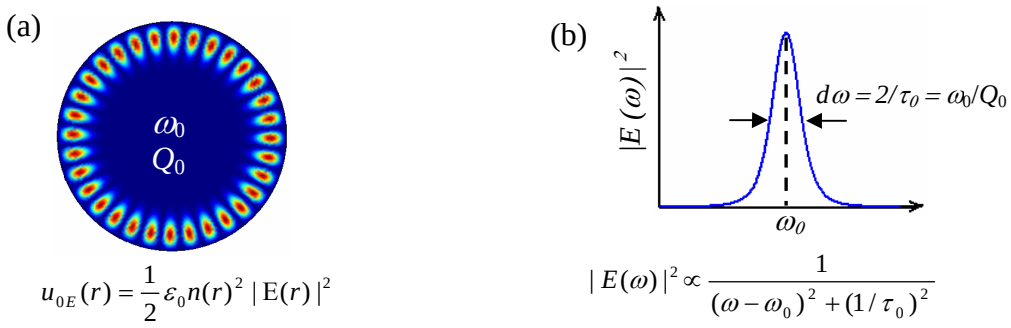

Fig. 2.1: (a) Top view of a typical spatial profile of the electric energy density of a dielectric microdisk resonator with a resonance frequency ω_0 and quality factors Q_0. (b) Spectral response of the resonator.

Combining Equations (2.6) and (2.7) we have[1]

$$Q_0 = \omega_0 \frac{U}{-dU/dt} = \omega_0 \frac{U_0 \exp(-2t/\tau_0)}{(2/\tau_0) U_0 \exp(-2t/\tau_0)} = \frac{\omega_0 \tau_0}{2}. \tag{2.9}$$

As can be seen from Equation (2.9), a larger Q results in a longer photon lifetime and vice versa.

The spatial localization of energy in a resonator is quantified by the mode volume (V_m), which is defined as

$$V_m = \frac{U_{0E}}{\frac{1}{2}\varepsilon_0 |n\mathrm{E}|^2_{\max}} = \frac{\frac{1}{2}\int \varepsilon_0 n^2(r) |\mathrm{E}(r)|^2 \, dr^3}{\frac{1}{2}\varepsilon_0 |n\mathrm{E}|^2_{\max}}. \tag{2.10}$$

From Equation (2.10), it can be seen that (at a fixed resonator electric energy (U_{0E})) a smaller mode volume results in a larger peak of electric field, and correspondingly, the entire field of the resonator is enhanced. In addition, a larger

[1] Also, as shown in Appendix B, using Poynting theorem and a rigorous analysis, the following expression can be shown for a resonator:

Radiation power + Absorption power = $(2/\tau_0)$ (Stored energy)

Combining the above equality and Equation (2.6), we reach Equation (2.9).

refractive index contrast between the resonator and its surrounding media results in a smaller mode volume.

Figure 2.1 shows an example of the spatial and temporal localizations of mode energy for a dielectric microdisk resonator suspended in air. Figure 2.1(a) shows the electric energy profile of the resonator mode, which is localized at the perimeter of the microdisk. Figure 2.1(b) shows its resonance energy spectrum. As seen from Figure 2.1(b), a narrower spectral linewidth ($d\omega$) for the resonator corresponds to a larger Q, which means a longer temporal localization of energy in the resonator (in other words, $d\omega = \omega_0/(2Q_0)=2/\tau_0$). In the next section, the properties of planar traveling-wave resonator structures, which are the case of interest and the focus of this thesis, are discussed.

2.2 Traveling-Wave Resonators (TWR) in a SOI Platform

In a SOI platform, a TWR can be implemented using a silicon disk, donut, or ring, which are the most conventional structures. Figure 2.2(a) shows a silicon microring (or microdonut) resonator structure in a SOI platform[2]. The resonator is seated on a SiO_2 substrate and covered by a cladding material such as air, oxide, or any other material with a refractive index less than that of silicon. Such a resonator has an axial, i.e., circular, symmetry, with the axis being at the center of the circle and normal to the plane of the resonator, as shown in Figure 2.2(a) by the *z* axis. Figure 2.2(b) shows the cross section of this resonator in a cylindrical coordinate with unit

[2] By changing R_{in} (as shown in Fig. 2.2(a)) from zero to a non-zero value, the resonator changes from a microdisk to a microring or microdonut.

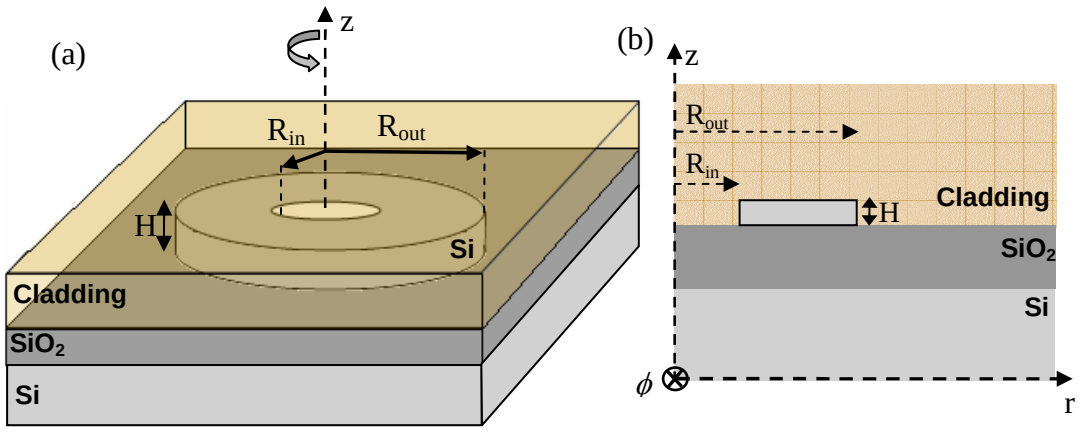

Fig. 2.2: (a) Structure of an axially symmetric silicon TWR structure seated on a SiO_2 substrate in a SOI platform. The resonator is covered by a cladding material. The axis of symmetry is at the center of the resonator and along the z direction. The thickness of the SiO_2 substrate is large enough to inhibit the leakage from the resonator to the underlying Si layer. (b) Cross section of the resonator structure. When R_{in} is zero the resonator is a disk; otherwise it is a ring or donut.

vectors (r, ϕ, z) corresponding to radial, azimuth, and vertical directions, respectively. In this resonator structure, with a refractive index larger than that of the regions surrounding the resonator, the EM wave can be confined and localized inside and in the vicinity of the perimeter of the resonator and travels along the perimeter in a clockwise or counterclockwise direction. Such a mode that travels along the circumference of the resonator is also called a whispering gallery mode (WGM)[3]. It is noted that the clockwise and counterclockwise traveling modes have frequency degeneracy[4]. Whereas the TWR structure in Figure 2.2 has a circular symmetry, a TWR structure can also be realized by forming any closed loop (made

[3] This terminology was adopted after Lord Rayleigh explained why whispers in the top gallery of St. Paul's Cathedral could be heard clearly along the perimeter of the gallery. In principle, the gallery forms a traveling wave acoustic resonator.

[4] The relation between the field components of degenerate clockwise and counterclockwise modes of the resonator is exactly the same that exists for the degenerate forward and backward modes of a waveguide (through z reversal properties), with the difference that ϕ is the propagation direction in a resonator.

of Si waveguide) without having an axial symmetry. In such a structure, the EM wave is laterally confined by the waveguide and travels along the loop. An example of this case is a racetrack resonator that is formed by a Si waveguide. In the upcoming subsections, we discuss the properties of both axially symmetric and axially asymmetric TWR structures. Most of the physical properties of these TWR structures are common and are introduced in the discussion of axially symmetric resonators. The other minor differences and properties of these structures are discussed separately.

2.2.1 Axially Symmetric TWR Structures: Microdisks and Microrings

As shown in Figure 2.2(a), because of the presence of circular symmetry in the resonator architecture, the field components of the resonator can be written in cylindrical coordinates in the following form:

$$F = \begin{pmatrix} E \\ H \end{pmatrix} = \begin{pmatrix} \mathrm{E}_r(r,z),\, \mathrm{E}_\phi(r,z),\, \mathrm{E}_z(r,z) \\ \mathrm{H}_r(r,z),\, \mathrm{H}_\phi(r,z),\, \mathrm{H}_z(r,z) \end{pmatrix} \exp(i\omega t - im\phi), \tag{2.11}$$

where ϕ is the phase variation of the field in the azimuthal direction and m (as will be shown later) is a discrete integer number that has to be determined via the boundary conditions. Because of this axial symmetry, any partial derivative with respect to ϕ can be written as

$$\frac{\partial}{\partial \phi} F = -imF\,. \tag{2.12}$$

Putting Equation (2.13) into Maxwell's equation in cylindrical coordinates makes the equations dependent only on r and z. When the resonator is 2D, i.e., infinite in

the *z* direction and with no field propagation and refractive index change along *z*, the field equations become simpler since they have no dependence on *z* and only depend on *r*. In such a case, similar to all 2D structures, Maxwell's equations can be separated into two isolated sets of solutions with different polarizations, namely, TE and TM. In the TE (TM) case, the electric (magnetic) field is in-plane with the disk plane and has no axial component, and the magnetic (electric) field is only along the axis of the resonator, i.e., H_z (E_z). Based on this property, TE (TM) modes are also called H_z (E_z) modes. Therefore, for a 2D case, Equation (2.11) becomes

$$\begin{cases} [\mathrm{E}_r(r,z), \mathrm{E}_\phi(r,z), \mathrm{H}_z(r,z)]\exp(i\omega t - im\phi), & \text{TE} \\ [\mathrm{H}_r(r,z), \mathrm{H}_\phi(r,z), \mathrm{E}_z(r,z)]\exp(i\omega t - im\phi), & \text{TM} \end{cases}. \tag{2.13}$$

For both 2D and 3D resonators, while a rigorous electromagnetic analysis is required to accurately and quantitatively analyze the resonator, using a qualitative ray and wave approach, the operation principle of the resonator and its physical parameters can be understood and found. At the beginning, we employ these qualitative methods, which provide a profound understanding of the resonator properties, and later, the accurate electromagnetic analysis is presented.

For a microdisk structure, as shown in Figure 2.3(a), the confinement and roundtrip travel of the EM wave at the disk perimeter can be explained via total internal reflection (TIR) of the wave at the sidewall of the disk. However, because the sidewall of the resonator has a finite curvature, TIR is not perfect and as a result, there is always some energy leakage to the outside of the disk, as shown in Figure 2.3(a). As a result of this energy leakage, the photon lifetime and, correspondingly,

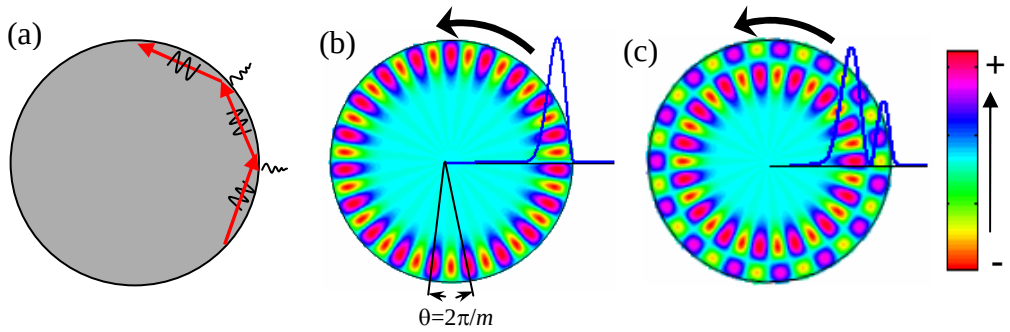

Fig. 2.3: (a) Schematic top view of a microdisk resonator. Traveling of EM wave at the perimeter of the disk and its confinement due to TIR is observed. Electromagnetic simulation of the typical magnetic field profiles of (b) 1st and (c) 2nd radial orders of the microdisk. As shown in (b), the field has m lobes with equal azimuth angular spacing of $2\pi/m$. The cross sections of the variation of the fields along the radial direction are shown in (b) and (c).

the Q of the resonator are reduced. At smaller disk radii, in which TIR has more energy leakage, we expect more energy leakage from the sidewall and consequently a lower Q. After a full roundtrip, if the EM field is in phase with the one at the start point of the trip, a constructive interference occurs, which leads to the resonance condition. Considering β as the propagation constant of the traveling EM wave inside the resonator, the interference or resonance can occur in a microdisk (or microring) at a specific frequency and at the following condition:

$$\beta L = 2\pi m, \tag{2.14}$$

where L is the effective length or perimeter of the resonator in which the EM wave travels, and m is an integer number, which is the same as that introduced in Equation (2.12). Similar to any propagating wave, a mode effective index (n_{eff}) can be defined for the traveling EM wave in the resonator as

$$n_{eff} = \frac{\beta}{(\omega_0 / c)} = \frac{\beta \lambda_0}{2\pi}, \tag{2.15}$$

where c is the speed of light, and ω_0 and λ_0 are the resonance frequency and wavelength, respectively. Combing Equations (2.14) and (2.15), the resonance wavelength and frequency are correspondingly related to the effective index and the resonator length as

$$n_{eff} = \frac{\lambda_0 m}{L}, \quad n_{eff} = \frac{2\pi mc}{L\omega_0}. \tag{2.16}$$

Figure 2.3(b) shows the accurate electromagnetic simulation of the electric field profile of the microdisk resonator when interference occurs with m azimuthal lobes. By changing the azimuthal number, m, resonance frequency changes, and the number of azimuthal lobes in the field also changes. Whereas the field in Figure 2.3(b) has one peak in the radial direction, which is called a 1st radial order of the microdisk with a specified set of (E, H, m, n_{eff}, ω_0), a microdisk resonator can support modal fields with different numbers of radial peaks, belonging to different sets of (E, H, m, n_{eff} , w_0). One example of the resonator field with two radial peaks is shown in Figure 2.3(c).

In contrast to a microdisk, a microring is designed to support one radial mode order. In a microring resonator, the resonance mode profile is confined by two sidewalls of the ring. In other words, the ring can be considered as a single-mode waveguide that is formed into a circular loop, and higher-order modes of such a waveguide are in cut-off. Figure 2.4(a) shows a ray approach to the propagation of the EM wave inside the ring in which TIR occurs at both sidewalls. However, there

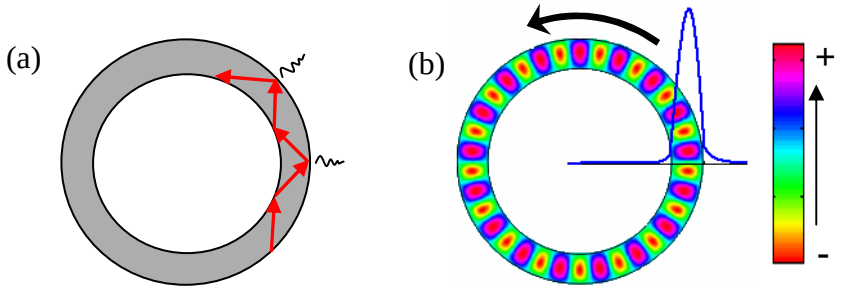

Fig. 2.4: (a) Schematic top view of a microring resonator. TIR of the traveling EM wave at the two sidewalls of the ring is observed. (b) Electromagnetic simulation of the typical magnetic field profiles the microring. The cross section of the variation of the field along the radial direction is shown in (b).

is some energy leakage through the outer sidewall similar to what was seen for a microdisk. Figure 2.4(b) shows the electromagnetic mode profile of the ring.

An intermediate architecture between a microdisk and a microring is a microdonut resonator. In a microdonut, as shown in Figure 2.5(a), the hole at the center of the structure is much smaller than the one for a microring. As shown in Figure 2.5(a), the EM wave does TIR at the outer sidewall without seeing the inner wall. This is similar to the traveling behavior of the EM wave in a microdisk. As shown in Figure 2.5(b), using electromagnetic simulation, the tail of the profile of 1^{st} radial order mode at the proximity of the inner wall is almost zero (in other words it does not see the inner sidewall of the donut). However, higher radial order modes that have more extension inside the donut can interact with the inner sidewall. In fact, the radius of the inner hole can be adjusted in a way that the inner sidewall strongly (very weakly) interacts with higher radial order modes (1^{st} radial mode). The interaction of the inner sidewall with the higher-order modes can even push them to cut-off and a strong radiation regime. This is similar to what was seen for a waveguide where, by controlling the width, the higher-order modes are pushed

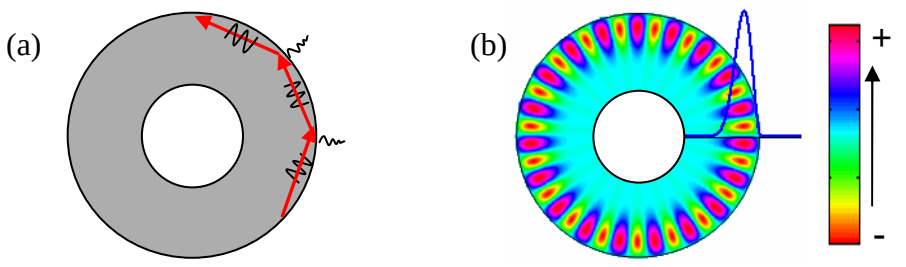

Fig. 2.5: (a) Schematic top view of a microdonut resonator. TIR of the traveling EM wave at one sidewall of the donut is observed. (b) Electromagnetic simulation of the typical magnetic field profiles the microdonut. The cross section of the variation of the field along the radial direction is shown in (b).

to cut-off. However, the difference is that in a waveguide, the fundamental mode always interacts with both sidewalls, while a microdonut can be designed in a way that the 1st order radial mode interacts only with one sidewall of the resonator.

2.2.1.1 Free-Spectral-Range (FSR)

As mentioned previously, for each m number in Equation (2.16), there is an individual resonance, and therefore the free-spectral range (FSR) of the resonator can be obtained by measuring the resonance spacing for two consecutive m numbers. This can be found as follows:

$$FSR^{(\omega)} = \Delta\omega = \omega_0^{(m+1)} - \omega_0^{(m)} = \frac{2\pi c}{n_{eff}^{m+1} L}(m+1) - \frac{2\pi c}{n_{eff}^{m} L} m \,. \tag{2.17}$$

In general, the n_{eff} is frequency dependent, and this fact has been considered in the above expression. Instead of simplifying Equation (2.17), an easier approach to find FSR is through directly differentiating Equation (2.14) as follows:

$$\Delta\beta L = 2\pi\Delta m, \quad (\Delta m = 1) \,. \tag{2.18}$$

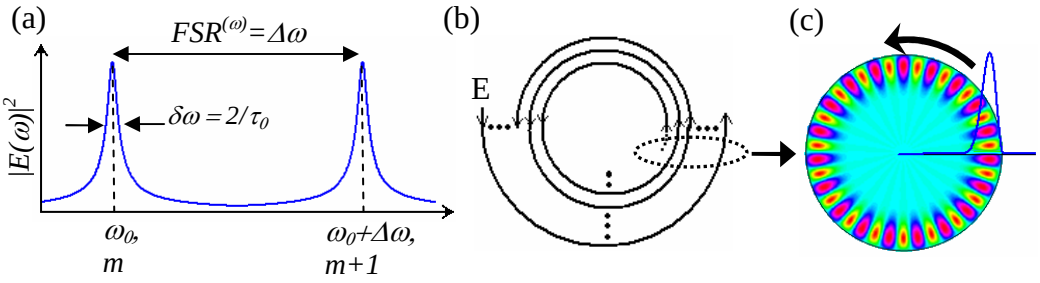

Fig. 2.6: (a) Spectrum of TWR resonator with two resonances and one FSR is shown. (b) Schematic representation of field enhancement and energy build up in a TWR due to the constructive interference of roundtrips of EM field; which results in a steady-state resonator field profile, as shown in (c).

Dividing both sides by FSR, i.e., $\Delta\omega$, and knowing that the group velocity of the EM wave is $v_g = \Delta\omega/\Delta\beta$, we have

$$L\,\Delta\beta / \Delta\omega = 2\pi 1 / \Delta\omega \;\Rightarrow\; L / v_g = 2\pi / FSR^{(\omega)}, \tag{2.19}$$

$$FSR^{(\omega)} = \frac{2\pi v_g}{L} = \frac{2\pi}{T_{roundtrip}}. \tag{2.20}$$

In Equation (2.20), $T_{\text{roundtrip}}=L/v_g$ is the total time of a roundtrip. Similarly, using the relation between the wavelength and the frequency, the FSR in the wavelength domain can be obtained as

$$FSR^{(\lambda)} = \frac{\lambda_0^2}{2\pi c} FSR^{(\omega)} = \frac{\lambda_0^2}{L}\frac{v_g}{c} = \frac{\lambda_0^2}{cT_{roundtraip}}. \tag{2.21}$$

Figure 2.6(a) shows a typical spectrum of two resonances of a TWR separated by their FSR.

2.2.1.2 Field Enhancement and Finesse

At resonance, because of many roundtrips of the EM wave, the field adds up constructively and, as a result, field enhancement in the resonator occurs. Figure

2.6(b) shows a qualitative description of this field enhancement where the E field, which is coupled into the resonator from outside, starts doing the roundtrip and constructively adds up; therefore, photons are accumulated at resonance and create the steady-state resonator field profile shown in Figure 2.6(c). Because of the energy leakage of the resonator (which corresponds to finite photon lifetime τ_0), the total number of roundtrips is finite and approximately equal to $2\tau_0/T_{\text{roundtrip}}$, where $2\tau_0$ is the energy leakage time constant. As a result, the resonator circulating power (which is proportional to $|E_{\text{resonator}}|^2$) is

$$|E_{resonator}|^2 = \frac{2\tau_0}{T_{roundtrip}} |E|^2 . \tag{2.22}$$

Therefore, resonator field enhancement is $2\tau_0/T_{\text{roundtrip}}$, which can be represented in the following form:

$$Enhancemen\ t = \frac{2\tau_0}{T_{roundtrip}} = \frac{2(2/\delta\omega)}{2\pi / FSR^{(\omega)}} = \frac{2}{\pi}\frac{FSR^{(\omega)}}{\delta\omega} = \frac{2}{\pi} Finesse \tag{2.23}$$

Finesse is defined as the ratio between the FSR and the linewidth of the resonator. Hence, field enhancement in a resonator is proportional to the finesse. From Equation (2.10) we saw that field enhancement in a resonator was inversely proportional to the mode volume. In a TWR structure, FSR is in fact a signature of the mode volume of the resonator since a smaller mode volume means larger FSR, as seen from Equation (2.20) (mode volume of a TWR is almost proportional to its perimeter L).

2.2.1.3 Roundtrip Loss and Q

In a TWR structure, because of the propagating nature of the resonance mode, a power propagation loss factor (α) can be defined that is attributed to any energy leakage or absorption during the roundtrip. While in the preceding discussions and using the temporal approach the Q of the resonator was related to the photon lifetime τ_0, using a spatial approach Q can also be related to propagation loss α, which is defined as

$$\alpha = -(\frac{dP}{dl}) / p . \tag{2.24}$$

In Equation (2.24), *dl* is a differential element of propagation length, and *P* is the power that circulates in the resonator. Using chain rules, we have

$$\frac{dP}{dl} = \frac{dP}{dt} \times \frac{dt}{dl} = \frac{dP}{dt} \times \frac{1}{v_g} . \tag{2.25}$$

Knowing that the circulating power is proportional to the squared magnitude of the field and using Equation (2.6), we conclude that $dP/dt = -(2/\tau_0)P$. Combining this and Equation (2.25), we have

$$\frac{dP}{dl} = -\frac{2}{\tau_0} p \times \frac{1}{v_g} . \tag{2.26}$$

Finally, combining Equations (2.24) and (2.26) and using Equation (2.9), we have a relation between α and Q as follows:

$$\alpha = \frac{2}{\tau_0} \times \frac{1}{v_g} = \frac{\omega_0}{Q_0 v_g} = \frac{2\pi}{Q_0 \lambda_0} \frac{c}{v_g} = \frac{2\pi n_g}{Q_0 \lambda_0} . \tag{2.27}$$

As seen form Equation (2.27), roundtrip loss (α) is inversely proportional to photon lifetime (τ_0) and Q.

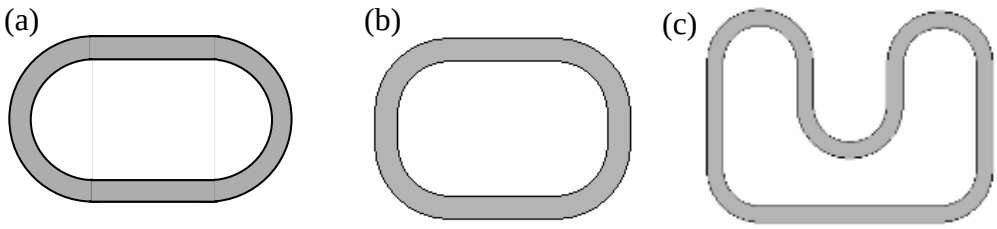

Fig. 2.7: Different waveguide-based TWR architectures with no circular symmetry. The straight portion of the resonator can enhance its interaction with another waveguide or resonator that is coupled to it along the straight region.

2.2.2 Axially Asymmetric TWR Structures

In the preceding discussion, it was mentioned that a microring can be approximated as a loop waveguide. While a ring waveguide loop has circular symmetry, in general it can have any other arbitrary shape as long as it is smooth. Figure 2.7 shows other examples of these waveguide loops. The benefit of using such architectures compared to a circular ring is that they can provide a larger interaction length and stronger power coupling when coupled to a straight waveguide that has the same waveguide dimensions as the one that forms the resonator. As an example, when a straight waveguide is coupled to a racetrack resonator along the straight portion of the racetrack, the coupling region behaves as a directional coupler with identical waveguide arms, and as a result, by controlling the length of the straight portion of a racetrack resonator, the coupling strength can be obtained at the desired level. This is discussed in more detail in chapter 3.

2.3 Electromagnetic Modeling of TWR Structures

An important step in designing TWR-based optical functionalities is to extract the accurate resonance frequency and electromagnetic mode properties of the resonator from the Helmholtz equation. For 2D microring and microdisk resonators, or for highly symmetric 3D structures such as microsphere geometry [39], analytical solutions for Helmholtz equations exists and many physical properties of these resonators can be understood through this analysis. However, for practical microring or microdisk resonators, which are 3D with a finite height, finding an analytical solution is almost impossible. There have been approximate semi-vectorial techniques, such as the popular effective-index method, that reduce the 3D geometry of the resonator into an approximately equivalent 2D geometry and simplify the vectorial Helmholtz equation to a scalar version in terms of one of the field components. This technique, while effective in finding the approximate resonance frequencies of the resonator, is not capable of providing quantitative information about all field components. Moreover, this method cannot accurately predict the *Q* of a resonator, which is a primary figure of merit for describing resonator characteristics[5]. In addition, such semi-vectorial methods impose certain conditions on the resonator size of the resonator to be able to simulate the structure with one field component. These facts force us to search for other efficient and fully vectorial numerical methods to extract resonant frequency, field components, and quality factor of the resonators.

[5] I have shown that when substrate and cladding of a microdisk are made of similar material, the extracted Q from the effective index-method is close but higher than the actual Q obtained through vectorial analysis. However, for an asymmetric case, e.g., substrate is oxide and cladding is air, or for structural dimensions in which the effective-index method deviates largely from the actual solution, the extracted Q is not valid.

Currently, the finite-difference time-domain (FDTD) technique [40] and finite-elements method (FEM) [41] are the popular numerical tools (in the time domain and frequency domain, respectively) used to analyze resonator structures. Analyzing axially symmetric resonators in Cartesian coordinates using either of these two methods is time consuming and memory inefficient, especially for the cases of large microdisk resonators in which the resonance mode profile is localized in a small portion of the resonator volume. A step to reduce the complexity of the problem is to transform Maxwell's equation into cylindrical coordinates and apply the axial symmetry properties of the structure, as shown in Equation (2.12), into FDTD equations. As a result, the 3D geometry is reduced to a 2D geometry with coordinate variables r and z representing the cross section or transverse plane of the resonator, as shown in Figure 2.2(b). However, a major problem with incorporating cylindrical symmetry in FDTD is that the Courant stability condition becomes dependent on the harmonic mode number, m, as [40]

$$\Delta t_m = \Delta t_0/(m+1), \tag{2.28}$$

with Δt_0 being the stable time step when $m = 0$. This dependence makes the simulation time consuming and inefficient, especially for a large value of m (which is the case of interest for many applications in TWR resonators[6]). In addition, all six field components of E and H are present during FDTD analysis, which requires more computational time and memory.

[6] As an example, for a Si microdisk with a radius of 5 μm and 10 μm and a thickness of 230 nm, the values of m (for the 1st order radial mode and with a resonance wavelength around 1550 nm) are around 50 and 107, respectively.

In contrast to FDTD, FEM analysis has proven to be very promising for the analysis of TWR resonators in reducing the required computational time and memory [42]. In this case, the axial symmetry condition is incorporated into the Helmholtz equation, and the 3D geometry is reduced to a 2D geometry with coordinate variables r and z , which represent the transverse plane of the resonator, as shown in Figure 2.2(b). Therefore, the vectorial Helmholtz equation to be solved has three equations and three field variables, (F_r, F_ϕ, F_z), with F being E or H in the reduced 2D geometry. In addition, employing hybrid vector edge-nodal elements in the FEM analysis can suppress the spurious modes (which are generated if scalar nodal elements are used, instead).

In this thesis, 3D microdisk and microring resonators are analyzed using the effective-index method and the vectorial FEM method. The effective-index method (with all its deficiencies) has the advantage of simplicity in formulation, fast analysis, and providing decent approximate results for the resonance frequency of a resonator. Vectorial FEM analysis (being computationally efficient and stable) provides accurate results for the resonance mode as well as all the field components.

For the FEM analysis, a new finite-elements formulation is proposed for the analysis of 3D microresonators with axial symmetry. The method is fast and memory efficient compared to the other finite-elements formulations. It only solves the transverse part of Helmholtz equations (i.e., two equations in the reduced 2D geometry) with only two coordinate variables, r and z. To verify the method, the results from this method for a microsphere (which has an analytical solution for the

resonance mode) will be compared with the analytical solutions. In addition, the results for other structures such as microdisks are compared with those obtained using the effective-index method.

In what follows, first the effective-index method for the analysis of microresonators is discussed, microresonators using this method are analyzed, and their properties are presented. Then, the new fully vectorial finite-elements analysis of these structures is presented and their accuracy is verified with known structures. This method becomes the main tool used to study and investigate the properties of microdisk and microring resonators at different scales.

2.3.1 Effective-Index Analysis of Microresonators

We assume that the refractive index of the resonator and the surrounding regions is piecewise homogeneous. By applying Equation (2.12) into Equation (2.3) and after expanding it in cylindrical coordinate, the *z* component of the equation in each domain can be expressed as

$$(\frac{1}{r}\frac{\partial}{\partial r}r\frac{\partial}{\partial r}-\frac{m^2}{r^2}+n^2k_0^2)F_z(r)+\frac{\partial^2 F_z}{\partial z^2}=0 \ , \ \begin{cases} F_z=\mathrm{H}_z \\ \quad or \quad , \\ F_z=\mathrm{E}_z \end{cases} \quad k_0=\omega/c \ , \tag{2.29}$$

where *n* is the refractive index of each domain, which is constant in the domain. As discussed in section 2.2.1, when resonator is 2D, i.e., $\partial/\partial z=0$, Maxwell's equations can be separated in two different polarizations of TE and TM[7]. However,

[7] In this case the z component of the Helmholtz equation can be written in a general form (which considers the inhomogeneity of refractive index) as

for the 3D case this separation is not possible and all the components of the electric and magnetic fields are tied and related. Nevertheless, if the thickness of the resonator is more than half of the optical wavelength in the resonator (i.e., greater than $\lambda_0/(2n)$ with n being the refractive index of the resonator), two sets of solutions are still distinguishable, namely, quasi-TE and quasi-TM solutions. In the quasi-TE (quasi-TM) solution, the electric (magnetic) field is predominantly in the plane of the resonator and has a very weak electric field along the resonator axis. Therefore, for the quasi-TE (quasi-TM) solution, the differential equation in Equation (2.29), with H_z (E_z) as the field variable, can provide approximate resonance frequencies of the resonator. Using the method of separation of variables, F_z in Equation (2.29) can be expressed as the product of two functions as $F_z(r,z) = R(r)\, Z(z)$. Putting this into Equation (2.29) and separating the independent equations, we obtain the following:

$$[\frac{d^2 Z(z)}{dz^2} + n^2 k_0^2 Z(z)] / Z(z) = n_{eff}^2 k_0^2 , \tag{2.30}$$

$$[(\frac{1}{r}\frac{d}{dr} r \frac{d}{dr} - \frac{m^2}{r^2}) R(r)] / R(r) = -n_{eff}^2 k_0^2 . \tag{2.31}$$

The term $n_{eff}^2 k_0^2$ on the right side of Equations (2.30) and (2.31) is the constant term, which has to be determined.

Equation (2.30) governs the vertical confinement of the mode in the microdisk (microring) resonator. This equation is the same as the mode equation of a slab

---

$$(\frac{1}{r}\frac{d}{dr}\frac{1}{p^2} r \frac{d}{dr} - \frac{m^2}{p^2 r^2} + \frac{n^2}{p^2} k_0^2) F_z(r) = 0 \quad , \quad \begin{cases} F_z = \mathrm{H}_z, \ p = n \\ \quad or \quad , \\ F_z = \mathrm{E}_z, \ p = 1 \end{cases} \quad k_0 = \omega / c$$

waveguide with a mode effective index n_{eff}. In fact, the 3D microdisk (microring) can be thought of as being created from a Si slab waveguide (as shown in Figure 2.6(a)) where the Si slab is sandwiched between the substrate and cladding. The top-right corner of Figure 2.8(a) partially shows the details of the slab and the slab mode that propagates with an effective index n_{eff} in it. For quasi-TE (quasi-TM) modes of the 3D resonator, the effective index of the TE (TM) mode of the slab waveguide has to be considered and found. After finding the n_{eff} of the slab from Equation (2.31), the 3D microdisk (microring) structure reduces to a 2D structure, as shown in Figure 2.8(b), with the governing equation given by Equation (2.31)[8].

Equation (2.31) (which governs the radial confinement of the resonator mode) is a Bessel differential equation in the cylindrical coordinate with a closed-form analytical solution. The analytical solution of Equation (2.31) for a microdisk that has one radial boundary is

$$R(r)=\begin{cases} A\,J_m(k_0 n_{eff}\, r) & r \le R_{out} \\ B\,H_m^2(k_0 n_{cladding}\, r) & R_{out} < r \end{cases}, \tag{2.32}$$

and for a microring that has two radial boundaries, the analytical solution of Equation (2.31) is

$$R(r)=\begin{cases} A\,J_m(k_0 n_{cladding} r) & r < R_{in} \\ B\,H_m^2(k_0 n_{eff} r)+C\,H_m^1(k_0 n_{eff} r) & R_{in} < r < R_{out} \\ D\,H_m^2(k_0 n_{cladding} r) & R_{out} < r \end{cases}, \tag{2.33}$$

[8] We note that n_{eff} in (2.30) depends on k_0, which is the main unknown of the problem. Hence we need to start with an initial guess for k_0, and based on that we find n_{eff}. By putting n_{eff} into (2.31) we find the new k_0.

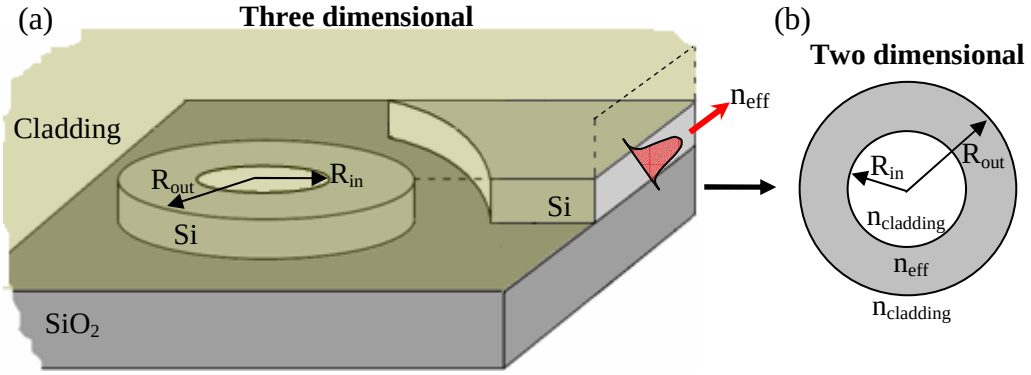

Fig. 2.8: (a) Structure of a 3D Si microring (disk) resonator made of a finite height slab and seated on a substrate and covered by cladding. The outer and inner radii are specified in the figure by R_{out} and R_{in} (R_{in} = 0 for disk). For clarity, the top-right corner of the figure shows the details of the Si slab, which is sandwiched between the substrate and cladding and supports a mode with an effective index n_{eff}. (b) Reduced 2D model of the 3D microring (disk) shown in (a).The refractive index of the 2D microring (disk) is n_{eff} calculated for the slab shown in (a), and the surrounding has the refractive index of cladding ($n_{cladding}$).

where J_m is the Bessel function of the 1st kind and order m, H_m^1 and H_m^2 are Hankel functions of the 1st and 2nd kind corresponding to the inward and outward propagation direction with respect to the axis of the resonator, and A, B, C, and D are the coefficients to be determined through the satisfaction of boundary conditions. The presence of Hankel functions (which have oscillatory and radiation properties[9]) as a solution in Equations (2.32) and (2.33) for $r > R_{out}$ means that the resonator has energy leakage to the outside in the radial direction. This energy leakage results in a finite Q for the resonator. Appendix C (which is devoted to the solution of 2D microdisk and microring resonators) shows the details of solving

[9] At a large r the behavior of a Hankle function is as $H_m^2(r) \sim \sqrt{\frac{2}{\pi r}}\ \exp[-i(r - m\pi/2 - \pi/4)]$

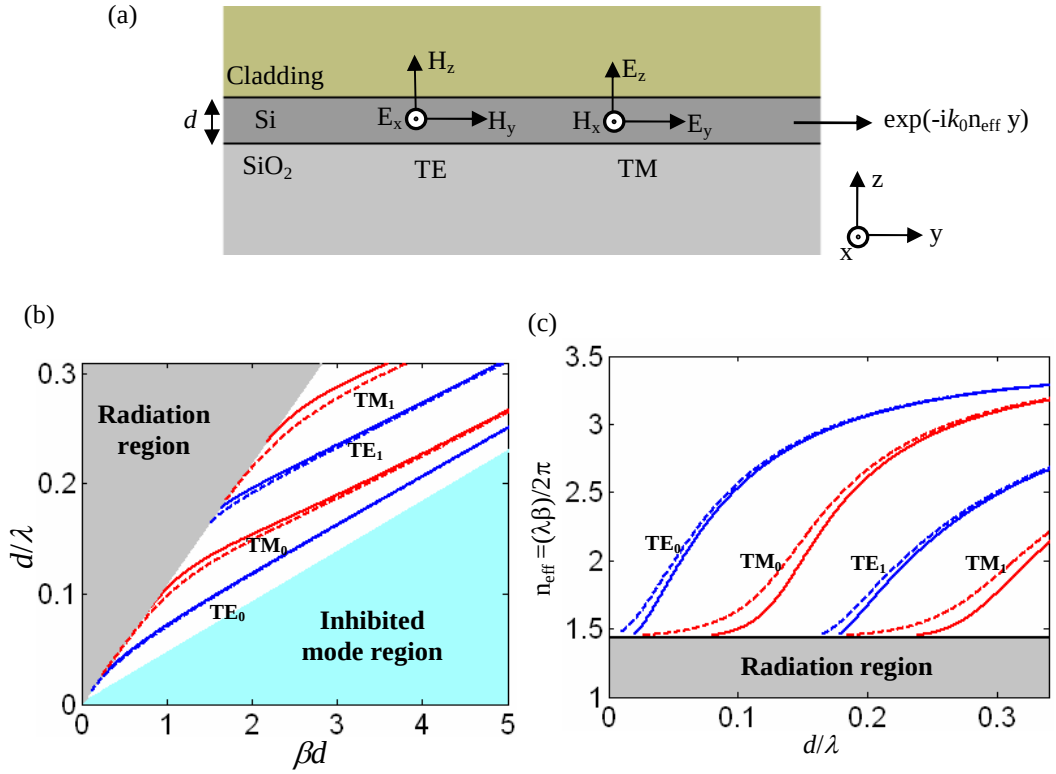

Fig. 2.9: (a) Structure of a Si slab waveguide with a thickness d on a SiO_2 substrate. The field components corresponding to TE and TM polarizations are specified in the figure. (b) The dispersion and (c) the effective index of different family modes of the waveguides for both TE and TM are shown. The solid and dashed curves correspond to the cases of air and oxide cladding, respectively. For this simulation, refractive indices of Si and SiO2 were 3.475 and 1.444, respectively.

Equations (2.32) and (2.33) by applying the boundary conditions to find the resonance frequency of the microdisk (mirroring).

When finding the resonances of the resonator, we need to do an iteration to find accurate results for the resonance. The iteration starts by choosing an initial k_0 and finding n_{eff} from Equation (2.30) and putting it into Equation (2.31) to find the new k_0. The iteration stops when the difference between the value of n_{eff} at the new k_0 and its previous value is in the acceptable range of error.

For many applications, we are interested in the 3D microdisk to support one mode for the polarization of interest in the vertical direction. Therefore, the slab waveguide is designed in a way to support one mode for that polarization in the frequency range of interest. Figure 2.9(a) shows more details of the field and polarization components of a slab waveguide in a SOI platform, and Figure 2.9(b) shows the dispersion diagram of the modes of the slab waveguide. Figure 2.7(c) shows the effective indices of different mode orders and polarizations.

Because of the oscillatory nature of Bessel and Hankel functions, the resonance mode profile of the microring and microdisk can have radial lobes inside the resonator. Based on the number of lobes, resonator modes are classified in the radial direction as different radial mode orders (or radial mode numbers) corresponding to lobe numbers. In summary, the modes in a microdisk (microring) resonator are classified based on the following:

1. polarization (quasi-TE or quasi-TM)
2. azimuthal mode number (m)
3. radial mode number

Figure 2.10 shows the simulation results for the quasi-TE (H_z) modes of a Si microdisk resonator with a radius of 10 μm and a thickness of 230 nm using the effective-index method. The microdisk is seated on a SiO_2 substrate and covered by air cladding. Figures 2.10(a)-(d) show, respectively, the magnetic field (H_z) profiles of the 1^{st}, 2^{nd}, 3^{rd}, and 4^{th} radial family modes across a line passing through the middle of the microdisk thickness and along the radial direction. The edge of the

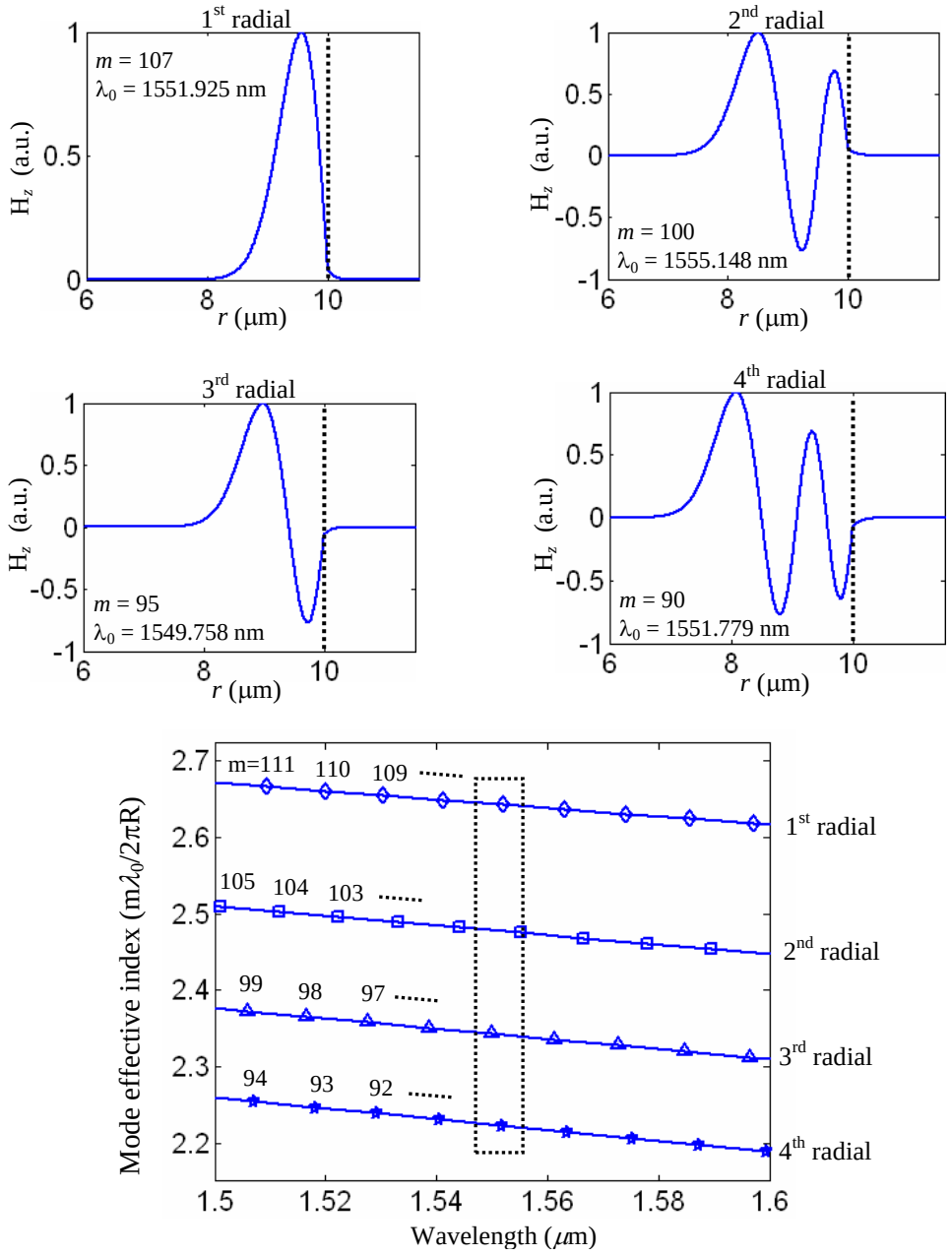

Fig. 2.10: Simulation results for the quasi-TE (H_z) modes of a microdisk resonator with a radius of 10 μm and a thickness of 230 nm, seated on a SiO_2 substrate and covered by air cladding using the effective-index method. Magnetic field (H_z) profile of (a) 1st, (b) 2nd, (c) 3rd, and (d) 4th radial modes along a line in the middle of the disk thickness and in the radial direction. The resonance wavelengths and azimuth number of these field profiles are specified in their figures. (e) Effective indices of the resonance modes for the 1st, 2nd, 3rd, and 4th radial order modes and at different azimuth harmonic numbers *m* as specified in the figure. For this simulation, refractive indices of Si and SiO_2 are 3.475 and 1.444, respectively. The dashed box in (d) is to highlight how these four radial modes are located in the spectrum in a small wavelength range around 1550 nm.

microdisk is specified in Figures 2.8(a)-(d) by vertical dashed lines. The resonance wavelengths and the azimuthal mode numbers of these field profiles are specified in these figures. For each radial mode of the resonator, an effective index can be specified as defined in Equation (2.16). However, the mode effective index is not a constant and depends on the radius. This is because of the radial distribution of the modes in the resonator, where the traveling length of the modal field is radius-dependent as $L(r) = 2\pi r$, with r being the distance of the field from the axis of the resonator. As a result, at any point of the mode distribution, the effective index is inversely proportional to its distance from the axis as

$$n_{eff} = \frac{\lambda_0 m}{2\pi r}. \tag{2.34}$$

Equation (2.34) says that the traveling field at farther axial distances has a lower effective index. In other words, the wavefront of the field, which does a circular roundtrip, has different velocities at different radial distances, and correspondingly, farther radial points have faster roundtrip propagation velocities. As a result, all the points of a mode, at different radial distances, travel their roundtrips (which have different roundtrip lengths) at the same time period and keep the wavefront undistorted.

Figure 2.10(e) shows the dispersion diagram of the effective index of the microdisk for the 1st, 2nd, 3rd, and 4th radial mode orders at r = R, i.e., at the edge of the microdisk, for different azimuthal mode numbers as specified in this figure. From this figure, it is seen that higher radial order modes have lower effective

indices. The dashed box in Figure 2.10(e) is to highlight how these four radial modes are located in the spectrum in a small wavelength range around 1550 nm. Some different radial modes have their resonance wavelength very close to each other[10]. The accuracy of the simulations shown in Figure 2.10, which is based on the effective-index method, is compared in the next section with the vectorial finite-elements analysis, which is more accurate.

2.3.2 Vector Finite-elements Analysis of Axially Symmetric Microresonators

In this section, a new vectorial FEM is proposed. In this new proposed method, as mentioned before, while the symmetry of the structure is employed to reduce the Helmholtz equation into two coordinate variables (r and z), the divergence equation for the magnetic field is additionally imposed to suppress the spurious modes and also to reduce the total number of equations to two and in terms of two field variables (H_r and H_z). All axially symmetric structures, including microdisks, microrings, microtoroids, and microspheres, can be easily and accurately analyzed. The method is very quick and computationally efficient so that large structures can be solved on a personal computer, and the solution, which is obtained in a few seconds, contains all the field components as well as the resonance frequencies of the structure. In addition, scalar nodal elements can be used without generating any spurious mode. For the analysis, we have chosen the magnetic field for the Helmholtz equation because the medium is magnetically homogenous (i.e.,

[10] Depending on the resonator size and the wavelength, the possibility of accidental degeneracy between different radial modes exists.

permeability at any point is vacuum permeability, μ_0), and as a result, the magnetic field is continuous all over the domain and scalar nodal elements already satisfy this property along the interfaces, including dielectric discontinuity. In the following, the new FEM formulation is discussed.

Considering the ϕ direction (as shown in Figure 2.2(b)) as the perpendicular direction and the (r, z) directions as transverse directions, the magnetic field components can be separated into perpendicular and transverse directions, as shown below:

$$\mathrm{H} = (\mathrm{H}_r \hat{r} + \mathrm{H}_z \hat{z}) + \mathrm{H}_\phi \hat{\phi} = \overline{\mathrm{H}}_t + \mathrm{H}_\phi \hat{\phi}\,, \tag{2.35}$$

where $\overline{\mathrm{H}}_t$ is the total vector magnetic field in the transverse plane. By applying the axial symmetry condition given by Equation (2.12) into the divergence equation, the ϕ component of the magnetic field can be written in terms of transverse components as

$$\nabla.\mathrm{H} = 0 \;\Rightarrow\; \mathrm{H}_\phi = \nabla_t.(\rho\overline{\mathrm{H}}_t)/(im)\,, \qquad (m \neq 0), \quad (\nabla_t = \frac{\partial}{\partial r}\hat{r} + \frac{\partial}{\partial z}\hat{z}\,). \tag{2.36}$$

The details of the above calculations are shown in Appendix D. By putting H_ϕ from Equation (2.36) into the Helmholtz equation, the transverse part of the equation (as explained in Appendix D) becomes

$$\frac{1}{r}\nabla_t \times (r\frac{1}{n^2}\nabla_t \times \overline{\mathrm{H}}_t) - \frac{1}{n^2 r^2}\nabla_t(r\nabla_t.(r\overline{\mathrm{H}}_t)) + \frac{m^2}{n^2 r^2}\overline{\mathrm{H}}_t = k_0^2\overline{\mathrm{H}}_t\,. \tag{2.37}$$

The above vector differential equation

1. consists of only two coupled scalar differential equations,

2. consists of only two field variables H_r and H_z,

3. consists of only two coordinate variables *r* and *z*.

The input parameters to Equation (2.37) for the simulation are the refractive index of the resonator and the regions surrounding it, and the azimuthal mode number *m*. The outputs of the simulation are the eigenvector $\overline{H}_t$ and eigenvalue k_0. Having $\overline{H}_t$ and k_0, and using the field relations from Maxwell's equations, all other field components are calculated. For a resonator made of a lossless material, it can be shown that H_r, H_z, E_r, and E_z can be obtained as pure real quantities and H_ϕ and E_ϕ as pure imaginary quantities.

By defining $\overline{H}_t^r = r\overline{H}_t$, Equation (2.36) can be written in another format as

$$\nabla_t \times [\frac{1}{n^2}\nabla_t \times (\overline{H}_t^r)] - \nabla_t \times [\frac{1}{n^2}\frac{\hat{r}}{r} \times \overline{H}_t^r] - \frac{1}{n^2 r}\nabla_t (r\nabla_t . \overline{H}_t^r) + \frac{m^2}{n^2 r^2}(\overline{H}_t^r) = k_0^2 \overline{H}_t^r . \tag{2.38}$$

Either Equation (2.37) or Equation (2.38) can be considered as the base differential equation for the finite-element simulation. For the rest of the discussions, we concentrate on Equation (2.37), which can be discretized in the domain of the solution using the Galerkin technique [41]. As result, the finalized FEM matrix is

$$[A][H_t] = k_0^2 [B][H_t], \tag{2.39}$$

where $[H_t]$ is a column matrix containing the magnetic fields at all the nodes of the elements, and [A] and [B] are the FEM global matrices, which are[11]

$$[A]=\sum_{e=1}^{N_e}\int_{\Delta_e}\overline{w}_t\cdot\{\frac{1}{r}\nabla_t\times(r\frac{1}{n^2}\nabla_t\times\overline{\mathrm{H}}_t)-\frac{1}{n^2r^2}\nabla_t(r\nabla_t.(r\overline{\mathrm{H}}_t))+\frac{m^2}{n^2r^2}\overline{\mathrm{H}}_t\}ds\,,$$

(2.40)

$$[B]=\sum_{e=1}^{N_e}\int_{\Delta_e}\overline{w}_t\cdot\overline{\mathrm{H}}_t ds\,, \tag{2.41}$$

where N_e is the total number of elements, Δ_e is the area of each element, and $\overline{w}_t$ is one of the vector basis functions in each element and has the following form

$$\overline{w}_t=w_r(r,z)\hat{r}+w_z(r,z)\hat{z}\,, \tag{2.42}$$

in which w_r and w_z are scalar Lagrange functions in each element. The double curl term in Equation (2.40), which is a 2nd order derivative term, can be converted to a 1st order derivative using the following vector field relations:

$$\nabla\cdot(\psi\mathrm{A})=\mathrm{A}\cdot\nabla\psi+\psi\nabla\cdot\mathrm{A}$$

$$\nabla\cdot(\mathrm{A}\times\mathrm{B})=\mathrm{B}\cdot\nabla\times\mathrm{A}-\mathrm{A}\cdot\nabla\times\mathrm{B}$$

$$\int_{\Delta}\nabla\cdot(\mathrm{A})ds=\oint_{\Delta}A.\hat{n}\,dl \qquad \text{(A and B are vector field, and } \psi \text{ is scalar).} \tag{2.43}$$

As a result, Equation (2.40) becomes

$$\begin{aligned}[A]=&\sum_{e=1}^{N_e}\int_{\Delta}(\nabla_t\times\frac{\overline{w}_t}{r}).[\frac{r}{n^2}\nabla_t\times(\overline{\mathrm{H}}_t)]ds-\sum_{e=1}^{N_e}\oint_{\Delta}[\frac{\overline{w}_t}{n^2}\times\nabla_t\times(\overline{\mathrm{H}}_t)\,].\hat{n}dl\\&+\sum_{e=1}^{N_e}\int_{\Delta}r\nabla_t\cdot(r\overline{\mathrm{H}}_t)\nabla_t\cdot(\frac{\overline{w}_t}{n^2r^2})ds-\sum_{e=1}^{N_e}\oint_{\Delta}\nabla_t\cdot(r\overline{\mathrm{H}}_r)\frac{\overline{w}_t}{n^2r}+m^2\sum_{e=1}^{N_e}\int_{\Delta}\frac{\overline{w}_t.\overline{\mathrm{H}}_t}{n^2r^2}ds\end{aligned}\,, \tag{2.44}$$

[11] Assembling the finite-element matrix of any differential operator is a standard technique that can be found in any FEM book (see for example [41]).

Using Maxwell's equation, the equivalent of the first line integral in Equation (2.44) is obtained as

$$\sum_{e=1}^{N_e} \oint_{\Delta_e} [\frac{\overline{w}_t}{n^2} \times \nabla_t \times (\overline{\mathrm{H}}_t)\ ].\hat{n}dl\ = \sum_{e=1}^{N_e} \oint_{\Delta_e} [\overline{w}_t \times i\omega_0 \varepsilon_0 \mathrm{E}_\phi\ ].\hat{n}dl\ . \tag{2.45}$$

Knowing that E_ϕ is a tangential component and continuous along all the boundaries shown in Figure 2.2(b), the net presence of this line integral in [*A*] is zero because

i) at the interface between two elements, the unit vectors $\hat{n}$ have opposite signs and their net sum from both neighboring elements is zero;

ii) very far from the resonator, that field decays and we put the perfect conductor at the exterior boundaries, $\mathrm{E}_\phi = 0$.

Similarly, the second line integral in Equation (2.44) can be equivalently written as

$$\sum_{e=1}^{N_e} \oint_{\Delta_e} \nabla_t \cdot (r\overline{\mathrm{H}}_t) \frac{\overline{w}_t}{n^2 r} = \sum_{e=1}^{N_e} \oint_{\Delta_e} im\mathrm{H}_\phi \frac{\overline{w}_t}{n^2 r}\ . \tag{2.46}$$

Knowing that H_ϕ is a tangential component and continuous along all the boundaries, this line integral is non-zero only at the interface between the two elements that have different refractive indices. Therefore, Equation (2.46) is only calculated for those lines that are along the boundaries with different refractive indices. At exterior boundaries where we have perfect conductors, H_ϕ is zero and as a result Equation (2.46) is zero.

For the FEM analysis we used a triangular meshing with scalar nodal elements and with quartic scalar Lagrange functions [41]. Each node in the mesh represents the two fields, H_r and H_z, corresponding to the location of that node. Therefore, the

total number of variables in Equation (2.39) is double the total number of nodes (except the nodes on perfect metal boundaries), which is much less than the total number of variables in the other FEM method (as mentioned before), which has all three field components and has to use hybrid vector edge-nodal elements to suppress the spurious solutions[12]. To find the Q of the resonator, the cylindrical perfectly matched layer (PML) boundary condition [43] is applied at the exterior boundaries. The FEM matrix was implemented in COMSOL[13] to get the benefit of its mathematical library and matrix eigenvalue solver as well as its graphical user interface for plotting and post-processing the field data.

To verify the FEM technique, the simulation results for a microsphere using this method were compared with the analytical asymptotic results that exist for a microsphere [39]. Figure 2.11(a) shows the structure of a Si microsphere with a radius of 10 μm, where z is the axis of symmetry, as shown in the figure. In a microsphere, a whispering gallery mode that travels around the z axis can be classified as a pure TE or a pure TM mode. In the pure TE (TM) mode, the electric (magnetic) field is parallel to the equator plane and normal to the z axis, and it has only one magnetic (electric) component, which is along the z axis, i.e., H_z (E_z).

[12] For the other formulation, the total number of variables is the number of edges (which correspond to transverse field components F_t) plus the total number of nodes (which correspond to perpendicular field components F_f). From graph theory the following relation can be shown for a mesh:

$$\textit{Number of Edges} = \textit{Number of Nodes} + \textit{Number of Elements} - 1$$

Therefore, the total number of variables in this formulation (excluding the nodes and edges at the perfect metal boundaries) is ~ 2×(*Number of node*) + *Number of elements*, while in our formulation the total number of variables is ~ 2×(*Number of node*).

[13] Currently, COMSOL software is not able to solve the modes of an axially symmetric microresonator (with m # 0) in cylindrical coordinates.

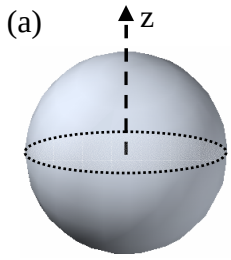

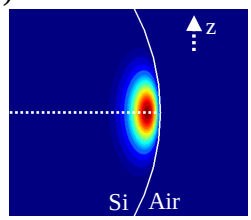

(c

Resonance wavelength

m^*	FEM	Asymptotic
130	1559.34	1559.37
131	1548.01	1548.06
132	1536.86	1536.90
133	1525.87	1525.91

*: *m* is the azimuth mode number

Fig. 2.11: (a) Structure of a dielectric microsphere with a refractive index of 3.475 and a radius of 10 μm suspended in air. (b) Cross section of the magnetic field profile of H_z corresponding to TE polarization. (c) Comparison of resonance wavelength of the microsphere for the mode shown in (b) at different azimuth mode numbers *m*.

Figure 2.11(b) shows the cross section of the magnetic profile of the 1st order radial TE (H_z) mode with azimuth mode number m = 130. The table shown in Figure 2.11(c) compares the results extracted from the proposed FEM technique and the asymptotic expression for different azimuth mode numbers (m). From these results good agreement between the asymptotic method and our FEM formulation is clear. For the analytical results of the microsphere, only the first six terms in the asymptotic series were considered[14].

For the second example, we chose a 3D microdisk resonator in a SOI platform. The microdisk has a radius of 10 μm and a thickness of 230 nm[15] and is seated on a SiO_2 substrate and covered by air. Figure 2.12(a) shows the cross section of the microdisk, which is moderately meshed for the FEM simulation. As shown in this figure, the meshing is denser at the location where the energy of the whispering

[14] The analytical solution of the microsphere results in an asymptotic series for the resonance frequency of the resonator. By considering a larger number of terms from this asymptotic series, more accurate results can be obtained (see [48]).

[15] For many applications, the thickness of the Si layer is in a range of 200-260 nm to provide single-mode and low-loss guiding in the wavelength around 1550 nm. However, for some applications, thicknesses below 200 nm (i.e., 110-200 nm) have been pursued to have less field confinement inside the Si layer.

gallery mode of the resonator is concentrated. The geometry domain of the structure in Figure 2.12(a) has been closed by perfect metals. These walls are far enough from the microdisk so that they have negligible effect in the resonance properties of the microdisk. It is noted that to measure the Q of the resonance mode, the PML boundary condition has to be considered at the outer boundaries. Figures 2.12(b)-(g) show, respectively, the cross sections of the electric (E_r, E_ϕ, E_z) and magnetic (H_r, H_ϕ, H_z) field components of one of the resonance modes of the microdisk. Also, Figures 2.12(h) and 2.12(i) show the electric and magnetic energy density profiles of this resonance mode. This mode is quasi-TE, as the electric field is predominantly projected into the in-plane components (E_r and E_ϕ), and the out-of-plane component (E_z), as shown in Figure 2.12(f), is very small. This mode is a 1st order radial mode, as energy densities have one lobe in the radial direction inside the microdisk. Figures 2.12(j) and 2.12(k) show the radial distribution of some of the field and energy components of the microdisk (as specified in these figures) along a line passing through the middle of the microdisk thickness and along the radial direction. From these two figures, we can see the level of the localization of the field energy components of the 1st order radial quasi-TE mode shown for a microdisk with a radius of 10 μm. The other important property of the resonator is the variation of the effective index at difference resonance wavelengths (which are specified with their azimuth mode number). Figure 2.13(a) shows the effective indices of the first three radial quasi-TE modes of the microdisk structure shown in Figure 2.12(a). The effective index was calculated at the edge of the disk (i.e., n_{eff} =

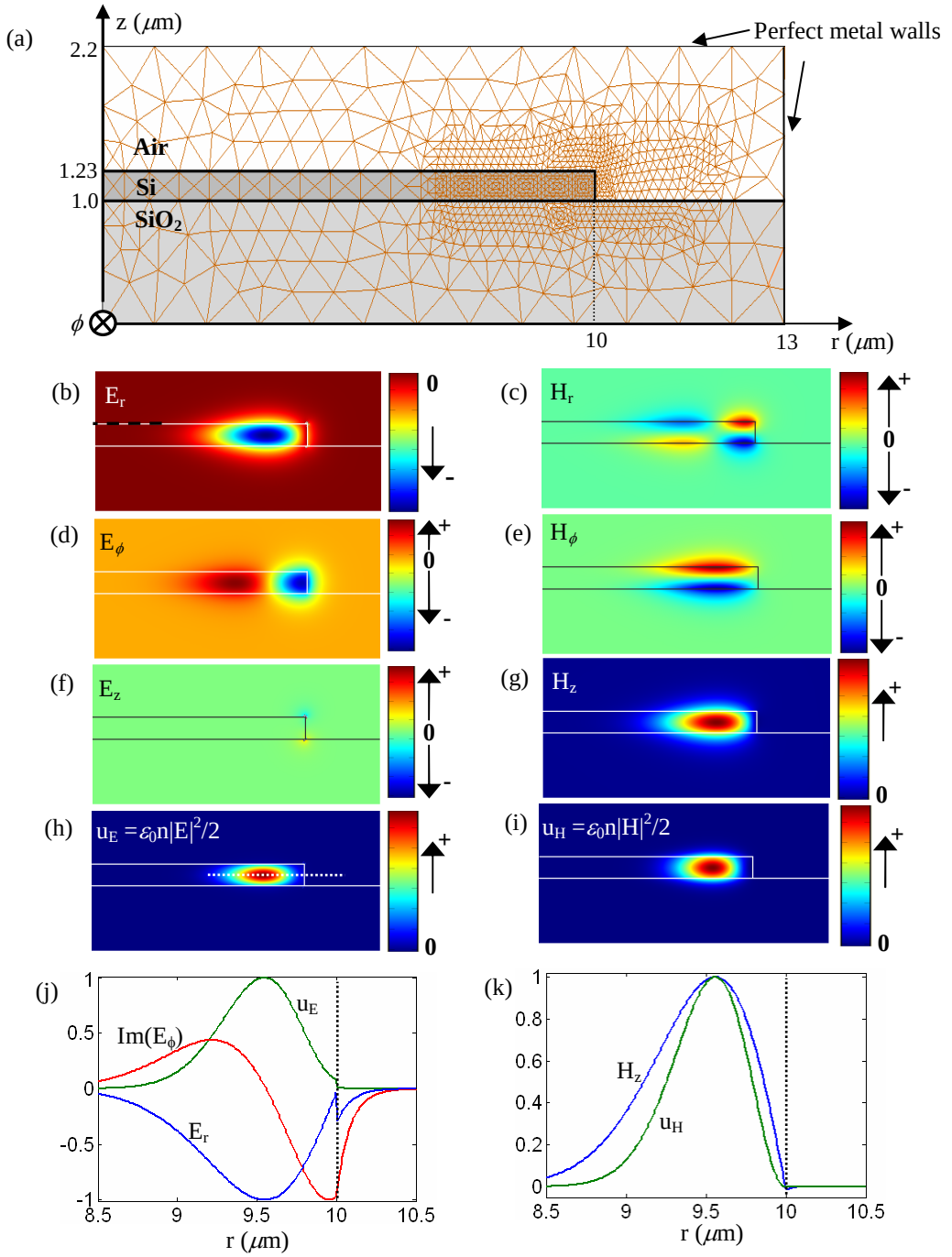

Fig. 2.12: (a) Cross section of a Si microdisk resonator on a SiO_2 substrate and moderately meshed for FEM analysis. Cross sections of the profiles (b)-(g) of all six field components of one of the resonance modes, (h)-(i) electric and magnetic energy densities of the mode, respectively. This mode is a 1st radial order TE mode, as u_E has one peak, and the electric field is predominantly in-plane (E_z is very small). (j)-(k) Variations of some of the field quantities across a line along the radial direction and passing through the middle of the disk height, e.g., the dashed line in (h). For this simulation m= 107, and the refractive indexes of Si and SiO_2 are 3.475 and 1.444, respectively.

$m\lambda_0/(2\pi R)$ with m, λ_0, and R as the azimuth mode number, resonance wavelength, and microdisk radius, respectively). The dashed curves in Figure 2.13(a) were obtained by FEM analysis, and the solid curves were obtained using the effective-index method. As seen from this figure, results from the effective-index method are close to those from FEM analysis, which provides more accurate results. Comparing the results from FEM and the effective-index method, we can say that the effective-index method is an appropriate tool to find the approximate location of the resonance wavelengths for 3D microdisk structures.

It is also interesting to compare the effective index of a microdisk and a straight ridge waveguide, which is frequently used in a SOI platform. This is shown in Figure 2.13(a) for a waveguide with a width of 500 nm and a thickness of 230 nm. The results for the waveguide were obtained using the available FEM tool in COMSOL for waveguide analysis. As seen from this figure, the effective index of the ridge waveguide with the given dimensions is lower than that of the 1st and 2nd radial mode and higher than that of the 3rd radial mode of the microdisk. Knowing the effective index of a microdisk mode and a waveguide mode is important where coupling these two structures to each other is concerned. In general when their effective indices are close together, the interaction of the waveguide with the resonator is stronger. Hence, one way to enhance the waveguide-resonator coupling is to phase match (i.e., effective index match) these two structures by appropriate design and engineering of their dimensions. The issue of waveguide-resonator coupling is discussed in greaterdetail in Chapter 3. Nevertheless, it is interesting to

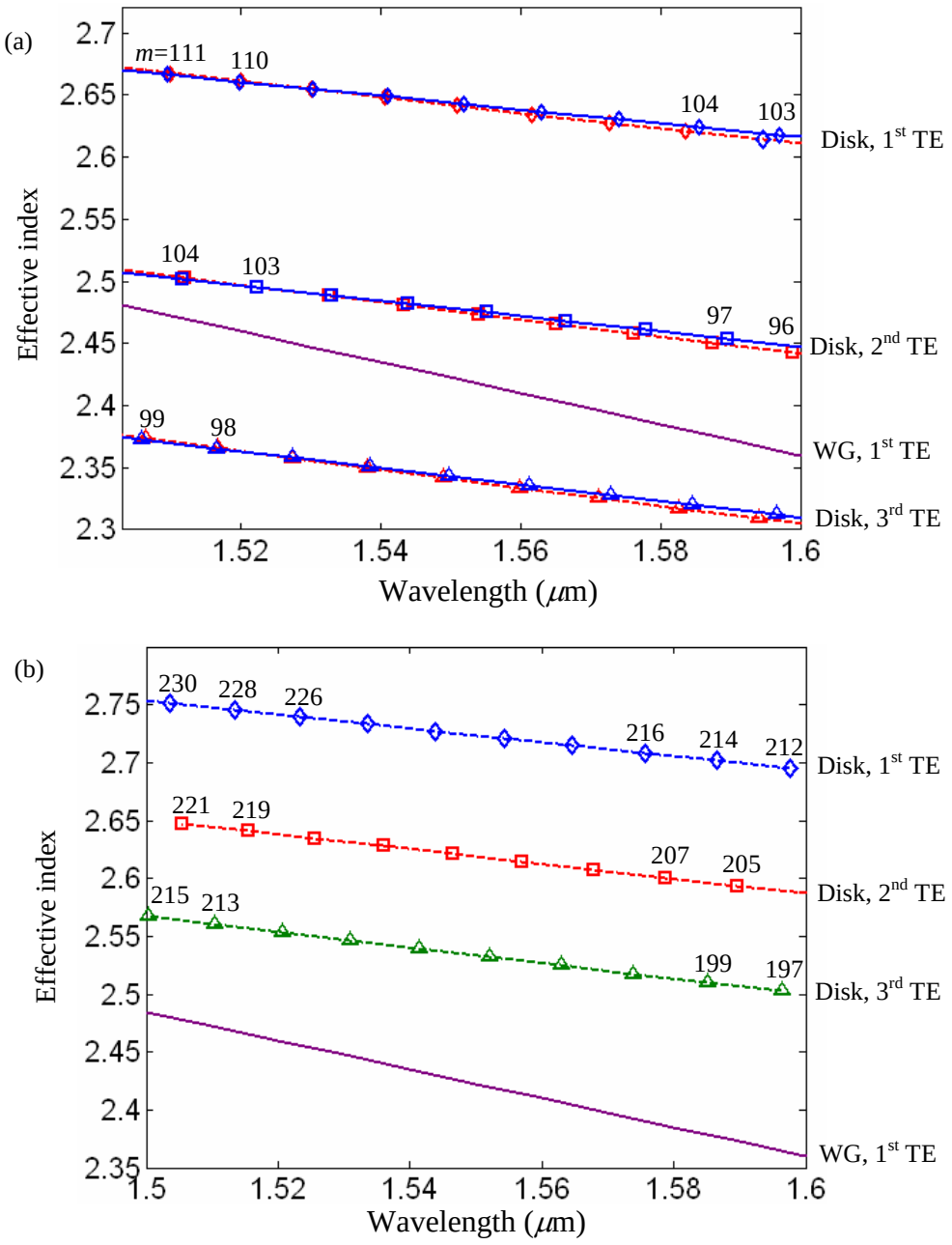

Fig. 2.13: (a) Effective indices of 1st, 2nd, and 3rd radial quasi-TE modes of a microdisk resonator with a radius of (a) 10 μm and (b) 20 μm, versus wavelength. For both (a) and (b) the microdisk has a thickness of 230 nm and is seated on a SiO_2 substrate and covered by air cladding. In (a), the solid and dashed curves correspond to the effective-index method and FEM analysis, respectively, and in (b) all the simulations are based on FEM analysis. In both (a) and (b) the azimuth mode number (m) corresponding to each resonance is shown. Also, the effective index of the 1st quasi-TE mode of a waveguide with a width of 500 nm and a thickness of 230 nm is shown in both figures. For this simulation, refractive indices are the same as those used in Fig. 2.8.

discuss the behavior of the effective index of a resonator versus its size and compare it with that of a waveguide. In general, going to a larger radius microdisk resonator, the radial confinement of the mode of the microdisk is more extended inside the microdisk and less outside. As a result of this inside confinement, the effective index of the mode is larger and closer to the refractive index of bulk Si. Figure 2.13(b) shows the effective indices of the first three radial quasi-TE modes of a microdisk with a radius of 20 μm and compares them with those of a ridge waveguide with a width of 500 nm. As seen from this figure, the effective index of the waveguide is smaller than that of the first three radial modes of the microdisk, whereas it is larger than that of the 3rd order radial mode of the 10 μm radius microdisk, as shown in Figure 2.13(a). Also, comparing the effective indices of the modes of the 10 μm and 20 μm microdisks shown in Figures 2.13(a) and 2.13(b), it is seen that the effective index of the modes of the larger disk is larger. In general, it is important to know the trend of the variation of the effective index of a resonator versus its radius. Figure 2.14 shows this trend for the first three radial quasi-TE modes of a microdisk resonator with different diameters. Also, the effective index of the fundamental quasi-TE mode of a microring resonator with a ring width of 500 nm[16] is shown in this figure. The simulations of Figure 2.14 were for resonance wavelength of the resonators that existed in a wavelength range of 1550 ± 20 nm[17].

[16] In many practical cases, for a thickness of 230 nm, choosing a width of 500 nm for a microring or a waveguide to have low loss is reasonable.

[17] As seen from Fig. 2. 14, going to smaller radii modes, the higher-order modes become strongly radiative and as a result their effective indices have not been calculated (e.g., the 3rd order radial

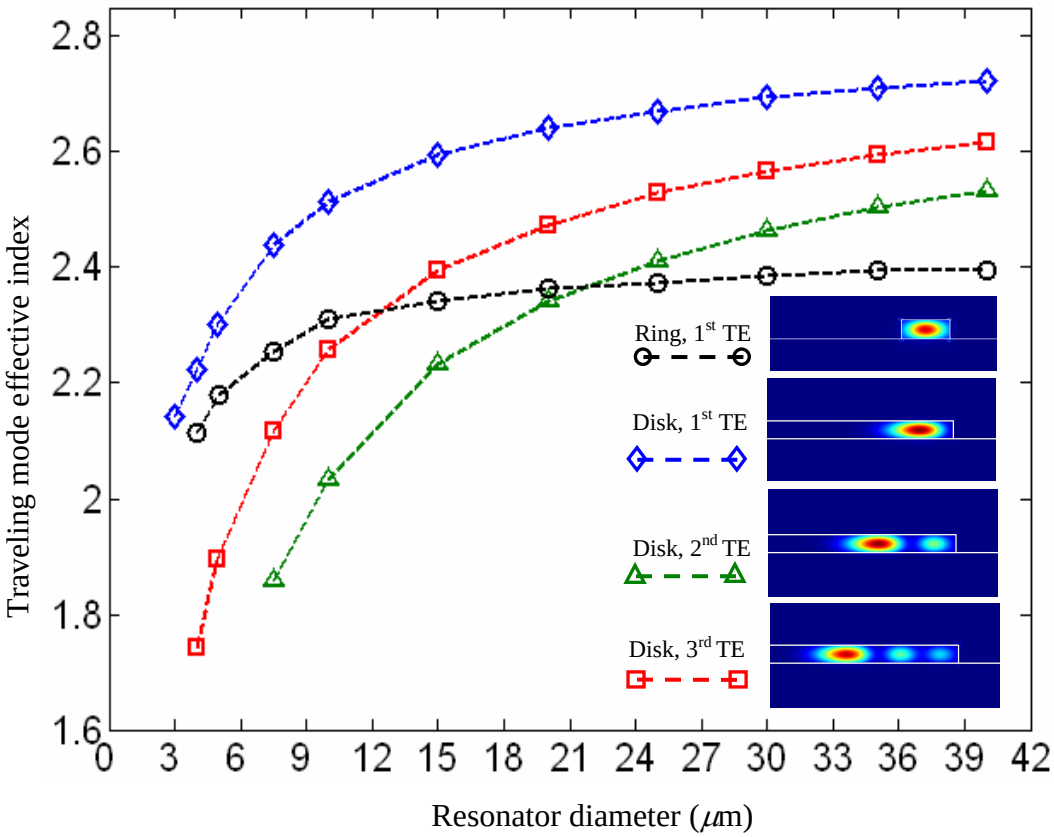

Fig. 2.14: Calculated effective index of the first three radial TE modes of a Si microdisk resonator and the fundamental TE mode of a microring resonator versus their outer diameters, as shown by different markers and colors and specified in the figure. All resonators have a thickness of 230 nm and are seated on a SiO_2 substrate and covered by air cladding. The width of the microring is also 500 nm. For both the microdisk and microring, the effective index at the external radius was calculated. The inset shows the cross section of the electric energy density for the 1st TE mode of the microring with an external radius of 10 μm, as well as for the 1st, 2nd, and 3rd radial TE modes of a microdisk with a radius of 10 μm. All the simulations were for the resonance wavelength that existed in a range of 1550±20 nm.

All the effective indices were calculated at the external radius of the resonator [18]. From Figure 2.14, it is seen that for a microdisk with any radius, the effective index of the 1st radial mode is the highest, and when going to smaller radii, the effective

mode for a microdisk with a diameter ~ 4 μm is strongly radiative and its effective index is not shown in Fig. 2.14).

[18] A microring has internal and external radii. For a microdisk, the external radius, in this context, means the microdisk diameter.

index becomes smaller. Also, as shown in Figure 2.14, going to larger radii, the effective index of the microring has much less variation compared to that of the microdisk. In fact, for larger radii, the effective index of the microring approaches that of a waveguide with the same width and thickness. However, in order to accurately compare the effective index of a microring and a waveguide of the same width, the effective index of the microring at the middle of its width has to be calculated. Figure 2.15 shows the details of the effective index of a microring resonator versus its external diameter. The effective indices in this figure were calculated at the external radius (dashed curve) and at the middle of the width of the microring (solid curve). The inset of Figure 2.15 shows the cross section of the electric energy density profile for the 1^{st} quasi-TE mode of the microring with an external radius of 10 μm. At larger microring diameters, the effective index of the microring at its center is almost the same as that of the waveguide with the same width and thickness (The effective index of the waveguide is shown in Figure 2.15 by the red horizontal line). However, at smaller microring diameters, the effective index of the microring has a large variation with the diameter, and as result, a small microring cannot be well approximated with a waveguide.

Another important parameter is the FSR of a resonator. Figure 2.16 shows the variation of the FSR of the 1^{st} and 2^{nd} quasi-TE radial modes of a microdisk resonator versus its diameter. As seen from this figure, FSR increases by decreasing the resonator diameter. This is evident from Equation (2.21), where the FSR of a mode is inversely proportional to its traveling length (and correspondingly, the

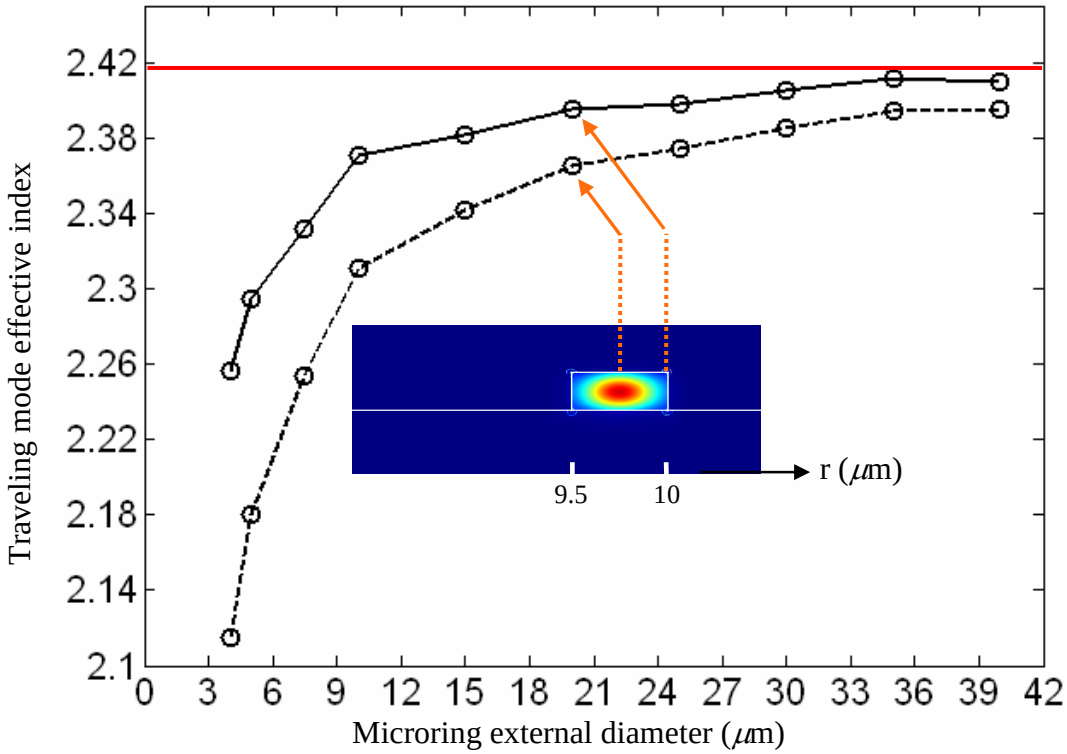

Fig. 2.15: Calculated effective index of the fundamental quasi-TE mode of a microring resonator versus its external diameter at two radial distances corresponding to the external radius (solid curve) and the middle of the ring width (dashed curve). For all the simulations the microring has a thickness of 230 nm and a width of 500 nm, and is seated on a SiO_2 substrate and covered by air cladding. The inset shows the cross section of the electric energy density profile for the 1st quasi-TE mode of a microring with an external radius of 10 μm (Also the effective indices of this resonator corresponding to the external radius and the middle of the ring are specified by arrows). The red line shows the effective index of the waveguide with a width of 500 nm and a thickness of 230 nm at the wavelength = 1550 nm. For all the microring simulations the effective index was calculated for one of the resonance wavelengths (λ_0) that existed in a range of 1550±20 nm (At larger diameters (>40 μm), resonance wavelength λ_0 = 1550±2.5 nm was available for the resonator).

diameter). Also, it can be seen from Figure 2.16 that the FSRs of the 1st and the 2nd radial order modes are almost at the same level, and at larger radii, they are even closer to each other. This is because at larger radii, the radial distribution of the mode of a microdisk extends more toward the inside and less to the outside.

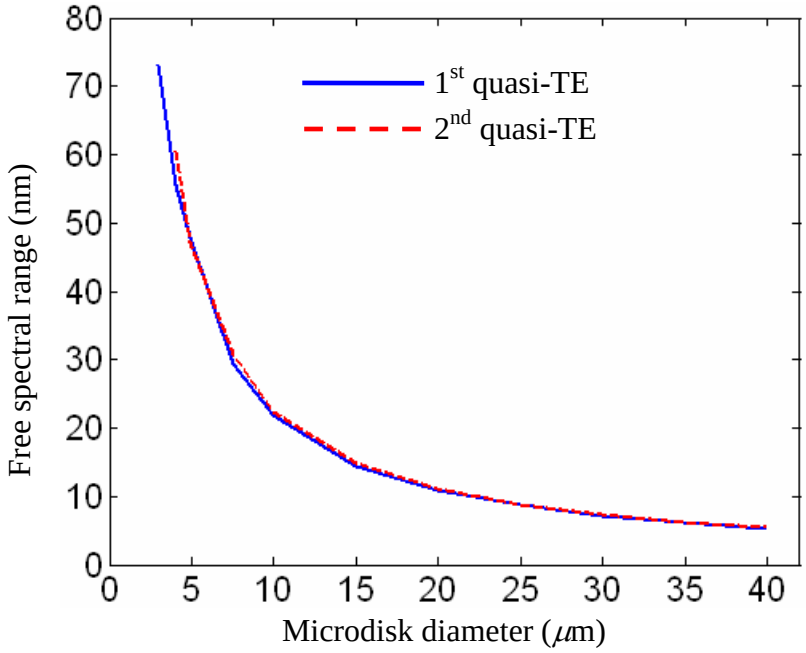

Fig. 2.16: Calculated FSR of the 1st and the 2nd radial quasi-TE modes of a Si microdisk resonator versus its diameter. All the simulations are for resonance wavelengths that exist in a range around 1550 nm. The microdisk has a thickness of 230 nm, and is seated on a SiO_2 substrate and covered by air cladding.

Therefore, there is a weaker interaction of the mode with the edge of the microdisk. As a result of this weak interaction, the microdisk mode sees less structural dispersion and consequently, the FSR values of different modes are closer to each other.

The mode volume of the resonator, as discussed before, is another important parameter that has to be obtained. The radial and vertical confinements of a mode, as well as the resonator traveling length (which is proportional to the radius), determine the energy localization and mode volume of the resonator. The vertical mode confinement is controlled by the thickness of the resonator. For resonators with the same thickness but different radii, the vertical confinement is almost at the same level. The radial confinement of the resonator mode, however, is dependent on

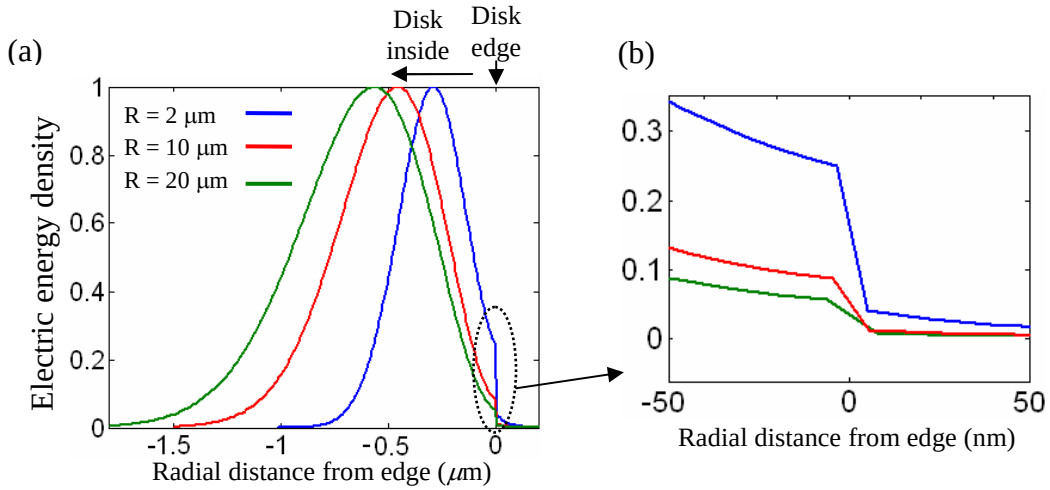

Fig. 2.17: (a) Radial distribution of the normalized-to-peak electric energy density u_E of the 1st order radial quasi-TE mode for Si microdisk resonators with a thickness of 230 nm and different radii R =2 μm, 10 μm, and 20 μm, as specified in the figure. The point 0 in the horizontal axis corresponds to the position of the edge of the microdisks. All plots are for the variations of u_E across a line in the radial direction and passing through the middle of the microdisk thickness (e.g., see the dashed line in Figure 2.12(h)). (b) A zoom view of the variation of the energy at the edge of the microdisk.

the resonator radius. Figure 2.17(a) shows the radial confinement of the electric mode energy density of the 1st order radial quasi-TE mode for a Si microdisk resonator with a thickness of 230 nm and different radii of 2 μm, 10 μm, and 20 μm. As seen from this figure, for smaller radii, two phenomena for the mode energy occur: 1) it is more localized in the radial direction and 2) it is pushed to the edge of the resonator. The shift of energy distribution to the edge of the microdisk increases the interaction of the energy with the disk sidewall, which is exposed to fabrication imperfection. Therefore, we expect to have a lower Q for smaller resonators. In addition, as shown in Figure 2.17(b), the push of the energy to the resonator edge causes more energy leakage to the outside of the resonator in the radial direction. As a result, the radiation leakage increases. However, the side coupling of a smaller

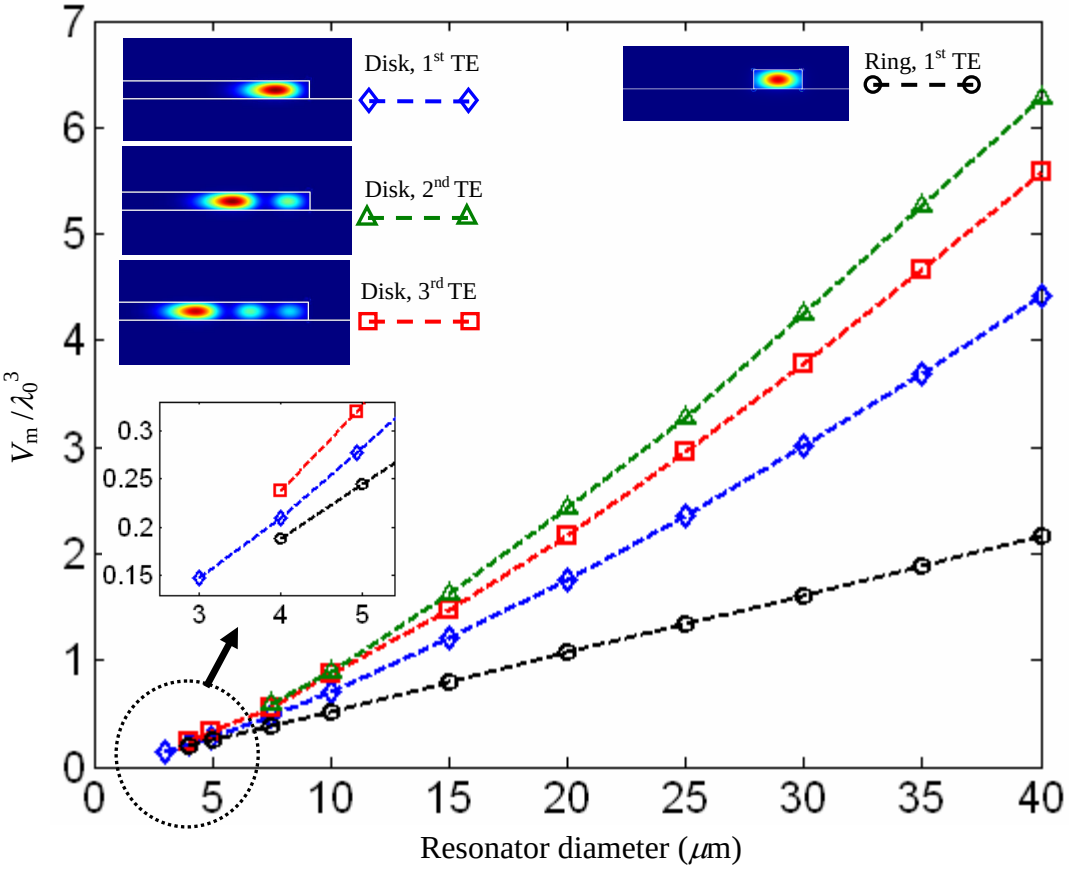

Fig. 2.18: Calculated normalized mode volume (V_m/λ_0^3) of the first three radial quasi-TE modes of a Si microdisk resonator, as well as the one for the fundamental quasi-TE mode of a microring resonator versus their outer diameters, as shown by different markers and colors and specified in the figure. Both resonators have thickness of 230 nm, the substrate is SiO_2, and cladding is air. The microring width is 500 nm. For all the simulations, the mode volume was calculated for one of the resonance wavelengths (λ_0) that existed in a range of 1550±20 nm.

resonator to another waveguide or resonator can be stronger, as the extension of the resonator energy to the outside (as shown in Figure 2.17(a)) is larger for smaller resonators. More quantitative results on coupling are discussed in chapter 3.

Figure 2.18 shows the variation of the mode volumes of the 1st, 2nd, and 3rd order radial quasi-TE modes of a Si microdisk as well as the one for the fundamental quasi-TE mode of a Si microring resonator (with a width of 500 nm) versus their

external diameters. All these resonators have a thickness of 230 nm and are on a SiO_2 substrate and covered by air. As seen from Figure 2.18, for a microdisk, the mode volume of the 1st order radial mode is the smallest compared to higher-order radial modes[19]. For the same external diameter, the mode volume of a microring (in which the presence of two sidewalls has resulted in more field confinement) is smaller than that of the modes of the microdisk. At smaller diameters, the ratio of the mode volumes of the modes of the microdisk and microring approaches one, especially for the 1st quasi-TE modes of the microdisk and microring. This can be simply explained through what we observed in Figure 2.17, where at smaller radii, the radial confinement of the mode energy was smaller and more localized toward the edge of the microdisk. In other words, in a microdisk, when going to smaller radii (i.e., ~1.5 μm), the effective radial width of the mode energy becomes smaller and is comparable and almost at the same level as the one for a microring with the same radius and a width > 500 nm. In addition, by adjusting the radii of the microdisk, higher-order radial modes can be strongly pushed to cut-off, while the 1st radial mode is strongly confined. This can be seen in Figure 2.19 by comparing the radial distribution of the normalized magnitude of the radial electric field $|E_r|$ of the 1st and 2nd radial quasi-TE modes of a microdisk resonator with a radius of 1.94 μm and a thickness of 230 nm (which is seated on an oxide substrate and covered by an oxide cladding). As shown in this figure, for such a microdisk with the mentioned

[19] For smaller radii, i.e., less than 5 μm, the 3rd radial mode of the microdisk showed strong radiation; as a result its mode volume has not been calculated. In general, at smaller microdisk radii, higher radial order modes approach the radiation cut-off.

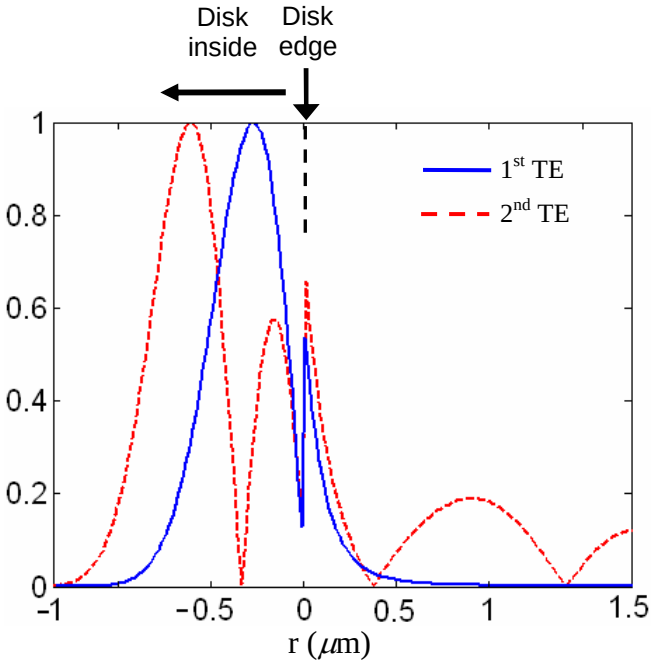

Fig. 2.19: Radial distribution of the normalized magnitude of the radial electric field $|E_r|$ of the 1st and the 2nd order radial TE modes, as specified in the figure, for a Si microdisk resonator with a thickness of 230 nm and a radius of R =1.94 μm. Both cover and substrate are oxide with a refractive index of 1.444, and the refractive index of Si is 3.475. The point 0 in the horizontal axis corresponds to the edge of the microdisks. All plots are across a line in the radial direction and passing through the middle of the microdisk thickness.

dimensions, the 1st radial mode is strongly confined while the 2nd radial mode is strongly radiative. From this discussion, we conclude that for microring resonators with small radii, e.g. r~1.5-2.5 μm, a threshold for the width of the microring can be found such that the 1st radial mode has almost the same mode volume as that of the 1st radial mode of a microdisk and the higher-order modes of the microring can be forced to the cut-off regime by two facts: (1) the small radius of the resonator pushes the higher-order radial modes to radiate and leak, and (2) the internal radius of the resonator restricts the presence of the higher- order modes by forcing them to the radiation. Such a microring resonator, which is an intermediate architecture

between a microdisk and a conventional microring, can be called a microdonut structure, as shown in Figure 2.5. In a microdonut, the 1st order radial mode has minimal interaction with the internal sidewall of the donut, compared to the external sidewall, which has a strong interaction with the mode. The advantages of a microdonut can be summarized as follows:1. It has a very small mode volume in the same level as a microring or a microdisk.2. Only one of the sidewalls (external sidewall) has strong interaction with the mode energy, and as a result, the fabrication imperfection only at the external sidewall impacts the Q of the resonator.3. The inner sidewall can be adjusted for hyper fine tuning of the resonance wavelength, while the external sidewall, because of its strong interaction with the mode, can be adjusted for the coarse tuning of the resonance wavelength.4. Reducing the external radius pushes the higher order modes to the cut-off regime, and adjusting the internal radius can further force these modes to the cut-off. In this manner, the 1st order mode can still remain high Q with minimal interaction with the inner sidewall and, as mentioned, with the same level of mode volume as that of a microring or microdisk of the same radius.

2.4 Practical Issues that Impact the Q of Si Resonators in a SOI Platform.

In a SOI platform, as shown in Figure 2.2, an actual Si TWR structure sits on an oxide substrate (which is also called the BOX layer). In order to realize a high Q silicon resonator in such a platform, some considerations regarding the material properties of silicon as well as the thickness of the underneath oxide substrate need to be taken into account. The total Q of a resonator is a combination of the intrinsic

radiation Q (or Q_{rad}) of the resonator and all other non-idealities (including absorption and imperfections), which can be expressed as

$$\frac{1}{Q_{total}} = \frac{1}{Q_{rad}} + \sum \frac{1}{Q_{non-idealities}} . \tag{2.47}$$

In the following, the impact of material absorption and the substrate (and its thickness) on the Q of the resonator are discussed and compared. In addition, other non-idealities are briefly discussed below.

2.4.1 Bulk Material Absorption of Silicon and its Impact on Q

Silicon as a semiconducting material has optical absorption, which degrades the Q of the resonator. The optical propagation loss (or ohmic loss) in bulk silicon, which is the result of this absorption, is determined as [44]

$$\alpha_b = 8.5 \times 10^{-18} N + 6 \times 10^{-18} P \ \ (cm^{-1}) , \tag{2.48}$$

where N and P are the density of free electrons and holes (in cm^{-3} unit). Corresponding to this bulk propagation loss, a bulk absorption Q (or Q_b) can be defined for the resonator, which is inversely proportional to α_b (as seen in Equation (2.27)) and independent of the resonator radius[20]. The bulk absorption loss in commercial SOI wafers can be found through their DC resistivity (ρ_0)[21], which is given in their datasheet and is inversely proportional to the density of free carriers[22]. The value of the DC resistivity of SOI wafers provided for low-loss photonic

[20] $Q_b = 2\pi n/(\lambda_0 \alpha_b)$ with n and λ_0 as the refractive index of silicon and wavelength, respectively.
[21] In silicon, the AC response of resistivity (using the Drude model) is $\rho = \rho_0 (1\text{-}i\omega\tau)$, where τ is electron relaxation time (which is abut 0.77 ps for electrons in a bulk Si).
[22] For an N-doped silicon, ρ_0 is related to free electron density (N) as $\rho_0 = m^*/(\tau e^2 N)$, where e is electron charge and m^* is effective electron mass ($m^* = 0.26 m_0$ with m is free electron mass).

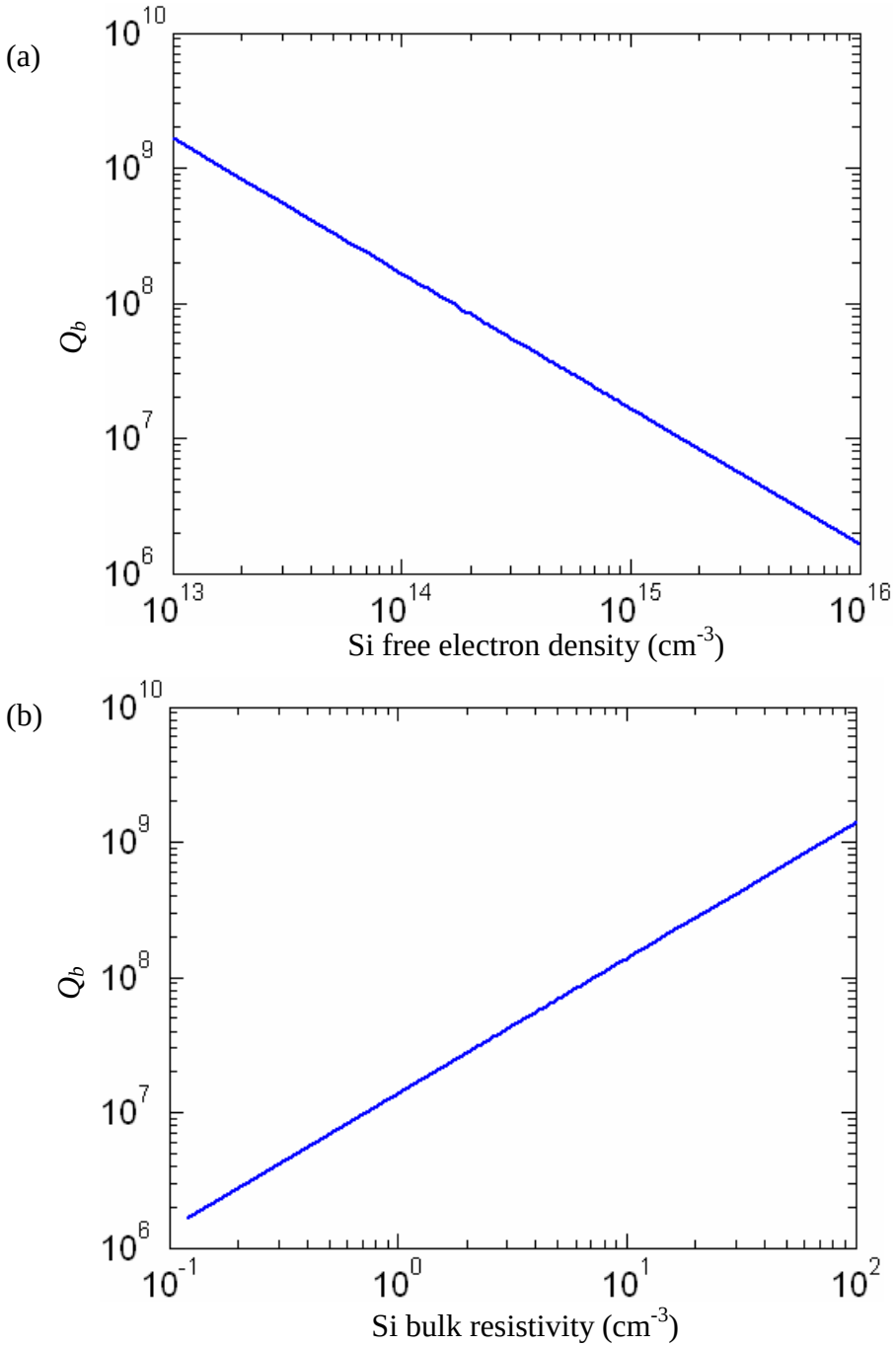

Fig. 2.20: Variation of bulk absorption Q (or Q_b) of an N-doped Si TWR resonator versus (a) free electron density and (b) resistivity.

applications is in the range of ρ_0 = 1-20 Ω–cm. Figures 2.20(a) and 2.20(b) show

the variation of the Q_b for an N-doped Si resonator versus the density of free electrons and the resistivity of the Si, respectively. As shown in these figures, for a typical DC resistivity of ρ_0= 10 Ω–cm (which corresponds to a free electron density of 1.2×10^{14}), $Q_b = 1.4\times10^8$ (which corresponds to a propagation loss of $\alpha = 0.001$). In other words, the bulk absorption has put an upper limit on the total Q of a resonator when no other non-ideality exists. However, depending on the size of the resonator, the ultimate Q may be limited by radiation (to the substrate or cladding) rather than by absorption, which is discussed in the following.

2.4.2 Impact of SiO_2 BOX Layer on Q

To achieve a high Q microdisk resonator, a tradition in the past has been to undercut the resonator to obtain a larger refractive index contrast between the resonator and the surrounding media to reduce the radiation. Figures 2.21(a) and 2.21(b) show the schematics of an undercut versus non-undercut Si microdisks in a SOI platform. While undercutting a microdisk resonator is relatively easy, using an undercut waveguide for coupling light to such an undercut resonator is not trivial. For mechanical stability and low-loss performance of the integrated photonic structures, it is highly desirable to keep the SiO_2 layer underneath the Si structures intact. However, it is important to assess the impact of the SiO_2 substrate on the Q of the resonator. For this purpose, a detailed theoretical study on the effect of the oxide substrate on the Q of the microdisk resonator was performed. Figure 2.22 shows the variation of the intrinsic radiation Q of the 1st radial quasi-TE mode of a Si microdisk resonator versus its radius. The simulation results for three radii (1.53, 2,

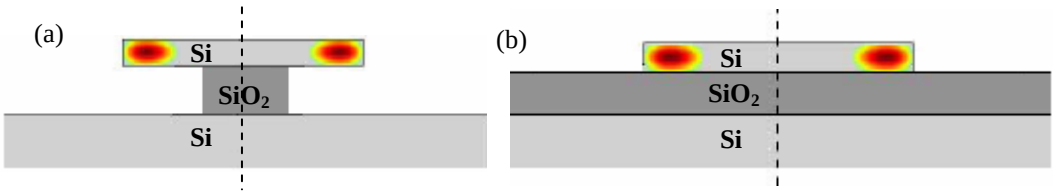

Fig. 2.21: (a) Cross section of the structure of (a) an undercut Si microdisk resonator and (b) a non-undercut Si microdisk resonator in a SOI platform. The energy profiles of the 1st radial TE mode inside the resonators are shown.

and 2.5 μm) are shown in Figure 2.22. The thickness of the microdisk is 230 nm and the thicknesses of the substrate and cladding are extended to infinity. For this simulation, as specified in the figure, three cases have been considered (cases of interest for many studies and applications): 1) both the cladding layer and the substrate are air, 2) the cladding layer is air and the substrate is oxide, and 3) both the cladding layer and the substrate are oxide. For each case, the azimuthal mode number and the resonance wavelength have been specified in the figure. In order to have a decent comparison between the results of different cases, the simulations for the three cases were performed for resonance wavelengths close to each other and around 1550 nm. Also, the bulk absorption Q of a silicon resonator for a typical resistivity larger than 10 Ω-cm is shown by the gray region in Figure 2.22. As shown in the figure, when both substrate and cladding are air, the value of Q_{rad} for the resonator with a radius of 1.53 μm is very large and close to the absorption limit (gray region) of the resonator. By going to larger radii, the Q_{rad} almost exponentially increases. As a result, when both the substrate and the cladding layer are air and the resistivity of silicon is 10 Ω-cm, the Q_{rad} of resonators with a thickness of 230 nm and small radii (~ 2 μm) is not limited by radiation, but limited by absorption and

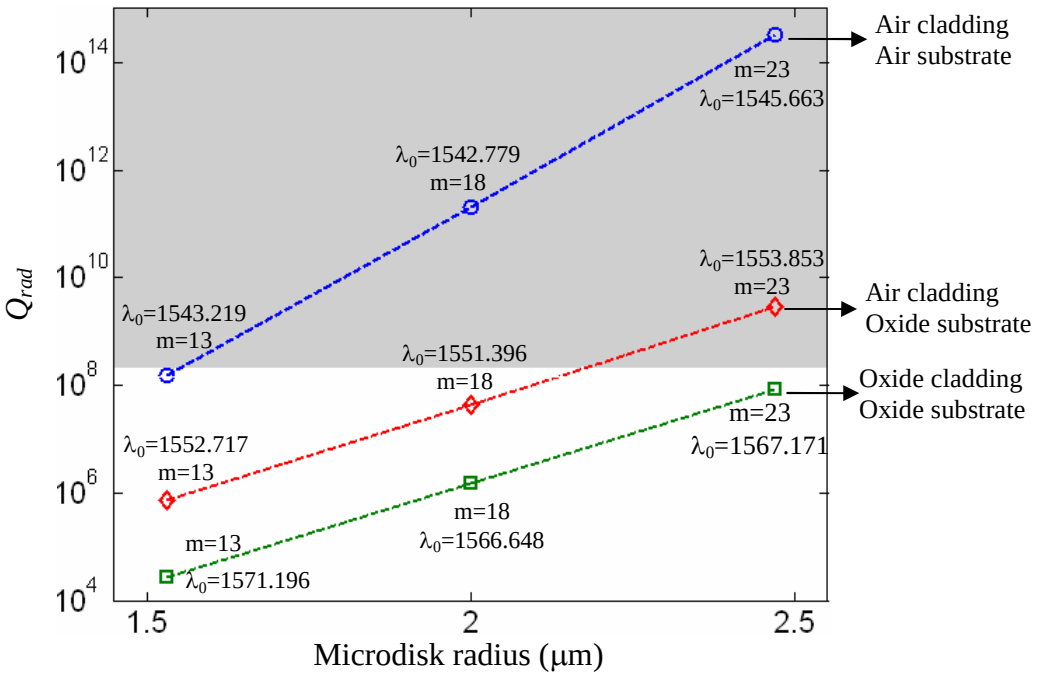

Fig. 2.22: Variation of the intrinsic radiation Q of a Si microdisk resonator versus its radius. The microdisk has a thickness of 230 nm and its substrate and cladding are been specified in the figure. The simulation results for three radii (1.53, 2, and 2.47 μm) are shown. For this simulation the refractive indices of Si and oxide were 3.475 and 1.444, respectively. For each resonance, the corresponding azimuth mode number (m) and resonance wavelength (λ_0) in nanometer are specified. Also, the bulk absorption Q of a silicon resonator for a typical resistivity larger than 10 Ω-cm is shown by the gray region.

other non-idealities. When either substrate or cladding (or both) is oxide, the Q_{rad}, as shown in Figure 2.20, is considerably lower, which is because of the lower refractive index contrast between the resonator and the surrounding media (which results in stronger radiation). In this regime, for small resonators, radiation has put a limit on the Q compared to the absorption (other non-idealities are ignored for this discussion). However, by going to larger radii, Q_{rad} exponentially increases, and as a result, it is not the main limiting factor in reducing the Q. Therefore, depending on

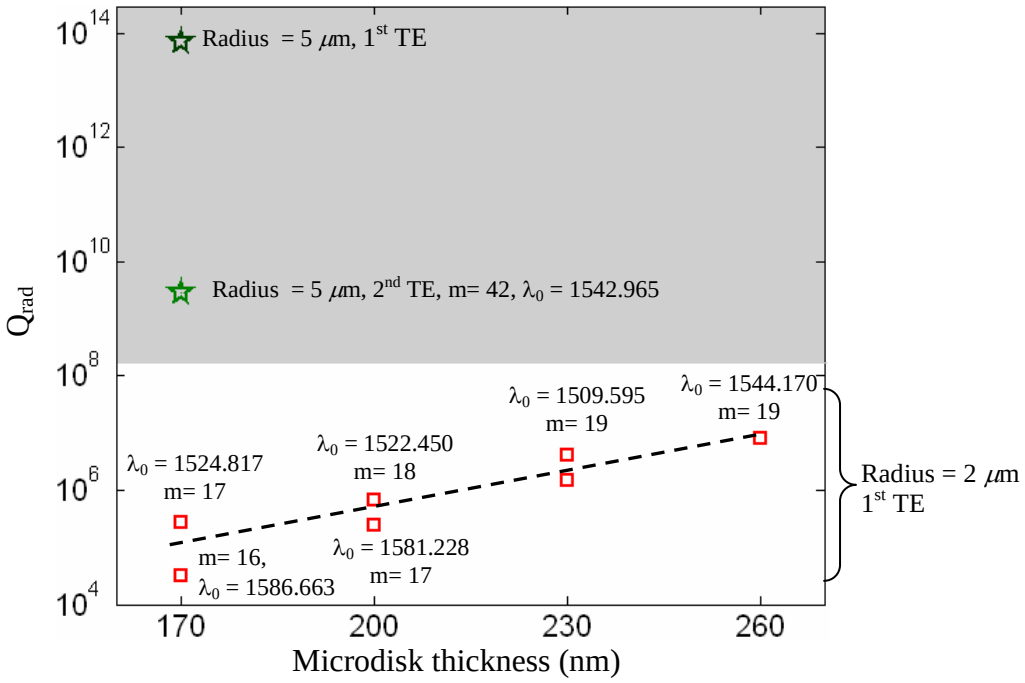

Fig. 2.23: Calculated intrinsic Q of a Si microdisk resonator with a radius of 2 μm versus its thickness (as shown by red square markers). The simulations were performed for thicknesses of 170, 200, 230, and 260 nm. Also, the simulation results for a microdisk with a radius of 5 μm and a thickness of 170 nm are shown (green pentagon markers). For each resonance the corresponding azimuth mode number (m) and resonance wavelength (λ_0) in nanometer are specified. For all the simulations, the cladding and substrate are both oxide. The refractive indices of Si and oxide were considered 3.475 and 1.444, respectively. Also, the bulk absorption Q of a silicon resonator for a typical resistivity larger than 10 Ω-cm is shown by the gray region.

the required Q, the size of the resonator has to be adjusted in order for the Q not to be limited by radiation.

Another parameter that can affect the Q_{rad} is the resonator thickness. Figure 2.23 shows (the red square markers) the variation of Q_{rad} versus the thickness for a microdisk resonator with a radius of 2 μm. The substrate and cladding are both oxide, with a thickness of infinity. As shown in this figure, for some of the thicknesses, the Q_{rad} has been calculated for two consecutive resonance wavelengths

(which correspond to two consecutive azimuthal mode numbers). From Figure 2.23, it is seen that at smaller thicknesses (such as 170 nm), a large difference exists between the Q_{rad} of two consecutive azimuthal mode numbers. This difference is because of the large FSR of this small resonator, which is comparable to the thickness of the resonator. From Figure 2.23, it is seen that by reducing the thickness, the Q_{rad} dramatically decreases. In fact, using the effective-index approach, we can interpret the results as follows. For a thinner resonator, the effective index of the slab is smaller, and as a result, when going to the 2D picture, the index contrast between the resonator and the regions surrounding the resonator is lower. However, by increasing the radius of the resonator, the effect of thinning the resonator on the Q can be compensated. This is shown in Figure 2.23 for the Q_{rad} of the 1st and 2nd radial quasi-TE modes of a microdisk with a radius of 5 μm and a thickness of 170 nm, as specified by pentagon markers in the figure.

Finally, the effect of the thickness of the SiO_2 BOX layer on the Q_{rad} of a resonator has to be investigated. Depending on the size of the resonator, the extension of the resonator mode to the substrate is different. As a result, a different substrate thickness is required in each case to provide a Q_{rad} that is more than the limit, which is ruled by the absorption and other non-idealities. Figure 2.24 shows the variation of the Q_{rad} of a microring resonator (which is a general case of a microdisk resonator) versus the thickness of the BOX layer. The inset shows the cross section of the waveguide that forms the microring. The radius of the ring is large enough so that the Q_{rad} of the microring can be obtained from the propagation

loss of the waveguide[23]. The simulation was performed for different widths and thicknesses of the microring, and different plots for Q_{rad} versus the thickness of the oxide BOX layer were obtained. As seen from the figure, by adjusting the thickness of the BOX layer, the Q_{rad} of the resonator can go above the absorption limit (shown by the gray region). For many applications, a thickness of 1 μm is enough so that the substrate leakage is not a limiting factor. This is because, in practice, the Q of a resonator is limited by the imperfections and non-idealities in the fabrication, which is usually much less than Q_b or Q_{rad}[24]. As an example, as shown in Figure 2.24, for a microring with a width of 500 nm and a thickness of 170 nm, when the BOX layer thickness is 1μm, Q_{rad} ~ 30 millions. This is much larger than the Q that we can obtain in practice for this microring (with the above dimensions) with the current fabrication technology[25]. Therefore, a 1 μm thickness for the box layer is more than enough. In addition, for applications that we are interested in, in thicker resonators (where the field is more vertically confined in the resonator compared to a thickness of 170 nm) the leakage to the substrate is lower and Q_{rad} is also higher and can be above the absorption limit. From Figure 2.24 we see that we can use a BOX layer thinner than 1 μm if the Q of a resonator (or propagation loss of a waveguide in that platform) defined by fabrication imperfections is much lower than what is defined by the radiation through the BOX layer.

[23] It can be simply shown that $Q_{rad} = 0.5 \times \text{real}(n_{eff})/\text{Imag}(n_{eff})$, where neff is the effective index of the mode propagating in the waveguide.
[24] Of course, the ultimate dream is to overcome all these imperfections and approach the ultimate theoretical Q of the resonator which is limited by Q_b and Q_{rad}.
[25] The Q of this microring is limited to tens of thousands.

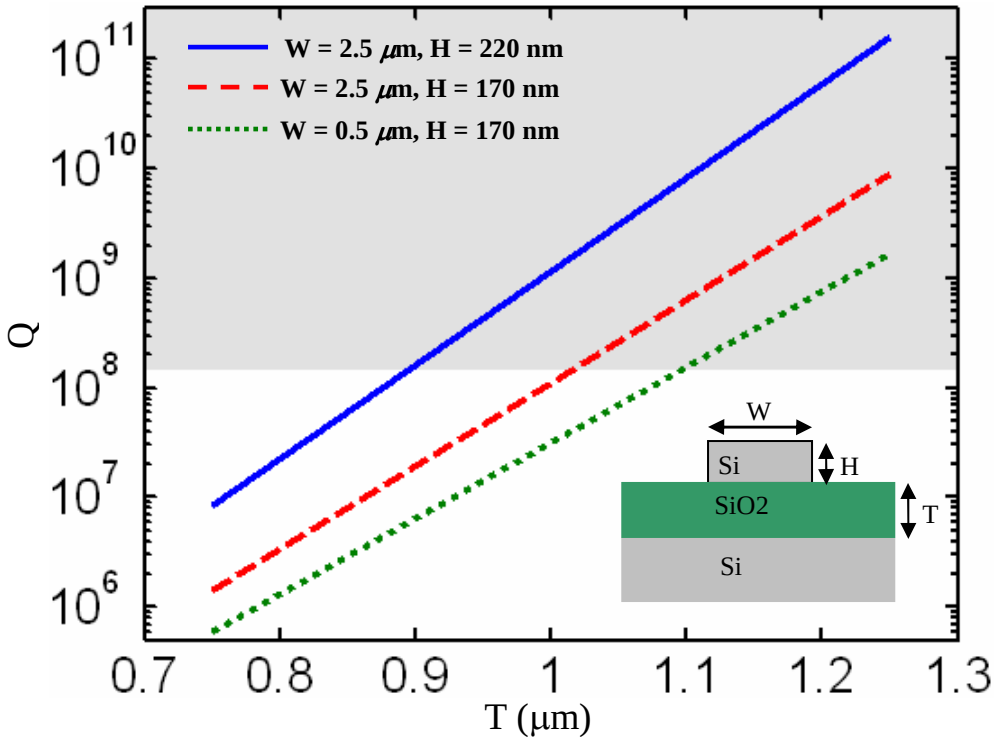

Fig. 2.24: Variation of the Q of a TWR versus the thickness of SiO_2 substrate in a SOI platform. The inset shows the cross section of the Si waveguide (that forms the TWR) in a SOI platform. The resonator radius is large enough so that the intrinsic Q of the resonator is limited by the energy leakage to the underlying Si layer. Also, the bulk absorption Q of a silicon resonator for a typical resistivity larger than 10 Ω-cm is shown by the gray region.

A reason to choose a thinner BOX layer is that thermal conductivity of the resonator is improved and heat can be transferred more quickly from the resonator to the underlying bulk Si layer in the SOI wafer. This is important in higher-power applications of the resonator, in which resonator temperature increases and thermo-optic effects can shift the refractive index and, correspondingly, the resonance wavelength of the resonator, which leads to an instability in the resonator functionality. Additional results about the thermal properties of the resonators are discussed in chapter 6.

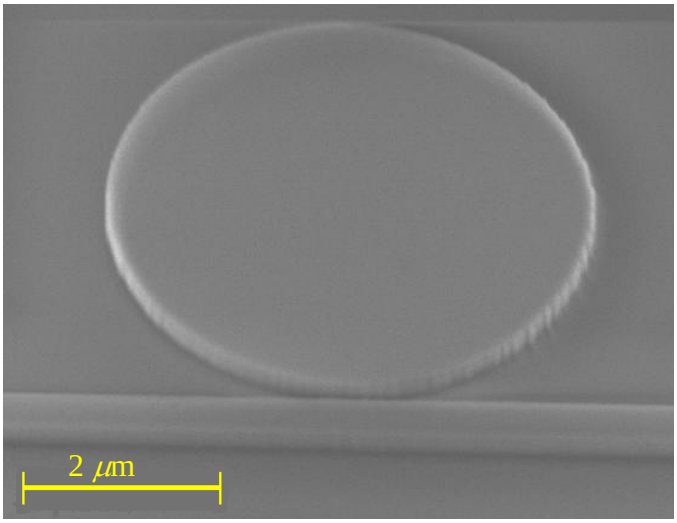

Fig. 2.25: Scanning electron microscopy (SEM) image of a Si microdisk resonator that has strong roughness at its sidewall as a result of fabrication imperfection. The microdisk is side coupled to a Si ridge waveguide.

2.4.3 Other Non-idealities of Si Microresonator in a SOI Platform

In the preceding analysis, the structure of a microresonator was considered ideal with regard to its geometry and the only material non-ideality considered was bulk optical absorption. However, in practice, many other non-idealities in the material as well as the fabrication of the resonator exist that degrade the Q of the resonator. In the following, we describe the non-idealities and later in chapter 5, in which the experimental results are discussed, more details are presented.

2.4.3.1 Degradation of Q by Fabrication-induced Distortion in the Resonator Geometry

Fabrication of resonators includes imperfections, which distort the resonator geometry from the ideal case. Figure 2.25 shows the scanning electron microscopy (SEM) image of a Si microdisk resonator (which is side coupled to a waveguide) on

a SiO_2 substrate in a SOI platform. As seen from this figure, a fabrication imperfection has resulted in strong roughness at the microdisk sidewall. The impacts of this sidewall roughness on the modes of the microdisk are the following:

1- Coupling of the resonator mode to radiation modes through the sidewall roughness perturbation and correspondingly scattering of resonator energy to the outside (Rayleigh scattering), which results in degradation of Q.

2- Coupling and energy exchange between the degenerate clockwise and counterclockwise mode of the resonator. Similar to the coupling phenomenon between two harmonic oscillators, the resonance spectrum can show a doublet instead of a Lorentzian response. This is discussed in more detail in the next chapter.

3- Coupling of resonator modes with different radial mode orders that have accidental degeneracy or resonance wavelengths very close to each other.

4- Crystalline damage at the sidewall of the microdisk, which results in the appearance of electronic defects and surface states in the middle of the Si electronic bandgap. As a result, light absorption at the surface of the microdisk increases[26].

To investigate these predictions of Q, experimental results for microdisk resonators with different sizes fabricated on a SOI wafer are presented in chapter 5.

[26] It is noted that optical surface absorption at the top and bottom surfaces of the microdisk exists. This is because the crystal has been terminated by surfaces at the top and the bottom. However, during fabrication, which is discussed in chapter 4, the sidewall of the microdisk is directly exposed to the fabrication imperfection and stronger more crystalline damage and non-idealities are observed at the sidewall.

2.5 TWR Microresonators Compatible with Active Integration

Controlling the refractive index of silicon with free carriers provides an opportunity to dynamically tune the resonance wavelength of Si-based resonators. For this purpose, TWR Si resonators can be modified to be integrated with P-N junctions for carrier injection into the resonator. Figure 2.26 shows the cross section of a microdonut resonator with external and internal radii of 2.5 and 1.2 μm. In this resonator architecture, a thin silicon pedestal layer is present at the interface between the resonator and the underlying SiO_2 substrate. The presence of this layer enables the fabrication of a P-N junction at the proximity of the resonator by ion implantation and doping of two regions as P-doped and N-doped, as shown in Figure 2.26. However, increasing the thickness of the pedestal can cause strong radiation and degradation of the Q. A 40 nm thickness for the pedestal is enough to fabricate a P-N junction [13]. Table 2.1 shows the resonance properties of this resonator architecture with a 40 nm pedestal thickness and oxide cladding. The simulation was performed for two different radii. As observed from this table, the presence of the pedestal has reduced the intrinsic Q. However, at the larger radius, an intrinsic Q larger than the absorption limit can be obtained, as observed for the radius of 5 μm. Although the intrinsic for a radius of 2.5 μm is below one million, for many applications, this Q or even one order below it can be satisfactory.

There are two main advantages of the pedestal microdisk: (1) the silicon pedestal reduces the thermal resistance of the microdisk, and (2) it enables the

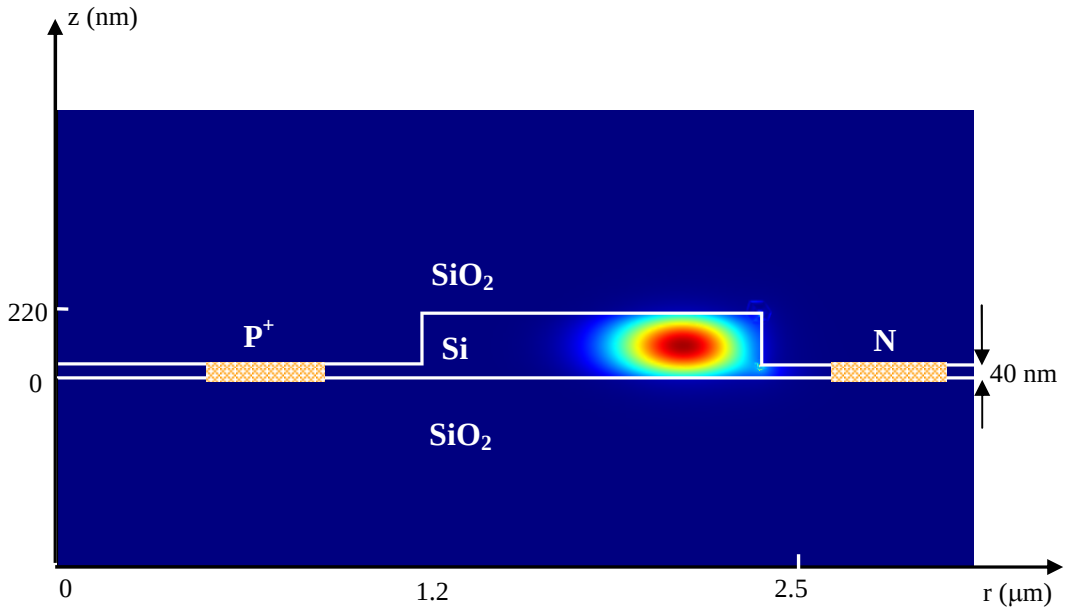

Fig. 2.26: Cross section of the electric energy of the 1st radial TE mode of a microdonut resonator with internal and external radii of 1.2 and 2.5 μm. A thin Si pedestal layer with a thickness of 40 nm is at the interface of the resonator and the underlying oxide substrate. This resonance mode has azimuth mode number m=24, resonance wavelength λ_0 = 1533.045, and Q = 4×10^5. The P-doped and N-doped regions are schematically shown at the proximity of the resonator for the purpose of injecting (removing) free carriers to (from) the resonator. The structure has an oxide cladding. For this simulation, the refractive indices of Si and oxide were 3.475 and 1.444, respectively.

integration of of the resonator with active electronic elements such as MOS transistors and P-N junctions [12,14]. These advantages make the pedestal microdisk the architecture of interest in several optical systems. For instance, in nonlinear optical applications, silicon suffers from free carriers generated by two-photon absorption. Using the pedestal microdisk architecture, a reverse-biased P-N junction can be potentially integrated with the resonator to remove the TPA-generated free carriers from the microdisk active region. In addition, as will be investigated in this research, the presence of the pedestal layer adds another degree

Table 2.1: Resonance properties (radial order, azimuth mode number, resonance wavelength, and Q) of a Si microdisk resonator with a thickness of 220 nm and a pedestal thickness of 40 nm. The substrate and cladding are both oxide.

Radius	Radial order	m	λ_0	Q
2.5	1^{st}	24	1531.045	4×10^{5}
2.5	2^{nd}	20	1533.397	480
5	1^{st}	50	1570.204	2×10^{12}
5	2^{nd}	45	1565.500	1.6×10^{8}

of freedom to control the coupling strength between the resonator and the waveguide by adjusting the thickness of the pedestal layer.

2.6 Chapter Summary

In this chapter, we presented the fundamental physical properties of dielectric TWR resonators and reviewed the properties of planar microdisk, microring, and racetrack resonators as promising TWR architectures in a SOI platform.

We proposed and implemented a new full-vectorial 3D electromagnetic modeling technique based on FEM for analyzing axially symmetric TWR resonators. The method was verified by solving highly symmetric structures, such as a microsphere, that have analytical solutions. In addition, the results from this technique were compared with those from the effective-index method, which was also presented in this chapter. While this vectorial method provides accurate information about all the field components as well as the resonance frequency of the mode of a resonator, it was shown that the effective-index method also provides

decent approximation for the location of the resonance frequencies of the resonator. However, the effective-index method fails to determine all the field components.

Using vectorial 3D modeling, we investigated the down-scaling of microdisk resonators by reducing their radii to achieve ultimate miniaturization and large-scale integration of many resonators, as well as to achieve small mode-volumes and large FSRs. It was shown that small microdisk resonators close to the radiation limit provide mode volumes almost at the same level as that for a microring resonator of the same radius. In addition, it was shown that at small radii, higher-order radial modes are strongly radiative, and as a result, a microdisk can be designed to support only the 1^{st} order radial mode over the entire FSR range. Compared to a microring, which has two sidewalls, a microdisk has one sidewall and therefore suffers less from fabrication imperfections. Hence, we conclude that ultra-small microdisk resonators with high Qs, small mode volumes, large FSRs, and supporting only the 1^{st} radial TE mode are achievable. In chapter 4 the fabrication and experimental results of these structures are discussed.

To assess the effect of the substrate on Q, a PML absorbing boundary condition was implemented to find the Q of the resonance modes. For both conventional and pedestal microdisk structures with the a radius even as small as 10 μm, the simulations resulted in a radiation $Q>10^{12}$ for a SiO_2 substrate with infinite thickness. Considering the effect of the finite SiO_2 substrate thickness (in the range of 1 μm), a radiation $Q>10^9$ was obtained. Therefore, it is concluded that the

ultimate bound on the achievable Q is limited mostly by fabrication limitations and other non-idealities in the device and not by radiation into the SiO_2 layer.

CHAPTER 3

COUPLING TO TRAVELING-WAVE RESONATORS

In this chapter the mode coupling to traveling-wave resonators is investigated. In general, three coupling cases are the focus of this research: 1) coupling of a TWR to a waveguide (waveguide-resonator coupling), 2) coupling of a TWR to another TWR (resonator-resonator coupling), and 3) intermodal coupling between the degenerate CW and CCW modes of a TWR (as a result of the presence of the fabrication induced perturbations[27]). In this chapter, cases 1 and 3 are investigated and case 2 is discussed in chapter 7, which concentrates on coupled-resonator structures. We first present the physical mechanism of waveguide-resonator coupling and intermodal CW-CCW coupling. Different regimes of waveguide-resonator coupling and the conditions to reach them are discussed and the impact of the CW-CCW modal coupling on the spectral response of the resonator in each regime of waveguide-resonator coupling is investigated. In what follows, the systematic engineering of a waveguide-resonator architecture to achieve different regimes of coupling is presented.

3.1. Waveguide-TWR Coupling

In the previous chapters many unique properties of planar Si TWR structures and their potential applications were introduced. In all such resonator applications, a

[27] The intermodal coupling between two modes with different radial order can occur if they have accidental frequency degeneracy or their resonance frequencies are very close to each other. This will be not discussed in this chapter, as for most of the cases, accidental degeneracy between two different radial modes is rare unless the radius of the resonator is so large that many radial family modes exists and the chance of degeneracy increases.

crucial requirement is the control of the rate of the coupling of energy into (out of) the resonator from (to) a waveguide, which is the main building block to carry the optical information on the photonic chip. In this regard, the systematic engineering of the waveguide-resonator coupling structure is vital.

In a waveguide-TWR coupling, the waveguide is either vertically seated on top of or at the bottom of the resonator [45-47], or it is laterally side coupled to the resonator [12, 19, 48, 49]. Whereas in the vertical coupling approach there is minimal lithography challenge to define the spacing between the resonator and the waveguide, challenges such as complicated fabrication with multiple fabrication steps and planarization requirements exist. On the other hand, the laterally side-coupled approach has the advantage of fewer fabrication steps while suffering from the lithography challenges associated with the fine-line spacing between the resonator and the waveguide. However, recent advances in nanolithography, especially with electron-beam lithography, have alleviated this problem.

In a waveguide-TWR coupling architecture, the strength of the coupling is determined predominantly by three conditions: 1) the modal field overlap of the resonator and the waveguide in the waveguide core, which acts as a perturbation to the resonator, 2) the interaction length between the resonator and the waveguide, and 3) the level of phase matching between the resonator mode and the waveguide mode.

Racetrack resonators, as an extension of microring structures, have been a promising solution to provide all three conditions mentioned above. In such

resonators, the use of directional couplers requires the coupling structure to be symmetrical to satisfy the phase matching over the long interaction length. We note that the amount of phase mismatch we can tolerate in this coupler is inversely related to the interaction length; otherwise, the coupling may become very weak. In addition, for a racetrack resonator with a fixed FSR, the overall roundtrip length of the racetrack needs to remain fixed. Hence, increasing the coupler length in the racetrack to enhance coupling requires reducing the bending radius of the resonator. However, using a small bend radius may dramatically degrade the intrinsic Q of the resonator due to the bend losses. In addition, the presence of a modal mismatch between the straight portion and the bent portion of the racetrack resonator can result in even more loss, which is more pronounced at smaller bend radii and dramatically reduces the Q [49]. Therefore, for applications that require very small resonator dimensions and high Q, we may be forced to employ microring or microdisk instead of racetrack resonators. For such purposes, we recently demonstrated miniaturized microdisk resonators with a radius of about 1.5 μm and $Q > 10^5$ working in a single-mode condition and forcing the higher-order mode to the radiation regime [50].

In this chapter, we systematically engineer a planar laterally coupled waveguide-TWR structure for microring, microdisk, and micro-racetrack resonators in a SOI platform to achieve the required level of coupling. Such a coupling scheme has minimum fabrication steps and is more compatible with planar fabrication. The waveguide resonator can be analyzed using coupled-mode theory (CMT) in either

the time [48, 51, 52, 53] or space approach [53-56]. Each approach has advantages in understanding different aspects of the coupling mechanism. For structures in which the coupling region is localized, the CMT in time is suitable. Examples of this case are small microring and microdisk resonators coupled to a straight waveguide. For other structures where the coupling region is long, the CMT in space provides more accurate results. An example of this case is the analysis of coupling to a racetrack resonator [57,58]. Both approaches are presented here, and using them, waveguide-resonator coupling is engineered.

3.2. Time-Domain Analysis of Waveguide-Resonator Coupling[28]

The temporal response of an isolated resonator with a lifetime τ_0 can be written as [52,53]

$$\frac{da}{dt} = (j\omega_0 - 1/\tau_0)a, \tag{3.1}$$

where a is normalized such that its squared magnitude corresponds to the resonator energy. From Equation (3.1) it can be shown that the resonator energy varies as

$$\frac{d\,|a|^2}{dt} = (-2/\tau_0)\,|a|^2. \tag{3.2}$$

Figure 3.1 shows the structure of a TWR side coupled to a straight waveguide. A waveguide source mode with an amplitude S_{in} is traveling in the forward direction (from the left to the right). S_{in} is normalized such that its squared magnitude corresponds to the power of this mode. The resonator supports two degenerate

[28] While the main equations are presented here, more details about the fundamental concepts of the time-domain theory of waveguide-resonator coupling are provided in Appendix E.

clockwise (CW) and counterclockwise (CCW) traveling modes at the resonance frequency ω_0. The forward mode of the waveguide can couple to the CW mode of the resonator. However, its coupling to the CCW mode is weak and negligible. This is because of the strong phase mismatch that exists between the forward mode of the waveguide and the CCW mode of the resonator as they propagate in opposite directions in the coupling region. The degenerate CW and CCW modes of the resonator are orthogonal to each other and as a result, they do not interchange energy unless there is considerable perturbation in the resonator, such as roughness at the sidewall of the resonator. In that case, the CW mode excites the CCW mode, and the generated CCW mode can be coupled to the backward mode of the waveguide and generate a reflection signal S_{ref} in the waveguide, as shown in Figure 3.1. However, if CW-CCW coupling now exists, S_{ref} is almost absent. In this case, time-domain coupling of the forward mode of the waveguide and the CW mode of the resonator can be presented (in the 1st order approximation) in the following set of equations:

$$\begin{cases} \dfrac{da_{cw}}{dt} = (j\omega_0 - 1/\tau_0 - 1/\tau_c)a_{cw} + \kappa S_{in} \\ S_{out} = S_{in} - \kappa^* a_{cw} \\ |\kappa| = \sqrt{2/\tau_c} \end{cases} . \qquad (3.3)$$

In Equation (3.3), a_{cw} is the amplitude of the CW mode of the resonator, κ is the coupling coefficient between the forward mode of the waveguide and the CW mode of the resonator, S_{out} is the waveguide-mode amplitude in the forward direction after the interaction with the resonator, and τ_c is the time constant of the rate of the

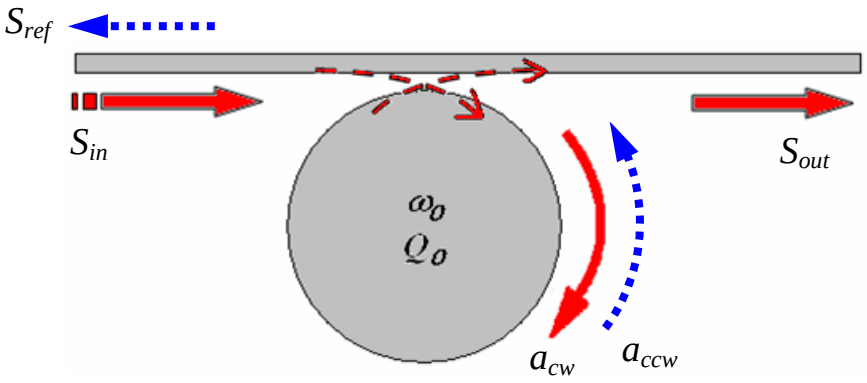

Fig.3.1: (a) Schematic of waveguide-resonator coupling for a TWR. The structure is excited by a waveguide source S_{in} from left. This source mode couples to the clockwise (CW) mode of the resonator. Interaction of S_{in} and a_{cw} results in the output waveguide amplitude S_{out}. If there is considerable perturbation in the resonator, the counterclockwise (CCW) mode of the resonator can be excited as a result of coupling to the CW mode. The generated CCW mode can couple to the backward waveguide mode and generate a reflection in the waveguide, as shown by S_{ref}. When there is no CW-CCW coupling, S_{ref} is almost absent.

energy coupling from the CW mode to the waveguide mode (which is to the forward mode). The symbol '*' in Equation (3.3) means the complex conjugate. Also, κ and τ_c are related to each other, as seen in the last expression in Equation (3.3). For more details on the derivation of Equation (3.3) see Appendix E. In this coupling scheme, we have assumed that only coupling between the resonator mode and the waveguide mode occurs and coupling to the radiation modes is negligible.

By solving Equation (3.3) in the frequency domain, the resonator CW amplitude and the waveguide transmission (which is $T = S_{out} / S_{in}$) can be obtained as

$$a_{cw}(\omega) = \frac{\kappa}{j(\omega - \omega_0) + 1/\tau_0 + 1/\tau_e} S_{in}(\omega), \tag{3.4}$$

$$T = \frac{S_{out}(\omega)}{S_{in}(\omega)} = \frac{j(\omega - \omega_0) + 1/\tau_0 - 1/\tau_c}{j(\omega - \omega_0) + 1/\tau_0 + 1/\tau_c}. \tag{3.5}$$

Similar to the intrinsic quality factor of the resonator, which is $Q_0 = \omega_0 \tau_0/2$, a quality factor for the waveguide-resonator coupling can be defined as

$$Q_c = \omega_0 \frac{\text{Re}\,sonator\ \ Energy}{Power\ \ Coupled\,to\,the\ \ Waveguide} = \omega_0 \tau_c / 2 . \tag{3.6}$$

Therefore, Equations (3.4) and (3.5) can be reformulated as

$$a_{cw}(\omega) = \frac{2\kappa / \omega_0}{j2(\omega - \omega_0)/\omega_0 + 1/Q_0 + 1/Q_c} S_{in}(\omega), \tag{3.7}$$

$$T = \frac{S_{out}(\omega)}{S_{in}(\omega)} = \frac{j2(\omega - \omega_0)/\omega_0 + 1/Q_0 - 1/Q_c}{j2(\omega - \omega_0)/\omega_0 + 1/Q_0 + 1/Q_c} . \tag{3.8}$$

The full-width half-maximum (FWHM) of the transmission (i.e., Equation (3.8)) can be simply obtained as

$$\Delta\omega_{FWHM} = \frac{\omega_0}{Q_L}, \tag{3.9}$$

where Q_L is defined as total Q or the loaded Q of the waveguide-TWR coupling structure, which is

$$\frac{1}{Q_L} = \frac{1}{Q_0} + \frac{1}{Q_e} \Rightarrow \ Q_L = \frac{Q_0}{1 + Q_0 / Q_e} . \tag{3.10}$$

Also, Q_L can be expressed as

$$Q_L = \omega_0 \tau_L/2, \tag{3.11}$$

where τ_L is the total (or loaded) lifetime of the resonator and is

$$\frac{1}{\tau_L} = \frac{1}{\tau_0} + \frac{1}{\tau_c} \ . \tag{3.12}$$

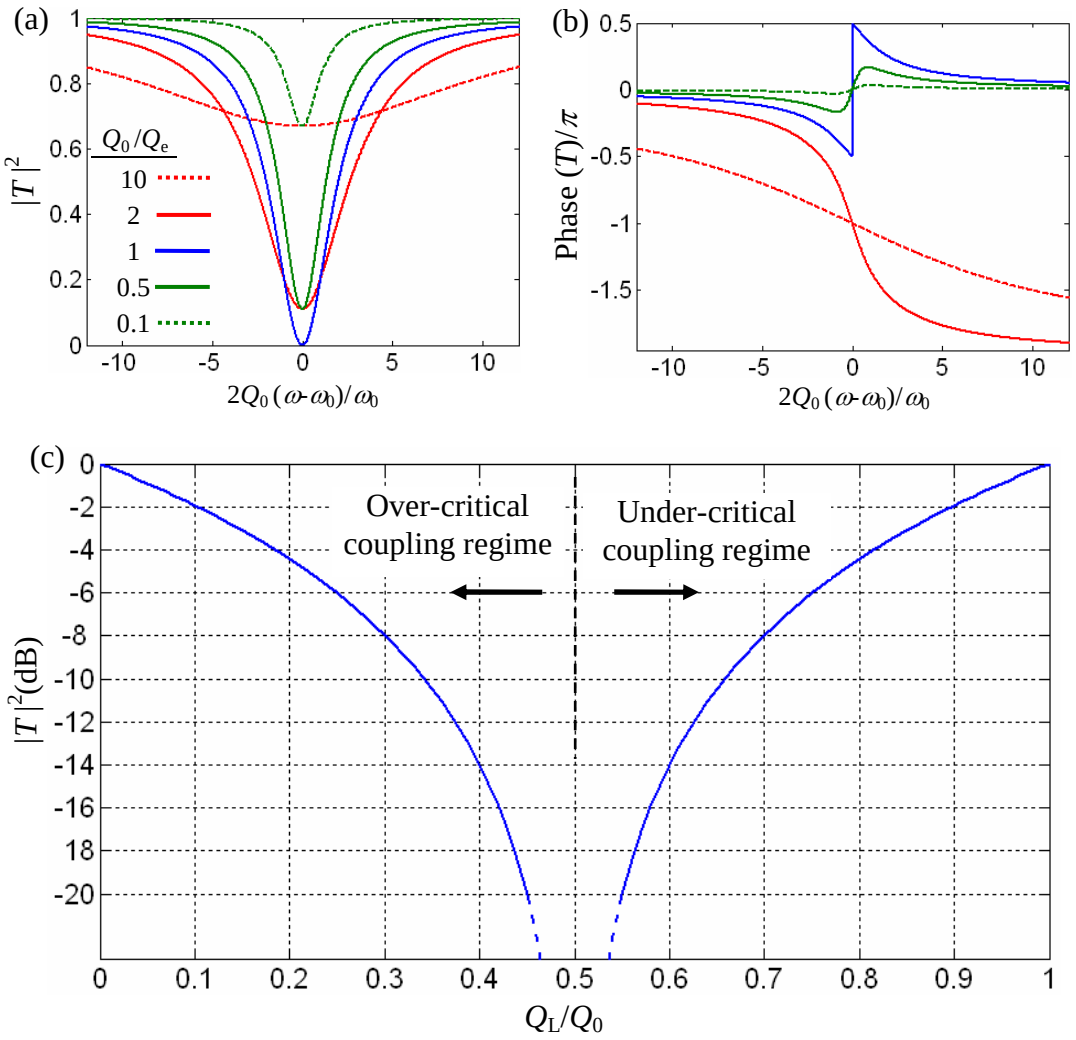

Fig.3.2: Spectral response of a waveguide-TWR coupling structure. (a) The squared magnitude and (b) the phase of the transmission (T) given by Equation (3.8) for different ratios of Q_0/Q_c, as specified in the inset of the figure in (a). (c) The variation of the squared magnitude of T at resonance versus the ratio Q_L/Q_0. The operation regimes of the coupling are specified in (c).

Figures 3.2(a) and 3.2(b) show, respectively, the squared magnitude and phase of transmission, i.e., Equation (3.8), for different ratios of Q_0/Q_c. Based on the ratio of Q_0/Q_c, a waveguide-TWR structure can be classified into three different operation regimes:

1- Critical coupling regime [56], in which $Q_0 = Q_c$. For this case $Q_L = Q_0/2$ and at the resonance, the transmission magnitude is zero (the blue curve in Figure 3.2(a)) and it has a discontinuous jump in its phase response (the blue curve in Figure 3.2(b)).

2- Under-critical coupling regime, in which $Q_0 < Q_c$. For this case, the transmission at resonance is non-zero, the spectral linewidth of the transmission is narrower than the case of critical coupling regime, and $Q_L > Q_0/2$. In the limiting case of $Q_0 << Q_c$, Q_L approaches Q_0 and transmission approaches 1. The squared magnitude and the phase of the transmission (for this coupling regime) are shown with the green curves and at different values of Q_0/Q_c in Figures 3.2(a) and 3.2 (b), respectively.

3- Over-critical coupling regime, in which $Q_0 > Q_c$. For this case, the transmission at resonance is non-zero, the spectrum is broader than the case of the critical coupling regime, and $Q_L < Q_0/2$. The squared magnitude and the phase of the transmission for this scenario are shown in Figures 3.2(a) and 2.3(b) with red curves for different values of Q_0/Q_e. In the limiting case of $Q_0 >> Q_c$, Q_L/Q_0 approaches zero, $|T|^2$ approaches 1, and the structure behaves as a very low-loss all-pass phase filter. Such an architecture can be employed as the building block of more sophisticated filters. As seen in Figure 3.2(b), the shape of the phase response for the over-critical coupling regime is different than that for the under-critical coupling regime.

Also, from Equations (3.8) and (3.10) and at the resonance ($\omega = \omega_0$) we have

$$|T(\omega_0)|^2 = \left|\frac{1-Q_0/Q_c}{1+Q_0/Q_c}\right|^2 = |2Q_L/Q_0 - 1|^2 . \quad (3.13)$$

Figure 3.2(c) shows a plot of Equation (3.13) for different values of Q_L/Q_0 and at different coupling regimes. From this figure, it can be seen that for the same level of $|T|^2$ at the resonance, two different values of Q_L/Q_0 can be obtained corresponding to the under-critical and over-critical coupling regimes. Hence, in the experimental characterization of a waveguide-TWR, by just monitoring the transmission magnitude and measuring its FWHM (which corresponds to Q_L) and its extinction at the resonance ($|T(\omega_0)|^2$), we cannot identify a unique Q_0 for the resonator. In other words, the operation regime of the coupling has to be identified in the measurement. While the transmission magnitude, as shown in Figure 3.2(a), has a Lorentzian shape for all the operation regimes of coupling, the phase response shape differs for each regime, as shown in Figure 3.2(b). Therefore, by identifying the phase response from the experiment, the operation regime of the coupling is determined. Knowing this information, a unique value for the Q_0 of the resonator can be obtained from Figure 3.2(c).

Another important physical term is the power that circulates inside the resonator, which is related to the resonator energy as

$$|a_{cw}|^2 = P_{cir}\frac{L}{v_g}, \quad (3.14)$$

where L is the effective traveling length of the mode and v_g is the group velocity of the traveling mode inside the resonator. By combining Equations (3.14) and (3.7)

we can obtain the ratio between the circulating power in the resonator and the input power in the waveguide as

$$\frac{P_{cir}}{P_{in}} = \frac{v_g}{L\omega_0}\frac{4/Q_c}{4(\omega-\omega_0)^2/\omega_0^2+(1/Q_0+1/Q_c)^2} \quad , \quad (P_{in}=|S_{in}|^2). \tag{3.15}$$

In Equation (3.15), it is clearly seen that the power enhancement in the resonator is inversely proportional to L, which is by itself proportional to the mode volume of the resonator. At the resonance, we expect the maximum power enhancement in the resonator, which is

$$\left.\frac{P_{cir}}{P_{in}}\right|_{\omega=\omega_0} = \frac{v_g}{L}\frac{4Q_e/\omega_0}{(Q_e/Q_0+1)^2} \ . \tag{3.16}$$

Equation (3.16) is at its maximum when $Q_c = Q_0$ (i.e., the critical coupling regime) in which the transmission is zero. In this case Equation (3.16) becomes

$$\begin{aligned}\left.\frac{P_{cir}}{P_{in}}\right|_{\max} &= \frac{v_g}{L}\frac{Q_e}{\omega_0} = \frac{FSR^{(\omega)}}{2\pi}\frac{Q_e}{\omega_0} = \frac{1}{\pi}\frac{FSR^{(\omega)}}{\omega_0/Q_L} \\ &= \frac{1}{\pi}\frac{FSR^{(\omega)}}{\Delta\omega_{FWHM}} = \frac{1}{\pi}\frac{FSR^{(\lambda)}}{\Delta\lambda_{FWHM}} = \frac{1}{\pi}Finesse\end{aligned} \ , \tag{3.17}$$

In Equation (3.17), we have used Equation (2.20), which relates the FSR to the group velocity of the resonator mode. Hence, the maximum power enhancement (which occurs at the critical coupling condition) is proportional to the finesse of the resonator. From Equation (3.17), we can see that a giant power buildup circulation power in the resonator is possible when a high-finesse resonator is used. As an example, a microresonator with an FSR of 5 nm and a loaded linewidth of 1 pm at the critical coupling (which means an intrinsic linewidth of 0.5 pm) when excited by

an input power P_{in} = 1 μW, generates a circulation power P_{cir} ~ 1.6 mW. Such a large power enhancement can be used for many nonlinear optic and sensing applications.

In the above analysis, we assumed no coupling between the degenerate CW and CCW modes of the resonator. However, because of the presence of roughness at the sidewalls of the dielectric resonator (induced by fabrication imperfections), the coupling of these two modes is unavoidable, which is discussednext.

3.2.1. Effect of Resonator CW-CCW: Resonance Splitting

In most practical cases, a fabricated TWR resonator has dielectric perturbation as a result of the presence of fabrication-induced roughness in the sidewalls of the resonator. This perturbation causes the degenerate CW and CCW modes of the resonator to couple to each other and interchange energy[29]. As a result of this coupling, the degenerate resonance frequency of CW and CCW splits into two frequencies. Such a phenomenon is called resonance splitting [59-61]. To analyze the resonance splitting, Equation (3.3) can be revised to consider the coupling of the CW and CCW modes. Figure 3.1 shows the coupling structure and the corresponding waveguide and the resonance parameters in the analysis. To incorporate the CW-CCW coupling, the new set of coupled-mode equations is as follows:

[29] It is noted that the presence of dielectric perturbation also causes the scattering of the resonator modes into the radiation modes. The result of this scattering is the leakage of resonator energy, and as a result, the Q_0 of the resonator is reduced.

$$\frac{da_{cw}}{dt} = (j\omega_0 - 1/\tau_0 - 1/\tau_c)a_{cw} + j\mu a_{ccw} + \kappa S_{in}, \tag{3.18}$$

$$\frac{da_{ccw}}{dt} = (j\omega_0 - 1/\tau_0 - 1/\tau_c)a_{ccw} + j\mu^* a_{cw}, \tag{3.19}$$

$$S_{out} = S_{in} - \kappa^* a_{cw}, \tag{3.20}$$

$$S_{back} = -\kappa^* a_{ccw}, \tag{3.21}$$

$$|\kappa| = \sqrt{2/\tau_c}\ . \tag{3.22}$$

In Equations (3.18) and (3.19), μ and μ^* (which are conjugate of each other) are the coupling coefficients between CW-CCW and CCW-CW modes, respectively. We have assumed that the waveguide excitation, S_{in}, comes from the left to the right, as shown in Figure 3.1. Therefore, it only interacts with the CW mode. τ_0 is the resonator intrinsic lifetime, which includes the perturbation-induced scattering loss. τ_c, as before, is the time constant of the rate of the coupling of energy from the CW mode of the resonator to the waveguide. The generated CCW mode couples to the backward mode of the waveguide and generates a backward reflection, i.e., S_{ref}, as shown in Figure 3.1. Similar to the same argument mentioned for the CW mode of the resonator and the backward mode of the waveguide, the CCW mode and the forward mode of the waveguide (as they propagate in opposite directions in the coupling region) have a very weak coupling, which is neglected in the analysis. Because of the symmetry, the CCW mode couples to the backward mode of the waveguide with the same time constant, τ_c, and coupling coefficient, κ, that CW

mode couples to the forward mode of the waveguide. For more details on the derivation of Equations (3.18)-(3.22) see Appendix E.

For a more systematic analysis, Equations (3.18) and (3.19) can be written in a matrix as

$$\frac{d}{dt}\begin{bmatrix} a_{cw} \\ a_{ccw} \end{bmatrix} = \begin{bmatrix} (j\omega_0 - 1/\tau_0 - 1/\tau_c) & j\mu \\ j\mu^* & (j\omega_0 - 1/\tau_0 - 1/\tau_c) \end{bmatrix} \begin{bmatrix} a_{cw} \\ a_{ccw} \end{bmatrix} + \begin{bmatrix} \kappa S_{in} \\ 0 \end{bmatrix}. \tag{3.23}$$

To solve (3.23), we transform it into the coordinate that consists of the eigenvectors of its characteristic matrix. This results in orthogonal bases for the solution. The eigenvalues and the eigenvectors of the characteristic matrix in Equation (3.23) can be simply found as

$$\lambda_{\pm} = (j\omega_0 - 1/\tau_0 - 1/\tau_c) \pm j|\mu|, \quad V_{\pm} = \frac{1}{\sqrt{2}}\begin{bmatrix} \mu/|\mu| \\ \pm 1 \end{bmatrix}. \tag{3.24}$$

Using the results in Equation (3.24), Equation (3.23) is transformed into the following form:

$$\frac{d}{dt}\begin{bmatrix} a_+ \\ a_- \end{bmatrix} = \begin{bmatrix} (j\omega_0 - 1/\tau_0 - 1/\tau_c) + j|\mu| & 0 \\ 0 & (j\omega_0 - 1/\tau_0 - 1/\tau_c) - j|\mu| \end{bmatrix} \begin{bmatrix} a_+ \\ a_- \end{bmatrix} + \begin{bmatrix} \kappa/\sqrt{2} \\ \kappa/\sqrt{2} \end{bmatrix} \frac{|\mu|}{\mu} S_{in}, \tag{3.25}$$

where

$$a_{\pm} = \frac{(|\mu|/\mu)a_{cw} \pm a_{ccw}}{\sqrt{2}}, \tag{3.26}$$

and correspondingly

$$a_{cw} = (\mu/|\mu|)\frac{a_+ + a_-}{\sqrt{2}}, \quad a_{ccw} = \frac{a_+ - a_-}{\sqrt{2}}. \tag{3.27}$$

The new matrix system in Equation (3.25) has no non-zero off-diagonal term, which means that the modes a_+ and a_- are orthogonal to each other and as a result they are not coupled to each other. While a_{cw} and a_{ccw} represent the amplitude of CW and CCW traveling waves with the corresponding azimuth phase variations of $\exp(-im\phi)$ and $\exp(+im\phi)$, respectively, from Equation (3.26) we can see that a_+ and a_- behave like standing waves with azimuth phase variations of $\cos(m\phi)$ and $\sin(m\phi)$, respectively.

In general, the generated standing-wave modes of the resonator can have different lifetimes instead of being designated by a unique lifetime τ_0. This means that these two standing-wave modes can have different quality factors. To qualitatively verify this, assume a Si microdisk resonator with air cladding in which the sidewalls of the microdisk has sidewall roughness. As a result of this sidewall perturbation in the microdisk, one of the generated standing-wave modes tends to have more energy concentration in the dielectric (Si) side of the perturbation (called the dielectric mode) and the other standing-wave mode tends to have more energy concentration in the air side of the perturbation (called the air mode)[30]. Both the air mode and dielectric mode are subject to the surface roughness-induced scattering loss. However, the dielectric mode is subject to more material absorption and surface non-idealities of Si, while the air mode is less subject to Si non-idealities as it has less energy concentration in the Si. Hence, we can give more generality to

[30] A sensible example of this mode classification is a grating made of a periodic stack of air and dielectric slabs. In this grating, two standing-wave modes with different frequencies are created. One mode has more energy concentration in the dielectric (called a dielectric mode) and the other has more energy concentration in the air (called an air mode)

Equation (3.25) by assigning different lifetimes τ_{0+} and τ_{0-} (instead of one τ_0) to the standing modes a_+ and a_-, respectively. However, because of the symmetry of the waveguide-TWR structure, these standing-wave modes can have the same coupling lifetimes (τ_c) as the waveguide. As a result, the new form of Equations (3.25) is

$$\frac{d}{dt}\begin{bmatrix} a_+ \\ a_- \end{bmatrix} = \begin{bmatrix} (j\omega_0 - 1/\bar{\tau}_+) + j|\mu| & 0 \\ 0 & (j\omega_0 - 1/\bar{\tau}_-) - j|\mu| \end{bmatrix}\begin{bmatrix} a_+ \\ a_- \end{bmatrix} + \begin{bmatrix} \kappa \\ \kappa \end{bmatrix}\frac{|\mu|}{\mu}\frac{S_{in}}{\sqrt{2}}, \quad (3.28)$$

where

$$1/\bar{\tau}_\pm = 1/\tau_{0\pm} + 1/\tau_c . \quad (3.29)$$

We can also define the following:

$$1/\overline{Q}_\pm = 1/Q_{0\pm} + 1/Q_c , \quad (3.30)$$

$$1/Q_{split} = 2|\mu|/\omega_0 . \quad (3.31)$$

By incorporating Equations (3.30) and (3.31) into Equation (3.28). and after taking its Fourier transform. we find the following:

$$a_\pm(\omega) = \frac{\sqrt{2}}{[j2(\omega-\omega_0)/\omega_0 + 1/\overline{Q}_\pm \mp j1/Q_{split}]}\frac{|\mu|}{\mu}\frac{\kappa S_{in}(\omega)}{\omega_0}, \quad (3.32)$$

and the resonator total energy is

$$U = U_+ + U_- = |a_+(\omega)|^2 + |a_-(\omega)|^2 = \left\{ \frac{2/Q_e}{(2(\omega-\omega_0)/\omega_0 - 1/Q_{split})^2 + 1/\overline{Q}_+^2} + \frac{2/Q_e}{(2(\omega-\omega_0)/\omega_0 + 1/Q_{split})^2 + 1/\overline{Q}_-^2} \right\}\frac{P_{in}(\omega)}{\omega_0}, \quad (3.33)$$

By combining Equations (3.27) and (3.32) the amplitudes of the CW and CCW modes (i.e., a_{cw} and a_{ccw}) can be obtained. Finally, by putting the values of a_{cw} and

a_{ccw} into Equations (3.20) and (3.21) we can find the transmission ($T = S_{out}/S_{in}$) and reflection ($R = S_{ref}/S_{in}$) coefficients in the waveguide as

$$T = 1 - \frac{[j4(\omega - \omega_0)/\omega_0 + 1/\overline{Q}_+ + 1/\overline{Q}_-]/Q_c}{[j(2(\omega - \omega_0)/\omega_0 - 1/Q_{split}) + 1/\overline{Q}_+][j(2(\omega - \omega_0)/\omega_0 + 1/Q_{split}) + 1/\overline{Q}_-]}\ , \tag{3.34}$$

$$R = -\frac{(1/\overline{Q}_- - 1/\overline{Q}_+ + j2/Q_{split})/Q_c}{[j(2(\omega - \omega_0)/\omega_0 - 1/Q_{split}) + 1/\overline{Q}_+][j(2(\omega - \omega_0)/\omega_0 + 1/Q_{split}) + 1/\overline{Q}_-]}\ . \tag{3.35}$$

Figures 3.3(a) and 3.3(b) show the simulation results for the energy spectrum of the resonator in the presence of CW-CCW coupling for two examples of equal ($Q_{0-}=Q_{0+}$) and unequal ($Q_{0-}=0.8Q_{0+}$) quality factors for the standing-wave modes of the resonator, respectively. The coupling Q (Q_c) has been assumed to be equal to the intrinsic Q of one of the standing-wave modes, the resonator mode. As can been seen from each figure, the resonance splitting and the appearance of a doublet are observed in the spectrum. In addition, asymmetry is observed in the energy spectrum when the quality factors of the standing-wave modes are different. Also, Figure 3.4(a) shows the squared magnitudes of the transmission and reflection in the waveguide for these cases, and Figure 3.4(b) shows their corresponding phase responses. As can be seen from Figure 3.4(a), when the quality factors of the standing-wave modes are not equal, the extinctions and the linewidths of the split resonances are different (see the dashed curve). As a result, a greater difference

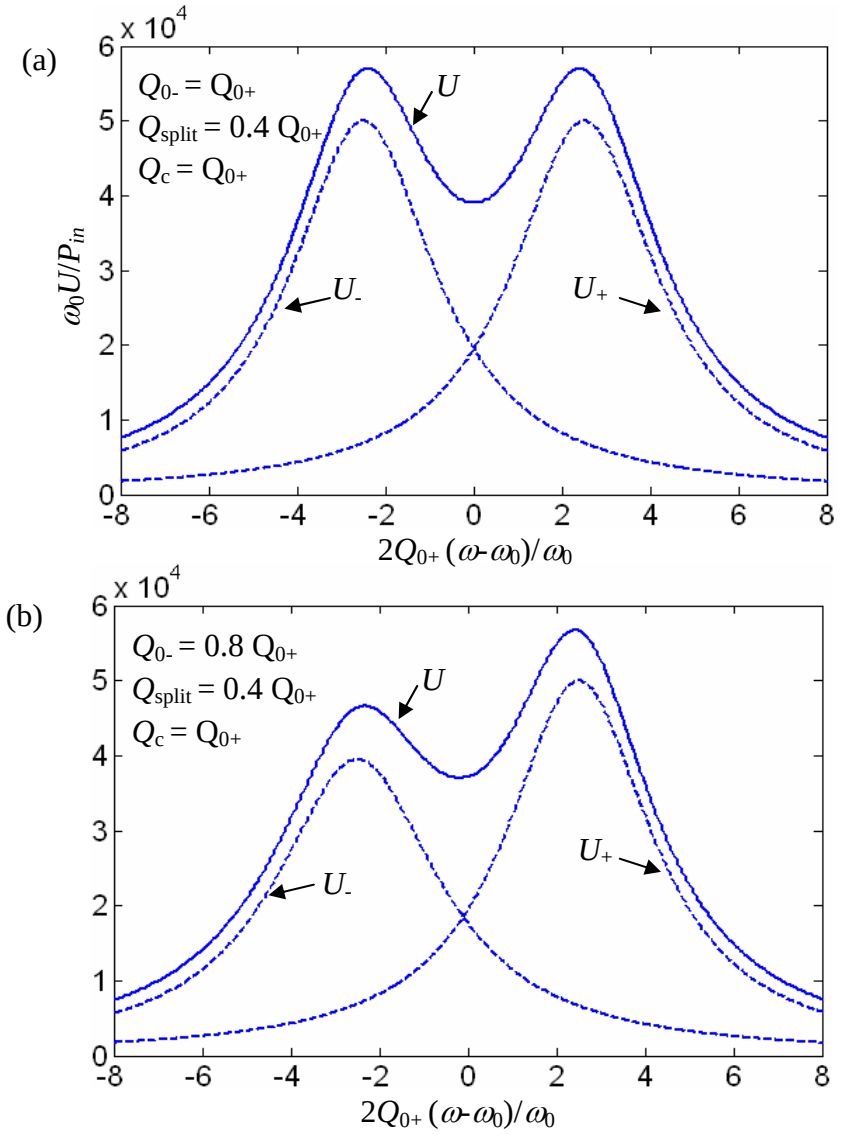

Fig.3.3: Energy of the resonator with (a) the equal quality factors (Q_{0+}=Q_{0-}) and (b) unequal quality factors (Q_{0+}=Q_{0-}) for the standing-wave modes of the resonator in a waveguide-TWR structure shown in Figure 3.1. The other parameters are specified in the insets of the figures.

between the quality factors of the standing-wave modes results in more asymmetry and a greater difference in the extinction of the split resonances.

For the symmetric case where Q_{0-}=Q_{0+}, we have found that closed-form expressions for the resonator response can be obtained, and based on those results, a

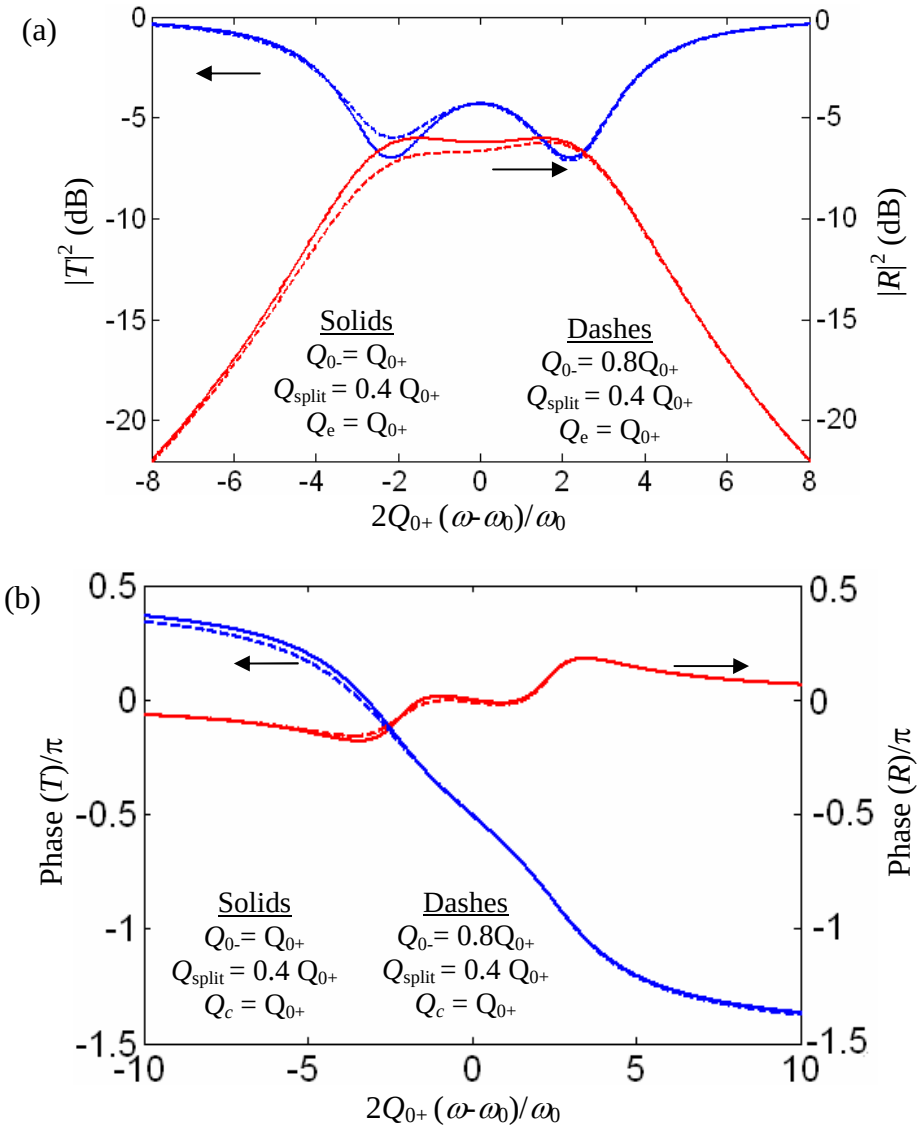

Fig.3.4: (a) Squared magnitudes of the transmission ($T = S_{out}/S_{in}$, the blue curves) and the reflection ($R = S_{ref}/S_{in}$, the red curves) and (b) their phases for equal quality factors ($Q_{0-} = Q_{0+}$, the solid curves), and (b) unequal quality factors ($Q_{0-} = 0.8\ Q_{0+}$, the dashed curves) for the standing-wave modes of the resonator in a waveguide-TWR shown in Figure 3.1. The other parameters are specified in the insets of the figures.

deeper understanding of the impact of different resonator parameters on the resonator can be obtained. In addition, for many cases where the asymmetry is not strong, the results of the symmetric case can be extended to them. In the following,

we focus on the symmetric case and analyze the response of the waveguide-resonator coupling structure.

In general, resonance splitting (because of the fabrication imperfection) is not a desired effect, and usually a waveguide-TWR structure is designed to work in the critical coupling or strong over-critical coupling regime with the presence of only the CW or CCW mode. However, depending on the strength of splitting, different spectral responses can be obtained. As an example, Figures 3.5(a) and 3.5(b) show the squared magnitude and phase of a waveguide-TWR structure designed to work at the critical coupling regime and without splitting ($Q_c = Q_0$, $Q_{split} = \infty$, see the blue dashed curve). However, the appearance of splitting and the increase in its strength (as shown by different colors in the figure), the transmission spectrum changes from a singlet response to a doublet response and the extinction is also reduced. The interesting cases in Figure 3.5(a) are the singlet responses, which are a Lorentzian-like shape (e.g, the case of $Q_{split}/Q_0 = 1.5$ shown by red curve). Observing these cases in the experiments of waveguide-TWR coupling (where usually only the transmission response is measured) may lead to a wrong conclusion that CW-CCW does not exist. As a result we may fit the Lorentzian transmission response from the experiment to the theoretical data given in Figure 3.2 (in which CW-CCW coupling is absent) and obtain a wrong conclusion about the operation regime of the resonator and its intrinsic Q. A clear example of this case is shown in Figure 3.6. As can be seen from this figure, the case of $Q_c/Q_0 = 0.8$, $Q_{split}/Q_0 = \infty$(blue curve), which has

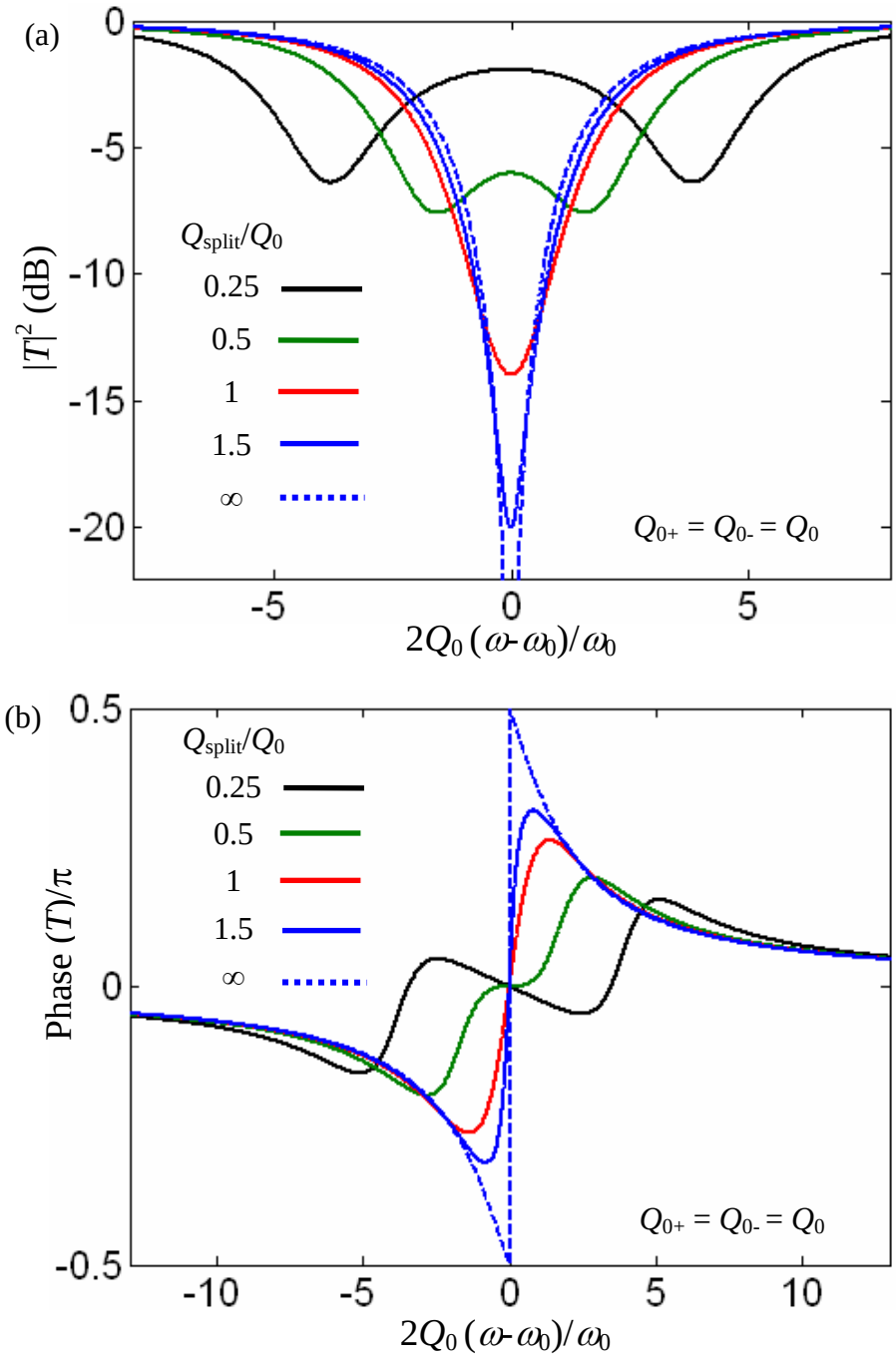

Fig.3.5: (a) Squared magnitude and (b) phase response of the transmission of a waveguide-TWR coupling structure when $Q_c = Q_0$ and under different conditions of Q_{split}/Q_0 as specified by different colors in the figures. The quality factors of the standing-wave modes are $Q_{0+} = Q_{0-} = Q_0$.

no CW-CCW coupling, and the case of Q_c/Q_0 =0.8, Q_{split}/Q_0 = 0.4 (green curve),

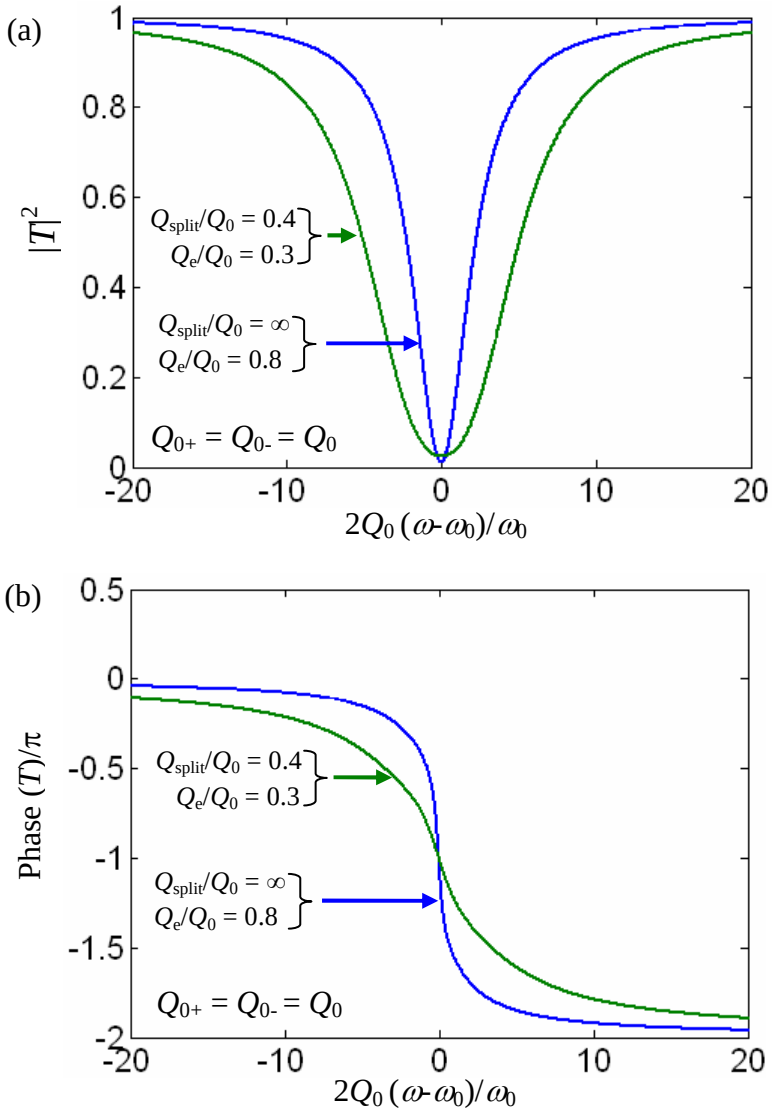

Fig.3.6: (a) Squared magnitude and (b) phase response of the transmission of a waveguide-TWR coupling structure under different conditions of Q_{split}/Q_0 and Q_c/Q_0, as designated by different colors in the figures.

which has CW-CCW coupling, show Lorentzian responses for the transmission with almost the same level of transmission at resonance. The latter case shows a broader response, which can lead us to a lower estimated Q_0 for the resonator if the Q is found by just looking at this Lorentzian response, assuming no CW-CCW coupling and using the results presented in the previous section. For such cases, at least the

reflection has to be measured to realize if the waveguide-TWR has CW-CCW coupling.

Having the observation shown in Figures 3.5 and 3.6, it is important to discover the conditions under which the spectrum of resonator energy or transmission and reflection show a doublet or singlet response. From Equation (3.33), the frequency locations of the peaks of the resonator energy, U, for the symmetric case ($Q_{0-} = Q_{0+} = Q_0$) can be found as

$$\left.\frac{\Delta\omega^{peak}}{\omega_0}\right|_{U(\omega)} = \begin{cases} \pm\dfrac{1}{2Q_{split}}\sqrt{2\sqrt{1+\dfrac{Q_{split}^2}{\overline{Q}^2}}-(1+\dfrac{Q_{split}^2}{\overline{Q}^2})}, & (\dfrac{1}{\overline{Q}}=\dfrac{1}{Q_0}+\dfrac{1}{Q_c}). \\ 0 \end{cases} \quad (3.36)$$

In Equation (3.36) $\Delta\omega^{peak}/\omega_0 = 0$ corresponds to the local minima of the energy and the other two frequencies correspond to the two peaks of the doublet. As discussed previously, there are situations where coupling between CW-CCW exists. However, no doublet is observed in the energy spectrum. For such cases, $Q_{split} \geq \sqrt{3}\overline{Q}$, where the doublet peaks in Equation (3.37), become complex numbers, which means that the resonator does not show any doublet and behaves as a singlet with one peak at the center, i.e., $\omega=\omega_0$.

It has to be noted that the locations of the peaks of the energy spectrum are slightly different from those for the $|T|^2$ and $|R|^2$. For example, the peaks of $|R|^2$ are located at

$$\left.\frac{\Delta\omega^{peak}}{\omega_0}\right|_{R^2} = \begin{cases} \pm\dfrac{1}{2Q_{split}}\sqrt{1-\dfrac{Q_{split}^2}{\overline{Q}^2}}, & \left(\dfrac{1}{\overline{Q}} = \dfrac{1}{Q_0} + \dfrac{1}{Q_c}\right) \\ 0 \end{cases} . \tag{3.37}$$

In Equation (3.37), if $\overline{Q} \le Q_{split} \le \sqrt{3}\overline{Q}$, $|R|^2$ does not show any doublet while the resonator energy (U) still shows a doublet. In both cases of singlet and doublet responses, it is interesting to find the optimum Q_c for which the maximum field enhancement in the resonator is achieved. This is discussed next for both cases of singlet and doublet in *U*.

a. Resonator Energy (*U*) Shows a Singlet Response ($Q_{split} \ge \sqrt{3}\overline{Q}$)

In this case, only one peak appears in the energy spectrum at $\omega=\omega_0$. Therefore, from Equation (3.33) the energy peak is

$$\left.\frac{\omega_0 U}{P_{in}}\right|_{peak} = \frac{4/Q_c}{1/Q_{split}^2 + 1/\overline{Q}^2} = \frac{4/Q_c}{1/Q_{split}^2 + 1/Q_0^2 + 1/Q_e^2 + 2/(Q_c Q_0)} . \tag{3.38}$$

The maximum value of Equation (3.38) with respect to Q_c occurs when the following condition is satisfied:

$$1/Q_c^2 = 1/Q_0^2 + 1/Q_{split}^2 , \tag{3.39}$$

and in this case the resonator energy, which is the maximum, is

$$\left.\frac{\omega_0 U}{P_{in}}\right|_{\max} = \frac{2}{1/Q_c + 1/Q_0} = 2\overline{Q} , \tag{3.40}$$

and for the waveguide we have

$$|T|^2 = 0, \ |R|^2 = \frac{1}{1 + Q_{split}/Q_c} . \tag{3.41}$$

b. Resonator Energy (*U*) Shows a Doublet Response ($Q_{split} < \sqrt{3}\overline{Q}$)

In this case, and as discussed before, the maximum peak of the resonator energy occurs at the frequencies given by Equation (3.36). Because we are investigating the symmetric case, i.e., $Q_{0-}=Q_{0+}= Q_0$, both peaks have equal energies. Therefore, we can analyze one of them. Putting one of the doublet frequency peaks from Equation (3.36) into Equation (3.33) the peak of *U* can be obtained as

$$\left.\frac{\omega_0 U}{P_{in}}\right|_{peak} = \frac{Q_{split}^2 / Q_c}{\sqrt{1+Q_{split}^2/\overline{Q}^2}-1} \ . \tag{3.42}$$

The maximum value of Equation (3.42) with respect to Q_c is when the following condition is satisfied:

$$\frac{Q_c}{Q_0} = \frac{1-(Q_{split}/Q_0)^2}{1+(Q_{split}/Q_0)^2} \ , \ (Q_{split} \le \sqrt{3}\overline{Q} \ ) \tag{3.43}$$

and for this condition, the resonator energy (which is at its maximum) is

$$\left.\frac{\omega_0 U}{P_{in}}\right|_{\max} = \frac{Q_0}{2}(1+Q_{split}^2/Q_0^2) \ . \tag{3.44}$$

Also, for the transmission in the waveguide at the peak frequency of *U* and when the condition in Equation (3.43) exists, we have

$$|T|^2 = \left[2-\frac{1+(Q_{split}/Q_0)^2}{1-(Q_{split}/Q_0)^2}\right]\left[2(1+\frac{1+(Q_{split}/Q_0)^2}{1-(Q_{split}/Q_0)^2})\right]^{-1} = \frac{1-(Q_0/Q_c)/2}{1+Q_0/Q_c}. \tag{3.45}$$

It has to be noted that Equation (3.45) does not correspond with the peak value of the transmission. The frequencies when the peak value of the transmission, reflection, and the energy occur do not coincide. However, with a good

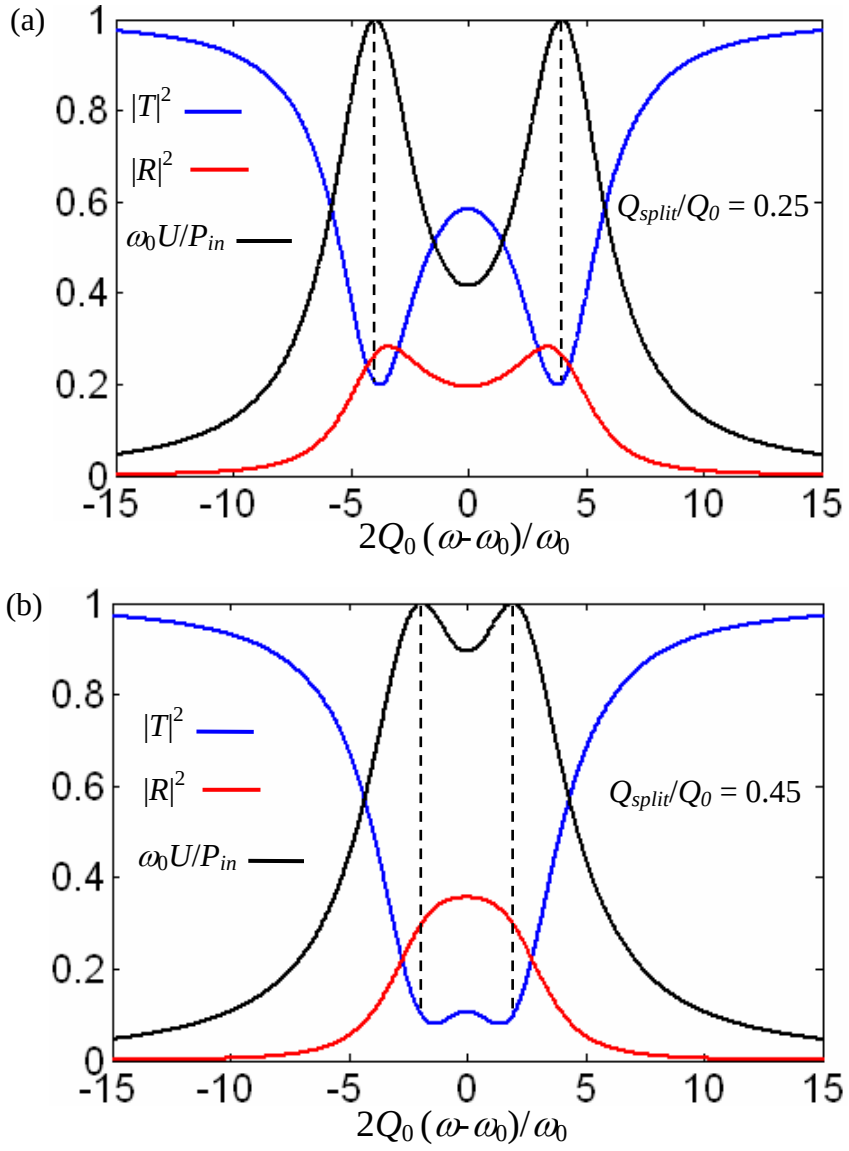

Fig.3.7: Spectra of $|T|2$, $|R|2$, and normalized-to-peak of $\omega_0 U/P_{in}$, for (a) Q_{split}/Q_0 = 0.25, and (b) Q_{split}/Q_0 = 0.45, and with Q_c given by Equation (3.43). For the case of Q_{split}/Q_0 = 0.45 as shown in (b), the reflection behaves as a singlet.

approximation (especially when Q_{split}/Q_0 is small), the magnitude of the transmission given by Equation (3.45) is close to the peak value of the transmission. Figures 3.7(a) and 3.7(b) show the spectra of $|T|^2$, $|R|^2$, normalized-to-peak of $\omega_0 U/P_{in}$ for two cases with Q_{split}/Q_0 = 0.25 and Q_{split}/Q_0 = 0.45, respectively, and at the condition given for Q_c in Equation (3.43) to maximize the resonator energy.

Comparing these two figures we see that when the ratio Q_{split}/Q_0 becomes smaller, all three quantities of $|T|^2$, $|R|^2$, and $\omega_0 U/P_{in}$ are doublets and the locations of their peak frequencies are closer to each other.

It is interesting to note that in the presence of CW-CCW, the required value of Q_c to have maximum energy in the resonator in both Equations (3.39) (for the singlet case) and (3.43) (for the doublet case) is less than Q_0, while in the critical coupling (which was discussed before and no CW-CCW coupling existed), the maximum energy occurs at critical coupling, i.e., $Q_c = Q_0$.

One last thing to be discussed is the variation of the spectral responses of U, $|T|^2$, and $|R|^2$ for a fixed Q_{split}/Q_0 and at different levels of Q_c/Q_0. This is important since for a fixed quality of the fabrication of resonators, the values of the Q_0 of the resonator and Q_{split} are fixed, while the value of Q_c can be modified by changing the spacing between the waveguide and the resonator. Figure 3.8 shows the results of this investigation for a fixed Q_{split}/Q_0 and different values of Q_c/Q_0. In addition, the results for the critical coupling case when no CW-CCW coupling exists is shown in this figure with the blue dashed curves. For a ratio of $Q_{split}/Q_0 = 0.5$ considered in Figure 3.8, the ratio of $Q_c/Q_0 = 0.6$ is the optimum condition, which corresponds to the maximum field enhancement in the resonator. For the values of Q_c far below this optimum condition, the spectral response of the resonator behaves like a singlet with a weak interaction with the waveguide, and for the values of Q_c far above the optimum condition, the spectral response of the resonator behaves like a doublet and again with a weak interaction with the waveguide. Only around the

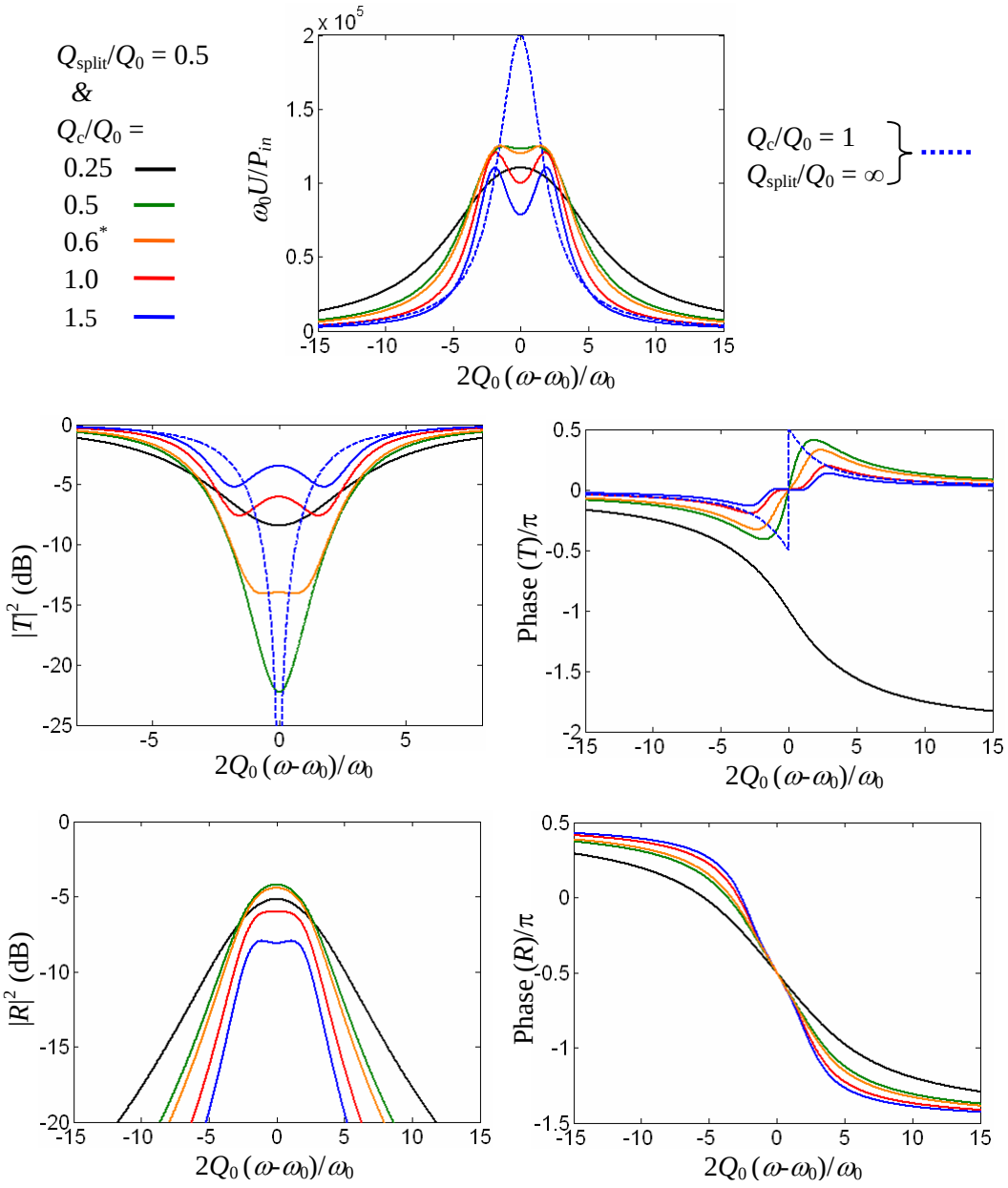

Fig. 3.8: Spectrum of (a) U, (b) $|T|^2$, (c) phase of T, (d) $|R|^2$, and (e) phase of R, for a waveguide-TWR coupling structure at a fixed Q_{split}/Q_0 = 0.5 and at different values of Q_c/Q_0 as specified in the figure. *: Q_c/Q_0 = 0.6 corresponds to the condition given by Equation (3.43), where the doublet peaks of U are maximum. The dashed curve corresponds to the case when the structure has no CW-CCW coupling and it is at the critical coupling, i.e., $Q_c = Q_0$.

optimum condition is the interaction of the resonator with the waveguide strong. An interesting case in this example is the case Q_c/Q_0 = 0.5, which is a little below the

optimum condition. For this case, as shown by the green curve in Figure 3.8(a), while not much change in the resonator energy occurs compared to the optimum case (the orange curve), its corresponding $|T|^2$ as shown in Figure 3.8(b) (the green curve) has a much larger extinction than the optimum case (the orange curve).

In chapter 5 where the experimental results on the characterizations of microresonators are presented, the theoretical results of resonance splitting presented here are used to fit to the experimental data for finding the intrinsic Q of the resonators.

3.2.2. Coupling of a Resonator to More Waveguides

The analysis of a single resonator coupled to one waveguide can be generalized to a multi-waveguide system. For the sake of clarity, while keeping the generality, we discuss the case of a resonator coupled to two waveguides, as shown in Figure 3.9. In general, the optical signal can be launched from all ports of the waveguides to the coupling region, as shown in Figure 3.9. The waveguides are assumed to support only one mode, as is the case of interest for many applications. By extending the coupled-mode equations used in the previous section, the new system of equations that governs the structure shown in Figure 3.9 are

$$\frac{da_{cw}}{dt} = (j\omega_0 - 1/\tau_0 - 1/\tau_{ca} - 1/\tau_{cb})a_{cw} + j\mu a_{ccw} + \kappa_b S_{b1}^{+} + \kappa_a S_{a2}^{+}, \tag{3.46}$$

$$\frac{da_{ccw}}{dt} = (j\omega_0 - 1/\tau_0 - 1/\tau_{ca} - 1/\tau_{cb})a_{ccw} + j\mu^{*} a_{cw} + \kappa_a S_{a1}^{+} + \kappa_b S_{b2}^{+}, \tag{3.47}$$

$$S_{a1}^{-} = S_{a2}^{+} - \kappa_a^{*} a_{cw}, \tag{3.48}$$

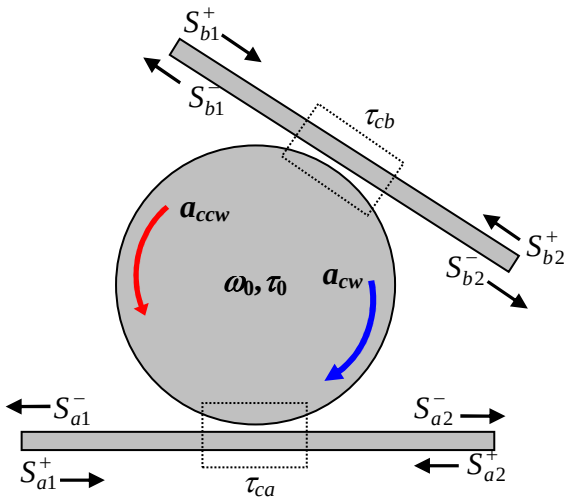

Fig. 3.9: Schematic of a TWR coupled to two waveguides *a* and *b* with coupling time constants τ_{ca} and τ_{cb}, respectively.

$$S_{a2}^{-} = S_{a1}^{+} - \kappa_a^{*} a_{ccw}, \tag{3.49}$$

$$S_{b1}^{-} = S_{b2}^{+} - \kappa_b^{*} a_{ccw}, \tag{3.50}$$

$$S_{b2}^{-} = S_{b1}^{+} - \kappa_b^{*} a_{cw}, \tag{3.51}$$

$$|\kappa_a| = \sqrt{2/\tau_{ca}}\ , \tag{3.52}$$

$$|\kappa_b| = \sqrt{2/\tau_{cb}}\ . \tag{3.53}$$

If the coupling between the CW and CCW modes of the resonator is very weak, Equations (3.44) and (3.45) are decoupled from each other, and as a result, a_{cw}, S_{a1}^{-}, and S_{b2}^{-} are only excited by and depend on S_{a2}^{+} and S_{b1}^{+}. Similarly, a_{ccw}, S_{a2}^{-}, and S_{b1}^{-} are only excited by and depend on S_{a1}^{+} and S_{b2}^{+}. In this case, if we assume S_{a1}^{+} as the only excitation source to the system, we obtain the following in the frequency domain:

$$a_{ccw} = \frac{\kappa_a S_{a1}^{+}}{j(\omega-\omega_0)+1/\tau_0+1/\tau_{ca}+1/\tau_{cb}}, \tag{3.54}$$

$$S_{a2}^{-} = S_{a1}^{+} - \kappa_a^{*} a_{ccw} = \frac{j(\omega-\omega_0)+1/\tau_0+1/\tau_{cb}-1/\tau_{ca}}{j(\omega-\omega_0)+1/\tau_0+1/\tau_{ca}+1/\tau_{cb}} S_{a1}^{+}, \tag{3.55}$$

$$S_{b1}^{-} = -\kappa_b^{*} a_{ccw} = \frac{-\kappa_b^{*}\kappa_a}{j(\omega-\omega_0)+1/\tau_0+1/\tau_{ca}+1/\tau_{cb}} S_{a1}^{+}. \tag{3.56}$$

In this case, the resonator captures the power from the waveguide *a* and drops it to the waveguide *b* (which is the drop port). Such an architecture is called a 1st order add-drop filter, which is made of one resonator. If both waveguides have equal coupling time constants, i.e., $\tau_{ea} = \tau_{eb} = \tau_e$, then from Equations (3.55) and (3.56) we have the through port (T) and the drop port (D) transmission coefficients as

$$T = \frac{S_{a2}^{-}}{S_{a1}^{+}} = \frac{j2(\omega-\omega_0)/\omega_0+1/Q_0}{j2(\omega-\omega_0)/\omega_0+1/Q_0+2/Q_e}, \tag{3.57}$$

$$D = \frac{S_{b1}^{-}}{S_{a1}^{+}} = \frac{-2/Q_e}{j2(\omega-\omega_0)/\omega_0+1/Q_0+2/Q_e}. \tag{3.58}$$

Figure 3.10 shows a plot of the squared magnitudes of Equations (3.55) and (3.56). In the case of $Q_c << Q_0$, the drop port transmission approaches 1 and the through port transmission approaches zero. This shows the impact of the intrinsic Q of a resonator in designing a low-loss add-drop filter. In fact, in almost all the applications of add-drop filtering, Q_c is designed to be very small compared to the intrinsic Q of the resonator.

To analyze the effect of resonance splitting in the add-drop structure shown in Figure 3.9, we note that if we define a total coupling lifetime for the resonator as

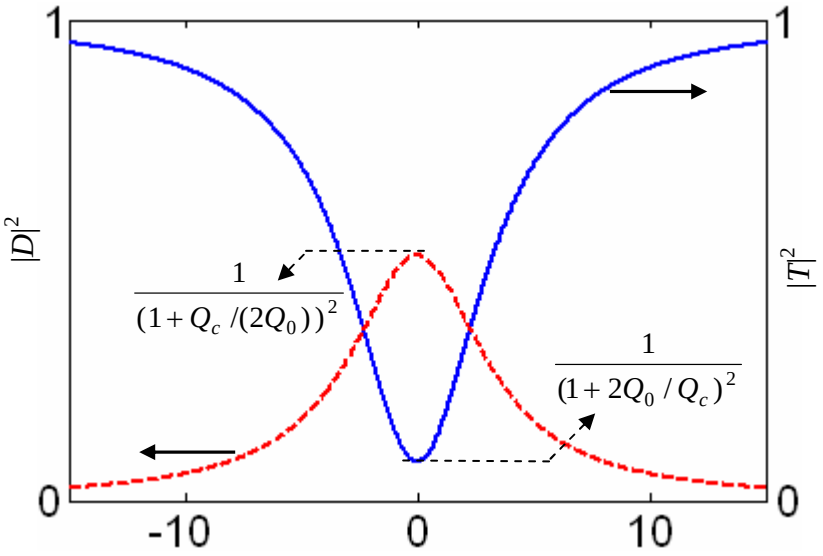

Fig.3.10: The through port (T) and drop port (D) transmission coefficients for the coupling structure shown in Figure 3.9 and excited by S_{a1}^{+}.

$$1/\bar{\tau}_c = 1/\tau_{ca} + 1/\tau_{cb}$$

(3.59)and put it in Equations (3.46) and (3.47), these equations are similar to Equations (3.18) and (3.19), with the only difference being that the structure in Figure 3.9 can have more waveguide excitation sources. However, the method of analysis is the same, and the same forms of eigenvalues and eigenvectors are obtained for the standing-wave modes. As a result, the final matrix equations for the standing-wave modes in Figure 3.9 can be written as

$$\frac{d}{dt}\begin{bmatrix} a_+ \\ a_- \end{bmatrix} = \begin{bmatrix} (j\omega_0 - 1/\bar{\tau}_+) + j|\mu| & 0 \\ 0 & (j\omega_0 - 1/\bar{\tau}_-) - j|\mu| \end{bmatrix}\begin{bmatrix} a_+ \\ a_- \end{bmatrix} + \begin{bmatrix} \kappa_b \\ \kappa_b \end{bmatrix}\frac{|\mu|}{\mu}\frac{S_{b1}^{+}}{\sqrt{2}} + \begin{bmatrix} \kappa_b \\ -\kappa_b \end{bmatrix}\frac{S_{b2}^{+}}{\sqrt{2}} + \begin{bmatrix} \kappa_a \\ \kappa_a \end{bmatrix}\frac{|\mu|}{\mu}\frac{S_{a2}^{+}}{\sqrt{2}} + \begin{bmatrix} \kappa_a \\ -\kappa_a \end{bmatrix}\frac{S_{a1}^{+}}{\sqrt{2}}, \tag{3.60}$$

where

$$1/\bar{\tau}_{\pm} = 1/\tau_{0\pm} + 1/\bar{\tau}_c, \tag{3.61}$$

and the relations between the standing-wave modes and traveling-wave modes are the same as those given in Equations (3.26) and (3.27). By finding the standing-wave solution from Equation (3.60) and then finding the corresponding traveling-wave mode via Equation (3.27), all the transmitted signals at the ports of the waveguides can be found through Equations (3.48)-(3.51).

In chapter 5, experimental results for add-drop filters are presented. Also in chapter 7, experimental results for higher-order add-drop filters, which are based on coupled resonators (as an extension of a 1st order add-drop filter) are presented.

3.2.3. Engineering and Optimization of Waveguide-TWR Coupling for Microring and Microdisk Resonators

In the preceding discussions in this chapter, the analysis of waveguide-resonator coupling using coupled-mode theory in time was presented, and the impact of the strength of waveguide-resonator coupling (which was represented by coupling Q (Q_c)) and the intrinsic Q of a resonator on the spectral response of the structure were investigated. In this section, we perform a quantitative analysis on Q_c and the ways to engineer and optimize it to achieve a desired value for Qc in a waveguide-TWR structure. A typical example of such structures is shown in Figure 3.11 for a microring resonator. The resonator and the waveguide are made of silicon and are seated on an oxide substrate and covered by air or a dielectric cladding. In addition, a thin silicon pedestal layer with a thickness of p (as specified in Figure 3.11(b)) has been added at the interface between the waveguide-TWR structure and the underlying oxide substrate. The free input parameters to optimize the waveguide-

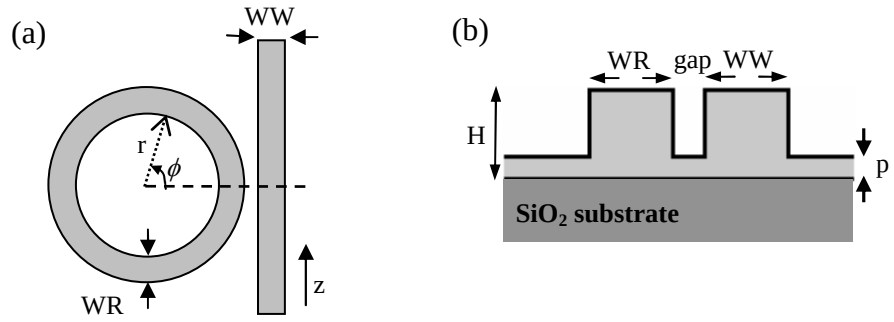

Fig. 3.11: Schematic of the coupling between a silicon ring resonator and a waveguide on an oxide substrate; (a) top view, (b) cross section view at the coupling region between the waveguide and the resonator along the horizontal dashed line shown in the figure in (a). The structure's dimensions are designated in the figure.

TWR coupling (and correspondingly, the Q_c) are the dimensions of the resonator and the waveguide, the spacing between them, the pedestal thickness, and the cladding material.

From Equation (3.6), Q_c is related to the coupling lifetime τ_c as $Q_c = \omega_0 \tau_c/2$. Also from Equation (3.11), τ_c is related to the waveguide-resonator coupling factor κ as $|\kappa|^2 = 2/\tau_c$. Therefore, Q_c is related to κ as

$$Q_c = \frac{\omega_0}{|\kappa|^2}. \tag{3.62}$$

Hence, after calculating κ, the value of Q_c can be obtained from (3.60). From coupled-mode theory and in the 1st order approximation (see Appendix E), κ is extracted to be

$$k = -\frac{j\omega_0\varepsilon_0}{4}\int dz dA\, \Delta(n^2)\frac{E_r^* e^{jm\phi}}{\sqrt{U}}\frac{E_w e^{-j\beta z}}{\sqrt{P}}. \tag{3.63}$$

In the above coupling integral, ω_0 is the resonance frequency of the resonator, ε_0 is the permittivity of vacuum, β is the waveguide propagation constant, z is the

propagation direction along the waveguide, m and ϕ are the azimuthal harmonic number and the azimuthal phase of the resonator mode, respectively. $\Delta(n^2)$ is the index perturbation caused by the waveguide at the vicinity of the resonator[31], and U and P are the energy and power of the resonator and waveguide modes, respectively, which are expressed as follows:

$$U = \frac{1}{2}\varepsilon_0 n_r^2 E_{\max,r}^2 V_m \tag{3.64}$$

$$P = \frac{1}{2}\varepsilon_0 n_w^2 E_{\max,w}^2 A_m v_g \tag{3.65}$$

In Equations (3.62) and (3.63), n_r and n_w are the refractive index of the core of the resonator and the waveguide, V_m is the effective mode volume of the resonator, and A_m and v_g are the effective mode area and the group velocity of the waveguide mode, respectively. The integration in Equation (3.63) is a volume integration that extends over the cross section of the waveguide (as a perturbing element) and over a length in the waveguide propagation direction in which the resonator field is considerable. Because of the reciprocity, the coupling factor κ can also be obtained by calculating the coupling integral over the resonator volume (as a perturbing element). However, for the latter case, a few modifications have to be made in Equation (3.63). Appendix E provides the derivation of κ for both cases.

To gain insight into the impact of different physical parameters on κ and Q_c, Equation (3.61) can be simplified as follows:

[31] In other words, $\Delta(n^2) = n^2_W - n^2_b$, where n_W is the refractive index of the waveguide and n_b is the refractive index of the background region that the waveguide has occupied.

$$\kappa = -\frac{j\omega_0}{2}\frac{\int dzdA\Delta(n^2)e_r^* e_w e^{j(m\phi - j\beta z)}}{\sqrt{n_r^2 n_W^2}\sqrt{v_g V_m A_m}} \quad , \quad \left(e_{r/w} = \frac{E_{r/w}}{|E|_{\max, r/w}}\right), \tag{3.66}$$

and correspondingly, Q_c is

$$Q_c = \frac{\omega_0}{|\kappa|^2} = \frac{4n_r^2 n_W^2 v_g V_m A_m}{\omega_0 \left|\int dzdA\Delta(n^2)e_r^* e_w e^{j(m\phi - j\beta z)}\right|^2}. \tag{3.67}$$

Equation (3.67) shows that Q_c is proportional to the mode volume of the resonator. Therefore, a smaller mode volume results in a stronger coupling. However, Q_c does not have the same proportionality to A_m, which is because of the area integration in the denominator of Equation (3.67). In the equation, the larger the integral in the denominator (which is taken over the cross section of the waveguide and along its propagation direction), the stronger the coupling, and therefore, the smaller the Q_c. Three terms define the strength of this integral:

1- The interaction length between the resonator and the waveguide, which is represented by the integration volume;

2- The extension of the resonator field in the waveguide core. Usually, the lateral field extension of the resonator is exponential; hence, when the waveguide is moved closer to the resonator, we expect the same exponential behavior in the integral and Q_c;

3- The level of phase-mismatch between the waveguide mode and the resonator mode, which is represented by the term ($m\phi$-βz) in Equation (3.67). In fact, the value of the integral in Equation (3.67) has a *Sinc*-function dependence on the phase mismatch. If the two modes have a large phase mismatch, the

integral becomes small. Further increasing the interaction length beyond the first lobe of the *Sinc* function pushes the integral close to zero, which results in an infinite value for Q_c.

From this discussion, we can conclude that optimizing the phase matching and the field overlap of the waveguide-TWR are more critical than optimizing the mode volume of the resonator. In the following sections, we calculate and evaluate Q_c of the waveguide-TWR structures for different planar traveling-resonator architectures using Equations (3.62) and (3.63).

3.2.3.1. Simulation and Optimization Results of Coupling Q (Q_c) for Microring Resonators

In this section, we investigate the Q_c for a microring in the coupling structure shown in Figure 3.11. Many ideas and concepts explored in this section can be extended and applied to microdisk structures. The inner radius of the microring for this simulation is fixed and chosen to be r = 10 μm. However, the other parameters of the structure such as the waveguide width (WW), the resonator width (WR), the gap, and the pedestal thickness (p) can vary during the analysis. As mentioned before, the free input parameters to optimize the coupling are the resonator and the waveguide sizes, the spacing between them, the thickness of the Si pedestal layer, and the cladding material. The impact of these parameters on the phase matching and field overlap of the waveguide-TWR structure is investigated systematically.

In all the following simulations the refractive indices of silicon and oxide are considered to be 3.475 and 1.444 for all the wavelengths. The exact mode profile,

including all the field components and resonance wavelength of the ring resonator, are obtained by solving the vectorial Helmholtz equation using the finite-element method, as discussed in chapter 2. Correspondingly, the mode profile and the propagation constant of the waveguide are also obtained at the resonance wavelength of the resonator. Then, using numerical integration, the value of κ in Equation (3.63) and consequently the value of Q_c in Equation (3.62) are calculated. In all the simulations, the polarization of the waveguide and the resonator modes is TE (the electric field is predominantly in the plane of the resonator and the waveguide).

Figure 3.12 shows the numerical calculation of Q_c at different wavelengths for two pedestal thicknesses of p = 0 nm and p = 40 nm for the cases of oxide cladding (which is relevant to most applications) and air cladding. For this simulation, the gap is 200 nm and H = 250 nm. As shown in Figure 3.12, for a ring resonator structure that has a zero pedestal thickness and an air cladding, Q_c is of the order of a million, which is typically far above the intrinsic Q of a ring resonator with such dimensions with the current fabrication technology [62]. As shown in Figure 3.12, it is interesting to note that Q_c for a pedestal thickness of 40 nm and the air-cladding case is much smaller, by nearly one order of magnitude, than the case of a zero pedestal and the same air cladding. This shows the great impact of adding such a thin pedestal layer on improving the coupling.

As is known, the presence of the oxide cladding extends the resonator field more to the outside of the resonator, which enhances the coupling. As long as the

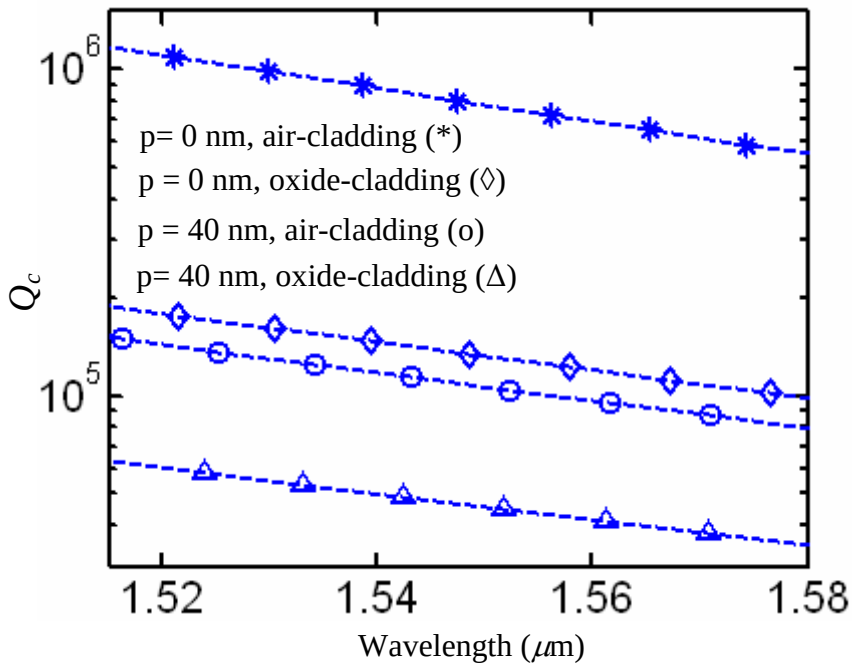

Fig. 3.12: Calculated Q_c of the structure shown in Figure 3.11, with r = 10 μm, WW=WR=500 nm, H=250 nm, at different wavelengths for two different pedestal thicknesses of p=0 nm and p=40 nm, and the air-cladding and oxide-cladding cases. The gap between the waveguide and the resonator in all cases is 200 nm.

resonator bend radius is not so small that the Q of the resonator is limited by radiation, an oxide or any other low-loss dielectric can be used as cladding. Figure 3.12 shows the effect of adding an oxide cladding layer on improving the coupling. It is noteworthy that the Q_c for the oxide-cladding and zero pedestal (the diamond markers) case is larger than for the case of the 40 nm pedestal and air cladding (the circle markers). This shows that the 40 nm pedestal layer is more significant in coupling improvement compared to a zero pedestal with oxide cladding. When both pedestal layer and an oxide cladding are present, we expect a significant improvement in coupling, as shown in Figure 3.12 (the delta markers). The Q_c in

this case is in the range of the achievable intrinsic Q of the resonator with a conventional fabrication technology.

To further investigate the impact of the pedestal layer on the coupling, we calculated the Q_c of the waveguide-TWR structure shown in Figure 3.11 for different pedestal thicknesses. Figure 3.13 shows the results of these calculations for different pedestal thicknesses and gaps between the waveguide and the resonator. For this simulation, we changed the thickness of the pedestal layer from zero to 80 nm, at which point the field distribution of the resonator showed a strong radiative behavior outside the resonator rather than being dominantly evanescent. As can be seen from Figure 3.13, increasing the pedestal thickness reduces the Q_c exponentially. However, it has to be noted that, depending on the bend radius of the resonator, the thickness of this layer has to be optimized in order to not degrade the Q by strong radiation of resonator energy through this layer, and therefore leave the resonator Q limited by other factors such as fabrication imperfections. As is discussed in section 4, experimental results show that ultra-high Q is preserved for pedestal thickness at least up to 50 nm.

In all the above calculations of Q_c, the overall height of the resonator was fixed to H = 250 nm. However, as intuitively expected, reducing H extends the mode distribution of the resonator laterally and therefore we expect an enhancement in the coupling strength. To better see the effect of this change, two scenarios can be compared. One case is to keep the overall height (H) of both waveguide and resonator fixed and change the pedestal thickness (see Figure 3.14(a), case I). The

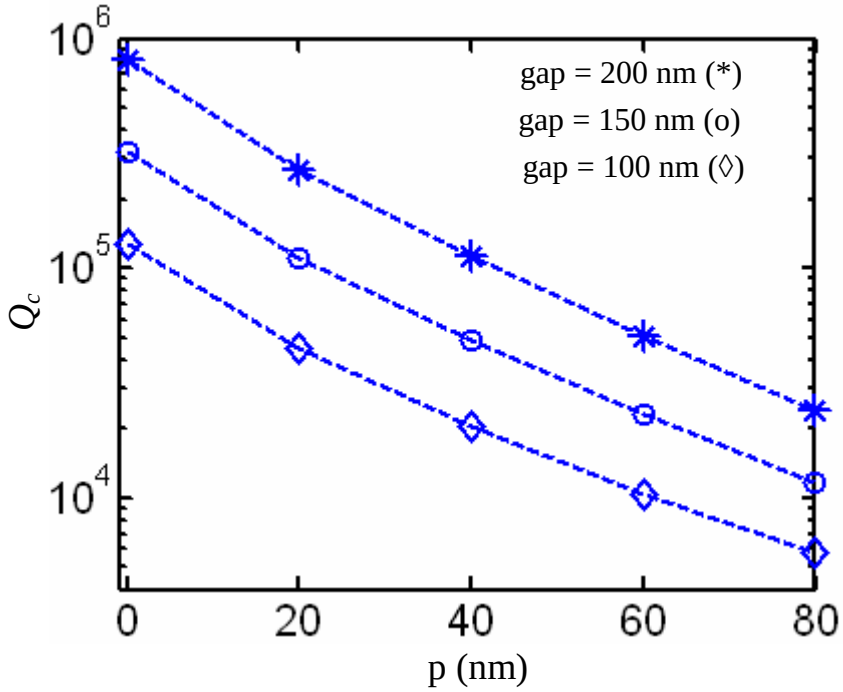

Fig. 3.13: Calculated *Q*c of the waveguide-resonator structure shown in Figure 3.11, with r= 10 μm, WW = WR = 500 nm H = 250 nm, and an air cladding, at different pedestal thicknesses and different gaps. The simulations were performed at resonance wavelengths ~1550 nm.

results of this case have already been shown in Figure 3.13. The other case is to keep the pedestal zero and reduce the overall height H of both waveguide and resonator by an amount of h (see Figure 3.14(a), case II). Figure 3.14(b) shows the comparison of the calculation Q_c for both cases. The simulation is performed for two different waveguide-TWR gaps of 100 nm and 200 nm. The solid and dashed curves in Figure 3.14(b) correspond to case I and case II in Figure 3.14(a), respectively. In both cases, the coupling is considerably modified. However, as is evident from the slope of the curves in Figure 3.14(b), changing the pedestal thickness has a stronger effect on enhancing the coupling compared to the case of changing the waveguide height and leaving the pedestal thickness at zero. Hence, it

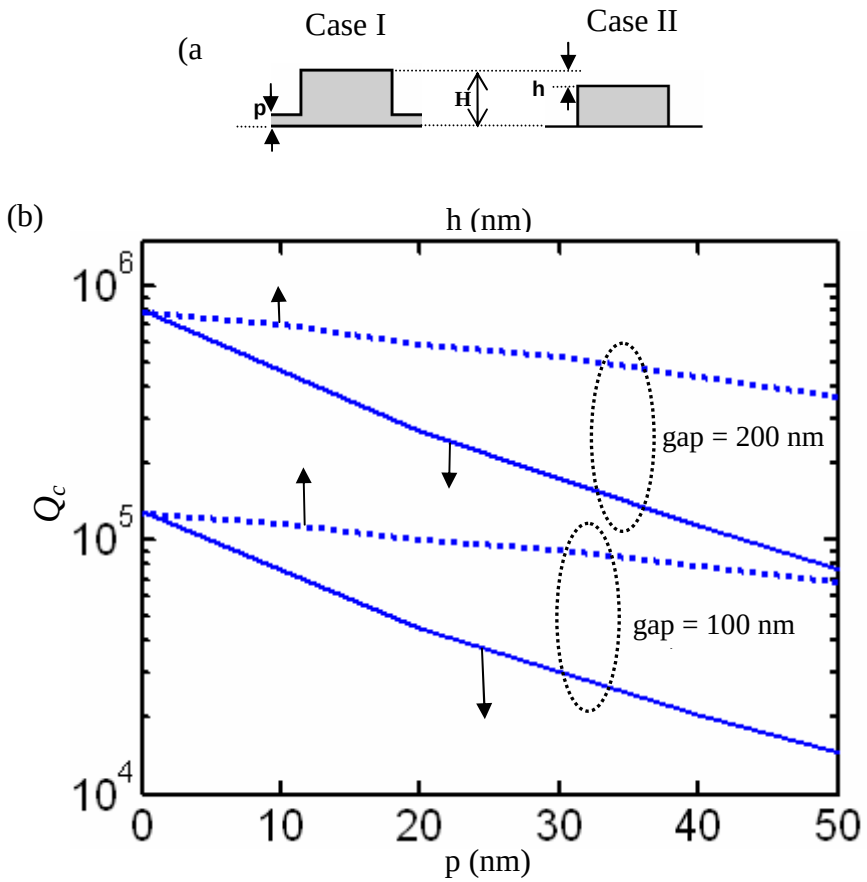

Fig. 3.14: Comparison of two waveguide architectures employed for the implementation of the waveguide-resonator structure shown in Figure 3.11. (a) Case I: a waveguide with overall height of H = 250 nm and width WW=500 nm with a pedestal p varying; Case II: a waveguide without a pedestal layer and with a reduced varying height. (b) Solids: Q_c of the coupling structure versus p when the waveguide architecture in case I in (a) is employed; Dashes: Q_c of the coupling structure versus h when the waveguide architecture in case II in (a) is employed. For these simulations, the ring inner radius is 10 μm, and two different gaps of 100 nm and 200 nm have been tried.

can be concluded that a simultaneous decrease in the waveguide height as well as an increase in the pedestal thickness will further enhance the coupling.

Another key parameter that affects Q_c is the waveguide and the resonator widths. Multiple physical effects simultaneously occur by changing these widths. As is known, reducing the resonator width reduces the mode volume (V_m) and according

to Equation (3.67), it reduces the Q_c. In addition, reducing the resonator width extends the resonator mode energy more to the outside, which exponentially enhances the field overlap between the resonator and the waveguide. Reducing the width of the waveguide makes the field more uniform (i.e., smaller peak-to-average ratio) inside the waveguide core. This smaller peak-to-average ratio of the waveguide mode enhances the coupling integral in Equation (3.67). However, reducing the waveguide width simultaneously reduced the coupling integral due to a reduction in the integration volume. In addition, the change of the waveguide and resonator widths strongly impacts the phase-matching condition, which can dramatically change Q_c. To further investigate the effect of waveguide and resonator widths on phase matching, we note that in a microring or a microdisk resonator, the effective index of the mode traveling inside the resonator is inversely proportional to the radial distance (i.e., $n_{eff} = \lambda_0 m/(2\pi r)$, see Equation 2.34 in chapter 2). As a result, the mode distribution of the resonator outside the resonator has a lower effective index than that of the resonator core. Therefore, to provide better phasematching, the waveguide, which is laterally seated outside the resonator, has to have a lower effective index compared to a resonator mode in the resonator core. This can be satisfied by reducing the waveguide width in comparison to the resonator width. Although reducing the waveguide width has the drawback of reducing the integration volume shown in Equation (3.67), because of the exponential effect of phase matching on Q_c, the coupling can be strongly improved. More precisely, there is an optimum width that maximizes both the phase matching

and the integration volume effects, which is discussed later. In the case where the resonator width is smaller than the waveguide width, the phase mismatch increases. In this case, while the field of the resonator extends more outside, the larger phase mismatch results in reducing the coupling. To quantitatively see these effects, we calculated the Q_c for three representative cases: 1) the waveguide width is smaller than the resonator width, 2) the waveguide and resonator widths are the same, and 3) the waveguide width is larger than the resonator width.

Figure 3.15 shows the Q_c of the waveguide-TWR structure shown in Figure 3.11 for different cases of resonator and waveguide widths. For this simulation, the cladding is air, the gap is 200 nm, and a 40 nm pedestal layer is considered. As can be seen from this figure, the case of WR = 500 nm and WW = 440 nm has a much lower Q_c than the one for the case of WR = 500 nm and WW = 500 nm. This is because the former case has improvement in both phasematching and field overlap compared to the latter case. Even the Q_c of the case of WR = 500 nm and WW = 500 nm is lower than for the case of WR = 440 nm and WW = 500 nm. In the latter case, although reducing the resonator width has extended more of the resonator mode field inside the waveguide, at the same time, it has increased the phase mismatch, which has been dominant in reducing the coupling strength. Another case is to simultaneously reduce the resonator and the waveguide widths. For this case with WR = 440 nm and WW = 440 nm, although suffering from phase mismatch, compared to the case with WR = 500 nm and WW = 440 nm, stronger coupling as a result of strong field overlap is observed.

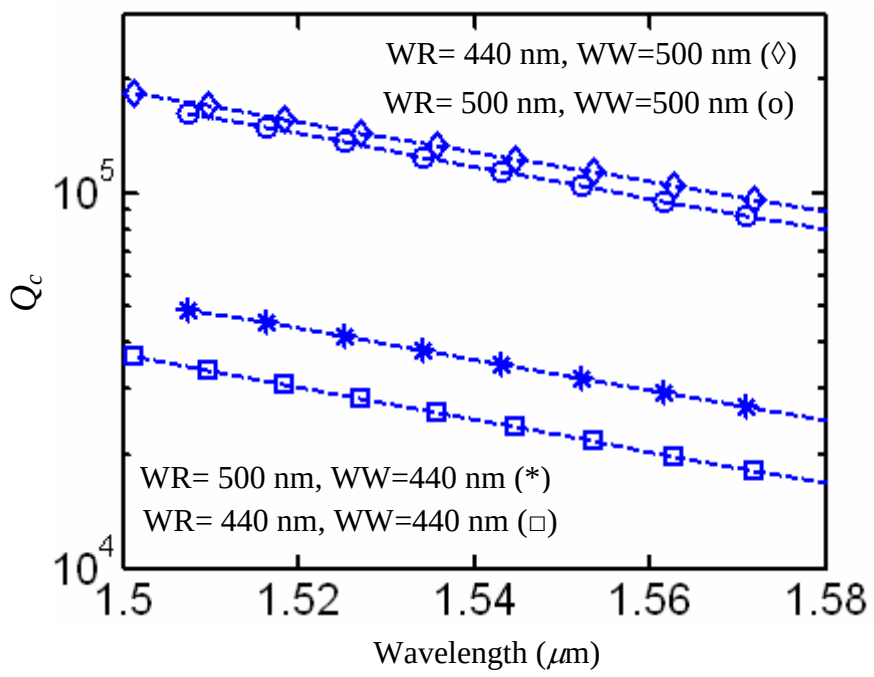

Figure 3.15: (a) Calculated Q_c of the waveguide-resonator structure shown in Figure 3.11 at different wavelength and for different resonator and waveguide widths. For this simulation r = 10 μm, gap = 200 nm, H = 250 nm, p = 40 nm, and the cladding is air.

From the results observed in Figure 3.15, it can be concluded that in general, reducing the widths of both the waveguide and resonator enhances the coupling, because of the strong field overlap of the resonator and the waveguide modes. In addition, further reduction of the waveguide width results in a stronger coupling because of better phase matching. However, the remaining question that may arise is whether for a resonator with a fixed width, an optimum waveguide width exists since we cannot keep reducing the waveguide width and satisfy phase matching. Figure 3.16 answers this question by calculating the Q_c of the structure shown in Figure 3.11 versus the waveguide width for a fixed resonator width WR = 500 nm. Each curve corresponds to a different gap. For this simulation, the cladding is air

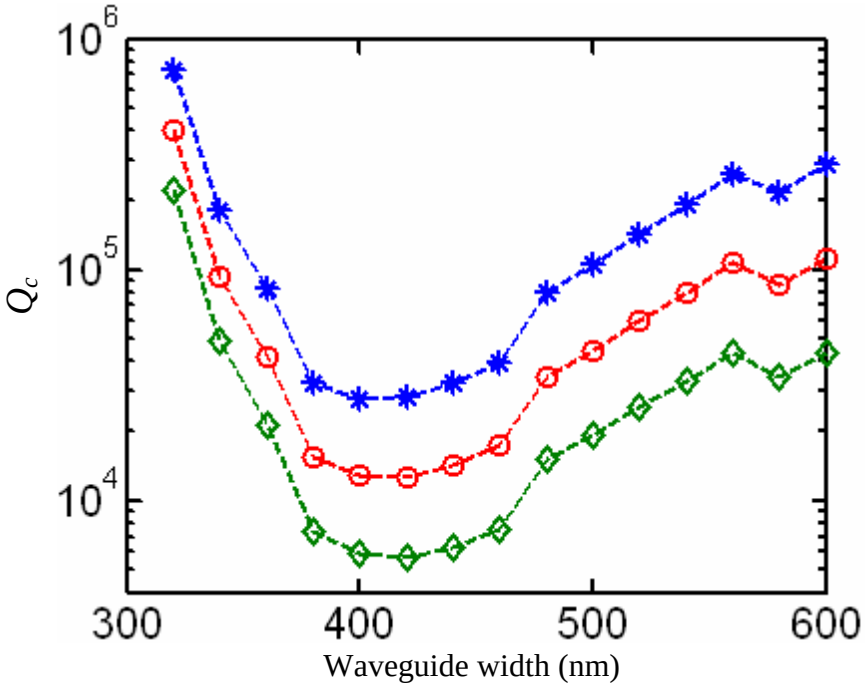

Fig. 3.16: Calculated Q_c of the structure shown in Figure 3.11, with r=10 μm, WR = 500 nm, H = 250 nm, and a pedestal thickness of 40 nm, with air cladding, at different gaps of 100 nm (+), 150 nm (o), and 200 nm (*), versus waveguide width (WW). The calculation of Q_c for all cases was performed at a resonance ~1550 nm.

and a 40 nm pedestal layer is considered. As can be seen from Figure 3.16, there is an optimum range of WW ~ 420-440 nm to obtain the strongest coupling, i.e., minimum Q_c. In fact, as shown in Figure 3.16, further reduction in WW does not improve Q_c, which highlights the effect of increased phase mismatch as well as reduction in the integration volume. Another interesting fact seen from Figure 3.16 is that, at the optimum point, the Q_c has minimum sensitivity to small changes in the waveguide width. Therefore, for a waveguide-TWR fabricated with dimensions close to these optimal sizes, any fabrication error in the dimensions of the waveguide and the resonator has minimal change in Q_c. Although the resonator dimensions and the pedestal thickness are fixed for this simulation, we notice in our

simulations that the conclusion is very general and for other resonator dimensions, a suitable optimum waveguide width can be obtained.

3.2.3.2. Simulation and Optimization Results of Coupling Q (Q_c) for Microdisk Resonators

In this section, we explore the coupling to a microdisk resonator. Because of their multi-modal and intrinsic ultra-high Q properties [63], microdisk resonators require a careful coupling optimization to excite an individual mode or several radial mode orders with the required level of Q_c. As mentioned before, in contrast to a microring of the same radius, the energy tail of the whispering gallery mode of a microdisk decays more rapidly in the radial direction and outside the disk region. As a result, compared to a microring, coupling of the microdisk to a straight waveguide, which is laterally seated next to it, is weaker and consequently, Q_c is larger. Hence, achieving critical coupling or even strong over-critical coupling, especially for applications such as coupled resonators or all-pass filters, may be challenging with a reasonable spacing between the resonator and the waveguide. For larger radii microdisks, achieving the required Q_c becomes more challenging since the mode energy tail outside the disk decays faster. We did an analysis to see the effect of resonator radii on Q_c. Figure 3.17(a) shows the calculated Q_c of the first three radial mode orders of a microdisk resonator coupled to a waveguide for different microdisk radii. For this simulation, two cases of a zero pedestal and a pedestal of 40 nm have been considered. For the smallest microdisk radii considered for this simulation (i.e., r = 2.5 μm), some of the radial mode orders, especially the higher-

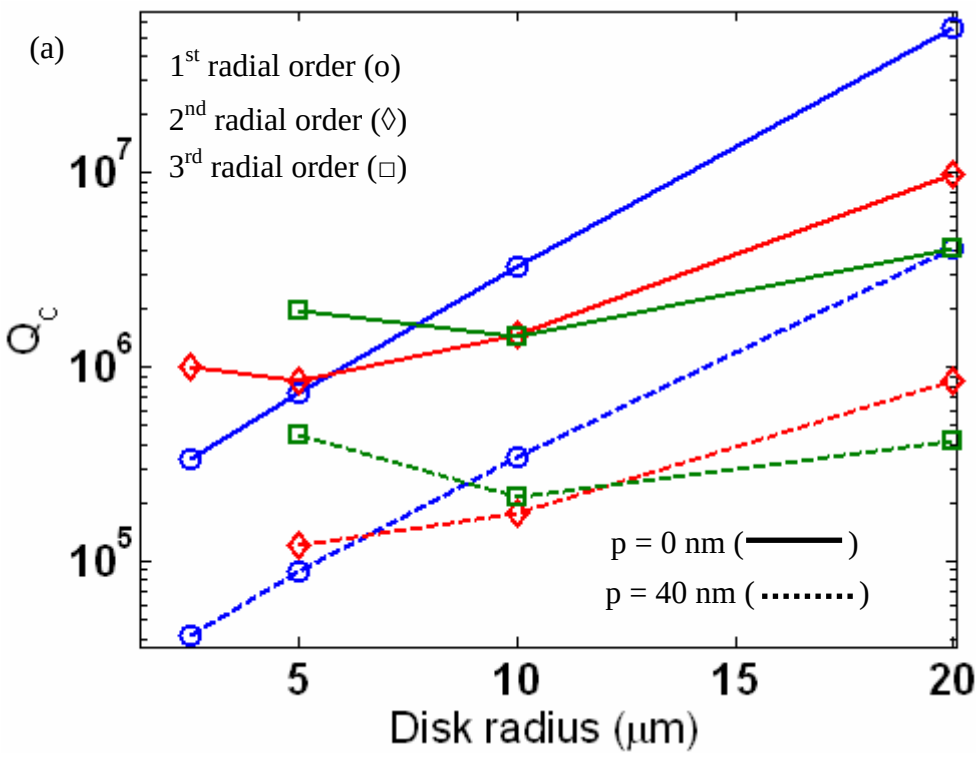

(b)

	Radius r = 5 μm	Radius r = 10 μm	Radius r = 20 μm
Mode order = 1	λ_0 = 1554.646, m = 52	λ_0 = 1545.135, m = 110	λ_0 =1548.135, m = 226
	$n_{eff\text{-}R}$ =2.383, $n_{eff\text{-}WG}$=2.528	$n_{eff\text{-}R}$ =2.601, $n_{eff\text{-}WG}$ = 2.537	$n_{eff\text{-}R}$ =2.730, $n_{eff\text{-}WG}$=2.534
Mode order = 2	λ_0 =1547.719, m = 47	λ_0 = 1547.763, m = 103	λ_0 =1550.586, m = 217
	$n_{eff\text{-}R}$ =2.144, $n_{eff\text{-}WG}$= 2.534	$n_{eff\text{-}R}$ =2.440, $n_{eff\text{-}WG}$= 2.534	$n_{eff\text{-}R}$ =2.625, $n_{eff\text{-}WG}$=2.532
Mode order = 3	λ_0 =1540.748, m = 43	λ_0 =1553.321, m = 97	λ_0 =1550.707, m = 210
	$n_{eff\text{-}R}$ =1.953, $n_{eff\text{-}WG}$= 2.541	$n_{eff\text{-}R}$ =2.306, $n_{eff\text{-}WG}$=2.529	$n_{eff\text{-}R}$ =2.541, $n_{eff\text{-}WG}$=2.531

Fig. 3.17: (a) Calculated Q_c of a the first (o), second (◊), and third (□) radial mode orders of a microdisk resonator for different disk radii, for two cases of pedestal=0 nm (solid curves) and pedestal = 40nm (dashed curves). The coupling structure is shown in Figure 3.11 where the ring is replaced by a disk. For this simulation, gap = 150 nm, WW = 500 nm, and H=250 nm. The calculation of Q_c for all resonators was performed at resonance wavelengths ~1550 nm. (b) A table showing the resonance wavelength (λ_0), azimuth mode number (m), waveguide effective index ($n_{eff\text{-}WG}$), and the resonator effective index ($n_{eff\text{-}R}$) for the pedestal structure and for microdisk radii 5 μm, 10 μm, and 20 μm. For each microdisk radius, $n_{eff\text{-}R}$ was calculated at the center of the width of the waveguide when the gap = 150 nm as $n_{eff\text{-}R} = m\lambda_0 / [2\pi(r+gap+WW/2)]$.

order modes, showed a strong radiative behavior and therefore their Q_c was not calculated. As expected and seen in Figure 3.17(a), for all the microdisk radii and for all three radial modes, the Q_c in the presence of the 40 nm pedestal layer is about one order smaller than that of the zero pedestal. Increasing the thickness of the pedestal layer (as long as the resonance mode does not go to the strong radiation regime) can further enhance the coupling. For a typical pedestal of 40 nm, the Q_c of the first few orders of radial modes can be in the range of the intrinsic Q of the microdisk resonators with the current technology (This is shown with experimental results in chapter 5).

As seen in Figure 3.17, for some microdisk radii, when going to lower-order radial modes, the Q_c becomes higher. However, for some other radii (such as r = 5 μm), the Q_c of the 3rd order radial mode becomes higher than that of the 1st and the 2nd order radial modes. This has to be investigated through the resonator parameters in Equation (3.67), which are 1) the resonator mode volume, 2) the strength of the resonator mode overlap with the waveguide, and 3) the phase matching between the resonator mode and the waveguide mode. From Figure 2.18 in chapter 2, we saw that the mode volumes of the higher-order modes are larger. However, their magnitudes are at the same level and the difference between them is below a factor of two. Therefore, the mode volume cannot be a reason to have the Q_c of the 3rd order mode larger than that of the lower-order modes, as seen in Figure 3.17 for the microdisk with the radius of 5 μm. Regarding the mode overlap of the waveguide and the resonator, we know that the mode profile of the 1st order mode of the

resonator decays more quickly in the lateral direction outside the disk than that of the higher-order modes[32]. Therefore, we expect a higher Q_c for the 1st order radial mode, as it has a weaker field overlap with the waveguide mode, which makes the integral in Equation (3.67) smaller compared to that in higher-order modes. However, this does not seem to be a dominant factor for the microdisk with r = 5 μm in Figure 3.17, as the Q_c of the 3rd radial order mode is larger than that of the 1st order mode. Hence, the only reason to have the Q_c of the 3rd order mode larger than the 1st and the 2nd order modes is the larger phase mismatch between the 3rd order radial mode and the waveguide mode compared to that for the 1st and the 2nd radial mode. To verify this, we have shown the details of the parameters obtained for the pedestal microdisk architecture in the table in Figure 3.17(b). This table also shows the effective indices of the waveguide mode and the resonator mode at the resonance frequency of the resonator mode. As seen from this table, for r = 5 μm, the effective-index difference between the waveguide mode and the 3rd order radial mode is much larger than the effective index difference between the waveguide mode and the 1st order mode. Such a large term when appearing in the phase term (i.e., $\exp(im\phi - i\beta z)$) in the integral in Equation (3.67) makes the integral very small, which weakens the coupling. This shows the dramatic impact of phase matching on controlling the strength of the coupling.

[32] This is because the 1st order radial mode has the highest azimuth mode number (as seen in chapter 2) and as a result the decay of the mode profile, which can be approximated with a Hankle function, is faster (Hankle functions with larger azimuth mode numbers have faster decay).

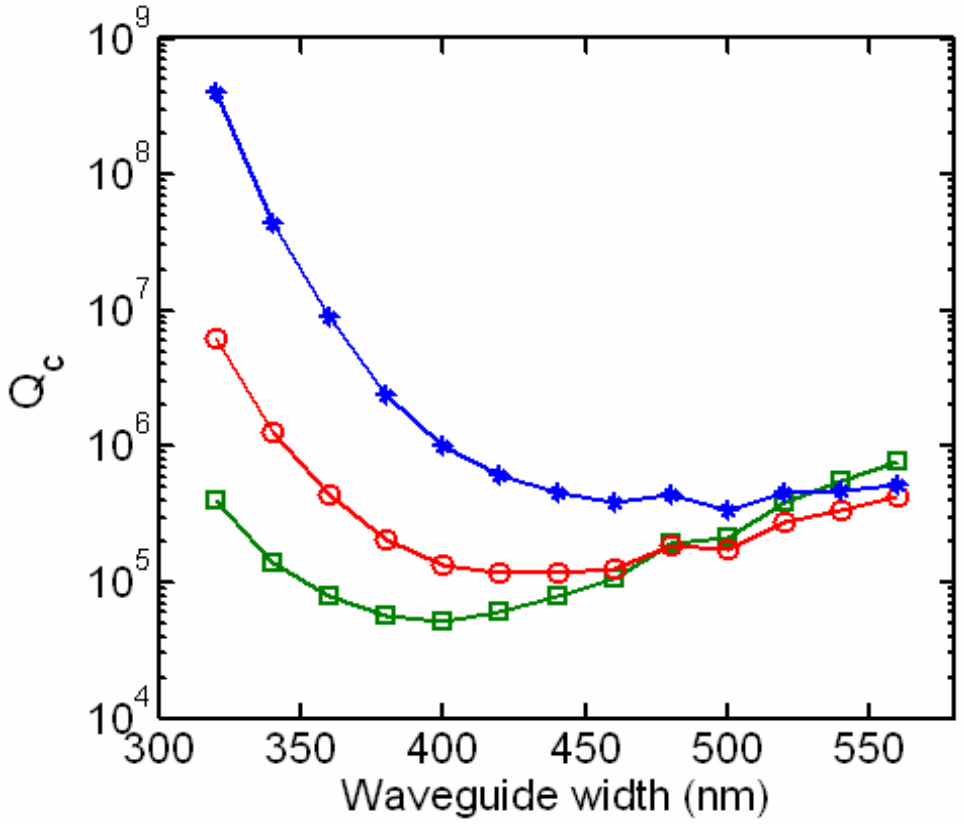

Fig. 3.18: Calculated Q_c of the first (*), the second (o), and the third (□) radial mode orders of a microdisk resonator with radius 10 μm in the structure shown in Figure 3.11 where the ring is replaced by a disk. The structure parameters as shown in Figure 3.11 are gap = 150 nm, H=250 nm, pedestal=40 nm, and the waveguide width (WW) is a varying parameter. The calculation of Q_c for all resonators was performed at resonance wavelengths ~1550 nm.

Similar to a microring resonator, efficient coupling to a microdisk resonator requires the optimization of the waveguide width. Furthermore, each radial mode order of the microdisk has a different mode profile distribution and phase. Therefore, the optimized waveguide dimensions are expected to be different for each microdisk mode. To verify this, we performed a simulation for a microdisk with a fixed radius of 10 μm coupled to a waveguide with different widths. The coupling structure is shown in Figure 3.11, where the ring is replaced by a disk.

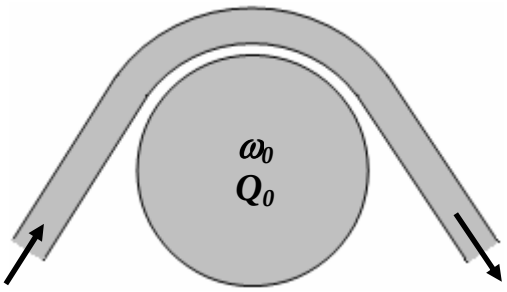

Fig. 3.19: Schematic a waveguide-TWR coupling structure where the waveguide is bent concentric with the resonator to increase the interaction length. If the waveguide mode and the resonator mode are phase matched, the coupling is enhanced; otherwise, if they are phase mismatched by increasing the interaction length, the coupling may approach zero.

Figure 3.18 shows the calculated Q_c of the first three radial mode orders for such a microdisk coupled to the waveguide. The simulations were performed for a resonance mode near 1550 nm. As can be seen from Figure 3.18, the optimum waveguide width to minimize the Q_c (i.e., to enhance the coupling) is different for different radial orders of the microdisk mode. This optimized waveguide width is mostly due to satisfying the phase matching between the resonator mode and the waveguide mode.

3.2.3.3. Additional Structural Modifications to Improve the Coupling to Microring and Microdisk Resonators

In the preceding analysis of the optimization of Q_c in a waveguide-TWR coupling for microring and microdisk resonators, the coupling waveguide was considered to be straight in the coupling region, and as a result, the interaction length between the waveguide and the resonator in the coupling region was short. To increase the interaction length, the coupling waveguide can be bent and concentrically wrapped around the resonator. This coupling scheme is shown in Figure 3.19.

Such a coupling scheme was studied for microring resonators [64] and the improvement in coupling was experimentally verified [65]. In this technique, the waveguide width should be made smaller than the microring width to match the effective indices of their modes propagating concentrically and thereby satisfy the phase-matching condition. If the phase mismatch between the resonator mode and the waveguide mode is large, then the integral in Equation (3.67) becomes very because of the large interaction length in this coupling scheme small, and as a result, the coupling becomes very weak. Therefore, it is very important to adjust the phase matching when the interaction length is long.

The coupling scheme shown in Figure 3.19 has also been employed for ultra-high Q microdisk resonators [66,67] to further enhance the weak coupling observed in these resonators. However, because of the larger interaction length and the requirements of the phase matching, the coupling of only one radial mode or at most a few radial modes of the microdisk that are closely phase matched to the waveguide mode is enhanced and coupling to the rest of the radial modes approaches zero [66,67].

3.2.3.4. Additional Notes on Calculating Q_c using Equation (3.63)

In the preceding analysis, we employed Equation (3.63) as the 1st order approximation to calculate the Q_c of a waveguide-TWR structure. As seen from this equation, the fields of the unperturbed resonator and the waveguide have been incorporated into the equation. While in the 1st order approximation this assumption is reasonable, more accurate results can be obtained when 2^{nd} order effects are

considered. As we discussed above, Q_c is very sensitive to phase matching, which depends on the phases of the waveguide and the resonator. Hence, one important modification to Equation (3.63) is the correction of phase variation of the waveguide mode and the resonator mode in the coupling region (presently in this equation, the unperturbed terms βz and $m\phi$ have been considered for the waveguide and the resonator phases, respectively). This phase correction becomes more important when the interaction length becomes longer and thus the effect of phase becomes important. To make this correction, we have performed a more rigorous analysis of waveguide-TWR coupling (shown in Appendix E), and the correction term in the phase has been obtained. This phase correction adds more wavelength dispersion to the value of Q_c.

3.3. Space-Domain Approach for Waveguide-Resonator Coupling

Because of the traveling-wave nature of the resonance mode in a TWR, its coupling to a waveguide can be modeled as a directional coupler. In this scenario, the input and output ports of one of the branches of the coupler form a loop, which is the resonator. This method of analysis is applicable for racetrack resonators as well, in which case the coupling region is long and the coupling branches are parallel. In the time-domain approach, the resonator mode was represented with one parameter, i.e., a in (3.1), and no spatial variation was considered in a. Therefore, any perturbation in the resonator would result in a change in a and consequently, the entire mode profile of the resonator would scale with the same level as a. In other words, in the presence of the perturbation, no spatial variation in the mode profile of the resonator

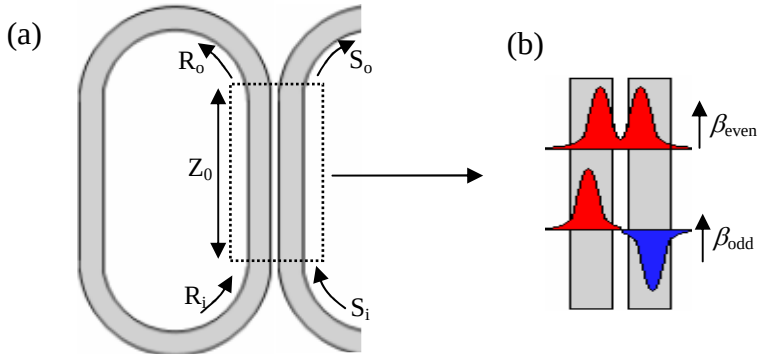

Fig. 3.20: (a) Structure of a racetrack resonator coupled to a waveguide. (b) Detailed structure of the coupling region, which is a directional coupler with identical branches. The super-even and super-odd modes of the directional coupler and their propagation constants are shown.

was considered. In contrast, in the space-domain approach, the spatial mode profile variation of the resonator as a result of the perturbation is considered in the coupling analysis. As an example, for a racetrack resonator that is coupled to a waveguide with a long coupling length, the resonator energy profile in the coupling region has a spatial variation because of the interaction with the waveguide. However, far from the coupling region, the energy profile is almost constant. For such cases, space-domain analysis is superior to the time-domain analysis, where the resonator energy mode variation is not considered in the coupling region. The limitation of space-domain analysis is when the resonator is very small or the coupling region is so short and the bending radius of the resonator is so small that the coupling cannot be modeled accurately using a directional coupler model. For such cases, the time-domain approach is more suitable.

Applying space-domain analysis to a racetrack resonator coupled to a waveguide provides interesting closed-form results. For the racetrack-waveguide coupling

structure shown in Figure 3.20(a), the coupling region is made symmetric to provide perfect phase matching between the waveguide mode and the resonator mode; otherwise (if phase mismatch exists) the coupling strength may become very weak because of the large interaction length. Figure 3.20(b) shows the details of the symmetric directional coupler in the coupling region. Also, the profiles of the super-even and super-odd modes of the coupler are shown in Figure 3.20(b). In this section we focus on a symmetric coupling structure, and more general cases of the waveguide-resonator coupling with space-domain analysis are discussed in Appendix F. For the coupling structure shown in Figure 3.20, the coupling matrix is

$$\begin{bmatrix} S_o \\ R_o \end{bmatrix} = \exp(-i\beta Z_0 - \alpha Z_0) \begin{bmatrix} \cos(\frac{\Delta\beta Z_0}{2}) & i\sin(\frac{\Delta\beta Z_0}{2}) \\ i\sin(\frac{\Delta\beta Z_0}{2}) & \cos(\frac{\Delta\beta Z_0}{2}) \end{bmatrix} \begin{bmatrix} S_i \\ R_i \end{bmatrix}. \tag{3.68}$$

In Equation (3.68) S_i, R_i, S_o, and R_o are the signals at the ports of the coupler (as shown in Figure 3.20) and are normalized such that their squared magnitude corresponds to their optical power. Also, Z_0 is the length of the coupling region, and β and α are the wave propagation constant and propagation loss, respectively, in the waveguide and the racetrack. In addition, we have

$$\Delta\beta = \beta_{even} - \beta_{odd}\,. \tag{3.69}$$

The super modes of the directional coupler and their wave propagation constants can be found by electromagnetic FEM simulation of the directional coupler. Because of the symmetry of the directional coupler, β of the waveguide is related to the propagation constants of the super modes of the coupler as

$$\beta = (\beta_{even} + \beta_{odd}) / 2 . \tag{3.70}$$

In addition, the following relation between R_o and R_i exsist:

$$R_i = R_o \exp[-i\beta(L - Z_0) - \alpha(L - Z_0)], \tag{3.71}$$

where L is the total length of the racetrack. By combining Equations (3.68) and (3.71) we reach the following expression for the transmission through the waveguide:

$$T = \frac{S_o}{S_i} = \exp[-i\beta Z_0 - \alpha Z_0] \frac{\cos(\Delta\beta Z_0 / 2) - \exp(-\alpha L)\exp(-i\beta L)}{1 - \cos(\Delta\beta Z_0 / 2)\exp(-\alpha L)\exp(-i\beta L)}, \tag{3.72}$$

and its squared magnitude is

$$\begin{aligned} |T|^2 &= \exp(-2\alpha Z_0) \\ &\times \frac{\cos^2(\Delta\beta Z_0 / 2) - \exp(-2\alpha L) - 2\exp(-\alpha L)\cos(\Delta\beta Z_0 / 2)\cos(\beta L)}{1 - \cos^2(\Delta\beta Z_0 / 2)\exp(-2\alpha L) - 2\cos(\Delta\beta Z_0 / 2)\exp(-\alpha L)\cos(\beta L)} . \end{aligned} \tag{3.73}$$

The resonance condition for (3.73) occurs at

$$\beta L = 2\pi m , \tag{3.74}$$

and at this condition, Equation (3.74) becomes

$$|T|^2 = \exp(-2\alpha Z_0) \frac{[\cos(\Delta\beta Z_0 / 2) - \exp(-\alpha L)]^2}{[1 - \cos(\Delta\beta Z_0 / 2)\exp(-\alpha L)]^2} . \tag{3.75}$$

The critical coupling condition occurs when the numerator of Equation (3.75) is zero and for that case, we have

$$\cos(\Delta\beta Z_0 / 2) = \exp(-\alpha L) . \tag{3.76}$$

Equation (3.76) is a very useful expression in the sense that it relates the resonator loss to its length and the coupling parameters. Knowing that the Q of the

resonator is $Q_0 = 2\pi n_g/(\alpha\lambda_0)$ and putting it into Equation (3.76), we obtain the following expression at the critical coupling:

$$Q_0 = -\frac{2\pi n_g (L/\lambda_0)}{\ln[\cos(\Delta\beta Z_0/2)]}. \tag{3.77}$$

Therefore, to obtain critical coupling to a racetrack resonator with a known Q_0, the dimensions of the coupling region and the length of the resonator should be such that Equation (3.77) is satisfied. In fact, using Equation (3.77), we can design a racetrack-waveguide coupling to achieve the critical coupling condition.

3.3.1. Optimization of Coupling to Racetrack Resonators

While Equation (3.77) provides a design rule for the critical coupling condition, for many other applications we need a different level of coupling. Examples of these cases are all-pass filters and coupled-resonator filters. For such purposes, one way to evaluate the coupling is to directly start with some initial parameters for the resonator and directional coupler, put them into Equation (3.77), find the spectrum, and after measuring the linewidth and the power extinction, decide how to modify the parameters. The other way is to extend the analysis of the space domain, relate it to the results of the time-domain analysis, and from that relation find an expression for the coupling Q (Q_c) of the resonator. For a racetrack resonator coupled to a waveguide, as shown in Figure 3.21, we can find Q_c for the counterclockwise mode as follows: assuming that the resonator has an initial energy of u_0 and there is no input power from the waveguide, from the time-domain coupled-mode theory, the mode energy of the resonator can be expressed as $u(t) = u_0\exp(-2t/\tau_c)$, where τ_c, as

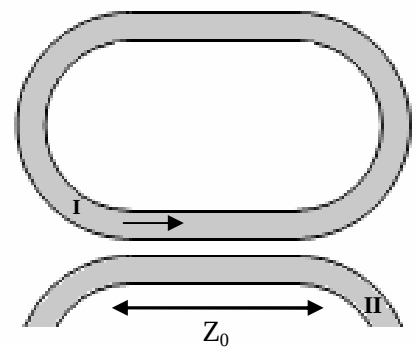

Fig. 3.21: Structure of a racetrack resonator side coupled to a waveguide. Both waveguide and the resonator have the same waveguide dimension.

defined before, is expressed as $\tau_c=2Q_c/\omega_0$. Starting at point I in the resonator in Figure 3.21, and doing a roundtrip in the counterclockwise direction, the average power transferred to the waveguide from the resonator in a roundtrip time of $t_r=L/v_g$ (L is the resonator length and v_g is the group velocity of the mode inside the resonator) is

$$p = u_0(1-e^{2L/(v_g\tau_c)})/(L/v_g). \tag{3.78}$$

Separately, we also know that from the space-domain coupled-mode theory of parallel waveguides [54], the power transferred from point I in the resonator to point II in the waveguide is

$$p = p_0 \sin^2(\Delta\beta Z_0/2), \tag{3.79}$$

where p_0 is the resonator circulating power at point I, Z_0 is the coupling length, and $\Delta\beta$ is the difference between the propagation constants of the super modes of the directional coupler structure in Figure 3.21. By equating Equations (3.78) and (3.79), knowing that $u_0= p_0v_g/L$ and $v_g = c/n_g$, and noting the relation between Q_c and τ_c ($Q_c = \omega_0\tau_c/2$), we find an expression for Q_c as

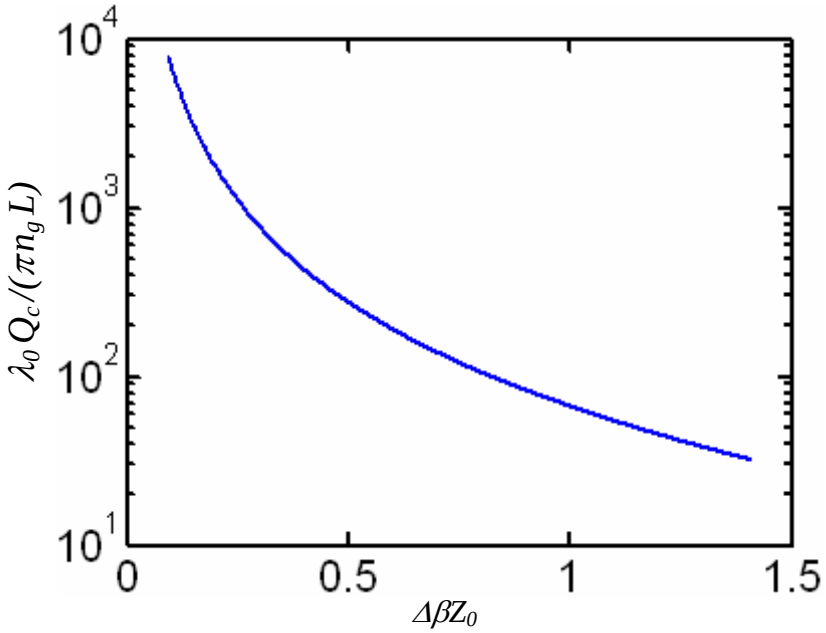

Fig. 3.22: Variation of the normalized Q_c of the waveguide-TWR structure, as shown in Figure 3.20, versus its normalized coupling length $\Delta\beta Z_0$.

$$Q_c = -\frac{\pi n_g L / \lambda_0}{\ln[\cos(\Delta\beta Z_0 / 2)]}. \tag{3.80}$$

The above equation relates the parameters of the directional coupler as well as the resonator lengths to the Q_c of the waveguide-racetrack coupling structure. It is interesting to see that Equation (3.80) has exactly the same form as Equation (3.77). In Equation (3.77), the resonator parameters are adjusted to achieve the critical coupling condition, while in Equation (3.80), the resonator parameters are adjusted to obtain the desired level of coupling specified by the coupling Q (Q_c). From Equation (3.80) it can be seen that for a fixed coupling length (Z_0), Q_c is linearly proportional to the resonator length (L), which is proportional to the mode volume of the resonator. This is, in fact, what we expected, as shown in the time-domain picture in Equation (3.67), where the proportionality of Q_c to the mode volume is

evident. Figure 3.22 shows the variation of Q_c normalized to the resonator length (i.e., Q_c/L) versus $\Delta\beta Z_0$, which we call the normalized coupling length of the directional coupler. From this figure, we notice that increasing $\Delta\beta Z_0$ dramatically reduces Q_c. Therefore, the most sensitive way to enhance and control the coupling is to change either $\Delta\beta$ or Z_0.

First, we consider the case of coupling control by changing Z_0. For a racetrack resonator with a fixed FSR, i.e., L is fixed, if Z_0 is increased to enhance the coupling, the bend radius has to decrease to keep the resonator length unchanged. This may degrade the intrinsic Q of the resonator due to the modal mismatch between the straight portion and the bent portion of the resonator, especially at small bend radii [49]. In addition, for a large Z_0, any fabrication imperfection that causes an imbalance between the waveguide and the resonator widths can dramatically reduce the coupling strength because of the large sensitivity of the coupling to $\Delta\beta$, as seen in Figure 3.22.

Another solution to enhance the coupling is to increase $\Delta\beta$. This can be done either by reducing the gap between the resonator and the waveguide or by reducing the width of both the waveguide and resonator so that their fields extend more outside the core in the lateral direction and as a consequence, they perturb each other more strongly. We have calculated the effects of these changes on the Q_c of the waveguide-racetrack coupling structure. Figure 3.23 shows the exponential variations of Q_c versus the gap. From this figure, we see that changing the gap has exponentially changed the Q_c. We also notice that the addition of a 40 nm pedestal

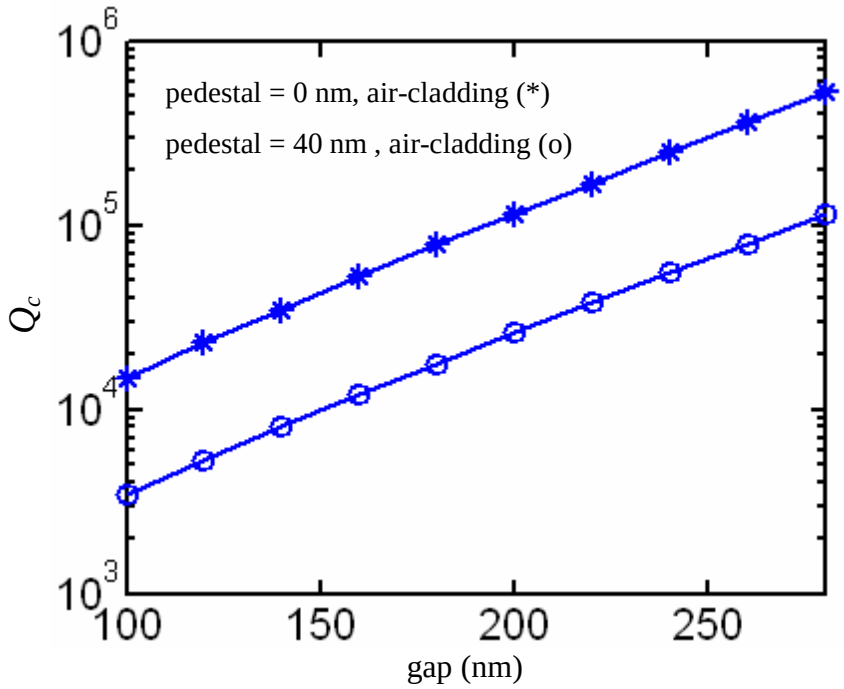

Fig. 3.23: Variation of Q_c versus the gap for a coupled waveguide-racetrack structure shown in Figure 3.20. The structure is made of a waveguide with a width of 500 nm and with different pedestal thicknesses. The cladding is air. The coupling length Z_0 = 5 μm and the bending radius of the racetrack is 6 μm. The simulations are performed for a resonance wavelength ~ 1550 nm.

layer results in almost one order of magnitude reduction in Q_c compared to the zero pedestal case, as seen in Figure 3.23. Figure 3.24 shows the effect of the width of the waveguide and racetrack on the variation of Q_c for both oxide cladding and air cladding. From this figure, we can see the almost exponential variation of Q_c versus the waveguide width.

As we have seen in Figures 3.23 and 3.24, both control of the gap and the width of waveguide and resonator result in large variation in Q_c. However, changing either of these two parameters requires that some fabrication issues be taken into consideration. Reducing the gap makes the lithography more challenging. On the other hand, reducing the resonator width degrades the intrinsic Q of the resonator

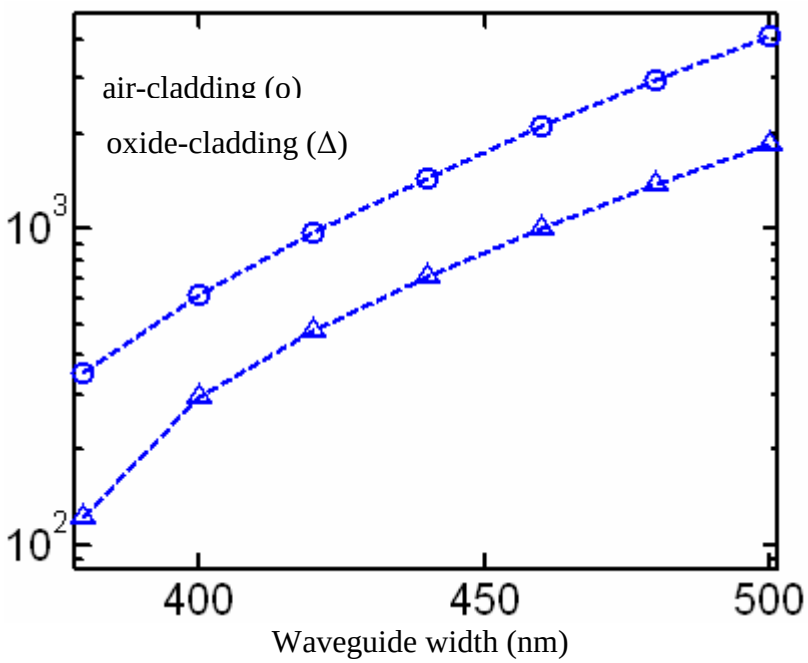

Fig. 3.24: Variation of Q_c versus the waveguide width for a coupled waveguide-racetrack structure. The coupling length Z0 = 5 μm, the gap is 100 nm, and the bend radius of the racetrack is 6 μm. A 40 nm pedestal layer is at the interface between the structure and the oxide substrate. The simulations are performed for the wavelength 1550 nm.

because of more sensitivity of the mode profile at the sidewalls, which are exposed to fabrication imperfections. Hence, based on the achievable lithography control and etching quality, as well as the targeted FSR and Q_c for the structure, we can choose the appropriate device dimensions.

It has to be noted that for very strong over-critical coupling regime applications, where the waveguide and the resonator are very close to each other, the 2nd order effects can come into the picture. In addition, the effect of the bent portion of the coupling structure on the coupling strength may be considerable [68]. Therefore, an effective coupling length has to be considered instead of Z_0 to accurately calculate Q_c using (3.80) [68].

3.4. Chapter Summary

In this chapter, we systematically investigated the planar waveguide-TWR coupling for silicon microring, microdisk, and racetrack resonators in a SOI platform. The microdisk and microring resonator were analyzed using coupled-mode theory in the time domain and racetrack resonators were analyzed using the coupled-mode theory in the space domain. The effect of resonance splitting (as a result of coupling between the degenerate CW and CCW modes because of the sidewall roughness) on the transmission spectrum of the resonator coupled to a waveguide was studied in detail, and the conditions under which a doublet or singlet response is observed in the spectrum were obtained. A figure of merit to evaluate the coupling strength is the quality factor of the coupling (Q_c). Whereas some applications require critical coupling (i.e., $Q_c \approx Q_0$) of a single resonator to a waveguide for sensing and strong light matter interaction, other applications such as all-pass filters and coupled-resonator filters, in addition to being low-loss structures (i.e., $Q_0 \geq 10Q_c$), require the value of Q_c (in the range of a few hundred to a few thousand) corresponding to the required bandwidth of the filter for telecommunication and interconnect applications. Providing such levels of Q_c needs a detailed optimization of the resonator and the waveguide parameters, including 1) waveguide width, 2) resonator radius (and width in the case of a microring), 3) waveguide and resonator thicknesses, 4) the refractive index of the cladding layer, and 5) the thickness of the silicon pedestal layer at the interface between the waveguide-TWR structure and the SiO_2 substrate. Stronger coupling requires the following conditions:

1- larger and stronger overlap of the resonator mode and the waveguide mode;
2- better phase matching between the waveguide mode and the resonator mode;
3- longer interaction length between the waveguide and the resonator (if phase-matching is satisfied); and
4- smaller peak-to-average ratio of the waveguide mode and the resonator mode inside their cores.

Using the coupled-mode theory and the FEM analysis, the coupling Q (Q_c) of waveguide-TWR coupling for microring, microdisk, and racetrack resonators was calculated. In the case of the large phase mismatch between the resonator and the waveguide, we observed that coupling is strongly reduced such that even bringing the waveguide very close to the cavity does not significantly improve their coupling. Moreover, putting the waveguide and the resonator too close to each other leads to strong perturbation of the cavity structure, resulting in additional loss and the resultant degradation of the *Q*. We showed that both reducing the waveguide-TWR thickness and increasing the pedestal layer thickness exponentially improve the coupling. In addition, we showed that the presence of a thin Si pedestal layer strongly improves the coupling compared to the case of reducing waveguide-TWR thickness while no pedestal exists. Whereas reducing the thickness of the waveguide and TWR forces their energy mode distributions toward the sidewalls (which are exposed to fabrication imperfections) and increases the resonator loss, increasing the thickness of the pedestal layer too much can cause large leakage of the resonator mode energy through this layer and therefore degrade the resonator Q. Therefore,

depending on the quality of the fabrication and the resonator bend radius, optimum dimensions for the thickness of the waveguide-TWR and the pedestal layer have to be obtained.

For microring and microdisk resonators of specific radius, we showed that there is an optimal range of waveguide dimensions that provides good phase matching and field overlap, which results in maximum coupling (i.e., minimum Q_c). Such an optimum waveguide has the maximum tolerance to fabrication imperfections. For waveguide-racetrack coupling structure, we derived a simple analytical expression for Q_c in terms of the resonator length and the coupling parameters of the directional coupler in the structure. We investigated the effects of the waveguide widths, the gap, and the interaction length on Q_c.

In chapter 5, experimental results for waveguide-resonator are provided and different coupling regimes are experimentally investigated and compared with theoretical predictions.

CHAPTER 4

FABRICATIONS OF PLANAR SILICON MICRORESONATORS

Fabrication of Si photonic structures is a wide research area that addresses the challenges in the implementation of micron and submicron devices. One important objective of these attempts is to implement low-loss passive optical elements in SOI platforms. Recent advances in nanoscale lithography and plasma etching have enabled a rapid trend toward realizing such low-loss and compact photonic elements. In this context, the implementation of planar silicon ultra-high Q optical resonators (which are ultra-low loss optical elements) requires the development of more advanced methods and processing steps to reduce fabrication imperfections.

Standard processes are available for fabricating micro-electro-mechanical systems (MEMS) or microelectronic devices in any cleanroom environment. In most MEMS devices, the feature sizes are so large that the fabrication-induced roughness (in the range of tens of nanometers) does not deteriorate device performance[33]. For microelectronic devices (which is the other extreme), the electron wavelength is so small that the effect of fabrication-induced roughness is not tangible on electronic device performance[34]. However, for nanophotonic structures where the device sizes are comparable to the optical wavelength in the photonic device, a sidewall roughness in the range of ten(s) of nanometers can

[33] Bosch process, standard MEMS plasma etching process, induces sidewall roughness, which cannot be tolerated in nanophotonic devices.

[34] In current nanoelectronics where the feature sizes are close to electron wavelength, any fabrication-induced roughness can strongly impact the propagation and scattering of electrons in a nanowire. Therefore, research to improve the fabrication quality to reduce imperfections and surface and sidewall roughness is going on.

dramatically affect device performance. Therefore, it is crucial to reduce the roughness even close to the nanometer or sub nanometer range, especially for ultra-high Q traveling-wave resonator (TWR) structures.

One of the main objectives of this thesis was to develop a process for the fabrication of planar ultra-low loss Si photonic devices with very smooth and vertical sidewalls. To achieve this goal, we performed a detailed theoretical and experimental study of the fabrication of these structures (including lithography, etching, and pre and post processing steps), and based on these studies, two main process flows for fabricating planar microresonators were developed[35]:

1- A process flow that includes a two-step etching process with a positive electron resist (ZEP520A) layer as a softmask and a thin oxide layer as a hardmask. This process was mainly considered for the development of ultra-high Q resonators and ultra-low-loss devices.

2- A process flow that includes one-step etching with hydrogen silsequioxane (HSQ) as a negative electron resist mask, which resulted in better feature resolution [69]. This process was intended for (but limited to) coupled-resonator structures where the performance of the device is very sensitive to any imbalance between the resonators dimensions (which are supposed to be identical) as well as resonator-resonator spacing.

[35] Both processes were developed using shared fabrication facilities and on two different plasma etching machines (Plasma-Therm ICP for the 1st, and STS SOE ICP for the 2nd). At the beginning of this research, the 1st process flow was developed, and later the 2nd process flow for the fabrication of coupled-resonators structures was developed. Each plasma machine had its own restrictions on using certain allowed gases and processes.

The details of these two processes are given below.

4.1 The 1st Process Flow

Figure 4.1 shows a diagram of the 1st process flow developed to fabricate Si ultra-high Q microresonators and other planar photonic devices in a SOI platform. As shown in this figure, this process utilizes one step of lithography (step 3) and two steps of plasma etching (steps 4 and 6) with two masks. The 1st mask is the electron resist mask, which is defined by transferring the pattern through electron lithography (see step 3 in Figure 4.1). The 2nd mask (which is also called the hardmask) is defined by transferring the pattern of the 1st mask on it through the 1st step of etching (see step 4). Finally, the ultimate structure is obtained by transferring the pattern of the 2nd mask (hardmask) to the silicon layer via the 2nd step of etching. In the following, we describe the details of each step of the process flow.

Step 0: Wafer preparation

Step 0, in Figure 4.1, is the wafer preparation step appropriate for the implementation of ultra-low-loss Si photonic devices in the telecommunication wavelength. Based on the availability of SOI wafers in the inventory of the SOITEC Company[36], we found two types of SOI wafers appropriate for photonics applications; their specifications are given in Table 4.1. The BOX thicknesses of the wafers (as given in Table 4.1) are large enough to not limit the Q of a resonator (as discussed theoretically in chapter 2). Also, the doping level of the Si layer is in a range that provides $Q_b > 10^8$ (as discussed in chapter 2). For most of the

[36] SOITEC is a worldwide supplier of SOI wafers.

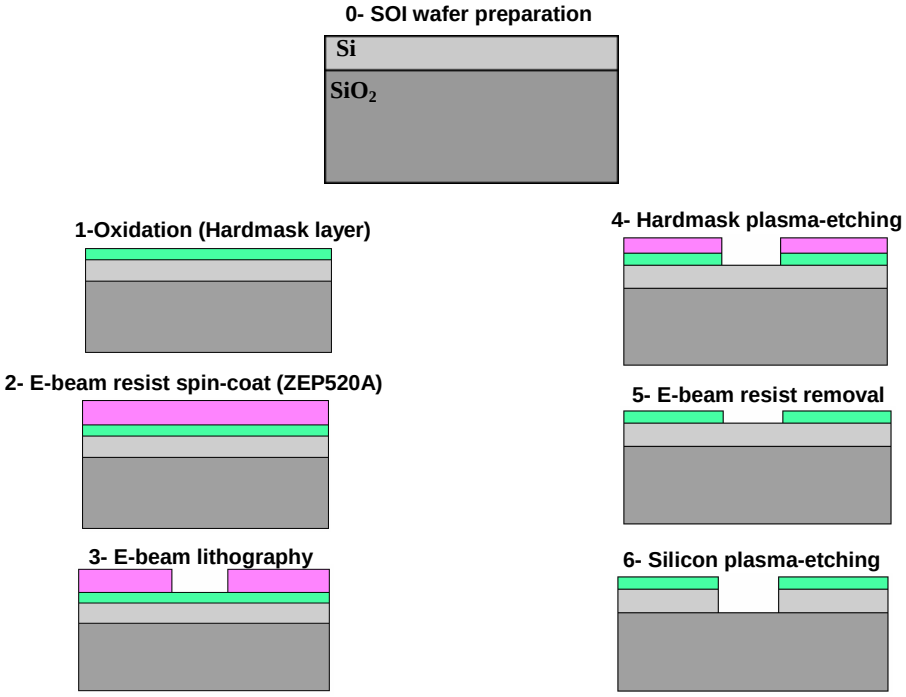

Fig. 4.1: 1st process flow for the fabrication of planar silicon microresonators and waveguides in a SOI platform. The handle Si layer, which is below the BOX layer, is not shown in the figures.

microresonator designs, in this thesis, the target thickness of the Si layer was between 200-250 nm. Therefore, when using wafer I (in Table 4.1), we needed to reduce the thickness of the Si layer by wet oxidation in a furnace and then remove the grown oxide using a buffered oxide etchant (BOE)[37]. Also, before putting the wafer in the oxidation furnace, it was cleaned with the standard Piranha and RCA clean processes [70]. RCA and Piranha processes are also used in later steps of fabrication and post-fabrication. As is known, the presence of contaminants and etch products, as well as improper termination of the Si-bonds on the sidewalls of the resonator, can result in optical absorption at the sidewalls of the resonator where

[37] BOE is a diluted hydrofluoric acid (HF) in water (with a ratio 6:1), which etches SiO_2 with an etch rate of 100 nm/min.

Table 4.1: Specifications of the SOI wafers used for the fabrication of Si

	Diameter	Wafer thickness	Crystal orientation	Si device thickness	SiO_2 BOX thickness	Device resistivity (Ω-cm)
Wafer I	100 mm	400 μm	<100>	340 ± 44 nm	1000 ± 20 nm	18±4.5
Wafer II	150 mm	675 μm	<100>	250 ± 30 nm	3000 ± 70 nm	14-20

the concentration of resonator energy exists [71-73]. Using the RCA and Piranha methods, the chemical and the electronic properties of the sidewalls and the surface can be improved [71-73]. Hence, these two clean processes are explained in detail below.

RCA clean involves the following steps:

1. Removal of organics with a 1:1:5 solution of NH_4OH + H_2O_2 + H_2O at 80^{o}C. This treatment results in the formation of a thin oxide layer (10 Angstrom) on the silicon surface along with a certain degree of metallic contamination that should be removed in the next step.

2. Removal of the thin oxide layer with a diluted HF such as BOE at 25^{o}C.

3. Removal of ionic (metallic) contamination with a 1:1:6 solution of HCl + H_2O_2 + H_2O at 80^{o}C. Because of the presence of H_2O_2 in this step, a thin oxidation similar to step 1 occurs that can be removed by BOE.

Piranha clean removes organic residues off the Si surface. Piranha is a mixture of sulfuric acid (H_2SO_4) and hydrogen peroxide (H_2O_2). A typical mixture is 3:1 concentrated sulfuric acid to 30% hydrogen peroxide. Hydrogen peroxide is added after the temperature of sulfuric acid is close to 120^{o}C. The Piranha process also

results in the formation of a thin layer (a few atomic layers) of oxide when cleaning the silicon surface.

Step 1: Thin Oxidation (Hardmask)

Step 1 in Figure 4.1 is the growth of a thin oxide layer as a hardmask on top of the Si layer (for the second step of etching) to reduce the roughness on the sidewalls of the final Si device. In general, part of this sidewall roughness comes from the lithography step and part of it appears in the etching. In conventional one-step etching, the resist is directly coated on top of the silicon layer. After patterning the resist via lithography followed by etching, the resist pattern is directly transferred to the Si layer. However, most resists are soft polymers and as a result, the sidewalls of the pattern defined in the resist (during the lithography step) are subject to random roughness. In the etching step, because of the weak etch resistance of these soft resists, the edges and sidewalls of the resist pattern are subject to more random corrosion[38]. As a result, in one-step etching, a considerable percentage of the sidewall roughness in the resist appears on the sidewalls of the Si device. However, in a two-step etching process, the pattern is first transferred from the resist to the hardmask via the first step of etching, and a percentage of the roughness in the resist pattern is transferred to the hardmask. Now, in the second step of etching (in which the hardmask is more etch resistance) the induced roughness from the hardmask to the Si layer is much smaller. In addition, in the second etching step, the edges of the

[38] In a plasma etching chamber, while ions are accelerated down in the vertical direction to etch the sample, they can have random walks in the horizontal direction and add roughness to the sidewalls. Even in the vertical etching, etch rate is not purely deterministic and spatially uniform. In fact, a small randomness in the etch rate exists.

hardmask are more resistive to random corrosion. Hence, the overall roughness induced from the initial resist to the final Si device is much weaker. In other words, the hardmask has acted as a buffer layer to weaken the effect of the resist roughness on the final pattern on the sidewall of the Si device.

After the wafer preparation in step 0, a thin thermal oxide (~ 50 nm) is grown on top of the Si layer as a hardmask. To accurately control the thickness of the hardmask, the dry oxidation technique is used, which has a slower oxide growth rate compared to wet oxidation and hence is easier to control. In general, instead of thermal oxide, we can use a deposited oxide, which can be obtained through either a plasma-enhanced chemical vapor deposition (PECVD) process or a low-pressure chemical vapor deposition (LPCVD) process. However, the advantage of thermal oxidation is that it can chemically treat the silicon surface to recover the crystalline damages as well as dangling bonds and also reduce the roughness of the Si surface. This is very important for the realization of ultra-high Q resonators in which the surface properties of the silicon are important.

The thickness of the hardmask is determined by the etch selectivity between the Si and SiO_2 in the 2^{nd} etching step. If etch selectivity is large, a thinner mask can be used, which provides better feature resolution and a higher quality of fabrication for the sidewalls. As will be shown later, based on the achieved selectivity, a hardmask thickness of ~ 50 nm is appropriate.

In thermal oxidation, roughly 40% of the total oxide thickness is consumed from the Si layer [70]. This should be kept in mind for the accurate design of resonators.

Steps 2 and 3: Resist Coating and Electron-beam Lithography

Steps 2 and 3 in Figure 4.1 are the lithography steps. An essential need to realize an ultra-high Q planar microresonator (which has a very small sidewall roughness) is high-resolution lithography. While optical deep UV lithography (with a laser wavelength of 193 or 248 nm) is able to write submicron features, providing patterns with smooth sidewalls, which is the main requirement for an ultra-high Q resonator, is still a challenge[39]. Currently, electron-beam lithography (EBL) is the most promising technique that provides very high resolution and is ultimately limited by electron wavelength diffraction. Using this technique, small feature sizes such as the spacing between a waveguide and a resonator (which can be as small as 100 nm or below) can be easily defined[40]. Hence, for the implementation of ultra-high Q resonators in this thesis, EBL was employed.

Among different choices for electron-beam resists, ZEP520A, which is a positive resist, showed very promising results becauseit provides 1) high resolution (~ 10 nm) and 2) good resistance to plasma etching.

After putting the wafer on a spinner and centering it to the axis of the spinner, ZEP520A was dropped on the wafer using a syringe. In order to have high-quality ZEP520A with minimum particle residues and contaminants on the wafer, a mass filter (with a porosity of around or less than 0.45 μm) was used at the head of the

[39] Using deep UV lithography, microring resonators with Qs in the order of tens of thousands have been reported [74]. The next generation of optical lithography employs Excimer lasers with wavelengths of ~ 157 nm.

[40] However, because everything is written in a serial way, the process is slow and therefore not suitable for large volumes. For mass fabrication, a parallel process is needed that can print all patterns simultaneously.

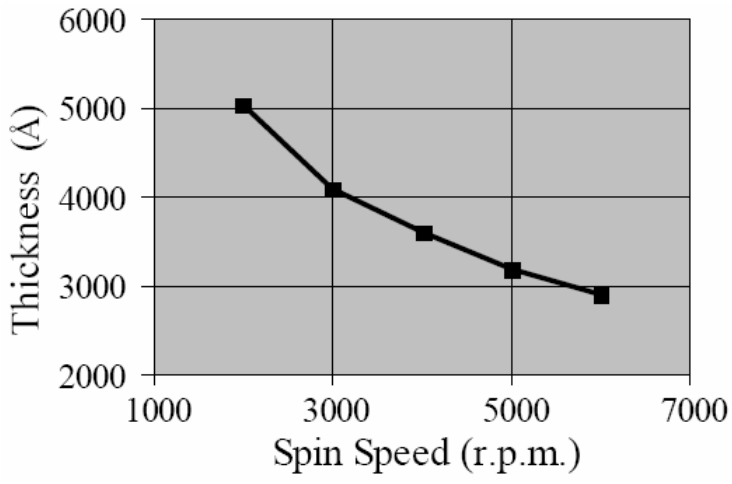

Fig. 4.2: Plot of the ZEP520A thickness versus the spin speed for a 4" wafer [from ZEP520A technical report provided by Zeon Chemicals Co.].

syringe. Figure 4.2 shows the thickness of the ZEP520A versus the spin speed. The target thickness of ZEP520A was ~ 350-400 nm. After spinning for about 60 seconds, the wafer was prebaked on a hot plate at a temperature of 180^{o}C for about 2 minutes. After this step the wafer was ready for electron-beam (e-beam) writing of the patterns.

The patterns were written using a JEOL-9300 electron-beam lithography system. The e-beam diameter in this system is ~ 4nm, and as a result, very small feature sizes (if the resist resolution allows) can be written[41]. The default beam current in the system is 2 nA[42]. After e-beam writing, the wafer was immersed in Amyl Acetate or ZEDN50 for about 2 minutes for the development. Finally, the wafer was rinsed with isopropyl alcohol (IPA) for about 20-30 seconds.

[41] More details about this system can be found on the Georgia Tech nanolithography website: www.nanolithography.gatech.edu, www.mirc.gatech.edu.
[42] In general, a smaller e-beam current can result in a higher quality of writing at the cost of slowing the writing time.

For e-beam writing, different feature sizes require different levels of beam exposure dose. This is especially important when defining the gap between a waveguide and a resonator, which could be as small as 100 nm or below. Therefore, to calibrate and optimize the exposure dose, a series of patterns with different feature sizes and with different levels of doses were written and after developing the patterns and looking at them using a scanning electron microscope (SEM), the optimal dose levels for different feature sizes were obtained. One issue with EBL writing is the proximity effect[43]. In this effect, electron scattering in the resist and the substrate leads to an undesired influence in the regions adjacent to those exposed by the electron beam. As a result of this secondary exposure, the sizes of these features can change or become distorted. For a single isolated resonator such as a microdisk, which is highly symmetric, the effect of proximity may increase the entire size of the structure, with a negligible distortion in the geometry. However, for situations such as when a waveguide is adjacent to the resonator or two resonators are adjacent, the proximity effect may be considerable, and as a result, the dose correction, especially close to the coupling region between the waveguide and the resonator, is required[44]. Correspondingly, the dose correction was performed for these situations.

[43] Useful information about the proximity effect can be found on the nanolithography website of Georgia Tech: http://www.nanolithography.gatech.edu/proximity.htm.

[44] There is some Monte Carlo software that considers the effects of electron scattering and provides the optimized dose. In this approach, the pattern and all the layer thicknesses, including the device and the BOX thickness of the SOI, are given and the outcome of the simulation is the required dose level at different parts of the pattern.

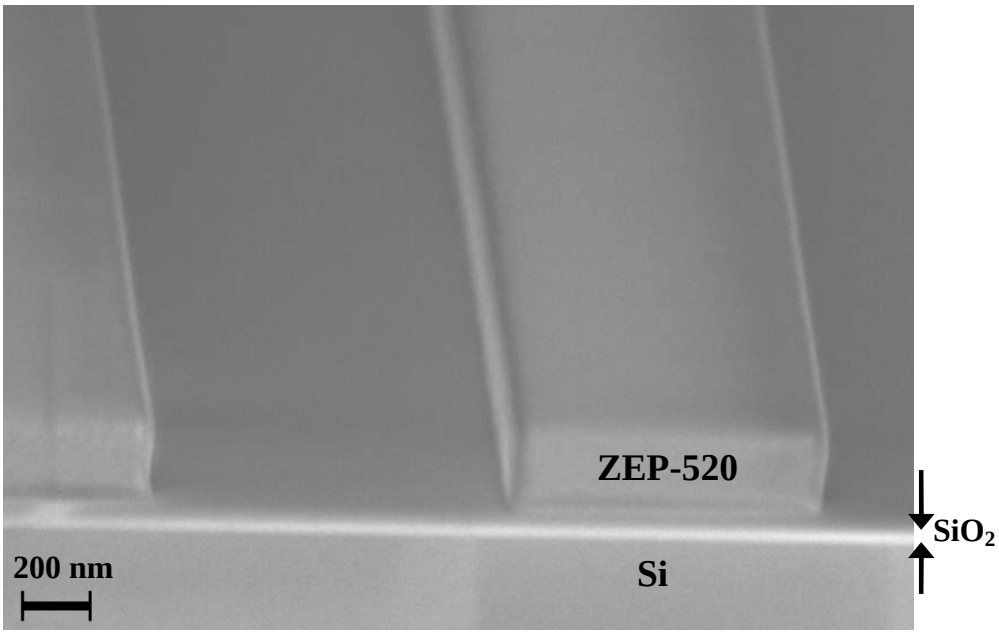

Fig. 4.3: SEM image of a cross section of developed ZEP bars seated on a thin SiO2 layer, which is on top of a Si layer.

Figure 4.3 shows a SEM image of the cross section of a typical patterned resist. As seen in this figure, ZEP520A patterns with pretty smooth and vertical sidewalls are obtained. The pattern is on top of a Si wafer with a thin oxide layer (as shown in Figure 4.3) at the interface. Because of the large electric resistivity of ZEP520A, capturing a clearer image of the sidewalls of the resist with the details of surface roughness was difficult.

It is noted that for many tests, instead of a full wafer, a piece sample of the wafer was used. As a result, after spinning the sample, only the center, which had its resist thickness close to the target thickness, was used for e-beam writing.

Step 4: Hardmask Plasma Etching

Step 4 in Figure 4.1 is etching the hardmask with resist mask on top of it. The objective of this step was to etch the hardmask with 1) good etch selectivity (compared to the resist etch rate), 2) smooth and vertical sidewalls of the hardmask, 3) less polymerizations and deposition of organics on the sidewalls of the hardmask, and 4) slow etch rate[45].

For both steps of plasma etching, an inductively coupled plasma (ICP) machine was used. The benefit of using such a system is that we have two separate RF generators to control the ion density and ion energy (acceleration) in the plasma. The plasma density is primarily generated and controlled inductively, while the ion energy and acceleration are controlled capacitively with separate RF powers. As a result, we have more degrees of freedom to optimize the plasma condition to obtain vertical sidewalls.

Plasma etching depends on the following parameters: gas chemistry, pressure, temperature, and RF powers. For etching the hardmask, different gas chemistries and mixtures were studied, and based on their availability in the plasma machine, the optimization of the etch recipe for the oxide was started. Among different oxide plasma etchants, CF_4 plasma has been shown to be very promising [75]. However, it etches the resist (ZEP520A) very quickly and as a result, the etch selectivity between the oxide and the resist is low. A common technique in plasma etching to overcome this problem is to add another gas into the plasma to do polymerization of the surfaces and sidewalls. In other words, CF_4 does etching and the other gas does

[45] When etch rate is slow, the etch depth can be controlled more precisely.

the polymerization. The generated polymer (which is deposited on the surface and sidewalls) makes the resist harder and resistive to etching. In addition, the presence of a thin polymer layer on the sidewalls of the hardmask (during the etching) prevents lateral etching of the hardmask, and as a result, the etching becomes more anisotropic with more vertical etch profiles. However, if the polymerization is strong and results in a thick polymer layer on the sidewalls of the hardmask, the sidewall roughness of the hardmask becomes larger. Therefore, the polymerizing gas and its ratio with respect to CF_4 as well as other plasma parameters have to be optimized.

For the polymerizer, three gases (that were available[46] in the ICP plasma) were studied and tested: H_2, C_4F_6, and CHF_3. Among these three gases, CHF_3 proved to be the most promising.

Finally, an inert gas such as Ar was also added to the plasma. Including this inert gas provides stability to the plasma, whereas the ratio and amounts of the other two gases (CF_4 and CHF_3) are used to control the etch rate, anisotropy, selectivity, and polymerization.

The plasma conditions were optimized for the Plasma-Therm ICP machine. As this machine is a shared facility, results can be inconsistent without proper care. Therefore, before any etching, the plasma chamber was opened and manually

[46] CHF_3 at the beginning was not available in the chamber, and (after realizing that C_4F_6 was not satisfactory) it was added to the chamber later.

Table 4.2: The guidelines to optimize the hardmask etch recipe. Although these are not general guidelines (as plasma has sophisticated dynamics), we can approximately say that if any of the following parameters deviate from the optimum condition, the etch parameters would change.

	Resist etch rate	SiO_2 etch rate	Anisotropy	Polymerization	Selectivity SiO_2/Resist	Plasma stability
Inductive power ↑	↑	↑	↓	Depends	↑	↑
Capacitive power ↑	↑	↑	↑	↓	↓	↑
Pressure ↓	↑	↑	↑	↓	Depends	↓
CF4 ↑	↑	↑	—	↓	Depends	*
CHF3 ↑	↓	↓	↑	↑	↑	*
Ar ↑	—	—	—	—	↓ small	↑

*: Pressure may not be maintained and plasma is not ignited

cleaned[47]. For any etch run, a 5-minute seasoning run was performed before the actual run. As is known in the plasma community, when plasma is triggered, it takes a few seconds to reach the bias point and the plasma color may even flicker (which means instability). The seasoning run can overcome this problem by making the plasma more stable before the actual etch run when the sample is in the chamber. Table 4.2 provides guidelines for the optimization of our etching process. Plasmas have sophisticated dynamics such that changing plasma parameters can result in deposition rather than etching; also, what holds true for one plasma may not be true for another plasma. However, the guidelines given in Table 4.2 (and for the gas

[47] Cleaning was performed by vacuum cleaning and then wiping the chamber with acetone. If the chamber was strongly polymerized, a razor was used to scrap off the polymer from the walls of the chamber before vacuum cleaning and acetone wiping.

(a)

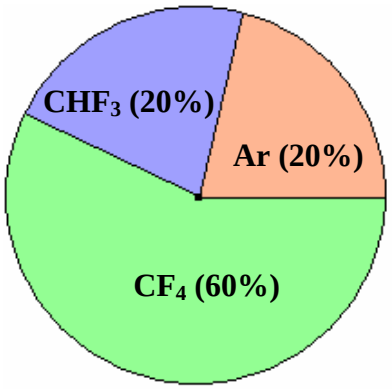

(b)

Pressure	Inductive power	Capacitive power	CF_4 flow rate	CHF_3 flow rate	Ar flow rate	Chamber wall Temperature
5 m Torr	125 KW	75 kW	15 sccm	5 sccm	5 sccm	60°C

(c)

Oxide etch rate	~ 40 nm/min
ZEP520A etch rate	~ 120 nm/min
Selectivity	0.33

Figure 4.4: (a) A diagram showing the ratio of gases used for etching the hardmask. (b) A table showing the plasma parameters optimized for etching the oxide with ZEP520A on top as a resist mask. These parameters are optimized for an ICP plasma machine with the brand Plasma Therm ICP in the cleanroom facility of Georgia Tech. The temperature in this table is the chamber wall temperature (as set by the cleanroom staff). However, for a room temperature etching, identical results were obtained. (c) The obtained etch rates and selectivity for oxide and ZEP520A.

mixture chemistry used) are approximately valid around the optimum condition. During the etching optimization, refractometry[48] and profilometry[49] were used to measure the thickness of the samples before and after the etching to calculate the etch rates.

[48] Using a Nanospec refractometer in the cleanroom.
[49] Using an Alpha-step profilometer in the cleanroom.

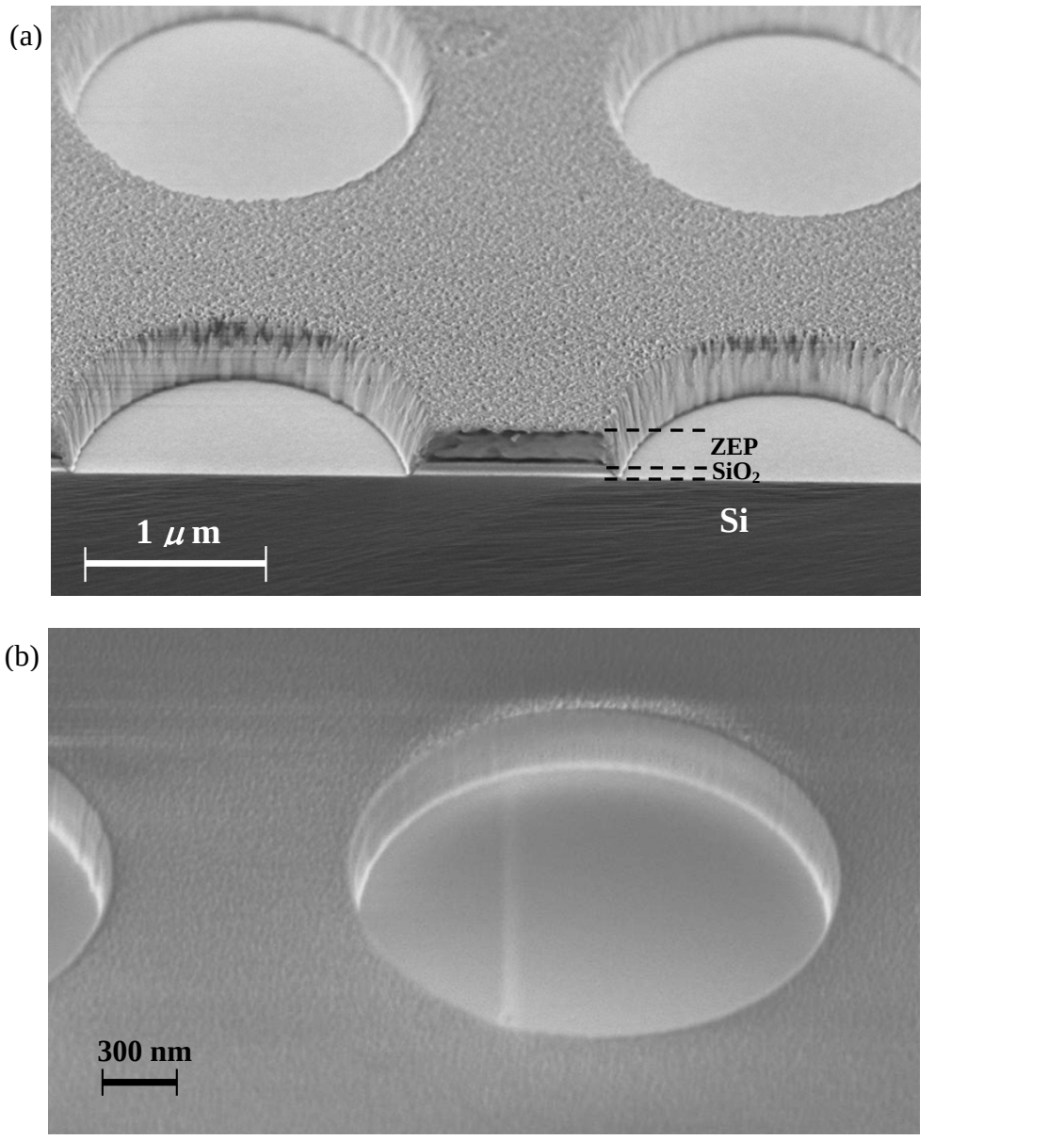

Fig. 4.5: Hardmask etching with (a) a non-optimized recipe and (b) an optimized recipe. In both (a) and (b), the ZEP520A layer is on top of an oxide layer, which is on top the silicon layer. These layers are specified in (a). In (a), strong polymerization and sidewall roughness in the ZEP520A (and correspondingly in the oxide) sidewall is observed.

Figure 4.4(a) shows the gas ratios optimized for the oxide etching. Also, the table in Figure 4.4(b) shows the values of the optimized plasma parameters. The minimum

pressure obtained while keeping the plasma stable was 5 mTorr[50]. The table in Figure 4.4(c) shows the etch rates of oxide and ZEP520A and their etch selectivity. As seen from this table, the etch selectivity is less than 1. This is the price that was paid to keep the sidewall polymerization of the hardmask low. However, because the oxide thickness is small (~ 50 nm) and the ZEP520A thickness is ~350 nm, even with that low selectivity, the resist is not completely removed during etching.

To further see the effect of the polymerization on the sidewall, Figures 4.5(a) and 4.5(b) show the results of etching using non-optimized and optimized etch recipes, respectively. As seen from Figure 4.5(a) for the non-optimized recipe (where the ratio of CHF_3 in the recipe is larger than the optimized value), strong polymerization and sidewall roughness are observed. However, the results in Figure 4.5(b), which are from the optimized recipe, the profile is very smooth and polymerization is negligible.

Step 5: Electron Resist Removal

Step 5 in Figure 4.1 is the removal of the ZEP520A resist left on top of the structure. For this step, either of the following two methods was used:

1- the wafer was put in an oxygen plasma asher for 1 minute to remove the polymers and organics. Then, the wafer was immersed in Piranha with a temperature of 120^{o}C for 5 minutes. It was then rinsed with dionized (DI) water and dried by nitrogen flow.

[50] A smaller pressure results in more anisotropic and faster etching.

2- The wafer was immersed in Microposit 1165 remover at 80^{o}C for 10 minutes with good mechanical agitation. Then, after rinsing it with water and drying it with nitrogen flow, the wafer was immersed in Piranha for 5 minutes to remove any possible organics left.

Finally, after removal of the resist, an oxide hardmask layer with the pattern is left on top of the Si layer.

Step 6: Silicon Etching

Step 6 in Figure 4.1 is the etching of the Si layer. After studying different gases and their influences on Si, and based on their availability in the ICP machine, a chlorine-(Cl_2) based plasma was chosen for etching the silicon to obtain smooth and vertical sidewalls [76-79]. Since pure chlorine provides good selectivity between Si and SiO2, the oxide hardmask can be very thin. Another advantage of using pure chlorine is that there is no polymerization. For the optimization of the Si etch recipe, the same guidelines as mentioned in Table 4.2 were followed. Table 4.3(a) shows the optimized plasma parameters and Table 4.3(b) shows the etch rates of the silicon and oxide and the etch selectivity. After etching the silicon, the remaining hardmask layer is kept on top of the structure to protect the surface electronic properties of the top surface of the silicon from environmental effects. In general, a thin thermal oxide on the top of the microdisk is also expected to improve the interface properties and consequently the *Q* of the cavity.

In what follows, some of the fabricated structures with the optimized recipes for hardmask and silicon etching are shown. Figure 4.6(a) shows the SEM pictures of a

Table 4.3: (a) The plasma parameters optimized for etching the silicon with oxide on top as a hardmask. These parameters are optimized for an ICP plasma machine with the brand Plasma-Therm ICP in the cleanroom facility of Georgia Tech. The temperature in this table is the chamber walls temperature (as set by the cleanroom staff). However, for a room temperature etching, identical results were obtained. (b) The obtained etch rates and selectivity for silicon and oxide.

(a)

Pressure	Inductive power	Capacitive power	Cl_2 flow rate	Temperature
5 m Torr	75 KW	125 kW	50 sccm	60^oC

(b)

Silicon etch rate	~ 73 nm/min
Oxide etch rate	~ 12 nm/min
Selectivity (Si/SiO_2)	~ 6

microdisk resonator with a radius of 20 μm coupled to a ridge waveguide with a width of 550 nm. Figure 4.6(b) shows the coupling between the microdisk and the waveguide with a coupling gap of 220 nm. The thicknesses of the silicon and hardmask layers are 225 nm and 60 nm, respectively. Also, Figure 4.6(c) shows the sidewall of the microdisk with a very small roughness, as observed in the figure. From the SEM pictures, the measured sidewall angle of the waveguide or microdisk was more than 85^o. To see the capability of the recipe, other photonic structures with small feature sizes were also fabricated. Figure 4.7 shows the SEM picture of a Si triangular lattice photonic crystal of air holes with a line defect in it. The lattice spacing is 410 nm and the hole diameter is 260 nm. The structure is on a SiO_2 substrate in a SOI platform. As seen from Figure 4.7, the small air holes are circular with minimal roughness. As another example, the SEM picture in Figure 4.8(a) shows the structure of a coupled-resonator structure made of four racetrack

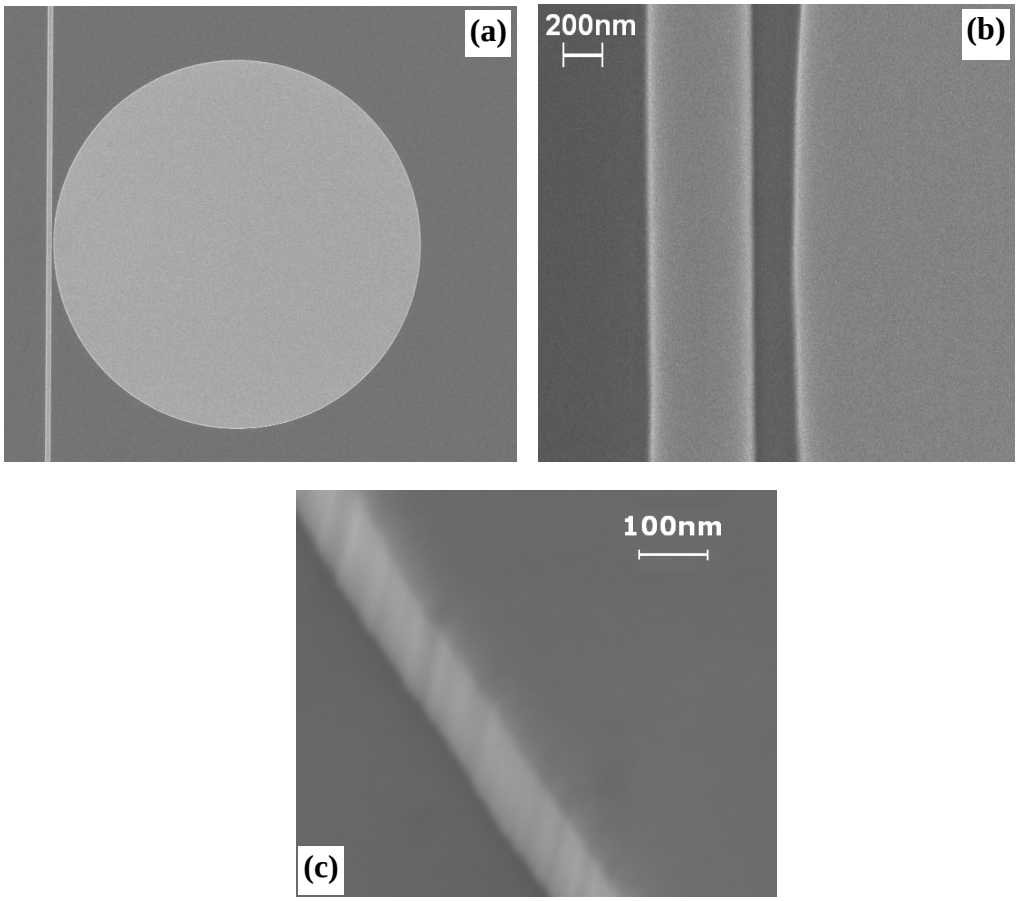

Fig. 4.6: (a) SEM micrograph of a Si microdisk resonator side coupled to a waveguide; the disk radius is 20 μm and its thickness is 225 nm. The waveguide width is 550 nm and the gap between the disk and the waveguide is 220 nm. (b) A closer view of the structure at the waveguide-cavity coupling region. (c) Sidewall of the microdisk captured at an azimuth angle 30^{o} and sample tilt angle 30^{o} [52].

resonators, and the structure is coupled to two waveguides from the sides, as shown in this figure. More details of the coupling region between the first resonator and waveguide are shown in the inset of Figure 4.8.

For the microresonators that have a thin Si pedestal layer, the etching time is controlled so that the desired thickness of the Si pedestal layer is obtained.

4.2 Post-processing

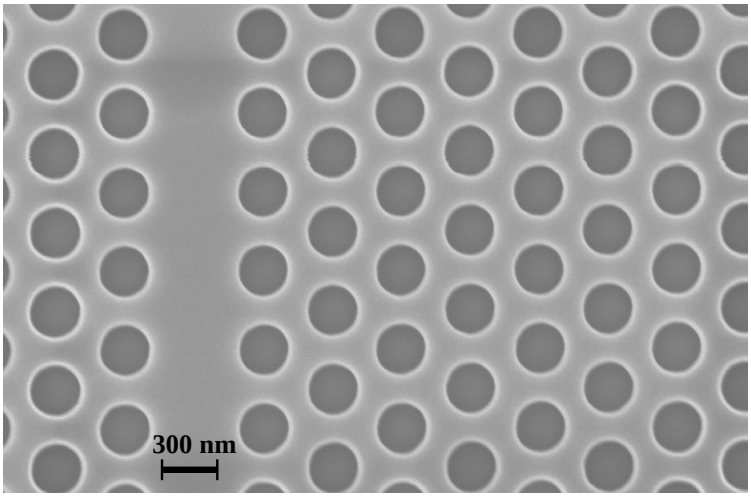

Fig. 4.7: SEM image of a Si triangular lattice photonic crystal of air holes with a line defect in it. The lattice spacing 410 nm and the hole diameter is 260 nm. The structure is in the device Si layer of a SOI wafer.

After the final step of etching, some post-processing steps can be performed to reduce the sidewall roughness. These post-processing steps have two aspects: One aspect is to reduce the roughness at the sidewalls of the resonator to reduce the scattering. The other aspect (which is called surface passivation) is to improve the electronic properties by treating crystalline damages and defects at the surface (to reduce surface electronic states) and removing possible organic or metal residues to reduce the optical absorption at the surface.

Smoothing the sidewalls of the resonator can be done quickly by one (or a few) cycle(s) of thermal oxidation and wet etching by BOE (or any other dilute HF). In a thermal oxidation process the silicon is consumed. Since the oxidation on the sharp points of a rough surface is faster (because more surface area is available), the oxidation process consumes more Si at the rougher points and as result, a smoother surface can be obtained.

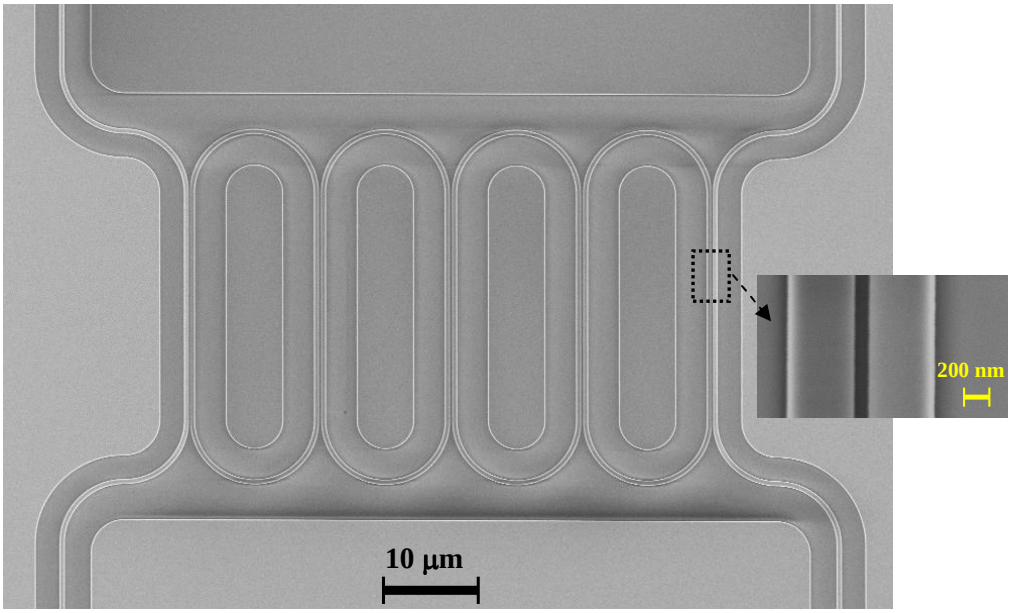

Fig. 4.8: SEM image of a coupled-resonators structure made of four racetrack resonators and coupled to two waveguides from the sides. The inset shows the details of the coupling region between the first resonator and the waveguide.

In order to have a good control on the oxidation process, dry oxidation was used at a temperature of 850^{o}C. In this thesis, for most of the experiments only one step of oxidation with a 10 nm thickness (corresponding to ~ 4 nm Si consumption) and without BOE etching was done. Before putting the sample in the oxidation furnace, it was cleaned using the Piranha process.

After oxidation, the grown thermal oxide layer is removed by putting the device in BOE. Another advantage of BOE etching is that it can passivate the dangling bonds, which are available at the surface, and as a result, optical absorption at the surface (which is due to the surface electronic states) is reduced. However, to protect the surface from any contamination, it is better not to remove the thermal oxide layer in the last cycle of oxidation of the resonator. A problem with many

cycles of oxidation and BOE etching is that the underlying oxide close to the edge of the resonator is also subject to removal by BOE. Although BOE etching is done very quickly (as the grown oxide is very thin), it can result in an oxide roughness underneath the resonator, as BOE may attack different regions with different etch rates. Therefore, the number of cycles has to be low. However, if the entire structure is covered by an oxide cladding (such as LPCVD oxide), all the regions under the resonator (that were BOE etched) will be filled by the cladding oxidation. Therefore, the number of cycles of oxidation and oxide removal is not a concern.

For the thermal oxidation post-processing, pedestal microdisk architectures are more advantageous, since in pedestal microdisks the oxide layer underneath is isolated from the exposed top layer. Therefore, BOE cannot reach that region. By fine controlling the thermal oxidation growth rate, a structure with specific pedestal thickness and smooth sidewalls can be obtained.

For the passivation of the surface, Piranha and RCA clean processes can be used, which perform oxidation and organic removal followed by BOE etching (to terminate the dangling bonds at the surface). Even thermal oxidation can be used for surface treatment and sidewall passivation. At the start of the oxidation process, nitrogen gas is passed through the tube to further clean it. The nitrogen flow can treat the crystalline damage of the silicon. Also, oxidation is done at a high temperature, which by itself treats the surface properties.

4.3 Cladding Coverage of Si Microresonators

In many applications, the resonator cladding is not air and the resonator is covered by a material that has a refractive index lower than that of Si. Conventional cladding materials are SiO_2 or polymers, both with refractive indices below or around 1.5.

The process for forming polymer cladding is similar to resist coating, step 2, of the process flow shown in Figure 4.10. The final thickness and material properties of the polymer depend on the spin speed, spin time of the spinner, bake temperature, and bake time.

The oxide cladding is formed either by the PECVD or LPCVD technique. The deposited oxide should be of high quality with minimal material loss. The LPCVD oxide provides a higher quality of oxide with less porosity and fewer grains and is closer in properties to thermal oxide. For ultra-high Q resonators, LPCVD oxide is preferred. The SEM picture in Figure 4.9 shows a cross section of a ridge waveguide in a SOI platform and covered by an LPCVD oxide layer. The dashed line in this figure is to distinguish the BOX layer from the LPCVD oxide cladding. For this LPCVD process, a standard LPCVD recipe available in the LPCVD Tystar furnace at the Georgia Tech cleanroom was used.

Despite a higher quality of LPVCD oxide, for many lower Q applications, PECVD oxide deposition is preferred and adequate. This is because the PECVD process is much faster (with a faster oxide deposition rate) compared to LPCVD. Also, knowing that the large refractive index contrast between the silicon and oxide results in small concentration of resonator energy in the oxide, the loss due to PECVD oxide is usually much smaller than the loss due to the surface

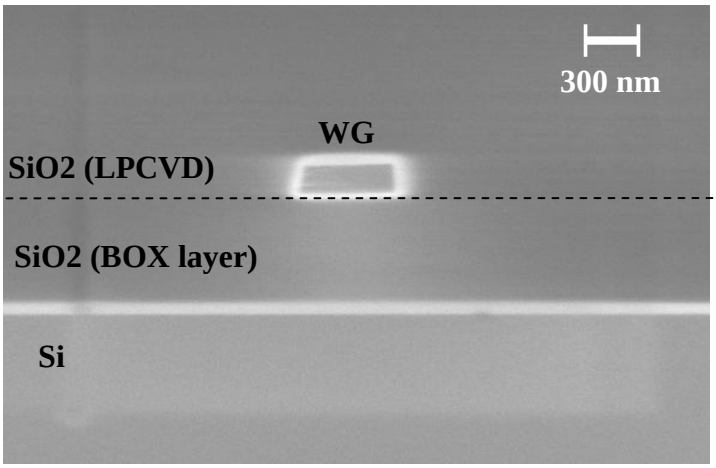

Fig. 4.9: SEM image of the cross section of a ridge waveguide in SOI. The cladding of the waveguide is LPCVD oxide. The dashed line is to distinguish the BOX layer from the cladding.

roughness of the resonator. In this thesis, for low Q resonator applications ($Q\sim<10^5$), a PECVD oxide cladding was used.

4.4 The 2nd Process Flow

Figure 4.10 shows the 2nd process flow developed based on negative electron resist HSQ to provide a higher lithography resolution. In the following, the process steps are explained.

Step 0: SIO Wafer Preparation

This step is similar to step 0 in the 1st process flow.

Steps 1 and 2: Resist Coating and Electron-beam Lithography

Steps 1 and 2 in Figure 4.10 are the lithography steps. For HSQ, different processes are typically used to get different resolutions. For high resolution and small feature sizes, the following process was used:

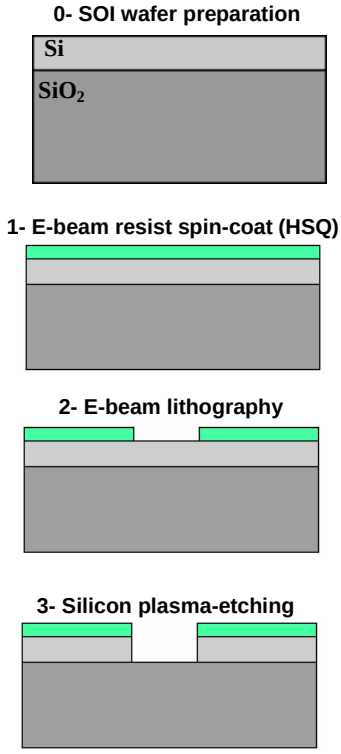

Fig. 4.10: The 2nd process flow for the fabrication of planar silicon microresonators and waveguides in a SOI platform. The process is based on negative electron resist (HSQ).

1. HSQ with a 6% concentration was spin coated on the Si wafer at a speed of 3000 rpm, which results in ~ 110 nm thickness.

2. After spin coating, the wafer was put on a hot plate with a temperature of 80^{o}C for 4 minutes.

3. After that the wafer was ready for e-beam writing. For large feature sizes, a base beam exposure dose of 2000 μC/cm^2 showed clear results. For smaller feature sizes the dose has to be higher and adjusted according to the feature size.

4. After e-beam writing, the wafer was developed in 25% TMAH at a temperature of 80^{o}C for about 30 seconds.

5. Finally, the wafer is rinsed with low-flowing DI water.

Step 3: Silicon Etching

HSQ has etching properties and resistivity that are almost similar to oxide. Therefore, any etch recipe developed for oxide can be used for HSQ. Similarly, any etch recipe developed for silicon with an oxide as a mask can be used for etching silicon with HSQ as a mask. Therefore, the silicon etch recipe optimized in the 1st process flow has been used in this case. In contrast to the 1st process flow that uses two-step etching to reduce sidewall roughness, this process is one-step etching and the roughness on the sidewalls of the HSQ pattern is transferred to the final Si device. However, the main purpose of developing this process was not to obtain an ultra-high Q cavity, but to fabricate coupled-resonator structures where the resolution of lithography is important and to provide identical resonators with minimal deviation in dimensions. In such a case, the Q of the resonators is enough to reduce the insertion loss of the coupled resonators in the allowed range (e.g., a 2nd order coupled-resonators filter (with a 3dB bandwidth ~ 1 nm) made of two resonators with Q ~ 40000 has an insertion loss below 0.5 dB). This is discussed in more detail in chapter 7). Nevertheless, this fabrication process can also be optimized toward obtaining ultra-high Q resonators.

Optimization of this etching process was done for a plasma machine with a brand of STS SOE ICP[51] and using the same guidelines mentioned in the 1st process

[51] The reason to switch to this machine was that the other machine (i.e. ,the Plasma-Therm ICP) was later subjected to many contaminants from different processes from different research disciplines. On the other hand, the STS SOE is a newer machine and intended only for nanofabrication purposes. A main drawback of this machine was that it was optimized for etching III-V materials. Optimization of

Table 4.4: (a) Plasma parameters optimized for etching the silicon with oxide on top as a hardmask. These parameters are optimized for an ICP plasma machine with the brand STS SOE ICP in the cleanroom facility of Georgia Tech. (b) The obtained etch rates and selectivity for silicon and HSQ (or oxide, which has an etch behavior as HSQ).

(a)

Pressure	Inductive power	Capacitive power	Cl_2 flow rate	Temperature
3 m Torr	200 KW	60 kW	20 sccm	20^{o}C

(b)

Silicon etch rate	~ 150 nm/min
Oxide etch rate	~ 30 nm/min
Selectivity (Si/SiO_2)	~ 5

flow for the silicon etching. Pure chlorine was selected for the plasma gas. Because the specifications of this plasma machine were different than those used for the 1st process flow, the optimized plasma parameters for etching the silicon were also different. Parameters for the optimized recipe are given in Table 4.4. Figure 4.11 shows some of the fabrication results based on the 2nd process flow. Figure 4.11(a) shows the SEM image of an add-drop filter (with a zero) made of two Si microdisk resonators with a radius of 2 μm. One of the resonators is side coupled to two waveguides. Also, Figure 4.11(b) shows the detailed dimensions of the coupling region in (a) as specified by the dashed window. As seen from these figures, good fabrication results have been obtained. The experimental data for the structures fabricated using the 2nd process flow are provided in chapters 5 and 7.

---

an etch recipe for silicon in this machine had more challenges as the etch rate was very high (e.g., a typical value was 300 nm/min). The other issue was that the regulations on the new machine did not allow oxide etching, which needed gas such as CF_4/CHF_3. Therefore, a two-step etching process with an oxide hardmask was not allowed and CHF_3 or any appropriate gas polymerizer was not available on this machine.

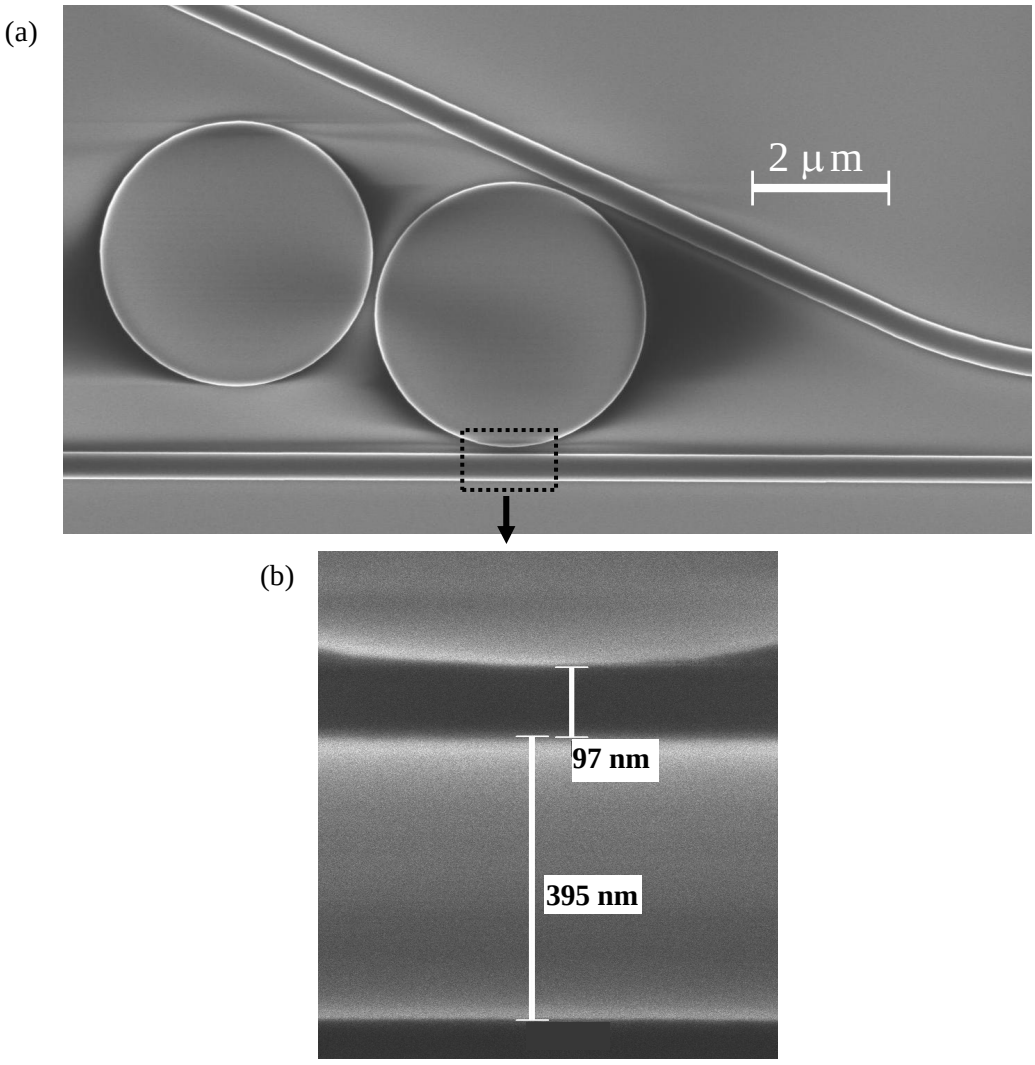

Fig. 4.11: Fabrication results using the 2nd process flow with an STS SOE ICP etching machine. (a) SEM image of an add-drop filter (with a zero) made of two microdisk resonators with radius 2 μm. One of the resonators is side coupled to two waveguides. (b) Detailed dimensions of the coupling region in (a) as specified by the dashed window.

4.4 Silicon Microresonator with a Pedestal Layer and the Nanotrenching Effect

As discussed in chapters 2 and 3, for the purpose of integrating resonators and waveguides with P-N junctions, as well as improving their side-coupling to other optical elements, a thin Si pedestal layer is considered at the interface between the

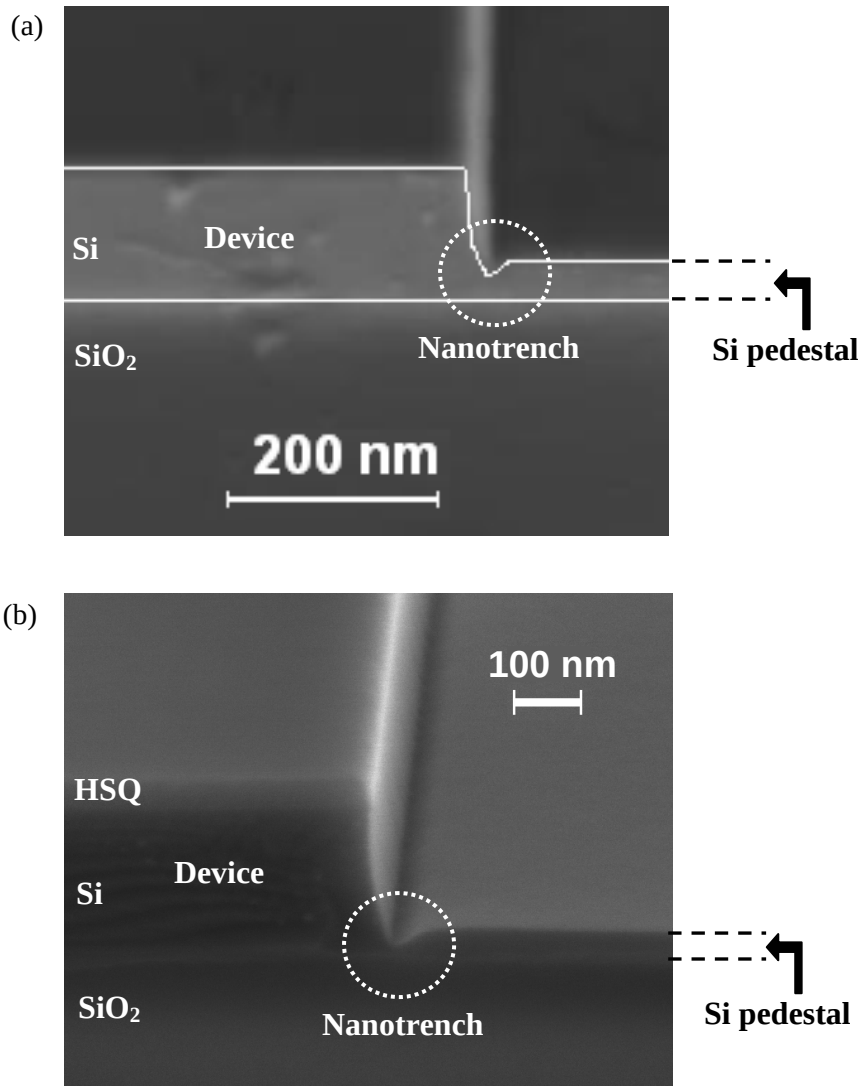

Fig. 4.12: (a) SEM cross section of the pedestal type structure fabricated using (a) the 1st process flow and (b) the 2nd process flow. The images in (a) and (b) were captured at sample tilt angles of 30° and 45°, respectively.

SiO2 substrate and the Si resonator. Correspondingly, such structures were also fabricated. Figures 4.12(a) and 4.12(b) show the SEM cross sections of these devices (e.g., waveguide or resonator) fabricated by the 1st and the 2nd process flows, respectively. As can be seen from these figures, nanotrenching is observed at

Table 4.5: (a) Plasma parameters optimized (in the 2nd process flow) for etching the silicon microresonator with a thin Si pedestal layer. HSQ (or oxide) is the mask. These parameters are optimized for an ICP plasma machine with the brand STS SOE ICP in the cleanroom facility of Georgia Tech. (b) The obtained etch rates and selectivity for silicon and HSQ (or oxide, which has an etch behavior as HSQ).

(a)

Pressure	Inductive power	Capacitive power	CF_4 flow rate	HBr flow rate	Temperature
3 m Torr	200 KW	40 kW	5 sccm	30 sccm	20°C

(b)

Silicon etch rate	~ 75 nm/min
Oxide etch rate	~ 18 nm/min
Selectivity (Si/SiO_2)	~ 4

the interface of the device and the pedestal layer[52]. This nanotrench formation has been reported before [77-80] when pure Cl_2 chemistry is used for the plasma etching of silicon. The presence of such a trench can pinch off the transmission of the carriers from the P-N diode to the devices and, therefore, this trenching has to be suppressed.

In a thorough study in [78, 89], the trenching effect in silicon was experimentally studied in a plasma etching machine with Cl_2 or hydrogen bromide (HBr) (another promising gas for fine and smooth etching of silicon) and under different plasma parameters. From this study, the trenching effect was observed at almost all the

[52] It is noted that when the silicon layer is fully etched, both the 1st and the 2nd process flows are fine and can be used. In fact, in the fully etched case and in the trench region, when reaching the underlying oxide layer, the etching of the oxide becomes very slow (because of the large selectivity of etching between the Si and SiO_2). As a result, the regions out of the trench, which are silicon, are etched faster until all the silicon layer is gone. However, the height of the SiO2 layer near the trench is a little lower than that of other locations, which has a negligible effect on the optical performance. By increasing the Si/SiO_2 etch selectivity, this height difference in the oxide layer approaches zero.

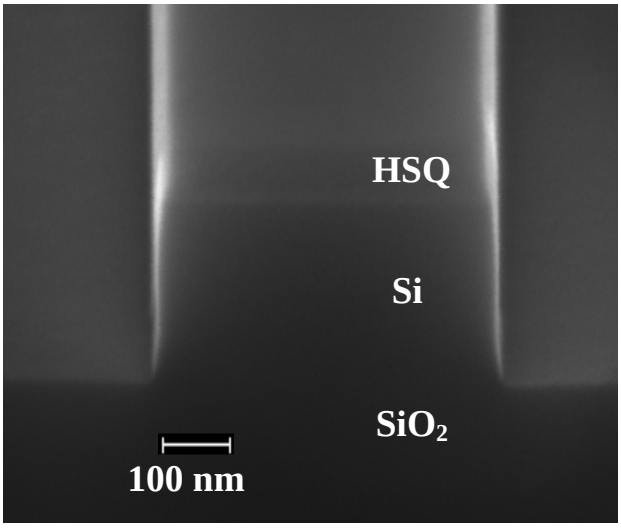

Fig. 4.13: Fabrication results using the modified 2nd process flow (with the plasma parameters given in Table. 4.5) and using a STS SOE ICP etching machine. As shown in the SEM, no nanotrenching is observed and the sidewalls are almost vertical.

plasma conditions when Cl_2 was used. However, when HBr in [78, 79] was used, the trenching effect was weaker, and under some conditions it could be suppressed. While the trenching is generally observed when using Cl_2 or HBr (as the plasma etching gas), such a phenomenon is not observed when etching using fluorine chemistry (such as SF6 or CF_4 gases) as the plasma etching gas. In another report [81], the combination of $Cl_2/HBr/CF_4/O_2$ was suggested and successful results for the fabrication of CMOS gate oxide without the observation of nanotrenching were obtained. In this thesis, a simpler approach was pursued by the combination of CF_4 with Cl_2, and with HBr (as was available in this machine) at different plasma conditions and parameters. The optimization was performed in the STS SOE ICP machine with HSQ as the resist. The early results showed more promising data when the combination of CF_4 and HBr was considered. Table 4.5(a) shows the

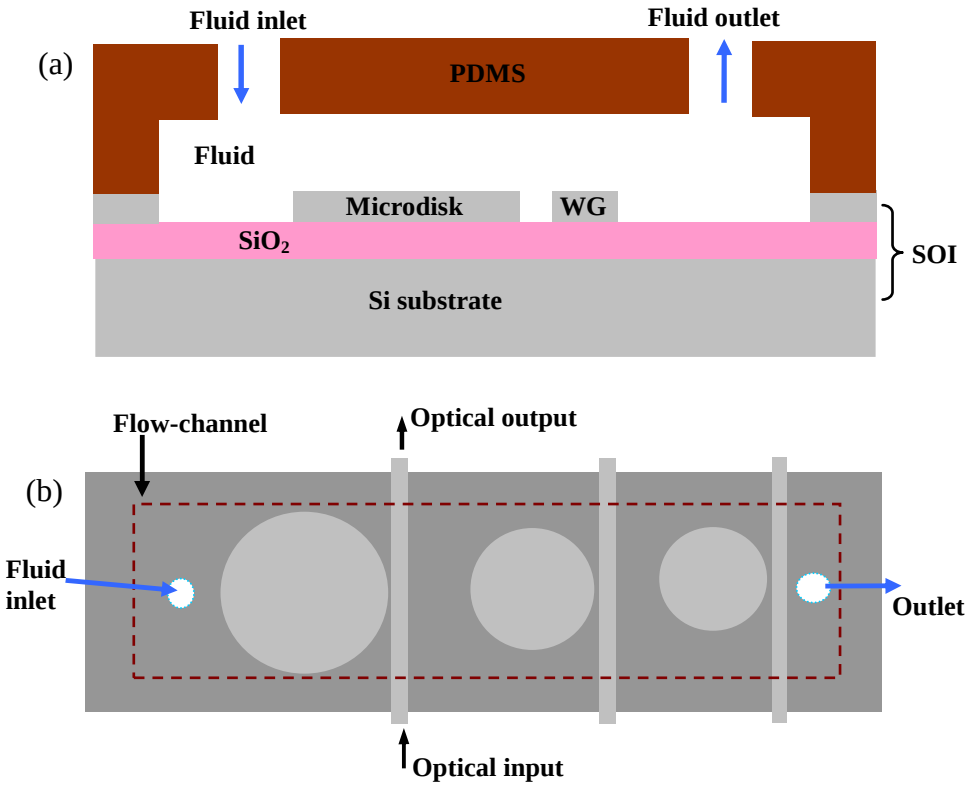

Fig. 4.14: (a) Longitudinal cross section showing the silicon microdisk resonator integrated with a PDMS microfluidic channel. (b) Top view of microfluidic channel integrated with an array of microdisk resonators.

optimized plasma parameters and Table 4.5(b) shows the etch rates and the Si/SiO_2 etch selectivity. Figure 4.13 shows a cross section of a ridge silicon waveguide using the recipe given in Table 4.5. As seen from this figure, no trenching is observed and the sidewalls are almost vertical. However, the addition of CF_4 into plasma can increase the surface roughness and polymerization. Therefore, the price we have paid to overcome the nanotrenching problem is to have more surface roughness due to the presence of CF_4 (mainly because of C which does polymerization). In chapter 5, experimental results of the resonators fabricated using this recipe are provided.

4.5 Integration of Microresonators with Microfluidic Channels

We also integrated the fabricated microresonators with microfluidic channels for the purpose of future lab-on-chip sensing applications. In order to enable the on-chip microfluidic integration, a conventional Polydimethylsiloxane (PDMS) fluidic flow-channel was formed using the soft-lithography technique [82]. The schematic of the longitudinal cross section and top view of the microdisk with integrated microfluidic channel is shown in Figures 4.14(a) and (b), respectively. Inlet/outlet ports were punched and after O_2 plasma activation of the bonding surfaces, the PDMS was aligned under a microscope and bonded to the SOI device [83]. Peeling tests showed that the PDMS fractured prior to bond peeling, thereby indicating that the PDMS-SOI devices were well-bonded. The microfluidic channel dimensions are 1mm × 6mm, so that an entire array of Si microdisk resonators could be overfilled with the fluid using a single channel.

4.6 Chapter Summary

In this chapter two process flows for the fabrication of silicon microresonators, which were developed and optimized, were presented. The electron-beam lithography and ICP plasma etching were the key processes to obtain smooth, vertical, and well-defined Si patterns.

The first process flow was based on a two-step etching process using a thin oxide layer (on Si) as a hardmask and ZEP520A (on the thin oxide) as the positive electron resist softmask. This process was intended for (but not limited to) the fabrication of ultra-high Q resonators.

The other process flow was a one-step etching process using HSQ as the negative electron resist mask. This process flow was intended for (but not limited to) the fabrication of coupled-resonator structures where accurate control of the dimensions and interspacing of the resonators is required, which can be fulfilled by HSQ as a high-resolution electron resist.

To fabricate microresonators with a Si pedestal layer, some modifications to the process flows were carried out to overcome the nanotrenching problem that exists in etching Si with Cl_2 or HBr. This was achieved by adding CF_4 to the plasma.

As mentioned before, some of the optimized plasma parameters for etching silicon or oxide are equipment dependent. With recent advances in plasma etching machines, further optimization of the plasma parameters can provide a higher quality of fabrication for ultra-high Q resonators.

Some post-processing steps using dry thermal oxidation, nitrogen flow treatment, and Piranha and RCA and BOE processing were discussed to reduce roughness as well as passivate the surfaces of the Si microresonator and remove the contaminants and organic residues from the resonator sidewalls.

Covering the resonator with oxide and polymer was discussed. For oxide cladding, two types PECVD and LPCVD oxide deposition and their impact on the performance of the fabrication were discussed, and experimental fabrication results were shown for an LPCVD oxide cladding.

In the next chapter, experimental characterizations of the Si microresonators fabricated using the above developed process flows are provided.

CHAPTER 5

CHARACTERIZATIONS OF SILICON MICRORESONATORS AT LOW OPTICAL POWERS

In this chapter, the experimental characterization of Si microresonators is presented. All the experiments are performed at low optical powers so that the linear response of the resonator is obtained. The characterization of resonators at high powers and their results are discussed in the next chapter.

For the characterization of Si microresonators, they are side coupled to a ridge waveguide on a SOI chip, as shown in Figure 5.1. In this scheme, light is coupled from one side of the chip (in Figure 5.1) to the waveguide, and after the interaction with the resonator, it is collected from the other side of the chip using a photodetector. As depicted in the figure, to reduce the coupling loss from the light source to the chip, the input waveguide is tapered from a 4 μm width at the input facet to 550 nm over a 1 mm length. For some designs, tapering at the output port of the chip was also considered (as shown by dashed lines). Also, to reduce the noise at the detector, some Si beam-block bars were considered on the chip to block light coming from the input source that travels along and outside the waveguide.

For the characterization of the SOI chip shown in Figure 5.1, two measurement setups were built. These setups were very similar except in their light coupling mechanism (into and out of the chip) and the light collection at the detector. These two setups are called (1) free-space coupling setup and (2) tapered lens fiber setup. The setups are explained in detail next.

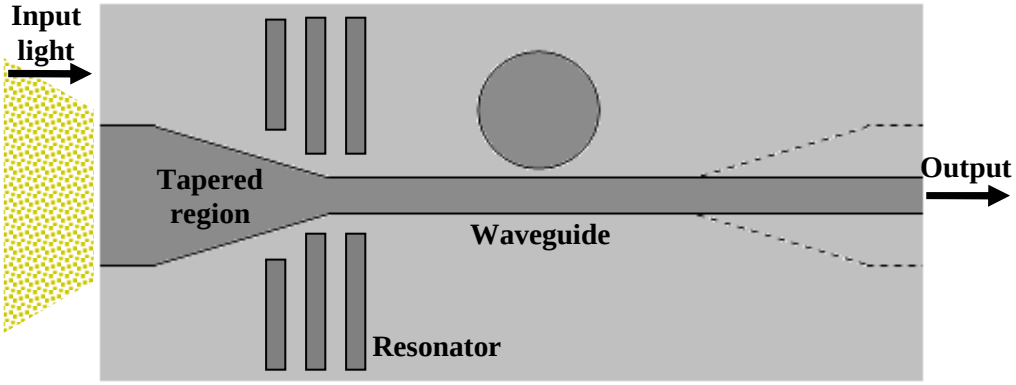

Fig. 5.1: Schematic of a SOI chip with microresonator and waveguide. Light is coupled from one side of the chip to the waveguide and is collected from the other side of the chip. To improve the coupling of light to the waveguide, tapering of the waveguide was considered. For many designs the input width of the taper was 4 μm. To reduce the noise, some Si bars were also patterned to block any propagation of the light (coming from the input light and traveling along the lateral sides of the waveguide) to the output detector.

5.1.1 Measurement using the Free-space Coupling Setup

This setup was developed in the early stage of this research. Figure 5.2(a) shows the schematic of the setup. A tunable laser (Agilent Technologies Model 81680A, linewidth 100 kHz) is used as the source. A single-mode fiber couples the light from the laser source to a graded refractive index (GRIN) fiber lens with a fiber polarization controller in the middle. The collimated beam through the fiber lens is directed to a broadband polarizer to assure the proper polarization state of the beam sent to the chip[53]. The collimated polarized light is then focused to the input facet of the waveguide (on the chip) via an objective lens. We used standard objective lenses (Newport M-40x, 0.65NA) for coupling into and out of the device. The chip is

[53] Using both fiber polarization controller and broadband polarizer, we have simultaneous control on the polarization and the attenuation of light.

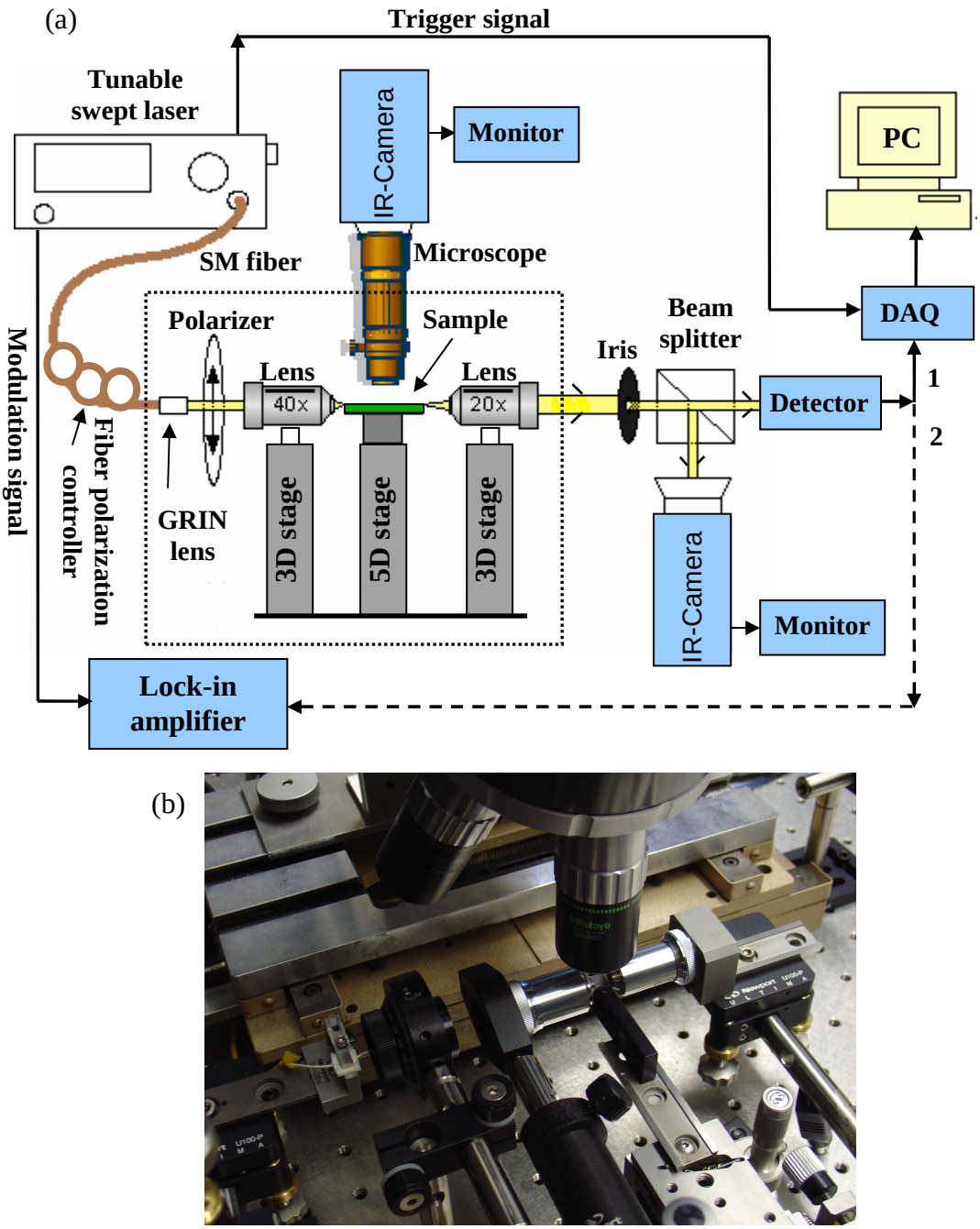

Fig. 5.2: (a) Diagram of the free-space coupling setup used for spectral characterization of microresonator. (b) A portion of the setup that corresponds to the dotted window in (a).

placed on a sample holder on top of a precision translation/tilt stage (562-XYZT precision stage from Newport). An infrared (IR) camera (SU320 NIR, from Sensors

Unlimited, Inc.) connected to a long working distance microscope (Mytutoyo FS-70 microscope head, with 20x and 50x near-infrared long working distance lenses) is used to allow top-view monitoring of the coupling of IR light into (and out of) the waveguide on the chip. The output light from the chip is collected via an objective lens and is collimated out. The output collimated light is spatially filtered using an aperture stop (iris) to remove the stray light (noise). The iris is put at the image plane of the lens (i.e., the plane where the image the output facet of the waveguide is formed via the lens). The light after the iris is sent to a beam splitter. Half of the beam goes to an IR camera for monitoring the beam spot and its profile, and also for further control of the alignment of the setup. The other half of the beam is converted to an electric signal through a photodetector (Thorlabs PDB 150C). Then, the converted optical-to-electric signal is sent to two paths: 1) a computer through a data acquisition (DAQ) card (National Instrument PCI-6251, 16-Bit, 1 MS/s) for saving and post-processing and 2) a lock-in amplifier with a modulation frequency of 20 kHz (Stanford Research Systems, SR830) for reading the signal in real time and optimizing the setup alignment to obtain maximum signal-to-noise ratio at the output.

During the alignment of the setup, the laser source is in the internal modulation mode, and it sends the light modulated with an electric signal with a frequency of 20 KHz. Also, the electric signal is sent to the lock-in amplifier thorough a BNC cable. In addition, the laser source and the lock-in amplifier are connected through a GPIB

cable. The laser source is set at a fixed wavelength in the range of interest, and the setup is aligned until the maximum signal is read in the lock-in amplifier.

After optimizing the alignment, the laser is switched to the wavelength-sweep mode operating in the continuous regime. The start and the end of the wavelength range and the wavelength sweeping speed are set in the laser, and then sweeping is turned on. The start of each laser wavelength sweep triggers the DAQ card to start the data acquisition and send the data to the computer. The measured input-output coupling loss of the waveguide using this setup was in the range of 20-25 dB.

5.1.2 Measurement using the Tapered Lens Fiber Setup

This setup was initially intended for studying the performance of the resonator at high powers. A tapered fiber setup is more efficient in coupling the power to the waveguide on the chip compared to the free-space coupling. However, it was also employed later for the low-power characterization of the resonators. Figure 5.3(a) shows this setup. As mentioned before and seen from Figure 5.3(a), the light from the laser source to the photodetector is guided through an optical fiber except at the region where the light is coupled from the fiber to the chip and from the chip to the fiber. However, the measurement technique and the acquisition of data are the same as in the free-space coupling setup. A tunable laser (Agilent Technologies Model 81680A, linewidth 100 kHz) is used as the source. A single-mode fiber couples the light from the laser source to a fiber polarization controller and then to a tapered

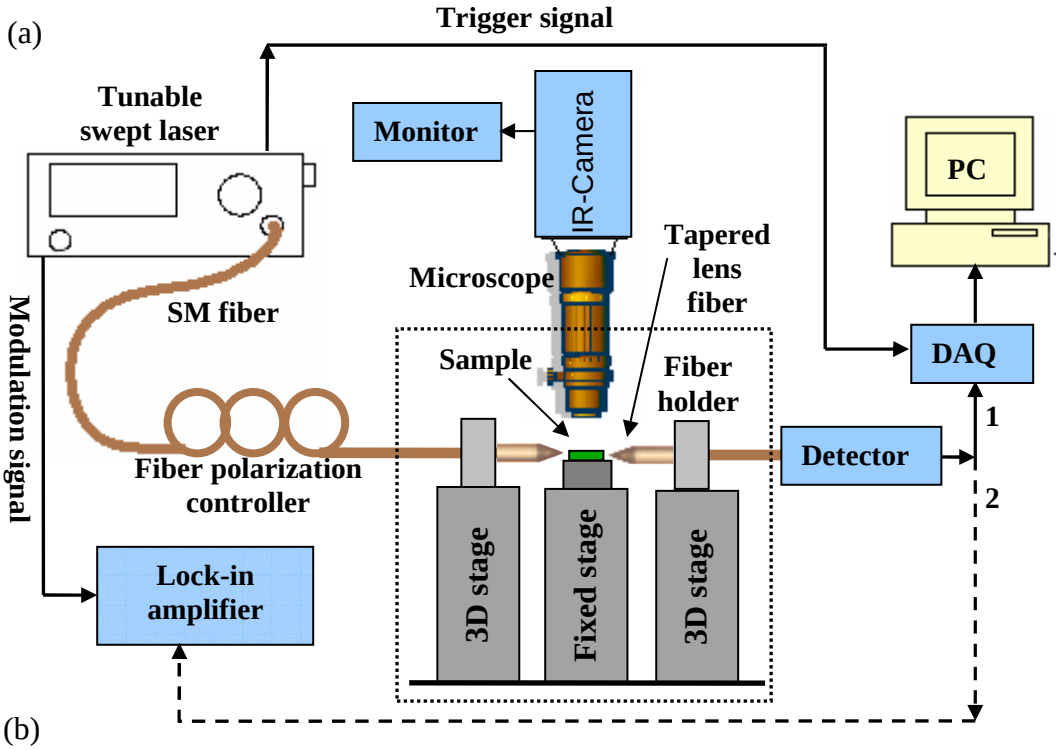

Fig. 5.3: (a) Tapered lens fiber setup used for spectral characterization of microresonator. (b) Portion of the setup that corresponds to the region in the dotted window in (a).

lens fiber (OZ Optics, TSMJ-3U-1550-9/125-0.25-18-2.5-14-1)[54]. The tapered fiber is mounted on top of a precision translation/tilt stage (562-XYZT precision stage from Newport) by a fiber holder. The chip is on top of a sample holder that is mounted on a fixed stage. An infrared (IR) camera (SU320 NIR, from Sensors Unlimited, Inc.) connected to a long working distance microscope (Mytutoyo FS-70 microscope head, with 20x and 50x near infrared long working distance lenses) is used to provide top-view monitoring of the coupling of IR light into (and out of) the waveguide on the chip. The output light from the chip is collected via another tapered fiber and sent to the fiber-coupling port of the photodetector. After the detector, the rest of the setup and its operation are to the same as the one described in the free-space coupling setup and depicted in Figure 5.2(a).

5.1.3 Some Tips and Notes on the Chip Preparation and the Measurement Setup

Unless otherwise specified, all the measurement results reported in this research use TE-polarized light. For most of the experiments, the sizes of the chips (input facet to the end facet of the sample) were usually in the range of 5-10 mm (correspondingly, the length of a straight waveguide on the chip was the same as the size of the chip). The size of the initial fabricated chip was a few millimeters longer to allow room for cleaving by a diamond scribe. The early measurements in this research were done using the free-space coupling setup, and later measurements were done using the

[54] The specification of this tapered fiber is as follows: 1 meter long single-mode fiber, 0.40 mm OD jacketed 8/125 1550 nm, tapered tip on one end, no connector on the other end; 10 mm stripped length, spot diameter of 2.5±0.5 microns, working distance (i.e., focal point) of 14±2 microns.

tapered fiber setup. In the free-space coupling accurate control of the polarization state of the input light was sent to the chip. However, in the tapered fiber setup the polarization of the light (launched into the chip) was not fully controlled (i.e., neither pure TE nor pure TM)[55]. For measurements when the cladding of the chip was air, both setups operated fine in obtaining the TE response of the resonator. This is because in the air cladding case, the fiber-to-chip coupling and propagation loss of the waveguide for the TM polarization were so large[56] that no TM signal was detected in the photodetector. However, for the case of oxide or polymer cladding, in which the TM propagation loss of the waveguide was much lower (compared to the air cladding), the distinction of transmitted power between the TE and TM polarizations using the tapered fiber setup was not large. This was verified by changing the state of the fiber polarization controller in the tapered fiber setup and observing a few dB change in the transmitted power to the photodetector. To overcome this problem, we came up with two solutions:

1- Replacing the tapered fiber in the output port of the chip with a free-space coupling scheme with free-space coupling using lens and polarizer. In other words, the coupling mechanism in the output of the chip is similar to the output of the free-space coupling (as shown in Figure 5.2(a)) adding a polarizer after the objective

[55] As seen in the tapered fiber setup in Fig. 5.3(a), the light (after passing through the fiber polarization and before reaching the tip of the tapered fiber) is subject to polarization change as a result of twisting or looping of the fiber in the path. Therefore, both TE and TM or even circular polarizations can be coupled to the fiber.

[56] In most waveguide designs, the height of the waveguide was in the range of 200-250 nm, and the width was in the range of 400-550 nm. As a result, the TM polarization was much lossier than the TE one. The measured data for the case of the air cladding waveguide confirmed that the TM loss was ~ 20 dB larger than the TE loss. This loss was a combination of coupling loss (from the outside to the chip and from the chip to the outside) and the propagation loss of the waveguide.

lens. In this case, by adjusting the polarizer at the TE state, the TE response of the resonator is obtained. The only possible failure of the setup in this case is when in the resonator has two resonance modes with different polarizations and resonance frequencies very close to each other. Even in this case, because the two polarizations are orthogonal, their coupling is very weak, unless some tensorial nonlinearity exists in the resonator.

1- Removing the oxide (polymer) cladding at the input and output of the chip while leaving the oxide (polymer) cladding at the region close to (and on top of) the resonator intact. For the case of oxide cladding, this can be done during PECVD oxide deposition by masking the input and output ports of the chip. A simple way to mask is to put two small pieces of silicon on top of those regions to protect them from the oxide deposition. For the polymer cladding case, a simple way to remove the polymer from the beginning and the end of the structure is to carbon tape a few millimeters of the region on top of the resonator and then rinse the chip with acetone or other polymer solvent.

For most of the oxide cladding structures, we used the second approach and kept the tapered fiber setup intact.

5.2 Measurement Results and Discussion

Figure 5.4(a) shows the transmission spectrum of a microdisk resonator with a radius of 20 μm coupled to a ridge waveguide with a width of 550 nm. Figure 5.4(b) shows the SEM image of this structure. This structure was fabricated using the first

process flow (which has a hardmask and two-step etching, as discussed in chapter 4). From the measurement of this resonator, several different resonant modes with *Q*s ranging from 1.5×10^5 up to 2.0×10^6 were observed, corresponding to different radial order modes. Figure 5.4(c) shows the spectrum of one of the high Q modes. As can be seen from this figure, because of the weak power extinction of this mode, the unloaded *Q* can be directly obtained by measuring the linewidth of the spectrum. From the measured linewidth, an unloaded $Q\sim2\times10^6$ was observed for this resonance mode. The power extinction for each of these resonant modes, shown in Figure 5.4(a), varies with deviations from the critical coupling condition caused by changes in the waveguide-cavity coupling as well as changes in the intrinsic *Q* of these modes.

One of the issues in the traveling-wave resonators such as a microdisk is resonance mode splitting [59-61]. As discussed in chapter 3, this phenomenon results from coupling between degenerate clockwise (CW) and counter-clockwise (CCW) traveling-wave modes of the resonator because of the sidewall roughness or any other perturbation. As a result of this coupling, two standing-wave modes are generated inside the resonator. This mode-splitting effect is more pronounced for the modes that have their mode energy concentrated close to the sidewall region. The fundamental TE-polarized radial mode of a microdisk has the smallest mode volume and the strongest electric field next to the sidewall and hence exhibits a high sensitivity to the sidewall roughness. A typical observed mode- splitting spectrum is shown in Figure 5.4(d). As can be seen from this figure, a splitting of $\Delta\lambda$ = 2.9 pm is

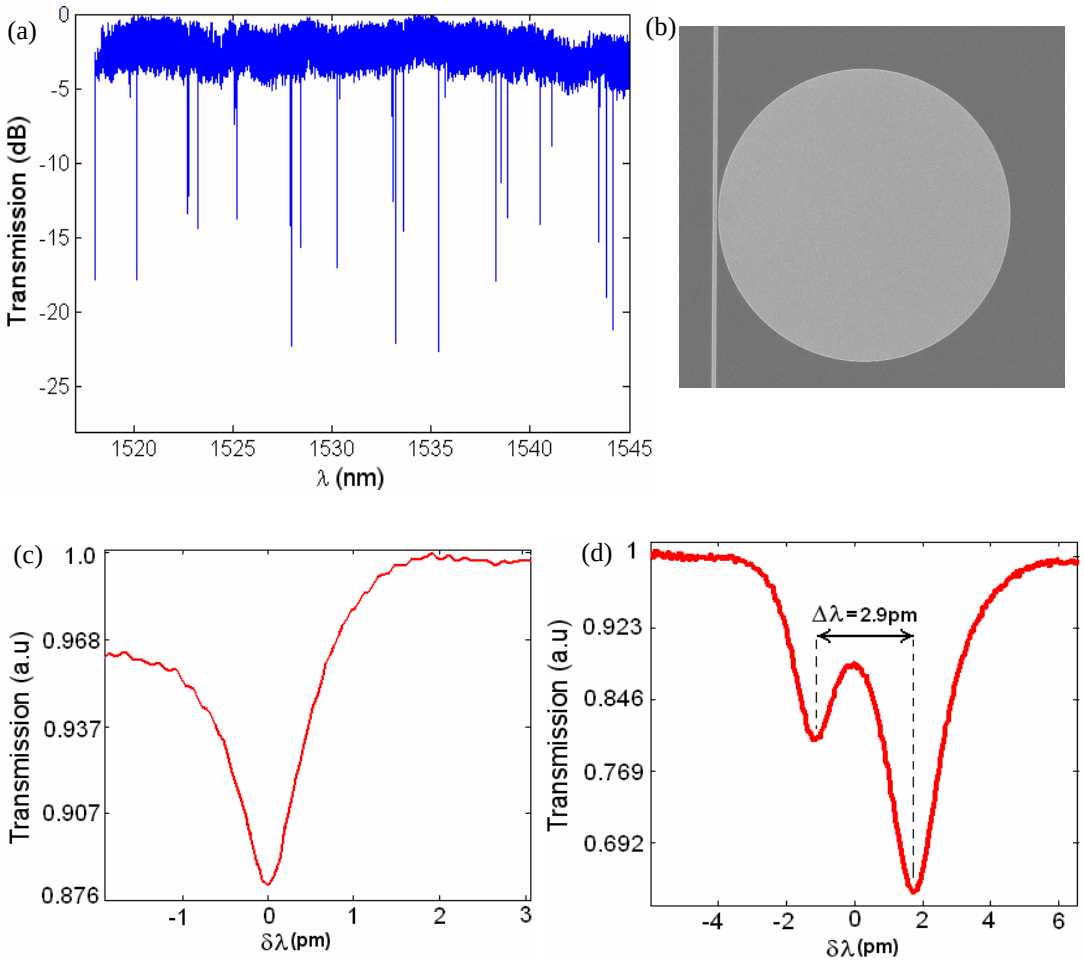

Fig. 5.4: (a) Transmission spectrum of a Si microdisk resonator with a radius of 20 μm coupled to a ridge waveguide with a width of 550 nm. The measurement is done for the TE polarization. (b) The SEM picture of the structure. The gap between the waveguide and the resonator is 220 nm. (c) An ultra-high Q=2.0×10^6 was observed at λ=1520.188 nm. From the simulation results, this resonance wavelength corresponds to a 2nd radial order mode with azimuth number m=218 and a free spectral range (FSR) of 5.1 nm. The mode order and FSR are found by comparing the experimental results with the theoretical simulation (which agree with the experimental data). (d) Observation of resonance mode splitting at resonance wavelength λ=1533.642 nm for one of the microdisk modes [63].

observed for this mode, which is a quantitative measure of the surface roughness [38]. Also, as seen from Figure 5.4(d), the splitting is asymmetric with respect to the resonance center. This is because the two standing-wave modes have different Qs,

which was discussed in chapter 3. One standing-wave mode has more energy concentration in the air side of the roughness and is called the air mode (assuming the cladding is air). The other standing-wave mode, which has less energy concentration in the dielectric side of the roughness is called the dielectric mode[57]. The dielectric standing-wave mode is expected to have a lower resonance frequency (i.e., a higher resonance wavelength). In our experiments, we observed several high Q modes with mode-splitting values in the range of $\Delta\lambda$ = 2-4 pm.

5.2.1 Performance of the Pedestal Microdisk Resonators

We also fabricated and characterized a microdisk resonator with a thin Si pedestal layer at the interface between the resonator and the SiO_2 substrate. The fabricated pedestal microdisk had a radius and input/output coupling waveguide dimensions identical to those in the structure shown in Figure 5.4(b), with the only difference being that by controlling the etching depth of the microdisk, we left a thin pedestal layer of silicon under the resonator. FEM simulations show that the radiation Q of this structure is very large ($Q > 10^{12}$). Hence, we anticipate that the Q is limited only by fabrication imperfections, surface roughness, and other non-idealities. Figure 5.5(a) shows the SEM cross section of this device. From the SEM measurement, the thickness of the thin pedestal layer after the fabrication was in the range 63 nm ± 3 nm. As can be seen from this figure, nanotrenching is observed at the interface of the device and the pedestal layer. This nanotrench formation, as discussed in chapter

[57] This behavior is somewhat similar to the distribution of the two standing-wave patterns in a grating made of a periodic arrangement of dielectric and air slabs. In this case, one standing wave is called a dielectric mode (which has its energy concentration in the dielectric slab) and the other one is called an air mode.

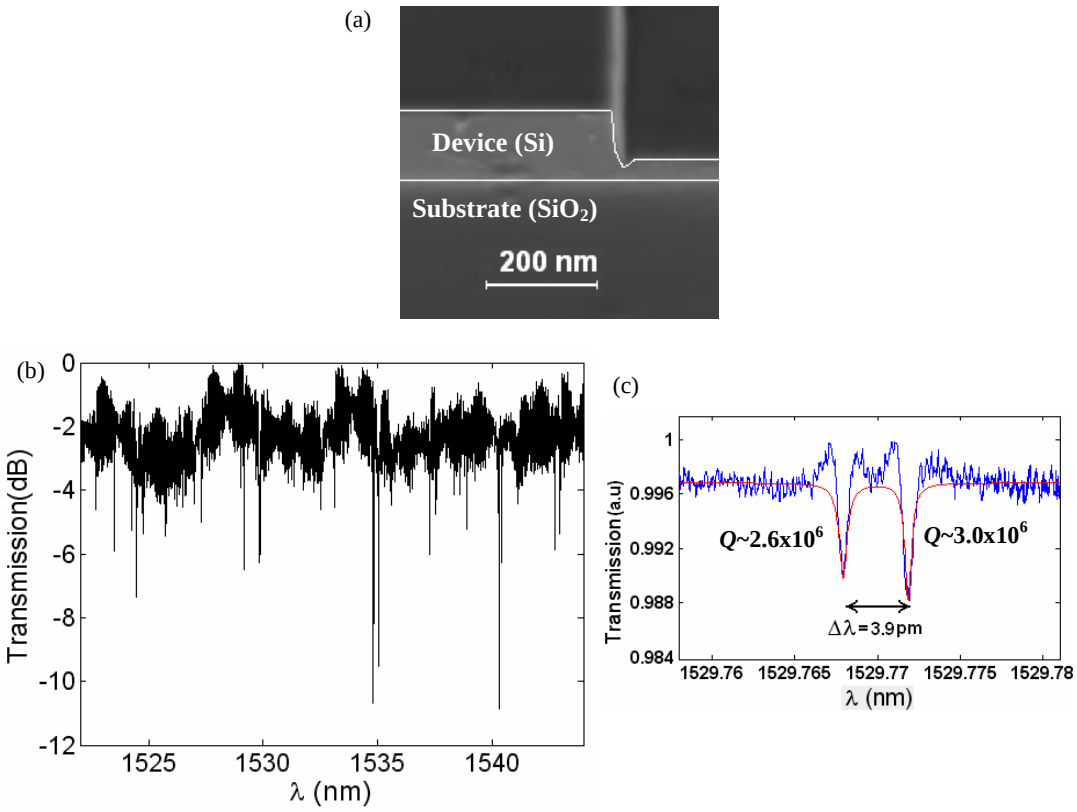

Fig. 5.5: (a) SEM cross section of the pedestal-type structure captured at a sample tilt angle of 30°. The microdisk radius and thickness are ~ 20 μm and ~ 225 nm, respectively, and the thickness of the shallow pedestal layer is ~ 60 nm. (b) Spectrum of the pedestal microdisk resonator coupled to a waveguide for the TE polarization. (c) Spectrum of the 2nd order radial mode; mode splitting due to the coupling of CW and CCW is observed. The theoretical Lorentzian spectrum, which is shown as the solid red curve in (c), resulted in unloaded *Q*s in agreement with the experimental *Q*s. The disk radius and the input/output coupling waveguide are identical to the conventional microdisk shown in Figure 5.4 [63].

4, is typical in Cl_2 chemistry-based plasma etching of silicon. Figure 5.5(b) shows the spectrum of this pedestal. Figure 5.5(c) shows the resonance spectrum of the 2nd order radial mode. As can be seen from this figure, resonance splitting is observed for this mode, and the power extinction in the spectrum is very weak. Therefore, the cavity is almost unloaded, and by measuring the linewidth of the spectrum, the unloaded *Q* was simply estimated to be about 3.0×10^6 in this pedestal microdisk

architecture. This Q corresponds to a roundtrip propagation loss of α~0.16 dB/cm. To our knowledge, this is the highest recorded Q for a pedestal microdisk cavity on substrate. To confirm these experimental results, temporal coupled-mode theory including the effect of mode splitting, as discussed in chapter 3, was employed. This theoretical Lorentzian spectrum, which is shown as the solid red curve in Figure 5.5(c), resulted in unloaded Qs in agreement with the experimental Qs. The presence of the nanotrench along the sidewall of the resonator, as seen in Figure 5.5(c), could have degraded the Q. By suppressing the nanotrench, we anticipate this pedestal microdisk to be an enabling ultra-high Q resonator suitable for integration with P-N junctions and other active electronic components.

In the course of our experiments with the conventional and pedestal microdisk, we noticed that while several of the higher radial order modes exhibited critical coupling, for the lowest order radial modes, which are of significant interest (because of their high Q and low mode volume), we were unable to obtain critical coupling. In other words, the coupling Q of the waveguide-resonator coupling (i.e., Q_c) for a resonance mode was far from the intrinsic Q of that resonance mode. The reason for this is the lack of optimization of the coupling. In chapter 3, the engineering and optimization of waveguide-resonator coupling were presented. Following the guidelines proposed in that chapter, new resonator structures were designed and fabricated.

Figure 5.6(a) shows the structure of a microdisk resonator with a radius of 20 μm coupled to a straight ridge waveguide with a width of 540 nm. The gap between

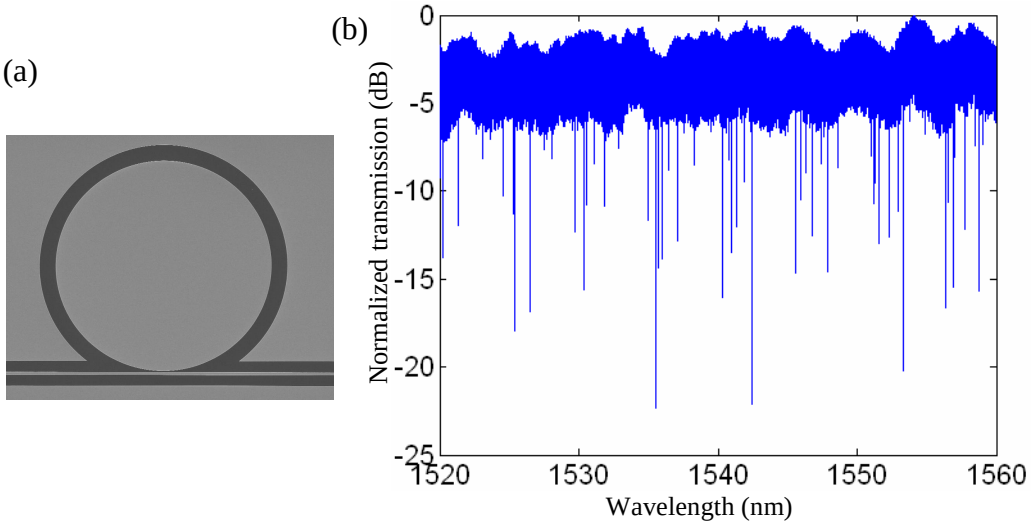

Fig. 5.6: (a) Scanning electron micrograph of a microdisk resonator with a radius of 20 μm coupled to a waveguide with a width of 540 nm. The gap between the waveguide and the resonator is 140 nm and the structure is seated on a 48±2 nm silicon pedestal layer. (b) Transmission spectrum of the structure [85, 86].

the waveguide and the resonator is 130 nm. The waveguide dimensions were optimized to minimize Q_c. This resonator structure was also fabricated with the first process flow (details of the fabrication were explained in chapter 4). In addition, a further post-processing step was performed that included growing a very thin (~10 nm) oxide layer (in a dry oxidation furnace at 850^{o}C) on the structure to passivate the etched sidewall of the microdisk as well as to reduce the sidewall roughness. The grown oxide on the sidewalls of the structure was not removed. Therefore, the actual size of the waveguide and resonator became a few nanometers smaller (by actual size we mean the size of the Si region). From the SEM measurement, the thickness of the pedestal was measured to be 48±2 nm. Figure 5.6(b) shows the experimental measured spectrum of the microdisk in which the critical coupling for many different families of modes is observed.

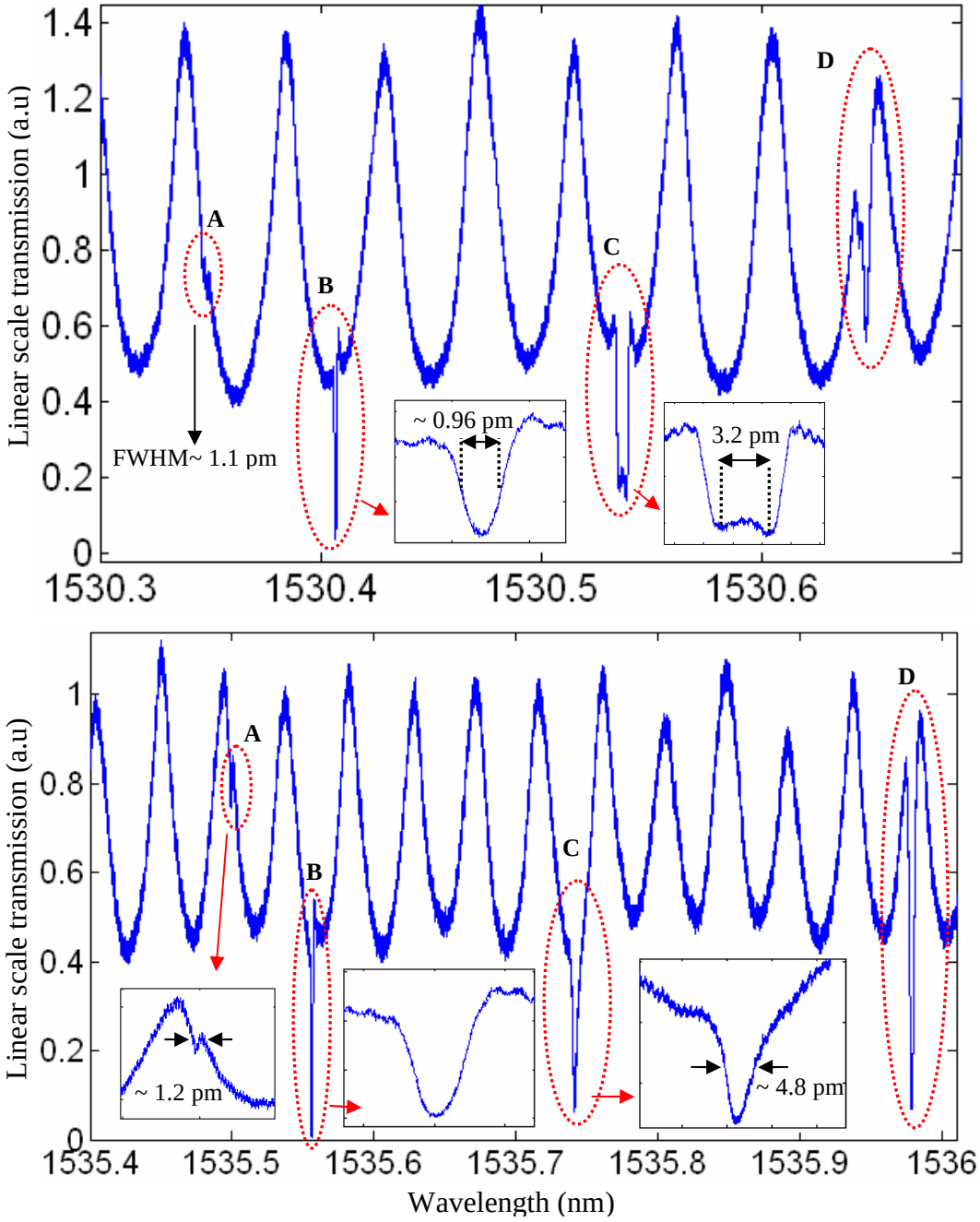

Fig. 5.7: Detailed observation of the spectrum of the microdisk shown in Fig. 5.6(b). (a) A zoomed portion of the spectrum containing four resonance modes belonging to four different radial mode orders. These modes are labeled by letters **A**, **B**, **C**, and **D**. The insets in (a) show the details of resonances **B** and **C**. Fabry-Perot fringes resulting from the waveguide facets are observed in the figure. (b) Spectrum of the same four modes at one FSR away from the ones shown in (a). The modes in (b) have their azimuth mode number one less than the modes in (a). The measured FSRs for **A**, **B**, **C**, and **D** are 5.151, 5.149, 5.205, and 5.332 nm, respectively. The insets in (b) show the details of resonances **A**, **B**, and **C**.

For a closer look at the resonance properties of this microdisk, we investigated some of the resonance modes shown in Figure 5.6(b) at two adjacent FSRs. From theoretical calculations, the FSRs of the first four radial order modes of the microdisk shown in Figure 5.6(a) are about 5nm[58]. Based on this fact and the transmission behavior of the modes in Figure 5.6(b), the modes at two adjacent FSRs (while belonging to the same radial mode order family) in Figure 5.6(b) could be identified. Figure 5.7 (a) (which is a zoomed view of Figure 5.6(b)) shows four of the resonance modes, which belong to different radial orders and have been labeled with letters **A**, **B**, **C**, and **D**, and Figure 5.7(b) shows the corresponding modes at the adjacent wavelength FSR (in other words, the azimuth mode numbers of the modes in Figure 5.7(b) are one integer less than the azimuth mode number of the modes in Figure 5.7(a)). From these two figures, the measured FSRs for theses four modes are ~5.151, 5.149, 5.205, 5.332 nm, corresponding to modes **A**, **B**, **C**, and **D**, respectively. As shown in these figures, strong Fabry-Perot fringes (with a period of ~ 44 pm) resulting from the interference between the facets of the waveguide are observed[59]. The insets in Figures 5.7(a) and 5.7(b) show the zoomed views of some of these modes.

As shown in Figure 5.7(a), the four resonance modes shown have different power extinctions. As an example, mode **A** (with a FWHM ~ 1.1 pm) has a very weak extinction, which means that its coupling Q is much larger than its intrinsic Q,

[58] It is noted that different radial order modes have different FSR values. However, for a large microdisk with a radius of 20 μm (such as the one in Fig. 5.6) the difference between the FSRs is below tens of picometers or a few hundreds picometers.

[59] The wavelength period of a Fabry-Perot can be obtained as $\Delta\lambda = \lambda^2/(2Ln_g)$, where L is the waveguide length, and n_g is the group index of the waveguide.

and the linewidth of **A** almost represents the intrinsic Q of this mode[60]. However, for mode **B,** which has a stronger power extinction, fitting is required to extract the intrinsic Q of this mode.

Comparing the power extinctions of the modes in Figure 5.7(a) with their corresponding ones in Figure 5.7(b), we see stronger extinctions for the modes in Figure 5.7(b) (e.g., mode A in Figure 5.7(b) has a stronger extinction compared to its corresponding mode A in Figure 5.7(a)). This can mean that the waveguide-resonator coupling condition for the modes in Figure 5.7(b) has resulted in stronger power extinctions. We notice that for this microdisk with such a small FSR, the intrinsic Q of a resonance mode when going to the adjacent FSR has a negligible change and is almost constant. However, the coupling Q of a mode (which is strongly dependent on the phase-matching condition between the resonator mode and the waveguide mode) can have a large variation even over one FSR range. Hence, while the intrinsic Q of the resonance mode has not changed, the coupling Q has become stronger. This can be further verified through the behavior of mode **C**. Mode **C** in Figure 5.7(b) shows a doublet behavior, which is a signature of resonance splitting (the spacing between the peaks of the doublet is ~3.2 pm). However, at one FSR away from the mode C, the corresponding mode (as shown in Figure 5.7(b)) shows a singlet behavior. This can be explained through the coupling of this mode the waveguide. As discussed in chapter 3, when resonance splitting

[60] If the intrinsic Q was much larger than the coupling Q, mode **A** was in the strongly over-critical regime. Therefore, (as discussed in chapter 3) the linewidth of **A** would almost represent the coupling Q, and the intrinsic Q was in the range of tens of millions. However, obtaining such a Q is impossible, knowing that the bulk absorption Q of the used Si wafer is in the same range, and with current fabrication technology reaching these numbers is very challenging.

occurs, if the coupling Q between the waveguide and the resonator is smaller than the splitting Q between the CW-CCW modes (i.e., $Q_c < Q_{split}$), the resonance spectrum behaves as a singlet; otherwise it shows a doublet with a weaker extinction compared to the singlet. Hence, for the resonance mode **C** in Figure 5.7(a), $Q_c > Q_{split}$, and in Figure 5.7(b) $Q_c < Q_{split}$. While over a small FSR Q_{split} is almost constant, Q_c can have a large variation over that small FSR range (as a result of improved phase matching) and the change of resonance mode C from a doublet to a singlet is additional evidence that coupling has increased (i.e., Q_c has decreased).

It is noted that by going to an adjacent FSR, all different radial modes don't necessarily obtain a stronger or weaker coupling to a waveguide at the same time. Each mode can have its own behavior, depending on its coupling and phase-matching condition. In addition (as briefly discussed in chapter 3), when perturbation on the phase of the waveguide is also considered in the coupled-mode calculations, more dispersion can appear in the coupling. As a result, coupling can have local minima or maxima (This is under more investigation and the initial theoretical supplementary materials on the perturbation of phase are provided in Appendix E). This kind of behavior can be clearly seen for mode **D** when going one FSR smaller than the one in Figure 5.7(a), as shown in Figure 5.8. The power extinction of mode **D** in Figure 5.8 is larger than the ones in the other two FSRs in Figure 5.7(a) and Figure 5.7(b) (which are at a longer wavelength). However, for modes **B** and **C** in Figure 5.8, their power extinctions are weaker compared to the

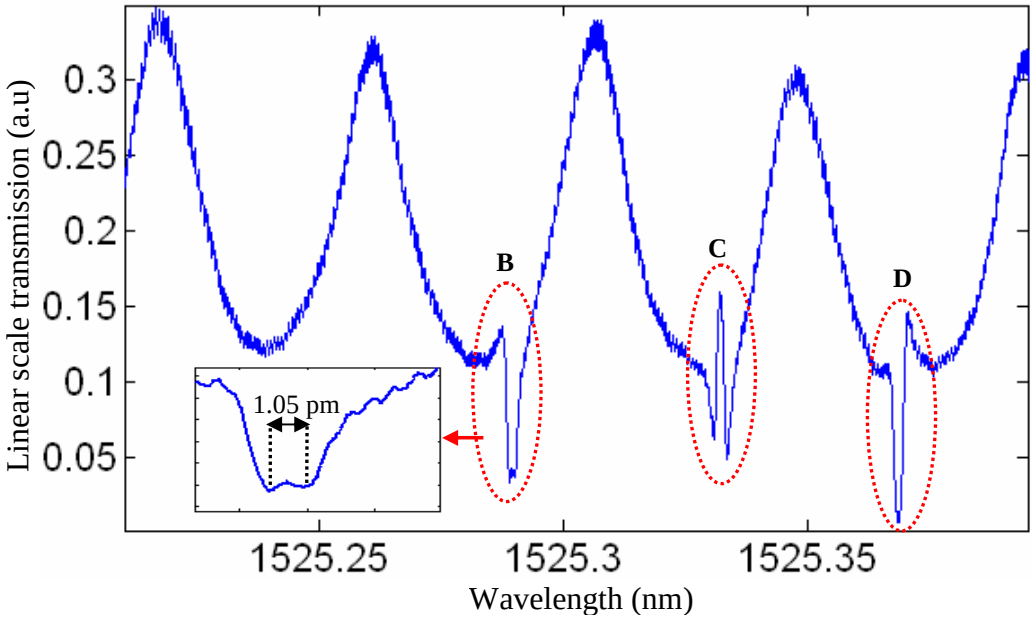

Fig. 5.8: Spectrum of the four resonance modes at one wavelength FSR lower from their corresponding ones shown in Fig. 5.7(a). The inset shows the zoomed view of mode B, which shows a doublet as a result of resonance splitting.

ones in Figure 5.7. Also, the appearance of stronger resonance splitting is further evidence of weaker coupling for modes **B** and **C**.

To find the highest Q among the resonance features shown in Figure 5.6(b), the narrow linewidth features were selected, and by fitting the experimental data to the theoretical data using temporal-coupled mode theory explained in chapter 3, the intrinsic Q of the modes was obtained. Figure, 5.9(a) shows the experimental and the fitted data of one of the ultra-high Q modes (which is the mode **B** as shown in Figure 5.7(b)). For accurate fitting, the effect of the waveguide Fabry-Perot was also considered on the resonator response. Figure 5.9(b) shows a zoomed view of Figure 5.9(a). As seen from Figure 5.9(b), the resonance response of this mode is a singlet; however, it is not in a symmetric Lorentzian shape. This is because of the existence

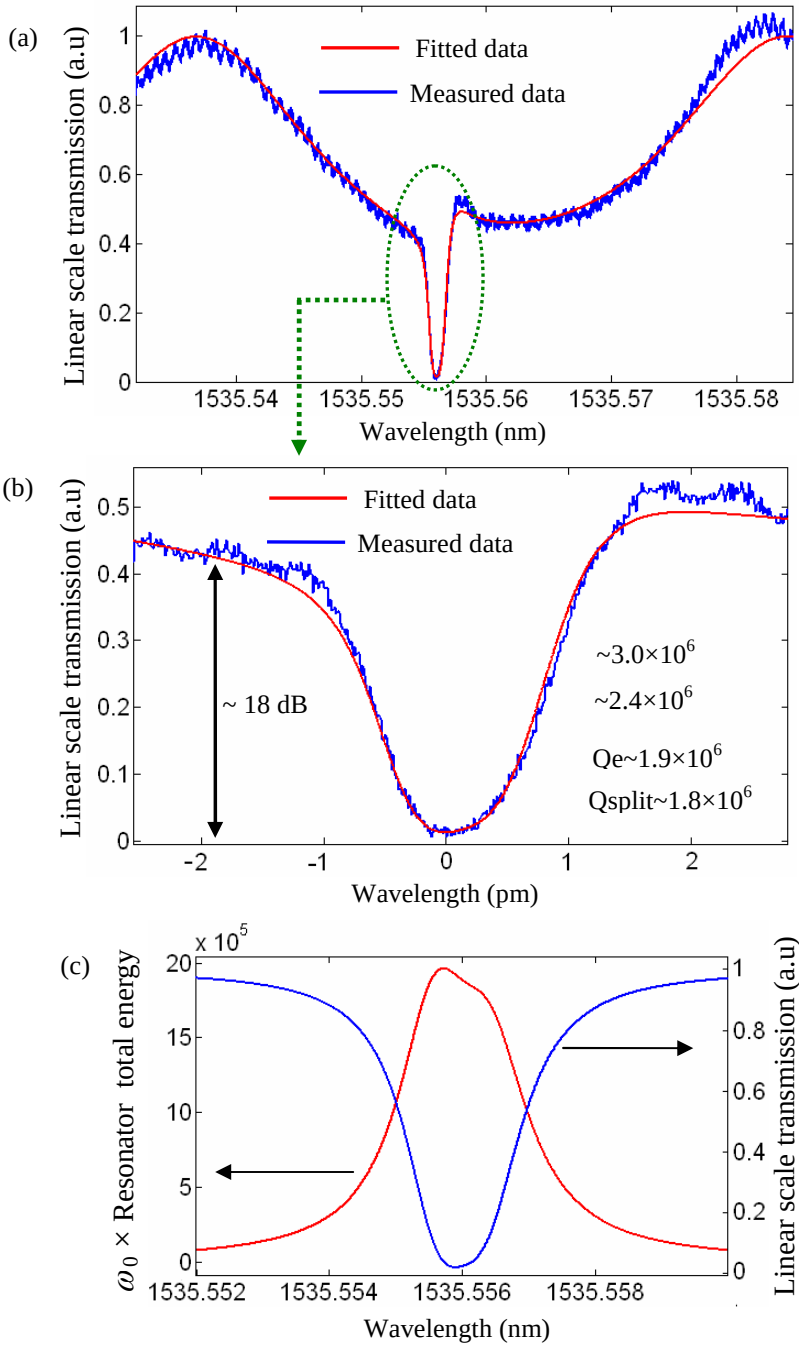

Fig. 5.9: (a) Measured versus the fitted data for the transmission response of one of the ultra-high Q modes of the microdisk resonator shown in Fig. 5.6(a). This mode is mode B in Fig. 5.7(b). (b) A zoomed view of Fig. 5.9(a) with the fitted data given in the inset of the figure. The power extinction of this mode is ~18 dB. (c) Simultaneous plot of the fitted resonator energy transmission response of the resonator mode.

of resonance splitting, where the two standing waves have different intrinsic Qs. Further evidence of the existence of splitting for this mode is that when we look at the transmission behavior of this mode at the adjacent FSR as shown Figure 5.8, splitting with the presence of a doublet is observed. By fitting the theoretical data to the experimental data, an intrinsic Q~3×10^6 was obtained for the resonance mode shown in Figure 5.9(b). Figure 5.9(c) shows the transmission and resonator energy response of the resonator from the theory and in the absence of the waveguide Fabry-Perot fringes.

From the experimental results observed in Figures 5.6 to 5.9 we conclude that, whereas the presence of the pedestal layer did not degrade Q, it improved the coupling to provide critical coupling to an ultra-high Q mode.

5.2.2 Experimental Results on Racetrack Resonator Architectures

We also fabricated racetrack resonators with different bend radii and lengths. For a racetrack with a fixed length, the dimensions of the waveguide and the coupling structure were optimized to provide the critical coupling condition according to the following expression for the Q_c (which was obtained and discussed in chapter 3):

$$Q_c = -\frac{2\pi n_g (L/\lambda_0)}{\ln[\cos(\Delta\beta Z_0/2)]}, \tag{5.1}$$

where L is the racetrack length, n_g is the group index of the mode in the racetrack, Z_0 is the coupling length, and $\Delta\beta$ is the difference between the propagation constants of the supermodes of the directional coupler structure in the racetrack structure. From our initial experiments with racetrack structures and the measured results, we

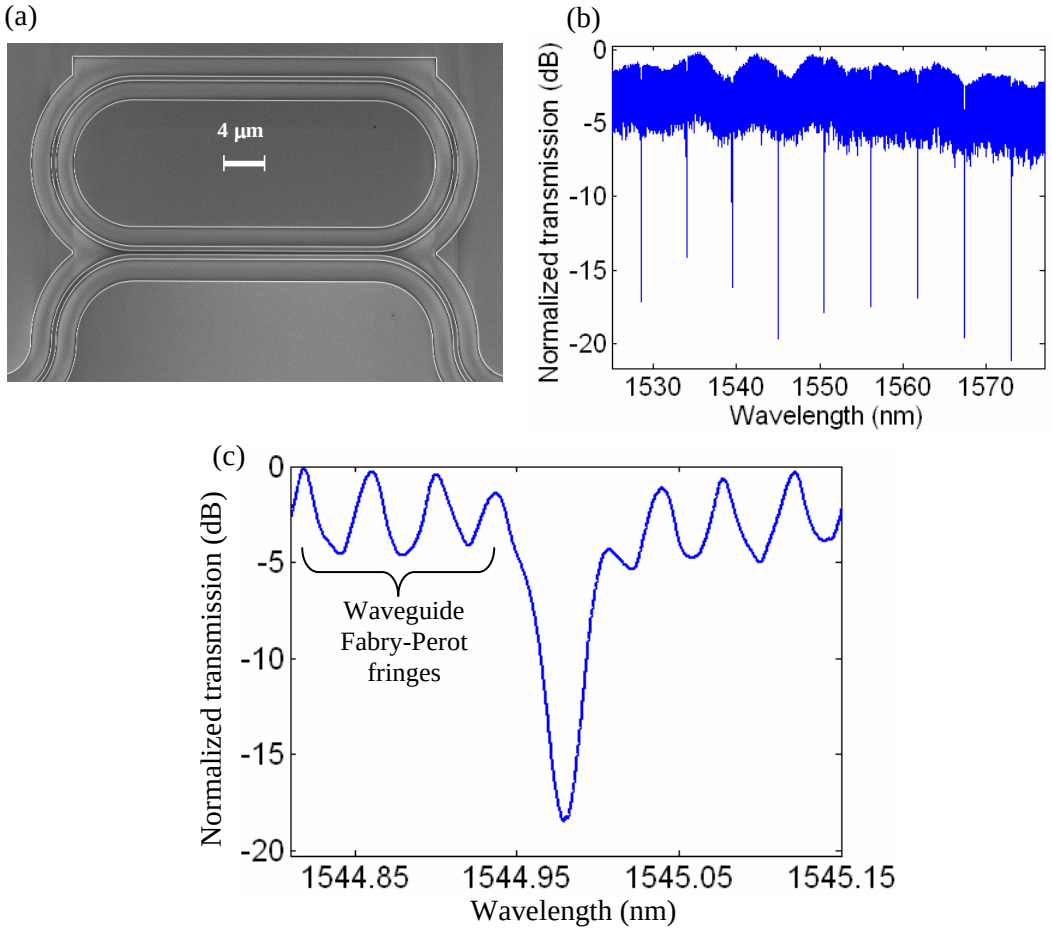

Fig. 5.10: (a) Scanning electron micrograph of a racetrack with an inner bend radius of 7.75 μm and width of 500 nm and a straight length of 24 μm coupled to an external waveguide with a width of 500 nm. The gap between the waveguide and the racetrack is 300 nm. The overall height of the waveguide is H=235 nm. (b) Transmission spectrum of the resonator coupling structure. (c) The zoomed view of one of the resonance modes. Strong Fabry-Perot fringes of the external waveguide are clearly observed in the spectrum in (b) [85, 86].

found that that the intrinsic Qs of a fabricated racetrack are in the range of 50,000-100,000 (being the lowest or the highest in this range depending on the fabrication conditions). Knowing this, we fabricated a racetrack with dimensions that resulted in a Qc ~ 65000. Figure 5.10(a) shows the SEM image of the fabricated racetrack and Figure 5.10(b) shows the measured transmission spectrum of the racetrack. For

this structure, a loaded Q of ~30,000 with more than 12 dB extinction was measured. From the measured spectrum, it was difficult to realize the operation regime of the coupling (i.e., being under-critical coupling or over-critical coupling). From Figure 3.2(c) in chapter 3, we can see that for a loaded Q ~ 30,000 with a 12 dB extinction, two intrinsic Qs of ~ 50,000 and ~80,000 are obtained, which correspond to over-critical and under-critical coupling regimes, respectively. Interestingly, the designed Q_c (i.e., 65000) is between this range (50,000-80,000). Hence, employing Equation (5.1) to design the coupling structure of a waveguide-racetrack structure is very promising and helpful.

5.2.3 Experimental Results on Ultra-small Microresonators: Towards Ultimate Miniaturizations and Large Scale Integrations[61]

In the preceding experiments in this chapter, the demonstrated microdisk resonators had large radii with a lot of resonance modes in a small FSR range. Nevertheless, they showed ultra-high Q and large Q/V quantities, which make them prominent for many applications where the multimode nature of the resonator is not a concern. However, for other applications where features such as compactness, smaller mode volume, larger FSR, and single resonance mode condition over the FSR range are required, the resonator dimensions need to be shrunk. This is especially important for the large-scale integration of many resonator-based functionalities and devices. In most previous reports, a microring or a micro-racetrack resonator have been

[61] All the devices of this section up to the end were fabricated using the second fabrication process flow, which (as discussed in chapter 4) had one step of etching with HSQ as the negative electron resist.

employed as the building block of the device [19, 49, 62]. While these structures provide a single-mode resonance condition over the FSR range, a major problem with them is that at very small bending radii, the inner sidewall of the resonator forces the mode energy distribution out of the resonator, resulting in more energy leakage. In racetrack resonators with a small bend radius, another problem is the presence of large mode mismatch between the straight portion and the bent portion, which results in more scattering and loss of the resonator [49]. In addition, the presence of fabrication imperfections at two sidewalls of the microring and racetrack degrades the *Q*. Moreover, for practical applications in which the resonator is covered with a cladding layer such as oxide, the field leakage is further enhanced, which results in further reduction of *Q*. In this section, we propose to use an ultra-small silicon microdisk as the constituting element of miniaturized resonator-based devices. In contrast to a microring or a racetrack, a microdisk resonator has only one sidewall and therefore the *Q* suffers less from fabrication imperfections.

As discussed in chapter 2, in small microdisk resonators, by adjusting the radius and the thickness of the microdisk, the higher-order radial modes are strongly suppressed because of their radiative leakage, thereby resulting in a pure single-mode operation for a very wide wavelength range. As an example, Figures 5.11(a) and 5.11(b) show the cross sections of the electric energy of the 1^{st} and the 2^{nd} radial order modes with a TE polarization (electric field is predominantly in the plane of the disk) for a microdisk resonator with a radius of 1.4 μm and a thickness of 200

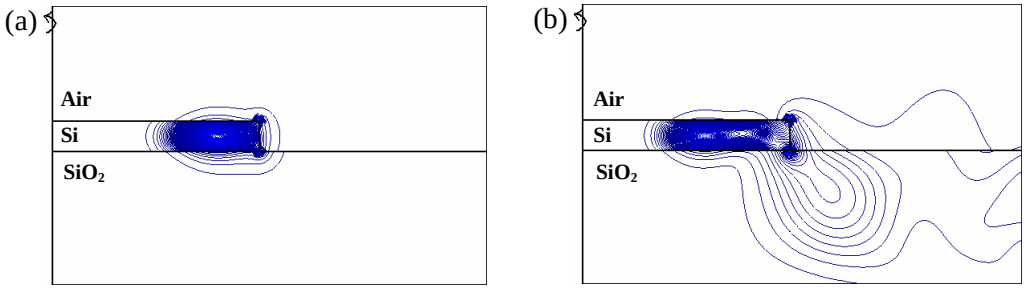

Fig. 5.11: The cross sections of the simulated electric energy distributions of (a) the 1st and (b) the 2nd radial order mode of a silicon microdisk resonator with a radius of 1.4 μm and a thickness of 200 nm. The resonance wavelengths of the modes are around 1550 nm, and the corresponding azimuth mode numbers are 11 and 8 for the 1st mode and the 2nd mode, respectively. The polarization considered is TE (electric field is predominantly in the plane of the disk).

nm. As shown in this figure, the 1st order mode is a confined mode, while the 2nd order mode is strongly radiative. The optimal thickness and the radius of the microdisk are found through the simultaneous maximization of the radiation Q of the 1st and minimization of that of higher-order modes. We also note that the overall Q of tiny resonators is more degraded because of the fabrication imperfection compared to larger microdisk resonators [38]. Therefore, a high quality of fabrication is required to achieve a high Q (or the required Q) with small microdisk resonators. We fabricated small microdisk resonators with radii ranging from 1.5 to 2 μm to experimentally study their performance. As the thickness of the silicon microdisk is very important to satisfy the single radial mode condition and to make sure the higher-order modes are strongly radiative, we considered a range of thicknesses from 210 to 235 nm. Figure 5.12(a) shows the SEM image of a microdisk resonator with a radius of 1.53 μm coupled to a straight ridge waveguide with a width of 400 nm. Also, Figure 5.12(b) shows the transmission spectrum of

this resonator for which one resonance mode with a pretty strong extinction is seen over the entire FSR range. This resonance mode is the 1st radial order TE mode, and the theoretical simulations accurately predict it with an azimuth mode number m=12. From the simulations, the FSR and the mode volume of this mode are FSR ≈ 70 *nm* and 6.3 $(\lambda_0/n)^3$ (with n = 3.475), respectively. Figure 5.12(c) shows a zoomed view of the resonance mode spectrum shown in Figure 5.12(b). As seen from Figure 5.12(c), resonance splitting, as a result of coupling between the CW and CCW modes and the occurrence of two standing-wave modes, is observed. By fitting the experimental data into the theoretical simulations of the resonator showing resonance splitting, the fitting parameters were obtained as shown in the inset of Figure 5.12(c). From the fitting results, the intrinsic Qs ~ 110,000 and 88,000 for the standing modes of the resonator were obtained. These are the highest Qs reported for such a small Si microdisk resonator (with a radius of 1.53 μm) on a SiO2 substrate in a SOI platform. We believe that by further optimizing the fabrication process, the Q can be improved by at least a factor of two.

For such tiny resonators, we can add another degree of freedom to control the single-mode operation condition by changing the cladding to a higher refractive index material, such as oxide. In addition, for an oxide-clad small microdisk, the waveguide-resonator coupling is stronger compared to the air-clad case. The typical disk radii that we pursued for the oxide-clad case range from 1.9μm to 2 μm to guarantee that *Q* is just above the radiation limit when the resonator has an oxide cladding. To better study these structures under the same fabrication conditions, we

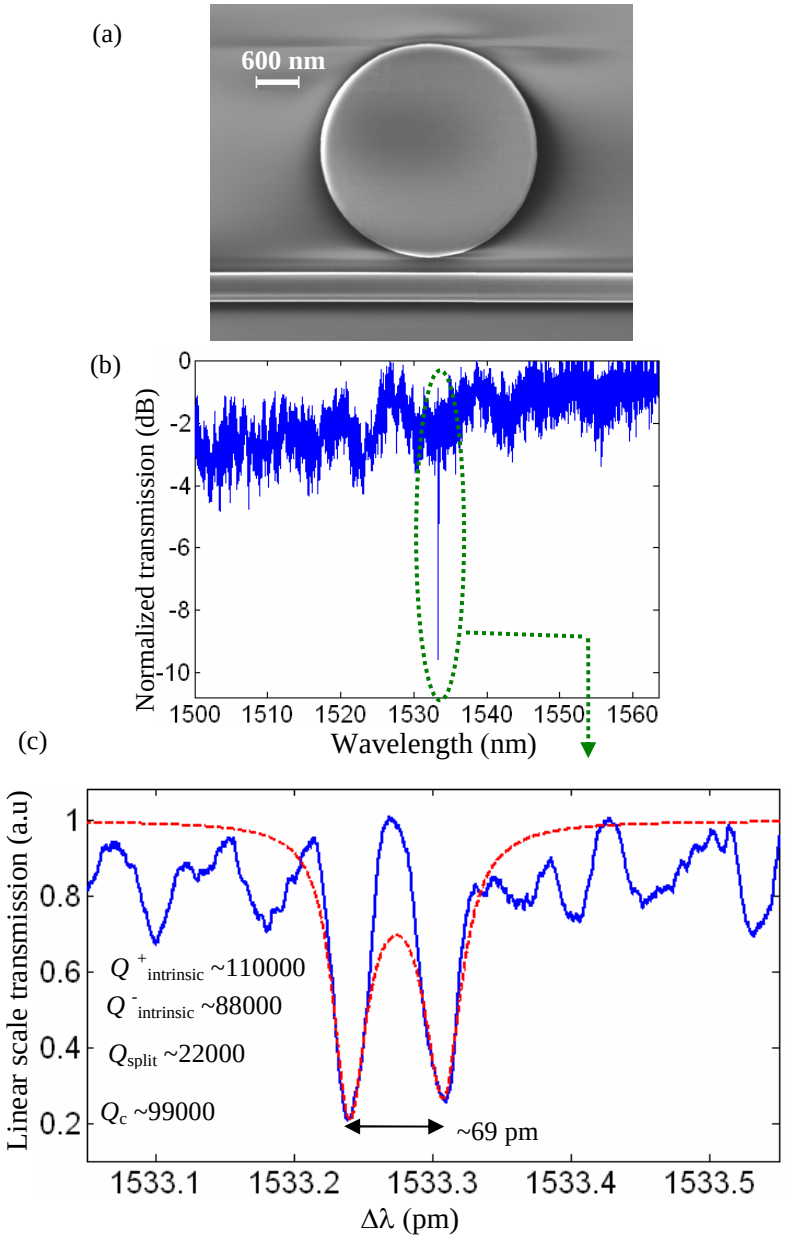

Fig. 5.12: (a) SEM image of a microdisk resonator with a radius of 1.53 μm coupled to a waveguide with a width of 400 nm. The gap between the waveguide and the resonator is ~ 210 nm. The thickness of the Si microdisk is 230 nm and there is a thin HSQ layer with a thickness of ~ 60 nm on top of the microdisk and the waveguide. (b) Transmission spectrum of the resonator showing the 1st radial order TE mode. (c) Detailed resonance spectrum of the 1st radial mode of this resonator, which shows resonance splitting. By fitting theory to experiment, the intrinsic Qs ≈ 110,000 and 88,000 were obtained for the two standing-wave modes. The value of the coupling Q ~ 99,000 in the fitted data is close to the calculated value from coupled-mode theory. The azimuth harmonic mode of this mode is m=12 and its mode volume is ~ 0.15 $(\lambda_0)^3 = 6.3\ (\lambda_0/n)^3$ with n = 3.475 [50, 87, 88].

made an array of these resonators coupled to a straight waveguide, as shown in Figure 5.13(a). The array includes 32 individual resonators. The radius of the resonators in the array is distributed in the range of 1.92 μm to 2 μm. The radius definition was obtained by the simultaneous change of the radius in the CAD file as well as the dosage control during e-beam writing. Adjusting the beam exposure dose adds another degree of freedom to provide nanometer or sub-nanometer control of changing the resonator radius. The fabrication of the oxide-clad resonators is the same as that used in the 2nd process flow mentioned in chapter 3, followed by a Piranha cleaning and depositing a 2 μm oxide in a PECVD chamber. Figure 5.13(b) shows the SEM picture of one of these resonators in the array. As seen in this figure, an inner hole with a radius of 0.6 μm has been perforated at the disk center. We call this architecture a microdonut, as discussed in chapter 2. While the coarse tuning of the resonance wavelength can be achieved by adjusting the outer radius of the donut[62], fine tuning the resonance (<10 pm wavelength accuracy) is achieved by changing the size of the hole, which is far from the peak of the mode energy of the resonator. This fine-tuning capability is very useful to compensate the CIFS effect observed in the design of coupled-resonator filters made of at least three resonators [84]. In addition, this hole in the center of the resonator forces higher-order radial modes to the cut-off regime with negligible change in the quality factor of the fundamental mode.

[62] As an example, for a Si microdisk with a radius of 2μm and a thickness of 220 nm, if the radius changes ±5 nm, the resonance wavelength changes ~±3 nm. Therefore, to obtain a smaller change in the resonance wavelength (e.g., ±1 nm) changing the external radius below 5 nm will go to the limitations of the resolution of lithography.

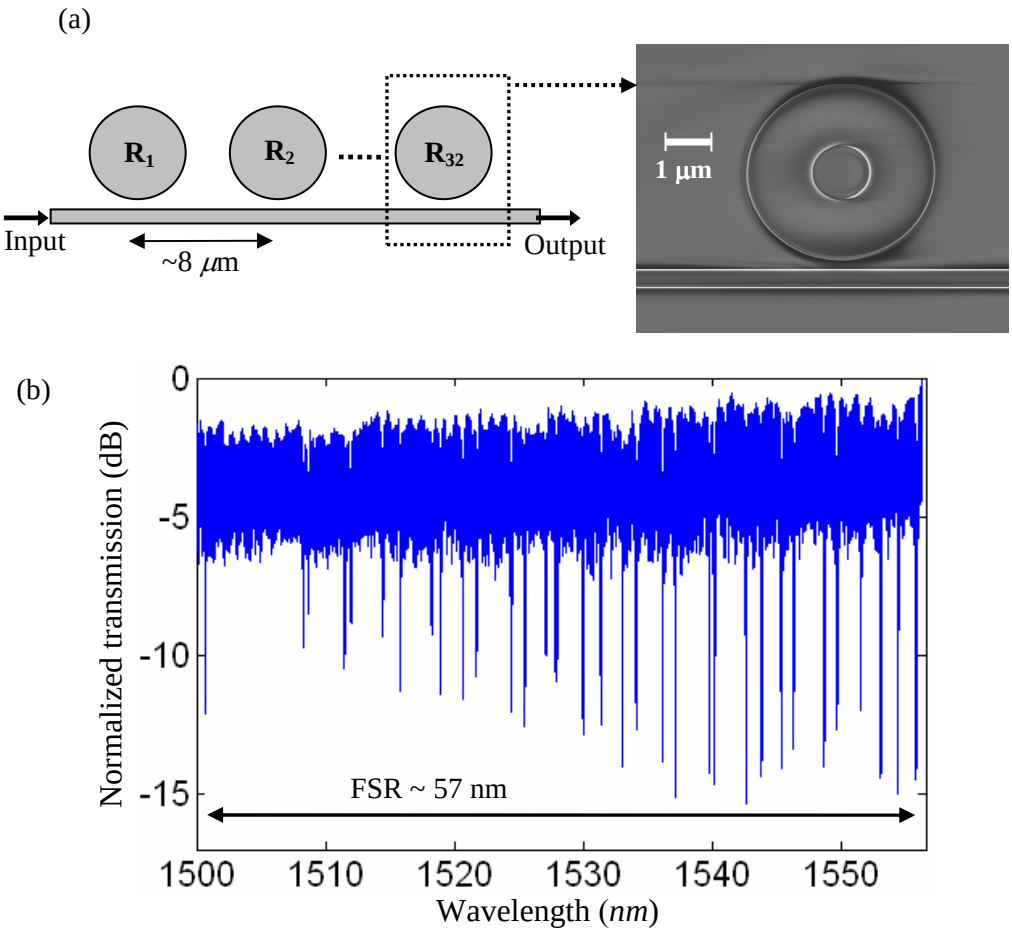

Fig. 5.13: (a) Left: An array of 32 resonators side coupled to a waveguide. Right: The SEM image of one of the resonators in the left structure. The structure has oxide cladding. An inner hole with a radius of 0.6 μm has been made at the disk center. The external radius of the resonators in the array is distributed in the range of 1.92 μm to 2 μm. (b) The resonance spectrum of the structure shown in (a) in the left [88].

Figure 5.13(c) shows the transmission response of the 32 resonators in the array shown in Figure 5.13(a). As seen from Figure 5.13(c), strong power extinctions for all the resonators are observed. Figures 5.14(a) and 5.14(b) show a detailed view of two of the resonance spectra in Figure 5.13(c). These two resonances belong to two different resonators in the array shown in Figure 5.13(a). As seen from Figure

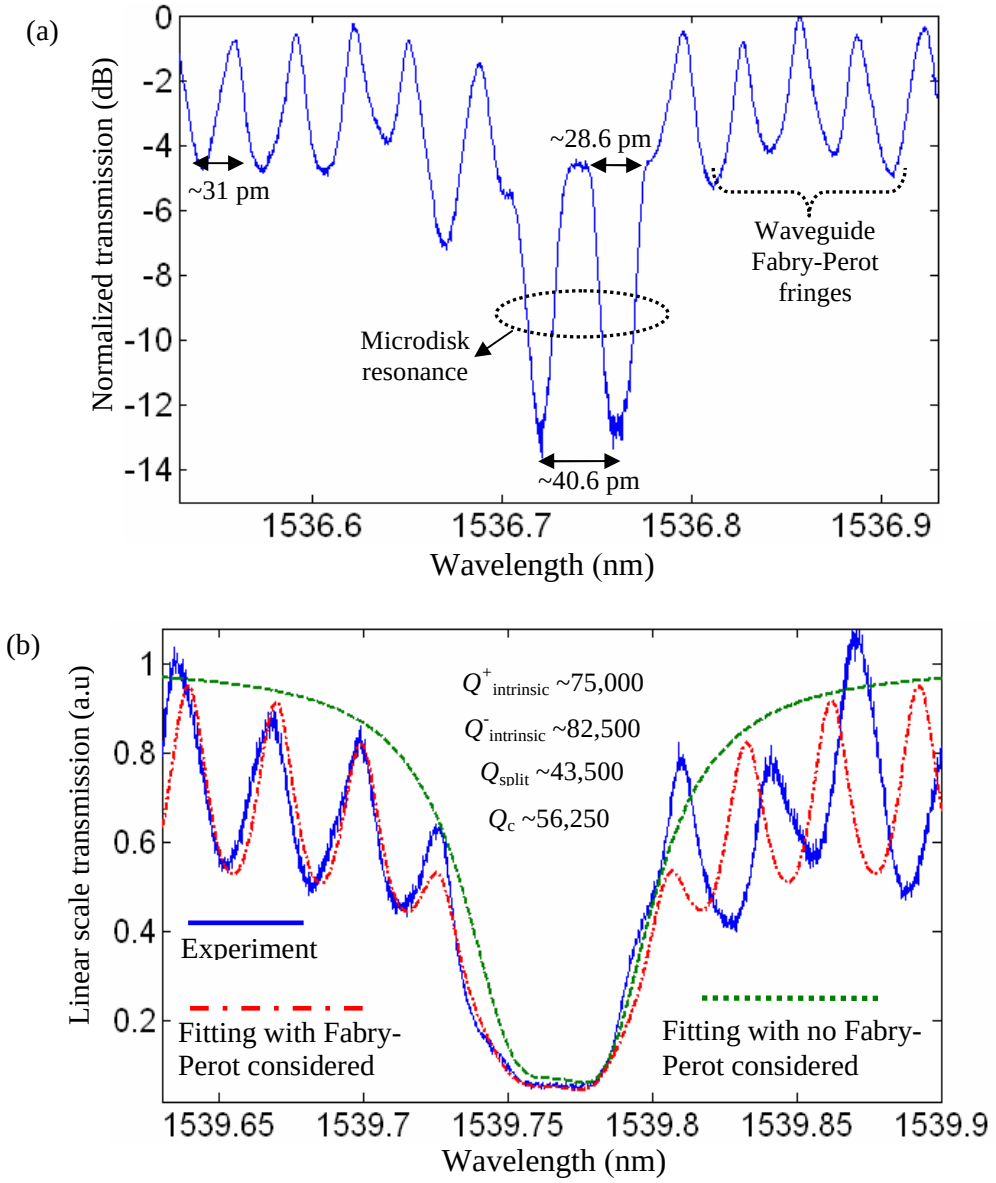

Fig. 5.14: (a) and (b) show the details of two of the resonance features in Figure 5.13(c). These resonances belong to two different resonators in the array shown in Figure 5.13(a). In (a), resonance splitting with a doublet in the transmission is observed. In (b) resonance splitting has resulted in the flattening of the transmission. Strong Fabry-Perot fringes of the waveguide with a period of ~ 31 pm are observed. (b) By fitting theory and experiment in (b) intrinsic Qs of ~ 82,500 and 75,000 were obtained for the standing-wave modes of the resonator [88].

5.14(a), resonance splitting with the appearance of a doublet is observed. The resonance features of the doublet in this figure are narrower than the splitting

wavelength, which is ~ 40.6 pm. This promises a high Q for this resonator. As discussed before, by reducing the coupling Q (Q_c) of the waveguide resonator toward and below the resonance splitting Q (Q_{split}), the doublet in the resonance spectrum becomes very weak and changes to singlet behavior. Figure 5.14(b) shows a scenario in which a very weak doublet is observed in the spectrum, and the transmission response around the center resonance is almost flattened. By fitting the experimental data to the theory, we were able to extract the Qs of ~ 75,000 and 82,500. It is noted that because the period of Fabry-Perot fringes of the waveguide is comparable to the linewidth of the resonance, the Fabry-Perot effect can strongly load the resonator and make the resonator spectrum broader. Therefore, in the fitting, the Fabry-Perot effect has to be considered. The red dashed-dotted curve in Figure 5.14(b) shows the result of the fitting when the Fabry-Perot effect is considered, and the green dotted curve is when the Fabry-Perot is absent. In other words, when Fabry-Perot exists in the experiment, the measured linewidth of the experimental resonance spectrum is larger than the actual linewidth of the resonator.

In the resonator array shown in Figure 5.13, , a variety of operation regimes for the waveguide resonator coupling were observed because of the presence of many resonators. Two other resonance spectra in Figure 5.13(c) are shown in Figures 5.15(a) and 5.15(b), showing a very weak doublet and singlet, respectively.

It is noted that in the experiment in Figure 5.13, the 1st order radial mode energy of the resonators does not interact with the hole at the center of the resonator. However, for future designs, the hole has to be larger to have weak interaction with

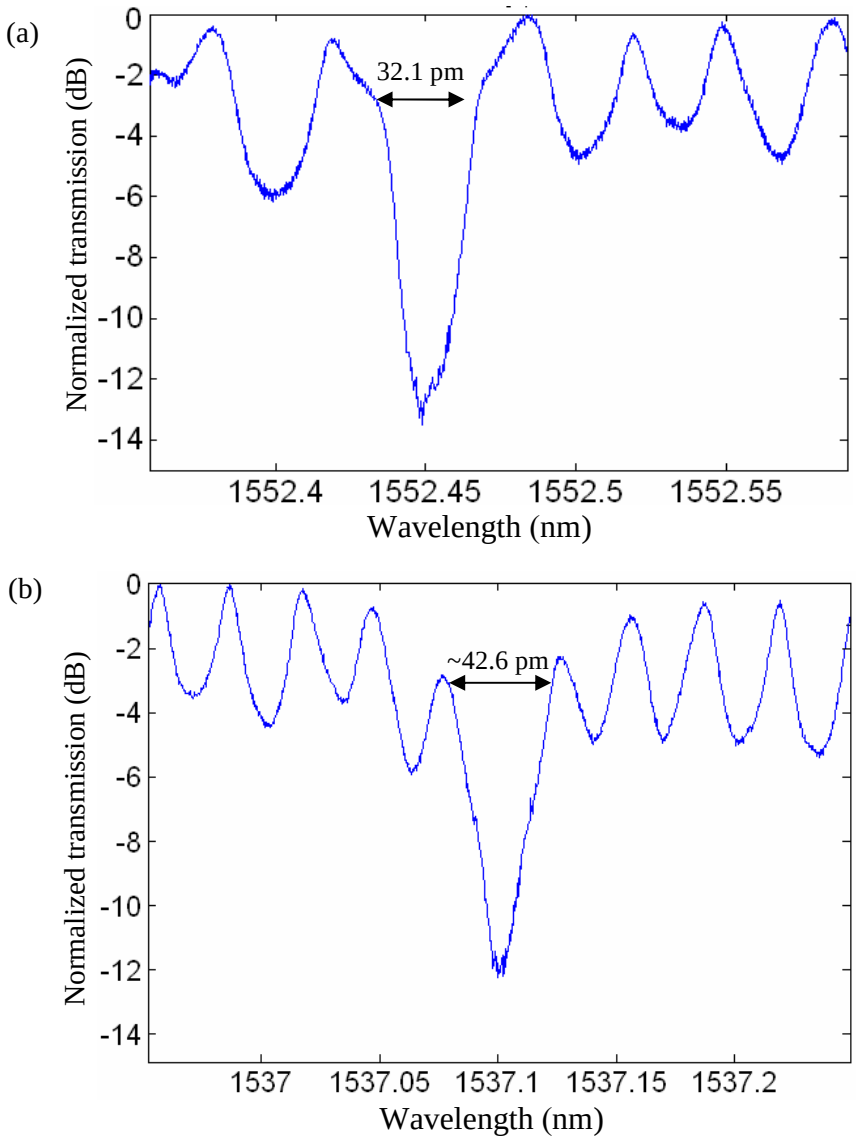

Fig. 5.15: (a) and (b) show the details of two of the resonance features in Fig. 5.13(c). These resonances belong to two different resonators in the array shown in Fig. 5.13(a). In (a) a weak doublet and in (b) a singlet are observed. In both (a) and (b) the resonance spectrum of the resonator has been loaded by Fabry-Perot fringes of the waveguide.

the resonator mode for fine tuning the resonance wavelength and also for pushing higher-order radial modes to cut-off.

One concern in the experiment of the resonator array in Figure 5.13 was the possibility of the appearance of a 2nd radial order mode in the spectrum. For such small structures with an oxide cladding, the 2nd and higher-order modes were predicted to be strongly leaky, and as a result, they had a very weak coupling to the waveguide. However, to gather further evidence of this, another structure was designed and fabricated, as shown in Figure 5.16(a). This structure is a 1st order add-drop filter made of a single resonator. The resonator radius and the waveguide resonator were similar to what were used in the resonator array in Figure 5.13(a) (i.e., radius ~ 2μm and gap ~ 240 nm). Figure 5.16(b) shows the transmission spectrum of the drop port of the add-drop filter shown in Figure 5.16(a). As seen from Figure 5.16(b), two resonance modes are observed, which are the 1st order radial modes with a wavelength FSR ~ 57 nm and the azimuth mode numbers m = 18 and m = 19, corresponding to the longer and the shorter resonance wavelengths, respectively. The resonance wavelength locations and the FSR of these modes agreed with the theoretical simulations. From the measurement, a linewidth of ~ 50 *pm* was measured for the resonances of this filter. As seen in the spectrum in Figure 5.16(b), only the 1st order radial mode appears, and other radial modes are below the noise floor. Compared to the resonators in the array in Figure 5.13(a), the resonator in Figure 5.16(a) is doubly loaded with two waveguides, and as a result, its overall coupling Q to the 2nd order radial mode is lower, which makes the chance of coupling to this low Q mode higher. However, no footprint of coupling to the 2nd order mode is observed in Figure 5.16(b). Therefore, we can conclude that the

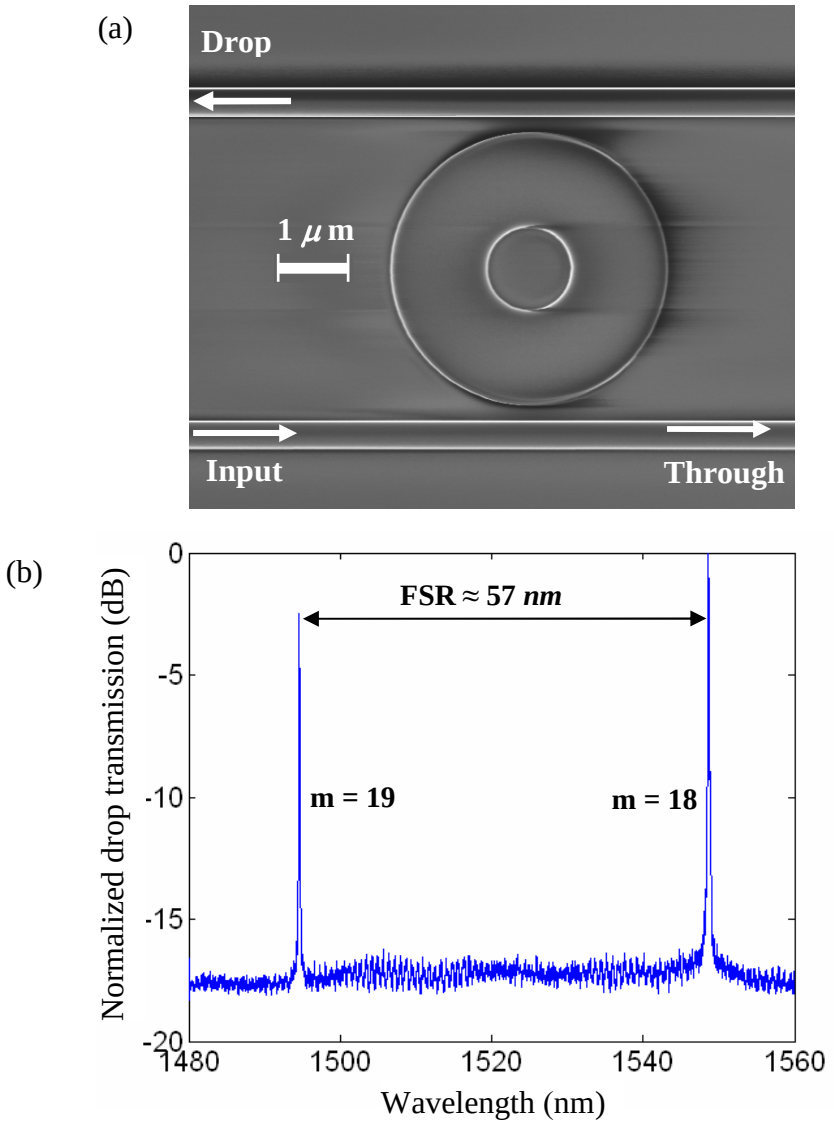

Fig. 5.16: The SEM image of a miniaturized add-drop filter. The waveguide width and thickness are 400 *nm* and 230 *nm*, respectively. The employed microdisk resonator has a radius of r = 1.97 μm with an inner hole with a radius of r = 0.6 μm at its center. The gap between the waveguide and the resonator is 240 *nm*. (b) Transmission spectrum of the drop port of the filter showing the two resonances belonging to the 1st order radial family modes with azimuth mode numbers (m) specified in the figure [50, 87, 88].

coupling of the 2nd order mode of the resonator in Figure 5.13(a) should be much weaker, as there is one waveguide that has loaded the resonator. Consequently, all

the resonance features observed in the spectrum in Figure 5.13(c) are the 1st order radial modes and all the 2nd order radial modes are very weakly coupled to the waveguide and are in the noise level of the transmission.

Having such miniaturized and high Q resonators in a SOI platform motivates the realization of more resonator-based functionalities in a small chip area. One example is the realization of a filter bank made of add-drop filters, as shown in Figure 5.17(a). In this figure, there is one input bus waveguide for all the resonators, and each resonator has its own drop port. The sizes of the resonators are adjusted to have different resonant wavelengths. In the filter bank shown in Figure 5.17(a), there are six Si microdonut resonators with a thickness of 230 nm and external radii varying from 1.92 mm to 1.97, with a radial step change of 10 nm. From the theoretical simulations, a 10 nm change in the radius of these resonators results in a ~ 6 nm shift in the resonance wavelength. Figure 5.17(b) shows the SEM image of one of the add-drop structures in the filter bank in Figure 5.17(b). Because of the small size of the resonators, this filter bank is very compact. In addition, because of the high Q nature of the resonators, very low loss and fine spectral linewidths can be achieved for the filter bank. Figure 5.17(c) shows the transmission spectrum of the drop ports of the filter bank. As can be seen, all the channels are almost equally spaced in the spectrum. For these channels, linewidths in the rage 50 pm to 100 pm were obtained. The main benefits of such a filter bank are as follows:

1- The individual resonators in the filter are high Q. As a result, the filter can be low loss with very narrow linewidths. As discussed in chapter 3, for an

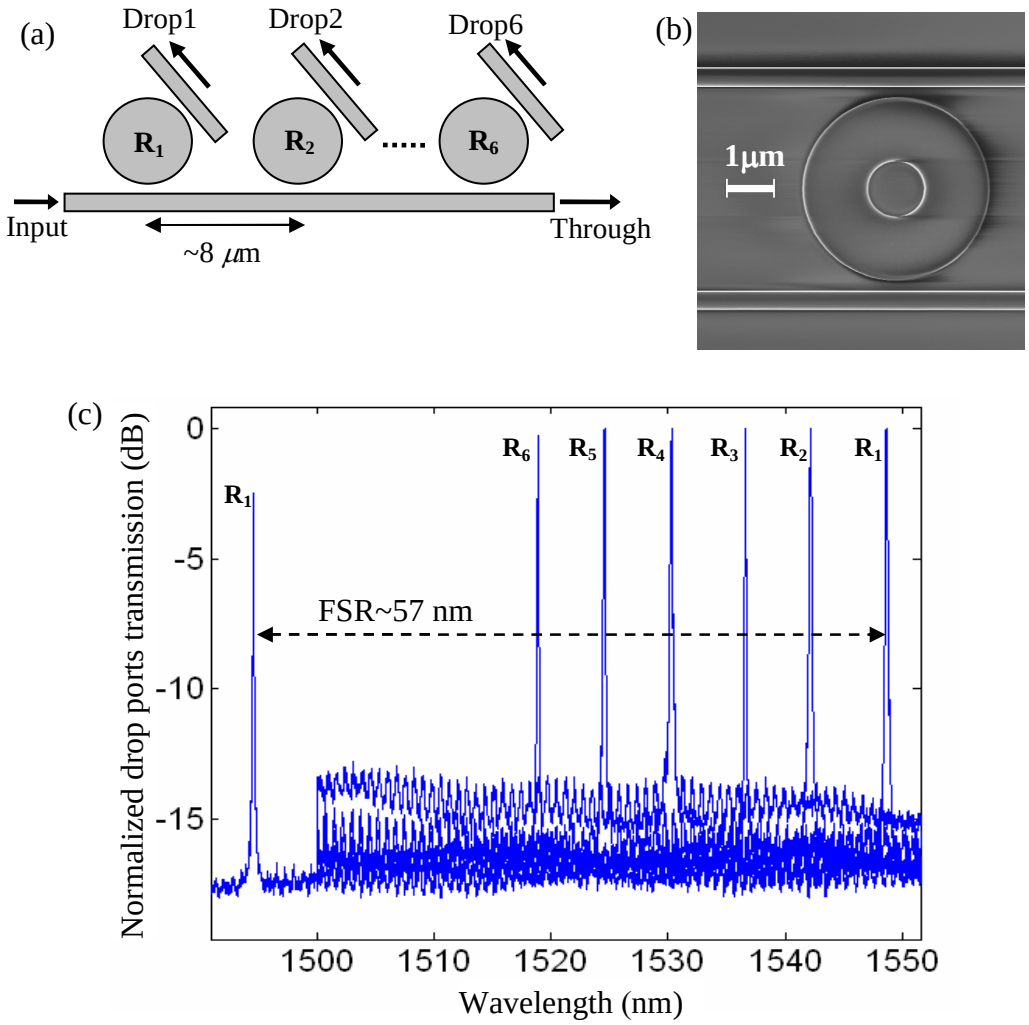

Fig. 5.17**:** (a) An array of add-drop resonator filters suitable for in-plane spectral analysis and signal processing. The radius of the resonators varies from 1.92 μm to 1.97 μm with a radial step change of 10 nm. (b) The SEM image of one of the fabricated resonators in the array, which has a radius of 1.97 μm. The structure is covered with an oxide cladding. (c) Measured transmission of the drop ports of the array shown in (a). The FSR is ~57 nm and the spectral linewidth was designed to be in the range of 50 to 100 pm [88].

add-drop filter, the drop port transmission (at resonance) and the linewidth are $1/(1+0.5Q_c/Q_0)^2$ and $\lambda_0\times(2/Q_c+1/Q_0)^{-1}$, respectively, where Q_0 is the intrinsic Q of the resonator, and the Q_c is the coupling Q of the resonator to the waveguides that are identical and have equal spacing to the resonator.

As an example, when Q_0 =100,000 (as we have obtained in the experiment) and Q_c = 10000, the filter has a loss of 0.4 dB and a linewidth of 0.3 nm at 1550 nm. In fact, the intrinsic Q is much larger than the coupling Q so that the resonance linewidth is dominantly defined by the coupling Q.

2- The filter is made of very large FSR resonators. As a result, many more channels can be accommodated.

3- By adjusting the external and internal radii of the microdonut resonators in the filter bank, their central wavelength resonances can be tuned. In addition, by integrating a microheater on top of the resonator's cladding, the resonance wavelength of the filter bank can be finely and dynamically controlled. Theoretical simulation shows a resonance shift of ~ +80 pm for one degree increase in the microdisk temperature.

Figure 5.18(a) shows another example of a large-scale number of resonators in an array coupled to a waveguide. This is an extension of the structure shown in Figure 5.13(a) to a larger number of resonators. In Figure 5.18(a), the number of resonators in the array is 90, and Figure 5.18(b) shows a zoomed view of the structure. The resonance wavelength spacing between the resonators was designed to be ~ 0.6-0.8 nm. This was done by adjusting the radii of the resonators. As an example, a 1 nm change in the radius of a microdisk with a radius of 2 μm and a thickness of 230 nm corresponds to a 0.6 nm change in its resonance wavelength, which is around 1550 nm. However, a 1 nm change in the radius is below the resolution of the lithography that we used, and as a result, randomness in the

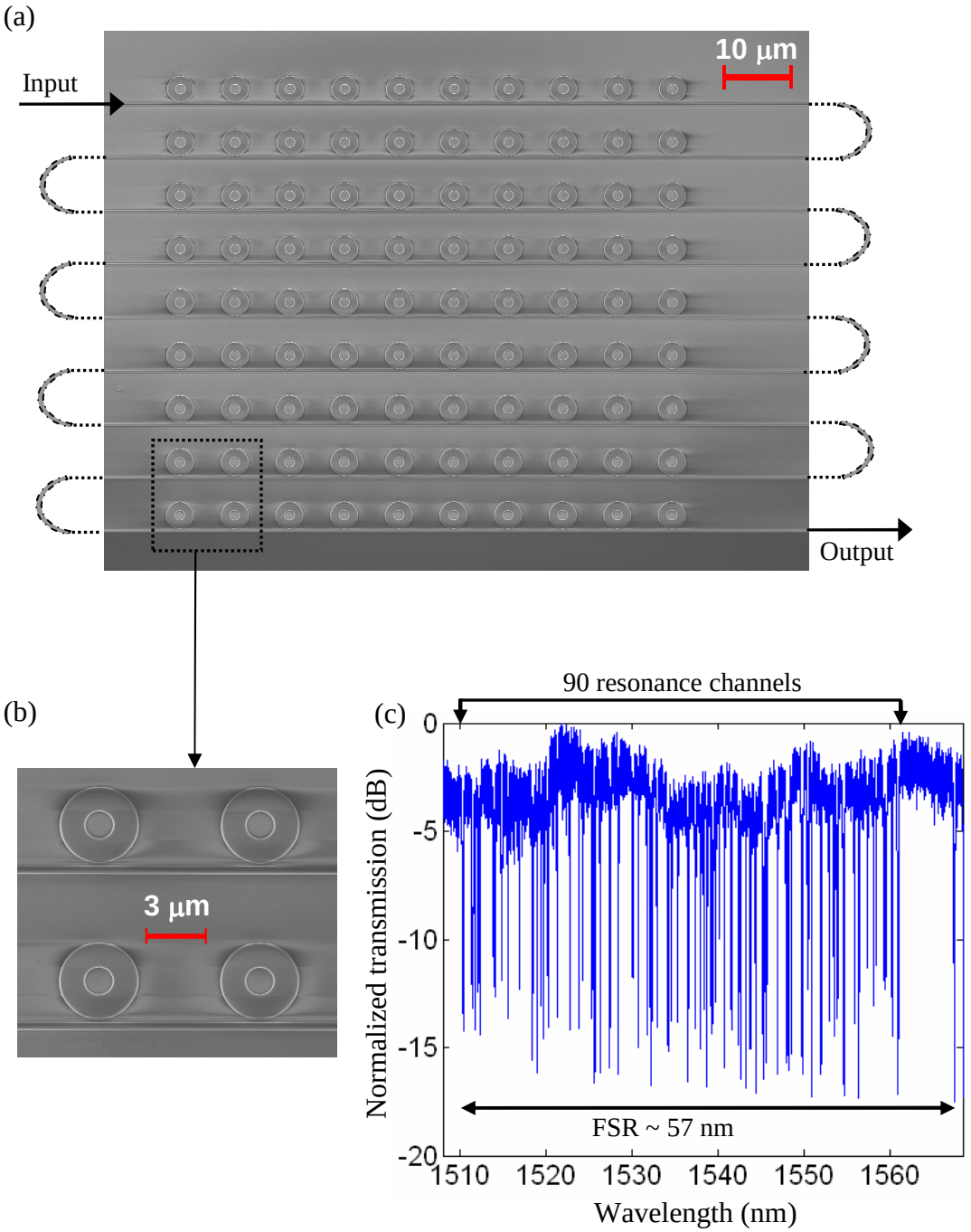

Fig. 5.18: (a) SEM image of an array of 90 microdonut resonators coupled to one bus waveguide (a ridge waveguide with a width of 400 nm). (b) A zoomed view of the structure in (a). (c) Transmission spectrum of the structure. The resonance spectrum at the right end and the one at the left end belong to one of the resonators, and the spacing between these two resonances is the FSR of that resonator [88].

fabrication can change the resonance wavelength spacing between the resonators from their designed values. Figure 5.18(c) shows the measured transmission spectrum of the resonator array shown in Figure 5.18(a). As seen from this figure, the randomness in the fabrication has distributed the resonance wavelength spacing from its original designed values to a range of 0.1 nm to 1.5 nm. Also, a wavelength region close to the right end of the spectrum with no resonance is observed. This wavelength region was intentionally designed to be empty to demonstrate the agreement between theory and experiment. By adding more resonators (into the array) to the resonance wavelengths in that empty region, the number of channels can be increased. Considering that each of these high intrinsic Q resonators in Figure 5.18 has a loaded linewidth of 0.1 nm, by adjusting their center resonance we can accommodate more than 500 resonators in the FSR range, which is ~ 57 nm for the design shown in Figure 5.18. Such a large-scale and compact integration of resonators can dramatically increase the information throughput for spectral analysis. When an unknown signal is sent to the bus waveguide in Figure 5.18(a), each resonator grabs a portion of the spectrum energy of the input signal, which corresponds to the resonance frequency and linewidth of the resonator. By imaging the resonator using a CCD chip on top of the resonator array, all the spectral information about the unknown input signal with a bandwidth below the FSR can be obtained. The main benefit of such spectral analysis is its ultra-high resolution, which cannot be easily obtained by other techniques in such a compact and efficient manner. This is discussed more in chapter 8, where future work is presented.

5.2.3.1. Miniaturized Si Resonators Compatible with Active Integration

As discussed in chapter 2, by adding a thin Si pedestal at the interface of resonator and the underlying substrate, the resonator can be integrated with a P-N junction, as schematically shown in Figure 2.25 in chapter 2. At smaller resonator radii, a simultaneous presence of oxide cladding and the Si pedestal layer can dramatically increase the energy leakage of the resonator mode. The pedestal thickness has to be large enough so that efficient electron transport from the P-N junction and through the pedestal layer occurs. In a recent report, a 30-nm pedestal thickness in a Mach-Zehnder device was shown to be sufficient for high-speed electron transport [13]. In our design, we considered a target pedestal thickness of 35 nm. For a microdonut with an external radius of 2 μm, a pedestal thickness of 35 nm, and oxide cladding, we observed a very low Q and leaky resonator. Therefore, we decided to increase the radius to reduce the leakage and as a result increase the Q. Considering these facts, a microdonut resonator with an external radius of 2.5 μm, an internal radius of 1.3 μm, and a Si pedestal layer was fabricated. The measured thickness of the pedestal layer (after fabrication) using the ellipsometry technique was 33 nm. Figure 5.19(a) shows the SEM image of this resonator coupled to a waveguide with a width of 400 nm. The gap between the waveguide and the resonator is 250 nm. To avoid any nanotrenching at the bottom of the sidewall of the resonator, HBr/CF_4 was used in plasma etching in the second process flow (as discussed in chapter 4). Therefore, we expected the Q to be lower because of the presence of CF_4. The structure was also covered by a 2 μm layer of PECVD oxide, which is closer to a realistic case

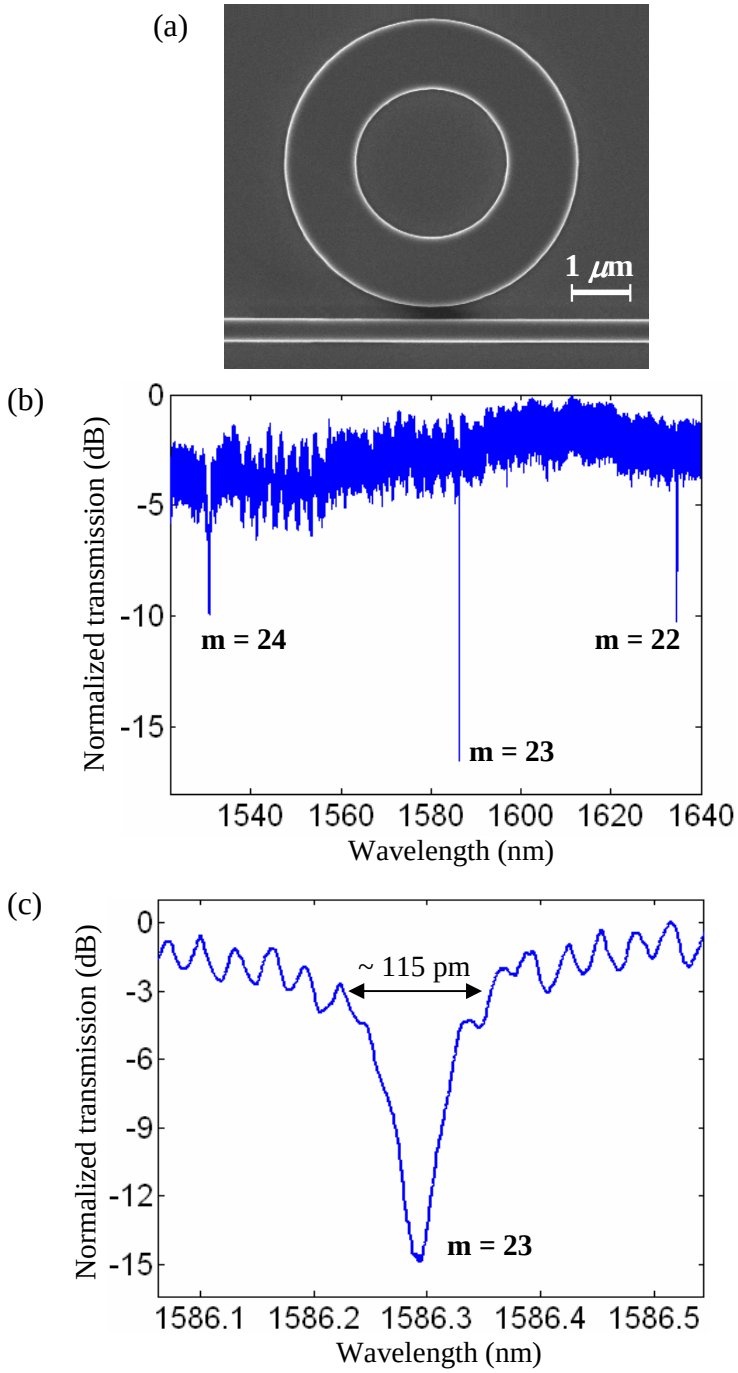

Fig. 5.19: (a) SEM image of a pedestal microdonut resonator with internal and external radii of 1.3 μm and 1.5 μm, respectively, coupled to a waveguide with a width of 400 nm. The gap between the waveguide and the resonator is 250 nm. The thickness of the pedestal layer is 33 nm and the overall height of the Si device layer is 216 nm. (b) Transmission spectrum of the resonator shows large extinctions for three resonances belonging to the 1st order radial mode and with different azimuth mode numbers (m) as specified in the figure. (c) A zoomed view of one of the resonance modes [88].

where the resonator is integrated with a P-N junction. Figure 5.19(b) shows the transmission spectrum of the resonator shown in Figure 5.19(a). As can be seen from this figure, three resonances belonging to the 1st order radial TE mode and with different azimuth mode numbers are observed. Figure 5.19(c) shows a zoomed view of one of the resonances in Figure 5.19(b) with an azimuth mode number m = 23. As seen from this figure, a measured loaded spectral linewidth of ~ 115 pm was obtained for this resonance mode with an extinction of ~ 15 dB. Correspondingly, the intrinsic Q of this resonator using the graph shown in Figure 3.2 in chapter 3 can be obtained, which is Q_0 ~ 24,000. While the Q_0 is not large, this resonator can still be employed for many applications where this level of Q is satisfactory. As an example, a 2nd order coupled-resonator filter (with a bandwidth of ~ 1 nm at 1550 nm) made of two resonators with the mentioned intrinsic Q has an insertion loss less than 1 dB. However, by improving the fabrication process, the intrinsic Q of this pedestal architecture with such small radii can be further improved.

5.3. Chapter Summary

In this chapter, we characterized the spectral properties of Si microdisk and racetrack resonators at low powers. We fabricated these resonator structures using the fabrication recipes that we developed and described in chapter 4. Based on the optimization techniques that we developed in chapter 3 for waveguide-TWR coupling, we designed these structures to achieve critical coupling. We demonstrated a world-record Q (> 3 millions) for microdisk resonators (r = 20 μm).

Such an ultra-high Q was demonstrated for a microdisk with a thin Si pedestal layer,which enables the active integration of the resonator with a P-N junction.

Scaling and miniaturization of microdisk resonators with high Q was another focus of this research. The goal was to achieve the same level of Q/V_m that was obtained in this thesis for ultra-high Q resonators with larger dimensions. The benefits of such small resonators are their compactness, large free-spectral range (FSR), and fewer modes (essentially, they can be made single mode). Based on this motivation, we designed and demonstrated microdisk resonators with dimensions close to the radiation limit (radius ~ 1.5 μm) while supporting one mode over the entire FSR~70 nm with an intrinsic $Q > 10^5$. This is the highest Q reported for a Si microdisk resonator of this size on a SiO_2 substrate, and it is one order of magnitude larger than the previously reported works. The Q/V_m of this structure ($Q = 10^5$, $V_m = 6.3(\lambda_0/n)^3$) was very close to the Q/V_m of the larger ultra-high Q microdisk ($Q = 3\times10^6$, $V_m = 185(\lambda_0/n)^3$). Table 5.1 summarizes the experimental results for a microdisk resonator from ultimate miniaturized scale to larger scales.

Table 5.1: Summary of experimental results for microdisk resonators from ultimate miniaturized scales to large scales.

Radius (μm)	Q	V_m $(\lambda_0/n)^3$	Q/V_m	FSR (nm)	Finesse	Mode properties	Coupling
1.53	10^5	6.3	1.59×104	73.1	4.7×10^3	Single-mode	Easy ↓ Hard
20	3×10^6	185	1.62×10^4	5.3	10^4	Multi-mode	

We showed the capability of these ultra-small resonators for large-scale photonic integration by designing, fabricating, and characterizing a large array of resonators (~ 90 channel), with each resonator having an FSR ~ 57 nm, a Q~10^5, and supporting one mode over the entire FSR range.

For the purpose of compatibility with active integration, we designed and fabricated miniaturized microdisk resonators with a thin Si pedestal layer, and we obtained a Q ~ 25,000. While this moderate value of Q is appropriate for many applications, it can be boosted by improving the fabrication and appropriate design of the resonator dimensions, including the resonator radius and the pedestal thickness.

Also, for fine tuning the resonance wavelength and having more control to design a single-mode resonator, we introduced a hole at the center of the microdisk resonators. Such a resonator (which is in the form of a microdonut) is very suitable for integrating many resonators with close resonance frequencies.

Our successful demonstration of ultra-high Q resonators and miniaturized high Q resonators is a key step for the efficient implementation of a variety of compact and on-chip functionalities for dense and large-scale micro (nano) photonic integration.

CHAPTER 6

SILICON TRAVELLING-WAVE RESONATORS AT HIGH POWERS: THEORY AND EXPERIMENT

In this chapter we investigate the performance of Si traveling-wave resonators at high optical powers. The interplay of two-photon absorption, free-carrier absorption, free-carrier dispersion, and thermo-optic properties of silicon results in rich phenomena in the static and dynamic response of the resonator. We begin the chapter with a detailed study of the static (steady-state) spectral response of Si resonators at high power while considering all the above effects at high powers. We then proceed to the dynamical response of Si resonators at high powers. Here we discuss two different dynamical regimes of operation. We show that we can observe temporal self-sustained oscillations on the transmission response of the resonator, which is pumped with a continuous-wave laser at a fixed wavelength. Such oscillations are achievable with appropriate values for the photon, electron, and phonon (thermal) lifetimes in a silicon resonator, as well as enough input power and appropriate detuning of the laser wavelength from the resonance wavelength. Two regimes of oscillations are observed: 1) slow oscillations, which are in the MHz range frequencies, and 2) fast oscillations, which are in the GHz range. We show that by appropriate control of photon, phonon, and electron lifetimes in the resonator, as well as the input power and the laser wavelength, the oscillation

regime can be only the slow type, only the fast type, or the simultaneous fast and slow type.

6.1. Introduction

High *Q* and low electromagnetic mode volume of Si optical resonators can build up a strong electromagnetic field inside them. Under such conditions, the Si material starts to exhibit a nonlinear optical response, resulting in rich dynamical phenomena in the spectral response of the resonator such as lineshape broadening and bistability. Such effects were originally investigated for ultra-high Q silica microspheres that have only a thermo-optics effect [89-92]. Recently, a few reports [93, 94] investigated the performance of Si photonic crystal resonators and undercut microdisk resonators including effects other than thermal effect, and rich information on the physical mechanisms occurring in the resonators was obtained. In this chapter we generalize the analysis and study the static and dynamic response of the resonator under different resonator and material parameters.

In a waveguide-TWR structure, we can categorize the level of transferred input power from the waveguide to the resonator into three levels o: 1) low, 2) moderate, and 3) high, which are discussed below: (use periods after the numbers below)

1- At low optical powers, we expect the resonator response to be similar to the theoretical results obtained in chapter 3 and experimentally shown in chapter 5. As an example, if no resonance splitting exists, the resonator response is Lorentzian-like.

2- At moderate optical powers, the bulk and the surface absorption power can be considerable. This absorbed power (which is the optical mode energy converted to the heat energy) results in increasing the resonator temperature. As a result of this temperature rise and because of the large thermo-optics coefficients ($dn/dT = 1.84\times10^{-4}$) of Si, the resonance frequency of the resonator is shifted.

3- At high optical powers where Kerr nonlinearity manifests, the self-phase modulation increases the refractive index of Si. However, this effect is very weak compared to other effects that change the refractive index [93]. A much stronger consequence of the Kerr nonlinearity is two-photon absorption (TPA) that absorbs part of the optical-mode energy (photons) of the resonator and generates a large number of free carriers (FC) inside the resonator. The generated free carriers change the refractive index of Si in the positive direction, which results in a blue shift in the resonance frequency of the resonator [44, 93]. Also, the generated free carriers increase the electrical conductivity (loss) of the Si, which by itself is another source of absorption called free-carrier absorption (FCA). The FCA generates heat, which results in an increase in the refractive index of the Si resonator, leading to a red shift in the resonance frequency.

Figure 6.1(a) shows the electronic band diagram of Si near the band gap. In this figure, all the processes mentioned above for the resonator have been specified in the context of band energy concepts. Figure 6.1(b) shows a conceptual visualization

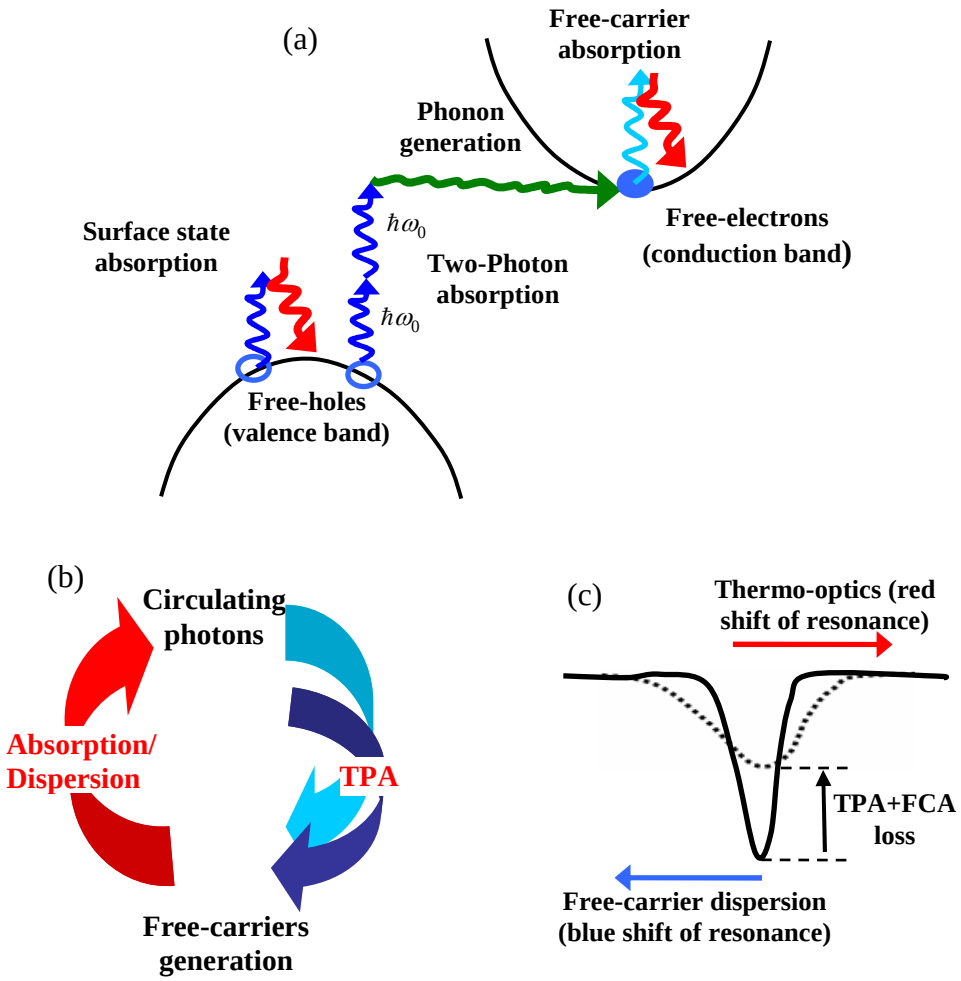

Fig. 6.1: (a) Electronic band diagram of Si showing all the absorption and generation mechanisms of photons, phonons, and electrons. The TPA process absorbs photons (which results in TPA loss and degrades the Q) and stimulates the electrons from the valence band and sends them to the higher unstable states. The phonons interplay to send the electrons from the unstable states into the stable conduction band. The generated electrons decrease the refractive index (which results in a resonance blue shift) and adds free-carrier absorption loss (which degrades the Q). The generated loss heats the resonator (which results in a resonance red shift). (b) A conceptual visualization of processes occurs during the circulation of photons in a resonator. (c) A qualitative description of the change of resonance spectrum from the low-power regime (solid curve) to high-power regime (dashed curve).

of processes that occur in a Si resonator at high powers. A qualitative description of the above effects on the spectral response of the resonator is shown in Figure 6.1(c).

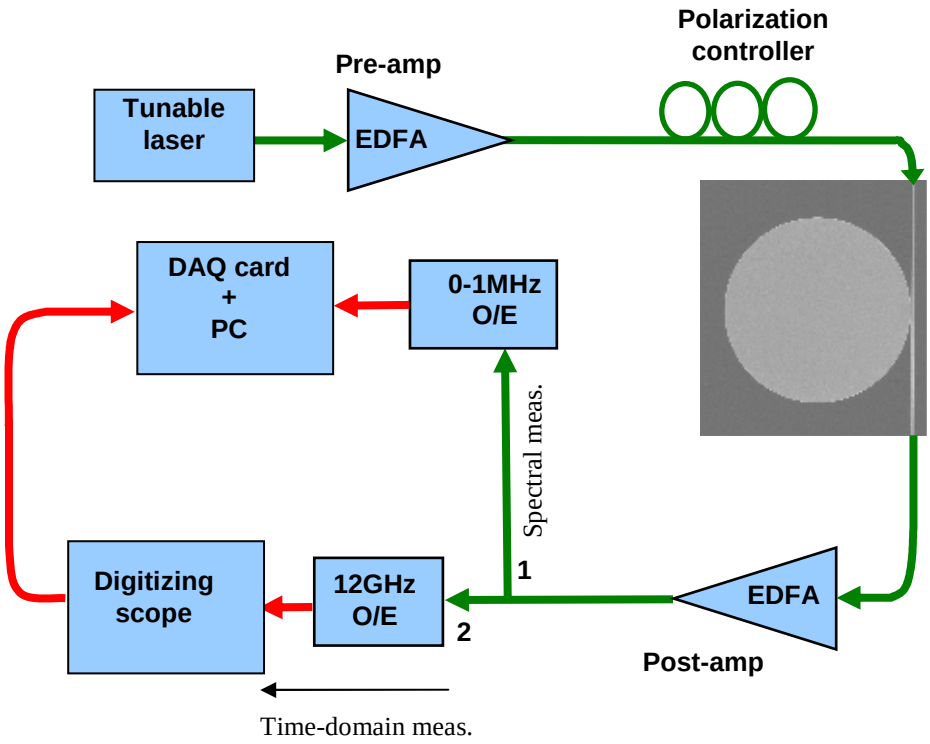

Fig. 6.2: (a) Setup used for monitoring the time-domain and spectral-domain response of the resonator. The SEM image of the measured microdisk is shown in the setup. The microdisk has a radius of 20 μm and a thickness of 230 nm on a SiO_2 substrate and covered by air.

In general, because of the presence of the nonlinearities (and the consequent non-idealities) at high powers, a Si resonator can have static and temporal dynamic responses, even with a CW input pump laser with a fixed wavelength. To observe such responses at high powers, we performed some initial experiments with an ultra-high Q resonator at different levels of input power. Figure 6.2 shows the experimental setup used for the characterization of the resonator. The setup is similar to the fiber-taper setup shown in Figure 5.2(a) in chapter 5, with the following differences: 1) Erbium-doped fiber amplifier (EDFA) has been used as the pre-amplification and post-amplification of the laser power at the input and the

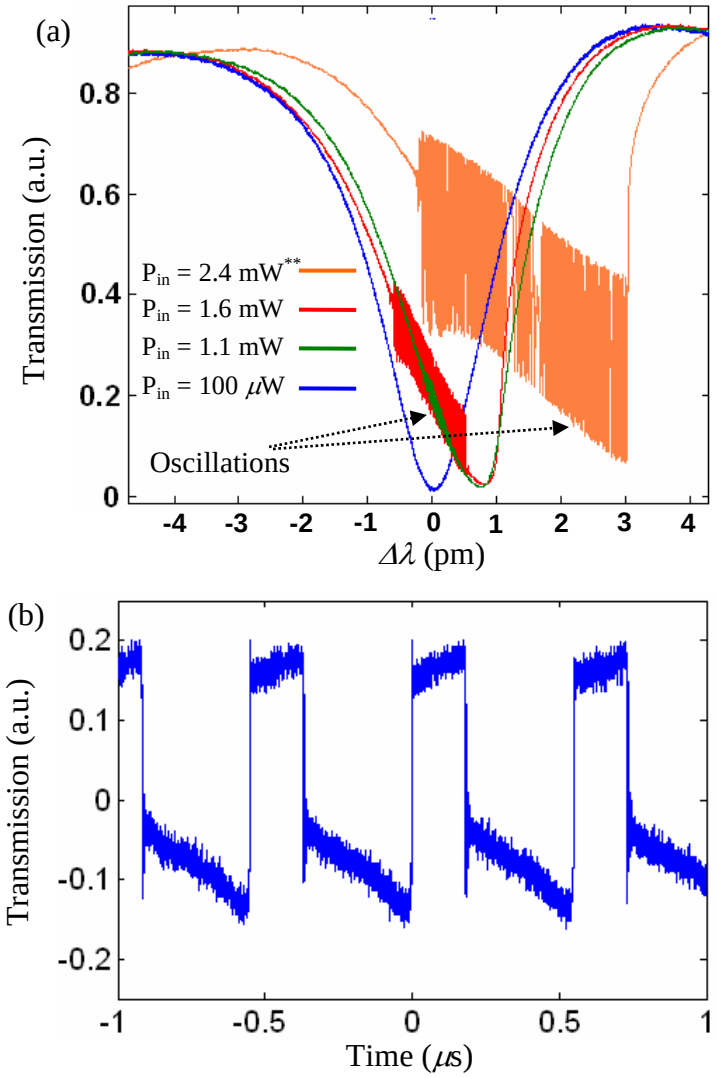

Fig. 6.3: (a) The resonance spectrum of one of the modes of a Si microdisk close to the critical coupling regime for different values of the input optical power as specified in the figure by different colors. For this measurement, the laser wavelength has been swept from the short to the long wavelengths. By increasing the power, resonance linewidth broadening as well as temporal oscillations have appeared in the spectrum. By fixing the laser wavelength at any point in the oscillation regions, temporal oscillations in the amplitude of the resonator are observed. Increasing the power has increased the wavelength range where temporal oscillations can occur. (b) Observation of the temporal oscillations in the transmission response of the resonator when the input laser is CW with a fixed wavelength. The microdisk has a radius of 20μm and thickness of ~ 230 nm coupled to a waveguide with a width of 550 nm. The unloaded Q of this resonance mode is Q_0~1.2x10^6 [96].

** It is noted that the powers in the inset of the figure in (a) are the powers before the chip. The measured insertion loss of the waveguide (facet-to-facet) is about 25 dB. Hence the actual power coming to the waveguide-resonator coupling region is much lower (~ 10-15 dB) than P_{in}.

output of the Si resonator chip; 2) The output optical signal after the EDFA post-amplifier goes to two paths. One path (path 1) is for the conventional spectral characterization, as discussed in Figure 5.2(a) in chapter 5. The other path (path 2) goes to a digitizing high-speed oscilloscope via an optoelectronic detector to monitor the temporal dynamic of the resonator. The EDFA post-amplifier provides a large signal and a better signal-to-noise ratio for the oscilloscope.

For the experiment we used an ultra-high Q microdisk with a radius of 20 μm and a thickness of ~ 230 nm coupled to a waveguide with a width of ~ 550 nm. The spacing between the waveguide and the resonator is ~ 200 nm. A shallow Si pedestal layer with a thickness of ~ 40-50 nm is at the interface between the BOX layer and the Si microdisk. The presence of this layer improves the thermal conductivity of the structure (see Appendix G), in addition to enabling the integration of P-N junction next to the microresonator to remove the free carriers from the active region. Figure 6.3(a) shows the transmission spectrum of one of the resonance modes of the Si microdisk measured at different levels of input optical power in the waveguide, as specified by different colors in the figure. The measurement was done by sweeping the laser wavelength from the left (short wavelength) to the right (long wavelength) around the resonance wavelength and the transmitted spectrum was monitored. Observing the results in Figure 6.3(a), the following points can be concluded: (use periods after the numbers

1- At very low input power (the blue curve), the resonance spectrum is Lorentzian-like, as expected.

2- By increasing the power (the green curve), broadening of the spectrum is observed. Moreover, the spectrum deviates from a Lorentzian-like shape and becomes asymmetric. In addition, in a small wavelength range, an instability behavior is observed in the transmission response. This instability (as we explain later) is oscillatory in time. In other words, if the input laser wavelength is fixed to any wavelength in that instability region, a temporal oscillation in the response of the resonator is observed.

3- By further increasing the input power (the red curve), the oscillation amplitude becomes larger. In addition, the wavelength range in which these oscillations exist becomes also larger.

4- Finally, by further increasing the power (the orange curve), stronger broadening and asymmetry in the spectrum are observed. Also, the spectrum at the right end side behaves like a bistable response as a sharp transition from a low value (~ 0) to a high value (~1) in the amplitude is observed. In addition, the wavelength range and the amplitudes of the oscillations become larger. Figure 6.3(b) shows one of these oscillations monitored by an oscilloscope at a fixed laser wavelength around the resonance and in the wavelength range that the possibility of the oscillation exists.

The observed oscillations in 6.3(b), as is explained later, are a cyclic dynamic between: 1) the blue shifting of the resonance because of the TPA-induced FC generation, 2) changing the photon lifetime (because of the change in Q as a results of FCA loss), 3) red shifting of the resonance because of the temperature rise (as a

consequence of FCA and heating generation), and 4) the back blue shifting of the resonator (to the original point) during the resonator cooling when the resonator energy is depleted. In fact, the process that makes these temporal oscillations appear in the response of the resonator is the sudden avalanche generation of free carriers by TPA. If the free carrier were smoothly generated in time, no oscillation would exist. However, the static response of the resonator would still experience the spectral broadening and asymmetry. Hence, the response of the resonator can be analyzed in two separate static (steady-state) and dynamic regimes. In what follows, we first investigate the static response of the resonator. Then, the dynamical response of the resonator with experimental results is presented.

6.2. Interplay of TPA, FC, and Thermal Effects on the Response of a Silicon Waveguide-TWR: Static Analysis

In general, a shift in the resonance frequency (ω_{R0}) of the resonator thorough a change in its refractive index can be obtained with a very good approximation by the following expression:

$$\frac{\Delta\omega_{R0}}{\omega_{R0}} = -\frac{\Delta n_{Si}}{n_{Si}}, \tag{6.1}$$

where $\Delta\omega_{R0}$ and Δn_{Si} are the shift in the resonance frequency and the refractive index of the resonator, respectively. Considering the thermo-optic and free carriers as the dominant effects changing the refractive index, Equation (6.1) can be written as follows:

$$\frac{\Delta\omega_{R0}}{\omega_{R0}} = -\frac{1}{n_{Si}}(\Delta n|_T + \Delta n|_{FC}), \tag{6.2}$$

where

$$\Delta n|_T = A_{th}\,\Delta T, \quad (A_{th} = 1.84\times10^{-4}), \tag{6.3}$$

in which ΔT is the temperature rise of the resonator. Also, the change in the refractive index in terms of the generated free carriers is

$$\Delta n|_{FC} = -8.8\times10^{-22}\,\Delta N - 8.5\times10^{-18}(\Delta P)^{0.8}, \tag{6.4}$$

where ΔN and ΔP are the density of generated electrons and holes per centimeter cubed volume, which are equal to each other. As an example, free-carrier densities $\Delta N = 10^{15}$, 10^{16}, and 10^{17} cm^{-3} correspond to refractive index changes $\Delta n = 9.4\times10^{-6}$, 6.2×10^{-5}, and 4.3×10^{-4}, which consequently correspond to resonance wavelength shifts $\Delta\lambda_0 \sim 4.2$ pm, 27.8 pm, and 190 pm at the operation wavelength of 1550 nm. Also, the generated free carriers add an absorption loss (per centimeter length) to the resonator as

$$\alpha_{FCA} = 8.5\times10^{-18}\,\Delta N + 6\times10^{-18}\,\Delta P = \alpha_{FCA0}\Delta N \quad (cm^{-1}), \tag{6.5}$$

where $\alpha_{FCA0} = 14.5\times10^{-18}$.

In addition to the resonance frequency, the quality factor of the resonator is also subject to change and degradation as a result of the additional loss. The two sources of additional loss at high powers are the FCA loss, which is given by Equation (6.5), and the TPA loss, which converts the photons to electrons. Hence, in a more general form, the quality factor of the resonator can be written as follows:

$$\frac{1}{Q_R} = \underbrace{\left(\frac{1}{Q_{Rad}} + \frac{1}{Q_{abs0}}\right)}_{Q_{R0}}\Bigg|_{\substack{Linear \\ regime}} + \left(\frac{1}{Q_{FCA}} + \frac{1}{Q_{TPA}}\right)\Bigg|_{\substack{Nonlinear \\ regime}} . \tag{6.6}$$

In Equation (6.6), the first parentheses correspond to the intrinsic Q (Q_{R0}) of the resonator in the linear regime. Q_{Rad} represents a combination of the intrinsic radiation and the sidewall roughness scattering of the resonator energy to the outside. Q_{abs0} represents the absorption of the resonator in the linear regime, which is a combination of surface and bulk absorptions. In the nonlinear regime, Q_{TPA} and Q_{FCA} appear, which represent the TPA and FCA losses, respectively. Using Equation (6.5), which is the absorption propagation of the FCA, and knowing the relation between the propagation loss and Q from Equation (2.27) in chapter 2, we can calculate Q_{FCA} as

$$\frac{1}{Q_{FCA}} = \frac{1}{\omega_{0R}}\frac{c}{n_g}\alpha_{FCA} = \frac{1}{\omega_{0R}}\frac{c}{n_g}\alpha_{FCA0}\Delta N . \tag{6.7}$$

We note that the generated free carriers are not uniformly distributed. In fact, because the TPA effect (which is a 3rd order nonlinearity effect) is proportional to the square of the electric energy of the resonator, the spatial distribution of the generated free carriers is almost the same as the distribution of the square of the mode energy profile of the resonator. However, an effective TPA mode volume can be defined in which the free-carrier distribution is considered to be uniform. Hence, the rate equation for the generated free carriers (ΔN) is

$$\frac{d}{dt}\Delta N = -\frac{\Delta N}{\tau_{FC}} + \frac{P_{TPA}}{2\hbar\omega_{0R}V_{TPA}} . \tag{6.8}$$

In Equation (6.8) τ_{FC} is the recombination lifetime of the carriers (which in brief is called FC lifetime or electron lifetime), V_{TPA} is the effective nonlinear mode volume[63] (related to TPA), which is defined as [93]

$$V_{TPA} = \frac{(\int n^2 \mid E \mid^2 \, dv)^2}{\int n^4 \mid E \mid^4 \, dv}, \tag{6.9}$$

P_{TPA} is the TPA absorbed power in the cavity in an effective TPA mode volume, V_{TPA} and it is related to the square of the resonator energy (U) as [93][64]

$$P_{TPA} = \frac{c^2 \beta}{n_g^2 V_{TPA}} U^2. \tag{6.10}$$

In Equation (6.10), β is the TPA coefficient in silicon, which is ~ 8.4×10^{-12} mW^{-1}, and n_g is the group index of the resonator. The value of β has been obtained from experiment [95] and for optical propagation in the crystalline direction <110> in silicon.

In the steady state, ΔN from Equation (6.8) can be obtained as

$$\Delta N = \frac{\tau_{FC} \, P_{TPA}}{2\hbar\omega_{0R}}. \tag{6.11}$$

From Equations (6.10), ΔN is related to resonator energy (U) as

$$\Delta N = \tau_{FC} G_{TPA} U^2, \tag{6.12}$$

[63] For many resonator sizes, the difference between the linear effective mode volume (V_m) and the nonlinear mode volume (V_{TPA}) is below 30%. Hence, for many discussions, we may use V_m instead of V_{TPA}.

[64] We note that this expression is for an isotropic nonlinear material such as SiO_2. For Si, which is crystalline, the Kerr tensor is anisotropic, and a closed-form expression for P_{TPA} cannot be obtained. However, for a symmetric resonator such as a microdisk fabricated in the <100> crystal plane, it can be shown that isotropic assumption is a good approximation.

where, for simplicity, we have defined the new coefficient G_{TPA} as

$$G_{TPA} = \frac{1}{2\hbar\omega_{0R}} \frac{c^2 \beta}{n_g^2 V_{TPA}^2}. \tag{6.13}$$

If the resonator is close to the critical coupling condition ($Q_R \sim Q_c$), then from chapter 3, we have $U = Q_c P_{in}/\omega_0$. As a result, from Equation (6.12) we can see that ΔN is proportional to $(Q_R/V_m)^2$, and from Equation (6.10), the TPA loss power is proportional to Q_R^2/V_m. To have an idea about the value of ΔN, let us calculate it for a microdisk resonator with a radius of 20 μm and a thickness of 250 nm, which has a mode volume $V_m \sim 4.5\ (\lambda_0)^3$, an intrinsic Q of $Q_{R0} = 10^6$, and an FC lifetime of τ_{FC} = 0.5 ns. For such a case, we have $G_{TPA} \sim 8\times10^{56}$. Now, if we assume the resonator is at the critical coupling, then for an input power level of 100 μm, the density of the generated free carriers is $\Delta N = 2.7\times10^{15}$. Of course, this is not the steady-state value that the resonator can reach, as we know that both Q and the resonance wavelength change, and as a result, the resonator energy changes as well.

From Equation (6.10) and using Equation (6.13), we can obtain Q_{TPA} as

$$\frac{1}{Q_{TPA}} = \frac{1}{\omega_{0R}} \frac{P_{TPA}}{U} = 2\hbar V_{TPA} G_{TPA} U\,. \tag{6.14}$$

Also, by combining Equations (6.14) and (6.12), Q_{TPA} can be expressed in terms of ΔN as

$$\frac{1}{Q_{TPA}} = 2\hbar V_{TPA} \sqrt{\frac{G_{TPA}}{\tau_{FC}}} \times \sqrt{\Delta N}\,. \tag{6.15}$$

Hence, by putting Equations (6.7) and (6.15) into Equation (6.6), the total Q of the resonator can be expressed in terms of one variable, which is the free-carrier density, (ΔN), as

$$\frac{1}{Q_R} = (\frac{1}{Q_{Rad}} + \frac{1}{Q_{abs0}}) + \quad 2\hbar V_{TPA}\sqrt{\frac{G_{TPA}}{\tau_{FC}}} \times \sqrt{\Delta N} + \frac{1}{\omega_{0R}}\frac{c}{n_g}\alpha_{FCA0}\Delta N \,. \tag{6.16}$$

The power absorbed by the resonator increases the resonator temperature until a steady-state temperature is reached in which the absorbed power is equal to the thermal flux power as

$$P_{abs0}\big|_{Linear} + P_{abs}\big|_{Nonlinear} = K_{eff}\,(\Delta T_0\big|_{Linear} + \Delta T\big|_{Nonlinear}) \,. \tag{6.17}$$

In Equation (6.17), the first term on the left side of the equality corresponds to the linear absorbed power because of the bulk absorption and surface state absorption, which results in a temperature rise ΔT_0 in the resonator. The second term in the left side of Equation (6.17) is the absorbed power because of the TPA and FCA effects, which result in another temperature rise ΔT in the resonator. Also, the parameter K_{eff} is the effective thermal conductivity of the resonator. Using Equation (6.6), the left side of Equation (6.17) can be expressed in terms of the resonator energy as

$$P_{abs} = \omega_{R0}(\frac{1}{Q_{abs0}} + \frac{1}{Q_{TPA}} + \frac{1}{Q_{FCA}})U \,, \tag{6.18}$$

and as a result, Equation (6.17) can be written as

$$\omega_{R0}(\frac{1}{Q_{abs0}} + \frac{1}{Q_{TPA}} + \frac{1}{Q_{FCA}})U = K_{eff}\,\Delta T_{total} \,, \tag{6.19}$$

where ΔT_{total} is the total temperature rise. Now, we need to find the resonator energy (U). From Equation (3.3) in chapter 2, the time variation of resonator amplitude is

$$\frac{da}{dt} = [\, j\omega_R - \frac{1}{\tau_R} - \frac{1}{\tau_c}]a + \kappa S_{in}, \tag{6.20}$$

where τ_R and τ_c are the resonator and the coupling lifetimes, respectively. In Equation (6.20), ω_R is the shifted resonator frequency of the resonator, expressed as

$$\omega_R = \omega_{R0} + \Delta\omega_{R0}, \tag{6.21}$$

where $\Delta\omega_{R0}$ is the frequency shift of the resonator, which has been given in Equation (6.2). Knowing that $Q_R = \omega_{R0}\tau_R/2$, $Q_c = \omega_{R0}\tau_c/2$, and $|\kappa|^2 = 2/\tau_c$, we can find the resonator energy in terms of the input power (Pin) in the waveguide as

$$U(\omega_P) = |\, a\,|^2 = \frac{1}{\omega_{R0}} \frac{1/Q_c}{(\frac{\omega_P - \omega_R}{\omega_{R0}})^2 + (\frac{1}{2Q_R} + \frac{1}{2Q_c})^2} P_{in}(\omega_P), \tag{6.22}$$

where ω_p is the frequency of the input power coming from the waveguide. Also, from Equations (6.2) and (6.21), we have

$$\frac{\omega_R}{\omega_{R0}} = 1 - \frac{1}{n_{Si}}(A_{th}\Delta T_{total} + \Delta n\,|_{FC}). \tag{6.23}$$

By putting Equation (6.22) into Equation (6.19), we find the following equation:

$$\frac{(Q_{abs0}^{-1} + Q_{TPA}^{-1} + Q_{FCA}^{-1})\, Q_c^{-1}}{(\frac{\omega_p - \omega_R}{\omega_{R0}})^2 + (\frac{1}{2Q_R} + \frac{1}{2Q_c})^2} P_{in} = K_{eff}\Delta T_{total}. \tag{6.24}$$

Also, by combining Equations (6.12) and (6.19) we find the following equation:

$$K_{eff}\Delta T_{total} = \omega_{R0}(Q_{abs0}^{-1} + Q_{TPA}^{-1} + Q_{FCA}^{-1})\sqrt{\frac{1}{\tau_{FC}G_{TPA}}} \times \sqrt{\Delta N}\ . \tag{6.25}$$

Equations (6.24) and (6.25) have two independent variables, ΔN and ΔT_{total}. All other variables such as Q_{FCA}, Q_{TPA}, ω_R, and Q_R (as given by Equations (6.7), (6.15), (6.23), and (6.6), respectively) are functions of these two variables. Therefore, by solving Equations (6.24) and (6.25), ΔN and ΔT_{total} can be found. Consequently, all other parameters, such as the resonance shift and the energy spectrum (U) of the resonator, can be obtained. Also, from Equation (3.8) in chapter 3, the transmission through the waveguide can be calculated, which is

$$T(\omega_p) = \frac{j2(\omega_p - \omega_R)/\omega_{R0} + 1/Q_R - 1/Q_c}{j2(\omega_p - \omega_R)/\omega_0 + 1/Q_R + 1/Q_c}\ . \tag{6.26}$$

For solving Equations (6.24) and (6.25), and as a result, finding the steady-state response of the resonator, we can consider two cases: 1) No TPA loss, and correspondingly, no TPA-induced FCA loss exist. This case occurs at moderate powers or even in other resonator materials, such as glass, that do not have TPA and FCA loss; 2) TPA loss as well as TPA-induced FCA loss exist. In what follows, we investigate these two cases separately.

6.2.1.1. Case 1: TPA Loss and TPA-induced FCA Loss are Absent

In this case, Equation (6.25) is absent and only Equations (6.23) and (6.24) exist. After removing the TPA and FCA effects from these two equations, they are

$$\frac{\omega_R}{\omega_{R0}} = 1 - \theta_{th}\,\Delta T_{total} \quad (\theta_{th} = \frac{A_{th}}{n_{Si}})\,, \tag{6.27}$$

and

$$\frac{Q_{abs0}^{-1}\, Q_c^{-1}\, P_{in}}{(\frac{\omega_p - \omega_R}{\omega_{R0}})^2 + (\frac{1}{2Q_{R0}} + \frac{1}{2Q_c})^2} = K_{eff}\, \Delta T_{total}\,. \tag{6.28}$$

We note that the Q of the resonator is Q_{R0}, which corresponds to the first parentheses in Equation (6.6). By combining Equations (6.27) and (6.28), one equation in terms of either ΔT_{total} or ω_R can be obtained. In terms of ω_R, the resulting equation is obtained as

$$\frac{Q_{abs0}^{-1}\, Q_c^{-1}\, P_{in}}{(\frac{\omega_p - \omega_R}{\omega_{R0}})^2 + (\frac{1}{2Q_{R0}} + \frac{1}{2Q_c})^2} = \frac{K_{eff}}{\theta_{th}}(1 - \frac{\omega_R}{\omega_{R0}})\,. \tag{6.29}$$

Hence, by solving Equation (6.28), the value of ω_R is found. Subsequently, other resonator parameters can also be obtained.

The simulation results for a waveguide-TWR structure in the presence of only the thermo-optic effect are shown in Figure 6.4, which shows the transmission spectrum through the waveguide versus the variation of the input power wavelength (λ_p) relative to the cold resonance wavelength (λ_{R0}). The simulation has been performed at three different levels of input power, as specified in the right side of the figure, and the corresponding results have been plotted with different colors. The input power is scaled in terms of P_{th0}, which can be considered as a measure for the presence of thermal broadening, and is expressed as

$$P_{th0} = \frac{K_{eff}}{Q_{R0}\theta_{th}}\,. \tag{6.30}$$

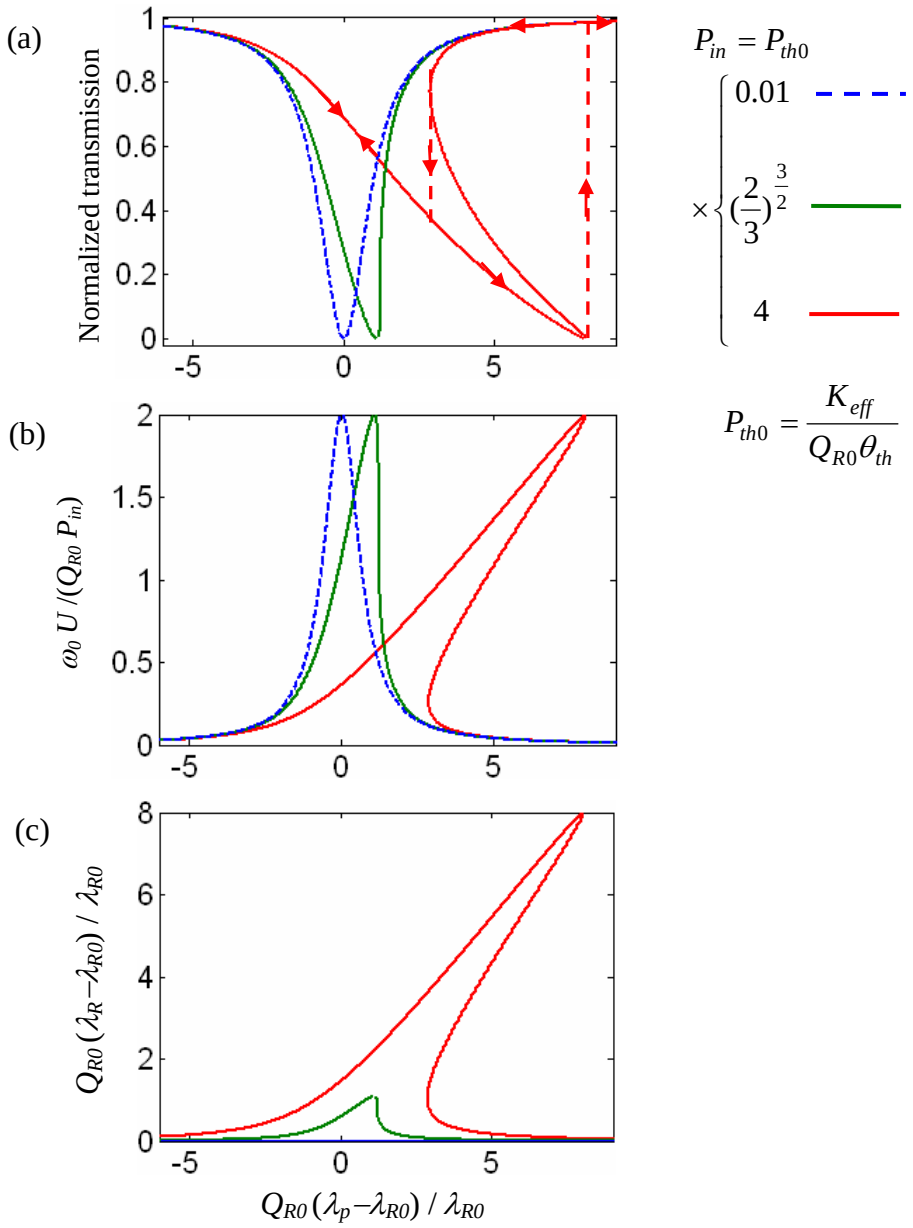

Fig. 6.4: (a) Normalized transmission, (b) resonator energy, and (c) relative resonance shift (with respect to the initial resonance) of a waveguide-TWR structure versus the relative input laser wavelength (with respect to the initial resonance wavelength) in the critical coupling regime (Q_c = Q_{R0}) and at different levels of input optical power, as shown by different colors. In the red curve, depending on sweeping the laser from left to right or vise versa, one of the edges of the bistability region as shown by the red dash lines is observed.

As seen from Figure 6.4(a), for input powers much below P_{th0}, the spectral broadening is very weak (as shown by the blue dashed curve) and the resonator spectrum is similar to the linear low power case. However, at input powers around or more than P_{th0}, thermal broadening and bistability are observed in the spectrum, and by further increasing the input power, the bistability region becomes wider. As a quantitative example, consider a Si microdisk resonator with a radius of 20 μm and a thickness of 250 nm and $Q_{R0} = 10^6$ in a SOI platform with a BOX thickness of 1 μm. For such a microdisk, the effective thermal conductivity for the first few radial order modes is $K_{eff} \sim 9.6\times10^{-4}$ WK^{-1}. Also, $\theta_{th} = 1.84\times10^{-4}/3.475 = 0.53\times10^{-4}$. Hence, $P_{th0} \sim 18$ μW, and at this power, the microdisk temperature rise is $\Delta T = P_{th}/K_{eff} \sim 19$ mK.

In an actual experiment, the bistability response shown in Figure 6.4(a) (the red curve) is observed by obtaining large transmission changes (or jumps, shown by dashed lines) when the sweeping laser wavelength passes through the wavelengths corresponding to the edges of the bistability region.

Using Equation (6.29), a threshold for the input power can be obtained below which the resonance spectrum does not show a bistable shape. This threshold is obtained by solving Equation (6.29) and applying the mathematical conditions to obtain ω_R as a one-to-one function of ω_p. Figure 6.5 shows this threshold curve as a function of the intrinsic Q of the resonator. For this analysis, we have assumed that the resonator is in the critical coupling regime ($Q_{R0} = Q_c$). In addition, we have

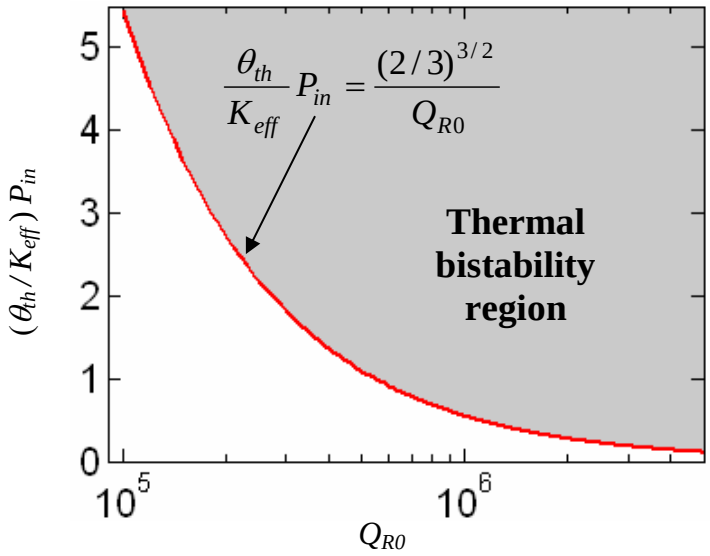

Fig. 6.5: The threshold (red curve) to observe bistable behavior in the spectrum. No bistable behavior is observed in the shaded region.

assumed that all the power that goes into the resonator is converted to heat[65]. The shaded region in Figure 6.5 corresponds to bistability. From this figure, we see that when K_{eff}/θ_{th} is large, we can send a larger optical power into the resonator, while no bistability and less broadening are observed in the resonance spectrum. Hence, by engineering the resonator to enlarge this term, we can enable the resonator for high-power applications with less suffering from broadening or the bistability effect (if not desired).

6.2.1.2. Case 2: TPA Loss and TPA-induced FCA Loss Exist

In this case, both Equations (6.24) and (6.25) are present and need to be solved simultaneously to find their roots (i.e., ΔN and ΔT_{total}). In this case, in addition to the input power and quality factor of the resonator, the FC lifetime and the mode

[65] This latter assumption works very well for ultra-high Q Si resonator where the quality factor is mostly limited by electronic surface absorption rather than scattering or radiation. However, for other cases that approximation is not good, the input power in Figure 6.5 is scaled by Q_{R0}/Q_{abs0}.

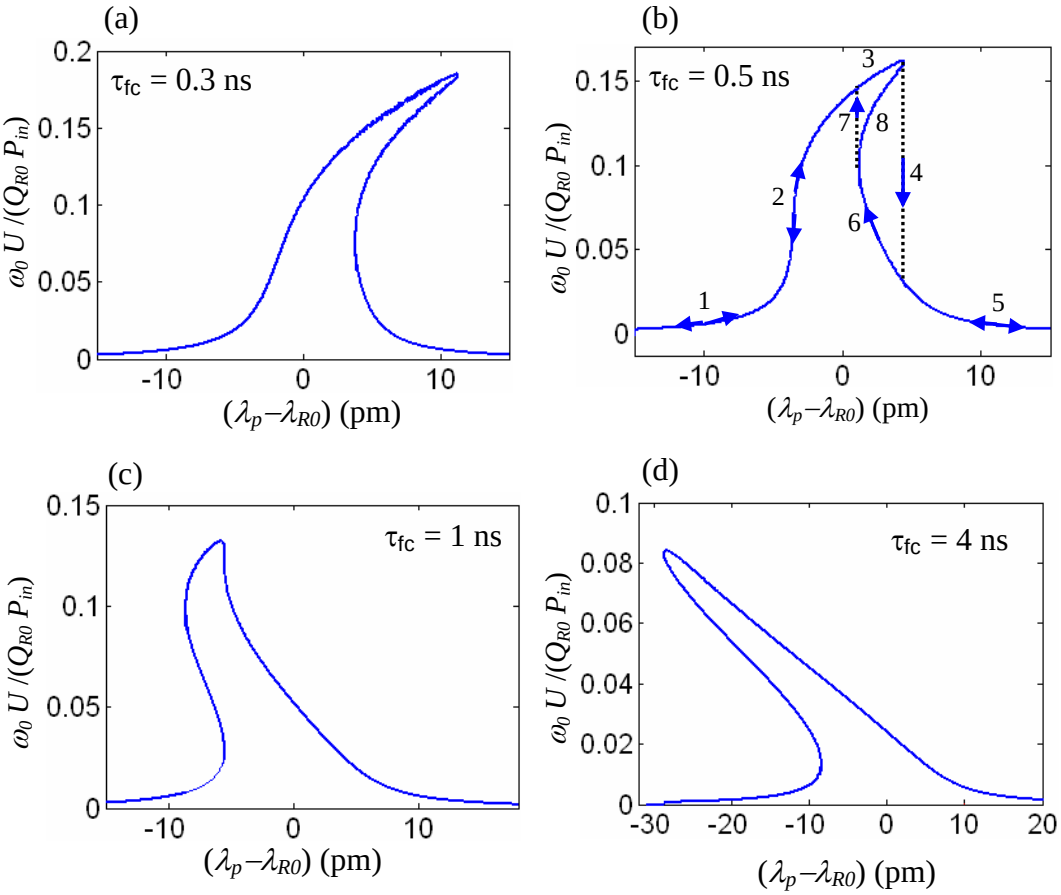

Fig. 6.6: The energy spectrum of a Si microdisk resonator (coupled to a waveguide) for an input power of P_{in} = 0.6 mW and at different FC lifetimes. The resonator cold Q (i.e., Q_{R0}) is assumed $Q_{R0} = 2\times10^6$, and the structure operates at the critical coupling regime ($Q_c = Q_{R0}$). The other parameters are $K_{eff} = 9.6\times10^{-4}$ and $V_m = 4.5\ (\lambda_0)^3$. These last two parameters correspond to the fundamental mode of a microdisk in a SOI platform with a BOX thickness of 1 μm. The microdisk has a radius of 20 μm and a thickness of 250 nm, and its cladding is air. In these plots, λ_{R0} is the resonance wavelength of the cold resonator and λ_p is the wavelength of the input power. The arrows in (b) correspond to the allowed directions of moving on the spectrum curve when the laser source is swept from the short wavelength to long wavelength or vice versa.

volume of the resonator impact the resonator spectral response. According to Equation (6.9), when TPA occurs, a larger FC lifetime results in a larger concentration of free carriers in the steady state. On one side, a larger density of FCs leads to a larger resonance blue shift (see Equations (6.2) and (6.4)). However, on

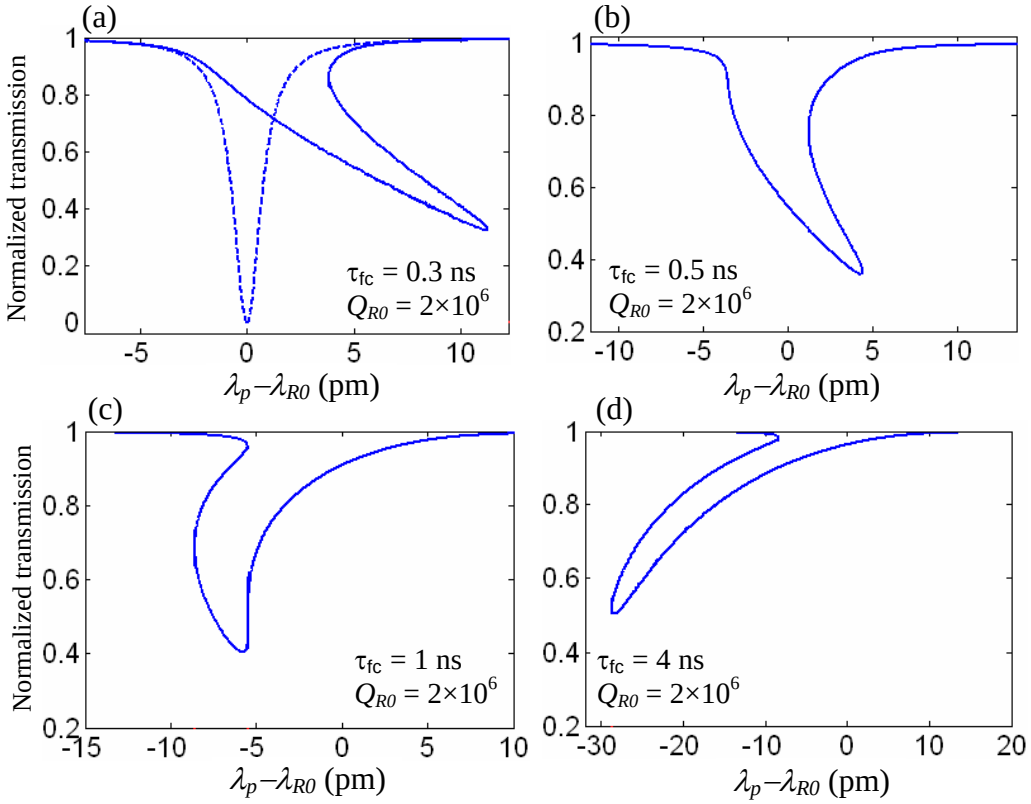

Fig. 6.7: The normalized transmission spectrum of a Si microdisk resonator (coupled to a waveguide) at different FC lifetimes (τ_{FC}). In the figures λ_{R0} is the resonance wavelength of the cold resonator and λ_p is the wavelength of the input power. Other parameters have been described and specified in the caption of Figure 6.6. The dashed curve in the top-left plot is the transmission at low powers, where the TPA, FCA, and thermal effects are absent.

the other side, a larger density of FCs increases the FCA and generates more heat, which causes a larger resonance red shift. To further investigate these two competing effects, we have simulated the spectral response of a silicon waveguide-TWR (by solving Equations (6.24) and (6.25)) at different levels of FC lifetime, while other resonator parameters as well as the input power are fixed. Figure 6.6 shows the results of the simulation for the energy spectrum of the resonator. Also, Figures 6.7 to 6.9 show the transmission, the resonance wavelength shift, and the

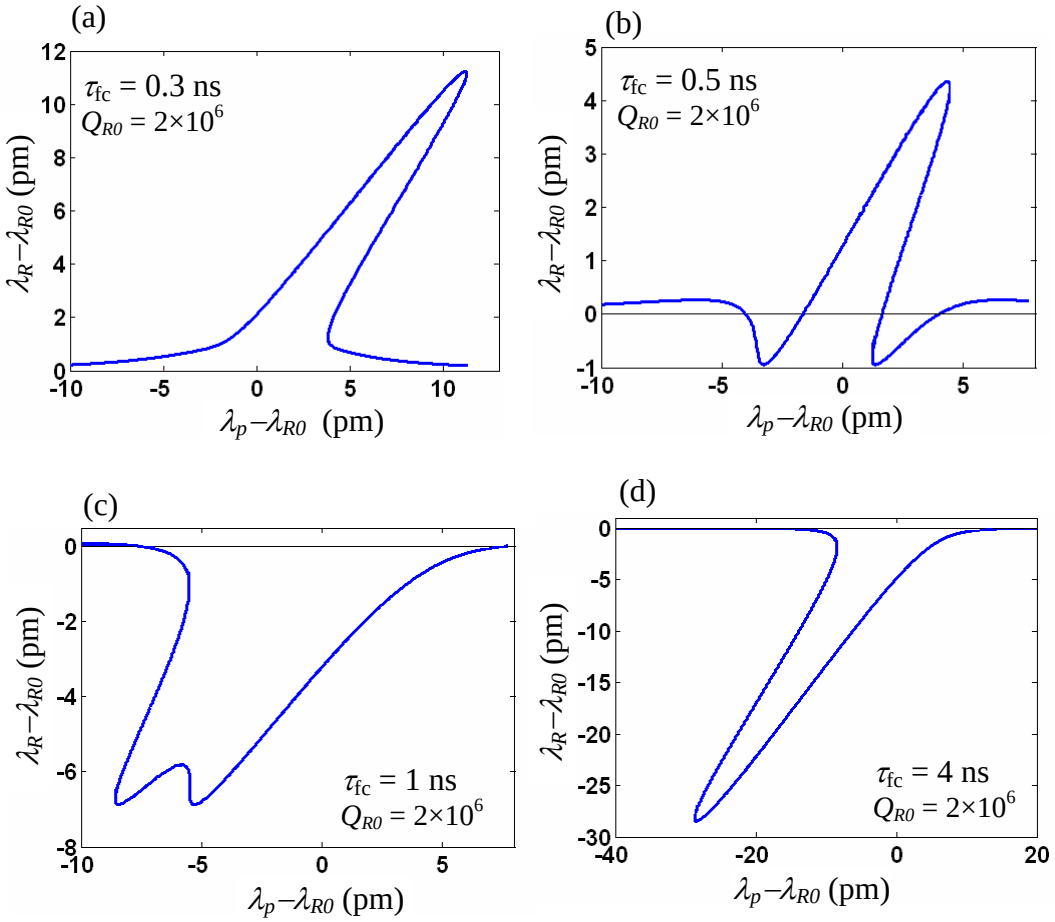

Fig. 6.8: The resonance wavelength shift of a Si microdisk resonator (coupled to a waveguide) at different FC lifetimes (τ_{FC}). In the figures λ_{R0} is the resonance wavelength of the cold resonator and λ_p is the wavelength of the input power. Other parameters have been described and specified in the caption of Figure 6.6. The dashed curve in the top-left figure is the transmission at low powers, where the TPA, FCA, and thermal effects are absent.

quality factor of the resonator. As seen from the plots in Figure 6.6, while at low values FC lifetime the resonance red shift is dominant (as the peak of the resonator is directed toward the right side), at higher values of FC lifetime, the resonance blue shift becomes dominant (as the peak of the resonator tends to be directed to the left side). This can be clearly seen from Figures 6.8(c) and 6.8(d), where the resonance

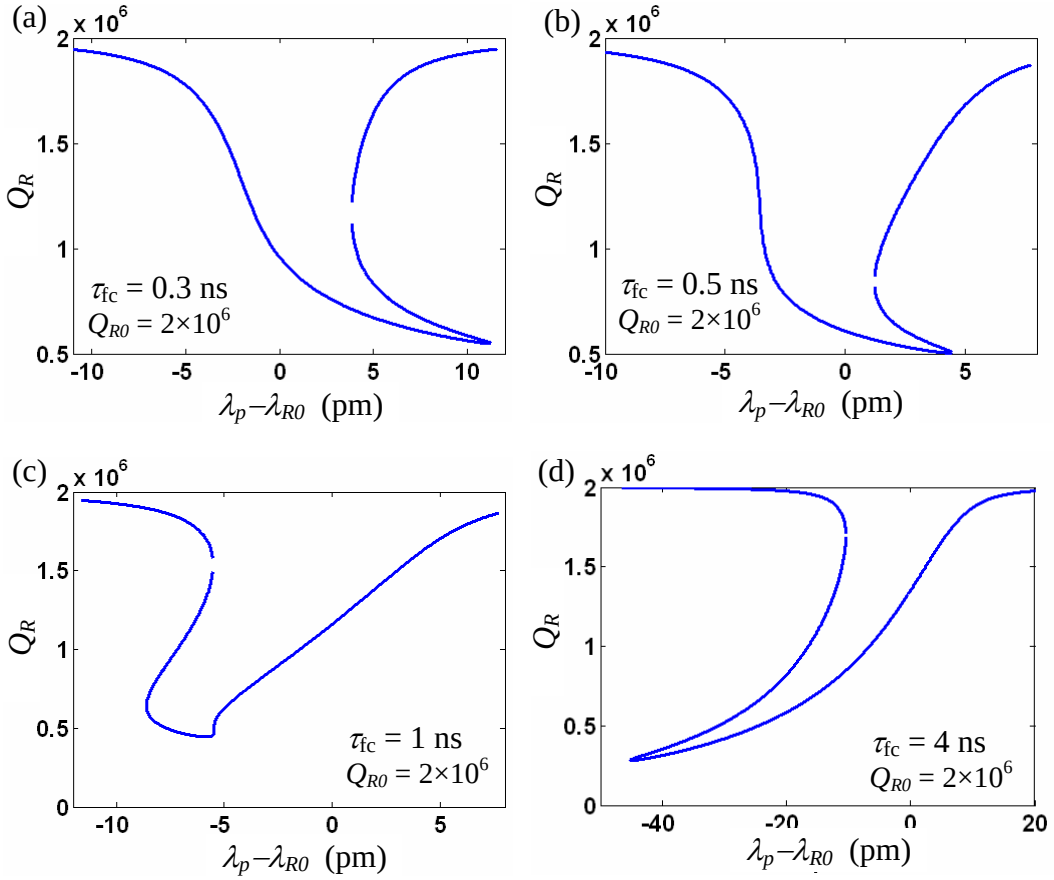

Fig. 6.9: The total quality factor (Q_R) of a Si microdisk resonator (coupled to a waveguide) at different FC lifetimes (τ_{FC}). In the figures λ_{R0} is the resonance wavelength of the cold resonator, and λ_p is the wavelength of the input power. Other parameters have been described and specified in the caption of Figure 6.6. The dashed curve in the top-left figure is the transmission at low powers, where the TPA, FCA, and thermal effects are absent.

wavelength shift has become negative compared to Figures 6.8(a) and 6.8(b), which correspond to smaller FC lifetimes. The reason behind this is that the blue shift is only affected by the density of free carriers, while the resonance red shift is affected by both FCA and TPA losses, and the TPA loss is independent of the free-carrier density. Hence, at small FC lifetimes where free-carrier density is small and

resonance blue shift and FCA loss are small, the TPA loss, which is power dependent, can be dominant.

All four cases in Figure 6.6 show bistability with the input power and the resonator parameters specified in this figure. In Figure 6.6(b), more details of the bistability are shown. The arrows in this figure correspond to the allowed direction of moving on the spectrum curve when the laser source is swept from the short wavelength to long wavelength or vice versa. The dashed lines (i.e., points 4 and 7 in the figure) correspond to the transition edges of the bistable region. When sweeping from left to the right, the passing points are 1, 2, 3, 4, and 5. On the other hand, when sweeping from right to the left, the passing points are 5, 6, 7, 2, and 1. Point 8 is the region that is never observed in the experiment. One question that needs to be answered is whether point 3 (and points like this on top of the curve) is always stable or, depending on the input power, partially stable. This question is under investigation and is part of the future research of this thesis.

From Figure 6.9, we can see how the quality factor of the resonator drops from its original value. This drop is the result of both the TPA and the FCA losses. However, for the three cases of τ_{FC} = 0.3 ns, 0.5 ns, and 1 ns, the level of the drop in the Q_R is almost the same (i.e., from 2×10^6 to ~ 0.5×10^6). This means that the TPA loss is still dominant (compared to FCA loss) for these three cases because the TPA loss is fixed (as the input power is fixed). However, for the fourth case (i.e., τ_{FC} = 0.3 ns) more drop in the Q is observed, which shows the effect of FCA loss.

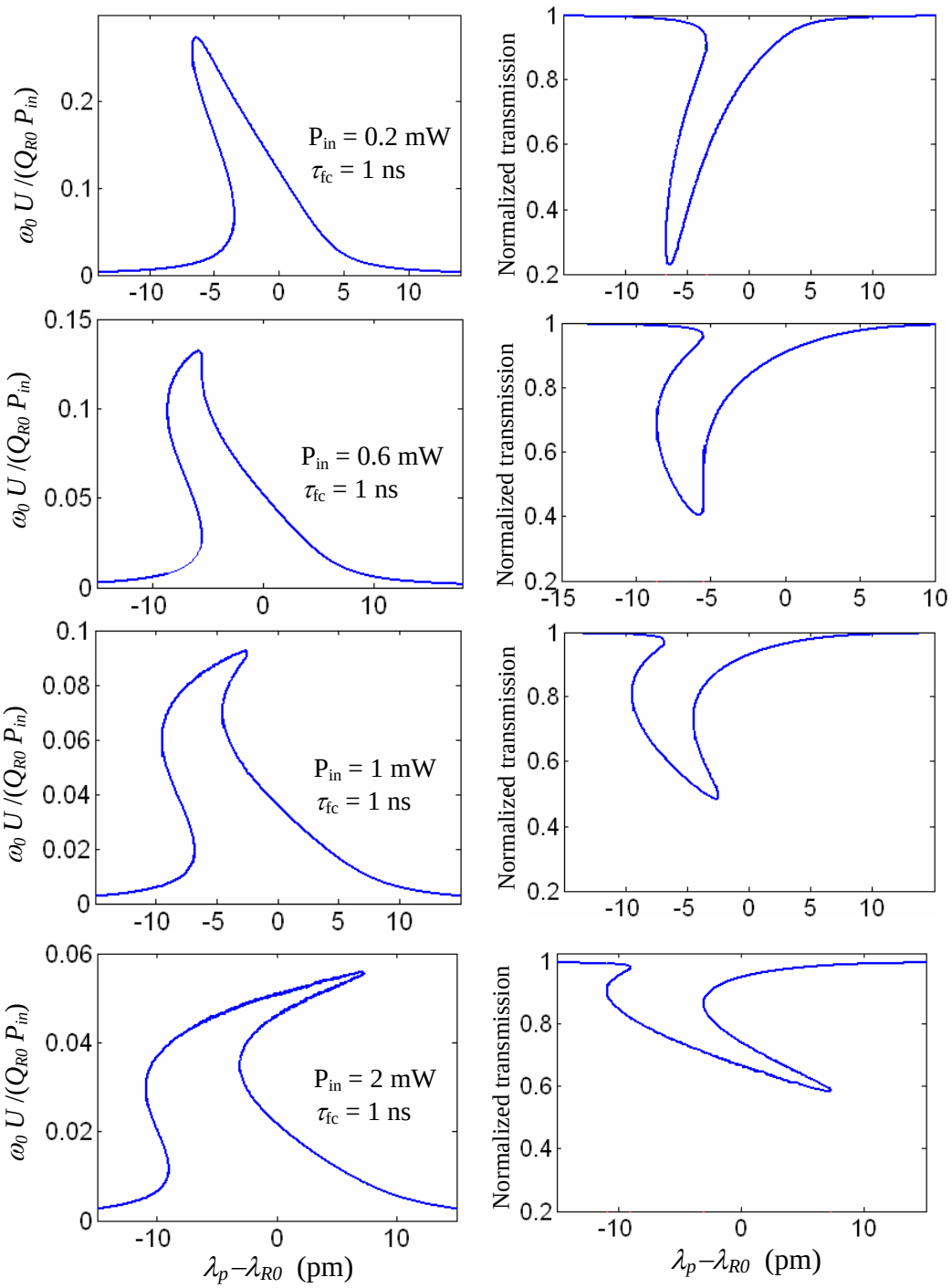

Fig. 6.10: The energy (left figures) and the normalized transmission (right figures) spectra of a Si microdisk resonator (coupled to a waveguide) at different input powers as specified in the left figures. For this simulation we assumed Q_{R0} = 2×10^6 and the FC lifetime τ_{fc} = 1 ns, K_{eff} = 9.6×10^{-4} and V_m = 4.5 $(\lambda_0)^3$. The last two parameters correspond to the fundamental mode of a microdisk with a radius of 20 μm and a thickness of 250 nm with air cladding in a SOI platform with a BOX thickness of 1 μm.

We also investigated the effect of the variation of the input power on the resonator spectrum while other parameters were fixed. Figure 6.10 shows the results of this simulation where the spectra of the resonator energy and the transmission through the waveguide for each power level have been plotted. As seen from these figures, by increasing the input power, the resonance spectrum tends to have a red shift.

Another interesting case is the effect of scaling of the resonator dimensions on its spectral properties. To investigate this case, we considered two Si microdisk resonators with radii of 1.53 μm and 20 μm and a thickness of ~ 230 nm[66]. For such dimensions, we obtained experimental Qs in the range of ~ 10^5 (for the small resonator) and ~ 1×10^6-3×10^6 (for the large resonator). Also, from the coupled electromagnetic-thermodynamic simulations, we found the effective thermal conductivity of these resonators (the discussions on these simulations is presented later in this chapter). Figures 6.11(a) and 6.11(b) show the resonator energy and transmission spectrum for these two resonators. The parameters for each resonator are shown in Figure 6.11(b). Both resonators had similar FC lifetimes (τ_{FC} = 1ns) and input powers (P_{in} = 1 mW). The thermal conductivity of the small resonator is almost 56 times smaller than that of the large resonator. This can result in a strong red shift in the resonance wavelength of the small resonator. This strong resonance red shift can be seen in Figure 6.11 in which the spectrum of the small resonator is

[66] In much of the modeling and many of the simulations the thickness of the resonator was considered 250 nm. However, in the experiment the thickness of the resonator was ~230 nm. Such a change has little effect on parameters such as mode volume and effective thermal conductivity of the resonator and does not violate the conclusions of our discussion.

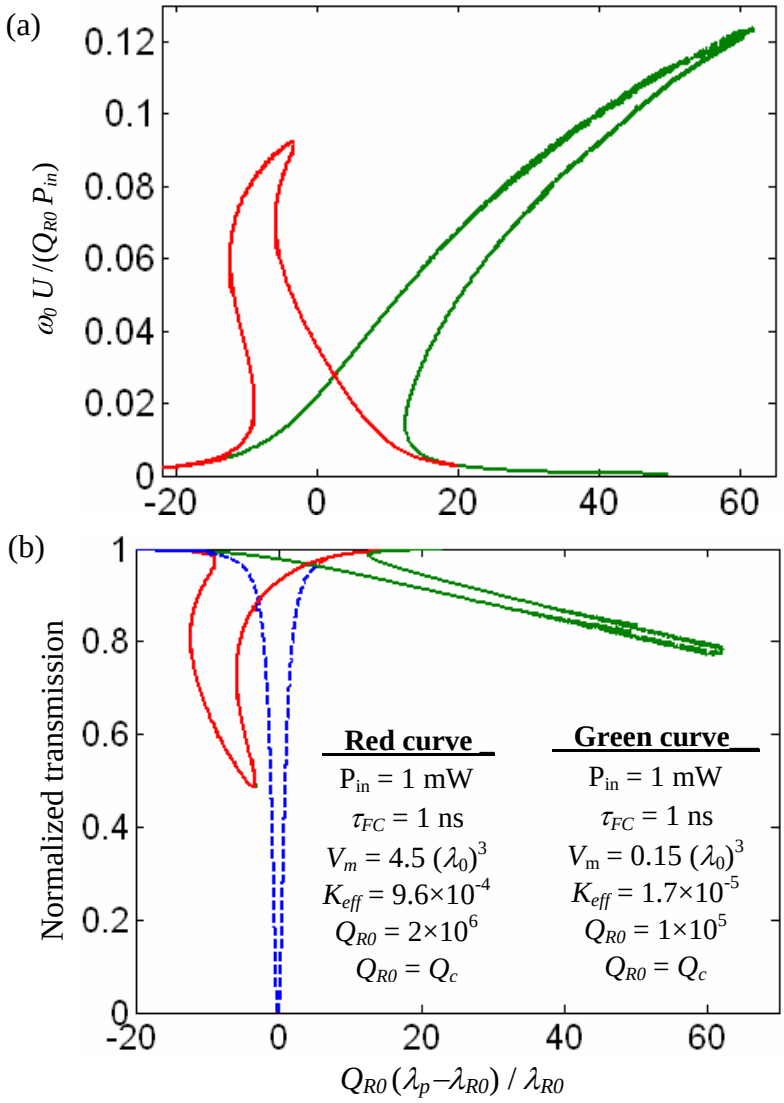

Fig. 6.11: Effect of resonator scaling on the spectral response of the resonator. (a) Energy and (b) transmission spectrum of a Si microdisk resonator with two different sets of parameters as plotted by red and green colors. These parameters are specified in the inset of (b). The given parameters for the red curve and the green curve correspond to the microdisks with a thickness of 250 nm and radii of 20 μm and 1.53 μm, respectively, and with air cladding. The thickness of the BOX layer is 1 μm. (and for this thickness K_{eff} has been calculated). The dashed blue curve in (b) corresponds to the low-power transmission spectrum [97].

strongly inclined to the long wavelengths. The Q_{R0}/V_m of the small resonator is about 1.5 times larger than that of the large resonator, which results in the generation of more free carriers in the small resonator. As a result, we expect more

blue shift for the small resonator. In addition, the Q_{R0}^2 / V_m of the large resonator is about 13 times larger than that of the small resonator, which results in a much larger TPA loss and heat in the large resonator. Hence, if both resonators had the same thermal conductivity, we expected the large resonator to have more red shift in its spectrum. However, despite the greater heat in the large resonator (which causes more red shift) and more free carriers in the small resonator (which causes more blue shift), the thermal conductivity of the small resonator is so small (compared to the large resonator) that it has become the dominant parameter in defining the spectrum and has strongly bent and broadened the spectrum (the green curve) toward the longer wavelengths.

In the following, some experimental results of the spectral response of the resonators at high powers are presented. Figure 6.12 shows the spectrum of one of the resonance modes of an ultra-high Q microdisk resonator measured at low and at high powers. The microdisk has a radius of 20 μm and a thickness of ~ 230 nm in a SOI platform with a BOX thickness of 1μm. A ~ 40 nm Si pedestal layer is also at the interface of the microdisk and the BOX layer. The laser power sent to the input facet of the chip was 60 μW for the low-power and 20 mW for the high-power measurement. From the measurement, the facet-to-facet insertion loss of the waveguide was ~ 20-30 dB. Therefore, we expect the power that has reached the waveguide-resonator coupling region to be ~10-15 dB below the input power before the chip. The green curve in Figure 6.12 corresponds to the low-power measurement. The intrinsic Q of this mode during the one-day measurement varied

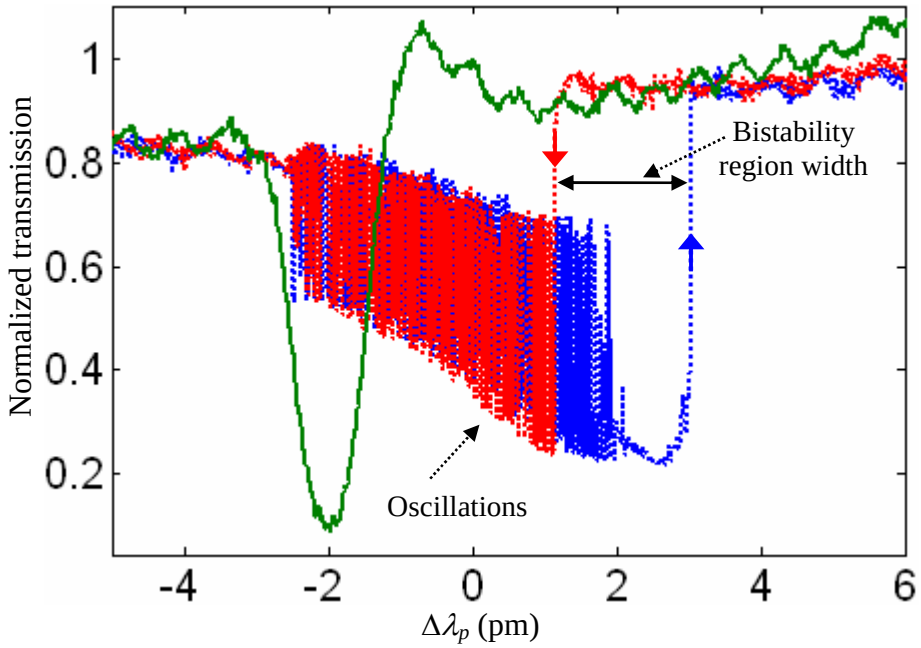

Fig. 6.12: Experimental measurement of the resonance transmission spectrum at low powers (the solid green curve) and at high powers when the input laser wavelength is swept from left to right (the dotted blue curve) and from right to left (the dotted red curves) of the resonance wavelength. Strong FC-TPA-thermal oscillations as well as resonance broadening are observed in both sweeping directions at the high-power measurement. The microdisk has a radius of 20 μm and a thickness of ~ 230 nm, and a thin Si pedestal layer with a thickness ~ 40 nm. The thickness of the BOX layer is 1μm. The effective thermal conductivity of this resonator is K_{eff} ~ 9.6×10^{-4}. See the text for more information on the input powers [97,98].

in the range of ~ 2.2-3.1 millions (this change was due to the cleanness condition of the resonator and the environment). For the high-power measurement, the laser source was swept in both directions around the resonance wavelength. The blue curve in Figure 6.12 corresponds to the sweeping from the short wavelengths to the long wavelengths, and the red curve corresponds to the reverse sweeping direction. For both sweeping directions in Figure 6.12, temporal oscillations as well as sharp transitions are observed. These two sharp transitions correspond to the edges of the

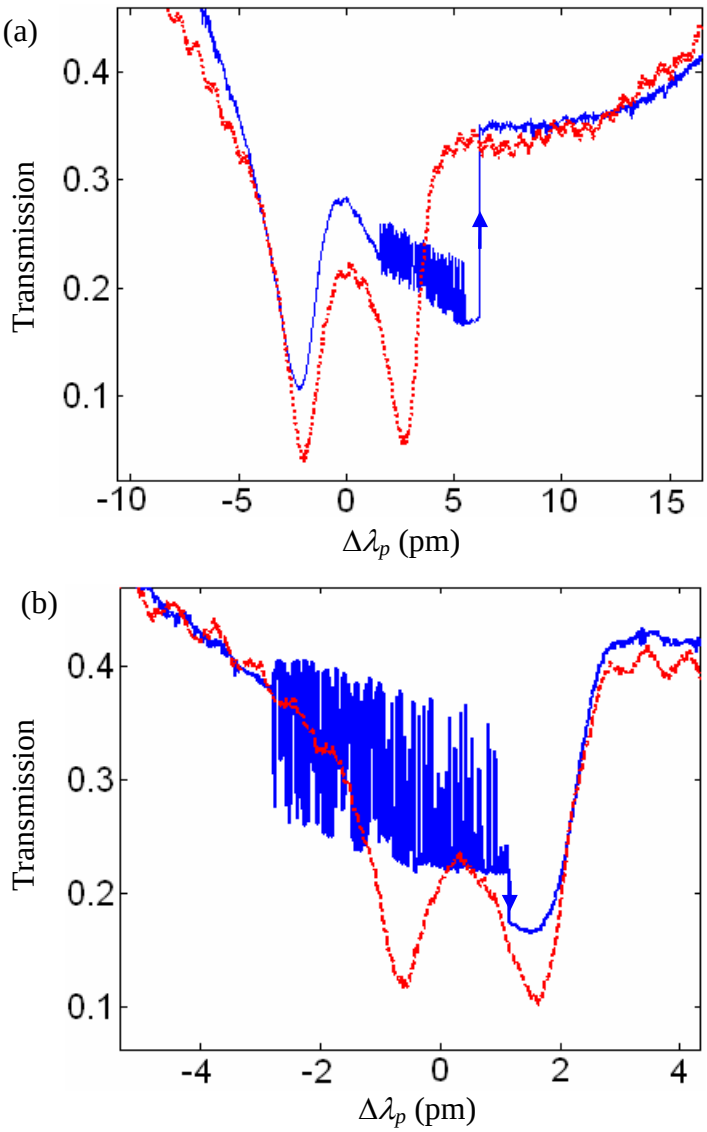

Fig. 6.13: (a) Experimental measurement of the resonance transmission spectrum at low powers (the dashed red curve) and at high powers (the solid blue curve). The laser wavelength is swept from left to right of the resonance wavelength. FC-TPA-thermal oscillations as well as resonance broadening are observed at high powers. (b) Repeati of the experiment for another resonance mode of the microdisk. The microdisk structure has the same specifications as the one described in Figure 6.12.

bistable region, and by measuring the difference between them, the width of the bistable region can be obtained.

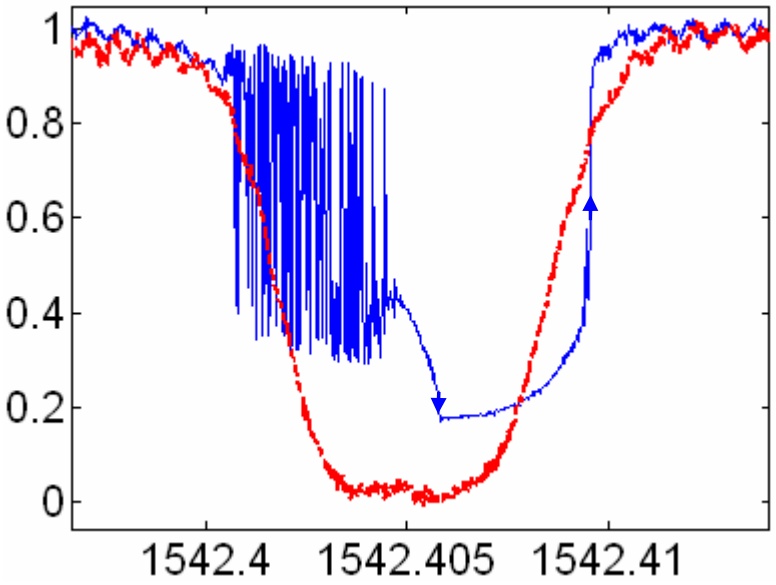

Fig. 6.14: Experimental measurement of the resonance transmission spectrum at low powers (the red curve) and at high powers (the blue curve). The laser wavelength is swept from left to right of the resonance wavelength. At low powers the spectrum shows resonance splitting with a flattening at the bottom of the transmission. Strong FC-TPA-thermal oscillations as well as resonance broadening are observed at high power. The microdisk structure has the same specifications as the one described in Figure 6.12, the only difference being that the BOX thickness is 3 μm and the pedestal thickness is ~ 50 nm.

Although we did not theoretically investigate the high-power performance of a resonator in the presence of resonance splitting, we observed many interesting features, some of which are shown here. Figures 6.13(a) and 6.13(b) show the measured low-power and higher resonance spectra of two different resonance modes of the microdisk resonator discussed in Figure 6.12 with the same power level. Figure 6.14 shows another example of observed broadening and oscillations in the presence of the resonance splitting. The low-power measurement in this figure shows flattening at the bottom of the transmission spectrum. The sharp transition

points corresponding to the edges of the bistable regions are shown by arrows in the blue curve in Figure 6.14.

In the next section, the dynamic behavior of the resonator at high powers, which results in the oscillation as mentioned before, is investigated.

6.3. Interplay of TPA, FC and Thermal Effects on the Response of a Silicon Waveguide-TWR: Temporal Dynamic Analysis

In the previous section, the governing equations of the resonator in the presence of TPA, FC, and thermal effects were investigated. From Equations (6.20) and (6.21) the time-domain behavior of the resonator and the waveguide amplitudes can be written as

$$\begin{cases} \dfrac{da}{dt} = \omega_{R0}\left[j\dfrac{\omega_{R0}+\Delta\omega_R(t)}{\omega_{R0}} - \dfrac{1}{2Q_R(t)} - \dfrac{1}{2Q_c}\right]a + \kappa S_{in} \\ S_{out} = S_{in} - \kappa^* a \\ |\kappa|^2 = 2/\tau_c \end{cases}, \tag{6.31}$$

where the resonance shift ($\Delta\omega_R$) and the total quality factor (Q_R) of the resonator vary in time. By extending Equation (6.2) to the time domain, the variation of resonance shift in time is

$$\frac{\Delta\omega_{R0}(t)}{\omega_{R0}} = -\frac{1}{n_{Si}}\left(\Delta n(t)|_T + \Delta n(t)|_{FC}\right). \tag{6.32}$$

Assuming the input laser wavelength is detuned from the resonance frequency ω_{R0} with an amount $\delta\omega_0$, we can remove the fast photon cycling from Equation (6.31) by writing the waveguide and resonator amplitudes as

$$S_{in} = \bar{S}_{in} \exp[i(\omega_{R0} + \delta\omega_0)t], \tag{6.33}$$

$$S_{out} = \bar{S}_{out} \exp[i(\omega_{R0} + \delta\omega_0)t], \tag{6.34}$$

$$a(t) = \bar{a}(t) \exp[i(\omega_{R0} + \delta\omega_0)t], \tag{6.35}$$

and by substituting them into Equation (6.31). Hence, the new form of Equation (6.31) becomes

$$\begin{cases} \dfrac{d\bar{a}}{dt} = [\, j(\Delta\omega_R(t) - \delta\omega_0) - \dfrac{\omega_{R0}}{2Q_R(t)} - \dfrac{\omega_{R0}}{2Q_c}]\bar{a} + \kappa\bar{S}_{in} \\ \bar{S}_{out} = \bar{S}_{in} - \kappa^* \bar{a} \\ |\kappa|^2 = 2/\tau_c \end{cases} . \tag{6.36}$$

To evaluate Equation (6.32), we need to find the temperature as well as the free-carrier density. From Equations (6.8), (6.10), and (6.13), the time-domain variation of free-carrier density can be written as

$$\frac{d}{dt}\Delta N = -\frac{\Delta N}{\tau_{FC}} + G_{TPA} |\, \bar{a}\,|^4 . \tag{6.37}$$

The calculated free-carrier density from the above equation is inserted into Equation (6.4) to find the refractive index shift resulting from FCs. To find the thermal effect on Equation (6.32), we need to find the absorbed power by the resonator. From Equation (6.18), we have the following expression for the absorbed power:

$$P_{abs}(t) = \omega_{R0}\left(\frac{1}{Q_{abs0}} + \frac{1}{Q_{TPA}(t)} + \frac{1}{Q_{FCA}(t)}\right) |\, \bar{a}(t)\,|^2, \tag{6.38}$$

where Q_{FCA} and Q_{TPA} are given by Equations (6.7) and (6.15) in the temporal form as

$$\frac{1}{Q_{FCA}(t)} = \frac{1}{\omega_{0R}} \frac{c}{n_g} \alpha_{FCA0} \Delta N(t), \tag{6.39}$$

$$\frac{1}{Q_{TPA}(t)} = 2\hbar V_{TPA} \sqrt{\frac{G_{TPA}}{\tau_{FC}}} \times \sqrt{\Delta N(t)}\,. \tag{6.40}$$

By putting the absorption power into the heat equation, the temperature variation can be obtained. As is discussed in the next section, by applying appropriate approximations into the heat equation, an equivalent equation for the dynamic thermal equation can be obtained, which is

$$\frac{d}{dt} \Delta \bar{T}(t) = -\frac{1}{\tau_{Th}} \Delta \bar{T}(t) + \eta P_{abs}(t), \tag{6.41}$$

where τ_{Th} is the thermal lifetime (or thermal response time) of the resonator, and η is a coefficient that depends of the mass heat properties of the resonator structure, which is described in the next section. By simultaneously solving Equations (6.32) and (6.36) to (6.41), the dynamic response of the resonator can be obtained. Figures 6.15(a) to 6.15(d) show the simulated results for the temporal transmission, the resonance shift, the temperature change, and the generated FCs of a microdisk resonator (coupled to a waveguide), respectively. The assumed microdisk parameters for this simulation are specified in the figure. As seen from Figure 6.15(a), the onset of slow (MHz) oscillations as well as fast (GHz) oscillations can be determined from the transmission responses. Details of the fast oscillations are shown in Figure 6.15(e), which is a zoomed view of the transmission response shown in Figure 6.15(a) in a time zone around t = 2.04 μs. One cycle of the oscillations shown in Figure 6.15(a) can be described as follows by starting from

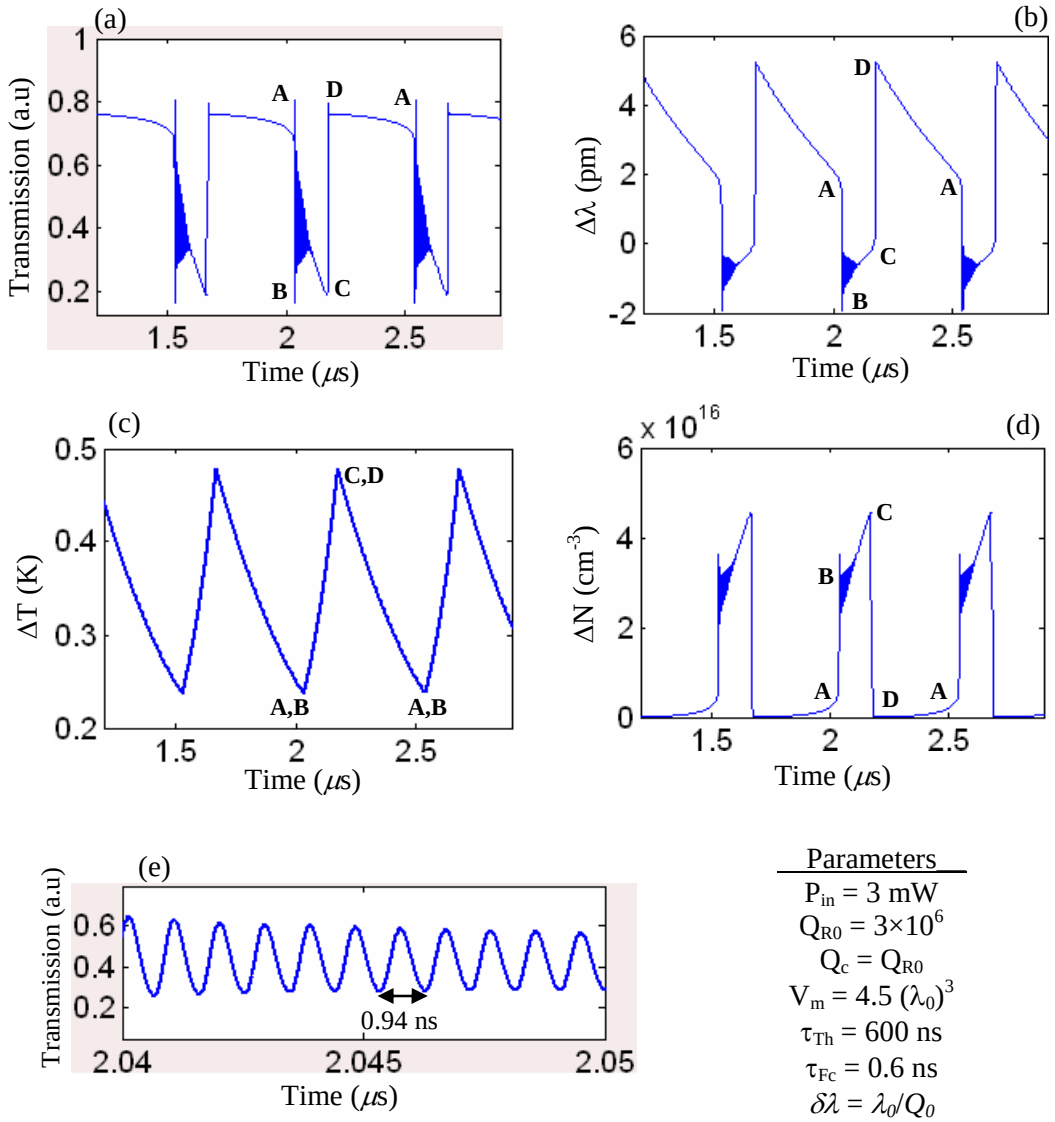

Figure 6.15: (a) Transmission response, (b) resonance wavelength change, (c) temperature change, and (d) free-carrier response of a microdisk resonator coupled to a waveguide. (e) A zoomed view of the transmission response shown in (a) around t ~ 2.04 μs. For this simulation the input power is P_{in} = 3 mW, the microdisk intrinsic Q_{R0} =3×10^6, the mode volume is V_m = 4.5 $(\lambda_0)^3$, the thermal lifetime τ_{Th} = 500 ns, the FC lifetime τ_{FC} = 0.6 ns, and the resonator works in the critical coupling regime ($Q_c = Q_{R0}$). The laser wavelength is detuned from the original resonance wavelength of the resonator by an amount of $\delta\lambda = \lambda_0/Q_0$, where λ_0 is the resonance wavelength.

point **A**. At point **A**, a strong TPA occurs, followed by a sudden and avalanche generation of free carriers. The generated FCs quickly change the refractive index

and shift the resonance wavelength in the negative (blue) direction. The laser wavelength has been appropriately detuned from the resonance wavelength[67] of the cold resonator to provide an avalanche generation of FCs (which is the necessary condition for the fast oscillations) as the resonance wavelength is blue shifted and further approaches the laser wavelength, which results in more resonator energy, more TPA, and more FCs. Hence the center of the resonance wavelength moves toward the laser wavelength. Therefore, because of the closer proximity of the laser wavelength and the resonance wavelength, a drop in the transmission occurs and the status of the transmission is at point **B**. At point **B**, competition between the FC lifetime and resonator photon lifetime occurs and fast oscillations are observed.

The mechanism of the fast oscillations at point **B** (which is also shown in Figure 6.15(e)) can be explained as follows: Because of the presence of the generated FCs, the Q of the resonator degrades and becomes smaller than coupling Q (Q_c). As a result, less power is coupled to the resonator, and consequently, the resonator energy decreases. However, the time of this energy decrease is controlled by the resonator loaded lifetime (which is a combination of the coupling lifetime and the resonator photon lifetime). As a result of less energy in the resonators, less FC is generated and the available FCs in the resonator are in the process of recombination with the FC lifetime. Hence, the Q of the resonator starts recovering and the resonance wavelength starts shifting back to the longer wavelengths closer to laser

[67] Usually, detuning is in the negative direction with respect to the cold resonance wavelength. However, because of the thermal broadening and red shift of the resonance, positive detuning is also possible.

wavelength. This results in the buildup of energy in the resonator and a consequent generation of new FCs, which start the new cycle of fast oscillation. The generated FCs (with or without producing the fast oscillations) heat the resonator and increase the temperature. This temperature increase results in a red shift in the resonance wavelength toward point **C**, as shown in Figure 6.15(b). During this trend, the fast oscillations become damped, as the resonance frequency is largely red shifted, and the detuning is not enough to provide fast oscillations. Also, from Figure 6.15(c), a temperature rise of the resonator from point **B** to point **C** is observed. However, as we saw in the static steady-state analysis, the spectrum of the transmission response at high power shows bistability (e.g., see Figure 6.7(b)). During resonator heating, toward point **C**, the resonance wavelength moves and the spectrum of the transmission dynamically changes and trends to its steady-state form, which has bistability. During these transitions, the laser wavelength and the edge of the bistable point of the transmission coincide, and as a result, a sharp transition from point **C** to point **D** occurs in Figure 6.15(a). Hence, the resonator energy quickly decreases, the number of FCs decreases, and the resonance wavelength (which is also at the edge of its bistable point) makes a sharp transition from point **C** to **D**, as shown in Figure 6.15(b). At this stage, the resonator energy has strongly decreased, and its wavelength has also red shifted and is far from the laser wavelength. Hence, because there is no heat generation, the resonator starts cooling and its resonance wavelength, which is now at the right side of the laser wavelength, moves to the shorter wavelength and approaches the laser wavelength. In the meantime, the

transmission spectrum dynamically trends to its original form and the resonator energy starts growing. When reaching point **A**, which corresponds to the other edge of the bistable region, a sharp transition to point **B** occurs. It has to be noted that this edge is not the steady-state edge, as the resonator spectrum is also under the variation. At point **B**, a strong energy buildup in the resonator occurs, which results in the TPA process as well as the avalanching generation of FCs. At this point, the cycle is repeated, as explained above.

Because of the complicated nature of the coupled nonlinear equations governing the response of the resonators at high powers, it is difficult to develop the conditions and constraints in mathematical closed forms under which different regimes of oscillations or lack of oscillation can occur. However, some general rules for the appearance of different operation regimes of the resonator can be stated, which are listed below.

6.3.1 Conditions for the Occurrence of Fast Oscillations

This process, which is the interplay of the photon (resonator) and FC lifetimes and the input power, results in TPA and generates FCs. This condition is independent of thermal lifetime of the resonator. To have fast oscillations with the lowest possible power, the FC lifetime should be close to the resonator lifetime.

If FC lifetime becomes too small, more power is needed to generate large free carriers to make a large shift as well as a large degradation in the Q (to drop the resonator energy). Otherwise, if the power is low, because of the fast recombination

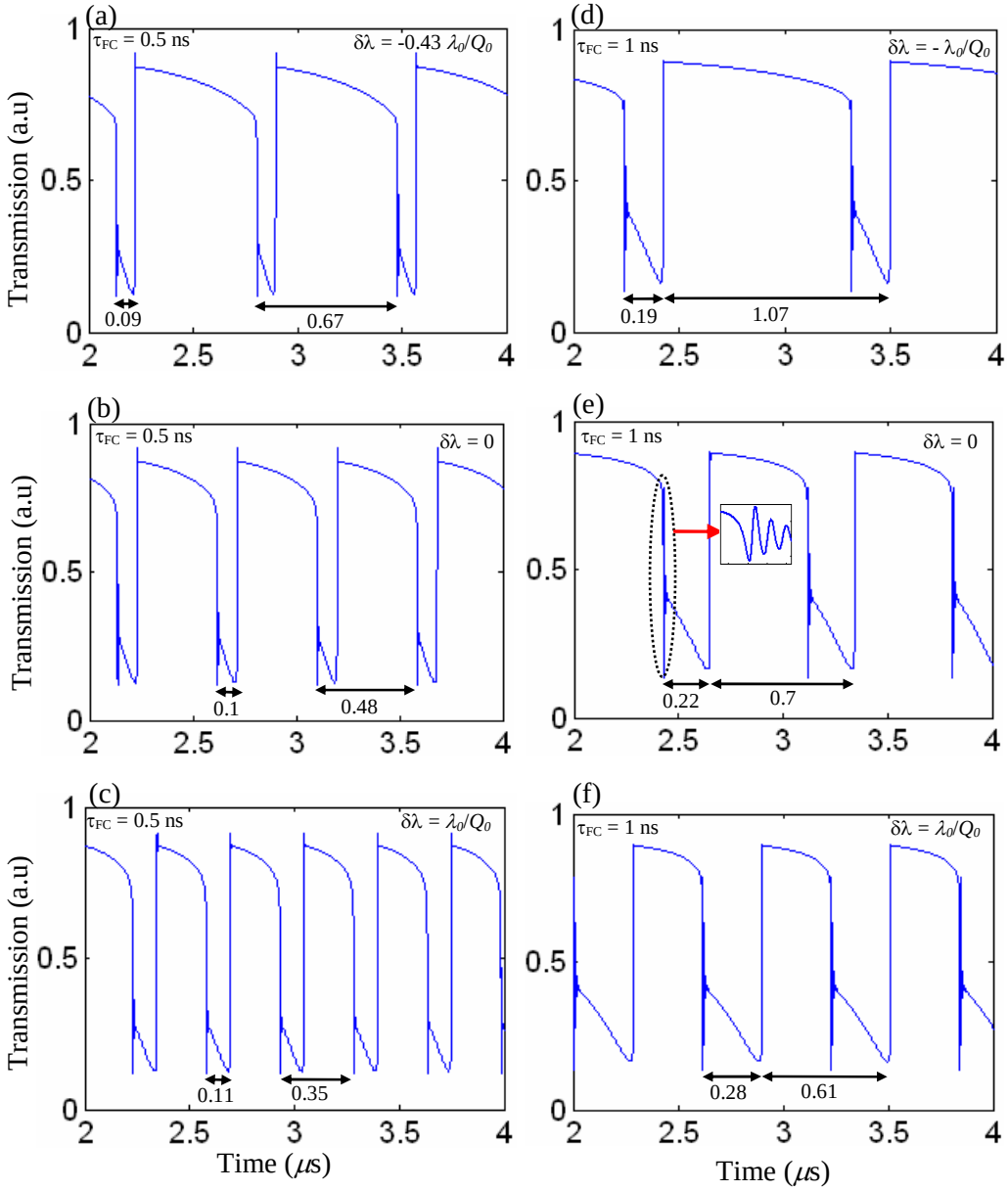

Figure 6.16: Transmission response of a microdisk resonator with an input power P_{in} = 1 mW, calculated with two different FC lifetimes of τ_{FC} = 0.5 ns (left figures), and 1 ns (right figures) and at different detuning ($\delta\lambda$) of the laser wavelength from the original resonance wavelength of the resonator as specified at the corner of the figures. The inset in (e) shows a damped fast oscillation. The microdisk has an intrinsic $Q_0 = 4\times10^6$, a thermal lifetime τ_{Th} = 600 ns, and works in the critical coupling regime ($Q_c = Q_{R0}$).

time of the FCs compared to the resonator lifetime, the resonator slowly goes to its

new state, and hence, no oscillation occurs.

By increasing the FC lifetime and being far from the resonator lifetime, the fast oscillation will not occur. This is because the resonator can quickly follow any trend ruled by the free carriers, which have a slower dynamic than the resonator lifetime. In this case, increasing the power does not help. As a result, the resonator can find its steady-state point in both the temporal and spectral domains.

6.3.1.1. Effect of Laser Detuning on the Fast Oscillations

In the preceding subsection where the mechanism of fast oscillations was discussed, a negative detuning of the laser wavelength with respect to the cold resonance wavelength was considered. However, because of the presence of thermal effects that can bend and push the resonator spectrum to the red region (e.g., see Figure 6.7(b)), oscillations with positive detuning of the laser wavelength are also possible. As a result, the wavelength that corresponds to the minimum transmission of the spectrum can be at the right side of the intrinsic resonance wavelength. Hence, there is a range where the laser wavelength can be larger than the resonance wavelength (i.e., positively detuned) and fast oscillations may still occur.

The detuning also controls the period and the duty cycle of the slow oscillations. This is mainly because of the distance of the laser wavelength from the edge of the bistability, which moves toward the laser wavelength. Hence, for negative detuning, we expect a larger period for the slow oscillation, while for positive detuning, we expect a shorter period. Figure 6.16 shows the effect of different levels of detuning on the period of slow oscillations for a microdisk resonator with two different FC

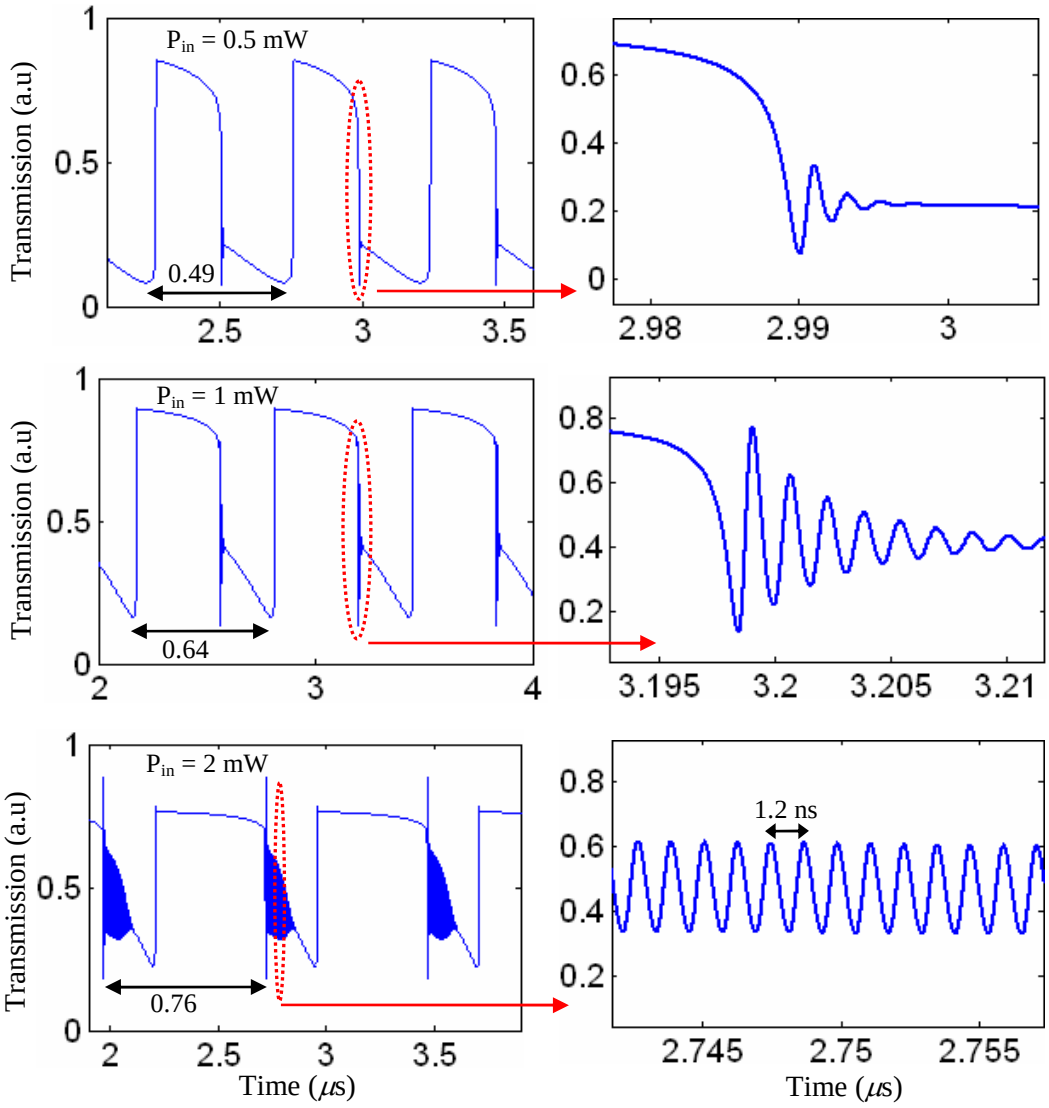

Figure 6.17: Left figure: Transmission response of a microdisk resonator with three different input powers of P_{in} =0.5 mW, 1mW, and 2 mW. The inset in (e) shows a damped fast oscillation. The right figures are the zoomed views of the regions in the left figures, as specified. The microdisk has an intrinsic Q_0 =4×10^6, a thermal lifetime τ_{Th} = 600 ns, τ_{FC} = 1 ns, and works in the critical coupling regime (Q_c = Q_0). The laser wavelength is detuned from the original resonance wavelength of the resonator by an amount of $\delta\lambda = 0.5\ \lambda_0/Q_0$, where λ_0 is the resonance wavelength.

lifetimes. As seen in this figure, by further detuning the laser wavelength in the positive direction, the period of slow oscillations reduces.

6.3.1.2. Effect of the Power on the Fast Oscillations

As mentioned before, the generation of fast oscillations is power dependent. Figure 6.17 shows simulation results for the dynamic response of the transmission of a microdisk resonator at different levels of input powers while other parameters are fixed. As seen from the plots in this figure, by increasing the input power, the number of cycles of the oscillations also increases.

6.3.2 Sustaining the Fast Oscillations and Suppressing the Slow Oscillations

In all previous simulations, fast oscillations, after some number of cycles, are damped and disappear. This is because of the heating of the resonator, which results in a large red shift in the resonance wavelength and eventually causes the fast oscillations to die away. Hence, to sustain the fast oscillations in a steady-state manner, the thermal effect has to be reduced. This can be done by either reducing the thermal lifetime and thermal conductivity to quickly reduce the large temperature in the system or by reducing the thermo-optic coefficient of the resonator to reduce the resonance shift. Also, in a further step, by properly choosing microdisk parameters, the slow oscillations can be suppressed. Figure 6.18 shows the simulation results for a microdisk resonator where self-sustained fast oscillations (width the absence of slow oscillations) are observed. The thermo-optics coefficient (TOC) of the resonator can be reduced by using a cladding material with a strong negative thermo-optics coefficient. Some polymers are available with strong negative TOC. Currently, there is ongoing research to design the resonators with these polymers as the cladding to reduce or suppress the resonance shift by the

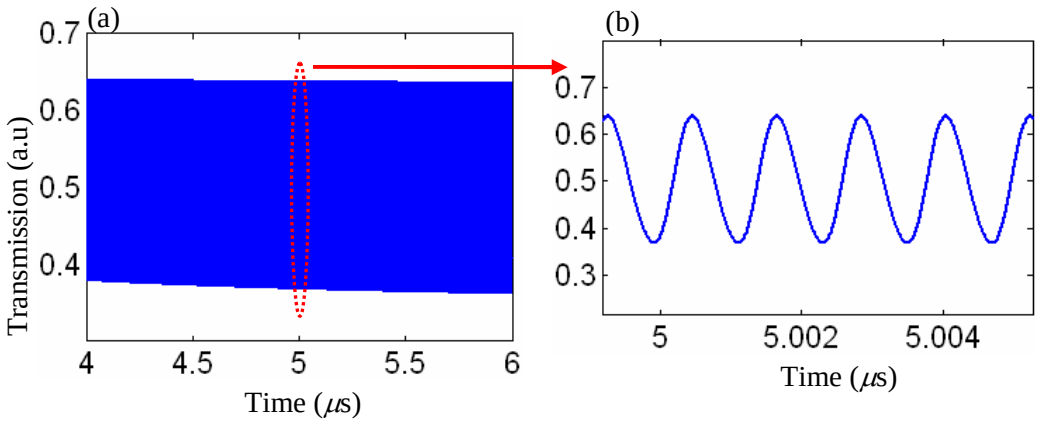

Figure 6.18: (a) Transmission response, (b) resonance wavelength change, (c) temperature change, and (d) free-carrier response of a microdisk resonator with an input power of P_{in} =2 mW. The microdisk has an intrinsic $Q_0 = 4\times10^6$, $V_m = 4.5\ (\lambda_0)^3$, a thermal lifetime τ_{Th} = 500 ns, τ_{FC} = 1 ns, and works in the critical coupling regime ($Q_c = Q_0$). The effective thermo-optics coefficient of the resonator is one-third that of silicon [98].

thermal effect. Such steady-state oscillations generated from a CW pump can enable a variety of applications in analog signal synthesis.

6.4 Experimental Results on the Slow and Fast Oscillations

In this section, we provide the experimental results for the temporal dynamic of an ultra-high Q microdisk resonator at high powers. Figure 6.12 shows the measured spectrum of one of the resonance modes of the microdisk we have considered for the high-power studies. The intrinsic Q of this mode during a one-day measurement was in the range of 2.2-3 millions. Figure 6.19 shows the temporal dynamic response of this resonance mode for a fixed pump wavelength close to the cold resonance wavelength. As seen from Figure 6.19(a), simultaneous steady-state slow (MHz) oscillations and long-sustained fast (GHz) oscillations (with a frequency of ~ 0.53 GHz and over 110 periods) are observed. More details of the long-sustained

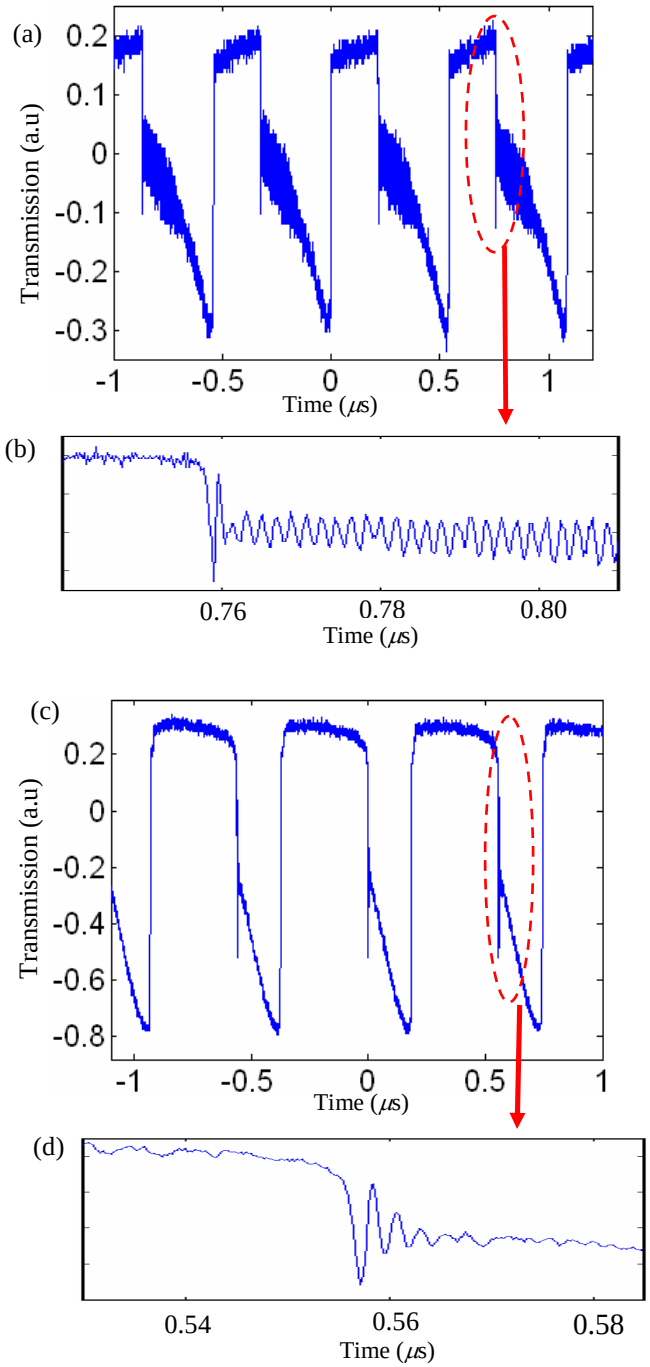

Fig. 6.19: Experimental results for temporal oscillations of a microdisk resonator. (a) Observation of simultaneous steady-state slow (MHz) and long-sustained fast (GHz) oscillations. (b) A zoomed view of the fast oscillation, which has a frequency of 0.52-0.54 GHz. The oscillation is sustained for over 110 periods. (c) Observation of simultaneous steady-state slow (MHz) and damped fast (GHz) oscillations. Bottom: A zoomed view of the damped GHz oscillations in the specified zone. The transmission spectrum and the parameters of this microdisk are given in Figure 6.12 [98].

oscillations are shown in Figure 6.19(b). As discussed above, the frequency of fast oscillations is mainly controlled by the FC lifetime, the photon lifetime, the input power, and the detuning of pump wavelength from the cold cavity resonance. As a result of the degradation of the Q of the cavity over time, as well as the resonance shift because of the ambient temperature fluctuations, we noticed the microdisk showed damped oscillations (when tested at a later time). This is shown in Figure 6.19(c), where simultaneous steady-state slow (MHz) and damped fast (GHz) oscillations are observed. Figure 6.19(d) shows more details of the damped fast oscillation. Figure 6.20 shows the spectrum of the measured data shown in Figure 6.19(a). The insets in Figure 6.20 show more details of the spectrum. The left inset in Figure 6.20 shows the spectral components of the slow oscillations and the right inset shows the spectrum of the fast oscillations. For the fast oscillations, a spectral linewidth of 10 MHz was measured from Figure 6.20.

Figure 6.21 shows the effect of detuning of the laser wavelength on oscillation behavior. The experimental results for three laser wavelengths with steps of 10 pm are shown in this figure. These wavelengths corresponded to the beginning, the middle, and the end of a range in which slow oscillation could occur in the resonator response. As seen from Figure 6.21, by increasing the laser wavelength, the period of oscillations as well as their duty cycle decreases. We also observed this in the theoretical simulations in the preceding section, as shown in Figure 6.16. Another phenomenon that occurs in Figure 6.21 is that by increasing the wavelength, the periods of fast oscillation decrease, and their damping becomes faster.

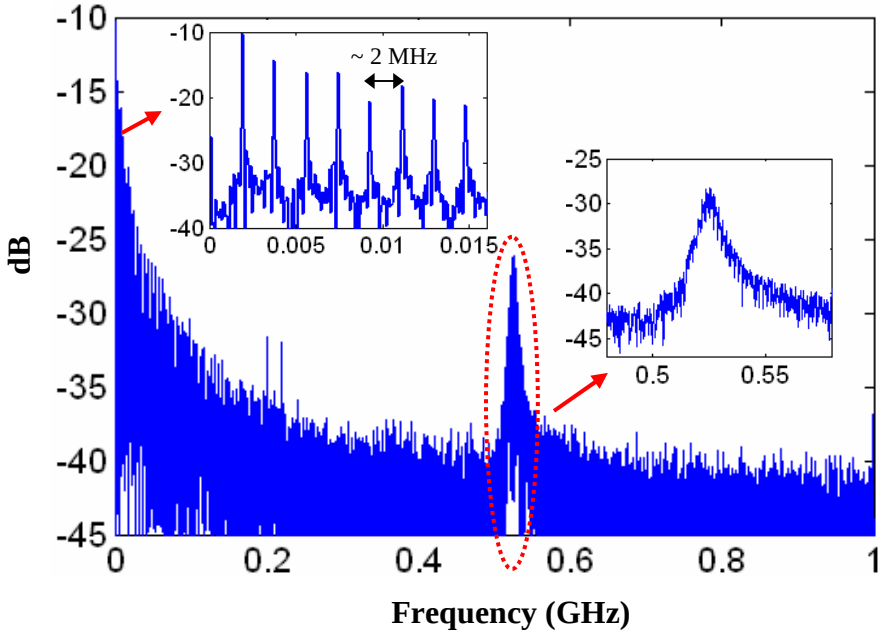

Figure 6.20: Spectrum of the time-domain measured data shown in Figure 6.18(a). The insets show details of the spectrum. The left inset shows the spectral components of the slow oscillations shown in Figure 6.18(a), and the right inset shows the spectrum of the fast oscillations. The 3 dB linewidth of the fast oscillation spectrum is 10 MHz [98].

6.5. Chapter Summary

In this chapter, we investigated the performance of Si traveling-wave resonators at high optical powers with the interplay of two-photon absorption, free-carrier absorption, and thermo-optics properties of silicon on the temporal and spectral responses of the resonators. Our study focused on two domains. In the first half of the chapter we focused on a detailed theoretical and experimental study of the static response of Si resonators. We initially derived closed-form expressions for the lineshape of resonators while considering pure thermo-optics (no FCA, TPA) broadening and then expanded this treatment to include other effects. Some of the key highlights that resulted from this study include the prediction and experimental

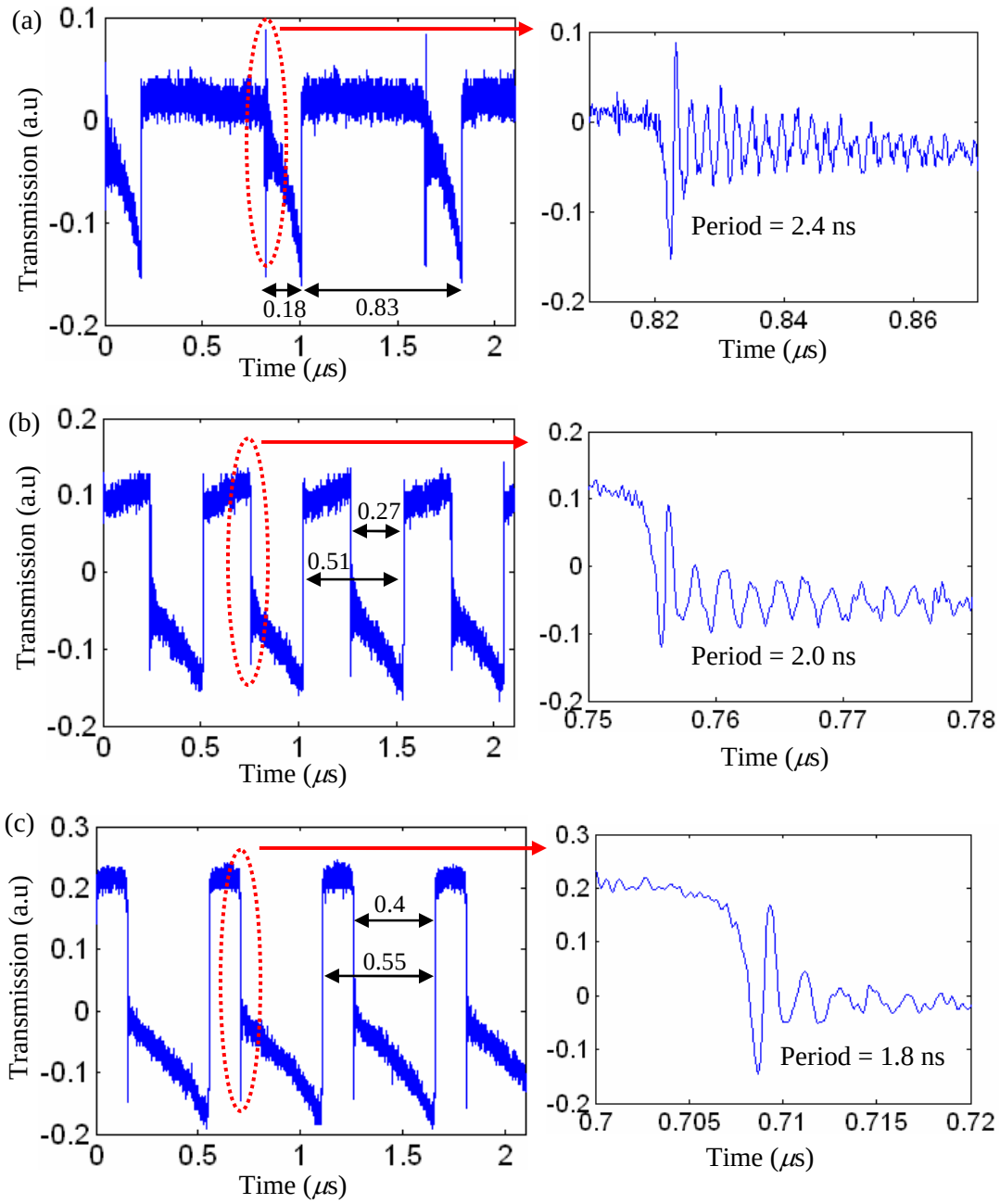

Figure 6.21: Temporal dynamic response of an ultra-high Q microdisk resonator at three laser wavelengths of (a) 1530.447, (b) 1530.457, and (c) 1530.467 detuned from the microdisk cold resonance wavelength. The right figures show the zoomed views of the fast oscillation regions specified in the left figures. The linear spectrum of this microdisk is shown in Figure 6.12 [98].

observation of distorted lineshapes with bistability. We then proceeded to analyze

the dynamical response of the resonators at high powers. At high powers, by appropriate detuning of the laser wavelength from the resonance wavelength, the avalanche generation of FCs induced by TPA is possible. Depending on the photon, phonon (thermal), and electron (FC) lifetimes of the resonators, the level of input power, and the laser detuning, an onset of self-sustained temporal oscillations may appear in the resonator response. These oscillations can occur even with a continuous-wave input laser power. We experimentally observed two regimes of oscillations: 1) slow oscillations, which are in the MHz range frequencies, and 2) fast oscillations, which are in the GHz range. We theoretically explained these two sets of oscillations and explained the conditions under which only fast, only slow, or both sets of oscillations appear. In brief, the mechanisms of these oscillations are as follows: (use periods after the numbers below)

1- The slow oscillations are a cycling dynamic of competitions among small blue shifting by FCs, large red shifting by heat generated by FCA, and large blue shifting by cooling (to return to the original point). A necessary condition for these oscillations is the existence of bistability in the resonator spectrum, which makes a transition from the heating to the cooling and from cooling to the original point.

2- The fast oscillations are a competition between the photon lifetime and FC lifetime. The generated FCs make a blue shift into the resonance wavelength until the laser wavelength and the resonance are more deviated and less energy goes into the resonator. In addition, the FCA reduces the Q, which

results in reducing the resonator energy (with the photon lifetime rate) as the resonator deviates from the critical coupling. Hence, the resonator receives less energy and as a result fewer FCs are generated and the remaining FCs recombine (with the FC lifetime) until the resonance goes back to the original point to start the new cycle of the oscillation.

We also theoretically showed that pure and self-sustained fast oscillations (without damping and without appearance of slow oscillations) are possible. Achieving a pure fast oscillation requires some tight conditions on the Q, FC lifetime, and thermo-optic properties of the resonator. To remove the slow oscillations, the thermo-optic coefficient and the thermal lifetime of the resonator have to be reduced. We extensively investigated the thermal properties of these resonators (through simultaneously solving thermodynamic and electromagnetic equations governing the resonator structure) and proposed methods to improve and optimize the thermal properties (see Appendix G).

The appearance of such fast oscillations can have potential applications in the generation and shaping of pulses in the time domain. The frequency-domain applications of such self-sustained oscillations include the generation of stable on-chip frequency references and optoelectronic mixing when the input continuous-wave laser is modulated with base band electronic information. There are other applications in which we like to use a resonator at high powers but do not wish to have any temporal oscillations. Some of these applications are in the linear optics regime, e.g., sensing and signal processing, while other applications are in the

nonlinear optics regime, e.g., four-wave mixing and Raman lasing. In such cases, the appearance of these oscillations can be a bottleneck, and we need to engineer these resonators and find the conditions where the power thresholds for these applications are below the threshold of the appearance of the temporal oscillations. This is an interesting research problem that needs to be further investigated.

CHAPTER 7

COUPLED-RESONATORS STRUCTURES IN SOI PLATFORMS

In this chapter, coupled-resonator structures, which are also called coupled-resonator optical waveguides (CROW) [20, 99], with a finite number of resonators are considered, and a systematic method of design to achieve filters with a flat-band spectrum is proposed. By employing temporal coupled-mode theory and analysis and identifying the equivalence between the CROW response and an electrical LC ladder filter response in circuit theory, we derive a simple analytical expression for the coupling coefficients between the resonators in a CROW structure to achieve a flat response in its transmission band. This is then extended to perform a detailed tolerance analysis of such CROW structures in a SOI platform. Based on the theoretical results, compact CROW filters made of high Q miniaturized Si microdisk resonators are designed, fabricated, and characterized.

7.1. Introduction

Coupled-resonator structures have been the focus of research for a variety of on-chip applications. These structures, owing to the use of controlled inter-resonator coupling, can operate in a much larger optical bandwidth [20, 48]. This large operation bandwidth is suitable for hosting and processing wideband optical pulses that may not be accommodated by a single resonator with a narrow resonance linewidth. Because of the slow flow of light in these structures, they are also considered potential candidates for on-chip optical buffering and slow-light

applications [100,101]. Some other wideband applications of these structures include wavelength division multiplexing (WDM) filters [21, 22, 102] as well as nonlinear interactions with wideband optical pulses [103,104]. Recent advances in the fabrication and fine control of high Q microresonators in a SOI platform have made CROW structures potential candidates for these applications [21, 22].

In a coupled-resonator structure, when the number of resonators extends to infinity, the structure can be considered a slow-light waveguide made of a chain of coupled resonators and called coupled-resonator optical waveguides (CROW) [99]. For an ideal CROW, where the resonators are periodically lined up, a mode-dispersion diagram can be obtained [99]. Hence, all the electromagnetic mode properties of the CROW, including phase, group velocity, and the bandwidth of the transmission, can be identified through its dispersion [99]. However, in practical implementations of these CROW structures, the number of resonators is limited, and the resulting finite-size CROW structure is terminated with waveguiding stages from both sides. This scenario is shown in Figure 7.1(a). In this structure, any transmission mismatch between the CROW and the input and output coupling stages to the waveguides can result in Fabry-Perot resonances that modulate the transmission response of the CROW. Figure 7.1(b) shows such Fabry-Perot modulations on the transmission response of the CROW structure at the drop port shown in Figure 7.1(a). Also, Figure 7.1(c) shows the transmission response at the through port. For these simulations, which have been done by temporal coupled-mode theory (as is explained later), the resonators are periodically spaced and

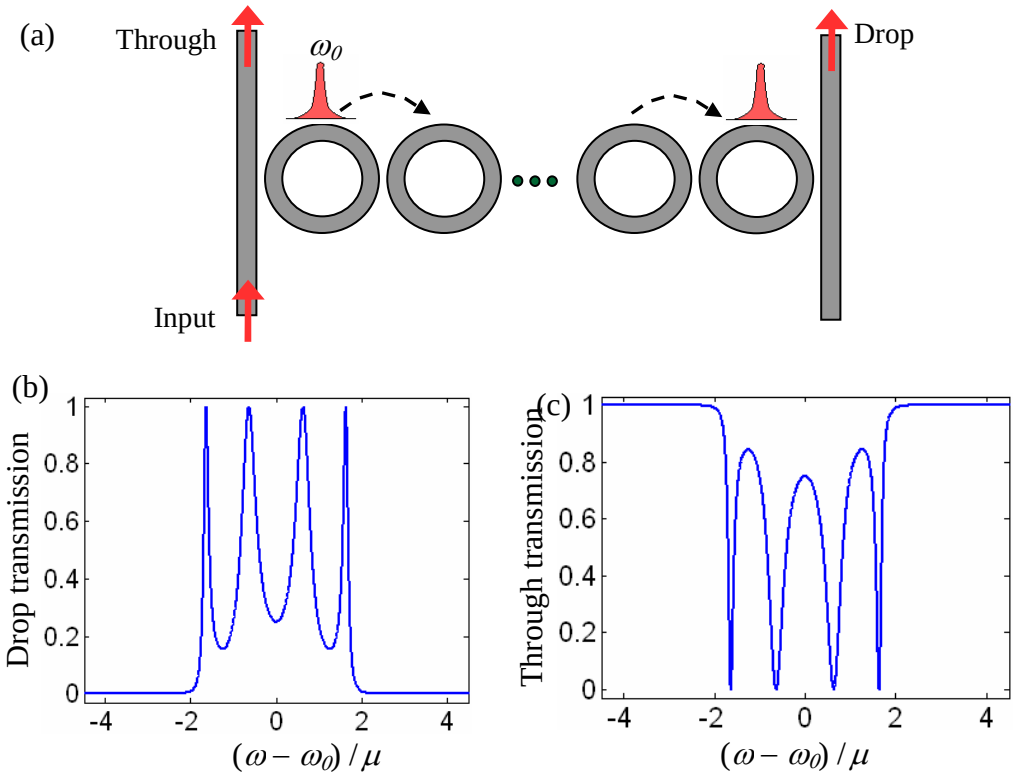

Fig. 7.1: (a) A chain of coupled-resonator structures made of identical traveling-wave resonators and side coupled to two waveguides at both ends of the chain. The simulation of the normalized transmissions response at (b) the drop port and (c) the through port versus the normalized frequency for the case when the structure consists of six resonators periodically arranged with a resonator-resonator coupling coefficient μ. Strong Fabry-Perot fringes are observed in the response. The coupling lifetime between the waveguides and their adjacent resonators is $\tau_c = 0.27 / \mu$. The resonance frequency of the resonators is ω_0. The resonators have been assumed to have no loss (infinite Q).

have an identical resonator-resonator coupling coefficient of μ. As seen from Figures 7.1(b) and 7.1(c), the finite-size effect of the CROW is strongly pronounced at the edges of the transmission band, which corresponds to the band edges of the dispersion diagram of the infinite CROW. In the vicinity of these edges, the group velocity is close to zero, and therefore, there is strong mismatch between the CROW and the input/output stages [99]. Hence, to have a flat-band response, we need to

find techniques to minimize these Fabry-Perot effects. In the past, such methods have been proposed [48, 105, 106]. In [48], using the temporal coupled-mode theory and borrowing the insertion-loss method from circuit theory, the coupling coefficient for the design of Butterworth- and Chebyshev-type responses have been extracted. However, as the number of resonators in a CROW increases, the order of rhe polynomial that represents the insertion loss of the CROW increases correspondingly, and therefore, finding the coupling coefficients from this higher-order polynomial becomes cumbersome. In [105], by borrowing the techniques for the filter design and impedance matching in a microwave circuit, equivalent parameters for optical-coupled resonators for the Butterworth and Chebyshev designs were proposed. While the technique was general, the extracted coupling parameters were specified based on coupling in space. In a recent work [106], by knowing the fact that the CROW can be described using a transfer matrix method and by employing Breit–Wigner scattering formalism [106], the conditions that minimize Fabry-Perot effects in the vicinity of the center of the CROW band were obtained, and a closed-form analytical expression for the coupling coefficients was given. Even though this method dramatically improves the transmission to almost a flat-band response, the Fabry-Perot resonances are still observed in the transmission band and become stronger at the edge of the CROW band.

In this research, by employing temporal coupled-mode theory and by borrowing techniques for the design of LC filters in circuit theory, we find a direct correspondence between the coupling parameters in a finite-sized CROW and

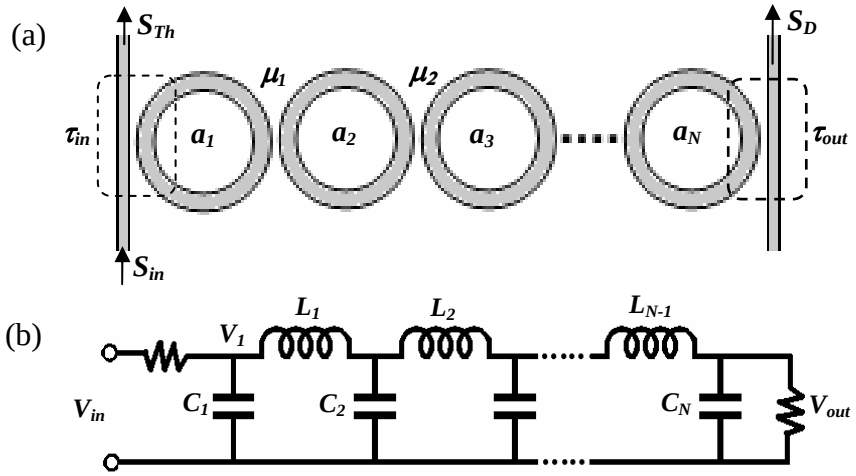

Fig. 7.2: (a) Structure of a finite-sized CROW with the detailed parameters specified. a_i is the amplitude of the ith resonator normalized such that $|a_i|^2$ represents the energy of the resonator. μi is the coupling coefficient between the resonators with indices i and i+1. τ_{in} and τ_{out} are the coupling lifetimes between the input and the output waveguides and their adjacent resonators. S_{in}, S_{Th}, and S_D are the waveguide amplitude at the input port, through port, and the drop port, normalized such that their squared amplitudes represent the power. (b) Structure of an LC circuit ends by two resistors.

the capacitors and inductors in an LC circuit of the same order. As a result, any type of filter response such as Butterworth, Chebyshev, and elliptic designs for a finite-sized CROW are possible. For the case of the Butterworth design, a simple and closed-form analytical expression is presented. Effects of the non-idealities on the response of the CROW are investigated. Based on the theoretical results obtained for the coupling coefficients, very compact coupled-resonator filters with miniaturized microdisk resonators are designed, fabricated, and characterized.

7.2 Coupled-mode Theory of Coupled-resonators Structures

Figures 7.2(a) and 7.2(b) show the structure of a finite-sized CROW and an LC circuit filter. The resonators constituting the CROW could be either standing-wave types, such as Fabry-Perot cavities or photonic crystal cavities, or traveling-wave

types such as microrings. In the traveling-wave type, it is assumed the one of the degenerate modes of the resonator participates in the coupling, which is a reasonable assumption, as the waveguide mode can excite one of the degenerate modes of the TWR because of the phase matching[68].

The analysis of the coupled-resonator structure using coupled-mode theory in time is very similar to what was presented in chapter 3 for waveguide-resonator coupling, with the difference that the effect of resonator-resonator coupling has come into the picture. Using coupled-mode theory, the master equations for the temporal response of the coupled-resonator structure shown in Figure 7.2(a) can be written as

$$\frac{da_1}{dt} = (j\omega_0 + 1/\tau_0 + 1/\tau_{in})a_1 + j\mu_1 a_2 + \kappa_{in} S_{in}$$

$$\frac{da_2}{dt} = (j\omega_0 + 1/\tau_0)a_2 + j\mu_1^* a_2 + j\mu_2 a_2$$

$$\vdots$$

$$\frac{da_n}{dt} = (j\omega_0 + 1/\tau_0)a_n + j\mu_{n-1}^* a_{n-1} + j\mu_n a_{n+1}$$

$$\vdots$$

$$\frac{da_N}{dt} = (j\omega_0 + 1/\tau_0 + 1/\tau_{out})a_N + j\mu_{N-1}^* a_{N-1}$$

$$S_D = -\kappa_{out}^* a_N$$

$$S_{Th} = S_{in} - \kappa_{in}^* a_N$$

[68] Also for two adjacent TWRs, because of the phase-matching issue, the CW mode of one of the resonators interacts only with the CCW mode of the other resonator.

$$|\kappa_{in(out)}| = \sqrt{2/\tau_{in(out)}}\,.^{69} \tag{7.1}$$

In the above equations, ω_0 and τ_0 are the resonance frequency and intrinsic lifetime of the resonators respectively, τ_{in} (κ_{in}) and τ_{out} (κ_{out}), as discussed in chapter 3, are the coupling lifetimes (coupling coefficient) between the input and output waveguides and their adjacent resonators, respectively. By transforming the resonators and waveguide amplitudes in Equation (7.1) into the Fourier domain, the field amplitude of the first resonator can be written in the following ladder format:

$$a_1 = \frac{\kappa_{in}\, S_{in}}{j\Omega + 1/\tau_{in} + \dfrac{\mu_1^2}{j\Omega + \dfrac{\mu_2^2}{j\Omega + \cdots + \dfrac{\mu_{N-1}^2}{j\Omega + 1/\tau_{out}}}}}\,,\ (\Omega = \omega - \omega_0)\,. \tag{7.2}$$

In the above expression, we have assumed that the intrinsic quality factor (Q_0) of the resonators is large enough to be neglected, i.e., $1/\tau_0 = 0$. The effect of finite Q_0 is discussed later.

In a similar way, by inspecting the circuit shown in Figure 7.2(b), it can be observed that the voltage at node 1 can be written in a similar form as in Equation (7.1), which represents the field amplitude of the first resonator in the CROW. The number of reactive elements in the circuit corresponds to the number of resonators in the CROW. As shown in Figure 7.2(b), the first reactive element at the input is always a shunt capacitor, but the last reactive element at the output is either a series

[69] These relations between κ_{in} (κ_{out}) and τ_{in} (τ_{out}) are for TWR cases. For a chain of standing-wave resonators that are direct coupled to a waveguide, we have $\kappa_{in(out)} = \sqrt{1/\tau_{in(out)}}$. An example of this case is a stack of coupled Fabry-Perot resonators along the waveguide.

inductor or a shunt capacitor depending on if the CROW has an odd or even number of resonators. For a CROW with an even number of resonators, the voltage at node 1, V_1, for the corresponding circuit can be written as follows:

$$V_1 = \frac{V_{in}/(RC_1)}{j\Omega + 1/(RC_1) + \dfrac{1/(C_1L_1)}{j\Omega + \dfrac{1/(C_2L_2)}{j\Omega + \cdots + \dfrac{1/(C_{N-1}L_{N-1})}{j\Omega + R/L_{N-1}}}}}.^{70} \tag{7.3}$$

By comparing Equations (7.2) and (7.3) and knowing that the values of circuit elements for different filter architectures such as Butterworth and Chebyshev can be calculated, we can find all the coupling parameters for the corresponding CROW. For Butterworth and Chebyshev filters, analytical expressions for the normalized circuit elements with equal and unit input and output resistors can be found in any filter handbook [107]. Equivalently, in the CROW structure, the coupling lifetimes at the input and the output should be the same (i.e., $\tau_{in}=\tau_{out}$); we refer to both of them as τ_c. By direct comparison of Equations (7.2) and (7.3) and knowing the value of the circuit elements in Equation (7.3), a universal expression for the coupling parameters in a CROW with even or odd number of resonators and for a Butterworth design can be obtained as follows:

$$\mu_n = \frac{\sin[(2N-1)\pi/2N]}{\sqrt{\sin[(2n-1)\pi/2N]\,\sin[(2n+1)\pi/2N]}}\frac{1}{\tau_c},\ (n = 1,\ldots,N\text{-}1). \tag{7.4}$$

[70] A similar expression can be written for V_1 in the circuit that represents a CROW with an odd number of resonators.

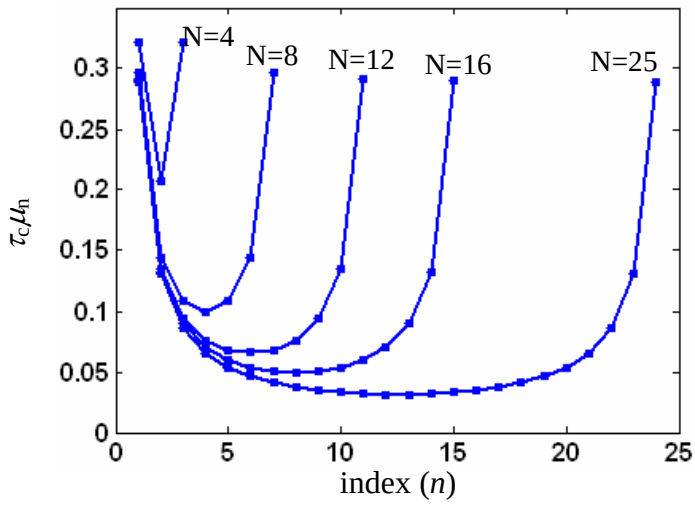

Fig. 7.3: Variation of the coupling coefficients between the resonators in a finite-sized Butterworth-response CROW made of N=4, 8, 12, 16, and 25 resonators as plotted by different curves. The horizontal axis is the index of the coupling coefficients, which varies from 1 to N-1.

As we can see from the above equation, all the coupling coefficients (μ_n) in the equation are linearly proportional to the inverse of τ_c. In fact, τ_c and the number of resonators (N) in the CROW are the two free parameters that determine the bandwidth of the CROW filter. Figure 7.3 shows the variation of μ_n (normalized to coupling lifetime, i.e., $\tau_c\mu_n$) given by Equation (7.4) versus the number of resonators in the CROW. As can be seen from the plots, for a fixed number of resonators (N), the variation of μ_n at the beginning and at the end of the CROW (which corresponds to indices close to 1 or N) is larger than that at the middle of the CROW. Especially, for a CROW with a larger number of resonators, μ_n at the middle of the structure is almost invariable.

To validate this theory, coupling parameters from Equation (7.4) were put into Equation (7.1) and the transmission response of the CROW was calculated.

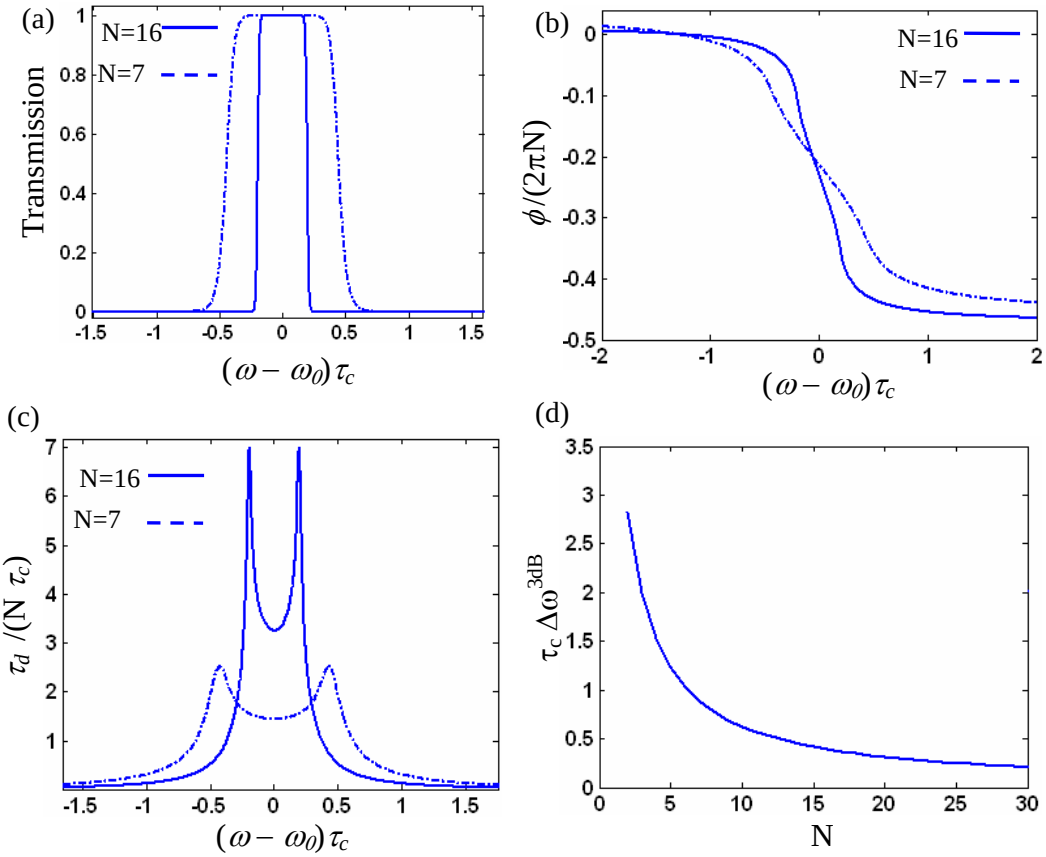

Fig. 7.4: (a) Transmission, (b) normalized phase ($\phi/2\pi N$), and (c) normalized group delay $\tau_d/(N\,\tau_c)$ of the drop port for a finite–sized CROW with Butterworth design parameters. Solid and dashed curves are for CROWs with N=7 and N=16 resonators, respectively. The resonance frequency of the resonators is ω_0. (d) Normalized 3 dB bandwidth ($\tau_c\,\Delta\omega^{3dB}$) of the CROW for a different number of resonators for the Butterworth design.

Figures 7.4(a), 7.4(b), and 7.4(c) show, respectively, the transmission, the normalized phase, and the normalized group delay responses of the drop port for two CROWs with N = 7 and N = 16 resonators versus the normalized frequency $\tau_c\,\Omega$. As seen from Figure 7.4(a), flat-band responses have been obtained for the CROW structure, which validates our theory and the coupling parameters given by Equation (7.4). Also, Figure 7.4(d) shows the normalized 3-dB bandwidth of the CROW for a different number of resonators. As seen from this figure, by

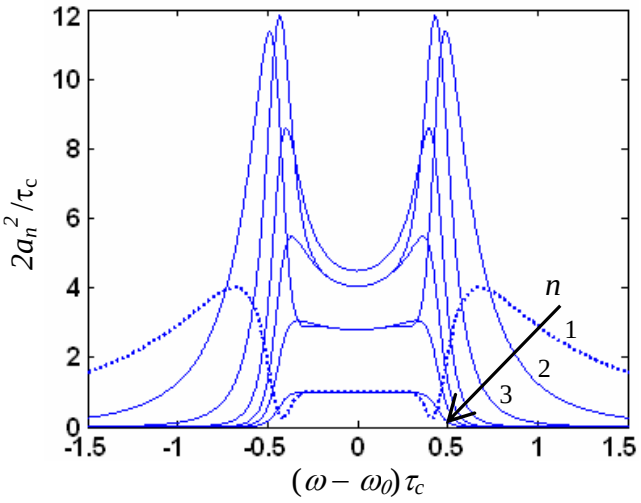

Fig. 7.5: Energy spectrum of the resonators (a_n^2) (scaled with $2/\tau_c$) for a Butterworth CROW with N = 7 resonators. The arrow in the figures shows the direction of increasing the resonator index number. The input power from the bus waveguide is unity. The last resonator has the same spectrum as the output power in the drop waveguide.

increasing the number of resonators while τ_c is kept fixed, the FWHM bandwidth (3-dB bandwidth) of the filter quickly drops.

Another issue to be addressed is the field enhancement that occurs in the resonators in a CROW. Figure 7.5 shows the energy spectrum of the resonators in a Butterworth CROW with N = 7 resonators. As can be seen from this figure, the first and the last resonators have the least field enhancement, while the resonator at the center has the strongest field enhancement. This can be explained from Figure 7.3, where the coupling coefficient for the central resonator is the weakest, and therefore, less energy leaks out and the energy buildup becomes stronger inside this resonator. This field enhancement property makes the CROW suitable for nonlinear optics applications in which strong field enhancement is required.

7.2.1 Sensitivity Analysis of the CROW Response to the Variation of CROW Parameters

In the preceding analysis, the CROW was considered to be made of ideal resonators with no intrinsic loss, and all the resonators were similar with the same resonance frequency. However, in practice, there are some non-idealities that can perturb the CROW parameters and consequently distort the CROW response. These non-idealities can be the outcome of either the imperfections induced during the fabrication of the structure or the systematic limitation in the resonators and the coupling geometry that cannot provide the desired coupling parameters. In this section, these non-idealities are studied and their effects on the response of the CROW are presented.

7.2.1.1. Effect of Finite quality Factor of Resonators on the Response of CROW

In this section, by considering a resonator finite-intrinsic lifetime (τ_0) and put it into the coupled-mode relations in Equation (7.1) and considering the same coupling coefficients given by Equation (7.4), the spectrum of a finite-sized CROW is analyzed. Figures 7.6(a) and 7.6(b) show the transmission responses of CROWs with $N = 2$ and $N = 6$, respectively, for different ratios of intrinsic lifetime of the resonator to the coupling lifetime (i.e., τ_0/τ_c). The solid and dashed curves correspond to the drop port and the through port transmissions, respectively. Also, the insets in the figures show the zoomed views of the transmission of the drop port. As seen from Figures 7.6(a) and 7.6(b), by decreasing τ_0/τ_c, the insertion loss of the

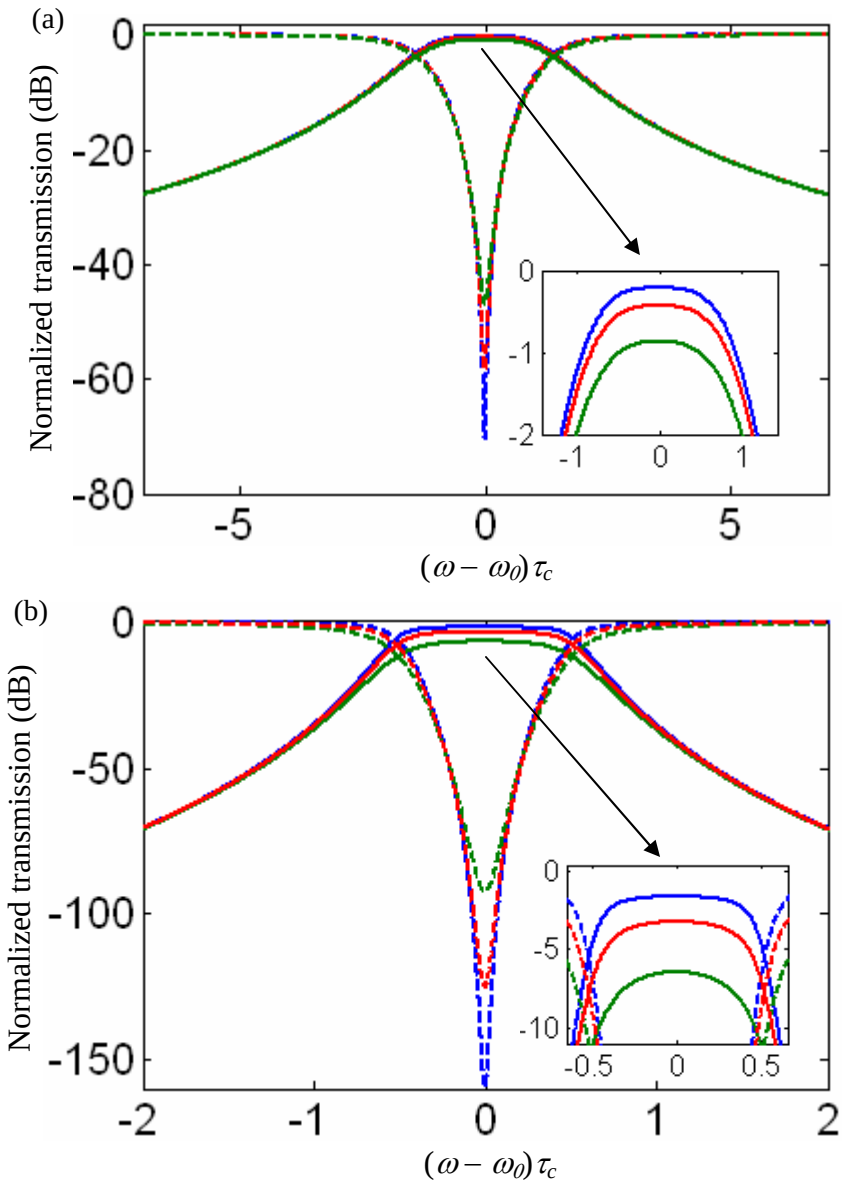

Fig. 7.6: Transmission responses of the drop port (solid curves) and the through port (dashed curves) for a CROW structure made of (a) N=2 resonators and (b) N=6 resonators. The simulation has been performed for τ_0/τ_c = [10, 20, 40] as plotted by the colors green, red, and blue, respectively. The insets in the figures show the zoomed views of the regions specified in the figure. The coupling coefficients of the CROW have been obtained from Equation (7.4).

structure increases correspondingly. In other words, part of the energy of resonators, instead of leaking into the neighboring resonators, leaks out of system as loss. This

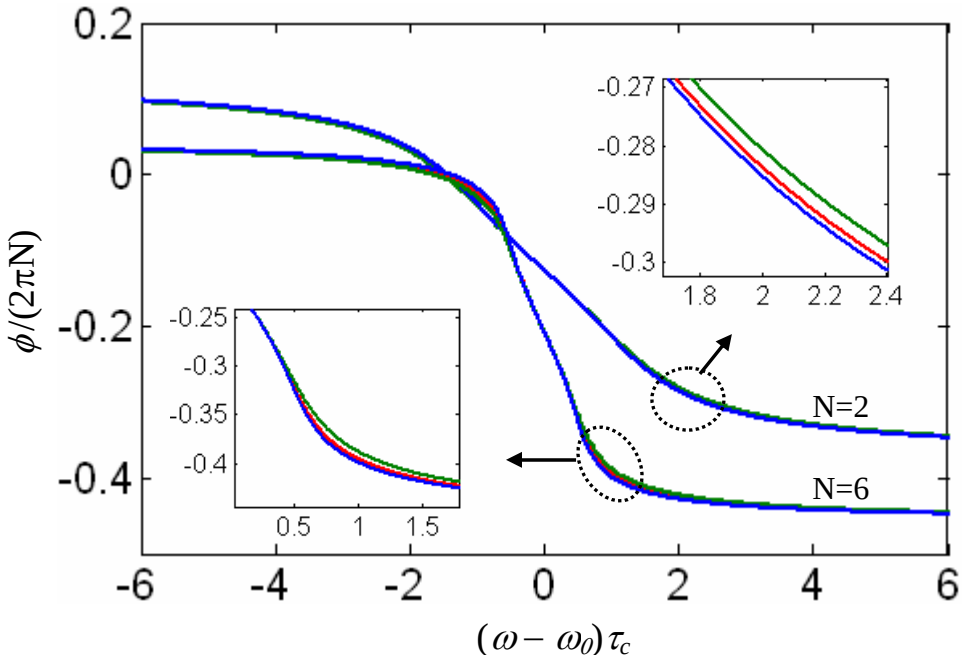

Fig. 7.7: The phase response of the transmission at the drop port for CROW structures with N = 2 and N = 6 resonators and described in Fig. 7.6. The simulation has been performed for τ_0/τ_c = [10, 20, 40] as plotted by the colors green, red, and blue, respectively. The insets in the figures show the zoomed views of the regions specified in the figure.

loss is stronger in the middle of the CROW where the coupling between the resonators is weaker. For the case of N = 2, as shown in Figure 7.6(a), the insertion loss at the drop port is smaller compared to the case of N = 6, which is shown in Figure 7.6(b). This smaller drop port insertion loss results for two reasons: 1) Increasing the number of the resonators, with their finite intrinsic lifetimes, increases the loss, and 2) a CROW with a larger number of resonators has weaker coupling coefficients between its resonators (this was shown in Figure 7.3). Hence, for the CROW with N = 6, the time rate of energy coupling from each resonator to the adjacent (to the adjacent what?) can become comparable to the intrinsic lifetime of the resonator, which represents the loss.

While the intrinsic lifetime of the individual resonators can dramatically change the insertion loss of the CROW, the phase response of the CROW is less affected. Figure 7.7 shows the phase response of the drop port for the CROW structures described in Figure 7.6. As seen from this figure, the effect of changing the intrinsic lifetime of the resonator on the phase response is small. This is because the phase (or the group delay, which is the slope of the phase) is mostly controlled by the coupling coefficients in the CROW structure.

7.2.1.2. Sensitivity of the CROW Response to the Variations in Coupling Coefficients

Another issue to be addressed is the sensitivity of the CROW response to the variation of coupling coefficients. These variations can come from the randomness in the fabrication that changes the spacing between the resonators. Hence, for the same level and strength of randomness, we expect the coupling coefficients between the resonators at the middle of the CROW to be more sensitive to the randomness, as they are weaker (as shown in Figure 7.3). In addition, we expect CROWs with a larger number of resonators to be more sensitive to randomness, as their coupling coefficients are weaker compared to CROWs with fewer resonators (as shown in Figure 7.3). In the following, we consider a CROW made of two resonators and study the effect of change on the coupling coefficients.

Figure 7.8 shows the transmission response of a CROW with $N = 2$ when the coupling lifetime of the input waveguide to the resonator is subject to change. As seen from this figure, by a ±20% change of τ_{in} (while keeping τ_{out} fixed), the

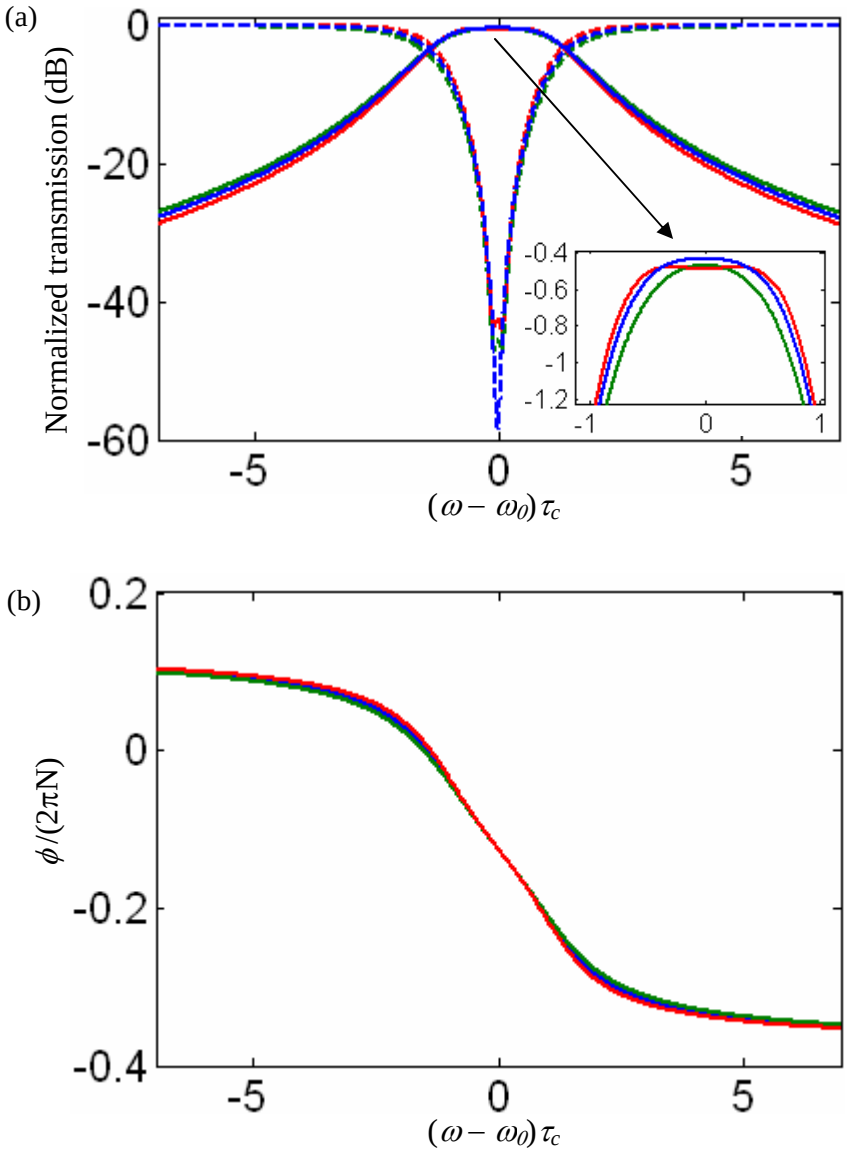

Fig. 7.8: (a) Transmission responses of the drop port (solid curves) and the through port (dashed curves) and (b) the phase response of the transmission at the drop port for a CROW structure with N = 2 resonators and with τ_0/τ_c = 20 for the cases when the coupling lifetimes at the input (τ_{in}) and the output (τ_{out}) ports are imbalanced. The simulations were performed for the cases of τ_{out}= τ_c and τ_{in} = [0.8, 1, 1.2] as plotted by different colors of green, red, and blue, respectively. The inset in (a) shows a zoomed view of the regions specified in the figure. The coupling coefficients of the CROW have been obtained from Equation (7.4).

transmission in the through port dramatically changes. However, the transmission

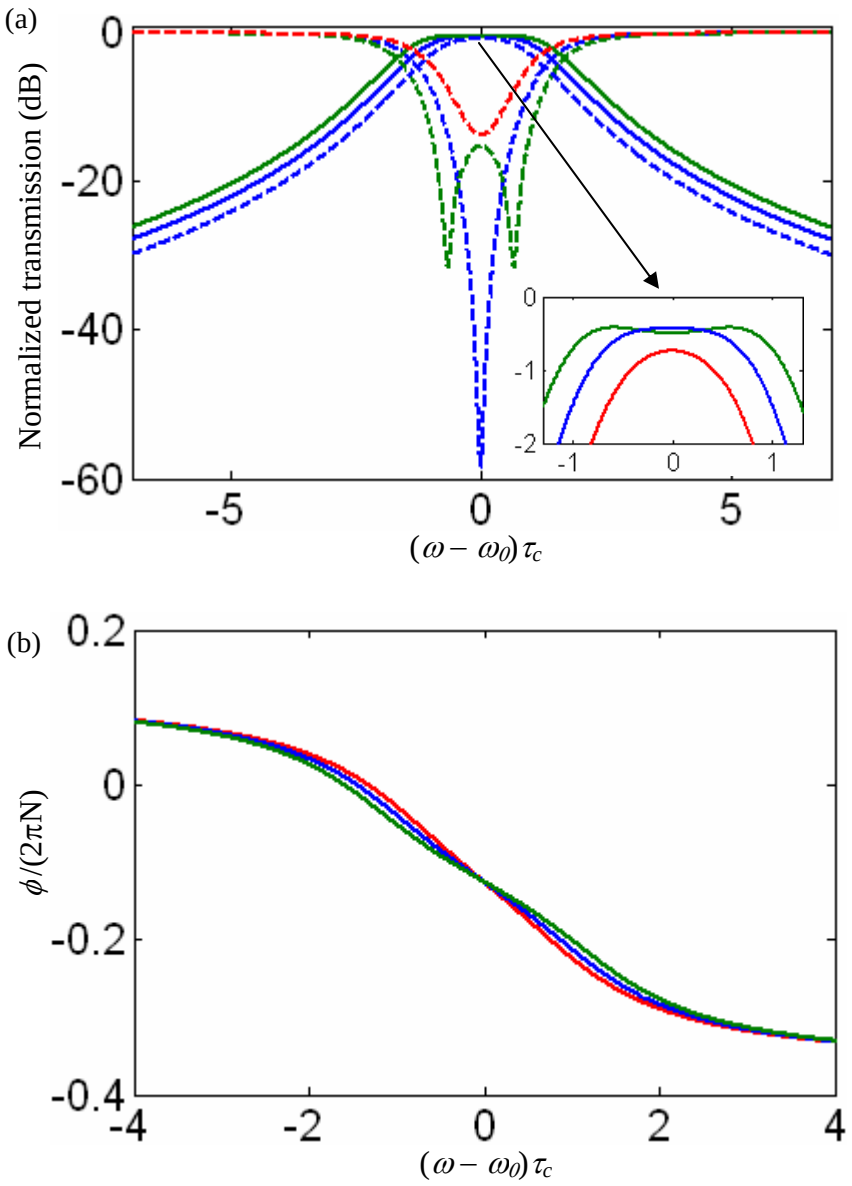

Fig. 7.9: (a) Transmission responses of the drop port (solid curves) and the through port (dashed curves) and (b) the phase response of the transmission at the drop port for a CROW structure with $N = 2$ resonators and with $\tau_0/\tau_c = 20$ for the cases when the coupling coefficient (μ) between the two resonators deviates from its original value. The simulations were performed for the three new coupling coefficients as $\mu' = [0.8\mu,\ 1\ \mu,\ 1.2\ \mu]$, which are plotted by different colors of green, red, and blue, respectively. The inset in (a) shows a zoomed view of the regions specified in the figure. The original coupling coefficient has been obtained from Equation (7.4).

response of the drop port has a smaller change. Nevertheless, the flatness of the drop

port transmission is modified. Also, the phase response of the drop port is shown in Figure 7.8(b), where small distortion is observed. By further increasing the coupling coefficients, we expect more distortion in the response of the resonator. More distortion in the CROW response is observed when the coupling between the resonator changes. Figure 7.9(a) shows the transmission response of the CROW when the coupling coefficient between the two resonators is subject to a ±20% change. As predicted before and seen from this figure, the distortion in the transmission response has become stronger. Also, the distortion in the phase response of the drop port transmission, as shown in Figure 7.9(b), is larger compared to the one shown in Figure 7.8(a).

The simulations in Figures 7.8 and 7.9 were for a CROW with $N = 2$. However, when the number of resonators increases, a stronger distortion in the CROW response is expected, as the coupling coefficients are smaller.

7.2.1.3 Sensitivity of the CROW Response to the Deviation of the Resonance Frequency of Resonators

The resonance frequencies of the resonators in a CROW may deviate from their original value mainly by (use periods after the numbers)

1- Imperfection in the fabrication that is random. Therefore, the geometry of the resonators may slightly differ from each other. We call this effect the fabrication-imperfection-induced frequency shift (FIFS) effect.

2- Effect of the coupling between the resonators that perturb each other and shift their resonance frequency [84]. This phenomenon, which is called

coupling-induced resonance frequency shifts (CIFS) [84], was recently investigated in greater detail in the context of coupled-resonator structures [84, 108].

Combining all the effects mentioned above, the new resonance frequency of the n-th resonator in the CROW structure is

$$\omega_{0n} = \omega_0 + \Delta\omega_{0n}, \tag{7.5}$$

where $\Delta\omega_{0n}$ is the net shift in the resonance frequency, which is

$$\Delta\omega_{0n} = \Delta\omega_{0n}\big|_{FIFS} + \Delta\omega_{0n}\big|_{CIFS}. \tag{7.6}$$

Hence ,for more accurate analysis, the new resonance frequencies of the resonators obtained from Equation (7.5) should be put into the coupled-mode relations in Equation (7.1). Intuitively, if the amounts of these resonance shifts are comparable to the CROW bandwidth, a strong distortion in the CROW response is expected. In the following analysis, we simulate the effect of these resonance shifts on the CROW response.

Figure 7.10(a) shows the transmission responses at the drop and the through ports of a CROW made of two resonators when the resonance frequency of the first resonator (close to the input waveguide) is slightly deviated from the original common frequency of the resonators. The simulation results are for three resonance deviations of $\Delta\omega_0$ = [0, -0.5/ τ_c, -1/τ_c]. The 3-dB bandwidth of the unperturbed case ($\Delta\omega_0$ = 0, the blue curve) is ~ 2/τ_c. As seen from Figure 7.10(a), by increasing the frequency deviation, 1) the insertion loss of the drop-port transmission increases, 2) the band flatness of the drop-port transmission with the above frequency deviations

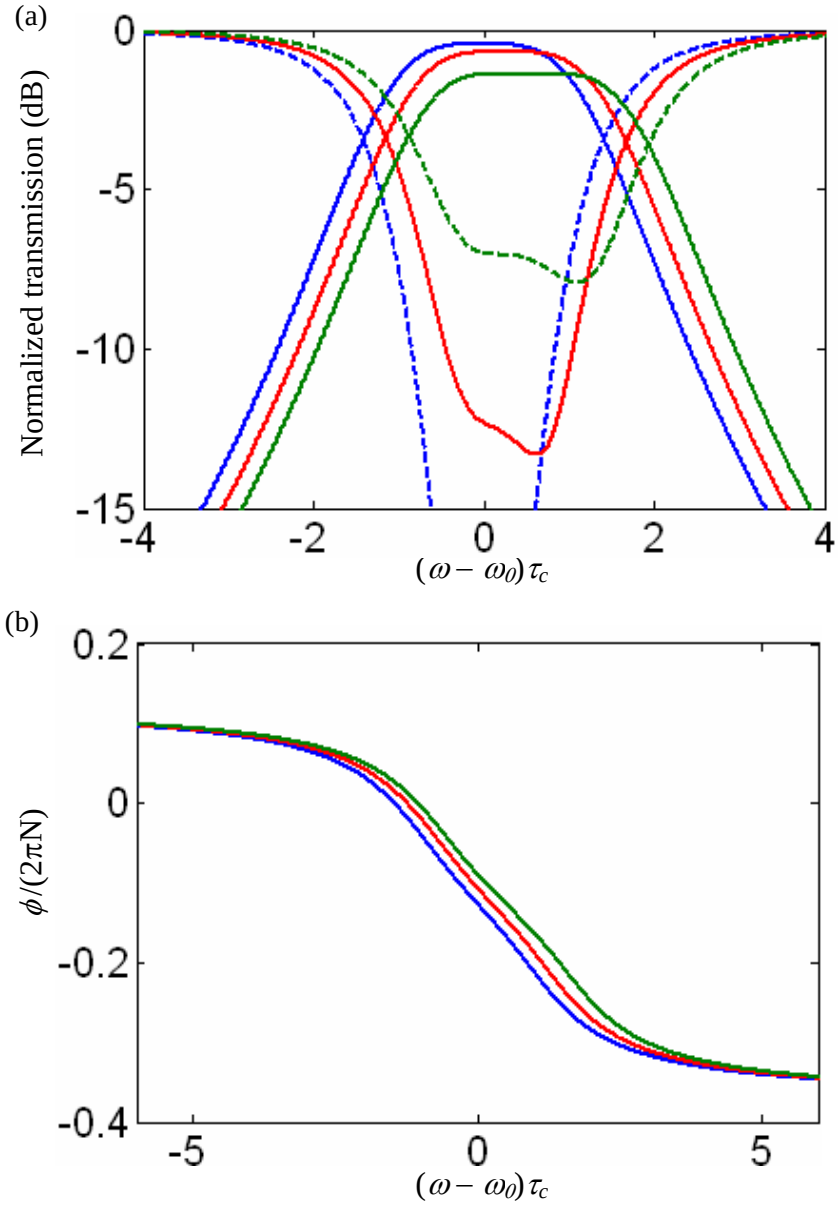

Fig. 7.10: (a) Transmission responses of the drop port (solid curves) and the through port (dashed curves) and (b) the phase response of the transmission at the drop port for a CROW structure with N=2 resonators and with $\tau_0/\tau_c = 20$ for the cases when the resonance frequency of the bottom resonator (close to the input waveguide) has been deviated from its original value (ω_0). The amount shifts are $\Delta\omega_0 = [-1, -0.5, 0]/\tau_c$,which are plotted by different colors of green, red, and blue, respectively. The inset in (a) shows a zoomed view of the regions specified in the figure. The original coupling coefficient has been obtained from Equation (7.4).

is less affected, and 3) the through-port transmission response is strongly perturbed. The phase response of this CROW structure under the resonance frequency deviations mentioned above is shown in Figure 7.10(b). As seen from this figure, the shapes of phase responses under these changes are still similar to those of the unperturbed CROW. However, by further increasing the resonance deviation close to or larger than the bandwidth of the unperturbed CROW, stronger distortion in the CROW response is expected. Depending on the accepted level of distortion, the allowed level of the resonance frequency deviation in a CROW is determined. For example, the results for the case of $\Delta\omega_0 = -0.5/\tau_c$ (the red curve) shown in Figure 7.10(a) may be satisfactory for some applications.

The response of a CROW with more resonators is more sensitive to the frequency deviation of the resonators, especially for the middle resonators whose coupling coefficients are weaker. To verify this fact, Figures 7.11(a) and 7.11(b) show the drop-port and the through-port transmission responses of a CROW made of $N = 4$ resonators under the following cases of resonance frequency deviations: 1) none of the resonators show deviation (the blue curve), 2) only the resonance frequency of the first resonator (close to the input waveguide) has a deviation of $\Delta\omega_0 = -1/\tau_c$, 3) only the resonance frequency of the second resonator (close to the input waveguide) has a deviation of $\Delta\omega_0 = -0.5/\tau_c$. Compared to the simulation results shown in Figure 7.10 (which was for a CROW made of two resonators), the simulation results in Figure 7.11 show a stronger distortion in the CROW response. For the third case (the green curve) in Figure 7.11, the distortion

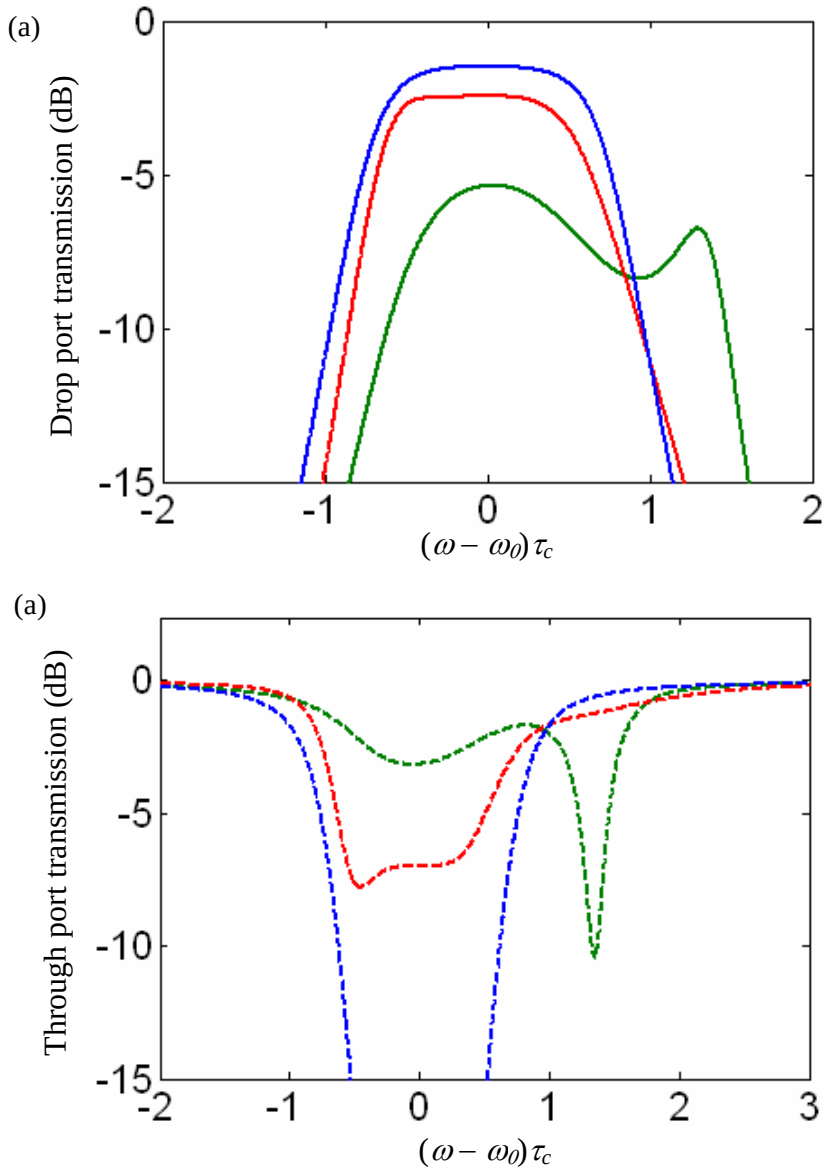

Fig. 7.11: Transmission responses of (a) the drop port and (b) the through port of a CROW structure with N = 4 resonators and with τ_0/τ_c = 20, for the three following cases: 1) the resonance frequency of the all the resonators is the same as ω_0 (the blue curves), 2) only the resonance frequency of the 1st resonator (close to the input waveguide) has been deviated by an amount of $1/\tau_c$ (the red curves), 3) only the resonance frequency of the 2nd 1st resonator (close to the input waveguide) has been deviated by an amount of $1/\tau_c$ (the green curves). The coupling coefficient has been obtained from Equation (7.4).

is so strong that, in addition to a large insertion loss, no flatness in the drop-port transmission is observed. Also, the through-port response has been almost destroyed. This strong distortion shows the effect of the larger sensitivity of the middle resonators to the resonance shift on the CROW response. In the next section, the design and experimental demonstration of CROWs made of silicon microresonator are presented.

7.3. Design and Experimental Demonstration of Coupled-resonator Filters

In this section, flat-band filters are designed, fabricated, and characterized using the coupling coefficients given by Equation (7.4) for a Butterworth CROW filter. The design process is as follows:

1- Find the number of the resonators and the coupling coefficients from Equation (7.4) and coupled-mode relations in Equation (7.1) based on the required bandwidth of the filter, its sharpness at the edges of the band, and the allowed insertion loss. The intrinsic lifetime of the resonators (τ_0) has to be put into Equation (7.1) to obtain the insertion loss of the filter. The value of τ_0 is obtained by characterization of the individual resonators, which was described in chapter 5. As an example, by considering the number of resonators to be $N = 5$ and an initial coupling lifetime (τ_c), the coupling parameters from Equation (7.4) are obtained and put into Equation (7.1) and the spectrum of the transmission is observed. If the bandwidth, the sharpness, and the insertion loss are satisfactory, we use the calculated coupling coefficients for the next step; if not, we change the number of

resonators or τ_c or both. Another alternative solution is to use other filter architectures such as a Chebyshev filter, which was not discussed in this research. Having the number of the resonators, the coupling coefficients between the resonators, and the coupling lifetime between the waveguide ports and the resonator, we need to find the spacing between the resonators as well as the spacing between the waveguide and their adjacent resonators.

2- Find the resonator dimensions that have a resonance frequency corresponding to the center frequency of the filter. This is done by the modeling tool explained in chapter 2.

3- Find the waveguide dimensions and the spacing between the waveguide and the adjacent resonator that result in the coupling lifetime τ_c. This can be done by finding the coupling coefficient (κ) between the waveguide and the resonator from Equation (3.63) (in chapter 3) for different waveguide dimensions and waveguide-resonator gaps until the required coupling lifetime (which is related to the coupling coefficient as $\tau_c = 2/|\kappa|^2$) is found(?). For this purpose, the engineering and optimization techniques for the waveguide-resonator coupling presented in chapter 3 are very helpful.

4- Find the inter-spacing between the resonators that provides the required coupling coefficients (e.g., as given by Equation (7.4) for a Butterworth design). From coupled-mode theory, the coupling coefficient between the m^{th} and the $(m+1)^{th}$ resonators in a CROW structure can be found as (see Appendix E)

$$\mu_m = -\frac{\omega_0}{4} \frac{\int_{V_{m+1}} \varepsilon_0 \Delta n^2 E_m^* E_{m+1}}{(\int_{V_m} \varepsilon_0 n^2 \mid E_m \mid^2 / 2)(\int_{V_{m+1}} \varepsilon_0 n^2 \mid E_{m+1} \mid^2 / 2)}, \quad (7.7)$$

where E_m and E_{m+1} are the electric field profiles of the mth and (m+1)th resonators, respectively, Δn^2 is the squared refractive index perturbation caused by the (m+1)th resonator in the vicinity of the mth resonator. The integral in the numerator is taken over the volume of the (m+1)th resonator, which is the perturbing element, and the integral in the denominator is the unperturbed energy of the mth resonator. Hence, by adjusting the spacing between the resonators, the coupling coefficient can be calculated from Equation (7.7) and compared to the desired value (which is given by Equation (7.4) for a Butterworth design).

7.3.1 Experimental Results

For the implementation of the CROW structure in this thesis, miniaturized high Q microdisk resonators were considered. In chapter 2, the reasons to support microdisk structures for miniaturization were explained and in chapter 5, experimental Qs > 10^5 were demonstrated for these structures, even with the presence of oxide cladding. Hence, in addition to compactness and large FSR, we expect to obtain low insertion loss filters. Also, such small structures have the potential to support only one radial mode in the entire FSR range.

As discussed in the previous section, the CROW response is very sensitive to any deviation in its parameters, especially to the resonance mismatch between the

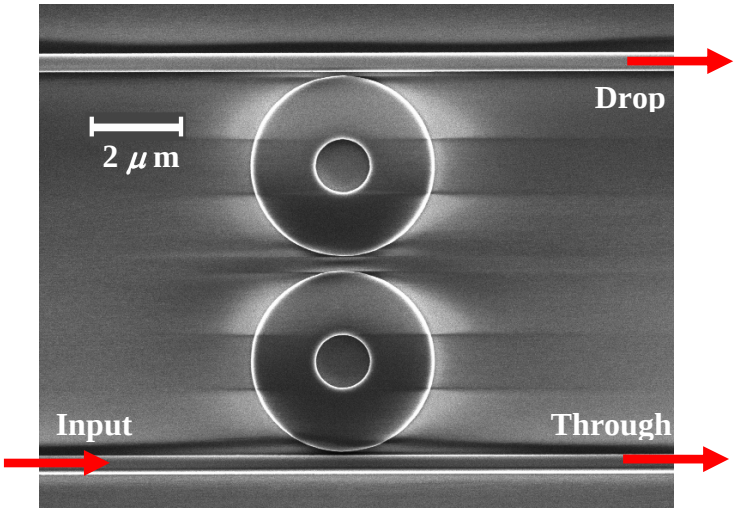

Fig. 7.12: SEM image of a typical coupled-resonator filter fabricated in this research. The filter is made of two miniaturized resonators with radii ~ 2 μm. The structure is covered by oxide. The details of the dimensions of the structure are shown in Table 7.1.

resonators. Hence, for the fabrication of the structure, we used our second process flow (as explained in chapter 4) that was developed based on HSQ negative electron resist for hyper-fine control of the dimensions. In addition, the structure was covered by a PECVD oxide cladding, as discussed in chapter 4.

Figure 7.12 shows the SEM image of a typical fabricated CROW filter made of two resonators. As seen in this figure (and discussed in chapters 2 and 5), there is an etched hole at the center of the resonator. In addition, as explained in chapter 2, by adjusting the radius of this hole, we can easily fine tune the resonance wavelength in the sub-nanometer range (which is cumbersome to achieve by changing the size of the microdisk radius). This fine-tuning capability is very useful to compensate the CIFS effect.

Table 7.1: Two sets of dimensions designed for the coupled-resonator structure shown in Figure 5.13. The thickness of the silicon layer was ~ 220-230 nm.

	Resonator internal/external radii (μm)	Waveguide width (nm)	Waveguide-resonator gap (nm)	Resonator-resonator gap (nm)
Design set 1	0.6 / 2	400	100	340
Design set 2	0.6 / 2	380	50	220

To obtain different filter bandwidths, two sets of dimensions were designed for the CROW structures shown in Figure 7.12. Table 7.1 shows these designed parameters for the waveguide and the resonators and the spacing between them.

Figure 7.13(a) shows one FSR of the spectrum of the transmission response of the drop port shown in Figure 7.12 and with the dimensions corresponding to design set 1 in Table 7.1. The locations of the resonances in this figure correspond to the resonances of the 1st order radial mode of the microdisk constituting the CROW filter. From Figure 7.13(b), we can see that except for the 1st radial order mode, all higher-order modes are in the noise floor. Figure 7.13(b) shows a zoomed view of the transmissions of the through port and the drop port. As seen from this figure, more than a 10 dB extinction is observed in the through-port response. From theory, the expected extinction is more than 60 dB. However, the resonance misalignment of the individual resonators and changes in the gaps introduced by fabrication imperfection have limited the through-port extinction. A 3 dB bandwidth of 0.4 nm was obtained for this filter realized with design set 1 in Table 7.1.

Figure 7.14 shows the spectrum of the drop port and the through port of the CROW filter shown in Figure 7.12 and with the dimensions corresponding to design

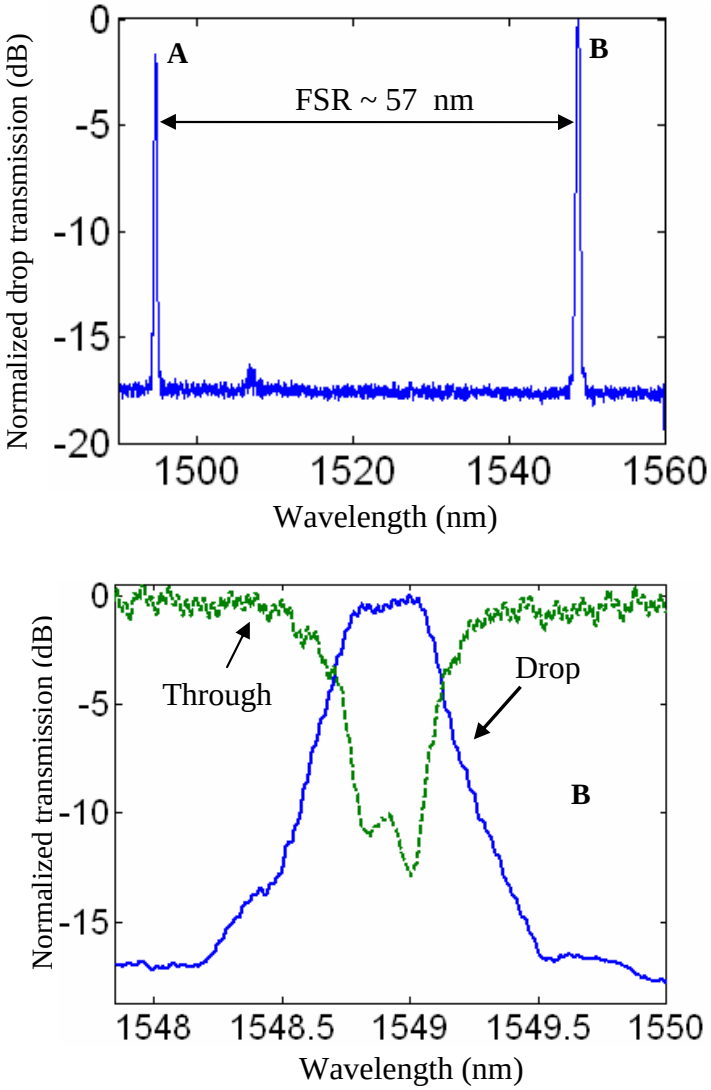

Figure 7.13: (a) Spectrum of one FSR of the normalized drop-port transmission for the coupled-resonator filter shown in Figure 7.12 and with design set 1 shown in Table 7.1. (b) A zoomed view of point **B** in (a) where transmissions of both the drop port and the through port are plotted. More than a 10 dB extinction is observed in the through-port response.

set 2 in Table 7.1. As seen from Figure 7.14, more than 16 dB extinction is observed in the response of the through port. However, by reducing the mismatch between the resonance frequencies of the resonators, as well as adjusting the gaps, better performance can be obtained for this filter. The drop-port response is quite flat,

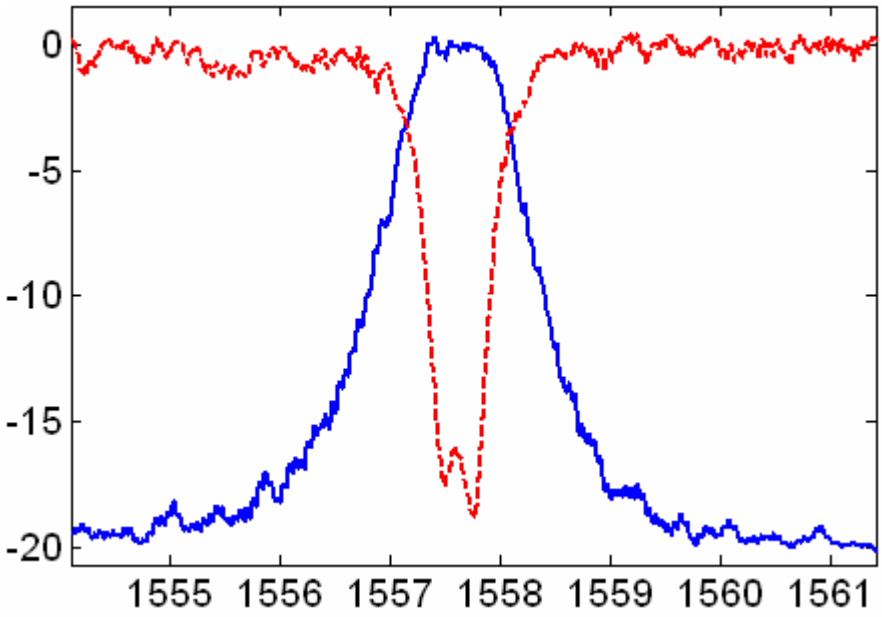

Fig. 7.14: The spectrum of the drop port and the through port of the coupled-resonator structure shown in Figure 7.12 and with design set 2 shown in Table 7.1. The 3 dB bandwidth is ~ 0.95 nm. More than a 16 dB extinction is observed in the through-port response.

with a 3 dB bandwidth of ~ 0.95 nm. From theory, the insertion loss of the filter is expected to be below 0.5 dB. Such an efficient performance for the filter shown in Figure 7.14 can inspire many applications based on ultra-compact coupled-resonator filters.

7.3.2. More on CIFS Effect

In some circumstances, the resonance shift of the resonator, because of the CIFS effect, can be even larger than the bandwidth of the CROW. As a result, this effect has to be considered in the analysis and be compensated. From coupled-mode theory and to the 1st order approximation, the resonance shift of a resonator due to the perturbation (i.e., CIFS) can be calculated as (see Appendix E)

$$\frac{\Delta\omega_{CIFS}}{\omega_0} = -\frac{1}{4}\frac{\int_{V_p}\varepsilon_0\Delta n^2 \mid E\mid^2}{\int_V \varepsilon_0 n^2 \mid E\mid^2 /2}, \tag{7.8}$$

where E is the resonator electric field; the integral in the numerator is taken over the perturbation volume with Δn^2 as the square refractive index perturbation. For a CROW filter made of two identical resonators, identical input and output waveguides, and identical gaps between the waveguides and the resonators at the input and the output, both resonators experience the same level of CIFS, as they experience identical perturbations. Hence, both resonators (after adding the CIFS effect) have the same resonance frequencies and no distortion in the filter response occurs. Therefore, in contrast to CIFS, in this case the FIFS effect in the resonators and other fabrication imperfections that change the gaps become important. However, for CROW structures made of more than two resonators, the CIFS effect becomes important, as the perturbation (and consequently, the CIFS) on the first and the last resonators is stronger. This is because these two resonators are adjacent to the waveguide with much smaller gaps compared to the inter-spacing between the resonators in the middle of the CROW. For such cases, the resonance frequencies of the resonators have to be tuned to compensate this effect. This can be done either passively by slightly modifying the dimensions of the resonators before the fabrication to compensate the CIFS effect or by dynamically tuning them after fabrication. The latter approach can be done by integrating microheaters on the cladding of the resonators and using the strong thermo-optics coefficient (dn/dT =

1.84×10^{-4}) of silicon for changing the refractive index and as a result, the resonance frequencies of the resonators.

7.4 Chapter Summary

In this chapter, we developed a systematic method for the design of a finite-sized CROW with a flat-band response using coupled-mode theory in time and also borrowing techniques from filter design in circuit theory. A direct correspondence between a ladder-type LC circuit and a finite-sized CROW was established. Using the closed-form expressions for the L and C components for the Butterworth filter design, a closed-form analytical formula for the coupling coefficient of a CROW with a Butterworth response was extracted. An analysis of the effect of non-idealities, such as resonator intrinsic loss, perturbation in coupling coefficients, and also shift in the resonance frequency of the resonators, on the response of the CROW was performed. Using this powerful technique, we designed and fabricated coupled-resonator filters with high Q miniaturized microdisk resonators (as demonstrated in chapter 5). As the CROW response is very sensitive to the resonance mismatch of the resonators in it, the second fabrication process flow, which consisted of high-resolution HSQ electron resist (as explained in chapter 4), was used. We were able to demonstrate very compact and low insertion loss filters with a flat-band response and with bandwidths ranging from 0.4 nm to 1 nm. In addition to being very efficient, these are the most compact filters that have been demonstrated in a SOI platform by traveling-wave resonators. Such compact and large FSR filters can provide a gateway for dense and large-scale silicon

nanophotonics. Despite many advances in fabrication, randomness in the fabrication still exists, which can distort the CROW response by mismatching the resonance frequencies of the resonators. Hence, to achieve a lower distortion in the CROW response, an alternative solution is the thermal tuning of the resonators (using the integrated microheaters on top of the cladding of the resonator) to compensate the resonance mismatch between them. This promising solution can be pursued in the future.

CHAPTER 8

FUTURE DIRECIONS

In this chapter, the remaining work and future directions as an extension of this research are presented. Listed are some of the promising applications with a potentially major impact.

8.1. Improving the Fabrication of Resonators

In this thesis, we showed world-record Qs for silicon microdisk resonators in both large-scale (radius ~ 20 μm) and ultimate miniaturized scale (radius ~ 1.5 μm). However, the achieved Qs are still limited by fabrication imperfections and their consequent non-idealities that appear at the sidewall of the resonator. For example, for a Si microdisk with a radius of 20 μm, the theoretical Q is more than 10^{12}, and the bulk absorption Q (according to the doping level of the SOI wafer) is ~ 30 million, while our achieved Q was about 3 million. Hence, there is still room to improve the fabrication of these resonators. The future steps to improve the fabrication of these resonators are as follows:

1- A better optimization of nanolithography to reduce the roughness at the sidewall of the patterned resist. Figure 8.1 shows some of the imperfections that appear in the pattern during lithography. In addition to sidewall roughness, resist residue appears as foot points at the bottom of the sidewall of the pattern, as shown in Figure 8.1 (left). Currently, e-beam lithography is the most promising technology that can

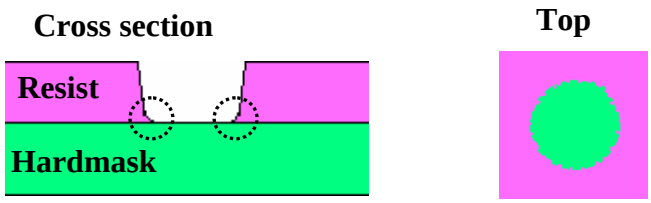

Fig. 8.1: Cross section (left) and the top (right) views of a circular pattern after written by e-beam lithography and developed. Foot points (as specified in the doted circles) in the left figure are due to the imperfection of e-beam exposure and development. Top view in the right figure shows the sidewall roughness.

provide smoother sidewalls for the pattern. Nevertheless, more effort is required to reduce the sidewall roughness and remove the foot points.

2- Adding a short-time etching step to gently smooth the sidewalls of the patterned resist as well as remove the foot points, as shown in Figure 8.1. The plasma parameters for this etch provide very slow etching with very low energy ions.

3- The etching of Si should be slow, with low energy ions to have less crystalline damage at the sidewalls of the resonator.

4- For post-processing steps, in addition to oxidation and wet chemical processing mentioned in chapter 4, the sidewalls of the resonator can be treated by a pulse laser with appropriate energy so that the damaged sites on the sidewall of the resonator self-reconstruct and form their crystalline shape. This technique can be borrowed from the electronics industry, where the surface of the silicon is treated by a laser.

5- The fabrication process of a Si resonator on a thin Si pedestal layer should be optimized to remove any nanotrenching along the sidewall of the resonator. Currently, we use HBr/CF_4 chemistry to remove the nanotrenching. However, the

presence of CF_4 degrades the Q. Hence, this plasma needs more optimization, or we need to switch to another gas chemistry that does not result in nanotrenching.

8.2. Employing Nanoimprint Lithography for Mass-manufacturing of Nanophotonic Devices

In contrast to optical lithography, which is a parallel process with one time-beam exposure, electron-beam lithography is a serial and slow process that is not suitable for mass manufacturing. A promising alternative to alleviate this problem is nanoimprint soft lithography, which was introduced in recent years [111]. In this technique, a master mask is prepared that is typically made of Si, SiO_2, or SiN. This mask acts as a stamp and, similar to stamping, its patterns are imprinted on the resist layer (which is coated on top of the SOI wafer). As a result, without any lithography of the resist, the patterns are stamped on the resist. The master mask can be made by any kind of advanced lithography (to provide a high quality of patterns) and can be used for stamping with the potential for master mold reuse for repeated fabrication suitable for volume. In this context, promising research is to develop an optimal process for fabricating a master mask using e-beam lithography and advanced plasma etching. Several commercial imprinting tools are commercially available, including Nanonex Inc., Obducat Inc., and Molecular Imprints. However, the use of nanoimprinting techniques for fabricating ultra-high Q resonators and high-fidelity dense photonic integrated circuits in Si is still in its infancy, and a lot of future work is required to optimize several features of the imprint process, including 1) reduction of residual layer thickness; 2) suitable imprint process, e.g., UV/thermal;

and 3) whole-wafer molding versus step-and-repeat molding of a small mold over a whole wafer. These topics can be pursued in the future work.

8.3 Integration of Ultra-high Q Resonators with P-N Junctions

We saw that at high powers, TPA generates free carriers. TPA is in the nature of silicon, and there is nothing we can do about it, unless structural engineering at the molecular level modifies its electronic band diagram. However, the generated free carriers induced by TPA can be swept out of the resonator by integrating a P-N junction in the reverse bias. The P-N junction has already been integrated with ring resonators for the free-carrier removal/injection from/into the resonator [12]. Despite this achievement, there has not been a report on the simultaneous achievement of ultra-high Q properties and integration with P-N junction for a Si microresonator. To realize such an active ultra-high Q resonator, the process of the deposition of oxide, which is used as a cladding, and the position of the electrodes with respect to the resonator have to be optimized, in addition to optimizing the nanolithography and etching the resonator, the resonator dimensions, the thickness of the Si pedestal layer, which enable P-N junction fabrication,. I envision that implementing such structures will considerably improve the performance of ultra-high Q resonators at high powers where free-carrier loss is a limiting factor. In addition, by integrating an ultra-high Q resonator with a P-N junction, we can initiate a profound study on the effect of the free-carrier dynamic and its impact on the spectral response of the resonator.

8.4 Thermal Compensation of Ultra-high Q Resonators

Silicon has a large thermo-optics coefficient ($dn/dT = 1.84\times10^{-4}\ K^{-1}$). For some applications, such a large coefficient enables us to dynamically control the resonance frequency of the resonator by heating the resonator with very low power consumption. However, for ultra-high Q resonator applications at high powers, self-heating results in spectral broadening that degrades the performance of the resonator. Two possible solutions to reduce self-heating effect are as follows:

1- Increasing the thermal conductivity of the resonator [96]: This can be done by reducing the thickness of the BOX layer as well as adding a thin Si pedestal layer at the interface between the resonator and the substrate, as discussed in Appendix G. To obtain an ultra-high Q resonator, the thickness of the BOX layer has to be large enough to not degrade the Q through radiation. From chapter 2, we saw that for a silicon resonator with a thickness of 220 nm, a BOX thickness of more than 800 nm is required to have the radiation Q through the substrate be more than 10^7. Hence, a SOI wafer with a BOX thickness below 1μm is appropriate.

2- Covering the resonator with a low-loss material with a strong negative thermo-optics coefficient: This is another potential solution if an appropriate material with the desired thermo-optics coefficient is available. Currently, many such polymers are available. Therefore, more research is required on these polymers and their compatibility with silicon. Usually, the refractive indices of these polymers are close to 1.5. As a result, when they are used as the cladding layer, the majority of the resonator energy is inside the silicon. Hence, we need to thin the silicon thickness so that more resonator field is extended to the outside. However, the effect

of thinning on the Q of the resonator has to be investigated and an optimum thickness must be found to provide good thermal compensation while preserving the ultra-high Q properties.

8.5 Lab-on-a-chip Biological Sensing using Si Microresonators

One of the prominent potential applications of Si microresonators in a SOI platform is their integration with microfluidic circuits for biological sensing [112-113]. Several optical techniques have been studied for biosensing applications, and they have proven to have a relatively high sensitivity and provide short assay times [112,113]. Principally, in these techniques, the analyte binds specifically to a capture molecule, which is immobilized on the resonator surface. These optical sensors can be divided into two main categories: 1) mass sensors, where the presence of the captured analyte is measured by detecting the change in the refractive index or absorption, and 2) fluorescence sensors, where the emission of an immobilized tracer molecule or fluorescently labeled analyte is measured [114]. For both mass sensors and fluorescence sensors, the signal strength increases with the magnitude of the optical field interacting with the analyte residing on the sensor surface. In this regard, Si microresonators are particularly interesting, as they provide high Q and strong field enhancement in a small interrogation volume that makes them more sensitive to the change in the total bound mass. Consequently, the required fluid volume becomes comparable to the resonator volume, which enables quantitative and real-time measurements, fast sample preparation, and detection of extremely low analyte quantities. Integrated into a microfluidic setup, thousands of

such microresonators can be lined up for multi-analyte sensing within a few square millimeters of Si chip that can be mass manufactured with low- cost CMOS technology. Finally, the SOI platform is amenable to coating of a thin (< 10nm) layer of SiO_2 without affecting the optical performance of the resonators[71]. This enables the extensive and well-established surface chemistry processes developed for glass-based biochip arrays to be adapted directly to silicon-based biosensors.

Based on these motivations and promising targets, I did some early research and experiments on sensing with Si microdisk resonators integrated with a microfluidic channel in a SOI platform. While earlier work has shown the tuning of low Q resonance features using microrings [115], my focus was the integration of ultra-high Q silicon resonators with PDMS microfluidics [82]. Figure 8.2(a) shows the general schematic of waveguide-resonator coupling designed and fabricated for sensing, and Figure 8.2(b) shows the schematic of the integration of the resonator with the microfluidic channel. The details of the fabrication have been explained in chapter 4. The main advantage of microdisk resonators compared with other similar devices is that because of the traveling-wave nature of the mode inside the disk, 100% coupling of energy from a bus waveguide to the cavity is possible. In addition, by changing the cladding to a larger refractive index material, ultra-high Qs are still achievable.

In the experiment, liquids with varying (known) refractive indices were flown over the microdisk resonator to characterize the sensor for bulk refractive index

[71] In my experimental results in the previous chapters, I showed ultra-high Q resonator while a thin layer of SiO_2 (as a hardmask) was on the top surface of the resonator.

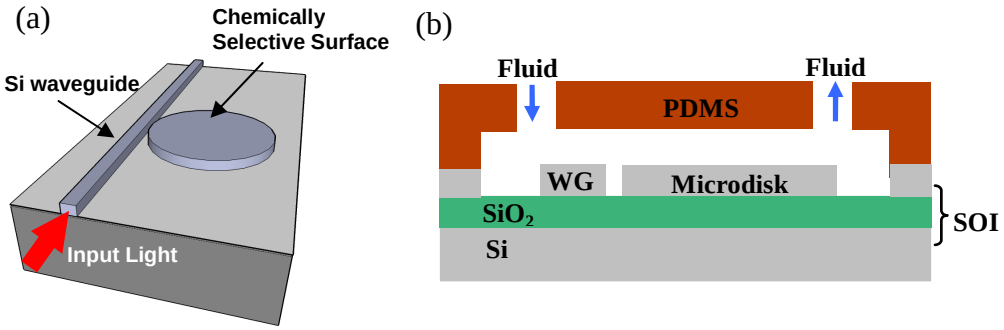

Fig. 8.2: (a) A silicon microdisk resonator coupled to a waveguide in a SOI platform. The surface of the resonator has been treated to be chemically selective. (b) Schematic of the microfluidic channel integrated with the resonator.

sensitivity. Following the injection of each refractive index fluid, the spectrum of the microdisk resonator was monitored using a swept-wavelength test setup. Figure 8.3 shows the variation of the resonance wavelength of the microdisk resonator when the refractive index of the fluid on top of the resonator was changed from 1.34 to 1.395. A resonance shift of approximately 0.4 nm was observed for a 0.055 index change. This corresponds to a bulk refractive index sensitivity of 8.2 nm/RIU (RIU stands for refractive index unit). In this particular experiment, we have observed a weaker evanescent field interaction due to the presence of a 25 nm SiO_2 layer on the top surface of the microdisk (used as hardmask in the fabrication process as well as to help bonding the PDMS to the resonator structure). For a minimal detectable resonance wavelength shift of 0.1 pm, the corresponding minimal detectable bulk cover refractive index shift is calculated to be 10^{-5} RIU. However, with suitable optimization and reducing the thickness of this hardmask, we should be able to approach 19.46 nm/RIU, as predicted by the theoretical calculations (where the

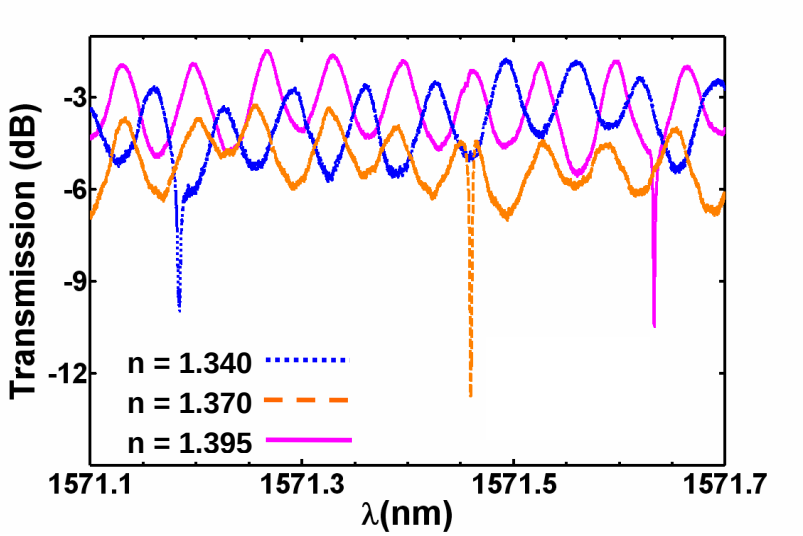

Fig. 8.3: Spectral response of the microdisk resonator sensor shown in Figure 8.2 where microdisk has a radius of 20 μm and a thickness of 230 nm. The waveguide has a width of 540 nm and the gap between the waveguide and the resonator is 220 nm. A ~25 nm oxide layer is left on top of the microdisk, which used as a hardmask for etching as well as for bonding the PDMS to the resonator structure. For this resonator being in the fluid, an ultra-high Q ~ 10^6 was measured. A resonance shift of ~ 0.4 nm is observed when the fluid refractive index is changed from 1.34 to 1.395. Hence, the resonance wavelength sensitivity was experimentally measured to be 8.2 nm/RIU for this sensor.

hardmask is absent). This sensitivity would enable a bulk refractive index resolution of 10^{-6} RIU.

One critical feature of this resonator-based sensor is its high sensitivity to the total bound mass due to the small interrogation volume caused by the ultra-compact device size. Hence, this naturally suggests that down-scaled microdisks would be more sensitive. The simulation results for the bulk cover refractive index sensitivity of a Si microdisk are shown in Figure 8.4. In these calculations we assumed the entire cover layer on top of the Si resonator was filled with a uniform refractive index. A bulk refractive index sensitivity of 50 nm/RIU is estimated for r = 1.5 μm microdisk, as seen in Figure 8.4. The bulk index sensitivity also increases with a

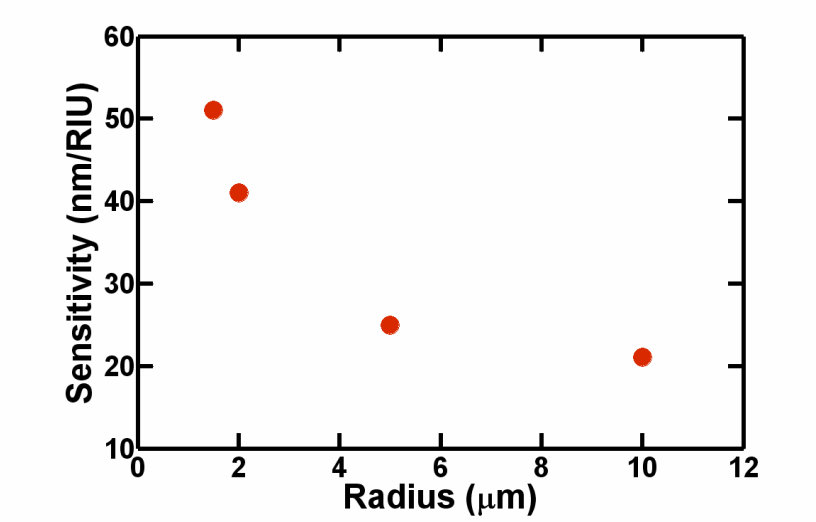

Fig. 8.4: Bulk refractive index sensitivity versus the microdisk radius for a microdisk thickness of 230 nm. The 1.5 μm radius microdisk shows a bulk index sensitivity of ~ 50nm/RIU.

reduction of the Si layer thickness as the electromagnetic field is extended more to the outside of the resonator and interacts with the bio-molecules.

Another important sensor metric for applications in label-free sensing is the mass sensitivity when a target molecule of interest attaches to a highly chemically specific surface coating on the top surface of the Si resonator. We expect the mass sensitivity of small resonators (because of their smaller mode volume) to be much larger compared to the larger resonators. Early calculations predict that for a wavelength resolution of 0.1 pm, we obtain a dramatic change in the mass sensitivity with the microdisk radius, with a sensitivity of 16 ag for the 1.5 μm radius microdisk.

To evaluate the performance of miniaturized microdisk resonators for sensing, we fabricated them and tested their spectrum with different cladding materials. Figure 8.5 shows the measured spectrum of a Si microdisk resonator with cladding

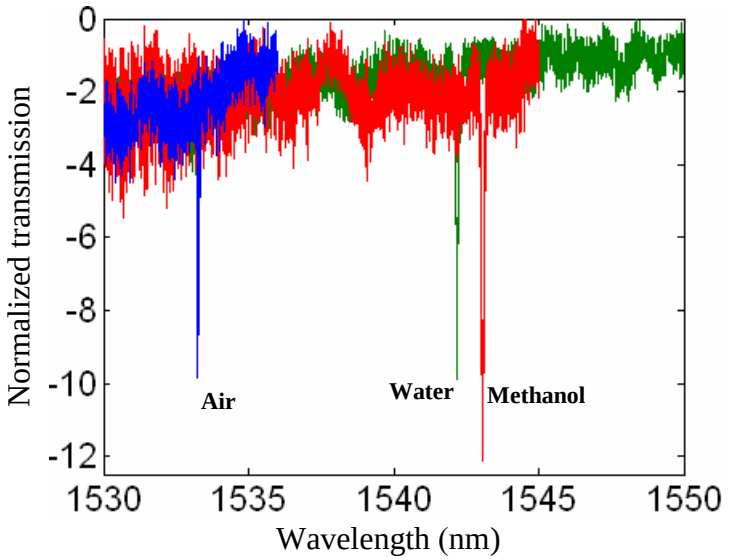

Fig. 8.5: Resonance spectrum of a microdisk resonator when the cladding material is air, water, and methanol, as specified. The microdisk has a radius of r = 1.53 μm and a thickness of ~ 220 nm and is coupled to a waveguide with a width of 400 nm. The gap between the waveguide and the resonator is ~ 210 nm. An intrinsic Q ≈ 10^5 was measured. A bulk-refractive index sensitivity of 27 nm/RIU is obtained for this disk. The presence of a ~60nm HSQ layer on the top of the disk results in the reduced bulk index sensitivity compared to the simulation, which shows a index sensitivity of ~ 50nm/RIU [116].

materials of air, water, and methanol. The microdisk has a radius of r = 1.53 μm and a thickness of 220 nm and is coupled to a waveguide with a width of 400 nm. The gap between the waveguide and the resonator is 210 nm. For this structure, only the 1^{st} order radial mode with a mode volume of 6.3 $(\lambda_0/n)^3$ and a very large FSR ≈ 70 nm was observed. When the cladding was air, an intrinsic high $Q \approx 10^5$ was observed for this mode. From the measured resonance shift induced by a change of the cladding material, a bulk-refractive index sensitivity of ~ 27 nm/RIU was obtained. The presence of the HSQ layer with a thickness ~ 60 nm on top of the disk resulted in the reduced bulk index sensitivity compared to the simulations shown in Figure 8.4 (which shows an index sensitivity of ~ 50 nm/RIU).

A main concern of using a microresonator in water is the large absorption of water at telecommunication wavelengths. At a wavelength range around 1300 nm, the water absorption loss is ~ 1 dB/cm. However, at a wavelength range around 1550 nm, the loss is ~ 40 dB, which is very large. One solution is to design the structure for operation in the 1300 nm range. However, when using a resonator at 1550 nm wavelength, a moderate Q in the range of 10^4 (and above) can still be obtained with small resonators. To give the reason behind this, we first introduce the effective total propagation loss of the resonator, which is defined as

$$\alpha_{total} = \frac{\alpha_{disk} \int_{V_{disk}} |E|^2 \, dv + \alpha_{water} \int_{V_{water}} |E|^2 \, dv}{\int_{V_{total}} |E|^2 \, dv} \quad , \tag{8.1}$$

where α_{disk} is the propagation loss of the disk as a result of fabrication imperfections and material non-idealities, and α_{water} is the absorption loss of water. The above equation can be arranged in the following format:

$$\alpha_{total} = \alpha_{disk} + \Gamma(\alpha_{water} - \alpha_{disk}) \quad , \quad \Gamma = \left(\int_{V_{water}} |E|^2 \, dv \Big/ \int_{V_{total}} |E|^2 \, dv \right) . \tag{8.2}$$

As we saw in chapter 2, in small radii resonators, more energy is extended to the outside compared to large radii resonator. Hence, the value of Γ for small resonators is larger. For large ultra-high Q resonators, the α_{disk} is much smaller than α_{water} (e.g., a Q ~3 million corresponds to α_{disk} ~0.2 dB/cm). Hence, with a very good approximation, for large ultra-high Q resonators we have

$$\alpha_{total} \approx \Gamma \alpha_{water} . \tag{8.3}$$

Table 8.1: Comparison of the parameters of two Si microdisk resonators with radii of 2 μm and 20 μm and with water cladding for the two cases of (a) water loss is absent, and (b) a water loss of ~ 40 dB/cm is present.

(a)

Disk radius (μm)	$a_{disk}(dB)$	Q	$V_m(\lambda^3)$	Q/V_m
20	0.2	3×10^6	4.37	4.87×10^5
2	4	1.5×10^5	0.2	7.5×10^5

(b)

Disk radius (μm)	$\alpha_{total}(dB)$	Q_{total}	$V_m(\lambda^3)$	Q/V_m
20	4.6	1.26×10^5	4.37	2.9×10^4
2	12	5.5×10^4	0.2	2.75×10^5

However, for small microresonators, where the resonator Q is smaller (as observed in the experiment) and α_{disk} is larger, Equation (8.2) needs to be accurately calculated. Tables 8.1(a) and 8.1(b) compare the parameters of two Si microdisk resonators with radii of 2 μm and 20 μm and with water cladding for the two cases: 1) water is considered to have no loss, and 2) water has a loss of 40 dB/cm. The intrinsic Qs given in Table 8.1(a) are based on our achieved experimental results[72]. As seen from Table 8.1(b), when the water loss is considered, the Q of the large resonator drops more than one order of magnitude when the resonator cladding is water. However, for the smaller resonator, the drop in the Q is only a factor of ~3. Hence, the Q/V of the large resonator degrades more compared to the small resonator when the water loss is considered. This can be seen from Table 8.1(b), where the Q/V of the smaller resonator has become almost one order of magnitude

[72] The Q~3×106 was shown for a microdisk with air cladding. However, if the cladding was lossless water, because of the large refractive index contrast between silicon and water, we would obtain almost the same results for Q.

larger than that of the large resonator. Hence, in such cases, larger Q/V can be achieved by using small resonators despite their lower values of Q (by one order of magnitude) compared to the ultra-high Q large resonators.

8.6 Large-scale Array of Small High-Q Microdisk Resonators for On-chip Spectral Analysis

In emerging applications such as lab-on-a-chip sensing, where there is a need for chip-scale devices to perform spectral analysis, a major challenge is achieving ultra-high spectral resolution (< 0.5 nm) in large-scale arrays. In this thesis, I showed miniaturized microdisk resonators with very high Qs, small linewidths, and large FSRs. As a result, I propose to use a large-scale array of these resonators for on-chip spectral analysis. Each resonator in the array corresponds to a spectral channel with a resonance frequency different than the adjacent resonators. As theoretically discussed in chapter 2 and experimentally demonstrated in chapter 5 (e.g., see Figure 5.16), by controlling the thickness and the outer radius of a miniaturized microdisk resonator, and in addition, by perforating the center of the microdisk to create a hole, we can design a high Q single-mode (1^{st} radial order mode) resonator. While coarse tuning the resonance wavelength is achieved by adjusting the outer radius of the disk (see Figure 5.17), fine tuning the resonance (<10 pm wavelength accuracy) is achieved by changing the size of the hole, which is far from the peak of the mode energy. Experimental results in chapter 5 (Figure 5.17) showed that linewidths of ~ 50 pm to 100 pm and FSR ~ 57 nm were obtained for the 1^{st} radial mode of a small microdisk resonator with a radius of 2 μm while all higher-order

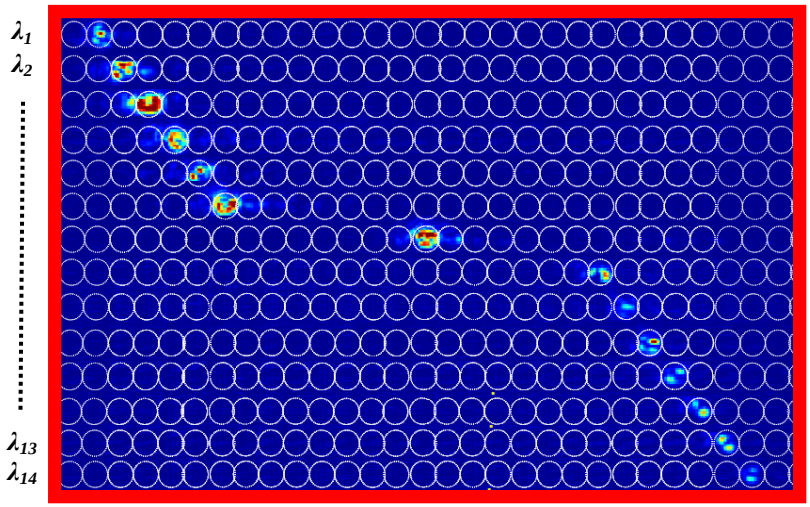

Fig. 8.6**:** Top view imaging of an array of 32 resonators coupled to a single bus waveguide. Each row corresponds to the scattering image for the input wavelength close to the resonance wavelength of each resonator.

modes were suppressed. In addition, the intrinsic $Q \approx 10^5$ was observed for the 1st order radial mode, which promises to obtain even finer linewidths. Integrating such a resonator structure with metal heaters enables the dynamic tuning of the resonator array. Figure 8.6 shows an out-of-plane image of the light scattering from the resonator array shown in Figure 5.13(a). The imaging was done by an infrared CCD camera. Each row in Figure 8.6 corresponds to the image for a separate input wavelength. As seen from this figure, at each wavelength corresponding to each row, one of the resonators in the row has most of the electromagnetic energy. Clear differentiation of spatial patterns for the resonance wavelengths with low crosstalk with adjacent resonators is observed, which is suitable for on-chip spectral analysis. While for this experiment 32 resonators were fabricated in the array, by using a large-scale array of such microdisk resonators, we can cover the entire FSR and

efficiently detect spectral signatures in the input at any wavelength within the FSR. Hence, using such small high Q resonators we envision the realization of an on-chip and compact broadband infrared spectrometer (bandwidth ~ FSR) consisting of hundreds of channels with a spectral resolution < 0.1 nm. In addition, by flip-chip bonding of a CCD chip on top of this spectrometer, optoelectronic conversion and data acquisition can be performed in a compact fashion. Fine tuning each spectral channel can be done by the thermal tuning of each resonator via integrating a microheater with the resonator.

Future work on this topic must focus on the development of ultra-compact high-resolution filter-bank arrays for on-chip spectral analysis, for detecting specific spectral signatures (e.g., SERS reporters) or monitoring the frequency peak shifts of resonator sensors due to binding events. The addition of on-chip spectral analysis would be a key enabler in developing practical lab-on-chip systems, which are not yet widely employed due to the expensive and cumbersome external optics for signal detection and spectral processing.

8.7. Tweezing and Trapping of Nanoparticles by Si Microresonators

Optical tweezing and trapping of nanoparticles in biology has inspired a lot of research during recent years. Using such a technique, biological nanoparticles (e.g., a cell) without any mechanical touch are trapped via the optical force. This optical force is induced by the gradient of the laser energy. As a result of the trapping, the nanoparticle is captured at a fixed position where its properties can be easily monitored and investigated. In addition, using this harmless optical force (which can

be applied at visible or IR wavelengths), the structure of the biological particle can be analyzed. A famous example of biological particle study is the unwrapping of DNA using optical force.

In current optical tweezing platforms, the optical trap is generated by a laser beam propagating in free space, and it uses macro-scale optical devices such as objective lenses. However, since the sizes of these biological particles are very small, an alternative efficient way of trapping is to miniaturize the trapping setup. In this regard, Si microresonators are very promising, as 1) they provide a strong evanescent (gradient) field close to the surface of the resonator; 2) because of their large Q/V they enhance and localize the electromagnetic field, which further enhances the amount of gradient; and 3) they are very compact and small. Recently, optical trapping using the evanescent field of a Si waveguide has been investigated, and promising results have been obtained [28]. However, the research on trapping nanoparticles with Si microresonators is new, as recent advances in the fabrications of these structures have provided large Q/V values for these resonators. Implementing a large-scale array of optical tweezers using Si microresonators can dramatically increase the speed and throughput of biological experiments. Such resonator structures are eventually integrated with microfluidic channels for sample delivery to the resonator.

8.8. Resonance Alignment of Resonators in Coupled-resonators Filters

As discussed in chapter 7, the performance of coupled-resonator filters is very sensitive to the misalignment of resonance frequencies of the individual resonators

from their common value. The presence of randomness in fabrication can cause nanometer-scale random changes in the dimensions of the resonators, which can strongly and randomly shift their resonance frequency. With the presence of such randomness, obtaining coupled-resonator filters with several resonators becomes very challenging. A promising solution that can be pursued as a research direction is to integrate these resonators with microheaters and use the thermo-optics properties of silicon to control the resonance frequency of each resonator individually. Using this thermal tuning approach, the random shifts in the resonance frequencies of the resonators can be compensated. In the fabricated coupled-resonator filters in this thesis, an oxide cladding was considered. The heater can be deposited on the oxide layer and optically far from the resonator in order to not distort the resonator mode. For microdisk resonators, the heater can be directly implemented on the silicon disk and close to its center, which is far from the optical mode energy of the disk. By optimizing the position and the geometry of the heater, a power-efficient coupled-resonator filter with a flat-band response made of many resonators can be realized. In addition, the heaters can act as switches to turn off the resonators (by shifting their resonance frequency from that of the other resonators) to strongly alter the filter response.

8.9 Compact and High-speed Modulators with Miniaturized Coupled-resonator Filters

Recently, electro-optic modulation in silicon has inspired a lot of research, with the intention of transferring high data bit rates from the electronic link to the optical link

for a 40 Giga bit/s Ethernet using a low-cost chip-scale device compatible with CMOS technology. For this purpose, two modulator architectures have been proposed. One is based on a Mach-Zehnder interferometer made of silicon waveguides [11,13], and the other one is based on microresonators [12]. In both cases, the modulation mechanism is based on injecting free carriers to change the refractive index. In the Mach-Zehnder architecture, one arm is integrated with a P-N junction for free-carrier injection into it, and in the resonator architecture, the P-N junction is integrated with the resonator to control its resonance frequency. The advantage of the Mach-Zehnder modulator is that it is broadband, and its disadvantage is that it is large. In contrast, the microresonator architecture is very compact and, in addition, it consumes very low power for its operation since it needs a very small free-carrier injection for its resonance shift. However, the drawback of the resonator-based architecture is that it is very narrowband, which is not suitable for most applications. In addition, the center wavelength of the incoming signal has to be lined up with the resonance wavelength of the resonator. However, for an off-chip laser source there is a ~ 0.1 nm uncertainty in the center wavelength of the laser. As a result, having a practical modulator based on a microresonator with a spectral linewidth less than 0.1 nm is very challenging.

Another potential solution to achieve compactness and low electric power consumption similar to the resonator-based modulator but with a bandwidth much larger than the laser source uncertainty is to use a coupled-resonator architecture, as shown in Figure 8.7. As shown in this figure, a P-N junction is integrated with one

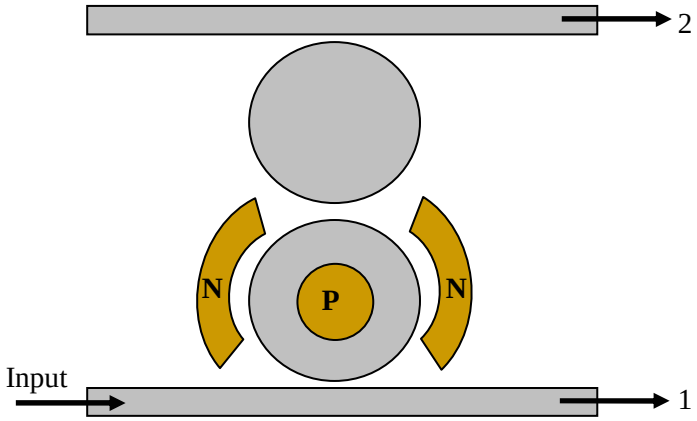

Fig. 8.7: A coupled-resonator structure integrated with a P-N junction for high-speed large-bandwidth electro-optic modulation.

of the resonators. When no carrier injection occurs, the coupled-resonator structure operates as an add-drop filter and sends the input light to port 2, as shown in the figure. However, when a large free-carrier injection occurs, the Q of the bottom resonator is strongly degraded and the coupled-resonator structure does not work as before. As a result, all the input light goes to port 1. Hence, by switching the P-N junction, the intensity at port 1 switches between 0 and 1. The research in this context covers theoretical electronic modeling of this switch (for predicting the ultimate achievable modulation speed), designing a coupled-resonator flat-band filter with low insertion loss, and integrating the P-N junction with optimum design and position for achieving high-speed modulation with low power consumption. For more compactness and low power consumption, miniaturized microdisk (microdonut) resonators with radii ~ 2-2.5 μm can be employed.

CHAPTER 9

CONCLUSION

The main focus of this Ph.D. research has been on the device physics, modeling, implementations, and applications of planar ultra-high Q silicon traveling-wave microresonators in a SOI platform. Microdisk, microring, and racetrack resonators are the three general TWR resonator architectures of interest that have been investigated in this thesis, with the greatest emphasis on microdisks. The theme of this research was to introduce these resonators as essential fundamental elements for dense integrated photonic circuits by theoretically and experimentally addressing the unique properties of these resonators such as the possibility of achieving ultra-high Qs and small mode volumes, efficient interaction with a waveguide or another resonator, and compatibility with large-scale integration. Such prominent resonator architectures are fully compatible with active electronic components (with minimal scarification of the optical properties) in a SOI platform. For practical considerations and for future aspects of integrating these resonators with other active electronic elements, the buried oxide layer underneath the resonator in all the designs in this thesis remained intact and no undercutting of the resonator was considered. To accomplish this research, several steps from theory to experiment were pursued, and by addressing different aspects of these resonator structures, major contributions were obtained, as I explain below.

First, I developed an efficient vectorial electromagnetic modeling tool based on the finite-element method to extract the modal properties of traveling-wave resonators with axial symmetry. Applying the symmetry properties of the structure and the divergence condition as constraints into the Helmholtz equation, I introduced a simple vector formulation consisting of two vector field components and two spatial variables for the FEM analysis. While many numerical techniques still fail or have a major challenge in modeling microdisk resonators, my simple formulation, which is implemented in a COMSOL environment, can easily simulate the structure and find the modal properties in a few seconds using a typical personal computer with average performance.

To achieve ultra-high Q values, a fine fabrication recipe for the resonator is required. For this purpose, I developed an optimized nanofabrication technique with nanometer range control for the implementation of these structures, with emphasis on obtaining ultra-low-loss resonators with accurate dimensions. Using this fabrication recipe, I demonstrated a world-record Q (> 3 million) for microdisk resonators (r = 20 μm), which was one of the major contributions of this research. Such a high Q brought confidence to the nanophotonics community that achieving ultra-high Qs for a Si resonator with compatibility for integration with active electronic elements is within reach.

The electromagnetic excitations of, and energy exchange to, these resonator structures were via silicon nanowaveguides side coupled to them. Therefore, I proposed a systematic method for engineering waveguide-resonator coupling to

achieve the desired level of coupling. This was the first reported analysis to fairly accurately and three-dimensionally analyze the coupling structure and provide quantitative numbers for the nanophotonics community.

Scaling and miniaturization of microdisk resonators with high Q was another focus of this research. The goal was to achieve the same levels of Q/V that were obtained in this thesis for ultra-high Q resonators with larger dimensions. The benefits of such small resonators are their compactness, large free-spectral range (FSR), and fewer modes (essentially, they can be made single mode). Based on this motivation, I designed and demonstrated microdisk resonators with dimensions close to radiation limits (radius ~ 1.5) while supporting one mode over the entire FSR~70 nm with an intrinsic Q > 10^5. This is the highest Q reported for a Si microdisk resonator of this size on a SiO_2 substrate, and it is one order of magnitude larger than the previous reported works. Surprisingly, the Q/V of this structure (Q = 10^5, V = $6.3(\lambda_0/n)^3$) was very close to the Q/V of a larger ultra-high Q microdisk (Q = 3×10^6, V = $185(\lambda_0/n)^3$).

Another aspect of this research was studying the performance of ultra-high Q resonators at high powers. At high powers, two-photon absorption (TPA) and TPA-induced free carriers result in resonance shift, self-heating, and degradation of Q, which results in resonance spectral broadening and possible temporal self-sustained oscillations in the resonator amplitude. In previous works [94], self-sustained MHz oscillation (which corresponded to the thermal lifetime of the resonator) had been observed and modeled. In this thesis, in addition to observing this phenomenon, we

also observed, for the first time, sustained GHz oscillations in ultra-high Q resonators with a continuous-wave laser. Such a phenomenon was theoretically modeled, and conditions for achieving pure GHz oscillations (without any simultaneous appearance of slow MHz oscillations) in the response of the resonator were addressed. An accurate modeling to obtain the effective thermal conductivity and thermal lifetime of the optical mode of the resonators (which are important at high powers) by simultaneously solving the Helmholtz equation and the heat equation was performed, and these parameters were extracted for use in modeling the thermal broadening as well as sustained oscillations.

Integrating silicon microdisk resonators with microfluidic channels for lab-on-a-chip sensing was performed, and promising results for sensing with microresonators (both miniaturized resonators and large resonators) were obtained.

Another major contribution of this research was the design and demonstration of compact resonator-based filters using miniaturized microdisk resonators. The demonstration of ultra-compact integrated photonic filters with such small high Q resonators using the design and fabrication recipe developed in this research was a major contribution to the field of integrated photonics. Very small dimensions and large FSR of the miniaturized high Q resonators enable their use as a platform for dense and large-scale integration of filter-bank arrays suitable for chip-scale signal processing, spectroscopy, and switching applications.

In addition to the design of simple resonator-based filters, I used circuit theory and coupled-mode theory in time to develop a systematic method for designing

coupled-resonator filters with a flat-band response. Based on the theoretical results, coupled-resonator add-drop filters with both moderate (~0.4 nm) and large (~ 1 nm) bandwidths and large extinction (>10-15 dB) with resonators radii < 2 μm were demonstrated. Initial experimental results for the filter-bank arrays were presented and future directions for the design of compact and very large arrays of filters and their integration with imaging arrays were discussed.

In brief, a summary of the main contributions in these research are as follows:

- Development of a fully vectorial electromagnetic FEM-based model for the analysis of dielectric traveling-wave resonators with axial symmetry.
- Development of an optimal fabrication recipe for the implementation of ultra-high Q silicon resonators.
- Demonstration of ultra-high Q silicon microdisk resonators on a SiO_2 substrate with world-record Q (> 3 million) in a SOI platform.
- First systematic analysis of thermal properties of microdisk resonators.
- Accurate modeling of thermal properties of Si microdisk resonators and extracting thermal lifetime and effective thermal conductivities of the optical resonance mode.
- First experimental observation and theoretical prediction of self-sustained GHz oscillations in ultra-high Q microdisk resonators.
- Design of ultra-small miniaturized microdisk resonators (r~1.5 μm) with single-mode condition over a large FSR.

- Demonstration of miniaturized microdisk resonators with the highest reported Q ($>10^5$), about one order of magnitude larger than previously reported values.
- First systematic engineering and analysis of 3D waveguide-resonator coupling for Si microdisk and microring resonators. Techniques for achieving the required level of coupling were proposed and verified.
- Development of a systematic technique for the design of coupled-resonator filters with a flat-band spectral response.
- Demonstration of the world's most compact coupled-resonator filter with a miniaturized silicon microdisk resonator ($r<2\mu m$) with oxide cladding.

It is my hope that the contributions of the dissertation spur the development of large-scale dense integration of Si photonic circuits for applications in signal processing, communication, and sensing systems.

APPENDIX A

Useful Mathematical Formula

1. Vector identities

$$\nabla \times (\nabla \psi) = 0$$

$$\nabla \cdot (\nabla \times \mathrm{A}) = 0$$

$$\nabla \cdot (\psi \mathrm{A}) = \mathrm{A} \cdot \nabla \psi + \psi \nabla \cdot \mathrm{A}$$

$$\nabla \times (\psi \mathrm{A}) = \nabla \psi \times \mathrm{A} + \psi \nabla \times \mathrm{A}$$

$$\nabla \cdot (\mathrm{A} \times \mathrm{B}) = \mathrm{B} \cdot \nabla \times \mathrm{A} - \mathrm{A} \cdot \nabla \times \mathrm{B}$$

$$\nabla (\mathrm{A} \cdot \mathrm{B}) = (\mathrm{A} \cdot \nabla)\mathrm{B} + (\mathrm{B} \cdot \nabla) + \mathrm{B} \times \nabla \times \mathrm{A} + \mathrm{A} \times \nabla \times \mathrm{B}$$

$$\nabla \times (\mathrm{A} \times \mathrm{B}) = (\mathrm{B} \cdot \nabla)\mathrm{A} - (\mathrm{A} \cdot \nabla)\mathrm{B} + \mathrm{A} \nabla \cdot \mathrm{B} - \mathrm{B} \nabla \cdot \mathrm{A}$$

$$\nabla \times (\nabla \times \mathrm{A}) = \nabla (\nabla \cdot \mathrm{A}) - \nabla^2 \cdot \mathrm{A}$$

2. Gradient, Divergence, Curl, and Laplacian in Cylindrical Coordinates

$$\nabla \psi = \frac{\partial \psi}{\partial \rho} \hat{\rho} + \frac{1}{\rho} \frac{\partial \psi}{\partial \phi} \hat{\phi} + \frac{\partial \psi}{\partial \mathrm{z}} \hat{z}$$

$$\nabla \cdot \mathrm{A} = \frac{1}{\rho} \frac{\partial}{\partial \rho} (\rho \frac{\partial \mathrm{A}_\rho}{\partial \rho}) + \frac{1}{\rho} \frac{\partial \mathrm{A}_\phi}{\partial \varphi} + \frac{\partial \mathrm{A}_z}{\partial \mathrm{z}}$$

$$\nabla \times \mathrm{A} = (\frac{1}{\rho} \frac{\partial \mathrm{A}_z}{\partial \phi} - \frac{\partial \mathrm{A}_\phi}{\partial \mathrm{z}}) \hat{\rho} + (\frac{\partial \mathrm{A}_\rho}{\partial z} - \frac{\partial \mathrm{A}_z}{\partial \rho}) \hat{\phi} + \frac{1}{\rho} (\frac{\partial}{\partial \rho} (\rho \mathrm{A}_\phi) - \frac{\partial \mathrm{A}_\rho}{\partial \phi}) \hat{z}$$

$$\nabla^2 \psi = \frac{1}{\rho} \frac{\partial}{\partial \rho} (\rho \frac{\partial \psi}{\partial \rho}) + \frac{1}{\rho^2} \frac{\partial^2 \psi}{\partial \phi^2} + \frac{\partial^2 \psi}{\partial \mathrm{z}^2}$$

APPENDIX B

Rigorous Derivation of the Relation between the Stored Energy and the Power Lost in a Resonator

Assuming that a resonator has a complex resonance frequency of $\omega_0 - i1/\tau_0$, Maxwell's curl equations are written as

$$\nabla \times E = -i(\omega_0 - 1/\tau_0)\mu_0 H\,, \tag{B.1}$$

$$\nabla \times H = J + i(\omega_0 - 1/\tau_0)\varepsilon_0 n^2 H\,, \tag{B.2}$$

where n is the refractive index and J is the electric current in the resonator caused by its electric conductivity (we have assumed that the resonator does not have any magnetic property or magnetic loss). In addition, the following vector identity between the electric and magnetic fields exists:

$$\nabla.(E \times H^*) = H^*.\nabla \times E - E.\nabla \times H^* \text{ (See Appendix A).} \tag{B.3}$$

Using the curl equations in (B.1) and (B.2) and putting them into (B.3), we have

$$\nabla.(E \times H^*) = H^*.(-i(\omega_0 - i1/\tau_0)\mu_0 H) - E.(J^* - i(\omega_0 + i1/\tau_0)\varepsilon_0 n^2 E^*)\,. \tag{B.4}$$

By rearranging (B.4), we can reach the following relation:

$$\nabla.(E \times H^*) + E.J^* = i\omega_0(E.\varepsilon_0 n^2 E^* - H^*.\mu_0 H) - (1/\tau_0)(E.\varepsilon_0 n^2 E^* + H^*.\mu_0 H)\,. \tag{B.5}$$

The real and the imaginary parts of (B.5) can be separated and written as follows:

$$\nabla.\frac{1}{2}\mathrm{Re}(E \times H^*) + \frac{1}{2}\mathrm{Re}\,E.J^* = -2(1/\tau_0)(\frac{1}{4}E.\varepsilon_0 n^2 E^* + \frac{1}{4}H^*.\mu_0 H)\,, \tag{B.6}$$

$$\nabla.\frac{1}{2}\mathrm{Im}(E\times H^{*})+\frac{1}{2}\mathrm{Im}(E.J^{*})=-2\omega_{0}(\frac{1}{4}E.\varepsilon_{0}n^{2}E^{*}-\frac{1}{4}H^{*}.\mu_{0}H)\,. \qquad \text{(B.7)}$$

Now, if we take the integral of (B.6) over the entire volume and use the mathematical relations between the volume integral of the divergence of a vector and its surface integral, we obtain the following form:

$$\oint\frac{1}{2}\mathrm{Re}(E\times H^{*})ds+\int\frac{1}{2}\mathrm{Re}\,E.J^{*}dv=-2(1/\tau_{0})\int(\frac{1}{4}E.\varepsilon_{0}n^{2}E^{*}+\frac{1}{4}H^{*}.\mu_{0}H)dv\,. \qquad \text{(B.8)}$$

In (B.8), the first surface integral on the left side is a surface integral on the Poynting vector, which represents the radiation of the power from the resonator. The second integral on the left side of (B.8) is the dissipated electric power inside the resonator. The integral on the right side of (B.8) is the stored energy in the resonator. Hence, (B.8) can be expressed in the following form for a resonator:

Radiated power + Dissipated power = -2× (Stored energy)/τ_0, (B.9)

or, in general, we can say that

The total lost power = -2× (Stored energy)/τ_0. (B.10)

APPENDIX C

Dispersion Equations for Two-dimensional (2D) Microring and Microdisk Resonators

In this Appendix, by solving Maxwell's equations in the cylindrical coordinates, we find the dispersion equations that govern the eigenmodes and resonance frequencies of 2D dielectric microdisk and microring resonators.

In a 2D case, the z component of Helmholtz equation can be written as

$$(\frac{1}{r}\frac{d}{dr}\frac{1}{p^2}r\frac{d}{dr}-\frac{m^2}{p^2r^2}+\frac{n^2}{p^2}k_0^2)F_z(r)=0,\begin{cases}F_z=\mathrm{H}_z,\ p=n,\ (\mathrm{TE})\\ \qquad or \qquad\\ F_z=\mathrm{E}_z,\ p=1,\ (\mathrm{TM})\end{cases},\ k_0=\omega/c\ .\quad (C.1)$$

For the TE case, using Maxwell's curl equations, the two electric field components are expressed in terms of H_z as

$$E_r=-\frac{Z_0 m}{k_0 n^2}\frac{\mathrm{H}_z}{r},\ (Z_0=\sqrt{\mu_0/\varepsilon_0}),\qquad (C.2)$$

$$\mathrm{E}_\phi=i\frac{Z_0}{k_0 n^2}\frac{\partial \mathrm{H}_z}{\partial r}\ .\qquad (C.3)$$

For the TM case, using Maxwell's curls equations, the two magnetic field components are expressed in terms of E_z as

$$\mathrm{H}_r=\frac{m}{Z_0 k_0}\frac{\mathrm{E}_z}{r},\qquad (C.4)$$

$$\mathrm{H}_\phi=-i\frac{1}{Z_0 k_0}\frac{\partial \mathrm{E}_z}{\partial r}.\qquad (C.5)$$

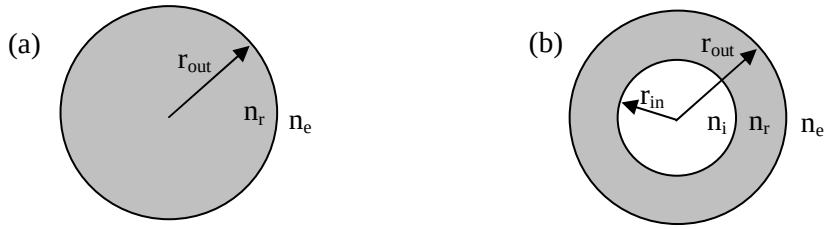

Fig. C.1: Structures of (a) a 2D microdisk and (b) a 2D microring with their parameters specified in the figures.

In the microring (microdisk) resonator structure, where the refractive index is constant in each sub domains, Equation (C.1) can be written as

$$(\frac{1}{r}\frac{d}{dr}r\frac{d}{dr}-\frac{m^2}{r^2}+n^2k_0^2)F(r)=0 \text{ , } (F\text{=E, H}). \tag{C.6}$$

The general solution of the above differential equation for the case of $m \neq 0$ and in each domain of the microdisk shown in Figure C.1(a) is

$$F(r)=\begin{cases} AJ_m(k_0n_r r) & r \le r_{out} \\ BH_m^2(k_0n_e r) & r_{out} < r \end{cases}, \tag{C.7}$$

and for the microring shown in Figure C.1(b) is

$$F(r)=\begin{cases} AJ_m(k_0n_i r) & r < r_{in} \\ BH_m^2(k_0n_r r)+CH_m^1(k_0n_r r) & r_{in} < r < r_{out} \\ DH_m^2(k_0n_e r) & r_{out} < r \end{cases}, \tag{C.8}$$

where *A*, *B*, *C*, and *D* are the unknown field coefficients in their corresponding domain that need to be determined. J_m is the Bessel function of the 1st kind and order *m*. H_m^1 and H_m^2 are Hankel's functions of the 1st and the 2nd kind[73] with order *m*, and they have propagation directions inward and outward with respect to the axis

[73] We have assumed the temporal phase variation of the fields to be $\exp(+i\omega_0 t)$.

of the resonator, respectively. To find unique solutions for Equations (C.7) and (C.8), we need to apply the boundary conditions. These boundary conditions satisfy the tangential components of the fields at the interfaces of the sub-domains of the resonator structure. For the TE case, these boundary conditions are

$$H_{z1} = H_{z2}, \tag{C.9}$$

$$E_{\phi 1} = E_{\phi 2} \ . \tag{C.10}$$

From Equation (C.3), we can find E_ϕ in terms of H_z and put it into Equation (C.10). The boundary conditions for the TM case are

$$E_{z1} = E_{z2}, \tag{C.11}$$

$$H_{\phi 1} = H_{\phi 2} \ . \tag{C.12}$$

From Equation (C.5), we can find H_ϕ in terms of E_z and put it into Equation (C.12). By applying the boundary conditions in Equations (C.9) and (C.10) for the TE, and in Equations (C.11) and (C.12) for the TM, the dispersion equation for microdisks and microrings can be obtained, respectively. As a result, for a microdisk structure, we come up with the following matrix equations:

$$\text{TE:} \quad \begin{bmatrix} J_m(k_0 n_r r_{out}) & -H_m^2(k_0 n_e r_{out}) \\ \frac{1}{n_r}[J_m(k_0 n_r r_{out})]' & \frac{-1}{n_e}[H_m^2(k_0 n_e r_{out})]' \end{bmatrix} \begin{bmatrix} A \\ B \end{bmatrix} = \begin{bmatrix} 0 \\ 0 \end{bmatrix}, \tag{C.13}$$

$$\text{TM:} \quad \begin{bmatrix} J_m(k_0 n_r r_{out}) & -H_m^1(k_0 n_e r_{out}) \\ n_r[J_m(k_0 n_r r_{out})]' & -n_e H_m^{1\prime}(k_0 n_e r_{out}) \end{bmatrix} \begin{bmatrix} A \\ B \end{bmatrix} = \begin{bmatrix} 0 \\ 0 \end{bmatrix}, \tag{C.14}$$

and for a microring structure we have the following matrix form:

$$M\begin{bmatrix} A \\ B \\ C \\ D \end{bmatrix} = \begin{bmatrix} 0 \\ 0 \\ 0 \\ 0 \end{bmatrix}, \tag{C.15}$$

where, for the TE case, the matrix M is

$$M = \begin{bmatrix} J_m(k_0 n_i r_{in}) & -H_m^2(k_0 n_r r_{in}) & -H_m^1(k_0 n_r r_{in}) & 0 \\ \frac{1}{n_i}[J_m(k_0 n_i r_{in})]' & \frac{-1}{n_r}[H_m^2(k_0 n_r r_{in})]' & \frac{-1}{n_r}[H_m^1(k_0 n_r r_{in})]' & 0 \\ 0 & H_m^2(k_0 n_r r_{out}) & H_m^1(k_0 n_r r_{out}) & -H_m^2(k_0 n_e r_{out}) \\ 0 & \frac{1}{n_r}[H_m^2(k_0 n_r r_{out})]' & \frac{1}{n_r}[H_m^1(k_0 n_r r_{out})]' & \frac{-1}{n_e}[H_m^2(k_0 n_e r_{out})]' \end{bmatrix}, \tag{C.16}$$

and for the TM case, M is

$$M = \begin{bmatrix} J_m(k_0 n_i r_{in}) & -H_m^2(k_0 n_r r_{in}) & -H_m^1(k_0 n_r r_{in}) & 0 \\ n_i[J_m(k_0 n_i r_{in})]' & -n_r[H_m^2(k_0 n_r r_{in})]' & -n_r[H_m^1(k_0 n_r r_{in})]' & 0 \\ 0 & H_m^2(k_0 n_r r_{out}) & H_m^1(k_0 n_r r_{out}) & -H_m^2(k_0 n_e r_{out}) \\ 0 & n_2[H_m^2(k_0 n_r r_{out})]' & n_r[H_m^1(k_0 n_r r_{out})]' & -n_e[H_m^2(k_0 n_e r_{out})]' \end{bmatrix}, \tag{C.17}$$

In Equations (C.13) to (C-17), the prime (´) means the derivative of the function with respect to its argument. The determinants of Equations (C.13) to (C.17) are the dispersion equations, which are functions of unknown k_0. In general, k_0 is a complex number. Hence, a complex root finder is required to search for the solutions of the dispersion equation. For this purpose, we use Davidenko's algorithm [117], which is very fast and efficient in finding the roots of the dispersion equation. After finding the k_0, the real part of it corresponds to the resonance frequency of the resonator

(ω=c×real(k_0)). Also, the intrinsic radiation quality factor of the resonator is Q_{rad}= 0.5×real(k_0)/imag(k_0).

APPENDIX D

Derivation of the Finite-Elements Formulation used in Chapter 2 for Modeling Axially-symmetric Resonators

In this Appendix we show the derivation of Equations (2.36) and (2.37).

D.1 Derivation of Equation (2.36) in Chapter 2

The divergence equation for the magnetic field in the cylindrical coordinates is

$$\frac{1}{\rho}\frac{\partial}{\partial\rho}(\rho \mathrm{H}_{\rho}) - \frac{jm}{\rho}\mathrm{H}_{\phi} + \frac{\partial \mathrm{H}_{z}}{\partial \mathrm{z}} = 0, \tag{D.1}$$

where ρ, ϕ, and z are the radial, the azimuthal phase, and the vertical coordinates' variable. By writing $\frac{\partial}{\partial \mathrm{z}}(\mathrm{H}_{z})$ as $\frac{1}{\rho}\frac{\partial}{\partial \mathrm{z}}(\rho \mathrm{H}_{z})$, Equation (D.1) becomes

$$\frac{\partial}{\partial\rho}(\rho \mathrm{H}_{\rho}) + \frac{\partial}{\partial \mathrm{z}}(\rho \mathrm{H}_{z}) - jm\mathrm{H}_{\phi} = 0. \tag{D.2}$$

Equation (D.2) can be written in a more compact form as

$$\nabla_{t}.(\rho\overline{\mathrm{H}}_{t}) = jm\mathrm{H}_{\phi}, \tag{D.3}$$

which is the same as Equation (2.36) in chapter 2. In Equation (D.3), we have

$$\overline{\mathrm{H}}_{t} = (\mathrm{H}_{r}\hat{r} + \mathrm{H}_{z}\hat{z}), \tag{D.4}$$

and

$$\nabla_{t} = \frac{\partial}{\partial\rho}\hat{r} + \frac{\partial}{\partial \mathrm{z}}\hat{z}. \tag{D.5}$$

D.2 Derivation of Equation (2.37) in Chapter 2

The curl equation for the magnetic field in the cylindrical coordinates is

$$\nabla \times H = \frac{1}{\rho}(-jmH_z - \rho\partial_z H_\phi)\hat{\rho} + \frac{1}{\rho}(\partial_\rho(\rho H_\phi) + jmH_\rho)\hat{z} + (\partial_z H_\rho - \partial_\rho H_z)\hat{\phi}. \tag{D.6}$$

By rearranging Equation (D.6) and using the properties of vector product and transverse curl (i.e., $\nabla_t \times$), we have

$$\nabla \times H = \frac{1}{\rho}(\partial_z \hat{z} + \partial_\rho \hat{\rho})(\rho H_\phi \hat{\phi}) + \frac{1}{\rho}(-jm\hat{\phi}) \times (H_\rho \hat{\rho} + H_z \hat{z}) + \nabla_t \times \overline{H}_t. \tag{D.7}$$

The above expression in its closed form is

$$\nabla \times H = \frac{1}{\rho}\nabla_t \times (\rho H_\phi \hat{\phi}) - \frac{jm}{\rho}\hat{\phi} \times \overline{H}_t + \nabla_t \times \overline{H}_t. \tag{D.8}$$

In a similar manner, considering $\mathrm{A} = \frac{1}{\varepsilon}\nabla \times \mathrm{H}$, we can write the curl of A as

$$\begin{aligned}\nabla \times (\frac{1}{\varepsilon}\nabla \times \mathrm{H}) = \nabla \times \mathrm{A} = \frac{1}{\rho}\nabla_t \times (\rho \frac{1}{\varepsilon}\nabla_t \times \overline{\mathrm{H}}_t) - \frac{jm}{\rho}\hat{\phi} \times [\frac{1}{\varepsilon\rho}\nabla_t \times (\rho \mathrm{H}_\phi \hat{\phi}) - \frac{jm}{\varepsilon\rho}\hat{\phi} \times \overline{\mathrm{H}}_t] \\ + \nabla_t \times [\frac{1}{\varepsilon\rho}\nabla_t \times (\rho \mathrm{H}_\phi \hat{\phi}) - \frac{jm}{\varepsilon\rho}\hat{\phi} \times \overline{\mathrm{H}}_t]\end{aligned} \tag{D.9}$$

In Equation (D.9), we have incorporated Equation (D.7). Equation (D.9) is one side of the Helmholtz equation. The Helmholtz equation can be decomposed into its transverse (ρ,ϕ) and normal (z) equations. Hence, using Equation (D.9), the transverse part of the Helmholtz can be found as

$$\frac{1}{\rho}\nabla_t \times (\rho \frac{1}{\varepsilon}\nabla_t \times \overline{\mathrm{H}}_t) - \frac{jm}{\rho}\hat{\phi} \times [\frac{1}{\varepsilon\rho}\nabla_t \times (\rho \mathrm{H}_\phi \hat{\phi}) - \frac{jm}{\varepsilon\rho}\hat{\phi} \times \overline{\mathrm{H}}_t] = k_0^2 \overline{\mathrm{H}}_t, \tag{D.10}$$

or, with more simplifications, we have

$$\frac{1}{\rho}\nabla_t \times (\rho \frac{1}{\varepsilon}\nabla_t \times \overline{\mathrm{H}}_t) - \frac{jm}{\rho}\hat{\phi} \times [\frac{1}{\varepsilon\rho}\nabla_t \times (\rho \mathrm{H}_\phi \hat{\phi})] + \frac{m^2}{\varepsilon\rho^2}\overline{\mathrm{H}}_t = k_0^2 \overline{\mathrm{H}}_t . \qquad \text{(D.11)}$$

By substituting H_ϕ in Equation (D.11) by its equivalent from Equation (D.3), we have

$$\frac{1}{\rho}\nabla_t \times (\rho \frac{1}{\varepsilon}\nabla_t \times \overline{\mathrm{H}}_t) - \frac{jm}{\rho}\hat{\phi} \times [\frac{1}{\varepsilon\rho}\nabla_t \times (\rho \frac{\nabla_t.(\rho\overline{\mathrm{H}}_t)}{jm}\hat{\phi})] + \frac{m^2}{\varepsilon\rho^2}\overline{\mathrm{H}}_t = k_0^2 \overline{\mathrm{H}}_t . \qquad \text{(D.12)}$$

By simplifying the above equation, we obtain the following expression:

$$\frac{1}{\rho}\nabla_t \times (\rho \frac{1}{\varepsilon}\nabla_t \times \overline{\mathrm{H}}_t) - \frac{1}{\varepsilon\rho^2}\nabla_t(\rho\nabla_t.(\rho\overline{\mathrm{H}}_t)) + \frac{m^2}{\varepsilon\rho^2}\overline{\mathrm{H}}_t = k_0^2 \overline{\mathrm{H}}_t . \qquad \text{(D.13)}$$

Equation (D.13) is the same as Equation (2.37) in chapter 2.

By using the following vector identity,

$$\rho \frac{1}{\varepsilon}\nabla_t \times \mathrm{H}_t = \frac{1}{\varepsilon}\nabla_t \times (\rho \mathrm{H}_t) - \frac{1}{\varepsilon}\hat{\rho} \times \mathrm{H}_t , \qquad \text{(D.14)}$$

we can write Equation (D.13) as

$$\nabla_t \times [\frac{1}{\varepsilon}\nabla_t \times (\rho \mathrm{H}_t) - \frac{1}{\varepsilon}\hat{\rho} \times \mathrm{H}_t] - \frac{1}{\varepsilon\rho}\nabla_t(\rho\nabla_t.(\rho \mathrm{H}_t)) + \frac{m^2}{\varepsilon\rho^2}(\rho \mathrm{H}_t) = k_0^2 \rho \mathrm{H}_t .$$

(D.15)

By defining the new field variable $\mathrm{H}_t^\rho = \rho\overline{\mathrm{H}}_t$ and putting it in Equation (D.15), we obtain

$$\nabla_t \times [\frac{1}{\varepsilon}\nabla_t \times (\mathrm{H}_t^\rho)] - \nabla_t \times [\frac{1}{\varepsilon}\frac{\hat{\rho}}{\rho} \times \mathrm{H}_t^\rho] - \frac{1}{\varepsilon\rho}\nabla_t(\rho\nabla_T.\mathrm{H}_t^\rho) + \frac{m^2}{\varepsilon\rho^2}(\mathrm{H}_t^\rho) = k_0^2 \mathrm{H}_t^\rho .$$

(D.16)

When a PML layer exists in the domain of the problem, Equation (D.16) needs to be generalized. In the cylindrical coordinates and in the PML region, the permittivity and the permeability have the following diagonal tensorial forms [43]:

$$\overline{\overline{\varepsilon}} = \varepsilon\overline{\overline{\Lambda}} \quad \overline{\overline{\mu}} = \mu_0\overline{\overline{\Lambda}}, \tag{D.17}$$

where

$$\overline{\overline{\Lambda}} = \begin{bmatrix} \frac{\tilde{\rho}}{\rho}\frac{s_z}{s_\rho} & 0 & 0 \\ 0 & \frac{\rho}{\tilde{\rho}}s_z s_\rho & 0 \\ 0 & 0 & \frac{\tilde{\rho}}{\rho}\frac{s_\rho}{s_z} \end{bmatrix} . \tag{D.18}$$

In Equation (D.18), $\tilde{\rho}$ is a complex spatial variable, which is a function of ρ, and S_z and S_ρ are the stretched functions in the PML region, which can be found in [40, 43]. By considering the above diagonal tensorial form for the permeability and the permittivity, we can find the general form of Equation (D.16), which is [118]

$$\frac{1}{\rho}\nabla_t \times (\rho\frac{1}{\varepsilon_\phi}\nabla_t \times \overline{\mathrm{H}}_t) - \frac{1}{[\varepsilon]_t \rho^2}\nabla_t(\rho\frac{\nabla_t.(\rho[\mu]_t\overline{\mathrm{H}}_t)}{\mu_\phi}) + \frac{m^2}{[\varepsilon]_t\rho^2}\overline{\mathrm{H}}_t = k_0^2\mu_t\overline{\mathrm{H}}_t, \tag{D.19}$$

where $[\varepsilon]_t$ and $[\mu]_t$ are the first 2×2 blocks of the permittivity and permeability tensors, respectively, and ε_ϕ is the 2nd diagonal element of the permittivity tensor. If the PML layer is far from the axis of the resonator, then, with very good approximation, $\tilde{\rho} = \rho$, and as a result, the tensor in Equation (D.18) is more simplified.

APPENDIX E
Time-domain Approach for Coupling to Resonators

E.1 Waveguide-Resonator Coupling

The temporal response of an isolated resonator with a lifetime τ_0 can be written as

$$\frac{da}{dt} = (j\omega_0 - 1/\tau_0)a, \tag{E.1}$$

where a is normalized such that its squared magnitude corresponds to the resonator energy. From Equation (E.1), it can be simply shown that the resonator energy varies as

$$\frac{d|a|^2}{dt} = (-2/\tau_0)|a|^2. \tag{E.2}$$

When the resonator is adjacent to another element such as a waveguide, as shown in Figure E.1, its energy can leak to the waveguide. To the 1st order approximation, a time constant, τ_c, can be designated to this energy leakage, which is also called the coupling lifetime. Now, being in the resonator frame, and assuming that only the clockwise (CW) mode of the resonator has an initial energy with the mode amplitude a_{cw}, the resonator amplitude varies in time as

$$\frac{da_{cw}}{dt} = (j\omega_0 - 1/\tau_0 - 1/\tau_c)a_{cw}, \tag{E.3}$$

It is noted that the CW mode of the resonator couples to the forward (left-to-right) propagating mode of the waveguide, and its coupling to the backward (right-to-left) mode of the waveguide is very weak and negligible. In this coupling scheme, we

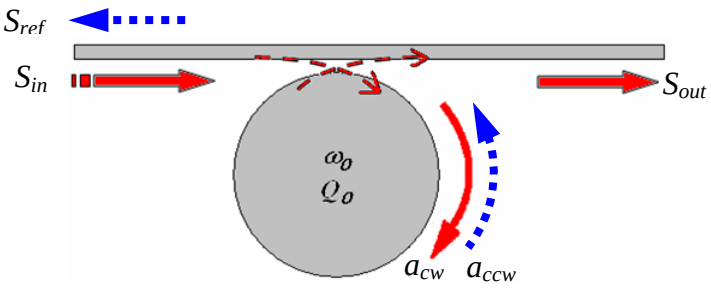

Fig.E.1: (a) Waveguide-resonator coupling for a TWR structure. The structure is excited via a waveguide source S_{in} from left, which couples to the clockwise mode of the resonator. Interaction of S_{in} and a_{cw} results in the output waveguide amplitude S_{out}. If there is considerable perturbation in the resonator, the CW mode can couple to the CCW modes, and the generated CCW mode can couple to the waveguide and generate the backward mode of the waveguide, as shown by S_{ref}.

have assumed that only coupling between the resonator mode and the waveguide mode occurs and that coupling to the radiation modes is negligible. The degenerate clockwise and counterclockwise (CCW) modes of the resonator are orthogonal to each other, and as a result, they do not exchange energy unless there is considerable perturbation in the resonator, such as sidewall roughness, to couple these two modes. In the case of coupling these two modes, Equation (E.3) has to be modified to consider this intermodal coupling, which is discussed later.

If the waveguide also has some initial excitation S_{in} as shown in Figure 10, it can couple to the CW mode of the resonator (coupling to CCW is very weak). This coupling mechanism can be incorporated to (E.3) as

$$\frac{da_{cw}}{dt} = (j\omega_0 - 1/\tau_0 - 1/\tau_c)a_{cw} + k_1 S_{in}, \qquad \text{(E.4)}$$

In Equation (E.4), S_{in} is normalized such that its squared magnitude corresponds to the waveguide mode power, and k_1 is the coupling coefficient from the waveguide

to the resonator. Now, going to the waveguide frame with an incoming excitation with an amplitude S_{in}, the output amplitude of the waveguide (S_{out}) after interaction with the resonator can be written as

$$S_{out} = S_{in} + k_2 a_{cw}, \tag{E.5}$$

where k_2 is the coupling coefficient from the resonator to the waveguide. The clockwise mode of the resonator has a very weak coupling to the backward propagation mode of the waveguide, and as a result, the reflection is almost zero, i.e., $S_{ref} = 0$. In Equation (E.5), even if there is no waveguide input excitation, i.e., $S_{in} = 0$, the output, S_{out}, can be generated via the coupling to the resonator if the resonator has an initial energy. Therefore, we expect a direct correspondence between k_2 in Equation (E.5) and τ_c in Equations (E.3) and (E.4), which is shown in what follows. By multiplying Equation (E.5) with the conjugate of the resonator amplitude, i.e., a^*, and also multiplying a with the conjugate of Equation (E.5) and then adding these two expressions, we have

$$\frac{d\,|\,a_{cw}\,|^2}{dt} = (-2/\tau_0 - 2/\tau_c)\,|\,a_{cw}\,|^2 + [a_{cw}^* k_1 S_{in} + c.c], \tag{E.6}$$

where *c.c* means complex conjugate. Equation (E.6) can be rearranged as

$$\frac{d\,|\,a_{cw}\,|^2}{dt} + (2/\tau_0)\,|\,a_{cw}\,|^2 = -(2/\tau_c)\,|\,a_{cw}\,|^2 + [a_{cw}^* k_1 S_{in} + c.c]. \tag{E.7}$$

The left side of Equation (E.7) is the change in the total resonator energy. By taking the squared magnitude of Equation (E.5), we have

$$|\,S_{out}\,|^2 = |\,S_{in}\,|^2 + |\,k_2\,|^2 |\,a_{cw}\,|^2 + [S_{in} k_2^* a_{cw}^* + c.c], \tag{E.8}$$

which can be arranged as

$$|S_{in}|^2 - |S_{out}|^2 = -|k_2|^2 |a_{cw}|^2 - [S_{in} k_2^* a_{cw}^* + c.c]. \quad \text{(E.9)}$$

The left side of Equation (E.9) is the difference between the incoming power and the outgoing power in the waveguide, and because of the conservation of energy, it has to be equal to the change in the resonator energy and the resonator lost energy. This energy conservation can be written as

$$|S_{in}|^2 - |S_{out}|^2 = \frac{d|a_{cw}|^2}{dt} + (2/\tau_0)|a_{cw}|^2. \quad \text{(E.10)}$$

As a result of the above equation, the right-hand sides of Equations (E.7) and (E.9) are also equal and can be written as

$$-(2/\tau_c)|a_{cw}|^2 + [a_{cw}^* k_1 S_i + c.c] = -|k_2|^2 |a_{cw}|^2 - [S_i k_2^* a_{cw}^* + c.c], \quad \text{(E.11)}$$

which can be arranged as

$$(|k_2|^2 - 2/\tau_e)|a_{cw}|^2 + [(k_1 + k_2^*) a_{cw}^* S_{in} + c.c] = 0. \quad \text{(E.12)}$$

Equation (38) has to be valid for any resonator amplitude (a_{cw}) and waveguide input power (S_{in}). When there is no excitation from the waveguide, i.e., $S_{in} = 0$, then, from Equation (E.12), we have

$$|k_2|^2 = (2/\tau_c). \quad \text{(E.13)}$$

Now, putting Equation (E.13) into Equation (E.12) yields

$$(k_1 + k_2^*) a_{cw}^* S_{in} + c.c = 0. \quad \text{(E.14)}$$

To satisfy Equation (E.14) for any a_{cw} and S_{in}, we need to have

$$k_1 = -k_2^* = \kappa, \ |\kappa|^2 = 2/\tau_c. \quad \text{(E.15)}$$

Also, because of the symmetry of the waveguide-TWR in Figure E.1, the coupling coefficient between the CCW mode of the resonator and the backward mode of the waveguide is κ.

E.2 Intermodal Coupling in Resonators

Due to any perturbation, the modes of the resonator with resonance frequencies near each other can couple to each other and interchange energy. However, the strength of the coupling depends on the level of perturbation, the field overlap, and the phases of these modes. These modes can be the degenerate CW and CCW modes of the TWR or they can be any other two modes. The perturbation can also cause the coupling of these modes to the radiation modes. However, with a good approximation, radiation coupling can be neglected. As a result, from the result in the previous section, the coupling equations for the two resonance modes can be written as

$$\frac{da_1}{dt} = (j\omega_{01} - 1/\tau_{01} - 1/\tau_{c1})a_1 + j\mu_1 a_2 + \kappa_1 S_{in}, \tag{E.16}$$

$$\frac{da_2}{dt} = (j\omega_{02} - 1/\tau_{02} - 1/\tau_{c2})a_1 + j\mu_2 a_1 + \kappa_2 S_{in}, \tag{E.17}$$

In Equations (E.16) and (E.17), a_1, ω_{01}, τ_{01}, and a_2, ω_{02}, τ_{02} are the amplitude, the frequency, and the intrinsic lifetime of the first and the second resonance modes, respectively, μ_1 is the coupling coefficient from the second mode to the first mode, μ_2 is the coupling coefficient from the first mode to the second mode, and κ_1 and κ_2 are the coupling coefficients between these modes and the waveguide mode. Similar

to the way that we reached Equation (E.7), we can proceed for Equations (E.16) and (E.17), and after adding terms and arranging them, we have

$$\frac{d\,|a_1|^2}{dt}+(\frac{2}{\tau_0}+\frac{2}{\tau_{c1}})\,|a_2|^2+\frac{d\,|a_2|^2}{dt}+(\frac{2}{\tau_0}+\frac{2}{\tau_{c2}})\,|a_2|^2= \\ [j(\mu_1-\mu_2^*)a_1^*a_2+c.c]+[\kappa_1 a_1^* S_{in}+c.c]+[\kappa_2 a_2^* S_{in}+c.c] \quad , \tag{E.18}$$

The left-hand side of the above expression corresponds to the total change of the energy of the resonator. When there is no waveguide excitation, i.e., S_{in} = 0, and if we assume that the coupling between the two modes of the resonator is lossless, then conservation of the energy forces the left side of Equation (E.20) to be zero. As a result of this, and balancing the left and the right side of Equation (E.18), we need to have

$$[j(\mu_1-\mu_2^*)a_1^*a_1+c.c]=0 \ . \tag{E.19}$$

To satisfy Equation (E.19) for any arbitrary case we need to have

$$\mu_1=\mu_2^*=\mu \ . \tag{E.20}$$

We have assumed that the waveguide excitation, S_{in}, comes from left to right, as shown in Figure 10, and therefore, it only interacts with the CW mode. The generated CCW mode can couple to the backward mode of the waveguide and generate the backward reflection, i.e., S_{back} as shown in Figure 10. Because of the symmetry, the CCW mode couples to the backward mode of the waveguide with the same time constant τ_c and coupling coefficient κ that the CW mode couples to the forward mode of the waveguide.

E.3 Coupling between Two or more Resonators

Analysis of the coupling between the resonators is very similar to the analysis of intermodal coupling presented in the previous section. However, the only difference is that both resonators are not necessarily coupled to the same waveguide or the same waveguide mode. For example, if the first resonator is coupled to the waveguide, and the second resonator is only coupled to the first resonator, then we have

$$\frac{da_1}{dt} = (j\omega_1 - 1/\tau_0 - 1/\tau_{c1})a_1 + j\mu a_2 + \kappa_1 S_{in}, \tag{E.21}$$

$$\frac{da_2}{dt} = (j\omega_2 - 1/\tau_0)a_1 + j\mu a_1, \tag{E.22}$$

The above equations can be extended to more resonators by adding them into the equation with their corresponding coupling coefficient. The important note is that the coupling coefficients between every two resonators satisfy Equation (E.20).

In the following, we provide a more rigorous analysis of the coupling between the two resonators.

Assuming that the electric and the magnetic fields of the first unperturbed resonator with a resonance frequency ω_{01} are

$$E_1^U = \mathrm{E}_1^U(r)\exp(i\omega_{01}t)\ ,\ H_1^U = \mathrm{H}_1^U(r)\exp(i\omega_{01}t), \tag{E.23}$$

they satisfy the following Maxwell's equations

$$\nabla \times E_1^U = -\mu_0 i\omega H_1^U\ ,\ \nabla \times H_1^U = \varepsilon_0 n_1^2 i\omega E_1^U, \tag{E.24}$$

where n_1 is the refractive index distribution of the resonator. The general form of Maxwell's equations for a perturbed resonator in the presence of a dielectric perturbation is

$$\nabla \times E_1^P = -\mu_0 \frac{\partial H_1^P}{\partial t}, \tag{E.25}$$

$$\nabla \times H_1^P = \varepsilon_0 n^2 \frac{\partial E_1^P}{\partial t} + \frac{\partial P_1}{\partial t}, \tag{E.26}$$

where E_1^P and H_1^P are the perturbed electric and magnetic fields and P_1 represents the perturbation for the first resonator, which appears as a polarization current. In the first approximation, the fields of the perturbed resonator can be written as

$$E_1^P = a_1(t)\frac{\mathrm{E}_1^U}{\sqrt{U_1}},\ H_1^P = a_1(t)\frac{\mathrm{H}_1^U}{\sqrt{U_1}}, \tag{E.27}$$

where U_1 is the mode energy of the resonator, which is

$$U_1 = \int \frac{1}{4}\varepsilon_0 n^2 \mathrm{E}_1^{U*}\mathrm{E}_1^U dv + \int \frac{1}{4}\mu_0 \mathrm{H}_1^{U*}\mathrm{H}_1^U dv. \tag{E.28}$$

Also, from Maxwell's equations, we can simply show that

$$\int \varepsilon_0 n^2 \mathrm{E}_1^{U*}\mathrm{E}_1^U dv = \int \mu_0 \mathrm{H}_1^{U*}\mathrm{H}_1^U dv. \tag{E.29}$$

The benefit of the normalization in Equation (E.27) is that the squared magnitude of a_1 corresponds to the resonator total energy of the perturbed resonator. Now considering the following vector identity

$$\nabla \cdot (\mathrm{E}_1^{U*} \times H_1^P) = \mathrm{E}_1^{U*} \cdot (\nabla \times H_1^P) - H_1^P \cdot (\nabla \times \mathrm{E}_1^{U*}), \tag{E.30}$$

and expanding it, we have

$$\nabla \cdot (\mathrm{E}_1^{U*} \times H_1^P) = \mathrm{E}_1^{U*} \cdot (\varepsilon_0 n^2 \frac{\partial E_1^P}{\partial t} + \frac{\partial P_1}{\partial t}) - H_1^P \cdot (\mu_0 i\omega \mathrm{H}_1^{U*}), \tag{E.31}$$

and by arranging it, we reach the following form:

$$\nabla \cdot (\mathrm{E}_1^{U*} \times H_1^P) = \frac{\varepsilon_0 n^2 \mathrm{E}_1^{U*} \mathrm{E}_1^U}{\sqrt{U_1}} \cdot \frac{\partial a_1}{\partial t} + \mathrm{E}_1^{U*} \cdot \frac{\partial P_1}{\partial t} - a_1(t) \frac{i\omega_{01} \mu_0 \mathrm{H}_1^{U*} \mathrm{H}_1^U}{\sqrt{U_1}}. \tag{E.32}$$

By integrating both sides of the above equation over the entire volume, we have

$$\oint (\mathrm{E}_1^{U*} \times H_1^P) ds = (\frac{\int \varepsilon_0 n^2 \mathrm{E}_1^{U*} \mathrm{E}_1^U dv}{\sqrt{U_1}}) \cdot \frac{\partial a_1}{\partial t} + \int \mathrm{E}_1^{U*} \cdot \frac{\partial P_1}{\partial t} dv - i\omega_{01} (\frac{\int \mu_0 \mathrm{H}_1^{U*} \mathrm{H}_1^U dv}{\sqrt{U_1}}) a_1(t) \tag{E.33}$$

Because of the evanescent nature of the fields, the surface integral in the left side of the above equation goes to zero. Hence, after the simplification of the above equation using Equations (E.24) and (E.25), we reach the following time-domain differential equation:

$$\frac{\partial a_1}{\partial t} = i\omega_{01} a_1(t) - \frac{1}{4\sqrt{U_1}} \int \mathrm{E}_1^{U*} \cdot \frac{\partial P_1}{\partial t} dv. \tag{E.34}$$

Now, we need to find the total dielectric perturbation, which acts as a polarization current. When the perturbation is caused by another resonator, the total induced polarization current includes two sources: 1) the field of the first resonator that induces a polarization current in the second resonator (P_{12}), 2) the field of the second resonator that induces a polarization current in the first resonator (P21). Hence, we have

$$P_1 = P_{12} + P_{21} = (\frac{a_1 \mathrm{E}_1^U}{\sqrt{U_1}}) \varepsilon_0 (n_2^2 - n_b^2) + (\frac{a_2 \mathrm{E}_2^U}{\sqrt{U_2}}) \varepsilon_0 (n_1^2 - n_b^2), \tag{E.35}$$

where n_1 and n_2 are the refractive indices of the resonators and n_b is the refractive index of the background in which the resonators are placed. Hence, the time derivative of the polarization current is

$$\frac{\partial P_1}{\partial t} = \frac{\varepsilon_0 (n_2^2 - n_b^2) \mathrm{E}_1^U}{\sqrt{U_1}} \frac{\partial a_1}{\partial t} + \frac{\varepsilon_0 (n_1^2 - n_b^2) \mathrm{E}_2^U}{\sqrt{U_2}} \frac{\partial a_2}{\partial t}. \tag{E.36}$$

By putting Equation (E.36) into Equation (E.34) we have

$$\frac{\partial a_1}{\partial t} = i\omega_{01} a_1(t) - \frac{\varepsilon_0 \int (n_2^2 - n_b^2) \mathrm{E}_1^{U*} \cdot \mathrm{E}_1^U dv}{4U_1} \frac{\partial a_1}{\partial t} - \frac{\varepsilon_0 \int (n_1^2 - n_b^2) \mathrm{E}_1^{U*} \cdot \mathrm{E}_2^U dv}{4\sqrt{U_1 U_2}} \frac{\partial a_2}{\partial t} \tag{E.37}$$

If we do the same procedure from the beginning for the second resonator we find a similar expression for the amplitude of the second resonator as

$$\frac{\partial a_2}{\partial t} = i\omega_{02} a_2(t) - \frac{\varepsilon_0 \int (n_1^2 - n_b^2) \mathrm{E}_2^{U*} \cdot \mathrm{E}_2^U dv}{4U_2} \frac{\partial a_2}{\partial t} - \frac{\varepsilon_0 \int (n_2^2 - n_b^2) \mathrm{E}_2^{U*} \cdot \mathrm{E}_1^U dv}{4\sqrt{U_1 U_2}} \frac{\partial a_1}{\partial t} \tag{E.38}$$

Equations (E.37) and (E.38) are the coupled-mode equations governing two resonators. As we see from the above equations, both sides of the equations have time derivatives. While we can directly solve the above set of equations, an alternative is to do one more step of approximation by substituting the time derivative variations in the polarization currents in the right sides of the above two equations with their approximate forms as

$$\frac{\partial a_1}{\partial t} \sim i\omega_{01} a_1, \; \frac{\partial a_2}{\partial t} \sim i\omega_{02} a_2. \tag{E.39}$$

This approximation is reasonable, as a_1 and a_2 have fast time-varying terms $\exp(i\omega_{01}t)$ and $\exp(i\omega_{02}t)$ inspired by their corresponding resonance modes in the first and the second resonator. Hence, by applying the approximation given in Equation (E.39) into the right sides Equations (E.37) and (E.38), we have the following equations:

$$\frac{\partial a_1}{\partial t} = i\omega_{01}a_1 - \frac{\varepsilon_0 \int (n_2^2 - n_b^2)\mathrm{E}_1^{U*} \cdot \mathrm{E}_1^U dv}{4U_1} i\omega_{01}a_1 - \frac{\varepsilon_0 \int (n_1^2 - n_b^2)\mathrm{E}_1^{U*} \cdot \mathrm{E}_2^U dv}{4\sqrt{U_1 U_2}} i\omega_{02}a_2 \tag{E.40}$$

$$\frac{\partial a_2}{\partial t} = i\omega_{02}a_2 - \frac{\varepsilon_0 \int (n_1^2 - n_b^2)\mathrm{E}_2^{U*} \cdot \mathrm{E}_2^U dv}{4U_2} i\omega_{02}a_2 - \frac{\varepsilon_0 \int (n_2^2 - n_b^2)\mathrm{E}_2^{U*} \cdot \mathrm{E}_1^U dv}{4\sqrt{U_1 U_2}} i\omega_{02}a_1 \tag{E.41}$$

In a more closed form, Equations (E.40) and (E.41) can be written as

$$\frac{\partial a_1}{\partial t} = i(\omega_{01} + \delta\omega_{01})a_1 + i\mu_{12}a_2, \tag{E.42}$$

$$\frac{\partial a_2}{\partial t} = i(\omega_{02} + \delta\omega_{02})a_2 + i\mu_{21}a_1, \tag{E.43}$$

where

$$\delta\omega_{01} = -\frac{\omega_{01}\varepsilon_0 \int (n_2^2 - n_b^2)\mathrm{E}_1^{U*} \cdot \mathrm{E}_1^U dv}{4U_1}, \tag{E.44}$$

$$\delta\omega_{02} = -\frac{\omega_{02}\varepsilon_0 \int (n_1^2 - n_b^2)\mathrm{E}_2^{U*} \cdot \mathrm{E}_2^U dv}{4U_2}, \tag{E.45}$$

$$\mu_{12} = -\frac{\omega_{02}}{4\sqrt{U_1}\sqrt{U_2}} \int_{V1} \varepsilon_0 E_1^{U*} \cdot E_2^U (n_1^2 - n_b^2) dv, \tag{E.46}$$

$$\mu_{21} = -\frac{\omega_{01}}{4\sqrt{U_1}\sqrt{U_2}} \int_{V2} \varepsilon_0 E_2^{U*} \cdot E_1^U (n_2^2 - n_b^2) dv \,. \tag{E.47}$$

Equations (E.44) and (E.45) are the frequency shifts in the first and the second resonators, respectively, induced by the presence of the second and the first resonator, respectively. Such a resonance shift is called coupling-induced resonance frequency shift (CIFS). The CIFS correction can be applied to the set of coupled-mode equations used in the analysis of the CROW structures in chapter 7. However, if they are small, they can be neglected.

Equations (E.46) and (E.47) show the coupling coefficients between the first and the second resonator. If the resonators are identical, we can see that $\mu_{12} = \mu_{21}^*$, which is what we required for the energy conservation obtained in Equation (E.20). If the two resonators are not identical, then, from Equations (E.46) and (E.47) we see that μ_{12} and μ_{21} are not necessarily the complex conjugate of each other. Hence, instead of solving Equations (E.42) and (E.43), it is suggested to solve Equations (E.40) and (E.41) as the set of coupled-mode equations to preserve the energy conservation and reciprocity.

If resonators have loss or they are coupled to another element, the loss term and the coupling can be easily added to (E.42) and (E.43), as we saw in Equations (E.21) and (E.22).

E.4 Derivation of Coupling Coefficient in Waveguide-TWR Structure

We present the coupling coefficient between a waveguide and a TWR through two approaches. One is the derivation of Manolatou and Haus [51] and the other is our

own derivation. Figure D.2 shows the structures of an isolated dielectric waveguide, an isolated dielectric resonator, and their coupling structure. The governing Maxwell's curl equations for each structure have been written next to it. We start from the general reciprocity theorem, which says if there are two different media with the following field relations

Medium 1:

$$\nabla \times E_1 = -i\omega\mu_0 H_1, \tag{E.48}$$

$$\nabla \times H_1 = J_1 + i\omega\varepsilon_1 E_1, \tag{E.49}$$

Medium 2:

$$\nabla \times E_2 = -i\omega\mu_0 H_2, \tag{E.50}$$

$$\nabla \times H_2 = J_2 + i\omega\varepsilon_2 E_2, \tag{E.51}$$

then, using the following vector identity

$$\nabla \cdot (\mathrm{A} \times \mathrm{B}) = \mathrm{B} \cdot \nabla \times \mathrm{A} - \mathrm{A} \cdot \nabla \times \mathrm{B} \tag{E.52}$$

we can obtain the universal reciprocity expression, which is

$$\nabla \cdot (E_1 \times H_2^* + E_2^* \times H_1) = -(E_1 . J_2^* + E_2^* . J_1) + i\omega(\varepsilon_2 - \varepsilon_1) E_1 E_2^*, \tag{E.53}$$

or in the integral form, (D.6) can be expressed as

$$\oint_S (E_1 \times H_2^* + E_2^* \times H_1)\, ds = \int_V [-(E_1 . J_2^* + E_2^* . J_1) + i\omega(\varepsilon_2 - \varepsilon_1) E_1 E_2^*]\, dv. \tag{E.54}$$

Case I:

In this case, which is the Manolatou and Haus derivation, we assume that the electromagnetic medium is composed of a waveguide perturbed by a resonator as a polarization current. Hence, Equation (E.53) becomes

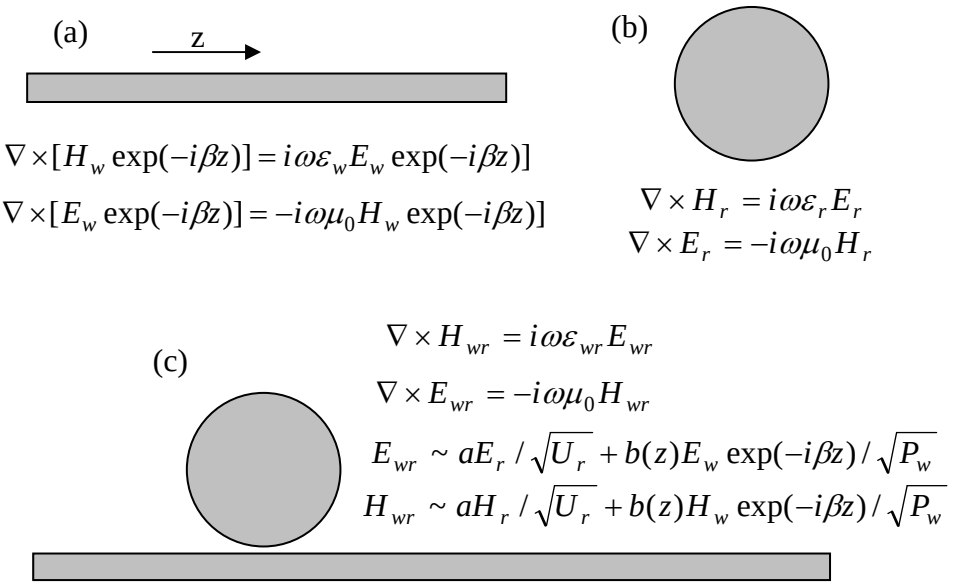

Fig. E.2: Structures of (a) a dielectric waveguide, (b) a dielectric resonator, and (c) a coupled dielectric waveguide resonator. Maxwell's curl equations governing each structure are written below them. For Case II, the field of the waveguide-resonator system in (c) has been approximated by the sum of the fields of the resonator and the waveguide.

$$\nabla \cdot (E_1 \times H_2^* + E_2^* \times H_1) = -(E_1 . J_2^* + E_2^* . J_1) \tag{E.55}$$

In Equation (E.55) we assume the (E_1, H_1) are the fields of the waveguide without any current source (as specified in Figure D.1(a)), and (E_2, H_2) are the unknown fields excited by the current source J_2. Hence, Equation (E.55) becomes

$$\nabla \cdot (E_w \times H_2^* + E_2^* \times H_w) \exp(-i\beta z) = -E_w \exp(-i\beta z) . J_2^* . \tag{E.56}$$

By integrating the above equation over a surface in the transverse plane (which extends to infinity) we have

$$\frac{d}{dz} \iint (E_w \times H_2^* + E_2^* \times H_w) \exp(-i\beta z)\, ds = \iint - E_w \exp(-i\beta z) . J_2^* ds\, . \tag{E.57}$$

Now, if we expand the unknown fields (E_2, H_2) in terms of all the modes of the waveguide (which are orthogonal to each other), the only non-zero term after the integration is the one that is projected to (E_w, H_w). Therefore, Equation (E.57) becomes

$$\frac{d}{dz}\iint (E_w \times S_w^*(z) H_w^* + S_w^*(z) E_w^* \times H_w)/\sqrt{P_w}\, ds = \iint -E_w \exp(-i\beta z).J_2^* ds\,, \quad \text{(E.58)}$$

where $S_w(z)$ is the amplitude of the unknown field after projection to the waveguide mode. Knowing the relation between the waveguide power and its modal field, Equation (E.58) can be written as

$$4\sqrt{P_w}\,\frac{d}{dz} S_w^*(z) = \iint -E_w \exp(-i\beta z).J_2^* ds\,, \quad \text{(E.59)}$$

where P_w is the waveguide mode power. If we take the complex conjugate of the above equation and take its integral along the z direction in the coupling region, we have

$$S_w(z_2) - S_w(z_1) = \frac{1}{4\sqrt{P_w}} \int_{z_1}^{z_2} \iint -E_w^* \exp(i\beta z).J_2 ds dz\,. \quad \text{(E.60)}$$

The polarization current is induced by the resonator as

$$J_2 = \varepsilon_0 i\omega_0 (n_w^2 - n_b^2) a E_r / \sqrt{U_r}\,, \quad \text{(E.61)}$$

where n_w and n_b are, respectively, the refractive indices of the waveguide and the background in which the waveguide is placed, ω_0 and E_r are the resonance frequency and the electric field of the resonator, and a is the resonator amplitude, which is normalized such that its squared magnitude corresponds to the resonator energy. By putting Equation (E.61) into Equation (E.60) we obtain the following:

$$S_w(z_2) = S_w(z_1) - [\frac{\varepsilon_0 i\omega_0}{4\sqrt{U_r}\sqrt{P_w}} \int_{z_1}^{z_2} \iint (n_w^2 - n_b^2) E_w^* \exp(i\beta z).E_r dv]a \,. \quad \text{(E.62)}$$

Also, from Equations (E.5) and (E.15) for a waveguide we had

$$S_{out} = S_{in} - k^* a_{cw} \,. \quad \text{(E.63)}$$

By comparing Equations (E.62) and (E.63), the coupling coefficient is obtained as

$$k = -(\frac{i\varepsilon_0\omega_0}{4\sqrt{U_r}\sqrt{P_w}} \int_{z_1}^{z_2} \iint (n_w^2 - n_b^2) E_w \exp(-i\beta z).E_r^* dv)a \,. \quad \text{(E.64)}$$

In chapter 3, we used Equation (E.64) to calculate the coupling coefficient between a waveguide and a TWR.

Case II:

In this case, we assume no current source exists, and we model the perturbation by the presence of the dielectric. Hence, Equation (E.53) can be written as

$$\nabla \cdot (E_1 \times H_2^* + E_2^* \times H_1) = i\omega(\varepsilon_2 - \varepsilon_1) E_1 E_2^* \,. \quad \text{(E.65)}$$

Now, in the above equation we assume that medium 1 is the waveguide-resonator system, as shown in Figure E.1(c), and medium 2 is the isolated waveguide shown in Figure E.1(a). The field equation for each case is shown in front of the structure in Figure E.1. As a result, Equation (E.65) becomes

$$\begin{aligned} \nabla \cdot [(aE_r / \sqrt{U_r} + b(z)E_w \exp(-i\beta z)/\sqrt{P_w}) \times H_w^* \exp(-i\beta z) \\ + E_w^* \exp(i\beta z) \times (aH_r / \sqrt{U_r} + b(z)H_w \exp(-i\beta z)/\sqrt{P_w})] \\ = i\omega(\varepsilon_w - \varepsilon_{wr})(aE_r / \sqrt{U_r} + b(z)E_w \exp(-i\beta z)/\sqrt{P_w}) E_w^* \exp(i\beta z) \end{aligned} \quad . \quad \text{(E.66)}$$

In Equation (E.66), ε_w and ε_{wr} are the permittivity distributions in the waveguide and the waveguide-resonator system. By arranging the terms in Equation (E.66) and

taking a surface integral (which extend to infinity) in the transverse plane, we have the following expression:

$$\begin{aligned}&\frac{d}{dz}\iint(E_w\times H_w^*+E_w^*\times H_w)\frac{b(z)}{\sqrt{P_w}}ds+a\frac{d}{dz}\iint(E_r\times H_w^*+E_w^*\times H_r)\frac{\exp(i\beta z)}{\sqrt{U_r}}ds\\&=i\omega\iint(\varepsilon_w-\varepsilon_{wr})[aE_r.E_w^*\exp(i\beta z)/\sqrt{U_r}+b(z)\mid E_w\mid^2/\sqrt{P_w}]ds\end{aligned},\quad\text{(E.67)}$$

Knowing that

$$\iint(E_w\times H_w^*+E_w^*\times H_w).\hat{z}\,ds=4P_w,\quad\text{(E.68)}$$

and defining the following

$$\iint(E_r\times H_w^*+E_w^*\times H_r).\hat{z}\,ds=4\sqrt{P_wU_r}\,F(z),\quad\text{(E.69)}$$

Equation (E.67) can be simplified as

$$\begin{aligned}&4\sqrt{P_w}a\frac{d}{dz}(\exp(i\beta z)F(z))+4\sqrt{P_w}\frac{db(z)}{dz}+4i\sqrt{P_w}\,q(z)b(z)\\&=(\iint i\omega(\varepsilon_w-\varepsilon_{wr})E_r.E_w^*\exp(i\beta z)ds)\,a/\sqrt{U_r}\end{aligned},\quad\text{(E.70)}$$

where $q(z)$ has been defined as

$$q(z)=\frac{-\omega}{4P_w}\iint(\varepsilon_w-\varepsilon_{wr})\mid E_w\mid^2\,ds\,.\quad\text{(E.71)}$$

Equation (E.70) can be more simplified as

$$\frac{db(z)}{dz}+iq(z)b(z)=(e^{i\beta z}k_\perp(z)-\frac{d}{dz}(e^{i\beta z}F(z))\;)a\,,\quad\text{(E.72)}$$

where

$$k_\perp(z)=\frac{i\omega}{4\sqrt{U_r}\sqrt{P_w}}(\iint(\varepsilon_w-\varepsilon_{wr})E_r.E_w^*ds)\,.\quad\text{(E.73)}$$

By defining $Q(z)$ as $q(z) = dQ(z)/dz$, Equation (E.72) can be written as follows:

$$\frac{d}{dz}[b\exp(iQ(z))] = \exp(iQ(z))[e^{i\beta z}k_{\perp}(z) - \frac{d}{dz}(e^{i\beta z}F(z))\ ]a\,. \tag{E.74}$$

By integrating the above equation along the *z* direction, we have

$$\begin{aligned} &b(z_2)\exp(iQ(z_2)) - b(z_1)\exp(iQ(z_2)) \\ &= a[\int_{z_1}^{z_2} k_{\perp}(z)\exp(i\overline{\beta}z) - \int_{z_1}^{z_2}\exp(i\overline{\beta}z)(i\beta F(z) + \frac{d}{dz}F(z))] \end{aligned}\quad , \tag{E.75}$$

where

$$\overline{\beta} = \beta + Q(z)/z\,. \tag{E.76}$$

The second integral in Equation (E.75) can be simplified as

$$\begin{aligned} &\int_{z_1}^{z_2}\exp(i\overline{\beta}z)(i\beta F(z) + \frac{d}{dz}F(z)) = \int_{z_1}^{z_2}\exp(iQ(z))\frac{d}{dz}(F(z)\exp(i\beta z)) \\ &= [F(z)\exp(i\beta z)\exp(iQ(z))]\Big|_{z1}^{z2} - iq\int_{z_1}^{z_2}\exp(iQ(z))F(z)\exp(i\beta z) \end{aligned}\quad , \tag{E.77}$$

However, as the field of the resonator approaches zero at the regions far from the coupling region, the first expression in Equation (E.77) is zero. Hence, Equation (E.77) becomes

$$\int_{z_1}^{z_2}\exp(iQ(z))\frac{d}{dz}(F(z)\exp(i\beta z)) = -iq\int_{z_1}^{z_2}F(z)\exp(i\overline{\beta}z)\,. \tag{E.78}$$

By putting equation (E.78) into equation (E.78) we have

$$b(z_2)\exp(iQ(z_2)) - b(z_1)\exp(iQ(z_1)) = a[\int_{z_1}^{z_2}k_{\perp}(z)\exp(i\overline{\beta}z) + iq\int_{z_1}^{z_2}F(z)\exp(i\overline{\beta}z)]\,. \tag{E.79}$$

In summary, the waveguide amplitude at the output of the coupling region is

$$b(z_2)$$
$$= b(z_1)\exp(-i(Q(z_2)-Q(z_1)) + a\exp(-iQ(z_2))[\int_{z_1}^{z_2} k_\perp(z)\exp(i\bar{\beta}z) + iq\int_{z_1}^{z_2} F(z)\exp(i\bar{\beta}z)] \tag{E.80}$$

If we do one more approximation and neglect the second integral in the above equation, we have the following expression:

$$b(z_2) \approx b(z_1)\exp(-i(Q(z_2)-Q(z_1)) + \exp(-iQ(z_2))[\int_{z_1}^{z_2} dz k_\perp(z)\exp(i\beta z + iQ(z))]a \tag{E.81}$$

Hence, the coupling coefficient between the resonator and the waveguide is

$$\kappa = -\frac{i\omega\varepsilon_0}{4\sqrt{U_r}\sqrt{P_w}}\int_0^{z_2}(n_{wr}^2 - n_w^2)E_r E_w^* \exp(i\beta z + iQ(z))\,dz\,, \tag{E.82}$$

where

$$Q(z) = -\frac{\omega\varepsilon_0}{4P_w}\int^{z} dz_1 \iint (n_{wr}^2 - n_w^2)\,|\,E_w\,|^2\; ds\,. \tag{E.83}$$

In all the analyses of waveguide-TWR coupling in chapter 3, the coupling coefficient was obtained using Equation (E.64). However, it is important to know the differences between Equations (E.64) and (E.82), which are that1) Equation (E.82) is integrated over the resonator volume, while Equation (E.64) is integrated over the waveguide volume; 2) In Equation (E.82) the phase of the waveguide has been corrected as a result of the perturbation by the resonator. This phase correction may have a major impact in some cases, as a waveguide-TWR coupling is very

phase sensitive. However, in Equation (E.64) no phase correction has been considered. Hence, we expect more dispersion to be observed when finding the coupling coefficient using Equation (E.82). A more accurate result is obtained when the effect of the phase correction is considered for the resonator mode. However, for this analysis, we did not consider any spatial variation for the resonator mode, and we considered the resonator amplitude only as a function of time. In future research, Equation (E.82) will be used to see the effect of the phase correction on the coupling coefficient.

APPENDIX F

Space-Domain Approach for Waveguide-Resonator Coupling

Figure F.1 shows an example of the space-domain description of coupling to a TWR structure. For this example, as shown in the figure, a TWR is coupled to two other guiding elements, A and B. A is a waveguide and B can be a waveguide or another resonator, a portion of which is shown. Using coupled-mode theory in space [53, 54] and assuming that the coupling between the resonator and these elements generates no backward reflection, the coupling matrices for each region are

$$\begin{bmatrix} S_o \\ R_o \end{bmatrix} = \exp(-i\frac{\beta_R + \beta_A}{2} Z_1) \begin{bmatrix} t_1 \exp(-\alpha_A Z_1) & k_1 \exp(-\alpha_A Z_1) \\ -k_1^* \exp(-\alpha_R Z_1) & t_1^* \exp(-\alpha_R Z_1) \end{bmatrix} \begin{bmatrix} S_i \\ R_i \end{bmatrix}, \tag{F.1}$$

$$\begin{bmatrix} D_o \\ P_o \end{bmatrix} = \exp(-i\frac{\beta_R + \beta_B}{2} Z_2) \begin{bmatrix} t_2 \exp(-\alpha_B Z_2) & k_2 \exp(-\alpha_B Z_2) \\ -k_2^* \exp(-\alpha_R Z_2) & t_2^* \exp(-\alpha_R Z_2) \end{bmatrix} \begin{bmatrix} D_i \\ P_i \end{bmatrix}, \tag{F.2}$$

where R_i, R_o, S_i, S_o and P_i, P_o, D_i, D_o are signals at each port of the coupling regions, and they are normalized such that their squared magnitudes correspond to their optical power. α_R, α_A, and α_B are the propagation losses in TWR, waveguide A, and waveguide B, respectively. β_R, β_A, and β_B are the wave propagation constants of the modes in TWR, waveguide A, and waveguide B, respectively. t_i and κ_i are the coupling and transmission coefficients [53-56]. Excluding the loss terms from the matrices in Equations (F.1) and (F.2) and assuming the conservation of the power in the coupling region, the coupling matrices have to be unitary, i.e.,

$$|t_1|^2 + |k_1|^2 = 1, \tag{F.3}$$

$$|t_2|^2 + |k_2|^2 = 1, \tag{F.4}$$

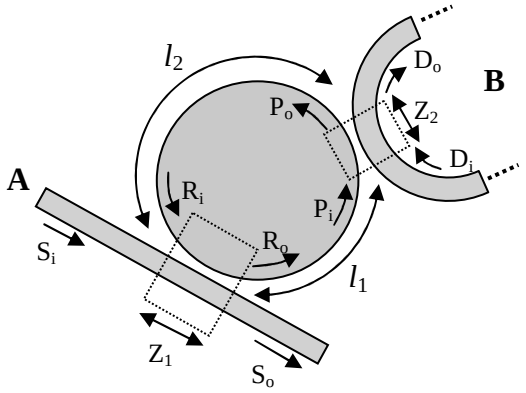

Fig. F.1: Space-domain description of coupling to a TWR where the resonator is coupled to two guiding elements, A and B. For example, A can be a waveguide, and B can be a waveguide or another resonator, a portion of which is shown. The coupling region can be modeled as a directional coupler.

In addition, the following relations between the signals exist:

$$P_i = R_o \exp[-(i\beta_R + \alpha_R) l_1], \tag{F.5}$$

$$R_i = P_o \exp[-(i\beta_R + \alpha_R) l_2], \tag{F.6}$$

where l_1 and l_2 are the propagation lengths in the resonator from $R_o \rightarrow P_i$ and $P_o \rightarrow R_i$, respectively. By combining Equations (F.1)-(F.6), we can find the transmission at each port of the structure in Figure F.1.

To compare the results of space-domain analysis with time-domain analysis, we consider a simpler case where only waveguide **A** exists in Figure F.1, and the guiding element B is absent. For such a case, we have

$$R_i = R_o \exp[-(i\beta_R + \alpha_R)(L - Z_0)], \tag{F.7}$$

where L is the total resonator traveling length and Z_0 is the effective length of the coupling region, as shown in Figure F.1. By combining Equations (F.1), (F.3), and (F.7), we have the following expression for the transmission coefficient through the waveguide **A:**

$$T = \frac{S_o}{S_i} = \exp[-i(\frac{\beta_A + \beta_R}{2})Z_1 - \alpha_A Z_1] \times \frac{t_1 - \exp(-\alpha_R L)\exp[-i\beta_R L - i(\beta_A - \beta_R)Z_1/2]}{1 - t_1^* \exp(-\alpha_R L)\exp[-i\beta_R L - i(\beta_A - \beta_R)Z_1/2]}, \quad \text{(F.8)}$$

and the squared magnitude of T is

$$|T|^2 = \exp(-2\alpha_A Z_1) \times \frac{|t_1|^2 + \exp(-2\alpha_R L) - 2\exp(-\alpha_R L)|t_1|\cos[\beta_R L + (\beta_A - \beta_R)Z_1/2 + \phi_{t1}]}{1 + |t_1|^2 \exp(-2\alpha_R L) - 2\exp(-\alpha_R L)|t_1|\cos[\beta_R L + (\beta_A - \beta_R)Z_1/2 + \phi_{t1}]}, \quad \text{(F.9)}$$

where ϕ_t is the phase of t_1. In Equation (F.9), by changing the frequency, the values of β_R and β_A change, and as a result, we can find the variation of transmission versus the frequency. The resonance condition in Equation (F.9) occurs when the argument of the cosine function in this equation becomes a multiple of 2π (which means a constructive interference during a roundtrip). Hence, we have

$$\beta_R L + (\beta_A - \beta_R)Z_1/2 + \phi_{t1} = 2\pi m, \quad \text{(F.10)}$$

where m is an integer. We note that the coupling of the waveguide to the resonator has modified the resonance condition from the original one, which was $\beta_R L = 2\pi m$. This effect corresponds to a coupling-induced shift in the resonance frequency of the resonator and is similar to what we discussed in time-domain analysis. By putting Equation (F.10) into (F.9), we can find $|T|^2$ at resonance as follows:

$$|T|^2 = \exp(-2\alpha_A Z_1)\frac{[|t_1| - \exp(-\alpha_R L)]^2}{[1 - |t_1|\exp(-\alpha_R L)]^2}. \quad \text{(F.11)}$$

Equation (F.11) corresponds to the peak of the transmission, which occurs at the resonance. Therefore, the critical coupling condition (which corresponds to $|T| = 0$ at the resonance) occurs when

$$|t_1| = \exp(-\alpha_R L). \tag{F.12}$$

APPENDIX G

Thermal Properties of Microdisk Resonators in SOI Platforms

In this Appendix, a detailed quantitative study of the thermal properties of Si microdisk resonators in a SOI platform is given. The effect of the SiO_2 substrate on improving the thermal conductivity of microdisk resonators on a SOI platform are studied, and the results are compared with those for the undercut microdisk structures.

The thermal behavior of a microdisk resonator can be studied using the heat equation, which is

$$\rho C_p \frac{d}{dt}(\Delta T(t)) - \nabla \cdot [K \nabla (\Delta T(t))] = p_{abs}, \tag{G.1}$$

where K, C_p, and ρ are, respectively, the thermal conductivity, specific heat capacity, and the mass density of different materials used in the structures, p_{abs} is the power density per volume absorbed by the resonator (and converted to heat), and ΔT is the spatial and temporal distribution of the temperate with respect to the ambient. In the steady state, in which the rate of absorbed power by the resonator is constant, the temperature distribution reaches a steady state in time, and as a result, the first term in the left side of Equation (G.1) is zero. Considering the axial symmetry of the microdisk resonator, Equation (G.1) can be analyzed more simply in the cylindrical coordinate. Note that the assumption of cylindrical symmetry is somehow approximate due to the presence of the coupling waveguide in the vicinity of the

resonator. However, the effect of this waveguide-resonator coupling on the symmetry of the structure can be neglected due to the small interaction length, especially for the large resonators. Therefore, *T* is assumed to have axial symmetry, and Equation (G.1) can be represented in the cylindrical coordinate as follows:

$$-\frac{1}{r}\frac{\partial}{\partial r}(rK\frac{\partial T}{\partial r})+\frac{m_T^2 KT}{r^2}-\frac{\partial}{\partial z}(K\frac{\partial T}{\partial z})=p_{abs}. \quad \text{(G.2)}$$

In Equation (G.2), *r* and *z* are the radial and axial coordinates, respectively, and m_T is the azimuthally harmonic number of temperature *T* in the microdisk resonator. The right side of Equation (G.2), which is proportional to the square resonator energy, has no harmonic dependence. Hence, m_T on the left side of Equation (G.2) is also zero. Therefore, the only available solution of Equation (8) is for $m_T=0$, and the resulting heat equation is

$$-\frac{1}{r}\frac{\partial}{\partial r}(rK\frac{\partial T}{\partial r})-\frac{\partial}{\partial z}(K\frac{\partial T}{\partial z})=p_{abs}. \quad \text{(G.3)}$$

Equation (G.3) can be solved for a given microdisk resonator to find the temperature distribution inside the structure. For the analysis, we implemented this differential equation in the COMSOL software environment.

G.1. Simulation Results for Thermal Conductance of Microdisk Resonators

To assess the role of the SiO_2 substrate and the shallow Si pedestal layer on the thermal conductivity of the microdisk resonator, the following structures were considered for the analysis: 1) an undercut microdisk held by an oxide micropost (shown in Figure G.1), and 2) a Si pedestal disk with thicknesses (*t*), which is

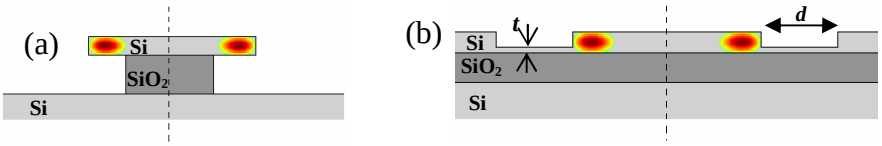

Fig. G.1: (a) Cross section of an undercut Si microdisk resonator held by an oxide micropost on a Si bulk layer. (b) Cross section of a Si microdisk resonator on an oxide substrate. A shallow Si pedestal layer with thickness *t* is at the interface between the microdisk and the oxide layer. The etched region that separates the disk perimeter from the surrounding top silicon layer is *d*. In both (a) and (b) the cross section of the generated heat energy, which has a distribution proportional to that of the electromagnetic mode energy of the resonator, is shown.

in general covered by either air or an oxide cladding (shown in Fig. 3(b)). In both cases, the microdisk has a radius of 20 μm and a thickness of 250 nm. For the undercut disk, the radius and the height of the underlying micropost oxide are 17μm and 1μm, respectively. Using a finite-element technique as discussed in chapter 2, the electromagnetic mode profile of the resonators is obtained. In this Appendix our focus is on the fundamental radial mode of the disk, although the final results for different modes regarding the thermal properties are similar. After finding the mode of the resonator, the generated heat power that has a distribution proportional to the energy mode profile of the microdisk is incorporated into Equation (G.3). In the equation, p_{abs} is normalized such that its integration over the resonator volume is 1 (meaning 1 Joul/s). Then, by solving Equation (G.3) using FEM and applying the cylindrical symmetry conditions in the structure, the steady-state temperature distributions of the resonator can be obtained. Figure G.2(a) shows the temperature distribution for a typical non-undercut microdisk with the dimensions given in the figure captions. As can be seen from Figure G.2(a), the peak temperature location

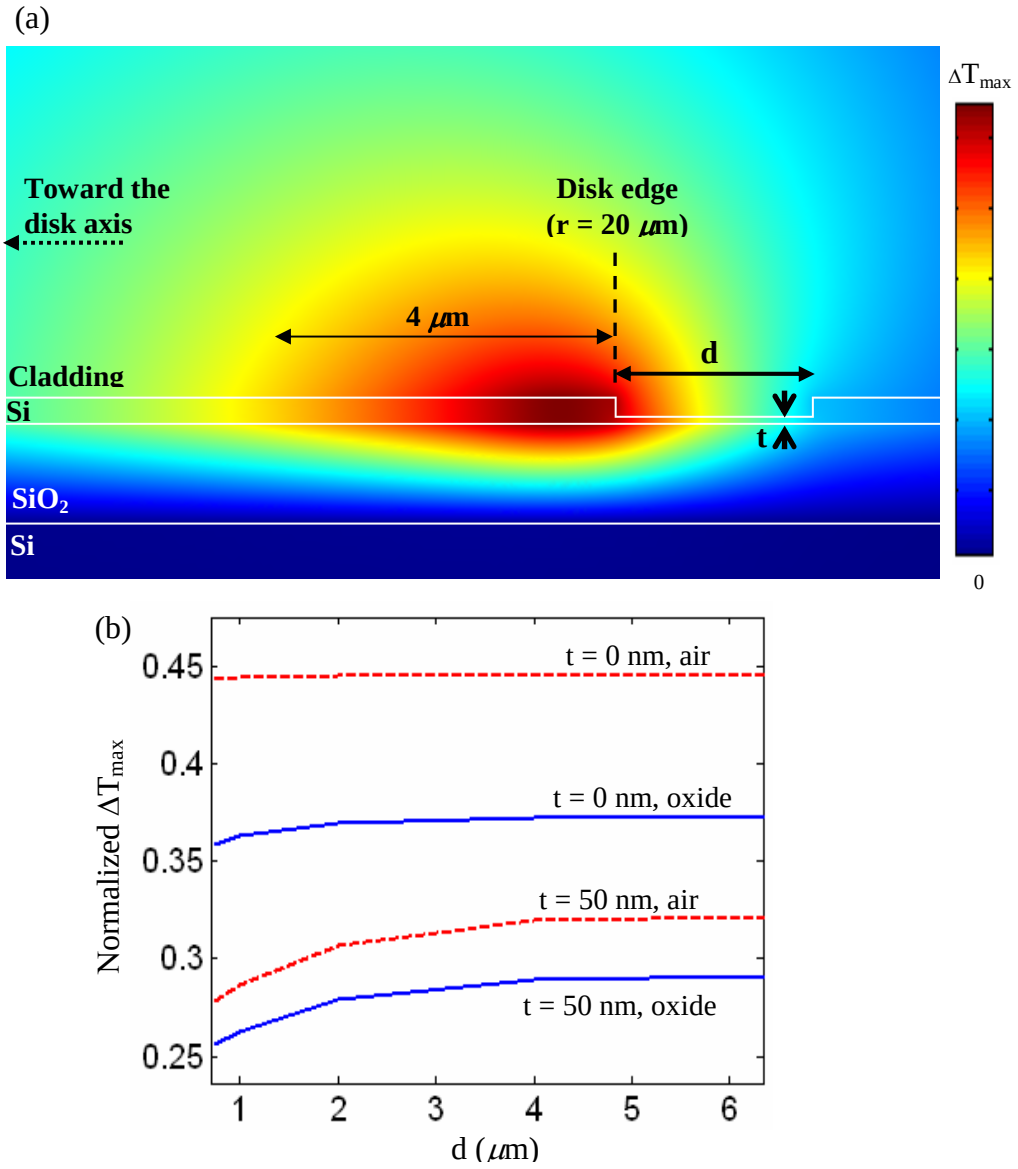

Fig. G.2: (a) Cross section of the temperature distribution in a Si pedestal microdisk resonator on substrate and with oxide cladding; the disk radius and thickness are 20 μm and 250 *nm*, the Si pedestal thickness is 50 *nm*; and the oxide substrate thickness is 1μm. (b) The normalized peak temperature of the non-undercut microdisk resonator versus *d*, which is the distance between the disk edge and the surrounding silicon layer. The simulation has been performed for air and oxide cladding materials and for two pedestal thicknesses of zero and 50 nm. The temperatures in (b) are normalized to the peak temperature of the undercut microdisk. The undercut microdisk has the same radius and thickness as the non-undercut microdisk. It is seated on a SiO_2 micropost with a radius of 17 μm and a height of 1 μm. For these simulations, the thermal conductivities of Si, SiO_2, and air were 163, 1.38, and 0.02 ($WK^{-1}m^{-1}$).

coincides with the position of the maximum concentration of the electromagnetic energy, which is in the vicinity of the disk edge.

Figure G.2(b) shows the normalized peak temperature rise of the pedestal disk with air cladding and oxide cladding for pedestal thicknesses of *t=0* nm and *t=50* nm, respectively. The temperatures have been normalized to the peak temperature rise of the undercut microdisk, which was simulated similarly. The results in Figure G.2(b) show a dramatic reduction (over 3x) in the peak temperature (proportional to the thermal resistance) by using the pedestal microdisk architecture in comparison with the undercut microdisk. When we narrowed the micropost radii in the undercut microdisk, we observed a dramatic growth in the peak temperature of the microdisk. This is because the underlying oxide layer is the main channel to transfer the heat from the microdisk to the underlying Si layer. Hence, by reducing the radius of the micropost, the effective heat flow area is reduced, which results in a reduction in the thermal conductance and consequently a temperature rise in the resonator. From Figure G.2(b), it is observed that the non-undercut microdisk with a thin Si pedestal and air cladding has a lower peak temperature when compared with the microdisk without the pedestal layer but covered with oxide cladding. In other words, the presence of the Si pedestal layer along with the underlying oxide layer has a major role in improving the overall thermal conductivity of the resonator. Our simulations were performed for different pedestal widths (*d*), which is the distance between the disk edge and the surrounding Si region. From Figure G.2(b), it is observed that the peak temperature rise increases with increasing *d* and eventually saturates at large *d*.

This saturation is because of the competition of the surrounding silicon region with the underlying substrate Si/oxide effects. Finally, the addition of the overall oxide cladding further improves the thermal conductivity as expected and shown in Figure G.2(b). Thus, depending on the application and the level of optical power used in the actual experiments involving Si microresonators, one can have different levels of thermal conductivity improvements by adding different layers (i.e., underlying SiO_2 layer, pedestal layer, and the oxide cladding layer) to the resonator. With a thinner underlying oxide (BOX) layer and a thicker Si pedestal layer, we expect a better thermal conductance for the structure. However, the thicknesses of the underlying oxide and Si pedestal layers should be in a range to restrict the optical mode energy leakage of the microdisk, in order to preserve the ultra-high *Q* properties of the microdisk. Figure G.3 shows the simulation results for the effect of the scaling of a microdisk resonator on its thermal conductance. The simulation has been performed for different BOX and Si pedestal thicknesses. As seen from this figure, by reducing the microdisk radius, the thermal conductance is dramatically reduced. This is because the effective heat flow area (which is related to the microdisk area) to transfer the heat from the resonator to the underlying substrate has reduced. Figures G.3(b) and G.3(c) show the cross section of the electromagnetic mode energy (which is proportional to the heat power) and the temperature distribution (which is resulted by the heat power) for a microdisk resonator with a radius of 2.5 μm seated on an oxide substrate with a

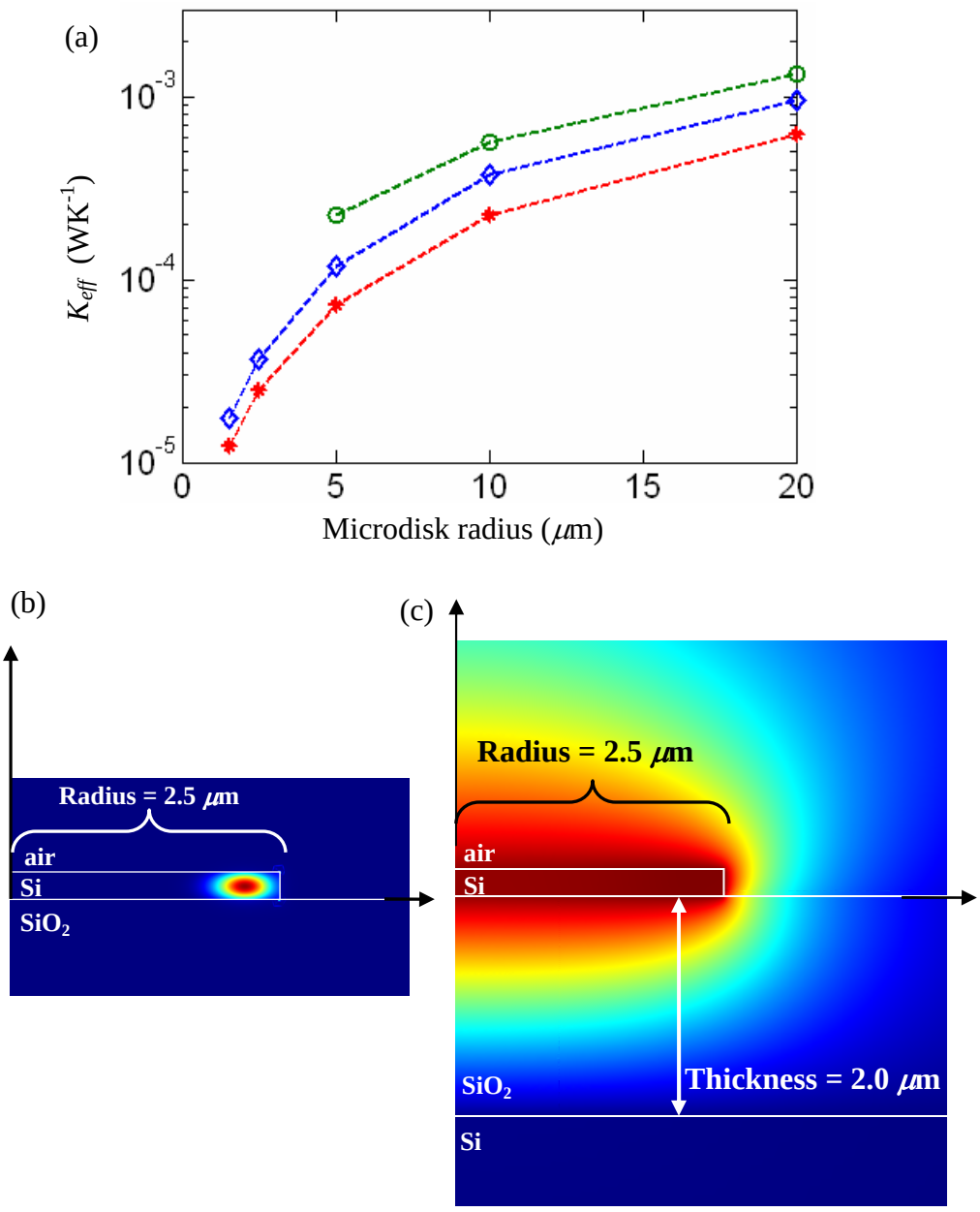

Fig. G.3: Effective thermal conductance of a microdisk resonator versus its radius. It has been calculated by dividing the total absorbed power (which is one) to the maximum temperature rise. The simulations have been performed for three cases: The BOX (oxide substrate) thickness is 2 μm (the stars), the BOX thickness is 1 μm (the diamonds), the BOX thickness is 1 mm and a Si pedestal layer with a thickness of 50 nm exists. The thickness of the Si microdisk in all the simulations is 250 nm. Cross sections of (b) the electric mode energy and (c) the temperature distribution resulting from heat generated by the mode energy in (b) for a microdisk with a radius of 2.5 μm.

thickness of 2 μm. From these two figures we can clearly see the difference between the electromagnetic mode volume and thermal mode volume of the resonator. As seen from Figure G.3(c), at smaller radii, the temperature distribution in the resonator is almost uniform compared to the case of larger radii, as shown in Figure G.2(a). In addition, from Figure G.3(c) we can clearly see that the heat has to escape from the very small region for a small resonator, while in the larger resonator, as shown in Figure G.2(a), there is more area for the heat to escape. As a result, the temperature in the large resonator should be much lower and its conductance much higher compared to the smaller resonator.

Also from Figure G.3(a) we can see the effect of increasing the BOX thickness on thermal conductance of the resonator. As an example, for the microdisk with the radius of 5 μm, the presence of a 50 nm Si pedestal, and a 1 μm BOX layer (dashed green curve with circle marker) has improved the thermal conductivity almost three times compared to the case of a zero Si pedestal and a 2 μm BOX. This shows the impact of engineering the structure to improve the thermal properties. In addition, with the presence of the cladding layer with an appropriate thickness, a metal heat sink layer can be deposited on top of the structure to extract more heat energy from the structure without sacrificing the *Q* of the resonator. In fact, the cladding layer can be any other high-quality optical material with a better thermal conductivity but with a refractive index much smaller than that of the resonator to preserve the ultra-high *Q* properties of the resonator. These issues and the corresponding design parameters are under more investigation.

We also studied the thermal lifetime of microdisk resonator by solving Equation (G.1) and by observing the response time of the resonator before reaching the steady state when excited with a step function in time. For this simulation, the p_{abs} was suddenly turned on, while its spatial distribution was similar to the electromagnetic mode energy of the resonator. By measuring the rise time to the steady state we were able to measure the thermal lifetime of the resonator when excited by its own electromagnetic mode energy (which produces heat). Surprisingly, when we scaled the resonator radius we observed a negligible change in the thermal lifetime. All the microdisk resonators with a thickness of 250 nm and a BOX thickness of 1 μm showed a thermal lifetime of ~ 1.7 μs (the very smaller resonators showed ~1.6 μs).

G.2 Effective Heat Equation

To study the temporal dynamic of a Si microdisk resonator at high powers, thermal effects need to be considered in the time domain and included in the analysis. Equation (G.1) is the accurate form of the heat equation that considers the temporal and spatial distribution of the temperature. However, we can perform some appropriate approximations to find a simpler approximate form for (G.1). With very good approximation we can decompose the temperature into the product of a temporal function and a spatial function, which represent the temporal variation and the spatial distribution of the temperature.

$$\Delta T(t,r) = \Delta T_t(t)\Delta T_r(r). \qquad \text{(G.4)}$$

Putting Equation (G.4) into Equation (G.1) and taking a volume integral from both side over the resonator volume we have

$$[\rho C_p \int \Delta T_r(r) dv] \frac{d\Delta T_t}{dt} - (\int \nabla \cdot [K \nabla (\Delta T_r(r))] dv) \Delta T_t = P_{abs}(t), \quad \text{(G.5)}$$

where P_{abs} is the total absorbed power in the entire volume of the resonator. The above equation can be further simplified as

$$[\rho C_p V_{Th} \Delta T_{r,\max}] \frac{d\Delta T_t}{dt} - (\int \nabla \cdot [K \nabla (\Delta T_r(r))] dv) \Delta T_t = P_{abs}(t), \quad \text{(G.6)}$$

where V_{Th} is the thermal volume of the resonator and $\Delta T_{r,\max}$ is the peak of the spatial distribution of the temperature and they are related as

$$V_{Th} \Delta T_{r,\max} = \int \Delta T_r(r) dv. \quad \text{(G.7)}$$

We could also write the above integral in the following form:

$$V_{disk} \Delta T_{r,avg} = \int \Delta T_r(r) dv, \quad \text{(G.8)}$$

where V_{disk} is the microdisk volume and $\Delta T_{r,avg}$ is the average temperature of the microdisk. However, $\Delta T_{r,\max}$ provides more accurate results for the change in the resonance shift of the resonator, as the location of $\Delta T_{r,\max}$ corresponds to the region where the resonator mode energy is located. From Figures G.3(b) and G.3(c), we see that the electromagnetic mode distribution is very localized so that the temperature over the entire distribution is almost constant and equal to $\Delta T_{r,\max}$. In addition, we see that the spatial distribution of the temperature inside the microdisk is almost uniform. Hence, for small resonators, V_{Th} is very close to the microdisk

volume (V_{disk}) and as a result, $\Delta T_{r,\max}$ is very close to $\Delta T_{r,avg}$ for small resonators. Even for larger resonators the approximation of the uniformity of the temperature inside the resonator is reasonable and does not change the general picture of temporal dynamic analysis of the resonators.

Knowing that the BOX layer is the major channel to transfer the heat from the resonator to the underlying Si layer, and assuming the temperature is almost constant inside the Si microdisk, the temperature gradient in the second term in Equation (G.6) can be approximated between the Si microdisk and the underlying Si layer below the BOX layer (which has the ambient temperature). Hence, Equation (6.38) can be approximated as

$$\rho C_p V_{Th} \Delta T_{r,\max} \frac{d}{dt} \Delta T_t(t) + \frac{\overline{K} A_{eff} \Delta T_{r,\max}}{H_{BOX}} \Delta T_t(t) = P_{abs}(t), \tag{G.9}$$

where $\overline{K}$ is the net thermal conductivity, A_{eff} is the effective area underneath the resonator that heat is transferred through, and H_{BOX} is the BOX thickness. In a more general form, Equation (6.40) can be written as

$$\rho C_p V_{Th} \Delta T_{r,\max} \frac{d}{dt} \Delta T_t(t) + K_{eff} \Delta T_{r,\max} \Delta T_t(t) = P_{abs}(t), \tag{G.10}$$

where K_{eff} is the effective thermal conductance of the resonator. Equation (G.10) can be written in the following form:

$$\frac{d}{dt} \Delta \overline{T}(t) = -\frac{K_{eff}}{\rho C_p V_{Th}} \Delta \overline{T}(t) + \frac{P_{abs}(t)}{\rho C_p V_{Th}}, \tag{G.11}$$

where $\Delta \overline{T}(t) = \Delta T_{r,\max} \Delta T_t(t)$.

In a more general form we can write Equation (G.11) as the following form:

$$\frac{d}{dt}\Delta\bar{T}(t) = -\frac{1}{\tau_{Th}}\Delta\bar{T}(t) + \frac{1}{\rho C_p V_{Th}} P_{abs}(t), \tag{6.42}$$

where, τ_{Th} is the thermal lifetime of the resonator. It is noted that τ_{Th} can be accurately extracted by directly solving Equation (G.1), as discussed at the end of the preceding section.

While improving the thermal conductivity is one solution to reduce the bistability in the resonance spectrum at high powers, another solution is to reduce the effective thermo-optics coefficient of the resonator. This can be done by using materials with strong negative thermo-optics coefficients as the cladding of the resonator. However, the thickness and the radius of the resonator have to be adjusted to have enough extension of the resonator mode profile in the cladding. This is a future research problem that needs to be investigated. The design and the choice of the cladding material should be such that they preserve the ultra-high Q properties of the resonator.

In conclusion, we showed that the thermal properties of high *Q* Si microresonators highly depend on the resonator structure. We showed that by preserving the oxide layer underneath Si in a microdisk resonator we can considerably improve the thermal conductivity of the structure without sacrificing *Q* (*Q*s above 10^6 are achievable with the oxide substrate as demonstrated in chapter 5). We further showed that the presence of a shallow Si pedestal layer at the interface between the microdisk and the oxide layer further improves the thermal

conductivity of the resonator. These modifications in the resonator structure can enable us to have more control on the thermal broadening of the resonator spectrum.

REFERENCES

[1] R. A. Soref and J. P. Lorenzo, "All-Silicon Active and Passive Guided-Wave Components for λ=1.3 and 1.6μm," *IEEE J. Quantum Electron.* **22,** 873 (1986).

[2] G. T. Reed and A. P. Knights, *Silicon Photonics: An Introduction*, John Wiley, West Sussex, 2004.

[3] L. Pavesi and D. J. Lockwood, *Silicon Photonics*, Springer-verlag, New York, 2004.

[4] B. Jalali, M. Paniccia, and G. Reed, "Silicon photonics," *IEEE Microwave Magazine*, **l7**, 58 (2006).

[5] M. Lipson, "Silicon photonics: An exercise in self control," *Nature Photonics*, **1**, 18 (2007).

[6] M. Lipson, "Guiding, Modulating and Emitting Light on Silicon-Challenges and Opportunities," *J. Lightwave Technol.* **23**, 4222 (2005).

[7] C. Gunn, "CMOS Photonics for High-Speed Interconnects," *IEEE Micro* **26**, 58 (2006).

[8] C. Gunn, "Fully Integrated VLSI CMOS and Photonics "CMOS Photonics"," *IEEE Symposium on VLSI Tech.*, 6 (2007).

[9] MIT Microphotonics Centre Industry Consortium 2005 Communications Technology Roadmap: 'Microphotonics: hardware for the information age' 2005 (http://mphotonics.mit.edu/)

[10] A. Narasimha, B. Analui, L. Yi, T. J. Sleboda, C. Gunn, "A Fully Integrated 4×10Gb/s DWDM Optoelectronic Transceiver in a standard 0.13μm CMOS SOI," *IEEE International Solid State Circuit Conference*, 42 (2007).

[11] A. Liu, R. Jones, L. Liao, D. Samara-Rubio, D. Rubin, O. Cohen, R. Nicolaescu, and M. Paniccia, "A high-speed silicon optical modulator based on a metal-oxide-semiconductor capacitor," *Nature* **427**, 615 (2004).

[12] Q. Xu, B. Schmidt, S. Pradhan, and M. Lipson, "Micrometre-scale silicon electro-optic modulator", *Nature* **435**, 325 (2005).

[13] W. M. J. Green, M. J. Rooks, L. Sekaric, and Y. A. Vlasov, "Ultra-compact, low RF power, 10 Gb/s silicon Mach-Zehnder modulator," *Optics Express* **15**, 17106 (2007).

[14] L. Zhou and A. W. Poon, "Silicon electro-optic modulators using p-i-n diodes embedded 10-micron-diameter microdisk resonators," *Opt. Express* **14**, 6851 (2006).

[15] S. F. Preble, Q. Xu, B. S. Schmidt, and M. Lipson, "Ultrafast all-optical modulation on a silicon chip," *Opt. Lett.* **30,** 2891 (2005).

[16] V. R. Almeida, C. A. Barrios, R. R. Panepucci, and M. Lipson, "All-optical control of light on a silicon chip," *Nature* **431**, 1081 (2004).

[17] O. Boyraz and B. Jalali, "Demonstration of a silicon Raman laser," *Opt. Express* **12**, 5269 (2004).

[18] H. Rong, R. Jones, A. Liu, O. Cohen, D. Hak, A. Fang, and M. Paniccia, "A continuous-wave Raman silicon laser," *Nature* **433**, 725 (2005).

[19] F. Xia, M. Rooks, L. Sekaric, and Y. Vlasov, "Ultra-compact high order ring resonator filters using submicron silicon photonic wires for on-chip optical interconnects," *Opt. Express* **15**, 11934 (2007).

[20] F. Xia, L. Sekaric, M. O'Boyle, and Y. A. Vlasov, "Coupled resonator optical waveguides (CROWs) based on silicon-on-insulator photonic wires", *Appl. Phys. Lett.* **89**, 041122 (2006).

[21] F. Xia, L. Sekaric and Y. Vlasov, "Ultracompact optical buffers on a silicon chip," *Nature Photonics* **1**, 65 (2007).

[22] Y.Vlasov, W. M. J. Green, and F. Xia, "High-throughput silicon nanophotonic wavelength-insensitive switch for on-chip optical networks", *Nature Photonics* **2**, 242 (2008).

[23] L. Chen, and M. Lipson, "Ultra-low capacitance and high speed germanium photodetectors on silicon," *Opt. Express* **17**, 7901 (2009).

[24] A. C. Turner, M. A. Foster, A. L. Gaeta, and M. Lipson, "Ultra-low power parametric frequency conversion in a silicon microring resonator," *Opt. Express* **16**, 4881 (2008).

[25] H. Fukuda, K. Yamada, T. Shoji, M. Takahashi, T. Tsuchizawa, T. Watanabe, J. Takahashi, and S. Itabashi, "Four-wave mixing in silicon wire waveguides," *Opt. Express* **13**, 4629 (2005).

[26] B. Schmidt, V. Almeida, C. Manolatou, S. Preble and M. Lipson, "Nano-cavity in a Silicon waveguide for ultra sensitive detection," *App. Phys. Lett.*, **85**, 4854 (2004).

[27] A. Nitkowski, L. Chen, and M. Lipson, "Cavity-enhanced on-chip absorption spectroscopy using microring resonators," *Opt. Express* **16**, 11930 (2008).

[28] A. H. J. Yang, S. D. Moore, B. S. Schmidt, M. Klug, M. Lipson, and D. Erickson, "Optical Manipulation of Nanoparticles and Biomolecules in Sub-Wavelength Slot Waveguides," *Nature* **457**, 71 (2009).

[29] M. Krishnan, J. Park, D. Erickson, "Opto-thermorheological flow manipulation" *Opt. Lett.* **34**, 1976 (2009).

[30] M. Li , W. Pernice, C. Xiong, T. Baehr-Jones, M. Hochberg, H. Tang , "Harnessing optical forces in integrated photonic circuits.", *Nature* **456**, 480(2008).

[31] K. J. Vahala, "Optical microcavities," *Nature*, **424**, 6950 (2003).

[32] K. Vahala, *Optical microcavities*, World scientific, 2004.

[33] Y. Akahane, T. Asano, B. S. Song, and S. Noda, "High-*Q* photonic nanocavity in a two-dimensional photonic crystal," *Nature* **425**, 944 (2003).

[34] T. Asano, B. S. Song, and S. Noda, "Analysis of the experimental *Q* factors (~ 1 million) of photonic crystal nanocavities," *Opt. Express* **14**, 1996 (2006).

[35] P. B. Deotare, M. W. McCutcheon, I. W. Frank, M. Khan, and M. Lončar, "High quality factor photonic crystal nanobeam cavities," *App. Phys. Lett.* **94**, 121106 (2009).

[36] S. McNab, N. Moll, and Y. Vlasov, "Ultra-low loss photonic integrated circuit with membrane-type photonic crystal waveguides," *Opt. Express* **11**, 2927 (2003).

[37] Y. Vlasov and S. McNab, "Losses in single-mode silicon-on-insulator strip waveguides and bends," *Opt. Express* **12**, 1622 (2004).

[38] M. Borselli, T. J. Johnson, and O. Painter, "Beyond the Rayleigh scattering limit in high-*Q* silicon microdisks: theory and experiment," *Opt. Express* **13,** 1515 (2005).

[39] S. Schiller "Asymptotic expansion of morphological resonances in Mie scattering," *App. Opt.* **13**, 2181 (1993).

[40] A. Taflove, C. Hagness, *Computational electrodynamics: The finite-difference time-domain method*, Artech House, 2000.

[41] Jianming Jin, *The Finite Element Method in Electromagnetics*, New York: Wiley,1993.

[42] K. Kakihara, N. Kono, K. Saitoh, M. Koshiba, "Full-vectorial finite element method in a cylindrical coordinate system for loss analysis of photonic wire bends," *Opt. Express* **14**, 11128 (2006).

[43] F. L. Teixeira, and W. C. Chew, "Systematic derivation of anisotropic PML absorbing media in cylindrical and spherical coordinates," *IEEE Microwave and Guided Wave Lett.* **7**, 371 (1997).

[44] C. Manolatou and M. Lipson, "All-Optical Silicon Modulators Based on Carrier injection by two-photon absorption," *J. Lightwave Technol.* **24**, 1433 (2006).

[45] P. P. Absil, J. V. Hryniewicz, B. E. Little, F. G. Johnson, K. J. Ritter, and P.-T. Ho, "Vertically coupled microring resonators using polymer wafer bonding," *IEEE Photon. Technol. Lett* **13**, 49 (2001).

[46] S. J. Choi, K. Djordjev, S. J. Choi, P. D. Dapkus, W. Lin, G. Griffel, R. Menna, and J. Connolly, "Microring resonators vertically coupled to buried heterostructure bus waveguides," *IEEE Photon. Technol. Lett.* **16**, 828 (2004).

[47] P. Koonath, T. Indukuri, and B. Jalali, "Monolithic 3-D silicon photonics," *Journal of Lightwave Technol.* **24**, 1796 (2006).

[48] B. E. Little, S. T. Chu, H. A. Haus, J. Foresi and J.-P. Laine, "Microring resonator channel dropping filters," *J. Lightwave Technol.* **15**, 998 (1997).

[49] Q. Xu, D. Fattal, and R. G. Beausoleil, "Silicon microring resonators with 1.5 μm radius," *Opt. Express* **16**, 4309 (2008).

[50] M. Soltani, Q. Li, S. Yegnanarayanan, A. Adibi, "Ultimate miniaturization of single and coupled-resonator filters in silicon photonics," *CLEO/QELS*, Baltimore, MD, 2009.

[51] C. Manolatou, M. J. Khan, S. Fan, P. R. Villeneuve, H. A. Haus, J. D. Joannopoulos, "Coupling of modes analysis of resonant channel add-drop filtering," *IEEE J. Lightwave Technol.*, **35**, 1322 (1999).

[52] H. Haus, *Electromagnetic noise and quantum optical measurements*, Springer, Berlin, 2000.

[53] H. Haus, W. Huang, "Coupled-mode theory," *Proceedings of IEEE* **79**, 1505 (1991).

[54] H. Haus, W. P. Huang, S. Kawasami, and N. A. Whitaker, "Coupled-mode theory of parallel waveguides," *Journal of Lightwave Technol.* **LT-5**, 16 (1987).

[55] A. Yariv, "Universal relations for coupling of optical power between microresonators and dielectric waveguides," *Electron. Lett.* **36**, 321 (2000).

[56] A. Yariv, "Critical coupling and its control in optical waveguide-ring resonator systems," *IEEE Photon. Technol. Lett.*, **14**, 483 (2002).

[57] F. Xia, L. Sekaric, and Y. A. Vlasov, "Mode conversion losses in silicon-on-insulator photonic wire based racetrack resonators," *Opt. Express* **14**, 3872 (2006).

[58] I. Kiyat, A. Aydinli, and N. Dagli, "High-Q silicon-on-insulator optical rib waveguide racetrack resonators," *Opt. Express* **13**, 1900 (2005).

[59] D. Weiss, V. Sandoghdar, J. Hare, V. Lef´evre-Seguin, J. Raimond, and S. Haroche, "Splitting of high-*Q* Mie modes induced by light backscattering in silica microspheres," *Opt. Lett.* **22**, 1835 (1995).

[60] B. E. Little, J.-P. Laine, and S. T. Chu, "Surface-Roughness-Induced Contradirectional Coupling in Ring and Disk Resonators," *Opt. Lett.* **22**, 4 (1997).

[61] T. J. Kippenberg, S. M. Spillane, and K. J. Vahala, "Modal coupling in traveling-wave resonators," *Opt. Lett.* **27**, 1669 (2002).

[62] S. Xiao, M. H. Khan, H. Shen, and M. Qi, "Compact silicon microring resonators with ultra-low propagation loss in the C band," *Opt. Express* **15**, 14467 (2007).

[63] M. Soltani, S. Yegnanarayanan, A. Adibi, "Ultra-high *Q* planar silicon microdisk resonators for chip-scale silicon photonics," *Opt. Express* **15**, 4694 (2007).

[64] M. K. Chin and S. T. Ho, "Design and modeling of waveguide-coupled single-mode ring resonators," *Journal of Lightwave Technol.*, **16**, 1433 (1998).

[65] W. Bogaerts, P. Dumon, D. V. Thourhout, D. Taillaert, P. Jaenen, J. Wouters, S. Beckx, R. Baets, "Compact wavelength-selective functions in silicon-on-insulator photonic wires," *J. Selected Topics in Quantum Electron.* **12**, 1394 (2006).

[66] J. Hu, N. Carlie, N. Feng, L. Petit, A. Agarwal, K. Richardson, L. Kimerling, "Planar waveguide-coupled, high-index-contrast, high-Q resonators in chalcogenide glass for sensing," *Opt. Lett.* **33**, 2500 (2008).

[67] E. Shah Hosseini, S. Yegnanarayanan, A. Adibi, "High quality factor microdisk resonators for chip-scale visible sensing," *IEEE LEOS*, 21st Annual Meeting, Boston, MA, 2008.

[68] Q. Li, M. Soltani, S. Yegnanarayanan, A. Adibi, "Design and demonstration of compact, wide bandwidth coupled-resonator filters on a silicon-on-insulator platform," *Opt. Express* **17**, pp. 2247 (2009).

[69] I. B. Baek, J. H. Yang, W. J. Cho, C. G. Ahn, K. Im, and S. Lee, "Electron beam lithography patterning of sub-10 nm line using hydrogen silsesquioxane for nanoscale device applications," *J. Vac. Sci. Technol. B* **23**, 3120 (2005).

[70] Stephen A. Campbell, *The science and engineering of microelectronic Fabrication*, Oxford University Press, 2001.

[71] M. Borselli, T. J. Johnson, and O. Painter, "Measuring the role of surface chemistry in silicon microphotonics," *Appl. Phys. Lett.* **88**, 131114 (2006).

[72] Y. Yamashita, A. Asano, Y. Nishioka, and H. Kobayashi, "Dependence of interface states in the Si band gap on oxide atomic density and interfacial roughness," Phys. Rev. B **59**, 872 (1999).

[73] D. Fenner, D. Biegelsen, and R. Bringans, "Silicon surface passivation by hydrogen termination: A comparative study of preparation methods," *J. Appl. Phys.* **66**, 419 (1989).

[74] W. Bogaerts, R. Baets, P. Dumon, V. Wiaux, S. Beckx, D. Taillaert, B. Luyssaert, J. Van Campenhout, P. Bienstman, D. Van Thourhout, "Nanophotonic Waveguides in Silicon-on-Insulator Fabricated with CMOS Technology," *J. Lightwave Technol.* **23**, 401 (2005).

[75] G. R Lee, B. O. Cho, S. W. Hwang, and S. H. Moona, "Sidewall-angle effect on the bottom etch profile in SiO_2 etching using a CF_4 plasma," *J. Vac. Sci. Technol. B* **19**, 172 (2001).

[76] J. H Lee, G. Y. Yeoma, J. W. Lee and J. Y. Lee, "Study of shallow silicon trench etch process using planar inductively coupled plasmas," *J. Vac. Sci. Technol. A* **15**, 573 (1997).

[77] W. Jina and H. H. Sawin, "Feature profile evolution in high-density plasma etching of silicon with Cl_2," *J. Vac. Sci. Technol. A* **21**, 911 (2003).

[78] M. A. Vyvoda, M. Li, and D. B. Gravesa, H. Lee, M. V. Malyshev, F. P. Klemens, J. T. C. Lee, and V. M. Donnelly, "Role of sidewall scattering in feature profile evolution during Cl_2 and HBr plasma etching of silicon," *J. Vac. Sci. Technol. B* **18**, 820 (2000).

[79] A. P. Mahorowalaa, H. H. Sawin, R. Jones, and A. H. Labun, "Etching of polysilicon in inductively coupled Cl_2 and HBr discharges. I. Experimental characterization of polysilicon profiles," *J. Vac. Sci. Technol. B* **20**, 1055 (2002).

[80] R. J. Hoekstra, M. J. Kushner, V. Sukharev, and P. Schoenborn, "Microtrenching resulting from specular reflection during chlorine etching of silicon," *J. Vac. Sci. Technol. B* **16**, 2102 (1998).

[81] O. Joubert, E. Pargon, J. Foucher, X. Detter, G. Cunge and L. Vallier, "Nanometer scale linewidth control during etching of polysilicon gates in high-density plasmas," *Microelectronic Eng.* **69**, 350 (2003).

[82] J. C. McDonald, G. M. Whitesides,"Poly(dimethylsiloxane) as a material for fabricating microfluidic devices," *Acc Chem Res*.,**35** (7), 491, (2002).

[83] K C Tang, E Liao, W L Ong, J D S Wong, A Agarwal, R Nagarajan and L Yobas, "Evaluation of bonding between oxygen plasma treated polydimethyl siloxane and passivated silicon," *J. Phys.: Conf. Ser.* **34** ,155-161, (2006).

[84] M. A. Popovic, C. Manolatou, H. A. Haus, "Coupling-induced resonance frequency shifts in coupled dielectric multi-cavity filters." *Opt. Express* **14**, 1208 (2006).

[85] M. Soltani, S. Yegnanarayanan, Q. Li, and A. Adibi, "Systematic engineering of waveguide-resonator coupling for silicon microring/ microdisk resonators" *IPNRA*, Honolulu, HI, 2009.

[86] M. Soltani, S. Yegnanarayanan, Q. Li, and A. Adibi, "Systematic engineering of waveguide-resonator coupling for silicon microring, microdisk, and racetrack resonators: theory and experiment," Submitted.

[87] M. Soltani, Q. Li, S. Yegnanarayanan, A. Adibi, "Implementation of single and coupled resonators filters using ultimate miniaturized silicon microdisk resonators," IPNRA, Honolulu, HI, 2009.

[88] M. Soltani, Q. Li, S. Yegnanarayanan, A. Adibi, "Scaling of high Q Si microresonators toward ultimate miniaturization and large scale integration: prospects and challenges" Submitted.

[89] V. S. Ilchenko, and M. L. Gorodetsky, "Thermal nonlinear effects in optical whispering gallery microresonators," *Laser Phys.* **2**, 1004 (1992).

[90] M. L. Gorodetsky, I. S. Grudinin, "Fundamental thermal fluctuations in microspheres," *J. Opt. Soc. Am. B* **21**, 697 (2004).

[91] T. Carmon, L. Yang, and K. J. Vahala, "Dynamical thermal behavior and thermal self stability of microcavities," *Opt. Express* **12**, 4742 (2004).

[92] A. E. Fomin, M. L. Gorodetsky, I. S. Grudinin, V. S. Ilchenko, "Nonstationary nonlinear effects in optical microspheres," *J. Opt. Soc. Am. B* **22**, 459 (2005).

[93] P.E. Barclay, K. Srinivasan, and O. Painter, "Nonlinear response of silicon photonic crystal microresonators excited via an integrated waveguide and fiber taper," *Opt. Express* **13**, 801 (2005).

[94] T. J. Johnson, M. Borselli, and O. Painter, "Self-induced optical modulation of the transmission through a high-*Q* silicon microdisk resonator," *Opt. Express* **14**, 817 (2006).

[95] M. Dinu, F. Quochi, and H. Garcia, "Third-order nonlinearities in silicon at telecom wavelengths," *Appl. Phys.Lett.* **82**, 2954 (2003).

[96] M. Soltani, Q. Li, S. Yegnanarayanan, and A. Adibi, "Improvement of thermal properties of ultra-high Q silicon microdisk resonators," *Opt. Express* **15**, 17305 (2007).

[97] M. Soltani, S. Yegnanarayanan, Q. Li, A. Eftekhar, and A. Adibi, "Impact of scaling of Si microresonators on their static and dynamic responses at high powers," Submitted.

[98] M. Soltani, S. Yegnanarayanan, Q. Li, A. Atabaki, A. Eftekhar, and A. Adibi, "Self-sustained GHz Oscillations in Ultra-high Q Silicon microresonators," Submitted.

[99] A. Yariv, Y. Xu, R. K. Lee, A. Scherer, "Coupled-resonator optical waveguide: A proposal and analysis." *Opt. Lett.*, **24**, 711 (1999).

[100] J. B. Khurgin, "Optical buffers based on slow light in electromagnetically induced transparent media and coupled resonator structures: comparative analysis," *J. Opt. Soc. Am. B.* **22** 1062 (2005).

[101] R. W. Boyd, D. J. Gauthier and A. L. Gaeta, "Applications of Slow Light in Telecommunications," *Optics and Photonics News* **17**, 18 (2006).

[102] S. Xiao, M. H. Khan, H. Shen and M. Qi, "A highly compact third-order silicon microring add-drop filter with a very large free spectral range, a flat passband and a low delay dispersion," *Opt. Express* **15**, 14765 (2007).

[103] S. Mookherjea, A. Yariv, "Second-harmonic generation with pulses in a coupled-resonator optical waveguide." *Phys. Rev. E* **65**, 026607 (2002).

[104] Y. Xu, R. K. Lee, A. Yariv, "Propagation and second-harmonic generation of electromagnetic waves in a coupled-resonator optical waveguide," *J. Opt. Soc. Am. B* **17**, 387 (2000).

[105] A. Melloni, M. Martinelli, "Synthesis of direct-coupled-resonators bandpass filters for WDM systems," *J. Lightwave Technol.* **20**, 296 (2002).

[106] P. Chak and J. E. Sipe, "Minimizing finite-size effects in artificial resonance tunneling structures," *Opt. Lett.* **31**, 2568 (2006).

[107] A. Zverev, *Handbook of filter synthesis*, Wiley, New York, 1967.

[108] Q. Li, M. Soltani, A. Atabaki, S. Yegnanarayanan and A. Adibi, "Investigation of coupling-induced resonance frequency shifts in dielectric traveling-wave resonators," Submitted.

[109] M. Soltani, Q. Li, S. Yegnanarayanan, and A. Adibi, "Optimized Design of Flat-Band Finite-Size Coupled Resonator Optical Waveguides with Reduced In-Band Distortions," Conference on Lasers and Electro-Optics, CLEO/QELS 2008, San Jose, California, May 2008.

[110] Q. Li, M. Soltani, S. Yegnanarayanan, and A. Adibi, "Design and Demonstration of a compact, wide bandwidth coupled-resonator filter for on-chip optical interconnects on the silicon-on-insulator platform," *Opt. Express* **17**, 2247 (2009).

[111] U. Plachetka, A. Kristensen, S. Scheerlinck, N. Whitbread, J. Huskens, N. Koo, H. Kurz, "Fabrication of photonic components by nanoimprint technology within ePIXnet," *Microelectronic Engineering* **85**, 886 (2008).

[112] F. Prieto, B. Sepulveda, A. Calle, A Llobera, C. Dominguez, A. Abad, A. Montoya and L.M. Lechuga, "An integrated optical interferometric nanodevice based on silicon technology for biosensor applications," *Nanotech*. **14**, 907 (2003).

[113] A. Ksendzov, Y. Lin, "Integrated Optics Ring-resonator Sensors for Protein Detection," *Opt. Lett*. **30**, 3344 (2005).

[114] S. Blair and Y. Chen, "Resonant-Enhanced Evanescent-Wave Fluorescence Biosensing with Cylindrical Optical Cavities," *Appl. Opt*. **40**, 570 (2001).

[115] K. De Vos, I. Bartolozzi, E. Schacht, P. Bienstman, and R. Baets, "Silicon-on-Insulator microring resonator for sensitive and label-free biosensing," *Opt. Express* **15**, 7610 (2007).

[116] S. Yegnanarayanan, M. Soltani, Q. Li, A. Adibi, "Optimized Si Microdisk with High Sensitivity for Label-free Lab-on-a-Chip Sensing Applications," CLEO/QELS, Baltimore, MD, 2009.

[117] H. A. N. Hejase, "On the use of Davidenko's method in complex root search," *IEEE Tran. Microwave Theory Tech.* **41**, 141 (1993).

[118] M. Soltani, S. Yegnanarayanan, and A. Adibi, "Efficient Finite Element Analysis of Three-Dimensional Optical Microcavities with Axial Symmetry," Submitted for publications.